Precision Manufacturing
Series Editor: Liangchi Zhang

SPRINGER
REFERENCE

Zhuangde Jiang
Shuming Yang *Editors*

Precision Machines

Springer

Precision Manufacturing

Series Editor

Liangchi Zhang
Southern University of Science and Technology (SUSTech)
Department of Mechanics and Aerospace Engineering
Shenzhen, China

This series of handbooks covers a comprehensive range of scientific and technological matters in precision manufacturing. The proposed handbook series aims to bridge the gaps by a systematically designed strategy to cover the required range of knowledge and essential understanding, and hence provide researchers and engineers a vehicle for achieving the optimization of the intelligent manufacturing chain. The readers will understand their role and position in precision manufacturing chain and hence understand how they could progress more efficiently and effectively. Junior researchers and engineers could seek their starting points of career development more easily and grab essential knowledge more systematically with a clear direction.

More information about this series at http://www.springer.com/series/15575

Zhuangde Jiang • Shuming Yang
Editors

Precision Machines

With 437 Figures and 42 Tables

Springer

Editors
Zhuangde Jiang
State Key Laboratory for Manufacturing Systems Engineering
Xi'an Jiaotong University
Xi'an, Shaanxi, China

Shuming Yang
State Key Laboratory for Manufacturing Systems Engineering
Xi'an Jiaotong University
Xi'an, Shaanxi, China

ISSN 2522-5464 ISSN 2522-5472 (electronic)
ISBN 978-981-13-0380-7 ISBN 978-981-13-0381-4 (eBook)
ISBN 978-981-13-0382-1 (print and electronic bundle)
https://doi.org/10.1007/978-981-13-0381-4

This Springer imprint is published by the registered company Springer Nature Singapore Pte Ltd.
The registered company address is: 152 Beach Road, #21-01/04 Gateway East, Singapore 189721, Singapore

Series Preface

Manufacturing has always been a major wealth-creating sector in developed economies and will remain the cornerstone of long-term economic growth. It is manufacturing that underpins the modern scientific and technological development, such as the advances in energy, bio, micro and nano technologies. Most of today's complex and important technological problems are inseparably connected to manufacturing issues. Successful innovative solutions in almost all disciplines rely on manufacturing, because deep insights can only be obtained with the aid of properly manufactured instruments. Since the new century, the advances in electronics, optics, telecommunication, biology, medical surgery, energy generation, resource exploration and environment protection have brought about further challenges and have produced veritable onslaught of fundamentals and technologies that require the capacity of precision manufacturing.

The production of precision components and systems is sensitive to many complex sets of conditions in which they are manufactured. Over the past decades, the design and manufacture of high-integrity systems have improved but are limited by the lack of understanding of the production processes as an integrated whole. The advancement of precision manufacturing requires that researchers and engineers master the fundamentals of the materials in use, the processing technologies for transforming such materials to functional products with minimized defects, the strategies and technologies to create machines that are accurate enough to realize precision production, and the solutions to environmental impact issues. Each aspect of the above plays a critical role in the precision manufacturing chain. The chain can be damaged if any of the aspects suffers from imperfections. If researchers and engineers do not have a comprehensive vision and understanding of the chain, optimization of precision manufacturing is difficult, which forms a major hurdle to realizing intelligent/smart manufacturing for a new industrial revolution. This has imposed severe restrictions on our ability to analyze the complex processes of precision manufacturing. It is because so much is now demanded of high-integrity systems that the slightest imperfection in their manufacture has become a serious matter.

The objective of this book series is to redress the shortcomings in the isolated single aspect studies in the chain of precision manufacturing. The book will cover a comprehensive range of scientific and technological matters to bridge the gaps by a

systematically designed strategy to reinforce the required knowledge and essential understanding and hence provide the reader with a vehicle for achieving optimization of the intelligent manufacturing chain. Specific emphasis of the book series will be on the fundamentals of materials and mechanics for precision manufacturing, minimal damage and damage-free design in precision manufacturing, precision machines and their control, numerical simulation for precision manufacturing, precision forming, precision optics, precision additive manufacturing, precision biomedical manufacturing, precision sensing and measurement, non-traditional precision manufacturing, eco-technologies and re-manufacture of precision elements.

The books are suitable for senior undergraduate students, postgraduate students, junior researchers, and engineers who are interested in or working in the field of precision manufacturing.

Volume Preface

Over the last decades, precision/ultra-precision machining techniques have been evolving a lot to fulfill the great demands for components with high surface quality, subsurface integrity and accuracy. With the development of multi-axis ultra-precision machines, ultra-precision machining can achieve unprecedented precision and surface integrity as well as the generation of freeform and complex micro-structured surfaces. The application of precision/ultra-precision machining covers the fields of automobiles, medicine, illumination, astronomy, optics, metrology, etc. Precision/ultra-precision machine tools are the base and a major prerequisite for precision/ultra-precision machining with a remarkable precision controlled down to a nanometer.

In this book, the design, manufacture and control technology of precision machine tools are introduced. The state-of-the-art of precision machining equipment including precision turning, milling, grinding, and lapping/polishing are discussed. The key components of precision machines are introduced, such as precision spindles, control systems, tools, grinding wheels, etc. In the machine design part, methods for design and simulation of the structure of precision machines as well as the key components are described in details. In the manufacture part, the fabrication and assembly technologies for different types of precision machines are introduced. In the control part, the control system, measurement and compensation technology for precision machines are discussed. The information provided in the book will be of interest to industrial practitioners and researchers in the field of precision machines.

The authors of the book chapters are the experts from different countries in the areas of precision machining or precision metrology. We would like to thank all the authors and contributors who made much efforts to ensure the content is integral and comprehensive. We would also like to thank the authors of references who kindly permitted the corresponding figures and tables to be included in the book.

July 2020

Contents

1 **Introduction to Precision Machines** 1
Shuming Yang, Guofeng Zhang, Changsheng Li, and Zhuangde Jiang

2 **Forward Design Methods for Precision Machines** 33
Bin Li

3 **Structure Design of Precision Machines** 57
Huiying Zhao and Shuming Yang

4 **Design of Tools, Grinding Wheels, and Precision Spindles** 93
Huiying Zhao and Shuming Yang

5 **Design of Precision Linear Drives** 131
Wanqun Chen and Yazhou Sun

6 **Design of Precision Rotary Drives** 155
Haitao Liu, Wenkun Xie, and Yazhou Sun

7 **Design, Development, and Analysis of a Hybrid Serial-Parallel Machine for Precision Polishing** 171
Peng Xu, Chi Fai Cheung, Bing Li, Chunjin Wang, and Lai Ting Ho

8 **Error Allocation in the Design of Precision Machines** 207
Shanshan Chen and Guofeng Zhang

9 **Grinding and Dressing Tools for Precision Machines** 233
Yunfeng Peng, Zhenzhong Wang, and Ping Yang

10 **Control Systems for Precision Machines** 265
Bing Li

11 **Robot-Based Precision Machines** 291
J. P. Xi

12 **Processing Techniques of Critical Components** 315
Shanshan Chen

13 Assembly Techniques of Precision Machines 353
Bin Li

14 Electric-Magnetic-Mechanical Coupling in Precision Machines 375
Dongxu Ren

15 Processing and Manufacturing Technology of Special Sensors . . . 401
Qiulin Tan

16 Environmental Control and Compensation of Precision Machining 435
Bing Li

17 Thermal Error and Compensation Method for Precision Machines 459
J. P. Xi

18 Performance Characterization of Precision Machines 483
Shuming Yang, Guofeng Zhang, and Zhuangde Jiang

19 Measurement Technology for Precision Machines 511
Shuming Yang, Changsheng Li, and Guofeng Zhang

20 On-Machine Measurement System and Its Application in Ultra-Precision Manufacturing 563
Xiangqian Jiang, Zhen Tong, and Duo Li

About the Series Editor

Liangchi Zhang is Chair Professor in the Department of Mechanics and Aerospace Engineering, Southern University of Science and Technology (SUSTech), Shenzhen, China. He is also the Fellow of the Australian Academy of Technological Science and Engineering (ATSE). Zhang obtained his B.Sc. and M.Eng. from Zhejiang University, Ph.D. from Peking University, China, and D.Eng. from the University of Sydney, Australia. Prior to joining SUSTech, he has worked at the University of New South Wales and University of Sydney, Australia; University of Cambridge, UK; National Mechanical Engineering Laboratory, MITI, Japan; and Zhejiang University, China. Zhang carries out research on both the fundamentals and industrial applications in the cross-disciplinary field of advanced manufacturing, advanced materials, tribology, nanotechnology, solid mechanics, and biomechanics. He has published extensively in his research areas, with some in multiple languages. His research outcomes have led to significant economic benefits for manufacturing industry. Zhang has been granted many awards and honors. He can be contacted at zhanglc@sustech.edu.cn.

About the Editors

Zhuangde Jiang Professor at Xi'an Jiaotong University (XJTU), is an academician at the Chinese Academy of Engineering and a former Vice President of XJTU (2004–2014). He serves as the Vice President of the Chinese Society of Mechanical Engineering, Vice President of the Chinese Society of Micro-Nano Technology, and Editor of Mechanical and Vehicle Engineering section of the journal *Engineering*. Professor Jiang has done focused and long-term research in micro/nano manufacturing and advanced sensors, precision (ultra-precision) machining, and measurement technology and equipment. He has made outstanding contributions in high-end MEMS sensor chips, nanoscale national standard substances, large-diameter turning and grinding compound machine tools, and precision (ultra-precision) measurement technology and instruments for complex surfaces. Additionally, he did innovative research in fundamental mechanism of micro/nano technology and biomedical detecting technology and devices. Accordingly, he won two National Awards of Technological Innovation and one National Award of Science and Technology Progress. Professor Jiang also received the Award of 1st National Innovation Competitiveness, the Prize for Scientific and Technological Progress of Ho Leung Ho Lee Foundation, and the Award for Outstanding Contribution to Degree and Graduate Education of XJTU.

Shuming Yang is currently a Full Professor at the School of Mechanical Engineering, Xi'an Jiaotong University (XJTU), China. He completed his B.Sc. and M.Sc. in mechanical engineering at XJTU and Ph.D. in nanotechnology and instrumentation at the University of Huddersfield (UoH) in the UK. He then began work at UoH, after which he joined XJTU and is working there till now. His research areas include micro-/nano-fabrication and measurement, optical technology and instrumentation, precision/ultra-precision manufacturing, etc. Professor Yang has led more than 20 research projects including National Key R&D Program of China and National Science and Technology Major Projects. He has published more than 130 academic papers and owns 50 patents of PCT, the UK, the European Union, and China. Professor Yang received the first class of Science and Technology Progress Award from the Ministry of Education, the first class of Machinery Industry Science and Technology Award of China, the first class of Shaanxi Science and Technology Award, and the second class of Science and Technology Progress Award from the Chinese Society for measurement (CSM). He was elected as a Fellow of the International Society for Nanomanufacturing (ISNM). Professor Yang is also an Associate Editor of the *Journal of Manufacturing Systems*, Editor of *Nanomanufacturing and Nanometrology*, Guest Editor of *Measurement Science and Technology*, and Guest Editor of the *International Journal of Advanced Manufacturing Technology.*

Contributors

Shanshan Chen School of Mechanical Engineering, Xi'an Jiaotong University, Xi'an, Shaanxi, China

Wanqun Chen Center for Precision Engineering, Harbin Institute of Technology, Harbin, People's Republic of China

Chi Fai Cheung State Key Laboratory of Ultra-precision Machining Technology, Department of Industrial and Systems Engineering, The Hong Kong Polytechnic University, Hung Hom, Kowloon, Hong Kong

Lai Ting Ho State Key Laboratory of Ultra-precision Machining Technology, Department of Industrial and Systems Engineering, The Hong Kong Polytechnic University, Hung Hom, Kowloon, Hong Kong

Xiangqian Jiang EPSRC Future Metrology Hub, Centre for Precision Technologies, University of Huddersfield, Huddersfield, UK

Zhuangde Jiang State Key Laboratory for Manufacturing Systems Engineering, Xi'an Jiaotong University, Xi'an, Shaanxi, China

Bin Li College of Mechatronic Engineering, Zhongyuan University of Technology, Zheng zhou, China

Bing Li School of Mechanical Engineering and Automation, Harbin Institute of Technology, Shenzhen, China

State Key Laboratory for Manufacturing Systems Engineering, Xi'an Jiaotong University, Xi'an, Shaanxi, China

Changsheng Li State Key Laboratory for Manufacturing Systems Engineering, Xi'an Jiaotong University, Xi'an, Shaanxi, China

Duo Li EPSRC Future Metrology Hub, Centre for Precision Technologies, University of Huddersfield, Huddersfield, UK

Haitao Liu Center for Precision Engineering, Harbin Institute of Technology, Harbin, People's Republic of China

School of Mechatronics Engineering, Harbin Institute of Technology, Harbin, People's Republic of China

Yunfeng Peng Xiamen University of China, Xiamen, China

Dongxu Ren Zhongyuan University of Technology, Zhengzhou, China

Yazhou Sun Center for Precision Engineering, Harbin Institute of Technology, Harbin, People's Republic of China

Qiulin Tan Key Laboratory of Instrumentation Science and Dynamic Measurement, Ministry of Education, North University of China, Taiyuan, China

Science and Technology on Electronic Test and Measurement Laboratory, North University of China, Taiyuan, China

Zhen Tong EPSRC Future Metrology Hub, Centre for Precision Technologies, University of Huddersfield, Huddersfield, UK

Chunjin Wang State Key Laboratory of Ultra-precision Machining Technology, Department of Industrial and Systems Engineering, The Hong Kong Polytechnic University, Hung Hom, Kowloon, Hong Kong

Zhenzhong Wang Xiamen University of China, Xiamen, China

J. P. Xi Zhongyuan University of Technology, Zhengzhou, China

Wenkun Xie Center for Precision Engineering, Harbin Institute of Technology, Harbin, People's Republic of China

Peng Xu State Key Laboratory of Ultra-precision Machining Technology, Department of Industrial and Systems Engineering, The Hong Kong Polytechnic University, Hung Hom, Kowloon, Hong Kong

Ping Yang Xiamen University of China, Xiamen, China

Shuming Yang State Key Laboratory for Manufacturing Systems Engineering, Xi'an Jiaotong University, Xi'an, Shaanxi, China

Guofeng Zhang State Key Laboratory for Manufacturing Systems Engineering, School of Mechanical Engineering, Xi'an Jiaotong University, Xi'an, Shaanxi, China

Huiying Zhao School of Mechanical Engineering, Xi'an Jiaotong University, Xi'an, Shaanxi, China

Introduction to Precision Machines

1

Shuming Yang, Guofeng Zhang, Changsheng Li, and Zhuangde Jiang

Contents

Introduction 2
Ultra-precision Cutting 3
Diamond Turning 4
Diamond Milling 6
Other Diamond Machining Processes 8
Ultra-precision Grinding 10
Grinding Mechanisms 11
High Static/Dynamic Loop Stiffness 13
High Motion Accuracy/Resolution 14
Tool Conditioning 14
Polishing and Figuring 16
Lap-Based Finishing 17
Fluid Flow-Assisted Finishing 20
Magnetic Field-Assisted Finishing 21
Ion Beam Machining 24
Plasma Discharge Finishing 27
Conclusion 30
References 30

Abstract

Ultra-precision machining is an advanced technology used to generate parts with high accuracy, low surface roughness and surface/subsurface damage to meet the

S. Yang (✉) · C. Li · Z. Jiang
State Key Laboratory for Manufacturing Systems Engineering, Xi'an Jiaotong University, Xi'an, Shaanxi, China
e-mail: shuming.yang@xjtu.edu.cn

G. Zhang
State Key Laboratory for Manufacturing Systems Engineering, School of Mechanical Engineering, Xi'an Jiaotong University, Xi'an, Shaanxi, China
e-mail: zgf0110@stu.xjtu.edu.cn

Z. Jiang, S. Yang (eds.), *Precision Machines*, Precision Manufacturing,
https://doi.org/10.1007/978-981-13-0381-4_1

requirements of astronomy, semiconductor technology, consumer electronics, etc. The application in some representative fields was described to clarify the concrete requirements for ultra-precision machining. The state of the art of three widely used ultra-precision machining processes including ultra-precision cutting, ultra-precision grinding and finishing/figuring is discussed.

Keywords

Precision machines · Manufacturing · Measurement

Introduction

Ultra-precision machining is an advanced technology used to generate parts with high accuracy, low surface roughness and surface/subsurface damages to meet the requirements of astronomy, semiconductor technology, consumer electronics, etc. According to Taniguchi, "precision of machining" can only be assessed from an evolutionary perspective as "processes/machines by which the highest possible dimensional accuracy is or has been achieved at a given point in time." The machining accuracy is now approaching atomic scale, as shown in Fig. 1. Ultra-precision machining today is associated with a machining accuracy under 1 μm, depending on the size and shape

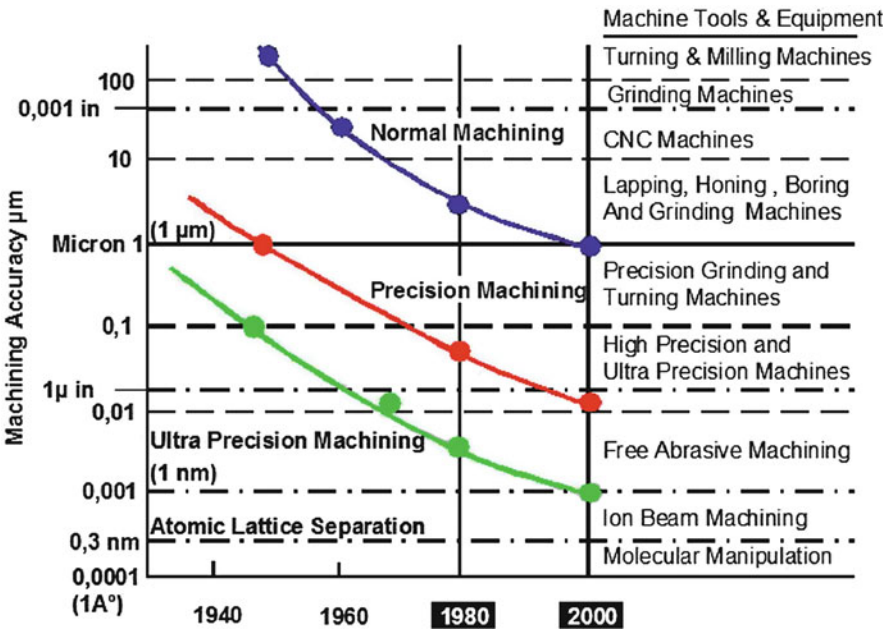

Fig. 1 Machining accuracy over time (Byrne et al. 2003)

of workpiece, and an achieved surface roughness Sa under 10 nm, depending on material properties and machining conditions.

According to the physical nature of the material removal process, ultra-precision machining processes can be classified into physical, chemical, and mechanical as shown in Fig. 2. While physical and chemical machining are limited to specific applications, mechanical machining is almost universal and has a long tradition. This is because a huge class of engineering materials can be processed and a large variety of geometries with flat, spherical, aspherical, and freeform surfaces can be generated. Mechanical ultra-precision machining is further subdivided into cutting and abrasive machining, with the latter comprising precision grinding and polishing and the former being dominated by diamond turning and milling. In this chapter, most of ultra-precision machining methods will be introduced from three machining processes, ultra-precision cutting, ultra-precision grinding, and polishing/figuring.

Ultra-precision Cutting

The term "ultra-precision cutting" refers to cutting processes which yield ultra-smooth surfaces, that is, surfaces with relative figure error $<10^{-5}$ and surface roughness Sa <10 nm. These tolerances can only be achieved with ultra-precision machines and ultraprecision tools. Since single crystal diamonds are commonly used as cutting tools, ultra-precision cutting is often called "diamond machining." Ultra-precision cutting is subdivided into diamond turning and diamond milling and some other diamond machining processes like diamond planning, grooving, and chiseling. The progress made in the development of tools and equipment is

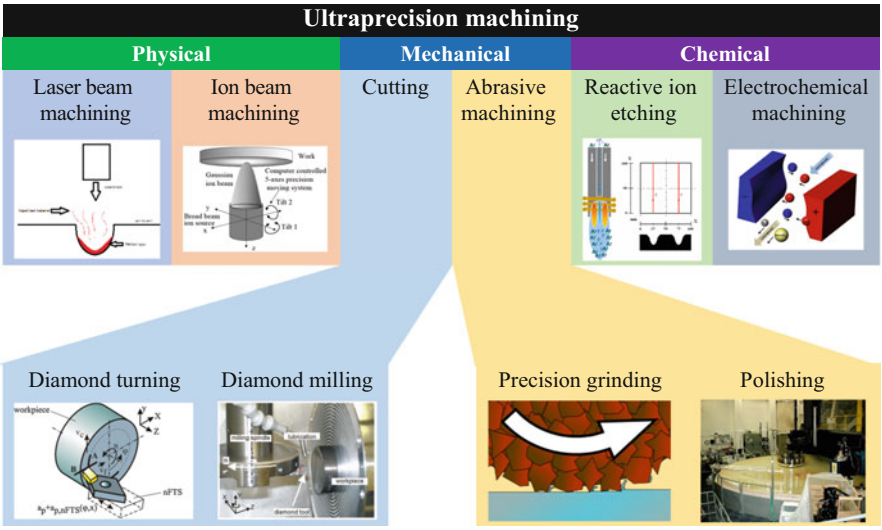

Fig. 2 Classification of ultra-precision machining

reflected by the improvement in the achievable surface roughness and figure accuracy, but even more by the tremendous increase in complexity of accessible surface shapes. Freeform shapes, structured surfaces, and even structured freeform surfaces are possible to be machined nowadays by the increase of the number of controllable machine axes. There are two challenges. First, it is not easy to maintain stiffness and contouring accuracy when more axes are added to a machine. Second, owing to the nature of the cutting tool (a polished single crystal diamond), only a very few cutting operations can be realized (compared with conventional multi-axis machining). It is essentially limited to single-edge circumferential milling and ball-end milling.

Diamond Turning

Diamond turning processes generate the cutting motion by the rotation of the workpiece, while the tool is guided in relation to the surface, thereby copying the geometry of the diamond tool into the surface to determine the shape of the desired part. The shape of the structure is either determined by the geometry of the diamond tool (profile turning) or by the modulation of the infeed depth (form-turning). Profile turning can generate circular or spiral-type structures by plunging the diamond tool into the surface according to the radial position of the tool on the surface (Fig. 3a) or by superposition of the tool geometry and the applied feed rate (Fig. 3b). More complex shapes can be generated easily when contouring the desired shape by controlling both linear axes (Fig. 3c). If the cutting depth is dynamically modulated according to the radial and angular position on the surface, structures without rotational symmetry can be realized in turning operations (Fig. 3d). Compared to the traditional optical fabrication technique of lapping and polishing and diamond turning can produce good optical surfaces near to the edge of the optical element, turn soft ductile materials that are extremely difficult to

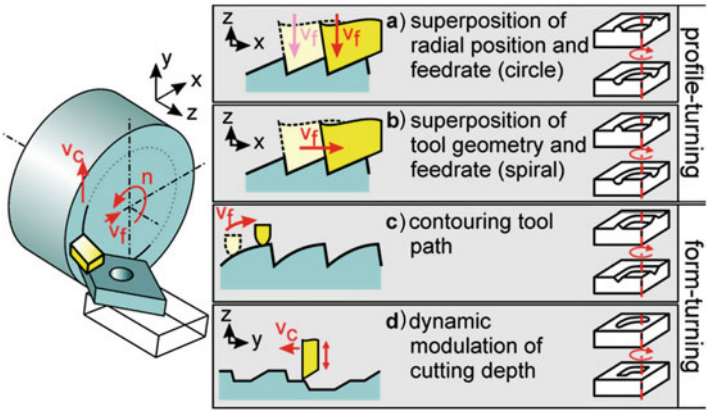

Fig. 3 Structure generation in diamond turning (Brinksmeier et al. 2012)

polish, and easily produce off-axis parabolas and other difficult-to-lap aspherical shapes.

Many specialized ultra-precision machines have been constructed which surpass the accuracy of commercially available equipment. The large optics diamond turning machine (LODTM) built at the Lawrence Livermore National Laboratories with a contouring accuracy less than 0.1 μm over 812.8 mm is supposed to be the most precise machine in the world. This machine has a work zone of 1.65 × 0.5 m, figure accuracy of 0.028 μm (RMS), and surface finish of 35–90 Å (RMS) (Carlisle 2009). The accuracy is obtained from the Super Invar metrology frame with seven laser interferometers, including those in the spindle, and compensates the tool path to eliminate these errors. Temperature stability is handled with air temperature control in the room and in the cooling panels around the metrology frame. Another diamond turning machine has been built by Cranfield University Precision Engineering (CUPE) in the UK for diamond turning of large mirrors up to 2032 mm diameter (Bryan 1979), Fresnel lenses up to 1950 mm diameter, precision drums up to 2000 mm in length, and mandrels for the production of Wolter mirrors for X-ray telescopes.

As an example of the state-of-the-art ultra-precision commercial diamond turning machine, Moore Nanotech 650 FG ultra-precision with three, four, or five axes CNC machining system has been widely used for on-axis turning of aspheric and toroidal surfaces, slow-slide-servo machining (rotary ruling) of freeform surfaces, and raster fly cutting of free forms, linear diffractives, and prismatic optical structures. It can be equipped with shear damped air isolation system with self-leveling to avoid the influence of the vibration. The workholding spindle uses graphite air bearing with center-mounted thrust face and a closed loop chiller to provide recirculating temperature control water to cooling channels located around the motor and bearing journals of the air bearing spindle, which maintains thermal stability and tool center repeatability. Axial and radial motion accuracy within 12.5 nm can be achieved. Using fully constrained oil hydrostatic box way slide, brushless DC linear motor, and laser holographic linear scale (0.008 nm feedback resolution), straightness of 0.3 μm over full travel along X and Z axes has been realized.

It is commonly known that ferrous materials rapidly wear diamond tools. The approaches for reducing such tool wear described in the literature can be divided into process modification methods, e.g., in methane and acetylene environments, cryogenic turning or elliptical vibration cutting; tool modification methods, e.g., TiN coating of diamond tools and ion implantation; and workpiece modification methods by changing the chemical composition of the workpiece within a thin zone beneath the surface to be diamond machined, e.g., thermochemical modification of steel. However, they are not feasible methods for industrial production because of their high costs or low reliability. Materials suitable for diamond machining are listed in Table 1. Ductile materials are normally well machined by diamond turning, and some brittle materials like optical glasses, silicon, and germanium can also been cut in the ductile regime if the feed rate is controlled in a small value. The tools used for cutting ductile metals usually have a rake angle of 0°, but a rake angle of 20–40° is preferable to machine brittle material

Table 1 Diamond-turnable materials

Metal	Inorganic materials	Polymers
Aluminum	Calcium fluoride	Polymethymethacrylate
Brass	Magnesium fluoride	Polycarbonates
Copper	Cadmium telluride	Polyimide
Beryllium copper	Zinc selenide	Polytetrafluoroethylene
Bronze	Zinc sulfide	Polystyrene
Gold	Gallium arsenide	
Silver	Sodium chloride	
Lead	Calcium chloride	
Platinum	Strontium fluoride	
Tin	Sodium fluoride	
Zinc	Germanium	
Electroless nickel	Silicon	
	KDP	
	KTP	

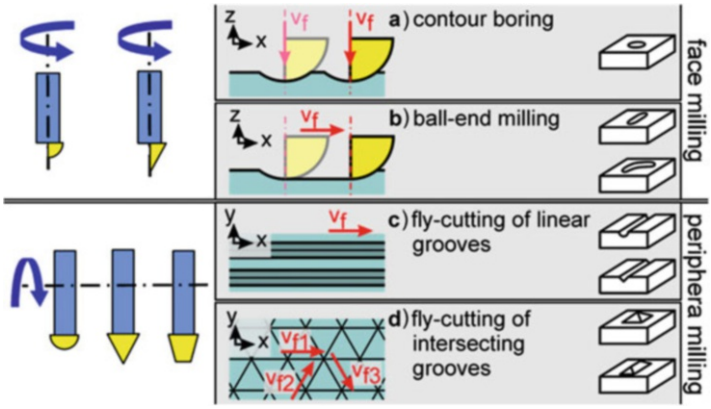

Fig. 4 Classification of milling processes (Brinksmeier et al. 2012)

and produce a compressive stress field to remove material in the ductile regime (Shibata et al. 1996).

Diamond Milling

In ultra-precision milling processes, a monocrystalline diamond tool rotates on a spindle and moves in relation to a fixed workpiece. According to the chosen configuration, these processes are divided into face and peripheral milling, as shown in Fig. 4. Peripheral milling is faster than face milling when machining surfaces of the same size. Face milling is preferred when generating freeform

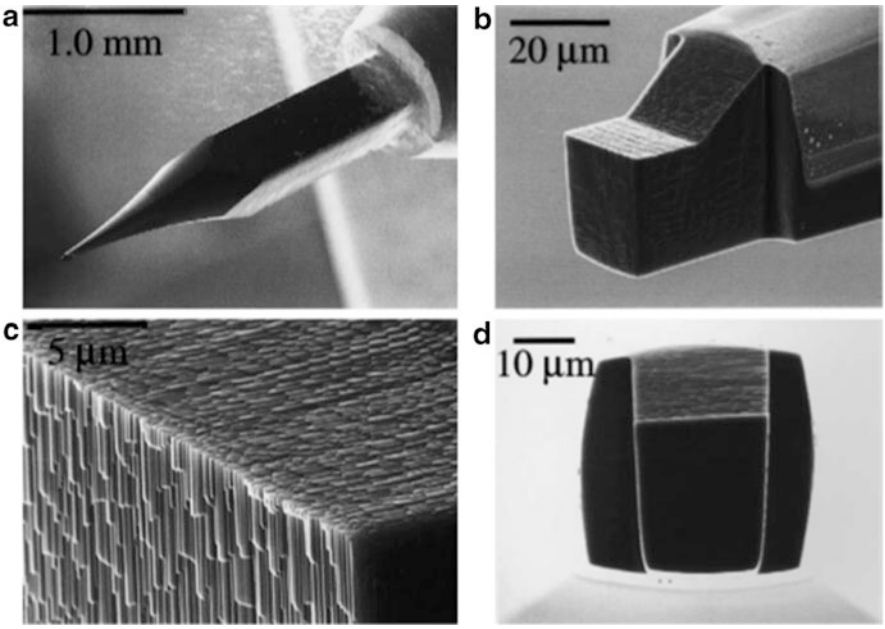

Fig. 5 (**a**) Low magnification view of a single crystal diamond tool shank and junction with mandrel. The tool cutting edges are fabricated on the last 30 µm near the tip. (**b**) Perspective view, high magnification scanning electron micrograph of the same diamond tool showing the FIB-shaped facets. (**c**) Left side cutting edge of same microtool. This image shows the intersection of three FIB-sputtered facets. (**d**) End view of the tool (Picard et al. 2003)

surfaces, as the curvature and slope angle are not limited by the swing radius. Fabrication of diamond micro-tools is a challenge in micromachining. Micro/nanoscale diamond cutting tools used in ultra-precision machining can be fabricated by precision grinding, but it is hard to fabricate a tool with a nanometric cutting edge and complex configurations. High-precision geometry accuracy and special shapes for microcutting tools with sharp edges can be achieved by focused ion beam (FIB) milling. Picard et al. used FIB sputtering to shape a variety of cutting tools made of high-speed steel, cemented tungsten carbide, or diamond with dimensions in the range of 100-150 µm and cutting edge radii of curvature of 40 nm, as shown in Fig. 5 (Picard et al. 2003). FIB is an effective means to fabricate micro- to submicroscale tool shapes. However, ion irradiation causes doping and defects in the tool that reduces tool performance. A combination of 500 °C heat treatment and aluminum deposition can be used to remove gallium ions induced by ion irradiation (Kawasegi et al. 2014). Lift-off process method and platinum can also be used to reduce the damage layer on diamond substrate. Laser beam has also been investigated recently to fabricate many three-dimensional cutting edges on the edge of a cylindrical single crystalline diamond (Suzuki et al. 2013), as shown in Fig. 6.

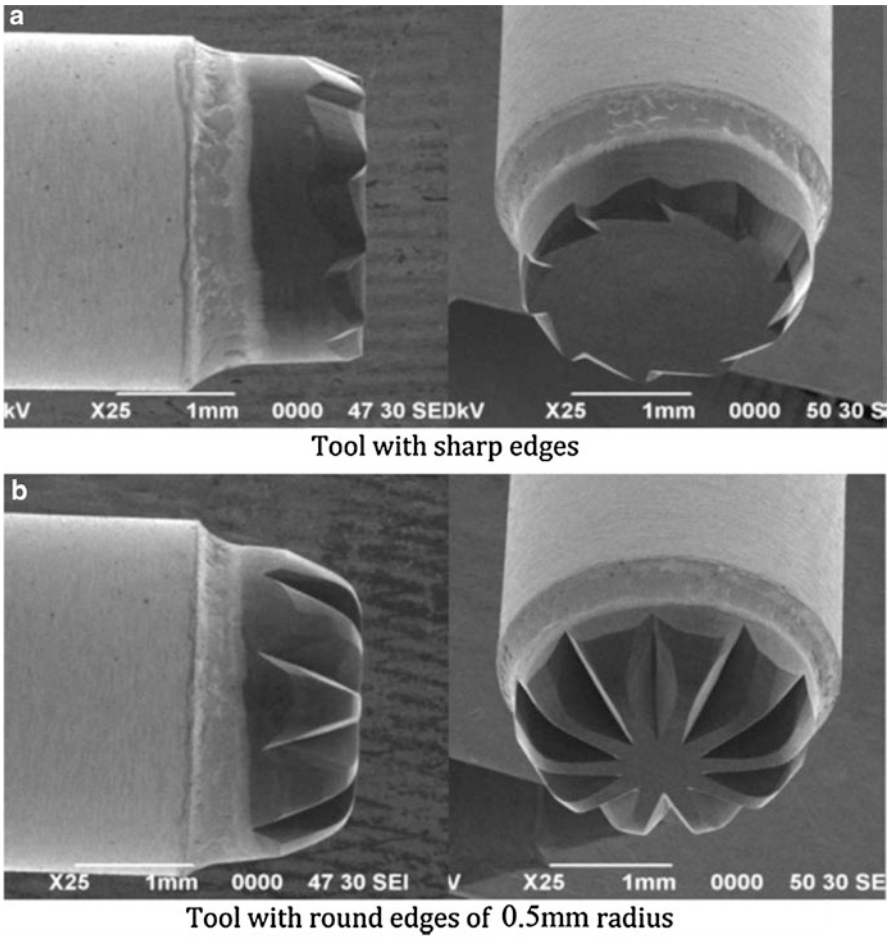

Fig. 6 SEM images of micro SCD milling tools fabricated by laser beam (Suzuki et al. 2013)

Other Diamond Machining Processes

Cutting edges are extremely sharp (less than 50 nm edge roundness), and the surface finish does not depend on cutting speed. Therefore, some processes with neither rotating tool nor rotating workpiece such as broaching, grooving, and chiseling can be used to machine linear structures. Takeuchi et al. (Takeuchi et al. 2003; Moriya et al. 2010) have made ultra-precision microgrooves with one or two flat ends for optical devices such as holographic optical elements using non-rotational cutting tools. Two cutting methods by the use of non-rotational cutting tool are devised so that V-shaped microgrooves with flat end can be created, as shown in Figs. 7 and 8.

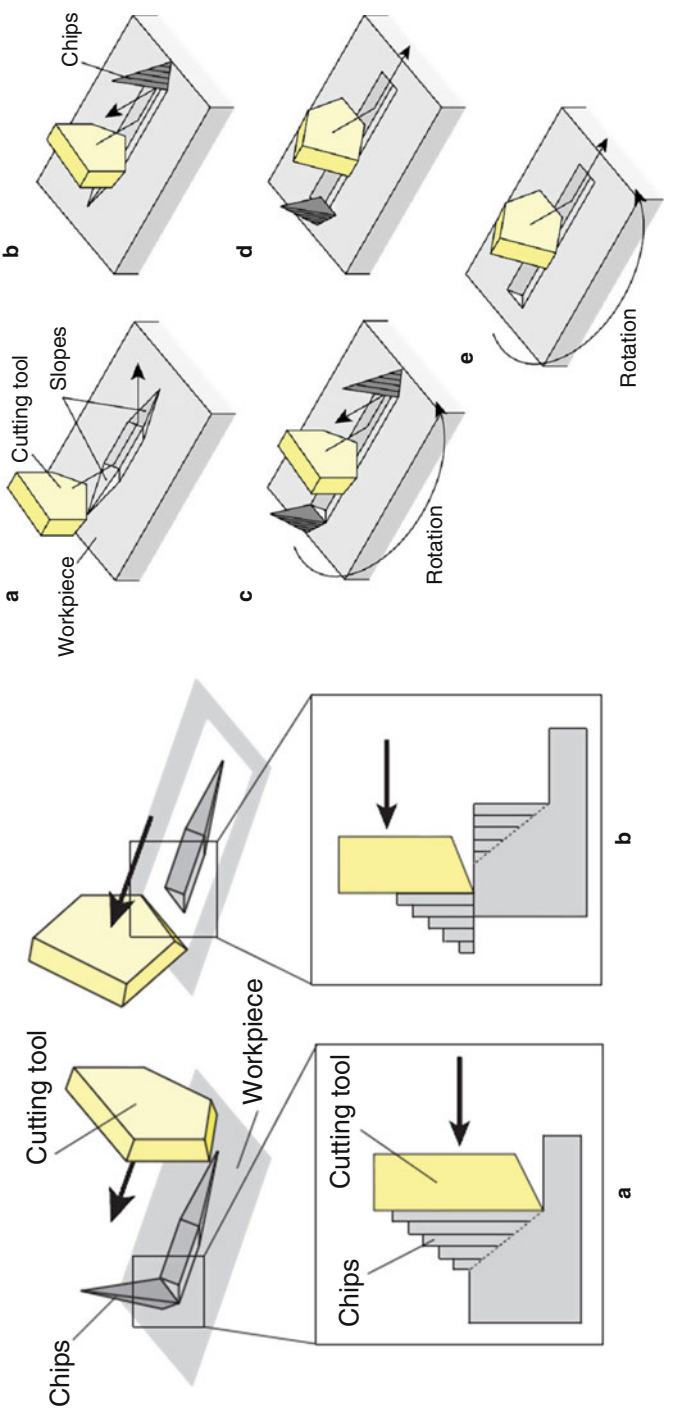

Fig. 7 Flat-end microgroove machining method by use of generated chips with (**a**) one flat end (Moriya et al. 2010) or (**b**) two flat ends (Moriya et al.)

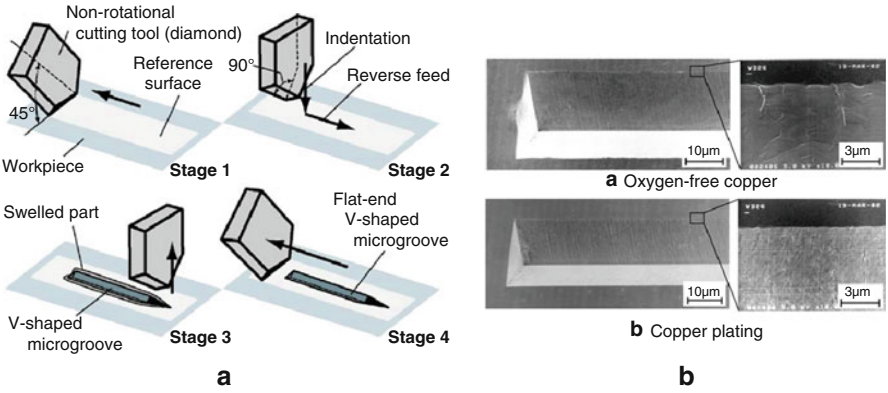

Fig. 8 Flat-end microgroove machining with reverse feed method. (**a**) Schematic figure. (**b**) Machined flat-end V-shaped microgroove (Takeuchi et al. 2003)

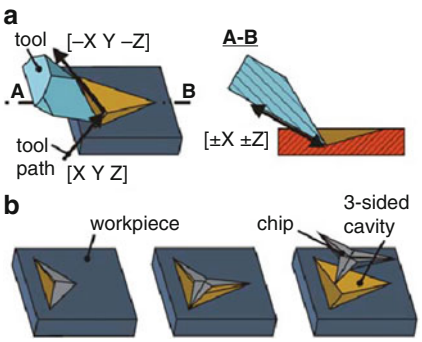

Fig. 9 Cutting kinematics of DMC demonstrated by cutting a three-sided cavity (Flucke et al. 2008)

For a long time, it has been believed that hexagonal corner cube prisms, which offer a 100% yield of retro-reflected light, would be impossible to generate by diamond machining owing to alternating convex and concave corners. However, (Flucke et al. 2008) have demonstrated that hexagonal prisms can be cut out by a diamond micro-chiseling (DMC) process with dedicated diamond tools and a genuine cutting strategy. Its cutting kinematics is shown in Fig. 9. A cube corner retroreflector machined by DMC is shown in Fig. 10.

Ultra-precision Grinding

Grinding is the feasible precision way to generate high-quality parts made from hard and brittle materials. An ideal up-grinding process can make functional surfaces with a surface finish adequate for optical applications.

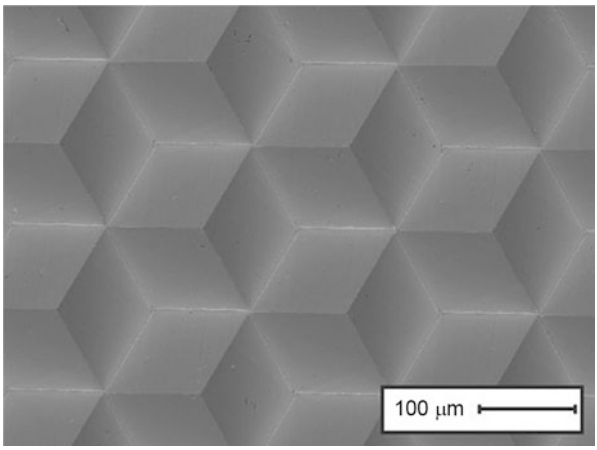

Fig. 10 SEM images of hexagonal corner cubes created by micro-chiseling (Brinksmeier and Preuss 2012)

Grinding Mechanisms

The damage-free material removal is one of the major differences for up-grinding compared with traditional grinding, so it is sometimes referred to as ductile-regime grinding or semi-ductile grinding. Subsurface damage resulting from the mechanism of brittle material removal can weaken the strength of material, serve as a reservoir for laser light absorbing precursors and polishing contaminators, enhance the electric field inside the cracks, and thus greatly affect the operational durability and lifetime of component in high power laser systems, semiconductor industry, military, and astronomical applications.

Transition from brittle to ductile material removal is important for ultra-precision grinding. The most important parameter for this transition in chip removal is the stress conditions in the workpiece material around the cutting edge. "Indentation fracture mechanics" and "machining" are two methods commonly used to investigate material removal mechanisms. The former approach likens abrasive workpiece interactions to a series of idealized small-scale indentations. The machining approach typically involves measurement of cutting forces together with microscopic observations of grinding debris and surfaces topography produced. The radial medium crack and its propagation result in strength degradation and reduce laser-induced damage threshold. The deflection of lateral cracks toward surface was supposed to be responsible for material removal, and the model of their critical load was used to determine whether the material is removed in the brittle mode or the ductile mode. In addition to the static indentation tests with a single grain, multigrain indentation tests and scratch tests were also conducted to make the study closer to the real grinding and cutting conditions. Other than micro-cracking and plastic deformation, some other damage mechanisms have been found such as pulverization and phase transformation mechanism. In order to realize ductile-regime grinding, some critical conditions about undeformed chip thickness and feed rate were obtained. They were related to the properties of machined materials, tip radius of the turning tools and machining parameters. Because the grit micro-geometry, loop

stiffness of machine tools, and cooling and lubricating conditions also have significant influence on the cutting depth and force, the effects were taken into account during the study of damage mechanisms. Although many aspects of damage mechanisms have been studied, a comprehensive model is not available yet due to the lack of experimental methods to directly investigate the nanoscale machining region.

Normally, ductile-regime grinding can only be met by special machine tools which can be controlled precisely and special grinding tools that do not wear significantly (or wear in a predictable way) (Brinksmeier et al. 2010). However, these requirements for machine tools maybe lowered by using novel grinding processes. Beaucamp recently have developed a shape adaptive grinding (SAG) (Beaucamp et al. 2014, 2015) method for freeform machining of difficult materials such as ceramics and hard metals. As shown in Fig. 11, a deformable tool is equipped on a 7-axis CNC platform and rotated with an attack angle. Due to the elasticity of the rubber membrane and deformability of the fabrics, the tool is able to comply with freeform surfaces of any type (convex and concave). However, at the smaller scale of the pellets, the tool is rigid. The grinding force is controlled by the air pressure, while the grinding spot area is controlled by the geometrical

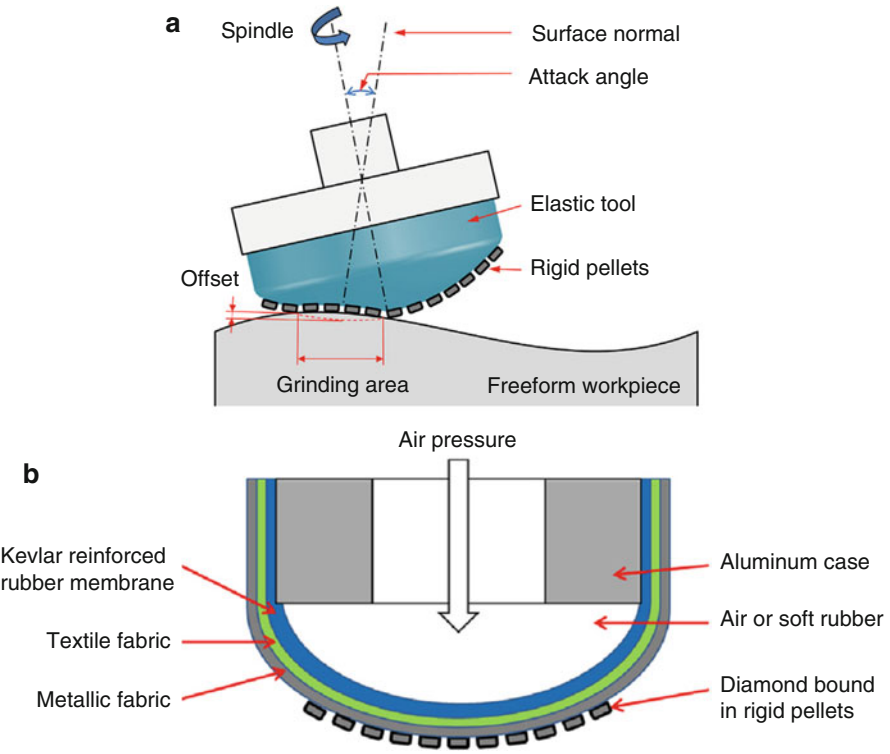

Fig. 11 (**a**) Principle of shape adaptive grinding (Beaucamp et al. 2015) and (**b**) diagram of shape adaptive grinding tool (Beaucamp et al. 2014)

position of the tool. Despite low stiffness requirement from the machining equipment, due to the "semi-elasticity" of the process, ductile mode grinding can be achieved with high surface finish. CVD silicon carbide was finished with roughness below 0.4 nm (Ra) and high removal rates up to 100 mm^3/min (Saito et al. 2007).

High Static/Dynamic Loop Stiffness

CUPE has built an ultra-stiff machine to achieve ductile-regime grinding. Its high loop stiffness (>200 N/μm) was provided by a combination of oil hydrostatic bearings (both linear and rotary), a bridge type configuration, and the stiff and smooth friction drive units. Another grinding machine with aerostatic guideways and aerostatic spindles has also been developed in CUPE. The static loop stiffness was measured to be better than 180 N/μm. In 1991, NPL in the UK has built the Tetraform 1 with high static stiffness and exceptionally high dynamic stiffness thanks to its unique pin-jointed tetrahedral structure. A fully triangulated structure ensured its high static stiffness. High resonant frequencies were achieved by minimizing structural lengths via "pin-jointing." The vibration of the machine was further reduced by the incorporation of passive damping of the structural members and at the "pin-joints." The Tetraform "C" was developed based on the same concept. Tetraform "C" can produce a repeatable surface finish of <10 nm (Ra) with an unprecedented 500 μm wheel depth of cut by CBN grinding wheel. With a 6–12 μm grain-sized diamond grinding wheel, nanometric quality surfaces (Ra <5 nm) with minimal subsurface damage depth (<0.5 μm) can be generated for fused quartz on Tetraform "C" (Zhao et al. 2007).

One of the major challenges of up-grinding is to reduce manufacturing time for large mirrors. The E-ELT and TMT are next-generation ground-based telescopes presently under development, which will require many hundred meter scale off-axis mirrors segments. Though the required precision can be met by the current grinding technologies, it is very challenging to manufacture so many mirrors within a few years to follow the development of the E-ELT and TMT projects. Some scientists in CUPE proposed a manufacturing chain with rapid low-damage precision grinding by a BoX machine, followed by an iterative polishing stage and finally reactive atom plasma (RAP) figuring (Comley et al. 2011). In order to reduce the grinding and post-grinding time, high precision workpieces need to be made with low subsurface damage and high material removal rate. The BoX machine configuration employs an R theta grinding mode with an inclined toroidal shape diamond grit cup wheel. Low number of machine interfaces (bearings) offers achievement of high static loop stiffness. Eased application of large area hydrostatic bearings can maximize smoothness and load capacity while minimize vibration levels at high load level. A 1.45 m scale Zerodur mirror segment (Comley et al. 2011) was made with removal rates of up to 187.5 mm^3/s. Form error <1 μm (RMS), subsurface damage was <10 μm, and a production cycle time was <20 h.

High Motion Accuracy/Resolution

Normally, the smooth linear and rotary motions demanded by ultra-precision grinding machines have been achieved using oil hydrostatic bearings and aerostatic bearings. For example, by utilizing oil hydrostatic bearings and friction drive unit, CPE NanoCentre 250 Ultra-Precision CNC Aspheric Generator achieved smooth and "backlash"-free linear motion with a resolution of 1.25 nm in X and Z and rotary motion with 0.1 arcsec resolution in the B axis (McKeown et al. 1990). Hydrostatic oil bearings can also be used in the glass-ceramic spindle which can perform the high rigidity, rotational accuracy, and vibration absorptivity. Using a grinder equipped with such glass-ceramic spindles, a very smooth surface of 0.266 nm (RMS) was obtained by ultra-precision grinding. CUPE has developed a heavy duty, high precision air-bearing workhead spindle (McKeown et al. 1990) with very high axial and radial stiffness of more than 500 N/μm, together with the radial and axial error motions which typically are within 0.05 μm. It comprises two opposed stainless steel hemispheres in mating high precision internal hemispheres made of porous graphite, which ensures no metal to metal contact during operation, thus ensuring zero wear, high reliability, and virtually infinite system life. Shinno (Shinno et al. 1999) demonstrated that a linear motor-driven ultra-precision aerostatic table could achieve <2 nm positioning resolution. Eda (Eda et al. 2001) applied aerostatic bearings to the spindles and other guideways so that no contact is made between the counterparts. The motion errors of the slideways and runout of the spindle were 0.15 μm over the stroke of 200 mm and ≤ 20 nm, respectively. Table 2 shows the accuracy requirements for the state-of-the-art ultra-precision machines. All the linear and rotary motions are in nanoscale for the most advanced machine tools, which are necessary to maintain the grinding in the ductile mode and achieve a small figure error. Smooth surfaces of 0.266 nm (RMS) and the global flatness <0.2 μm/ø300 mm (PV) (Eda et al. 2001) or form error <1 μm/1.45 m (RMS) have achieved.

Tool Conditioning

The biggest challenge for ultra-precision grinding is to reduce the grinding tool wear to a negligible amount or make the wheel worn in a predictable way. Therefore, diamond and CBN are the two most frequency used abrasives for ultra-precision grinding due to their super hardness and wear resistance. The disadvantages of traditional super-abrasive grinding wheels are high wear rates, which means that

Table 2 Accuracy requirements for state-of-the-art ultra-precision machines

Linearity of linear axes	<0.1 μm over 100 mm
Angular error movements of linear axes	<1 arcsec
Positional accuracy of linear axes	<10 nm
Axial and radial runout of rotational axes	<50 nm
Positional accuracy of rotational axes	<1 arcsec

dressing process are needed to avoid wheel loading. In surface grinding of BK7, coarse-grained diamond wheels precision conditioned by a diamond wheel were capable of generating high surface quality in terms of a low subsurface damage depth <3 μm and surface roughness around 1 nm (Ra) (Zhao and Guo 2015).

In most cases, continuous or periodic trueing and dressing are necessary to achieve high precision and maintain a stable process. Fine-grained metal-bonded diamond grinding wheels were very suitable for the precision machining of hard and brittle materials because of the high profile reliability, high wear resistance, and high material removal rates. Traditional trueing and dressing methods of such grinding wheels were proved to be difficult. Therefore, a lot of trueing and dressing technologies have been developed such as electro-discharge machining (EDM), electrochemical discharge machining (ECDM), and electrolytic in-process dressing (ELID). ELID was introduced for the application of abrasive cutoff of ceramics, and further improvement is suitable for metal-bonded or metal-resin-bonded (Saito et al. 2007) super-abrasive grinding wheels (diamond or CBN). The mental bond can be the standard cast iron bond, bronze bond, and cobalt bond. Metal-resin bond wheels were used to get a better surface finish by avoiding "chipping" and "scratches" on the workpiece by the chips. Figure 12 shows the principle of the proposed ELID grinding process (Ohmori and Nakagawa 1995). The grinding wheel is connected to the positive terminal of a power supply with a smooth brush contact, and a fixed electrode is made negative. The electrode is made from copper having 1/4 or 1/6 of the wheel peripheral length and a width that is 2 mm greater than the wheel rim thickness. The gap between the wheel and the electrode can be adjusted by mechanical means. A clearance of approximately 0.1–0.3 mm was kept between the positive and negative poles. The electrolysis

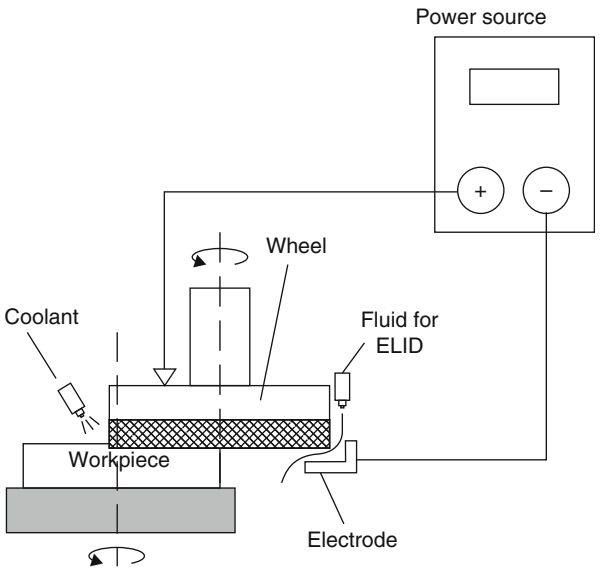

Fig. 12 Basic ELID system (Ohmori and Nakagawa 1995)

occurs upon the supply of a suitable grinding fluid and an electric current. With a ELID superfinishing system, surface finishes of 2 nm and 4 nm (Ra) were achieved with a #12000 metal-resin-bonded wheel (Saito et al. 2007) and a chromium bonding #8000 wheel (Saito et al. 2007), respectively. Several developments have been made for the adaptation of ELID to different grinding kinematics (Brinksmeier et al. 2010). ELID grinding with an additional electrical potential applied to the workpiece enables a controlled oxidation of the workpiece. It can be used to the formation of protecting oxide layers, e.g., titanium alloys.

In late 1982, University of Arizona started to develop the large optical generator (LOG) (Anderson et al. 1992) that dedicated to directly machine the aspheric curve into symmetric glass blanks with the diameter of 8 m. LOG is basically a large vertical grinder which consists of a bridge on which are mounted horizontal (5 m of travel) and vertical ways (1.5 m of travel) to position the grinding spindle. The spindle can be tipped $\pm 30^{\circ}$ from vertical in a plane parallel to the bridge to allow flexibility in setting up the generator. A cup-shaped, Blanchard-type grinding wheel was used for edging, roughing, and flat surfacing, and a bowl-shaped (or spherical cap) was fitted on the spindle for contouring. A convex mold segment for a 10 m f/0.35 parabola has been grinded by a long-radius bowl-shaped diamond wheel. The figure of this segmented parabolic mirror mold was about 4 μm (RMS) with a surface finish of 2 μm (RMS) and was claimed to be reduced to 2 μm (RMS) figure with a 1 μm finish (RMS). The 6.5 m f/1.25 primary mirrors for the Magellan telescopes and the 8.4 m f/1.14 primary mirrors for the Large Binocular Telescope (LBT) were ground and polished by LOG. These borosilicate glass honeycomb sandwich mirror blanks were formed by spin casting with an accuracy of about 1 mm and ground by a numerically controlled mill, and finally a front surface accuracy 10 μm (RMS) was achieved.

Polishing and Figuring

Polishing and figuring are the crucial processes to manufacture ultra-precision components, which determine their final precision and surface roughness, and they are referred to as finishing. Polishing is synonymous to smoothing, and the main object is to smooth the surface of the workpiece without changing its nominal mass, dimension, or shape, which means to reduce the high-frequency error, while figuring is a correction process aiming to reduce the form error (low frequency error) and mid-frequency error. The polishing and figuring are performed simultaneously for some methods and machine tools, while the others cater for one of polishing or figuring. In order to achieve high shape precision, iterative figuring and interferometer measurement runs should be performed to make the surface form converge to the theoretical form, and a so-called dwell time method (Ando et al. 1992) was commonly used. Based on the measured error map, the influence function of the sub-aperture tool is used to calculate the dwell time map. Sometimes other process parameters such as polishing pressure, local polishing forces were also varied to enhance the flexibility. The essence of material removal during machining is

breaking the chemical bonds of materials. Enough energy was needed to break the bond energy, which can be either mechanical or chemical energy. Mechanical finishing can further be divided into lap-based finishing using loose abrasives and a lap normally made of pitch, polyurethane, or non-lap-based finishing. The former class includes the traditional full-aperture lap polishing for spherical and flat workpieces, sub-aperture lap polishing (Ando et al. 1992, 1995; Negishi et al. 1995), and its variants, such as stressed mirror polishing (SMP) (Lubliner and Nelson 1980; Nelson et al. 1980), computer-controlled figuring with linear subtools, stressed-lap polishing (SLP) (Anderson et al. 1992), bonnet polishing (Walker et al. 2006; Beaucamp and Namba 2013), etc. A main difference of the variant compared to the traditional sub-aperture polishing is a larger polishing spot, which means lighter tool edge effects, fewer surface defects, and higher removal rates. There are a large number of non-lap-based finishing methods emerged in these two decades, which significantly improved the ultra-precision machining ability. The energy of the abrasives or ions can be supplied by magnetic field, e.g., magnetorheological finishing (MRF), magnetic abrasive finishing (MAF), magnetorheological (Umehara et al. 2006) abrasive flow finishing (MRAFF), and magnetic float polishing (MFP) (Jiang and Komanduri 1997) for ball finishing; electric field with ion beam, e.g., ion beam figuring (IBF), ion beam smoothing (IBS) (Frost et al. 1998, 2004), and gas cluster ion beam (GCIB) smoothing (Toyoda et al. 2002); and fluid flow, e.g., abrasive flow finishing (AFF) for flat or cylindrical workpieces, float polishing for flat workpieces, elastic emission machining (EEM) (Mori et al. 1988, 2001; Yamauchi et al. 2002), and fluid jet polishing (FJP) (Fähnle and van Brug 1999; Beaucamp and Namba 2013). In order to increase the material removal rate and obtain damage-free finished surface, many finishing techniques utilize chemical reaction with liquid or gas etchant to remove workpiece material, like local wet etching (LWE), plasma-assisted chemical etching (PACE) (Bollinger et al. 1992), plasma chemical vaporization machining (PCVM) (Takino et al. 1998; Mori et al. 2001; Yamamura et al. 2003), and reactive atom plasma technology (RAPT) (Fanara et al. 2006). They are promising ultra-precision technologies because of their damage-free, noncontact, and high-efficiency advantages. Polishing method dedicated to flat (CMP, float polishing), spherical workpieces (MFP) or some specific shapes (MAF, AFF) and others like MRAFF and LWE will not be expanded for discussion.

Lap-Based Finishing

Sub-aperture Polishing

A 500 mm sub-aperture polishing machine named the Canon Super Smooth Polisher (CSSP) has been developed by Canon Inc. in 1991 that aimed to meet the increasing demand of large-aperture supersmooth aspherical optical element for short-wavelength light applications. The local pitch tools with a diameter smaller than the workpiece were used during the polishing process, and it consisted of a stainless steel discussed as the base plate and a layer of 3 mm-thick pitch covering its surface.

An on-machine coordinate measuring system with a contact probe working in a constant contact force was equipped on CSSP (Negishi et al. 1995). A coordinate measuring method using 14-axis interferometers was also proposed for compensation of the major mechanical motion errors of the probe and the tables. A 100 mm flat test piece of synthetic fused silica with an initial form error of 0.98 μm PV and a roughness of 1.79 nm RMS was repetitively polished based on the form error measured by the on-machine coordinate measurement system. After seven corrective polishing runs, a flatness of 63 nm and a surface roughness of 0.17 nm RMS have been achieved. The CSSP polishing process also achieves a contour accuracy of 0.078 μm (PV) and a surface roughness of 0.13 nm (RMS) on a 500 mm diameter fused silica toroidal mirror. A contour accuracy of 0.077 μm (PV) and a surface roughness of 0.12 nm RMS were achieved on a 200 mm aspherical calcium fluoride (CaF_2) lens after 500 h polishing, and a 430 × 130 mm CVD-SiC toroidal mirror of sintered SiC coated with a film of CVD-SiC was polished to be 0.060 μm (PV) for form accuracy and 0.15 nm for surface roughness after 55 h polishing (Ando et al. 1995).

Stressed Mirror Polishing (SMP)

SMP was proposed in 1980 by Lubliner and Nelson to manufacture non-axis-symmetric optical surfaces, whose core concept was to reduce the difficulty of polishing non-axis-symmetric mirrors to the much simpler task of polishing spheres (Lubliner and Nelson 1980). In general, the idea is to apply an appropriate set of forces to a mirror blank so that after a sphere has been ground and polished into the blank, the forces can be removed, and the polished spherical surface deforms elastically into the desired nonaxisymmetric surface (Lubliner and Nelson 1980; Nelson et al. 1980). The performance of SML was tested by the fabrication of a thermal expansion glass (CerVit by Owens-Illinois) off-axis paraboloid with the diameter of 35.88 cm and the thickness of 2.54 cm. After two iterations of polishing and measurement, 0.16 μm (PV) is obtained (Nelson et al. 1980). SMP was applied to circular shape mirrors so that edge roll-off could be avoided. The polished blanks were subsequently cut out into hexagonal segment shapes but caused some warping due to changed boundary conditions in the stress field (Walker et al. 2012).

Stressed-Lap Polishing (SLP)

The stressed-lap polishing was proposed by Anderson in Steward Observatory in 1990 to realize the concept of figuring an aspheric surface similar to that of figuring a sphere by deforming the polishing lap, compared to the deformation of workpiece for the SMP (Anderson et al. 1992). Compared to a traditional sub-aperture polishing, a stiff polishing tool with a large polishing spot was achieved by actively deform its shape to the local curvature to correct small-scale errors better and enhance the polishing efficiency. The lap consists of an aluminum plate on which are mounted a set of actuators that apply moments to the edge of the plate to bend it elastically. The inner diameter of the lap plate is faced with pitch and, for grinding,

thin zinc pads (Anderson et al. 1992). The LOG in Steward Observatory has also been successfully used for loose abrasive grinding and polishing (Anderson et al. 1992) by replacing the grinding tool with a polishing tool whose shape is actively controlled to match the varying curvature of the aspheric optical surface. The stressed lap consists of an aluminum plate with the thickness of 50 mm and diameter of 1.5 m, with 18 moment-generating actuators around its perimeter to bend the plate elastically. The plate is faced with pitch on a layer of nylon that fills the sag between the flat plate and the concave mirror surface. The axisymmetric figure errors were corrected by varying the lap's dwell time and rotation rate as a function of its radial position on the mirror. Both symmetric and asymmetric figure errors were corrected by varying the polishing pressure and pressure gradients (radial and tangential). A 3.5 m f/1.5 paraboloid was first ground by LOG to an accuracy of 4.2 μm. After loose abrasive grinding for 21 days, its form error was reduced to 0.33 μm. Form error of 210 nm (RMS) was achieved by removing the zinc grinding pads (Anderson et al. 1992).

Bonnet Polishing

Bonnet polishing was developed by Bingham and Walker in University College in 2000 and commercialized by Zeeko Ltd. IRP 2400 is the biggest polishing machine developed in Zeeko Ltd., and it can be used for traditional spiral polishing or raster polishing for parts up to 2400 mm in diameter or freeform parts up to 2400 × 2400 mm. This is a smoothing and form correction process which targeted at meeting the growing demand for aspheric and freeform optics. The tooling is a rotating, inflated spherical membrane tool (the "bonnet"), which naturally molds itself to the local aspheric surface. Thus, the size of the polishing spot was enlarged, the tool edge effect was eliminated, and the polishing efficiency was improved. The bonnet is covered with a standard detachable polishing surface such as polyurethane. Normally, the precessions process was adopted to acquire a near-Gaussian influence function rather than the W of a poll-down tool (Walker et al. 2006). It is possible to achieve a similar effect to continuous precession (Beaucamp and Namba 2013), by instead incrementing the precession angle at each pass (Walker et al. 2006). Precession can be used for form-preserving polishing (Walker et al. 2006), 2D form correction by spiral tool path (Walker et al. 2006) (the tool moves in the radial direction in a constant speed, and the C axis speed is modulated according to the dwell time), and non-rotational error correction (Walker et al. 2006) by raster tool path (modulate the C axis rotation speed continuously during each rotation). Bonnet polishing has demonstrated its ability to correctively polish a plano WC surface of diameter 25 mm from a form error above l μm to below $\lambda/20$ (29 nm PV) in under 1 h while reducing roughness to 1.0 nm Ra. By applying very fine 7 nm fused silica as abrasives, it was possible to obtain a supersmooth anisotropic surface below 0.3 nm (RMS) on a 150 mm electroless nickel-plated molding die (Beaucamp and Namba 2013). These dies then can be used for the replication of thin aspheric mirrors by DC magnetron sputtering.

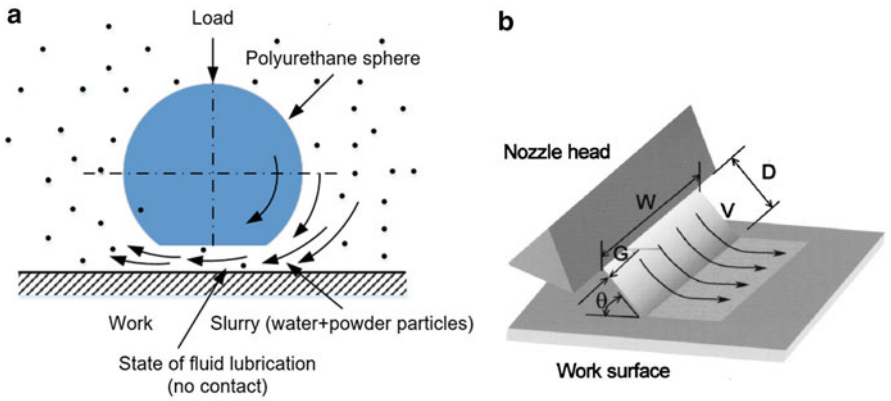

Fig. 13 Schematic view of a method for accelerating and transporting powder particles. (**a**) By the conventional rotating sphere type (Mori et al. 1988) and (**b**) the high-pressure jet-nozzle type (Yamauchi et al. 2002)

Fluid Flow-Assisted Finishing

Elastic Emission Machining (EEM)

EEM is an ultra-precision machining process employing surface chemical activities of ultrafine abrasives (Mori et al. 1988) to remove atomic size material without introducing crystallographic damage during machining. It was proposed by Yamauchi in Osaka University in the 1970s, and now NC EEM machines that can fabricate 400 mm diameter aspherical mirrors such as toroidal, parabolic, and flat mirrors have been equipped in Osaka University. Fluid mixture of ultrapure water and ultrafine powders was transported to the workpiece surface by a conventional elastic rotating sphere-type (Mori et al. 1988, 2001) or a high-pressure jet nozzle-type (Yamauchi et al. 2002) EEM head, as shown in Fig. 13. The kinetic energy of ultrafine powders at the interaction with the processed surface is calculated to be small enough to finish the surface without introducing crystal defects, while the shear rate of the flow on the processed surface is more than 1.0 m/s.μm and is sufficient to remove the ultrafine powders adsorbed chemically on the processed surface. Special care was taken to the machine to avoid the introduction of organic contamination and oxygen, which will block the chemical reaction between the powder surface and processed surface and destructively oxidize the processed surface, respectively (Yamauchi et al. 2002).

EEM can be used as figuring and smoothing technique for hard and brittle materials (silicon, Quartz glass, 4H-SiC, ULE, and Zerodur) normally with form error smaller than 10 nm and surface roughness below 0.1 nm. EEM with a nozzle-type head can be employed for numerically controlled figure correction in the spatial wavelength range from 0.5 to 10 mm and smoothing for the spatial wavelength shorter than 1 μm (Mori et al. 2001). EEM with a rotating sphere-type head can be used for smoothing in the spatial wavelength range shorter than 0.5 mm (Mori et al. 2001). It was reported that PV and RMS figure errors of 6 and 0.3 nm have been achieved for a 90 mm diameter elliptical silicon mirror (Yamauchi et al. 2002).

Fluid Jet Polishing (FJP)

Fluid jet polishing (FJP) is a figuring and smoothing process which was developed at Delft University of Technology in 1998. FJP resembles the two-body process employed in an abrasive slurry jet (ASJ) system that guides a premixed stream of slurry to the surface at pressures (0.5–6 bars) comparable with those of EEM or float polishing, which was much lower than ASJ. On flat glass samples (BK7), the surface roughness of a previously ground surface has been reduced from 475 nm (RMS) to 5 nm RMS (Fähnle and van Brug 1999). Since 2008, Zeeko Ltd. has implemented fluid jet polishing as an option on its family of polishing machines, to complement the Zeeko Classic and Zeeko Grolish processes. FJP was commonly used as a finishing process for diamond-turned electroless nickel or glass prior to the final bonnet polishing. A 100 mm diameter diamond-turned electroless nickel-plated plano mirror was fluid jet polished on the Zeeko IRP200 machine using cerium oxide slurry at a pressure of 20 bar. Its surface roughness slightly decreased from 3.2 to 2.8 nm (Ra), and the midspatial frequencies from diamond turning marks were entirely removed. Beaucamp (Beaucamp and Namba 2013) also used this method to remove the turning marks and correct the figure error simultaneously on diamond-turned electroless nickel-plated molding dies. The form error on a 50 mm diameter electroless nickel-plated molding die was improved from 127 nm to 27 nm (PV) by two polishing runs with different process parameters. The roughness was also improved from 3.35 to 1.68 nm (RMS). As shown in Fig. 14, the liquid jet of FJP breaks down at a very short distance from the nozzle (a few diameters) which, in this case, is highly sensitive to the nozzle-offset distance. It limits polishing configurations where the removal function is stable and results in significant restrictions on finishing of complex shapes. By magnetizing the round jet of magnetorheological fluid by an axial magnetic field when it flows out of the nozzle, the MR fluid jet was stabilized and became highly collimated and coherent. This feature allowed for stable removal rate at standoff distances of tens of centimeters. MR jet finishing (MRJF) was developed by QED in the early 2000s and became an attractive technology for the finishing of complex shapes like freeform optics, steep concaves, and cavities, while the radius of the wheel of MRF limits the concave radius of curvature that can be polished. MR jet has been shown to efficiently correct surface figure error to less than 30 nm (PV) in few iterations, with roughness of <1 nm RMS on a number of materials like glass (fused silica, BK7, ULE), single crystals (sapphire, calcium fluoride, magnesium fluoride, silicon, and germanium), polycrystalline alumina, tungsten carbide (WC), and stainless steel.

Magnetic Field-Assisted Finishing

Magnetorheological Finishing (MRF)

Magnetorheological finishing (MRF) was developed in the Center for Optics Manufacturing (COM) at University of Rochester in the early 1990s, and it was commercialized by COM and QED Technologies starting in 1996. MRF is a production-proven, sub-aperture polishing process for flat, spherical, aspherical,

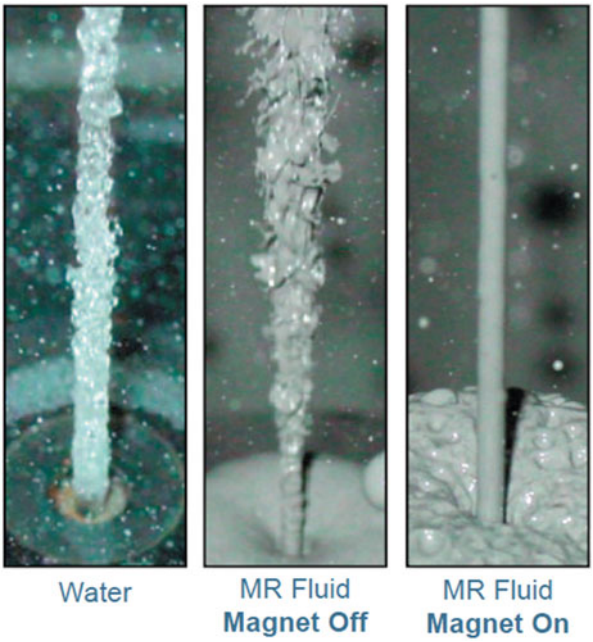

Fig. 14 Jet snapshot images (velocity = 30 m/s, nozzle diameter = 2 mm)

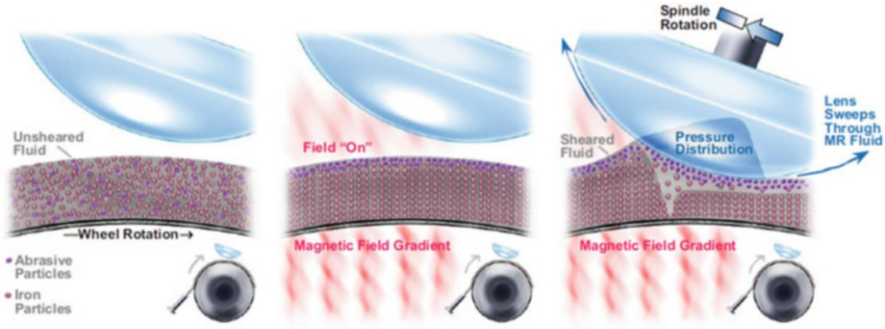

Fig. 15 Schematic of the MR fluid flow in the converging gap between the lens and wheel surfaces in MRF. The magnetic field stiffens the fluid, creating a thin sheared layer near the lens surface that is primarily abrasives and water (Jain 2009)

and cylindrical optics. The schematic of MRF is shown in Fig. 15. The workpiece is installed at a fixed distance from a moving wall so that a converging gap is formed between its surface and the wall form (Jain 2009). An electromagnet is placed to generate a nonuniform magnetic field in the vicinity of the gap. The MR polishing fluid is delivered to the wall just above the electromagnet pole pieces, and it is pressed against the wall by the magnetic field gradient and acquires the wall velocity. The MR fluid ribbon is stiffened by the magnetic field and thus

changed from a viscous fluid with the approximate consistency of honey to a clay-like fluid. The high shear stress was formed in the interface zone and results in material removal over a portion of the workpiece surface. MR fluid consists of magnetic particles of carbonyl iron (CI) in water, with small concentrations of stabilizers added to inhibit oxidation and prevent sedimentation and addition of nonmagnetic abrasives to accelerate the removal rate.

Although MRF is commonly used to fabricate small- or middle-sized workpieces (no larger than 400 mm), QED has developed large-aperture MRF tools in 2004. These newly developed Q22-750P MRF machines were claimed to be the largest and most precise MRF in the world, which can polish optics up to 750 × 1000 mm. Continuously varying topographical CPP pattern with an 8.6 μm peak-to-valley imprinted onto a 430 × 430 × 10 mm fused silica substrate was successfully fabricated using MRF with a damage-free surface. The unique material removal mechanism makes it possible to expose and remove surface and subsurface flaws in optics during final polishing to yield optics with superior UV laser damage resistance, which is very helpful for Megajoule Class Laser Systems. The damage-free characteristic of MRF also makes MRF spot technique and MRF taper polishing technique become the state-of-the-art subsurface damage (SSD) evaluation method. A spot or taper was polished to a certain depth to reveal SSD. A series of photomicrographs were electronically recorded along the polished spot or taper, the damage distribution and depth can then be evaluated according to the depth profile measured by the stylus profiler.

Other Magnetic Field-Assisted Finishing Techniques

There are some other magnetic-assisted finishing methods like magnetic abrasive finishing (MAF), magnetorheological abrasive flow finishing (MRAFF), and magnetic float polishing (MFP). MFP (Jiang and Komanduri 1997; Umehara et al. 2006) was a finishing process of advanced ceramic balls for hybrid-bearing applications, which based on the magnetohydrodynamic behavior of a magnetic fluid that can float nonmagnetic float and the abrasives suspended in the magnetic fluid, as shown in Fig. 16. Damage-free surface with high finish and accuracy on ceramic balls is efficiently accomplished by the magnetic float polishing technique because low and controlled magnetic buoyant force (1 N/ball) is applied via the flexible float. The best results of MFP were reported that a batch of 46, 3/4 in. Si_3N_4 balls were finished to a final diameter of 0.7500 in. with an average sphericity of 0.25 μm (best value of 0.15 μm) and an average surface finish Ra of 8 nm (best value of 6.7 nm) through an actual polishing time of 30 h (Umehara et al. 2006). MAF was an intensively investigated finishing process for planer, spherical, and cylindrical workpieces with a surface roughness commonly smaller than 100 nm Ra. In MAF, ferromagnetic particles could be sintered with fine abrasive particles (Al_2O_3, SiC, CBN, or diamond) or unbounded with abrasive particles. A magnetic field was applied across the machining gap between the workpiece and the rotating electromagnet pole, which acted as a binder and retained ferromagnetic abrasive particles in the machining gap.

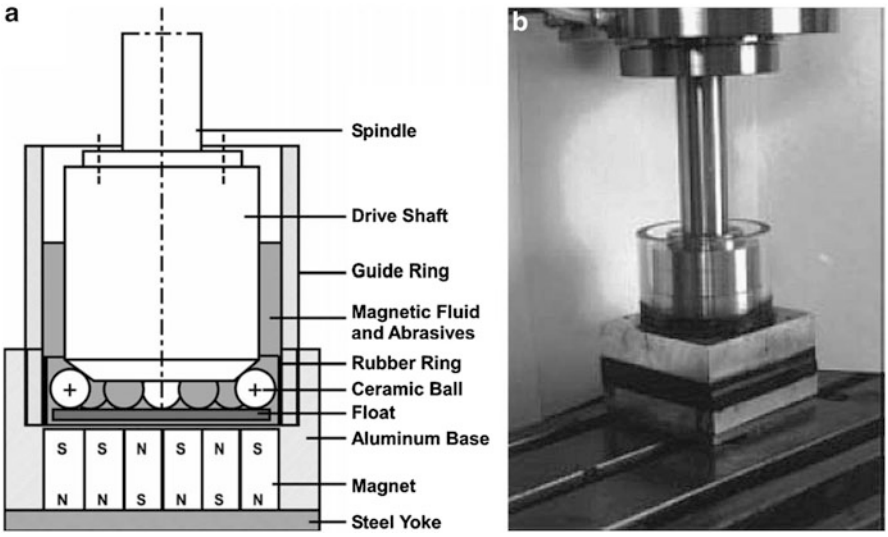

Fig. 16 Schematic (**a**) and a photograph (**b**) of the experimental setup used in finishing Si3N4 balls by MFP (Jiang and Komanduri 1997)

Ion Beam Machining

Ion Beam Figuring (IBF)

Ion beam figuring is accomplished through raster-scanning an ion beam (Ar^+ or Ne^+) across the workpiece. The dwell time method was used for the form correction of workpieces with nearly any shape (Schindler et al. 2002). The main advantages of figuring in this manner include the noncontact feature (useful for lightweight or ultrathin substrates) and an ability to fabricate exotic shapes. The main constraint is that it requires a vacuum environment for operation. Surface roughening and heating can also restrict the applicability or performance of IBF. The ion figuring process has been successfully used by Eastman Kodak Company to correct the residual surface figure error of a 1.8 m Zerodur off-axis segment for the Keck telescope primary mirror. Figure error correction is accomplished by varying the velocity of the constant-output ion source as it scans across the optic surface. The surface figure error was reduced from 0.726 μm RMS to 0.090 μm RMS in two test-figure iterations. IOM Leipzig (Schindler et al. 2002) has long been focused on deterministic figuring of plane, spherical, and aspherical surfaces with local surface errors. Different ion beam tool sizes from 0.5 mm to 25 mm FWHM were used to correct varying spatial wavelength shape errors present on the surfaces (Schindler et al. 2002). IBF has been widely used for the fabrication of EUV optics, and Fig. 17 shows a large commercial IBF machine developed by Neue Technologien GmbH (NTG).

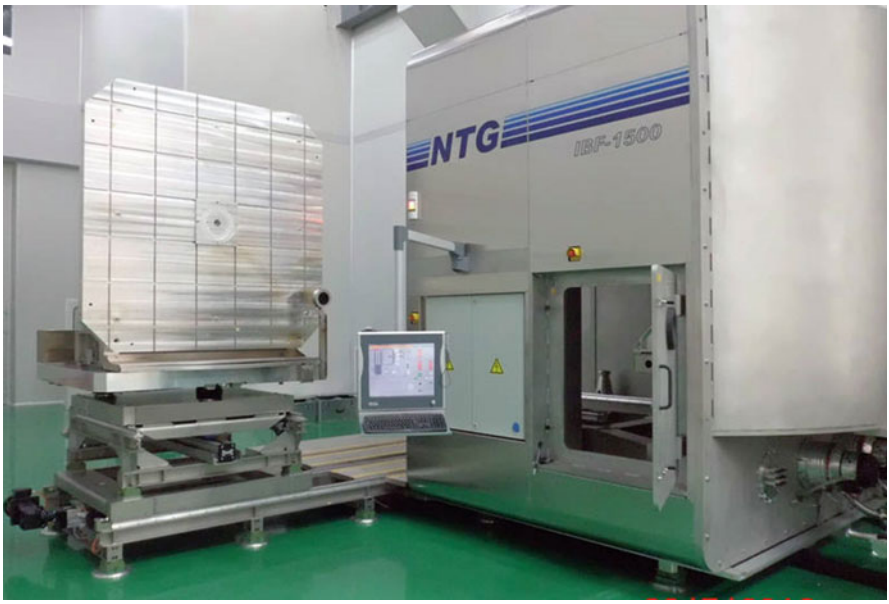

Fig. 17 The IBF-1500 is the latest generation of ion beam figuring plants at NTG, by which optics as large as 1.5 m diameter can be machined

Ion Beam Smoothing (IBS)

During ion sputtering, although atomic recoils, defect generation, and surface erosion will contribute to surface roughing in the atomic scale, a multitude of surface relaxation processes take place mediated by a mass transport along the surface (thermally activated surface diffusion, viscous flow, ballistic transport), and selective removal of atoms from the surface (ESD, gradient-dependent sputtering and glancing angle sputtering) can lead to smoothing of initially rough surfaces. Ion beam-assisted processes can be used for the preparation of ultrasmooth surfaces with RMS roughness values $\leq$0.2 nm. IOM has developed three ion beam-assisted smoothing techniques, ion beam direct smoothing, ion beam planarization, and ion beam-assisted smoothing with sacrificial layers. Ion beam direct smoothing of various materials (e.g., Si, III–V semiconductors (AlGaAs, Ga(As, P), In(P, As, Sb)), SiC, polycrystalline Cu(In, Ga)(Se, S), metals (Cu, Al), fused silica (SiO2), and sapphire (Al_2O_3)) has been investigated. According to the material, both inert gas and reactive gas (Frost et al. 1998) can be used for smoothing. For example, the initial RMS roughness of InAs (Rq = 2.8 $\pm$ 0.1 nm), InP (Rq = 3.3 $\pm$ 1.1 nm), and InSb (Rq = 36.5 $\pm$ 4.5 nm) could be reduced to 0.2 $\pm$ 0.1 nm, 0.8 $\pm$ 0.1 nm, and 1.4 $\pm$ 0.1 nm through ion beam smoothing with N_2 RIBE, respectively. More recently, The RMS roughness of Si surface was reduced from Rq = 2.25 nm to Rq $<$0.2 nm under Ar^+ ion beam erosion (Frost et al. 2004). In ion beam planarization, the rough surface is spin or spray coated by a suited sacrificial layer with a low viscosity (e.g., photo resist) to level out the surface roughness. Subsequently

the sacrificial layer is removed by ion beam etching at the planarization angle. At the planarization angle, the removal rate (sputter yield) of the sacrificial layer and the underlying substrate are nearly identical. Therefore, the smooth surface of the sacrificial layer surface is transferred into the substrate. Through two Ar^+ planarization runs, the roughness of a mechanically polished SiC can be reduced from 4.2 to 0.88 nm (RMS). But small pores existed on the sample surface due to the imperfect of photoresist. For some materials, ion beam smoothing, regardless of the processing conditions, results in increased surface roughness even after removal of only very thin surface layers because of the different etching rates of the two or more phases of the workpiece material. This is also problematic due to possible overetching effects in ion beam planarization, whereby an additional roughness can be generated. In these cases, it is beneficial to shift the process of ion beam smoothing to a thin sacrificial layer deposited on the substrate which has to be smoothed. Using Si as the sacrificial layer, this method was used to smooth the Zerodurs glass with surface roughness below 0.2 nm (Rq). This can be used as a subsequent smoothing process for IBF which will lead to an increase of roughness for Zerodurs glass (Frost et al. 2004).

Gas Cluster Ion Beam (GCIB) Smoothing

In 1992, Epion Corporation started to use GCIB for the smoothing of numerous material surface compositions to better than 0.5 nm without causing subsurface damage (Toyoda et al. 2002), like semiconductors (SOI wafer, gallium antimonide wafer, SiC single crystral, GaN), metals (permalloy film, Ta film), and metal oxides (Ta_2O_5 film). Figure 18 shows a schematic diagram of a 30 keV GCIB system (Toyoda et al. 2002). Neutral cluster beams can be formed by supersonic expansion of high-pressure gas ($\leq$5000 Torr) through a nozzle with a small orifice into a vacuum chamber. During the supersonic expansions, gas atoms collide with each other, and their random velocities are converted to one-directional motion. As a result, relative velocity differences become very small, and individual atoms become bound by Van der Waals forces to form clusters. For surface smoothing, Ar clusters are usually used. The neutral Ar clusters beam is collimated by

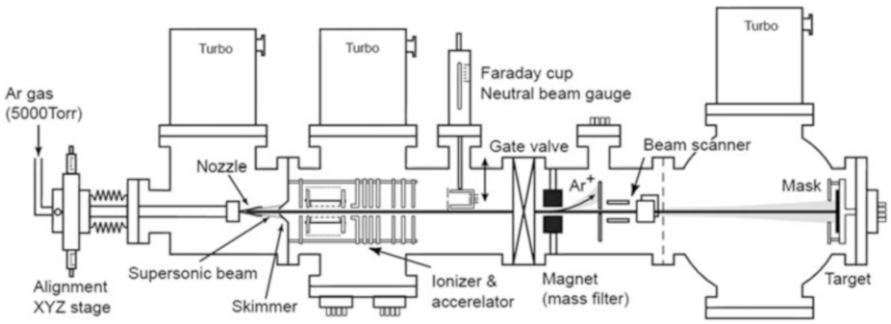

Fig. 18 Schematic diagram of 30 keV gas cluster ion beam (GCIB) system (Toyoda et al. 2002)

a skimmer, ionized by electron bombardment and accelerated by electric field. The lateral sputtering effect from the gas cluster impact is a significant factor in the smoothing process. Cluster ions have a much stronger lateral sputtering effect compared to monomer ions, so the surface smoothing effect of GCIB was much more apparent. Surface particles, shallow scratches, or "spikes" are rapidly removed, while long-range surface nonuniformity is difficult to improve. As a smoothing example, the roughness of a SOI wafer was reduced from 0.6 to 0.18 nm (Ra). With a low-energy configuration of a single atom, no subsurface damage has been observed, which is another advantage of GCIB compared to ion beam figuring.

Plasma Discharge Finishing

The relaxation of strain energy of former finishing iteration has deleterious and unpredictable effects on figure between iterations (Subrahmanyan et al. 2007). This is particularly pronounced when the substrate is made of a hard ceramic such as silicon carbide requiring a considerable amount of pressure to obtain any appreciable material removal rate, and a light weight mirror design is adopted for space telescope.

Plasma-Assisted Chemical Etching (PACE)

One of the pioneering works using chemical action to figure optical elements was PACE, which can rapidly (removal rates from 0 to 10 um/min) and controllably figure and smooth optical surfaces without mechanical contact. It uses a small confined plasma tool in a low-pressure environment (1–10 Torr) and has processed optical elements with aspheric surfaces. Two PACE modes have been experimentally investigated. For the "ion-enhanced" mode, the optical substrate is between the parallel electrodes of an RF discharge and is in electrical contact with the plasma. Therefore, the substrate surface is subject to a low-energy ion flux that contributes to the material removal characteristics. In contrast, for the "downstream" mode, the optical substrate is outside the plasma generation region; it is subject to chemically reactive and excited neutral species flowing from the plasma, but being electrically isolated from the plasma, not to ion bombardment. The dwell time method was used for the polishing process control. The dwell time map was computed from the measured error map and converted to the plasma tool velocity map for implementation (Bollinger et al. 1992). It was shown that PACE can polish a larger aspheric surface (up to 500 mm) to the final figure requiring only two to three measurement/figuring cycles to reach $\lambda/50$ wave surfaces (Bollinger et al. 1992). The spatial frequency range of smoothing can be modulated by the tool size. However, the experimental results showed that PACE, even when applied to smooth polished surfaces, could result in relatively large surface roughness values, possible due to the effect of subsurface damage. Although most of the figuring work has been done with fused silica and silicon, some other materials (Bollinger et al. 1992) like germanium, silicon carbide, silicon/silicon carbide, and plastics were also expected to be finished.

Plasma Chemical Vaporization Machining (PCVM)

Plasma chemical vaporization machining was developed as a pre-machining process for EEM to address its low removal rate. In order to realize this object, chemical process was utilized by PCVM to efficiently produce an undamaged surface, and a removal rate of 2.50 mm^3/h (Takino et al. 1998) and even as high as ~70 mm^3/h was achieved. In PCVM, because it operates in a high-pressure environment (~1 atm in PCVM compared to 1–10 Torr in PACE), plasma generation is confined to the proximity of an electrode, and a high concentration of neutral radicals is produced in the plasma (Takino et al. 1998). As a result, plasma CVM allows high-speed removal (high removal rate of several microns to several hundred microns per minute) for various functional materials such as fused silica, single crystal silicon, molybdenum, tungsten, silicon carbide, and diamond (Mori et al. 2001) with high spatial resolution. Electrodes with various shapes such as pipe electrode (Takino et al. 1998), rotary electrodes (Mori et al. 2001), and hemispherical tip electrode can be used for the plasma generation. The hemispherical tip electrode facilitated the simplification and downsizing of the plasma CVM device by removing the tilting motion of the electrode. In PCVM, figure errors of spatial wavelength range longer than 10 mm are removed efficiently by using the rotary electrode, and the spatial wavelength close to 1 mm can be corrected by using the pipe electrode (Mori et al. 2001; Yamamura et al. 2003). The residual figure error for the spatial wavelength close to 0.1 mm can be further removed by EEM. Two 100 × 50 × 10 mm single-crystalline silicon elliptical mirrors were manufactured by PCVM using the rotary electrode and the pipe electrode in combination, and a figure accuracy higher than 3 nm PV was achieved for the spatial wavelength range longer than 1 mm (Yamamura et al. 2003). Surface roughness of 1.4 nm PV was obtained on a silicon wafer (Mori et al. 2001). The defect density of the surface machined by plasma CVM under 1/100 in comparison with that machined by mechanical polishing and argon ion sputtering was reported to be achievable (Mori et al. 2001).

Reactive Atom Plasma Technology (RAPT)

RAPT emerged from the US National Ignition Facility project at the Lawrence Livermore National Laboratory and was developed by RAPT, Inc. (USA) since 2002 (Fanara et al. 2006). An atmospheric pressure argon inductively coupled plasma (ICP) excites a reactive gas which is injected through its center. The argon plasma acts as a thermal reservoir and excites the admitted species. These are conveyed by the plasma flow to the substrate where they react, yielding controlled and repeatable trenches which show pseudo-Gaussian profiles. The lower energetic cost associated with the generation of F_2 from NF_3 (283 kJ/mol) compared to CF_4 (485 kJ/mol) makes it become a better choice of reactive precursor. Therefore, higher etch rates on ULE (0.55 mm^3/s) were achieved. Furthermore, the lower enthalpy of dissociation of NF_3 makes it possible to operate the process at reduced plasma power. Due to the fact that RB-SiC and Zerodur are polycrystalline materials, application of the RAP to such

polycrystalline substrate can lead to increased roughness on the processed surface, so a subsequent polishing process should be performed to recover roughness. The RAP technology is well-developed for processing optical surfaces made of fused silica, silicon, borosilicate, silicon carbide, and ULE. Helios 1200 at Cranfield University Precision Engineering (CUPE) is a first large-scale machine designed to prove RAP figuring capability of large optics, and recently the form error on a 400 mm diameter ULE workpiece was reduced from 2260 nm PV and 373 nm RMS to 250 nm PV and 30 nm RMS (Jourdain et al. 2013). IOM, Leipzig, also used a similar technique named atmospheric plasma jet machining (Arnold et al. 2010) (PJM) for surface shaping and correction. Its principle is shown in Fig. 19. Depending on the respective task, volume removal rates and tool widths (Gaussian FWHM) can be varied between approximately 5×10^{-5}–50 mm^3/min and 0.3–12 mm, respectively. Shape error of a SiC off-axis parabola mirror with 10.1 mm diameter by a 1.0 mm FWHM plasma jet was reduced from 4972 nm PV and 984 nm RMS to 341 nm PV and 57 nm RMS after two figuring circles. However, similar to RAPT, subsequent polishing step is needed to reduce the increased surface roughness.

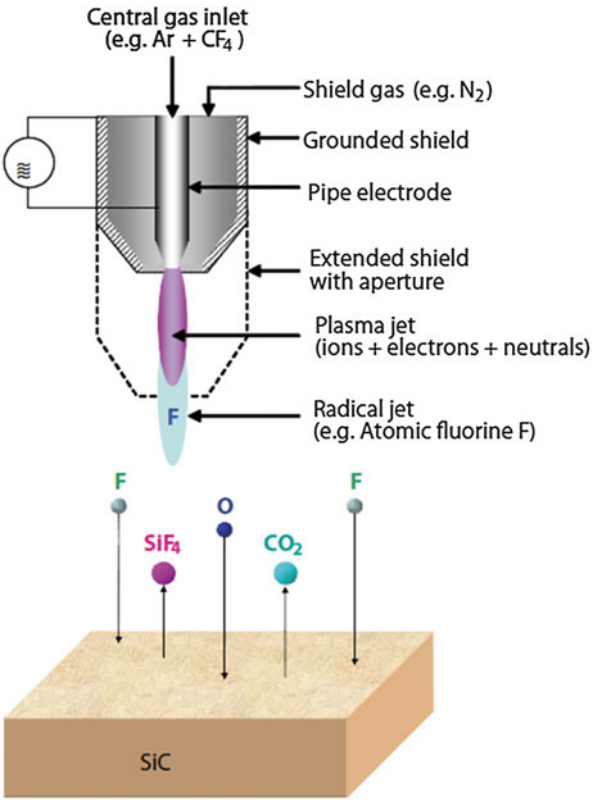

Fig. 19 Principle of the plasma jet generation and the removal process by chemical reactions of radicals with surface atoms. In addition to reactive gas (NF_3, CF_4, SF_6), oxygen is added (Arnold et al. 2010)

Conclusion

Ultra-precision machining is an advanced technology used to generate parts with high figure accuracy (<1 μm), small surface roughness (<10 nm), and few surface/subsurface damage for both optical and nonoptical applications. The applications are to be found in the astronomy, lithography, and consumer electronics. The major challenge of mirror manufacturing for astronomy is to produce ultra-precision large-aperture off-axis aspherical mirrors with high productivity. Ultra-stiff multi-axis grinding machine tools have been developed, and the damage mechanisms of hard and brittle materials subjected to grinding have been investigated to find out the appropriate process parameters. Ultra-precision grinding needs more predictable and reliable, so figure, roughness, and damage tolerances can be reached in one single machining step. Although a substantial progress was made by the introduction of ELID yielding superb surface finishes (Sa <2 nm) and very little subsurface damage and the use of "engineered" grinding wheels with large (average grain size >100 μm) "truncated" grains to reduce tool wear in ultra-precision ductile mode grinding, controlling figure accuracy remains a problem. Some chemical reaction-based polishing and figuring methods such as RAPT or PCVM which can rapidly (removal rates from 0 to 10 um/min) and controllably figure and smooth optical surfaces without mechanical contact are highly expected to be the high-efficiency finishing process. Processes combining fixed abrasive machining and free abrasive machining may also be a good way to achieve high precision and high productivity in a single process. It is difficult to reduce the MSFR to an extreme low level (<0.15 nm RMS) while simultaneously reaching stringent specification for the figure (<0.05 nm RMS) and the high-spatial frequency roughness (HSFR) (<0.09 nm RMS), which are required to ensure a low aberration level and high mirror reflectivity in addition to low flare. Diamond machining is preferable in these cases because of its deterministic characteristics. However, the spectrum of structures is limited by the applied kinematics and tool shapes. Although some methods like swing cutting and nanoparticle-based lubrication were introduced, the tool wear has not yet been reduced to an accepted level. Therefore, there is still plenty of room to develop ultra-precision technology. In the future ultra-precision machining will become even more accurate, faster, and versatile, and it will conquer new areas of application.

References

Anderson DS et al (1992) Stressed-lap polishing of 3.5-mf/1.5 and 1.8-mf/1.0 mirrors. In: 8th international symposium on gas flow and chemical lasers, international society for optics and photonics, San Diego

Ando M et al (1992) Super-smooth surface polishing on aspherical optics. Proc. SPIE 1720, Intl Symp on Optical Fabrication, Testing, and Surface Evaluation. https://doi.org/10.1117/12.132106

Ando M et al (1995) Super-smooth polishing on aspherical surfaces. Nanotechnology 6(4):111

Arnold T et al (2010) Plasma jet machining. Vakuum Forsch Prax 22(4):10–16

Beaucamp A, Namba Y (2013) Super-smooth finishing of diamond turned hard X-ray molding dies by combined fluid jet and bonnet polishing. CIRP Ann Manuf Technol 62(1):315–318
Beaucamp A et al (2014) Shape adaptive grinding of CVD silicon carbide. CIRP Ann Manuf Technol 63(1):317–320
Beaucamp A et al (2015) Process mechanism in shape adaptive grinding (SAG). CIRP Ann Manuf Technol 64(1):305–308
Bollinger LD et al (1992) Rapid optical figuring of aspherical surfaces with plasma-assisted chemical etching. In: Optics Rochester: SPIE's International Symposium on Imaging, Fabrication, and Competitiveness, 1991, Rochester, NY. Proc. SPIE 1618, Large Optics II. https://doi.org/10.1117/12.58037
Brinksmeier E, Preuss W (2012) Micro-machining. Phil Trans R Soc A 370(1973):3973–3992
Brinksmeier E et al (2010) Ultra-precision grinding. CIRP Ann Manuf Technol 59(2):652–671
Brinksmeier E et al (2012) Review on diamond-machining processes for the generation of functional surface structures. CIRP J Manuf Sci Technol 5(1):1–7
Bryan JB (1979) Design and construction of an ultraprecision 84 inch diamond turning machine. Precis Eng 1(1):13–17
Byrne G et al (2003) Advancing cutting technology. CIRP Ann Manuf Technol 52(2):483–507
Carlisle K (2009) Large optics diamond turning machine (LODTM). Lawrence Livermore National Laboratory (LLNL), Livermore
Comley P et al (2011) Grinding metre scale mirror segments for the E-ELT ground based telescope. CIRP Ann Manuf Technol 60(1):379–382
Eda H et al (2001) Development of single step grinding system for large scale ϕ300 Si wafer: a total integrated fixed-abrasive solution. CIRP Ann Manuf Technol 50(1):225–228
Fähnle OW, van Brug HH (1999) Fluid jet polishing: removal process analysis. In: Optical Systems Design and Production, 1999, Berlin. Proc. SPIE 3739, Optical Fabrication and Testing. https://doi.org/10.1117/12.360189
Fanara C et al (2006) A new reactive atom plasma technology (RAPT) for precision machining: the etching of ULE® surfaces. Adv Eng Mater 8(10):933–939
Flucke C et al (2008) Diamond micro chiselling of molding inserts for optical micro structures. In: Proceedings of the 23th ASPE annual meeting and 12th ICPE, Portland
Frost F et al (1998) Ion beam smoothing of indium-containing III-V compound semiconductors. Appl Phys A 66(6):663–668
Frost F et al (2004) Ion beam assisted smoothing of optical surfaces. Appl Phys A 78(5):651–654
Jain V (2009) Magnetic field assisted abrasive based micro-/nano-finishing. J Mater Process Technol 209(20):6022–6038
Jiang M, Komanduri R (1997) Application of Taguchi method for optimization of finishing conditions in magnetic float polishing (MFP). Wear 213(1):59–71
Jourdain R et al (2013) Reactive atom plasma (RAP) figuring machine for meter class optical surfaces. Prod Eng 7(6):665–673
Kawasegi N et al (2014) Improving machining performance of single-crystal diamond tools irradiated by a focused ion beam. Precis Eng 38(1):174–182
Lubliner J, Nelson JE (1980) Stressed mirror polishing. 1: a technique for producing non-axisymmetric mirrors. Appl Opt 19(14):2332–2340
McKeown PA et al (1990) Ultraprecision, high stiffness CNC grinding machines for ductile mode grinding of brittle materials. In: Eighth International Conference Infrared Technology and Applications, 1990, London. Proc. SPIE 1320, Infrared Technology and Applications. https://doi.org/10.1117/12.22336
Mori Y et al (1988) Mechanism of atomic removal in elastic emission machining. Precis Eng 10(1):24–28
Mori Y et al (2001) Development of plasma chemical vaporization machining and elastic emission machining systems for coherent X-ray optics. In: International Symposium on Optical Science and Technology, 2001, San Diego. Proc. SPIE 4501, X-Ray Mirrors, Crystals, and Multilayers. https://doi.org/10.1117/12.448496

Moriya T et al (2010) Creation of V-shaped microgrooves with flat-ends by 6-axis control ultra-precision machining. CIRP Ann Manuf Technol 59(1):61–66
Negishi M et al (1995) A high-precision coordinate measuring system for super-smooth polishing. Nanotechnology 6(4):139
Nelson JE et al (1980) Stressed mirror polishing. 2: fabrication of an off-axis section of a paraboloid. Appl Opt 19(14):2341–2352
Ohmori H, Nakagawa T (1995) Analysis of mirror surface generation of hard and brittle materials by ELID (electronic in-process dressing) grinding with superfine grain metallic bond wheels. CIRP Ann Manuf Technol 44(1):287–290
Picard YN et al (2003) Focused ion beam-shaped microtools for ultra-precision machining of cylindrical components. Precis Eng 27(1):59–69
Saito T et al (2007) Fabrication of high-quality surfaces on precise lens mold materials by a new ELID grinding wheel. In Towards Synthesis of Micro-/Nano-systems. Springer, London, pp. 315–318. https://doi.org/10.1007/1-84628-559-3_55
Schindler A et al (2002) Ion beam finishing technology for high precision optics production. In: Sawchuk A (ed) Optical fabrication and testing, vol. 76 of OSA Trends in Optics and Photonics Series, p. OTuB5.
Shibata T et al (1996) Ductile-regime turning mechanism of single-crystal silicon. Precis Eng 18(2):129–137
Shinno H et al (1999) Nanometer positioning of a linear motor-driven ultraprecision aerostatic table system with electrorheological fluid dampers. CIRP Ann Manuf Technol 48(1):289–292
Subrahmanyan P et al (2007) Rapid fabrication of lightweight SiC aspheres using reactive atom plasma (RAP) processing. Proc. SPIE 6666, Optical Materials and Structures Technologies III, 66660A. https://doi.org/10.1117/12.733123
Suzuki H et al (2013) Development of micro milling tool made of single crystalline diamond for ceramic cutting. CIRP Ann Manuf Technol 62(1):59–62
Takeuchi Y et al (2003) Creation of flat-end V-shaped microgrooves by non-rotational cutting tools. CIRP Ann Manuf Technol 52(1):41–44
Takino H et al (1998) Computer numerically controlled plasma chemical vaporization machining with a pipe electrode for optical fabrication. Appl Opt 37(22):5198–5210
Toyoda N et al (2002) Ultra-smooth surface preparation using gas cluster ion beams. Jpn J Appl Phys 41(6S):4287
Umehara N et al (2006) A new apparatus for finishing large size/large batch silicon nitride (Si3N4) balls for hybrid bearing applications by magnetic float polishing (MFP). Int J Mach Tools Manuf 46(2):151–169
Walker DD et al (2006) Use of the 'Precessions'™ process for prepolishing and correcting 2D & 2½D form. Opt Express 14(24):11787–11795
Walker D et al (2012) Edges in CNC polishing: from mirror-segments towards semiconductors, paper 1: edges on processing the global surface. Opt Express 20(18):19787–19798
Yamamura K et al (2003) Fabrication of elliptical mirror at nanometer-level accuracy for hard x-ray focusing by numerically controlled plasma chemical vaporization machining. Rev Sci Instrum 74(10):4549–4553
Yamauchi K et al (2002) Figuring with subnanometer-level accuracy by numerically controlled elastic emission machining. Rev Sci Instrum 73(11):4028–4033
Zhao Q, Guo B (2015) Ultra-precision grinding of optical glasses using mono-layer nickel electroplated coarse-grained diamond wheels. Part 2: investigation of profile and surface grinding. Precis Eng 39:67–78
Zhao Q et al (2007) Surface and subsurface integrity in diamond grinding of optical glasses on Tetraform 'C'. Int J Mach Tools Manuf 47(14):2091–2097

Forward Design Methods for Precision Machines

2

Bin Li

Contents

Introduction 34
Precision Machine Design Principles 35
Determinism 35
Abb Offset 36
Symmetry 36
Separation of Metrology Frame and Machining Loop 37
Precision Machine Design Method 37
Machining Process Analysis 37
Structure Design 37
Temperature Control 38
Accuracy Design and Error Budget 38
Large Aspheric Grinding Machine Design Case 39
Large Aspheric Mirror Grinding Process Analysis 40
UAG900 Configuration Design 42
Grinding Wheel Grit and Bond 44
Grinding Wheel Dynamic Balance 45
Grinding Wheel Dressing 45
Grinding Machine Configuration 46
UAG900 Grinding Machine Error Budget 48
Grinding Vibration Analysis 49
Grinding Machine Stiffness Budget 55
Conclusion 56
References 56

Abstract

With the development of modern manufacturing technology and improvement of the product performance, precision machine becomes much more vigorous than ever. In order to achieve qualified precision machine tools according to the

B. Li (✉)
College of Mechatronic Engineering, Zhongyuan University of Technology, Zheng zhou, China
e-mail: libin_zzti@zut.edu.cn

Z. Jiang, S. Yang (eds.), *Precision Machines*, Precision Manufacturing,
https://doi.org/10.1007/978-981-13-0381-4_25

restricting factors, such as process requirements, machining efficiency, and cost, the design work needs to be done firstly. The designer would not succeed even owing plenty of actual design experience of precision machines, but build his design concept through both theoretical literatures and practical experience. This chapter introduces the general design techniques for the precision machines, including the case-effect, symmetry, and abbe principles. The error compensation method will be the vital accuracy improvement method, and the separate metrology frame design concept is described especially. In the following sections, several design methods were introduced with concrete design examples. At the end, the design procedure and methods for the ultraprecision grinding NC machine are described.

Keywords

Precision machine · Design methods · Design principles · Large aspheric grinding machine

Introduction

The best designer gives the soul to the precision machine. For the given specifications, the best designer would take all the requirements and conditions into consideration and counterbalance the related parameters; the final design project would be capable of machining accuracy, stability and efficiency, and the cost would be minimal. The best designer generally acquires his or her excellent idea for and from the successful and unsuccessful experience. However, plenty of readings of the precision machine design reference book would expand the engineers' train of thought, that is the original purpose of this chapter.

The design process for precision machine is the key factor to determine whether the final performance specifications could be achieved. The design work not only focuses on the structural issues but also considers the manufacturing cost, stiffness, stability factors, etc. Different machining processes need to be treated individually. The engineer has to deal with concrete accuracy, stiffness, and cost problems and adopt suitable design strategies and method to balance the specifications described above and precision machine's final performance demands.

There are many successful design cases for reference; however, the design needs to be implemented according to the specific requirements. Not all the advanced configurations and concepts could be accepted, but the machining capability, test equipment, assembly conditions, and environment control level have to be taken into consideration, and the optimal design project could be determined thereafter. At last, the precision machine design is a systematic process, and each element involved needs to be kept balanced.

Many books, papers, and reports have been published for the precision machine and process engineering. Alexander H. Slocum published the most popular precision machine design book, which gives design philosophy and methods for the machine system and subsystems; it is the Bible for the precision machine engineers (Slocum 1992). For the precision manufacturing, David Dornfeld published a textbook for

graduate students, which provides the most complete introduction for precision engineering; however, the book gives more attention to precision manufacturing rather than machine science (Dornfeld and Lee 2008). Dr. Hale concluded his experience in LLNL laboratory and gave the profound design methods and principles for precision machines, as well as many typical cases (Hale 1999). It is known that the metrology is the basis for the whole engineering, especially for the precision engineering. Precision machine designer has to understand the precision metrology and know all the necessary measurement methods and instruments. David Whitehouse published the metrology book for the form and positional errors measurements, which tries to provide useful information for the surface and nanotechnology; however, the precision machine designers could be benefited as well (Whitehouse 1994).

The fundamental principle of the precision machine is the cause-effect relation, and all the error sources could be traced, compensated, or eliminated thereafter. The cause-effect principle was used and verified in the ultraprecision single diamond turning technology firstly which was classified as the deterministic machining technology. The nanometer level roughness could be obtained by precisely controlling the static and dynamic position relation between the diamond tool and workpiece. The error budget method could be adopted to determine the kinematic motion accuracy of each axis. The error budget could also be expressed by the homogeneous matrix method to describe the position relationship between the tool and workpiece. The whole configuration and subsystem's symmetry could minimize the influence of thermal and load distortion toward the machine accuracy. It is suggested that the abbe principle should be obeyed for the arrangement of the measuring unit. The metrology frame should be independent from the machining frame to avoid the introduction of the machining system error. The thermal stability could be improved by choosing proper material and controlling environment temperature. Modular design could promote the batch fabrication, and make the test, assembly, and maintenance more dependent.

Precision Machine Design Principles

Precision machine design methods were obtained through the philosophy and actual engineering experience; it is known that the great precision machine designer became successful by numerous failure and conclusions. However, many theories induced from the precision engineer and researchers would also quiet benefit.

Determinism

The basic idea is that machine tools obey cause-and-effect relationships that are within our ability to understand and control and that there is nothing random or probabilistic about their behavior. Everything happens for a reason, and the list of reasons is small enough to manage. Determinism is both a principle and a philosophy applicable to many systems and processes beyond automated manufacturing processes and machine tools in particular. The deterministic principle rests on the ability of physical laws to

explain the behavior of systems and processes. The deterministic philosophy instills a belief that all aspects of a system or process can be understood and ultimately controlled as desired. The systematic method used to identify root sources of error and to bring them under control has become known as the deterministic approach. While often used in the context of existing machines, determinism applies to precision machines that have yet to be conceived, and so too is a principle and a philosophy for design. The determinism could be used to direct the error source elimination and could also be used to verify whether the design is reasonable.

Abb Offset

> The measuring instrument is always to be so constructed that the distance being measured is a straight line extension of the graduations on the scale that serves as the reference. Should the measuring axis and that of the scale belong to two different axes, which are separated by a certain distance, then the length being read off will be identical to the length being measured in general only when the moving system undergoes pure parallel motion, with no rotation. If the system undergoes a rotation between the initial and final settings, then the scale reading and the measured length are different.
>
> The straightness measuring system should be in line with the functional point whose displacement is to be measured. If this is not possible, either the slideways that transfer the displacement must be free of angular motion or angular motion data must be used to calculate the consequences of the offset.

The Abb and Bryan principles emphasize the significance of sine errors in a measurement system. In the context of Abb, the concern is a changing angle (or angular motion). In addition, a sine error may include a constant angular misalignment commonly referred to as a squareness error. Usually of lesser significance is the cosine error, which occurs when the distance measurement and the scale are not parallel. The cosine function is second order for small angles, while the sine function is first order, as indicated by the following Equations. Typically, the constant angular misalignment is most significant for a cosine error.

$$\varepsilon_{\sin e} = r \sin\theta \cong r\theta$$

$$\varepsilon_{co\sin e} = l(1 - \cos\alpha) \cong l\frac{\alpha^2}{2}$$

Symmetry

There are many benefits to using symmetry in designs. Symmetrical designs are simpler to analyze, require less information to build, and often allow more accurate measuring and manufacturing methods. With regard to precision machines, symmetry can significantly reduce errors that occur in directions normal to the generator of the symmetry, for example, the line or plane. Not only must the material of the object

be symmetric, but the loads (forces or heat) must also be symmetric for the errors to be self-canceling. Symmetry about a single plane is usually easy to achieve in a design and if possible should be aligned to cancel errors in the most sensitive direction. The second plane of symmetry is more difficult or perhaps impractical to achieve globally, but efforts to create local symmetries are also beneficial.

Separation of Metrology Frame and Machining Loop

The metrology loop is a conceptual path through all the physical parts, sensors, and controls in the machine that determine the location of the tool or probe with respect to the workpiece. A change to any of these parts due to a force or a temperature change will cause a measurement error. To reduce errors, certain loads (force or heat) may be eliminated entirely or partially from the metrology loop by providing an independent structural loop to carry those loads. We may state the principle as follows: The metrology loop and the structural loop(s) should exist separately and independently to the greatest practical extent. Preferably the separation would be a physical one, but it could also be an informational separation, for example, through error compensation based on a force measurement and a structural model.

The dynamic error induced during the machining process would affect the measuring results; in order to attenuate the influence, it is better to separate the measuring frame from the machining frame. However, the separation design would improve the machine cost and make the configuration much more complicated. The counterbalance should be done to make the right choice between the frame separation and configuration simplification, as the simplification would achieve higher accuracy.

Precision Machine Design Method

Machining Process Analysis

To begin with the precision machine design process, the machine process analysis should be carried out firstly. The designer should remember the process requirement exactly, including the specimen's geometry and accuracy, machining efficiency, etc. The excel sheet and txt note could be used to list these process requirements; each requirements should be satisfied accordingly. Meanwhile, the machine tool would be selected thereafter. The machine process includes the material removal mechanism, the specimen fabrication efficiency, etc. The designer should be very familiar with the common machining process and make the right design selection.

Structure Design

After the machining process analysis, the design task could be implemented thereafter. The first design task is to choose or propose the most suitable configuration. Many classic cases could be listed and referenced.

For the precision turning machine, the most classic case is "T" configuration as shown, which separates the XZ axes comparing with the traditional turning lathe. The workpiece spindle is arranged on the top of the X axis slide, and tool station was placed on the top of the Z axis. The configuration would reduce the load of Z axis and make the accuracy improvement possible. However, such configuration is just suitable for the light cutting process, for example, the nonferrous material cutting or the small feeding cutting of the ferrous material due to the stiffness limitation. The most popular "T" type turning machine supplier includes Moore Nanotechnology, Precitech, Taylor Hobson, etc. However, the concrete turning configuration should be determined according to the specific process requirements.

Temperature Control

> By far the most common cause of non-repeatability is temperature. More specifically, the cause is changing temperature with time, which causes thermal distortion of the structural loop (which consists of all the mechanical elements involved in holding the tool and work in a given relative position). Interestingly, temperature problems also seem to be the least widely appreciated error source in machine tools.

Experience has shown that temperature control is the most reliable and effective means to reduce thermal errors. Further, it is usually one of the least expensive aspects of a precision machine tool and usually requires little additional hardware. The design challenge is figuring out how to provide sufficient control for the least costs. The cause-and-effect relationships can be calculated in considerable detail using modern computer software (finite element analysis and computational fluid dynamics) and empirical heat transfer formulas, but to do so requires considerable knowledge about the design and the environment. Data obtained from existing systems or specific tests may be easier to obtain and just as valuable. A number of simple models are presented in the remainder of this section to gain greater understanding of the important parameters and their relationships to the thermal control problem.

Accuracy Design and Error Budget

The accuracy is the most important specification of the precision machine design. Generally speaking, the machine consists of many kinematic axes, and each axis owns its accuracy demands. The accuracy overlap of each axis is the kinematic accuracy of the machine. Each axis's accuracy should be evaluated, analyzed, and allocated; thus, the compound coupling accuracy would be satisfied to be design value. The accuracy design method was termed as the error budget. The error budget was not the simple error addition and subtraction. The particular combinatorial rule to use is not obvious nor has it been rigorously determined. In the rare case that knowledge of all error components is complete, then simple addition is appropriate yielding a total error that may vary with time and space. When dealing with

magnitudes, it is unlikely that all errors will occur at the same time or place and with the same sign along the direction being combined. This makes direct addition too conservative. Quadrature addition (or root sum of squares) gives the expected value of errors acting independently from one another. That is to say on average they must all be orthogonal. Experience has shown this to be somewhat optimistic. A usual tactic is to arithmetically average the conservative and optimistic estimates, although a geometric average seems more appropriate. Another sensible approach is to use the vector norm, given in Eq. (1), with an exponent p between 1 and 2 (the values that give the conservative and optimistic estimates). For an error vector having up to 40 or so equal components, the vector norm with $p = 1.22$ closely matches the arithmetic average, while $p = 1.33$ closely matches the geometric average. Using $p = 2$ has an intuitive appeal.

Large Aspheric Grinding Machine Design Case

The following contents take the larger aspheric mirror grinding machine design for example to interpret the precision machine design process, principles, and methods furthermore.

The grinding process requirements for the large aspheric mirror were high accuracy, high efficiency, and low subsurface damage, and the process schedule and equipment design should respond to the above demands. The diameter of the aspheric mirror is smaller than 900 mm, while the height is less than 200 mm, and the gantry configuration was adopted to satisfy the machining space demands. To guarantee the mirror's profile accuracy, the relative position between the grinding wheel and workpiece should be precisely controlled. The precision grinding technology was the multi-edge cutting process, and the relative position accuracy was determined by the machine kinematic accuracy, the grinding wheel form accuracy, and the accuracy stability under the cutting force influence. To obtain the high kinematic accuracy and stiffness, the hydrostatic bearing was adopted. And the disk-type arc grinding wheel with a large diameter was used, thus the grinding linear speed would be guaranteed, and the grinding wheel inertia would be minimized. The cross grinding mode was adopted, the mirror was fixed on a hydrostatic rotary table, and X axis would carry the rotary table move against the grinding wheel spindle which was carried by the Z axis. The rotary table would reduce the linear axis stroke for the grating-type grinding mode, and Y gantry axis was also equipped to achieve precision in-situation measurement and grinding start point alignment.

The mirror high machining efficiency needs simple operation process and the corresponding material removal rate. The operation process involves the process procedure, workpiece load and unload, grinding wheel assembly and dressing, and compensation grinding. In order to reduce the workpiece fixture and grinding wheel off line procedure. The material removal rata was determined by the depth of cut and feed velocity, the mirror mold was generally flat, and the total removal depth during the whole machining process was several tens of millimeters. And larger cutting

depth and feeding velocity were generally adopted during the beginning stage to approach the ideal surface profile as soon as possible.

Subsurface damage corresponds to the medium frequency waviness error; it was induced by the grinding wheel and workpiece's vibration. Due to the equipment stiffness and accuracy limit, the large grinding depth would cause corresponding grinding force and vibration amplitude, and the subsurface damage would also be very severe. In order to restrict the subsurface damage, accuracy, stiffness, and damping characteristic need to be improved by using the hydrostatic bearing support. Smaller grinding depth would be adopted during the fine grinding stage, and the grinding wheel arc profile should be dressed precisely. Thus, the grinding wheel runout would be controlled.

Large Aspheric Mirror Grinding Process Analysis

The developed large aspheric mirror grinding machine should guarantee the high fabrication efficiency, high accuracy, and low subsurface damage of the symmetric aspheric mirror manufacture. To achieve the above process aims, the grinding process plan and machine design should make the following.

1. High efficiency
   High efficiency grinding means simple operation procedure, enough material removal rate, and surface profile accuracy convergence speed. The traditional large aspheric mirror fabrication process consists of the rough grinding shaping, fine grinding, profile measurement, compensation grinding procedure, etc., and each process needs special equipment. In order to improve the efficiency, the above process should be done in one machine, and the mirror transport, second fixture, and alignment time would be saved. During the rough grinding stage, high material removal rate would be adopted to make the surface profile convergence, and high material removal rate was determined by the grinding wheel grit texture type, grinding depth, and feed velocity. To satisfy the above specifications, the diamond grinding wheel of large grit size was used. And several grinding wheel assembly flanges were prepared for the grinding wheels used in different grinding stages. The grinding depth and feeding velocity were determined by the machine dynamic stiffness, and the drive system should have enough power. However, the drive motor type should not be too large, otherwise, the machine's part size would also increase, the moving mass would increase, and dynamic response characteristic would decrease. Due to the axis kinematic error, grinding force and temperature variation, the first fine ground surface would not satisfy the final surface profile accuracy requirements. And compensation grinding needs to be carried out to improve the ground surface accuracy, and the in-situation measurement device should be equipped thereafter. The mechanical stiffness was determined by the configuration, part, and assembly accuracy. And part material heat treatment should be done correctly to guarantee the sufficient stiffness and stability.

Large aspheric grinding system consists of complicated electrical and hydrostatic subsystems, and the total grinding stage needs more than 12 h. Meanwhile, the grinding environment is very tough, and in order to improve the cooling effect, the grinding fluent flow rate would have to be 20–25 L/min and the ground scrap size would have to be 0.1 mm which would pour into the grinding fluent, and prevention needs to be carried out to avoid the mixture of the grinding fluent and hydrostatic oil, otherwise, the guideways surface would be scraped or the restrictors would be chocked. And the machine should be stable enough.

2. High accuracy
   The most obvious characteristic of the large aspheric mirror NC grinding machine lies in that the numerical interpolation was introduced into the curved surface grinding. The aspheric mirror forming mechanism was that the grinding wheel was controlled to implement the high efficiency grinding according to the given track, and the kinematic axes should have enough static and dynamic accuracy to guarantee the mirror profile accuracy. The mechanical accuracy items consist of straightness, perpendicularity, and torsion error, and the hydrostatic bearing support technique could achieve higher accuracy specifications described above. The kinematic motion accuracy consists of the positioning and repeatability accuracy, the linear motor combined with the grating sensors would avoid the mechanical contact, which would eliminate the alignment and torsion error of the servo rotary motor. As the moving mass of the large aspheric mirror grinding machine is quiet large, flat linear motors with great drive force were adopted; however, there is great attraction force between the moving coil and static magnetic plate, the maximum value would be more than 10,000 N, the connection part should be stiff enough to resist the stress, and double linear plate motor arrangement was adopted to counterbalance the attraction force. And the grating displacement sensor was placed parallel to the main guideway with a minimum distance to reduce the Abb error.
3. Low subsurface damage
   Subsurface damage corresponds to texture structure crack with the medium frequency under surface, which is like the trace left by the track rolling on the soil road. The subsurface damage affecting factors include the vibration between the grinding wheel and workpiece, the press force caused by the grinding grit, and the stress release after grinding process. The corresponding machine specification is the grinding wheel form accuracy, dynamic runout, axis's stiffness, and accuracy, and the corresponding process parameter is the cutting depth. Grinding process with sub-micrometer cutting depth would restrict the subsurface damage; however, the corresponding material removal rate is too small which is contradictory to the high machining efficiency specifications. Under the condition of precise control of the grinding wheel form accuracy and runout, micro-cutting depth would decrease the subsurface damage. The micrometer level cutting depth was used during the fine and compensation grinding stage to decrease the subsurface damage, and the grinding wheel spindle was equipped with online dynamic balance device to reduce the grinding wheel's vibration toward the spindle runout.

UAG900 Configuration Design

The name of the developed large aspheric mirror grinding was abbreviated to "UAG900," according to the above process analysis, different interpolating grinding modes were compared, and the XZC polar grinding mode was selected finally. The grinding spindle wheel's shape and size were also analyzed, and the machine workspace was also taken into consideration.

Grinding Mode Selection

For many commercial aspheric grinding equipment, the workpiece or grinding wheel spindle swing mode was generally adopted, such as the GI milling-grinding compound machine from Satisloh which has two rotary motions, swing motion was added into Schneider's SCG milling-grinding machine series' spindle. Such grinding mode was more suitable for the small aperture aspheric mirror grinding, and machining space was enlarged by adding more axis freedoms. For the large aspheric mirror, the volume and mass of the grinding wheel spindle and mirror are much bigger, and the swing axis could not fulfill the accuracy and stiffness requirements. The most economic and practical process for mirror profile with large aperture is the numerical interpolation. The OAGM2500 and Big Optix of the Cranfield University used the XYZ linear coordinate and XZC polar coordinate interpolation mode, as shown in Fig. 1.

The prototype machine of the XYZ linear interpolation grinding mode is the gantry milling machine which has very large machining space. However, the XY stroke needs to be up to 900 mm × 900 mm, and the accuracy specification is the same over the total stroke. For the XZC polar interpolation mode, the rotary table size should be larger than 900 mm, and the stroke of the X feeding axis just needs 450 mm stroke to be capable of fabricating large aspheric mirror with a diameter of 900 mm, UAG900 selected the XZC polar coordinate grinding mode.

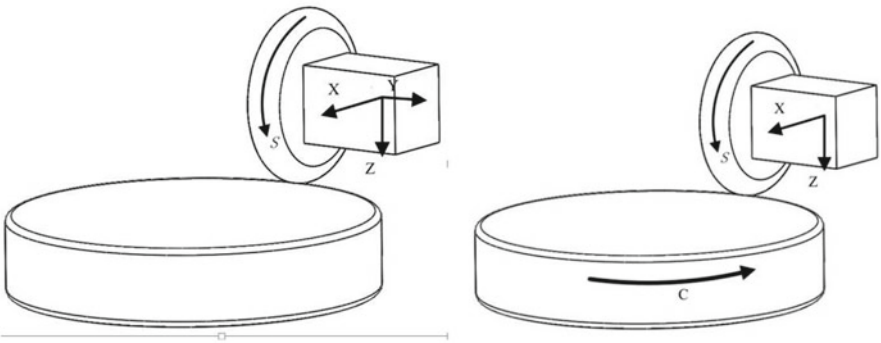

(a) XYZ linear interpolation mode (b) XZC polar coordinate interpolation mode

Fig. 1 Illustration of grinding interpolation mode

Hydrostatic Bearings Support Type

The bearing support type is vital for the machine system accuracy and the ground subsurface damage. The experiments have verified that the grinding system with hydrostatic bearings support would cause less subsurface damage, and the following polishing process would converge into the specified surface profile much more quickly. The reason was that the hydrostatic bearings have higher accuracy and stiffness, and the control of the grinding point in the machining space would be much more accurate, and the variation of the cutting depth would be smaller. On the premise of guaranteeing the grinding wheel form accuracy, the ground surface finish would be better, and the corresponding subsurface damage would be smaller and more average.

According to the grinding strategy evaluation, the crack depth during the grinding removal process is proportional to the cutting depth, grinding force, and grit size; however, the cross and overlapped crack would not only remove the material but also generate the residual crack, which is known as the subsurface damage. The subsurface damage depth could be expressed as the following:

$$D_{ssd} \propto G\left(\frac{Fd_C}{KS_C}\right)^P$$

in which the G is the constant value determined by the mirror material, grinding wheel, and grit material, F is the cutting force during the grinding process, dc is the cutting depth, k is the grinding system stiffness, S_c is the grinding contact area, and p is the accuracy affecting coefficient.

The value of grinding force F is generally taken as the ultimate output force of the drive system. However, the actual kinematic accuracy and stiffness is much lower during the grinding process, and the continuous grinding removal process would convert into a discrete impact process. The corresponding cutting force would increase exponentially which means that the induced crack depth would also expand exponentially.

The control accuracy of the cutting depth dc is determined by the kinematic accuracy and stiffness of the grinding machine, as well as the grinding wheel profile accuracy. If the kinematic accuracy is very low, there would be very severe cutting depth variation, the corresponding grinding contact area would also change, the cutting force for each grinding wheel grit would change exponentially, and the corresponding subsurface damage would increase exponentially, either.

If the grinding system stiffness is very weak during the grinding process, the grinding wheel would not achieve the ideal given position, and the result is that the cutting depth and force would decrease, the profile accuracy would not decrease either. The resonance generally arises for the grinding system with lower stiffness. The grinding process would also convert into the random impact procedure, the cutting force and depth would change greatly, and the corresponding subsurface damage would be very severe.

Conclusively, in order to reduce the subsurface damage depth and improve the ground surface quality, the accuracy and stability control of the grinding contact area

and cutting force should be promoted by using hydrostatic bearings support of each kinematic motion axis for UAG900.

In order to control the deformation caused by the temperature variation, the large aspheric mirror generally adopts the hard and brittle ceramic material, and the grinding wheel of natural diamond grit is needed. However, the grit shape and size should be selected properly. And the grinding wheel is of disk or cup type. 25 m/s – 30 m/s grinding wheel circular linear speed is generally required for the ceramic material workpiece grinding. Under the given grinding speed condition, the grinding wheel contact radius is inversely proportional to the spindle rotation speed.

As the hard and brittle material grinding linear velocity lies between 20 m/s and 30 m/s, the grinding wheel diameter and rotary speed will be determined by the volume of the working space. For the small aperture aspheric mirror grinding equipment, due to the workspace limitation, the grinding wheel diameter is generally 50–150 mm, the corresponding grinding wheel rotary table would be 10,000 r/min, and the aerostatic bearings' support spindle is generally adopted. For large aperture mirror grinding equipment, the volume of the machining space is large enough to make use of the grinding wheel with larger diameter of 300–450 mm. The grinding wheel's wear is very severe during the grinding of aspheric mirror with a large aperture. Effective grinding area would promote if the grinding wheel's diameter increases, and the number of the grinding wheel dressing and replacement would decrease. As the grinding wheel's diameter becomes larger, its mass also increases, the stiffness specification would also promote. In order to improve the grinding wheel strength, the aluminum is generally selected as the grinding wheel base material, and the grinding wheel spindle uses the hydrostatic bearings; the rotary speed is 1500–3000 r/min which would satisfy the linear velocity requirements.

For the precision grinding of medium and large aperture aspheric mirror grinding, the disk-type grinding wheel would make higher ratio of the velocity and mass. However, the disk-type grinding wheel is suitable for the large aperture aspheric mirror, there would be interfere for the small aspheric mirror. The grinding wheel wear occurs in the radial direction, and the influence toward the grinding wheel balance would be very small.

For the grinding wheel, the mass and velocity of the grinding wheel should compromise with each other. The greater the grinding wheel mass is, the start inertial would increase greatly. Comparing with the cup wheel and spherical wheel as shown in Fig. 2b, c. A disk-type grinding wheel with a diameter of 400 mm and width of 20 mm was adopted by UAG900, as shown in Fig. 2a, and the grit is natural diamond.

Grinding Wheel Grit and Bond

The grit of the grinding wheel would affect the surface roughness and material removal rate. Large grinding depth and grit size were generally adopted during the rough grinding stage to guarantee the material removal rate, and the surface roughness and profile accuracy requirements also decrease. The rough grinding was the typical brittle

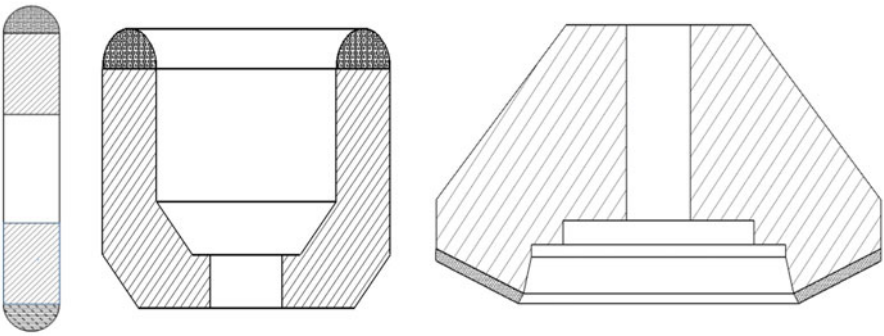

Fig. 2 Grinding wheel shape illustration

grinding mode, and the bond material was copper, iron, or even ceramic which would reduce the grinding wheel wear. During the semi-finish grinding stage, the surface roughness and profile accuracy need to be controlled under 0.5 and 50 μm, and the grit size was much smaller and the resin bond was chosen for the semi-finish grinding. According to the surface profile accuracy and self-stiffness requirements, the grinding wheel base is steel. The roughness should be less than 0.3 μm for fine and compensation grinding, and the grinding wheel is resin bond.

Grinding Wheel Dynamic Balance

The grinding wheel's balance is determined by the material distribution and radial runout. The vibration caused by the grinding wheel balance is the main source of surface waviness. The continuous grinding force would cause several micrometers distortion of the grinding spindle. Before the grinding wheel was fixed onto the grinding wheel, the static balance using the static balance frame should be carried out firstly, and the dynamic balance should be done using the dynamic balance. The in-situation dynamic balance system was applied to the UAG900, and the residual unbalance is less than 0.2 μm.

Grinding Wheel Dressing

The form accuracy and grit sharpness influence the grinding efficiency, and grinding wheel dressing method was determined by the surface profile accuracy, efficiency, and fixture requirements. The metal bond wheel with large grit size was applied to the rough grinding stage, as the wheel form accuracy is low and electrolysis dressing method was applied. For the resin bond grinding wheel used in the semi-finish and fine grinding stage, the dressing tool is a green silicon carbide wheel which could precisely control the grinding wheel form accuracy.

Grinding Machine Configuration

The configuration design would respond to the process and device requirements described above. The part manufacturing capability, assembly process, and cost should be taken into consideration. The basic requirements of the structure configuration are as follows:

- XZC polar grinding mode with 900 mm workspace
- In-situation measurement and compensation grinding
- Hydrostatic bearing support, micro-meter straightness, and positional accuracy
- In-situation grinding wheel dressing device

Based on the above requirements, the basic stroke specification could be determined. In the initial design stage, the manufacturing and assembly feasibility and cost should be considered. The movable gantry configuration is firstly selected according to the Cranfield OAGM2500, as shown in Fig. 3. The rotary table was placed in the center of the worktable to achieve the XZC polar grinding mode. The operation space is wide, and the load and unload of the mirror workpiece are convenient. The unit structure is simple, and their part manufacturing processes is feasible. However, this configuration needs more space, and its bigger mass makes

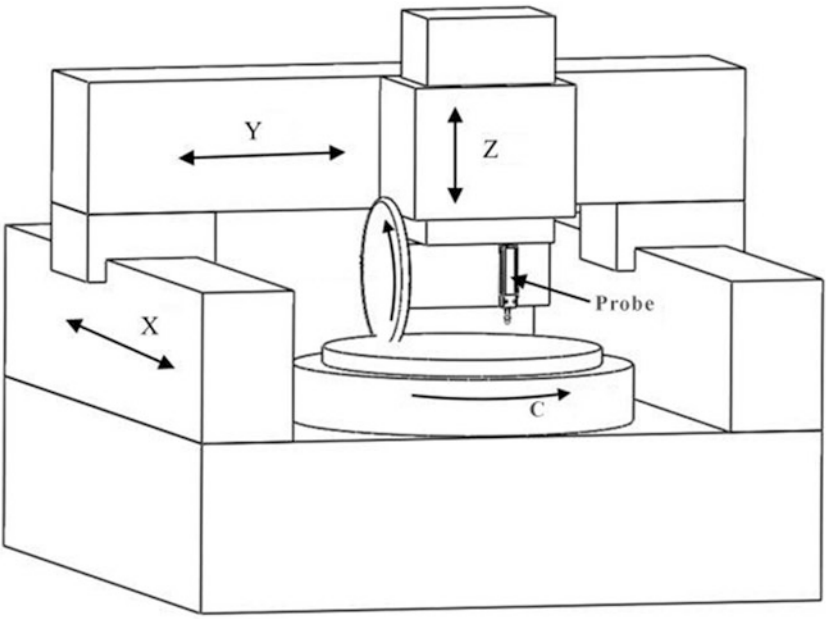

Fig. 3 Illustration of gantry configuration

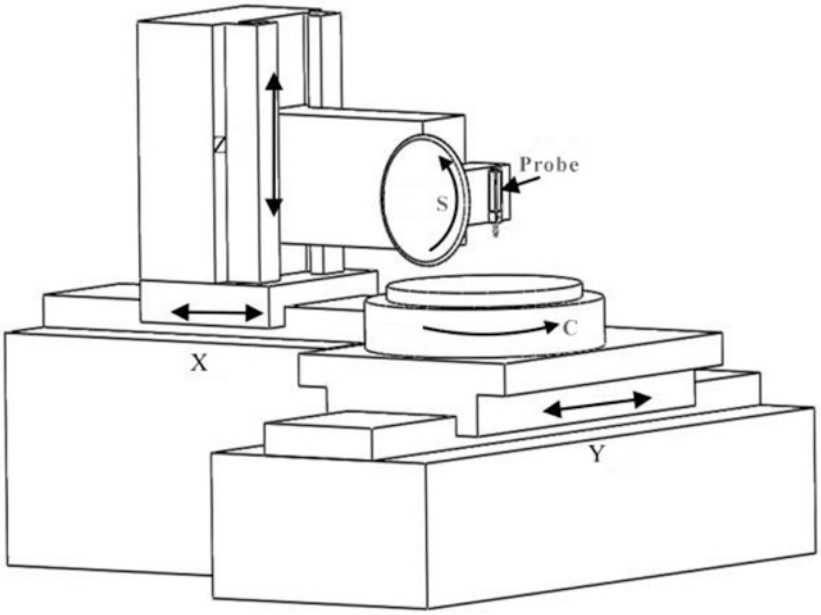

Fig. 4 Flat configuration illustration

the transporting much more difficult. Meanwhile, the large distance across the gantry needs the double drive system, and the corresponding manufacturing process costs more.

The flat grinding machine is capable of aspheric mirror grinding as the numerical system is equipped with the multi-axis linear interpolation capability. As shown in Fig. 4, the configuration is more compact, however, the supporting ram overhangs too long, the vibration caused by the grinding force would make the subsurface damage much severe, and the mirror crack even happens.

The static gantry configuration was chosen for the UAG900 which consisted of the XYZ linear axes, C rotary table C, and grinding wheel spindle S. All the kinematic motions were supported by the hydrostatic bearings as shown in Fig. 5. The gantry granite beam's cross-section size is 1 m × 1 m. The granite material has very little stress release. The 45° oblique beam could promote the stress distribution, and there was oil collection device at the bottom of the beam. The counterbalance weight for the Z axis was arranged across the beam which would reduce the torsion and twist. The symmetric aspheric mirror could be ground by XZC mode. The metrology frame is composed of the length gauge and Y axis, and the measurement results could be used for the compensation grinding. The grinding wheel dressing station was arranged at the end of X axis for the resin bond grinding wheel during the semi-finish and fine grinding.

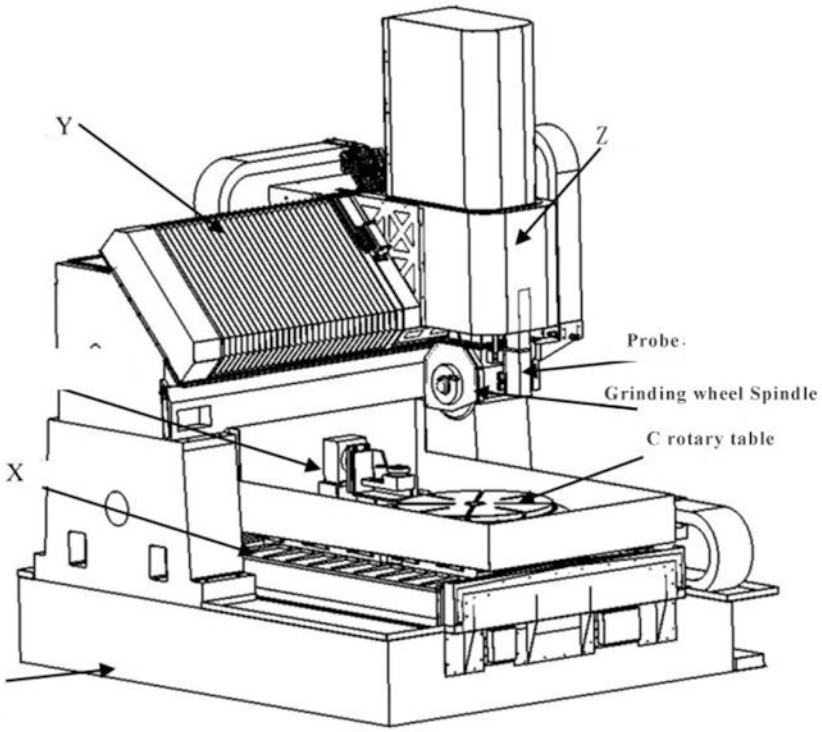

Fig. 5 Illustration of UAG900 configuration

UAG900 Grinding Machine Error Budget

The kinematic motion error of the interpolating axis and rotary error of the grinding wheel spindle would convert into the mirror surface profile error. The ultraprecision grinding was classified as the fix abrasive grinding. The relative position between the grinding wheel and workpiece should be controlled precisely. The stroke of the grinding wheel was determined by the mirror size and other auxiliary stroke requirements, and the kinematic motion accuracy was estimated and designed using the error budget method. By the error budget method, the error in the machining volume could be set, and the mirror surface error could be estimated. The kinematic motion error of each axis could also be adjusted accordingly. For the actual manufacturing process, the extreme error value would not be adopted. For the error budget, the axis that has not participated in the machining process would not be part of the error estimation, in case of the high manufacturing cost.

For the error compound, the definition of each error should be the same, which means that the error involved should be the P-V value or RMS value in one direction. For simple addition method was not coordinate with the real situation, as the single error would be overestimated. The compound error could be expressed as

$$e_{norm} = \left[\sum_{i=1}^{n} |e_i|^p\right]^{\frac{1}{p}}$$

The maximum mirror aperture is 900 mm, and the stroke is expanded to be 1200 mm considering the mirror unload and grinding wheel dressing. For the XZC grinding mode, the grinding wheel just need to pass the center of the rotary table, and the actual stroke is 500 mm. The Z stroke is 440 mm as the mirror height is generally less than 200 mm, the grinding wheel axis is 165 mm above the bottom face of the spindle, and the effective grinding stroke is 140 mm. Overestimation of the stroke would cause more manufacturing difficulty and cost. The final effective workspace of the linear axis is X500 mm × Z140 mm.

According to the stroke and error compound equations, accuracy of each axis was checked. The final accuracy specification and mirror surface profile are listed in Table 1. All accuracy specifications are parameters in the effective workspace.

According to the error budget table, the theoretical prediction profile error is 7.43 μm. In the actual grinding process, to improve the surface profile, the compensation grinding should be carried out to reduce the interpolating motion error and grinding spindle rotary error.

Grinding Vibration Analysis

The grinding vibration analysis was to determine the influence factors of the shimmy, and the stiffness specifications and parameters selection would be carried out thereafter, and the shimmy influence toward the surface roughness and waviness would be reduced. Comparing the single diamond turning and multi-edge milling process, the force distribution in the contact area of the grinding wheel and mirror is

Table 1 UAG900 machining loop accuracy checking table

	P-V	
Error source	X direction (μm)	Z direction (μm)
X straightness	1	1
X positioning error	2	2
Z straightness	0.5	0.5
Z positioning error	0.5	0.5
Grinding wheel form error	2	2
Grinding wheel spindle runout	2	2
Grinding wheel wear	1	1
Workpiece runout	2	2
Temperature variation	1	1
Deformation by grinding force and thermal variation	1	2
P-V and RSS	3.60	3.74
RMS	6.91	7.43

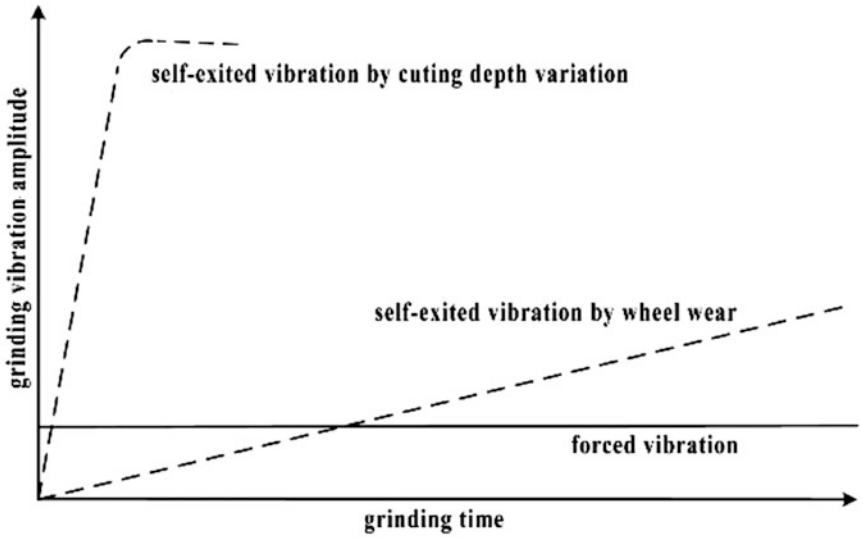

Fig. 6 Vibration amplitude variation in grinding

more complicated. The vibration in the grinding process consists of impulse vibration, forced vibration, and self-exited vibration as shown in Fig. 6. The impulse vibration generally originates from acceleration and deceleration, and it could be prevented by building the vibration-free basement, and the improvement of the machine stability and grinding track would also void the fierce acceleration.

The forced vibration was caused by the unbalance of the grinding wheel, spindle, or motors, and it would increase with the rotary table, not decrease with grinding time. The forced vibration would be attenuated by improving the balance level through the in-situation balancing device. The self-exited vibration was the result of the re-production effect between the grinding wheel and mirror. The cutting force will change with cutting depth during grinding process, and vibration would generate thereafter. The wear of the grinding wheel micro form would also cause the cutting force variation. The vibration described above could be measured using the force or acceleration sensor. Active or passive damping methods were generally adopted to restrict these vibrations.

The traditional grinding vibration analysis focused on the outer and inner cylindrical and flat grinding, and the control model was built with the cutting depth input. The control variable refers to machine stiffness, flexibility, workpiece, and grinding wheel's reproduction effect, and the cutting force is the output. With the aim of machining process stability, the machine's stiffness and damping specification would be determined or improved. The linear interpolating step changes continuously during the grinding process, and there are more grinding force influence factors than the traditional grinding process. The control theory is more complicated.

Vibration Model

For the XZC grinding mode, the main grinding force is F_N which would reflect the stiffness specification of the grinding wheel spindle, Z and Y axis as shown in Fig. 7. As the mass of the rotary table and X axis that carries the mirror is extremely large, the grinding force influence could be neglected. For any moment during the grinding process, the grinding wheel cutting depth equates the sum of the grinding wheel wear, material removal depth, the workpiece, and grinding wheel deformation, the equation could be transformed into transmission function, and according to the system stability theorem, the stiffness of the machine mechanical structure could be determined.

$$u_w = \delta_S + \delta_w + Y_m + Y$$

According to the brittle removal mechanism, the grinding wheel normal force is the main reason of the crack expansion which is also the reason of the residual subsurface damage as shown in Fig. 8. The grinding wheel wear grows with the grinding time. As the mirror profile accuracy is several millimeters or tens of millimeters, the actual cutting depth changes continuously.

The transmission function could be expressed as

$$\frac{Z_{\mathrm{W}}(S)}{K_W} \bullet \frac{1}{\mu_W e^{-\tau_W S} - 1} + \frac{Z_{\mathrm{S}}(S)}{K_S} \bullet \frac{1}{\mu_S e^{-\tau_S S} - 1} - \frac{1}{K_c} = \frac{G_m(S)}{K_m}$$

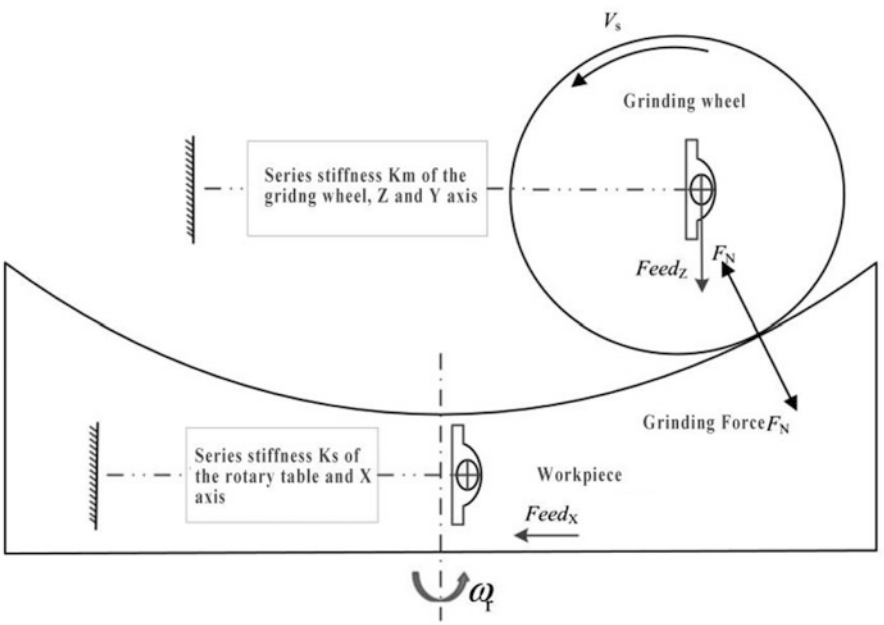

Fig. 7 Vibration model of the grinding system

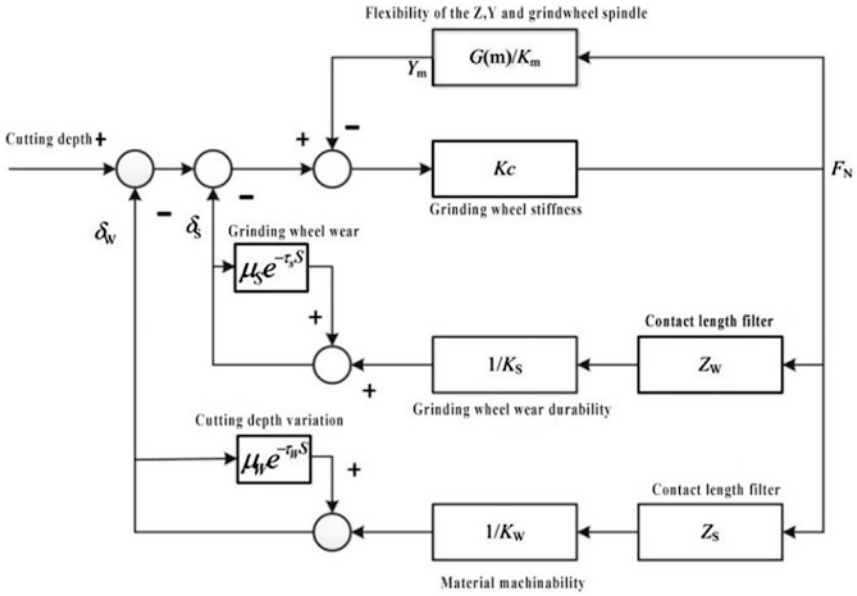

Fig. 8 Control theorem illustration for the wheel normal force

The grinding wheel contact length filter definition was given by Snoeys and Brown. The corresponding situation is that under the condition of the low grinding wheel speed and feeding velocity, the wear and cutting depth variation would not induce the vibration. According to the grinding contact area's depth variation, the filter *Zw* could be expressed as

$$Z_{\mathrm{W}}(jw) = \begin{cases} 1 & \omega/2\pi < V_W \quad /l_c 2 \\ 0 & \omega/2\pi < V_W \quad /l_c 2 \end{cases}$$

For the depth variation in the workpiece grinding contact area, the filter *Zs* could be expressed as

$$Z_{\mathrm{S}}(jw) = \begin{cases} 1 & \omega/2\pi < V_S \quad /l_c 2 \\ 0 & \omega/2\pi < V_S \quad /l_c 2 \end{cases}$$

For the above expression, ω equates the wheel speed, its unit is rad/s, V_w and V_s is the workpiece and grinding wheel's linear velocity, and L_C is the length of the cutting area.

Grinding System Stability Condition

The sufficient and necessary condition of the system stability is that all the extreme point's real part is minus, the grinding vibration system is the closed loop, and the

transmission function extreme point calculation result could be used to justify the system stability. The transmission function could be changed as

$$G_m(S) = \frac{K_m}{K_W} \bullet \frac{1}{e^{-\tau_W S} - 1} + \frac{K_m}{K_S} \bullet \frac{1}{e^{-\tau_S S} - 1} - \frac{K_m}{K_c}$$

taking $S = J\omega$ into the above equation

$$G_m(S) = \frac{K_m}{K_W} \bullet \frac{1}{e^{-j\tau_W \omega} - 1} + \frac{K_m}{K_S} \bullet \frac{1}{e^{-j\tau_S \omega} - 1} - \frac{K_m}{K_c}$$

According to the above equation and parameters table, the vector track to determine the grinding vibration frequency response is shown in Table 2.

According the Nyquist illustration, the cutting parameters could be connected with the system stability directly as shown in Fig. 9. For the grinding process, the grinding wheel speed should be connected with the machine, wheel and contact area stiffness, the suitable wheel speed, and grinding depth would be chosen properly. Combining with the above illustration, taking the wheel speed as the variable, the system stability could be determined using the $1/(K_m/2K_s + K_m/K_c)$. The first step is to determine the minimum real value of the transmission function.

$$\mathrm{R}_{\mathrm{emin}}(G_m(j\omega)) = \frac{K_m}{2K_W} + \frac{K_m}{K_S} + \frac{K_m}{K_c}$$

To determine the wheel speed corresponding to the system stability, the following method could be used.

Table 2 Typical parameter of the aspheric mirror grinding

	Item	Specification	Notes
Workpiece	K_m	10 N/μm	K_m, including mirror, X axis and rotary table
	D_w	20 mm	Grinding wheel width
	ω_m	2000 r/min	Grinding wheel speed
	ζ_m	0.05	Damping parameters
	Material	Zerodur	
Grinding wheel	K_c	100 N/μm	K_c, including grinding wheel, Z and Y axis
	D_s	400 mm	Grinding wheel diameter
	H	70 MPa•m$^{1/2}$	Grinding wheel crack toughness
	l_c	1.85 mm	Contact area length
	c	50 μm	Grinding depth
Grinding process parameters	V_w	0.13 m/s	Workpiece linear velocity
	V_s	28 m/s	Grinding wheel linear velocity
	f	2 mm/min	Interpolating axis linear velocity

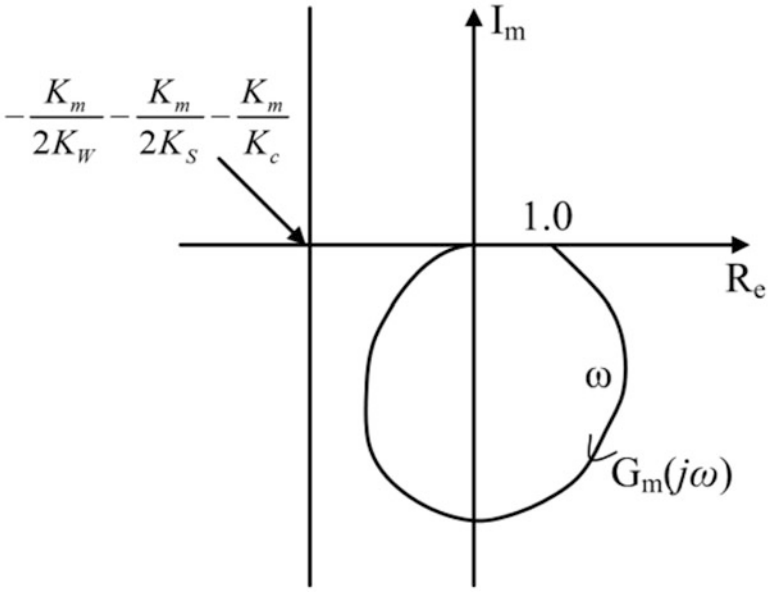

Fig. 9 Nyquist illustration of grinding vibration frequency response

1. As K_w and K_s are inverse ratio of the cutting depth, reducing the wheel cutting depth, the minimum ($K_m/2K_w + K_m/K_s$) could be determined. Drawing the vertical line by this value, the line would intersect with the track with n points, and the corresponding ω_i ($i = 1, 2,\ldots,N$) could be determined.
2. ω_i, determined in step (1), means the vibration condition for the given stiffness condition and the corresponding grinding force variation would cause the waviness change.

$$\omega_i \tau_{si} = \frac{\omega_i}{N_{si}} = 2\pi(n_s + \nu_{si})$$

in which n_s is positive integer, ν_{si} lies between 0 and 1.

$$\frac{1}{1 - e^{-j\tau_{si}\omega_i}} = \frac{1}{1 - e^{-j2\pi\nu_{si}}}$$

According the intersection point coordinate, ν_{si} could be determined.

$$-\frac{K_m}{2K_W}\frac{1}{1 - e^{-j2\pi\nu_{si}}} - \frac{K_m}{K_S} = G_m(j\omega)$$

3. Supporting that $n_s = 0$. According to ω_i and ν_{si}, τ_{si} and N_{si} could be determined.
4. Increasing n_s step by step, N_{si} was calculated according to step (3), the system stability could also be determined. With the increase of n_s, the unstable area and

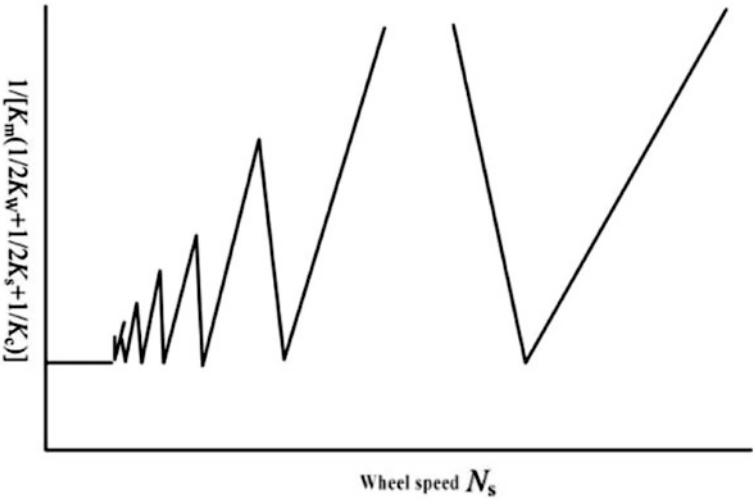

Fig. 10 Grinding machine vibration

stable area became overlapped, and the bigger n_s could be neglected as shown in Fig. 10.

Grinding Machine Stiffness Budget

According to the vibration condition, the stiffness specifications of the each axis could be determined, and K_M is the compound stiffness of the each axis (Fig. 11). The total stiffness could be expressed as following (Rivin 1999).

$$K_{\text{Series}} = \left(K_1{}^{-1} + K_2{}^{-1} + K_3{}^{-1}\right)^{-1}$$

The aspheric mirror grinding system contains the mirror and grinding wheel subsystems. The workpiece subsystem consists of rotary table, x axis, and fixture. The wheel subsystem consists of grinding wheel, spindle, and Z and Y axes. According to the series system stiffness calculating method, the subsystem stiffness of workpiece and wheel satisfies the following equation.

$$\begin{cases} \dfrac{1}{Kz} + \dfrac{1}{K_y} + \dfrac{1}{K_S} + \dfrac{1}{K_w} \geq \dfrac{1}{K_c} \\ \dfrac{1}{K_r} + \dfrac{1}{K_x} + \dfrac{1}{K_f} \geq \dfrac{1}{K_m} \end{cases}$$

According to the system stability justification method, the stiffness specification could be calculated respectively, as shown in Table 3.

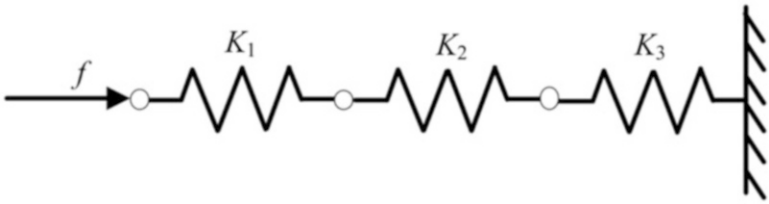

Fig. 11 Series spring stiffness illustration

Table 3 UAG900 unit stiffness design value

	Unit	Specifications (N/μm)	Notes
$K_m = 487$ N/μm	Rotary table	1000	Hydrostatic bearings
	X	1000	Hydrostatic guideways
	Fixture	20,000	45#
$K_c = 217$ N/m	Grinding wheel spindle	400	Hydrostatic bearings
	Z	1000	Hydrostatic guideways
	Y	1000	Hydrostatic guideways
	Grinding wheel	10,000	Aluminum base

Conclusion

The general design principles and methods were described by this chapter. The separated metrology frame was especially introduced, and the error compensation method would be widely applied in the future. In order to illustrate the design procedure, the large aspheric mirror grinding machine design case was given, and the design case contains the machining process, machine configuration, and stiffness design procedure.

References

Dornfeld D, Lee D-E (2008) Precision manufacturing. Springer Science + Business Media, New York

Hale LC (1999) Principles and techniques for designing precision machines. Lawrence Livermore National Laboratory, University of California, Livermore

Rivin EI (1999) Stiffness and damping in mechanical design, 1st edn. Marcel Dekker Press, Oxford

Slocum AH (1992) Precision machine design. Prentice Hall College, Prentice Hall

Whitehouse DJ (1994) Handbook of surface and nanometrology, 1st edn. Institute of Physics Publishing, Bristol/Philadelphia

Structure Design of Precision Machines

3

Huiying Zhao and Shuming Yang

Contents

Introduction 58
Forward Design of Ultraprecision Machine Tools 60
Machining Mechanism and Process Test 60
The Basic Requirements of Ultraprecision Machine Tools 61
Factors That Affect Precision and Ultraprecision Machining 62
Processing Mechanism 62
Materials to Be Processed 63
Processing Equipment and Its Components 63
Processing Tools 64
Structure Layout of Precision Ultraprecision 64
T-Shaped Layout 65
Cross Slide Structure 65
Vertical Structure Layout 67
Gantry Structure Layout 67
Gantry Structure Layout 67
Processing Technology Test 69
Error Distribution (Jianpu 2015) 73
Linear Axis Accuracy Analysis of Indicators 74
Large-Diameter Aspheric Ultraprecision CNC Grinding Machine Design (Bin 2015) 75
Large-Diameter Aspheric Mirror Grinding Process Analysis 76
High Efficiency 76
High Precision 77
Low Subsurface Damage 77
Machine Configuration Scheme 78
Grinding Mode Selection 78

H. Zhao (✉)
School of Mechanical Engineering, Xi'an Jiaotong University, Xi'an, Shaanxi, China
e-mail: bjzhaohuiying@163.com

S. Yang (✉)
State Key Laboratory for Manufacturing Systems Engineering, Xi'an Jiaotong University, Xi'an, Shaanxi, China
e-mail: shuming.yang@mail.xjtu.edu.cn

Z. Jiang, S. Yang (eds.), *Precision Machines*, Precision Manufacturing,
https://doi.org/10.1007/978-981-13-0381-4_2

Wheel Selection 79
Wheel Shape 79
Wheel Particle Size and Binder 80
Wheel Dynamic Balance 80
Wheel Dressing 81
Machine Structure Layout 81
Machine Tool Precision Estimation 83
Grinding Vibration Analysis 84
Vibration Model 86
Grinder Motion Axis Rigidity Distribution 88
Conclusion 90
References 90

Abstract

This chapter starts with the ultraprecision processing technology and then analyzes the route of ultraprecision machine tools' forward design and the relevant factors based on cutting mechanism, principal components, and processing technology. According to the ultraprecision machine tools in the market, several kinds of conventional ultraprecision machines' design configurations are introduced, and the design of the ultraprecision aspheric grinding machine is discussed in detail.

Keywords

Ultra-precision processing technology · Ultra-precision machine tools forward design · Ultra-precision aspheric grinding machine design

Introduction

The mechanical manufacturing industry is the foundation of social and economic development, which provides the necessary equipment and technology for the economic sectors. Because of the pursuit of better processing technology, mechanical manufacturing needs to be more precise (Thompson 2007).

Ultraprecision machining technology is a system engineering, which contains a cutting mechanism, instruments, machine tools, measurement, processing technology, and environmental factors (DeBra et al. 1990; Kim and Kim 1995). The machine tool is the most critical technical carrier. Every country in the world pays much attention to the development of ultraprecision machine tools. With the emergence of new materials, new products, and new application technology, ultraprecision machine tool has been developing all the time (Cheng et al. 2008) rapidly.

Ultraprecision machine tools can be classified from different perspectives (McKeown and Corbett 2004). According to the different generalizations, it can be divided into universal ultraprecision machine tool (with strong universality and complete function, it can process a variety of different parts such as aspheric lens, laser mirror, disk substrate, and oil distribution dish) and special ultraprecision machine tool (with simple structure, it is used for processing certain kinds of

parts) (Brinksmeier et al. 2010). According to different machining methods, ultra-precision machine tools can be divided into ultraprecision cutting machine, ultra-precision grinding machine, ultraprecision lapping and polishing machine, and ultraprecision special machining equipment (Yuan et al. 2010). The classification of ultraprecision machine tools is shown in Fig. 1.

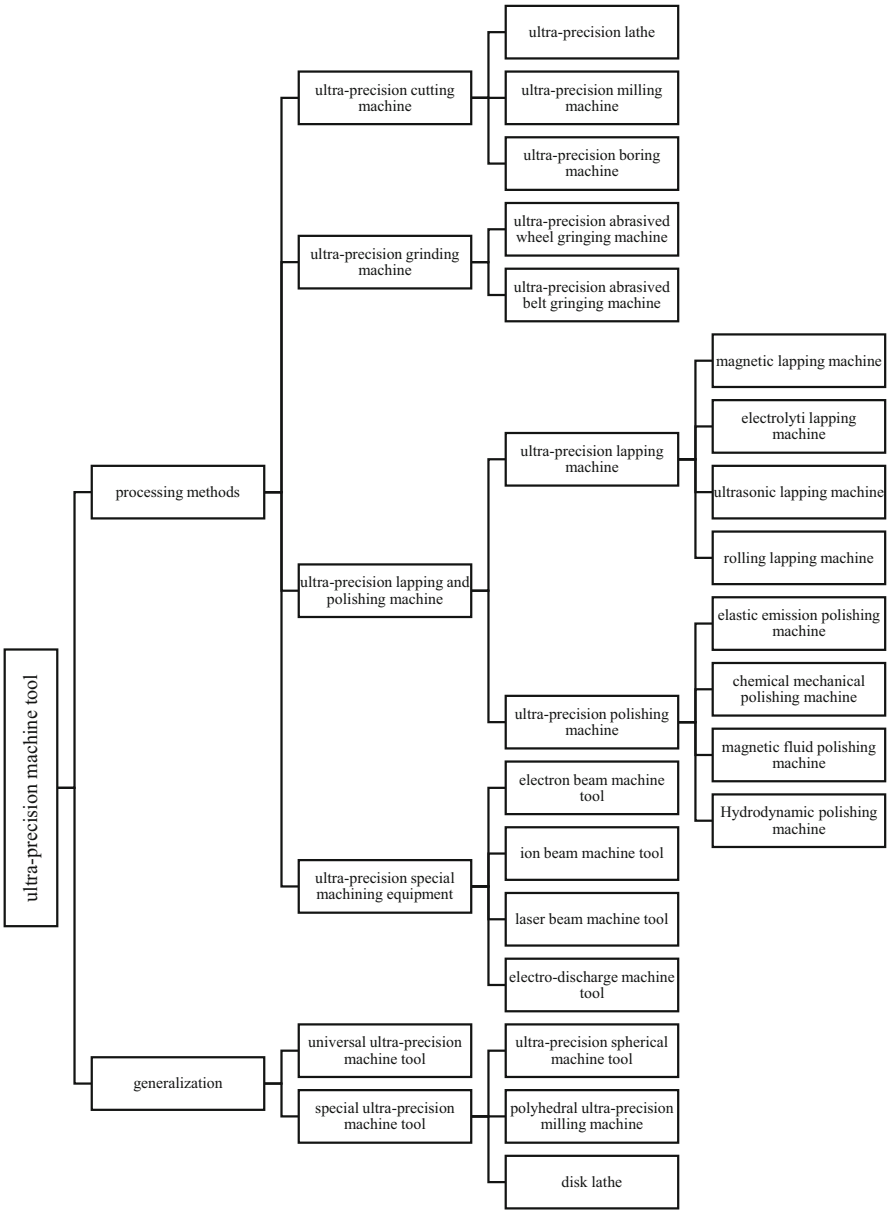

Fig. 1 Classification of ultraprecision machine tools

For ultraprecision cutting machine, natural single-crystal diamond tool is used for processing copper, aluminum, germanium, and other soft metal (Lee et al. 1999). The ultraprecision diamond lathe was used at the earliest and developed at the soonest. At present, it makes progress toward high precision, high stiffness, and enlargement (Cheung and Lee 2000). The processed materials also change to hard, brittle materials such as optical glass. The surface roughness and roundness of the processed workpiece can reach Ra 0.005–0.0008 μm and 0.01 μm, respectively.

The ultraprecision grinding machine tool is mainly used for processing ferrous metals, ceramics, optical materials, semiconductor functional materials, and the other hard, brittle materials. The surface roughness and profile accuracy of the processed workpiece can reach Ra 0.005–0.0001 μm and 0.5 μm, respectively.

Ultraprecision lapping and polishing machine tool is mainly used for processing ceramics, optical materials, semiconductor functional materials, and the other hard, brittle materials (Kuriyagawa et al. 2002). The surface roughness and profile accuracy (PV) of the processed workpiece can reach Ra 0.8–0.1 nm and 30 nm, respectively.

Ultraprecision special machining equipment uses physical and chemical non-traditional machining methods and complex machining methods to complete ultra-precision processing. It is suitable for processing both difficult-to-process parts and flexible deforming parts.

Forward Design of Ultraprecision Machine Tools

The forward design of ultraprecision machine tools has many unique features as follows (Dornfeld and Lee 2008).

Ultraprecision machine tools are almost at the limit of precision, so the precision transmission, long-term stability, precision margin design, self-discipline correction, evolution, and correction are all problems.

Due to the requirements of high precision, regarding stiffness, strength, and damping design methods, the distribution of environmental parameters and process parameters under ultraprecision conditions may affect the work of ultraprecision machine tools and also bring new challenges to the design and manufacture of machine tools.

The simpler, the better for the ultraprecision machine tool, including the simplified drive chain, dimension chain, force flow chain, and measurement chain. However, the means to achieve high-precision machine tool technology should use more complex high technologies, which require new design methods and technologies.

Machining Mechanism and Process Test

Generally, there are two aspects of ultraprecision machine tool design: (1) design the configuration of the machine tool according to the results of the research and the test of the machining process; and (2) based on the existing manufacturing technology of critical components and parts of machine tools, relevant configuration of ultra-precision machine tool can be developed and designed.

Ultraprecision processing is the atomic-scale processing, so the structure of materials is the most crucial question for ultraprecision processing (Furukawa and Moronuki 1988). For example, crystal material is generally regarded as lattice structure in the perspective of material structure, but it is not strictly latticed structure, because (1) the crystal boundary is not infinite. For example, the length of a unit cell of copper is 361 pm; there are 2.8 × 106 unit cells in a 1-nm-long crystal. Although the copper atoms are located in the edge and cannot overlap with other atoms through translation, the amount of atoms on edge is much fewer than all the atoms, and the number of atoms in the whole crystal is huge, so it can be regarded as lattice structure approximately; (2) the particle in the crystal is vibrating all the time, which changes the distances of the molecule and destroys the periodicity of the structure. However, the amplitude of the particles is much smaller than the periodicity of the structure so that the crystal can be regarded as a periodic structure. (3) There may be some impurities during crystal growths, the arrangement of particles is not strictly neat, and there are some defects and dislocations. So, the lattice theory is a kind of preferable description (Guangxian and Xiangyun 2010).

According to the material structure, ultraprecision processing is a kind of atomic-scale removal (Taniguchi 1983). The methods of removal should be confirmed before the ultraprecision machine tool design, such as turning with a diamond tool, milling with a diamond tool, grinding with a diamond wheel, or chemical-mechanical polishing (CMP). Based on the removal mechanism of the above methods, engineers should do some related experiments and gain the processing report, which can provide basic requirements for design, manufacture, and processing of ultraprecision machine tool.

There are many kinds of ultraprecision machine tools. Although their principles and methods are different, they have a lot of inheritable common necessary components and technologies (Brinksmeier et al. 2010). All countries in the world pay much attention to the research and development of these essential components and critical technologies. On the one hand, only first essential components can guarantee the high-quality machine tools. Therefore, emphasis should be placed on the development and research of essential components to continuously raise the level of processing equipment and expand its application scope. On the other hand, an excellent series of essential components can respond quickly to market needs and shorten the development cycle of the ultraprecision machine tool. The essential elements and critical technologies of ultraprecision machine tools include the following parts: the overall structure of the machine tool, ultraprecision moving parts, ultraprecision motion driving components, ultraprecision micro-feeding device, ultraprecision motion detection system, and ultraprecision computerized numerical control (CNC) technology.

The Basic Requirements of Ultraprecision Machine Tools

The research and development of ultraprecision machine tool are based on the application of processing and the design of technical parameters for the process. It relies on the technical parameters to design ultraprecision machine.

The ultraprecision machine tool is a piece of crucial necessary equipment; the basic requirements of ultraprecision machine tools are listed as follows (Dornfeld et al. 2006):

1. High precision: including high static precision and dynamic accuracy. The leading performance indicators are geometric accuracy, positioning accuracy and repeat positioning accuracy, and resolution, such as the rotation accuracy of spindle, motion accuracy of the guide rail, and indexing accuracy of the rotary table.
2. High stiffness: including static stiffness, dynamic stiffness, and thermal stiffness; at the same time, we should also consider the stiffness and contact stiffness of the processing system consisted by the workpiece, machine tools, tools, and fixtures.
3. High stability: the equipment is required to withstand transport and storage test and maintain high precision, anti-interference, and anti-vibration in the course of use.
4. High automation: in order to ensure the quality of processing and reduce the impact of human factors, the equipment should have a higher degree of automation.

Factors That Affect Precision and Ultraprecision Machining

There are many factors influencing the precision and ultraprecision machining: the machining mechanism, the processed materials, processing equipment, and their basic components, machining tools, means of detection and error compensation, process design, fixture design, skill level, and so on. The sketch map of the influencing factors is shown in Fig. 2.

Processing Mechanism

1. New process and new method. In recent years, new methods of new processing continue to appear; we should pay full attention to seek new means of processing.

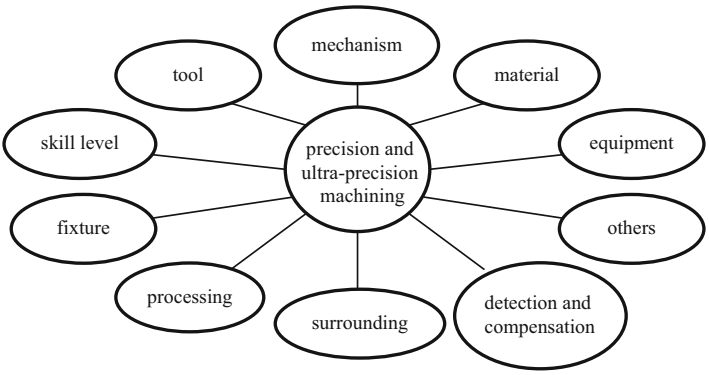

Fig. 2 Influence factors of precision ultraprecision machining

In the nontraditional processing, electron beam, ion beam, laser beam, and other high-energy beam processing, microwave processing, ultrasonic machining, etching, electrical discharge machining (EDM), electrochemical machining, and other methods emerge. These are innovated in the processing mechanism. The emergence of new processing mechanisms marks a technological breakthrough, which is the growth point of new technologies.

2. New concept of processing mechanism. Breakthrough in the processing mechanism is clearly stated in the removal processing, combined processing, and deformation processing. Especially the emergence of the "pile" of processing technology, which is represented by rapid prototyping manufacturing, became a milestone in the way of technical innovation.
3. Extremely thin processing has unlimited vitality. The goal and pursuit of ultraprecision processing are to seek and explore the processing limit. The current level of ultrathin cutting is nanoscale. With the development of science and technology, this limit will gradually move forward, and there are many problems worth studying.
4. The principle of evolutionary processing is worth promoting. With the help of special processing, computer technology, sensor technology, and machine tool equipment whose accuracy is lower than the required workpieces can be used to process the required parts directly or indirectly. This principle of evolution will affect the layout of precision machining and ultraprecision machining.

As we can see from above, processing mechanism research is the theoretical basis of ultraprecision machining and the source of new technologies. It is the essence of processing methods and the key to the development of machine tool.

Materials to Be Processed

For materials used for precision machining and ultraprecision machining, its chemical composition, physical and mechanical properties, and processing performance are strictly required. It should be uniform in texture, with stable performance and consistent, no external and internal micro-defects. The error of the chemical composition should be in the order of 10^{-2}–10^{-3} with little or no impurities. Its physical and mechanical properties, such as tensile strength, hardness, elongation, elastic modulus, thermal conductivity, and expansion coefficient, should reach 10^{-5}–10^{-6} order of magnitude. Smelting, casting, rolling, heat treatment, and other processes also should be strictly controlled. Temperature, slag filtration, grain size, uniformity, and direction of the material have a significant impact on the mechanical processing (Somiya 1984).

Processing Equipment and Its Components

Precision machining and ultraprecision machining are using a wide range of processing equipment, such as laser processing machines, precision EDM

machines, ion beam processing machines, coating, and other processing equipment. For machining equipment, the typical machine tool is ultraprecision lathe for machining various kinds of shafts, disk covers, curved surface parts, etc. The ultraprecision milling machine is equipped with a precision swivel table for machining flat surfaces and polyhedrons parts. Grinders and polishers are important precision machining equipment for machining cylindrical, hole, flat, and aspherical parts.

Precision and ultraprecision machining equipment and their basic elements and components are closely related. On the one hand, only first basic elements can provide excellent processing equipment; on the other hand, good series of basic components can respond quickly to the market demand and shorten the development cycle of precision machining and ultraprecision processing equipment.

Processing Tools

Processing tools mainly refer to cutting, abrasive, sharpening and trimming device. The selection of tools and abrasive materials is the key point. The history of the development of tool grinding tools is mainly represented by the development of cutting tool materials. From carbon steel, alloy steel, cemented carbide, ceramics, cubic boron nitride to diamond, as well as the use of multiple co-infiltration, coating, deposition, and other technologies to improve durability, the emergence of superhard materials provided conditions for precision machining and ultraprecision machining.

Structure Layout of Precision Ultraprecision

We can see from the above factors that affect the precision ultraprecision machining that the study of precision machining technology involves many disciplines and it is a comprehensive technology (Park et al. 2009). Only the integration of technical achievements in various fields can achieve precision and ultraprecision machining.

Precision and ultraprecision machine tools are the first conditions to achieve precision ultraprecision machining. The problem to be studied here is the overall configuration of the machine tool, the rotation accuracy of the spindle, the linear motion accuracy of the workbench, the micro-feed precision of the tool, the optimized design of the system software, and the optimization of the processing technology.

When designing ultraprecision machine tools, the overall layout is critical and plays a decisive role in the performance and accuracy of the machine (Koenigsberger and Tlusty 2016). Ultraprecision machine tools are often very different from the traditional machine tools in the structure layout, and the favorite layouts are the T-shaped layout, cross-shaped slide block layout, vertical layout, and other structures.

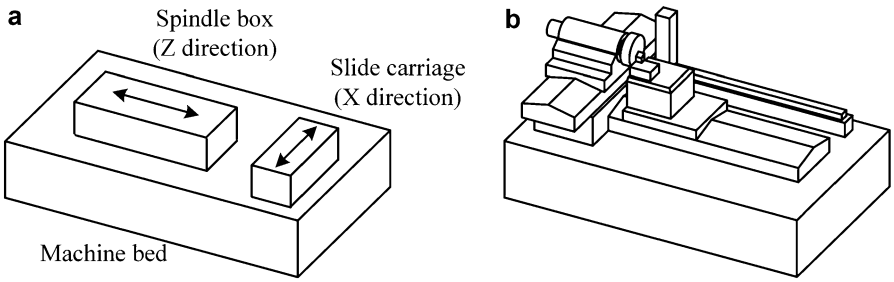

Fig. 3 T-shaped layout

T-Shaped Layout

These ultraprecision machine tools often use Z and X motion separation structure. The spindle box brings the workpiece for longitudinal movement (Z-direction) and lateral movement (X-direction) by the slide carriage, as shown in Fig. 3a. Z- and X-direction rails are placed on the machine bed, forming a T-shaped layout so that the two rails are at the same basic level. T-shaped layout structure is conducive to improving the manufacturing precision and precision of the guide rail. Moreover, the dual-frequency laser measuring system for detecting the Z-direction and the X-direction moving position can be mounted on a fixed bed, and only the reflecting mirror is in the Z- and X-direction of the moving parts. This not only makes the measurement system installation much simpler but also dramatically improves the measurement accuracy. This layout gives the machine a high overall stiffness and makes it relatively easy to control. For instance, most ultraprecision lathes manufactured by Pneumo use this layout. Now small-sized and medium-sized ultraprecision machine tools often use this overall layout.

There is another T-shaped overall layout; the spindle moves in X-direction; tool holder skateboard moves in Z-direction. Both the X-direction and Z-direction rails are put on the machine bed, as shown in Fig. 3b. Moreover, many ultraprecision lathe structures use this T-shaped structure.

Cross Slide Structure

For this kind of layout, its headstock position is fixed; tool carrier is mounted on the cross-shaped slide carriage. Z- and X-direction rails are concentrated on the table (or slide), which form a cross-shaped slide. Figure 4 shows the structural layout of the NANO800 ultraprecision CNC lathe designed by Beijing Machine Tool Research Institute. The spindle shaft is fixed on the bed of the machine tool. The Z-direction slide plate is made of guide rails on both sides and the upper surface of the bed; the X-direction slide plate is located

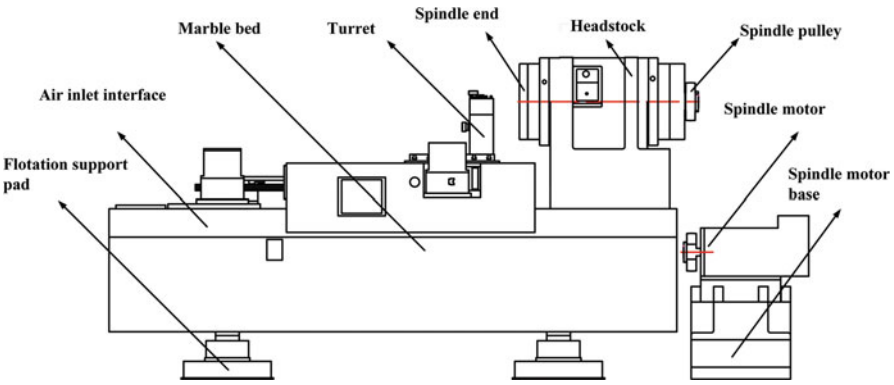

Fig. 4 Cross-shaped slider consisting of X and Z two-way table

Fig. 5 Cross slide X and Z two-way table structure diagram

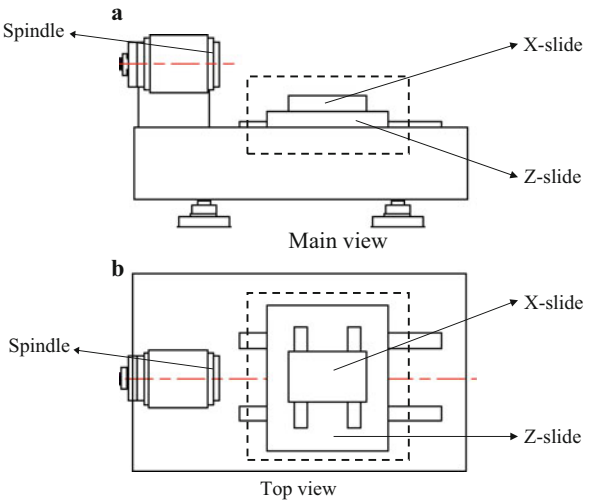

within the framework of the Z slide. Both the spindle shaft and Z- and X-direction guideway use the aerostatic structure. The machine can be equipped with a turntable on the X slide, which facilitates the machining of spherical parts. The machining diameter of the machine is Φ800 mm; the processing surface roughness Ra is less than 1 nm.

Figure 5 is another form of cross slide structure, the main shaft is fixed to the machine bed, Z slide is supported by rolling linear guide, and X slide is located above the Z slide. The spindle shaft system adopts the aerostatic structure; Z- and X-direction guide rails adopt the rolling linear guide rail auxiliary structure. The machine is conducive to processing the parts with high requirement of surface roughness. The machined parts' diameter is Φ300 mm the processing surface roughness Ra is less than 10 nm.

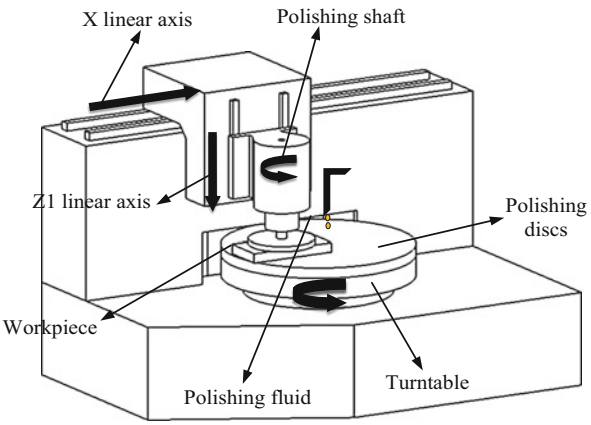

Fig. 6 Cross-shaped slider consisting of X and Z two-way table

Vertical Structure Layout

When processing the workpiece with large diameter and weight, the vertical structure layout is used in large-scale ultraprecision machine tools. In order to ensure high rigidity requirements of the ultraprecision machine tool, gantry and vertical wall structure are used, as shown in Fig. 6. It is the ultraprecision lathe structure; the turntable is put in the center of the bed, Y slide is put in the vertical wall, and the Z slide is put above the Y slide. This structure is characterized by the good rigidity of the wall structure and helps to ensure the accuracy and stability of the Y slide.

Gantry Structure Layout

As shown in Fig. 7, it is a small grinding machine CNC polishing machine structure; its structure is a gantry structure. The X slide plate is placed on the bed and equipped with CNC rotary table to bear polished parts; Y-axis is set on the gantry, Z slide is placed on the Y slide, and the polish spindle is on the Z-axis slide to achieve polishing.

Gantry Structure Layout

Large-diameter ultraprecision CNC aspheric milling machine is shown in Fig. 8. Its structure is the vertical gantry structure; beam and Z-axis are symmetrically designed. It can be used to process the aspheric surface optical components with 1000 mm diameter.

Machine bed and column are made by the whole granite, which can ensure high stiffness, high stability, and strong anti-vibration damping capacity. The hydrostatic spindle is driven by a built-in synchronous motor. The linear motion axes X, Y, and Z are hydrostatic guide rail to achieve high stiffness and high-precision motion control.

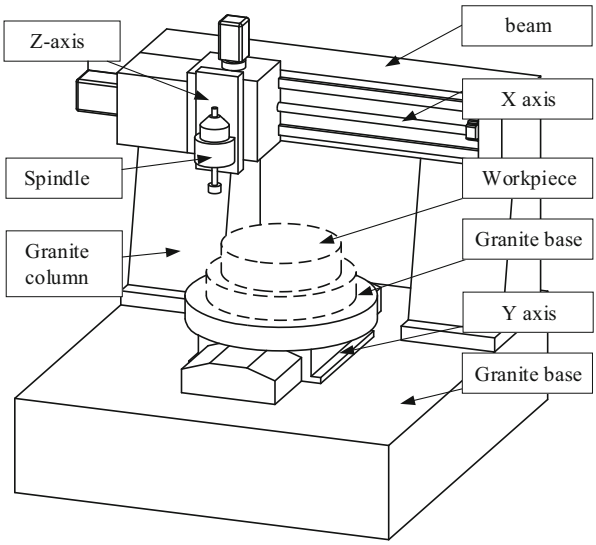

Fig. 7 Gantry CNC polishing machine structure diagram

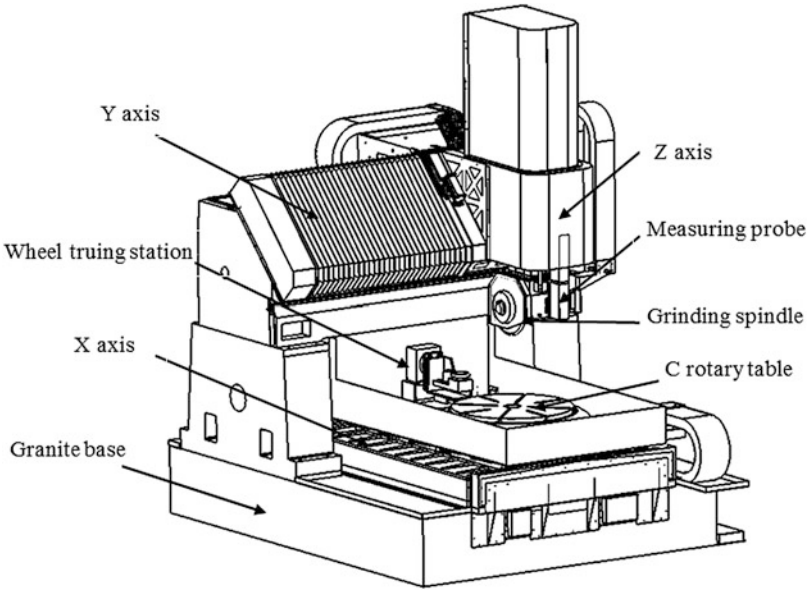

Fig. 8 Assembly drawing of large-diameter ultraprecision CNC aspheric milling machine-UAG900

X- and Y-axes are driven by T-linear motor Z-axis uses servomotor and high load precision ball screw. Three axes use high-precision grating line displacement sensor for full closed-loop control, which can achieve high-precision positioning accuracy. The machine uses a hydrostatic turntable and is driven by a built-in torque motor,

with high-precision grating angular displacement encoder for angle feedback. When machining a symmetrical aspheric surface, X-axis, Z-axis, and turntable are linked for ultraprecision grinding. The machine is equipped with a wheel dresser, which can finely adjust the wheel according to the characteristic requirements of the machined parts to ensure the machining precision of the parts.

The fine grinding process needs to complete the following three tasks:

1. Improve the shape accuracy: generate the smallest contour of the designed aspheric surface.
2. Reduce the surface damage: to minimize subsurface damage caused in milling and reduce the necessary polishing time.
3. Avoid the IF (intermediate-frequency) error: to minimize the surface ripple with frequency from 0.05 to 10/mm.

Processing Technology Test

The design basis of the machine tool is the processing technology oriented to a specific processing object. After the processing object is determined, the materials need to be tested, the technical processing requirements, and the processing technology need to be adopted are analyzed according to the technical requirements of the processing object. On the basis of this, we can design technical solutions for machine tools.

1. Multiparameter coupling model of kinematic pair's dynamic characteristics and the subsurface damage layer

Subsurface damage is the residual crack, and processing defect after the material is removed. The crack distribution depends on the contact area shape and contact force. Based on the crack propagation model in fracture mechanics, the subsurface damage layer is expressed as a function of contact force and contact area. Ideally, the contact area depends on the shape of the cutting tool and the depth of cut. The error of the kinematic pair can cause a change in the contact area. The XYZ spatial error component is introduced into contact area expression as the disturbance. Comprehensive analysis of the error component of the contact area is done. Based on the vibration model in classic dynamics, the cutting force is expressed as a function of the kinematic stiffness and damping characteristics. Coupling the expression of the contact area, a coupled model of the accuracy, stiffness, and damping index of motion pairs with subsurface damage is established.

With the dynamic model of ultraprecision aspherical grinder shown in Fig. 9a, the contact force between the grinding wheel and the workpiece is expressed as a nonlinear correlation function with kinematic stiffness, damping, and accuracy as parameters (Rowe et al. 1993). In Fig. 9, k, c, and m are the equivalent stiffness, damping, and mass of the kinematic secondary subsystem, respectively. Because the strength of grinding wheel and workpiece is much higher than that of the kinematic pair, the grinding wheel is equivalent to a rigid body. Moreover, the expression of

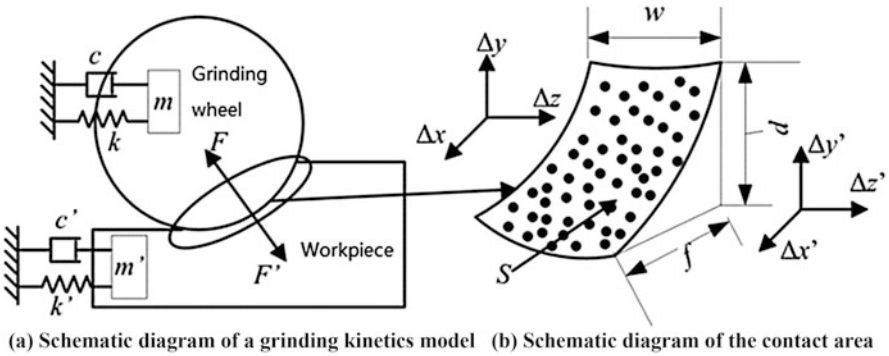

Fig. 9 Grinding contact area diagram. (**a**) Schematic diagram of a grinding kinetic model. (**b**) Schematic diagram of the contact area

cutting force with dynamic stiffness and damping as the variables is determined. Assuming that a single abrasive particle suffers the same grinding force, the grinding force of a single abrasive particle is determined according to the number of abrasive particles. The expression function of kinematic parameters and the subsurface damage of the kinematic pair are obtained. The grinding contact area is equivalent to the torus, as shown in Fig. 9b, where w, d, and f are the contact width, length, and depth of the grinding wheel with the workpiece, respectively. According to the geometrical parameters of the grinding wheel and the grinding parameters, the calculation formula of the contact area S is determined by the calculation geometry method. Combined with the contact area and the distribution density of abrasive particles, the number of abrasive particles in the contact area is determined. The dynamic errors of XYZ direction of the grinding wheel and workpiece movement pair are introduced into the calculation formula of the contact area as variables.

2. The peak and spatial distribution of subsurface damage

The material loss during grinding is caused by the intersection of indentation cracks (Xu et al. 1996). According to the above coupling model, the cutting parameters and system space coordinates are used as the boundary conditions to study the peak and spatial distribution of subsurface damage. The spatial error of the system during processing is related to the processing state. Different technological parameter combinations show different system states, and the final performance is the relative position change between the tool and the workpiece. The precision, stiffness, and damping response of the kinematic subsystems under different spatial positions and machining parameters were analyzed. The coupled model was established to study the peak and spatial distribution of subsurface damage.

Subsurface damage is the residual crack after the cross-crack removal in the ultraprecision grinding test (Huang et al. 2003). Two kinds of crack propagation models are shown in Fig. 10(a) and (b). The dynamic response of the kinematics

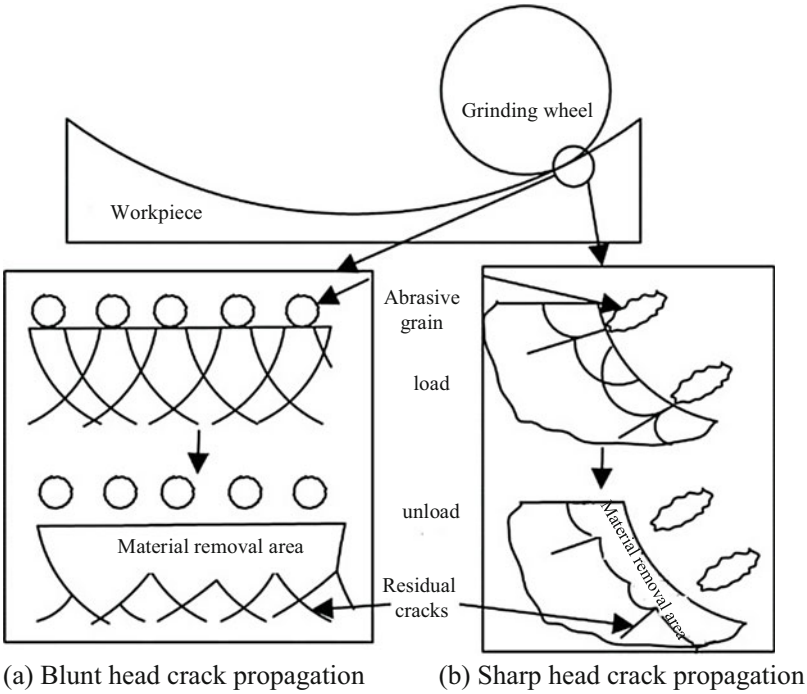

Fig. 10 Grinding fracture removal mode. (**a**) Blunt head crack propagation. (**b**) Sharp head crack propagation

depends on different grinding parameters and machining positions. Grinding parameters include cutting depth, feed rate, grinding wheel speed, and grinding point in the processing space. The cutting depth and feed rate are introduced into the formula of the contact area, and the kinematic response caused by feed speed and wheel speed is introduced into the dynamic model as a gain to achieve a comprehensive analysis of subsurface damage. The unilateral and multivariable boundary conditions were used to analyze the effect of grinding parameters on subsurface damage. The coordinate value of grinding point in the processing space is introduced to realize the global deterministic control of subsurface damage.

3. The influence of different supporting forms of the kinematic cutting system on subsurface damage

The effect of a grinding system constructed by rolling, sliding, liquid, and gas hydrostatic support motion pairs on subsurface damage was studied, respectively. Different bearing support forms have different dynamic parameters. According to the coupled model, the dynamic characteristics of different support forms are set as the boundary conditions to calculate and simulate the subsurface damage distribution of the set grinding system.

In order to study the influence of dynamic characteristics of different supporting forms on the subsurface damage of hard and brittle material grinding, three-dimensional software was used to build the grinding system of rolling, sliding, liquid, and gas hydrostatic support kinematic pair, respectively. After setting the same grinding parameters, the dynamic accuracy, stiffness, and damping characteristics of the constructed system are simulated and analyzed by using the analysis software ADAMS and ANSYS. Moreover, the obtained dynamic characteristic simulation value is brought into the subsurface damage coupling model proposed in the content (1) to realize the simulation analysis of the subsurface damage caused by the dynamic characteristics of different support forms.

4. Coupling model verification based on cutting process test and dynamic characteristic parameter monitoring

According to the cutting system constructed by the kinematic pair of different support forms, the dynamic accuracy, rigidity, and damping characteristics of the kinematic under cutting condition are obtained by experiments (Zhang et al. 2003). Moreover, then the cutting force and the contact area of the cutter are obtained. Cutting, polishing, and scanning electron microscope are combined with a measurement method to get the depth of subsurface damage detection cutting element. According to the subsurface damage layer obtained by the analysis of the law, the established coupling model is verified and optimized.

The dynamic accuracy, stiffness, and damping characteristics of the kinematic pair were obtained by experiments, and then the values of the cutting force and the contact area of the grinding wheel were obtained (Zaghbani and Songmene 2009). The distribution density of the abrasive grains was obtained using image acquisition and statistical analysis; the model of cutting force and contact area coefficient is directly related to the depth of subsurface damage layer. The displacement, velocity, and acceleration of the contact points in the linear and rotational movement are obtained, respectively, by a laser interferometer and eddy-current sensor. The use of precision diamond cutting, polishing, and scanning electron microscopy combined measurement can complete one-dimensional detection of subsurface damage depth. By polishing the grinded surface, the two-dimensional measurement of subsurface damage is achieved. Based on subsurface damage obtained by the peak value and distribution of validation, the prediction model is established. The dynamic characteristic parameters and the subsurface damage peak value and distribution are analyzed synthetically. Combined with the established coupling model, the method of dynamic subsurface dynamic characteristic parameter design and optimization of grinding process parameters are put forward with the aim of deterministic control of subsurface damage.

Through the above analysis, the coupling model between the whole machine configuration, the dynamic characteristics of each kinematic pair, and the cutting subsurface damage was established. The cutting force is expressed as a function of the rigid and damping characteristics of the kinematic pair. The coupled model of the precision, stiffness, and damping index of the kinematic pair and the subsurface

damage is established according to the expression of the contact area. The response of the kinematic characteristics of the kinematic pair to the cutting parameter is analyzed; the parameters are introduced into the coupled model to establish the prediction model of subsurface damage peak and distribution in the machining space of the cutting system.

The dynamic characteristic parameters of the cutting system constructed by the kinematic pairs of different support forms are calculated and analyzed. The coupled model is verified by the combination of cutting test and dynamic characteristic monitoring. The longitudinal section of the cutting tool is scanned by scanning electron microscopy, the peak and distribution of subsurface damage were obtained, and the coupled model was validated. Then, the whole structure with subsurface damage control as the goal, the design method of dynamic characteristic parameters, and the optimization of grinding technology were proposed.

Error Distribution (Jianpu 2015)

The surface quality of the processing is not always better when the ultraprecision machine tool rail movement accuracy is higher, which not only increases the cost of manufacturing and assembly, but the environmental impact of factors is also a challenge (Lee et al. 2000). In order to achieve better precision and ultraprecision manufacturing process, each index of the machine tool needs to make an error budget according to the processing target accuracy and environment of the workpiece and to predict and control the sensitivity of the sensitive motion precision (Ramesh et al. 2000). During the machine design stage, we introduce the machine tool axis of each component layout and the accuracy of the various parts of the distribution. The error budget provides an effective means of designing the precision of ultraprecision machine tools. It predicts and controls machine tool repetitive and non-repetitive errors. The basic assumption of machine tool design error budget includes two aspects: the linear superposition of all individual errors and single errors is predicted and reduced by measurement and identification. Machine error sources include geometric error, thermal deformation error, tool error, installation error, and so on. The displacement error in the sensitive direction is analyzed. The principle of the combination is a key step in the process of error budget calculation (Gao et al. 2007; Kong 2010). For single error magnitude, we choose peak value (PV) or root-mean-square (RMS), and the total error based on RMS is:

$$RMS_t = \sqrt{\left[\sum_{i=1}^{n} (RMS_i)^2\right]} \tag{1}$$

where RMS_i is the error of each displacement error value; the relationship between PV p_i and RMS_i is a linear proportional relationship, and setting the proportional constant k, p_i is:

$$p_i = k \cdot RMS_i \tag{2}$$

For the error of sinusoidal distribution $k = 2.83$, the probability density distribution $k = 3.46$, the $\pm 2\sigma$ Gaussian normal distribution $k = 4$, the total error in the case of p_i is:

$$RMS_t = \frac{1}{T}\sqrt{\sum_{i=1}^{n}(p_i)^2} \tag{3}$$

where T is determined by the distribution.

The upper and lower errors of the sum of errors are the optimal value ε_b and the worst value ε_w, respectively. When considering the random error ε_r, the lag error ε_h, and the systematic error ε_s, the optimal error value is:

$$\varepsilon_b = \sum \varepsilon_s + \sum \varepsilon_h + 4\sqrt{\sum \varepsilon_r^2} \tag{4}$$

The worst error is:

$$\varepsilon_w = \sum \varepsilon_s + \sum \varepsilon_h + 4\sum \varepsilon_r \tag{5}$$

where the random error is considered to be four times of the standard deviation. Therefore, the error selection cannot exceed four times of the standard deviation.

Linear Axis Accuracy Analysis of Indicators

According to the above analysis, the key factor that affects the contour error of workpiece is the straightness error and positioning error of the guide rail. If the errors of these two aspects are designed and calculated according to the combination error principle, the workpiece surface shape error must be $\leq \pm 0.4$ μm (RMS). For aspherical mirror grinding process, the workpiece is fixed relative to the center of rotation; the X-axis range of motion is from turntable edge to the center position; X- and Z-axes move within a specific displacement range $(x_m - x_n)$ $(z_m - z_n)$. Only consider the linear axis error the geometric error caused by the contour error can be expressed as:

$$e_w = f(e_s, e_p) \tag{6}$$

where e_s and e_p are the straightness error and positioning error in order to achieve the required accuracy, two errors need to be met:

$$f(e_s, e_p) \leq 1\mu m \tag{7}$$

Table 1 Machine tool axis accuracy design index

Axis	Accuracy indicators
X, Y, Z linear axis straightness error	0.1 μm/100 mm
X, Y, Z linear axis positioning error	±0.2 μm
Spindle rotation error	<0.1 μm
C axis rotation error	<0.1 μm

From the simulation results, the root-mean-square error of straightness is $e_s \leq 0.6$ μm, and the positioning error is -0.15 μm $\leq e_p \leq 0.15$ μm. Considering that the root-mean-square error minimizes the error and the difficulty of realizing the guide of the machine tool, straightness error and positioning error were set as follows: $e_s \leq 0.2$ μm/100 mm and -0.25 μm $\leq e_p \leq 0.25$ μm. Considering the machine tool thermal error and other factors, the straightness error will be increased to 0.1 μm/100 mm. According to the above analysis, the machine tool axis design indicators are shown in Table 1.

Large-Diameter Aspheric Ultraprecision CNC Grinding Machine Design (Bin 2015)

Large-diameter aspheric mirror grinding process requires high precision, high efficiency, and low subsurface damage. The process development and equipment design should respond to the above requirements. The machining lens diameter is less than 1000 mm, vector high is less than 200 mm, so we select the gantry structure to meet the processing space requirements. In order to ensure the outline of lens grinding accuracy, the precise control of the tool (grinding wheel) and the workpiece contact point between the relative positions are needed. The accuracy of the relative position depends on the accuracy of equipment and grinding wheel shape and the ability to maintain accuracy. The machine adopts hydrostatic bearing pair to obtain high movement accuracy and rigidity. The large-diameter disk-shaped circular grinding wheel is selected to minimize the wheel's moment of inertia and ensure the grinding line speed. The rotary table is used to drive the workpiece to rotate. A turret shafting is introduced to reduce the linear axis travel in the raster-grinding mode. The crossbeam axis (Y) is used to align the in-position measurement and grinding wheel starting point.

Efficient grinding for lens requires a simple operating procedure and a corresponding material removal rate (Komanduri et al. 1997). The operation flow involves the process flow, loading and unloading of workpieces, installation and dressing of grinding wheel, compensation grinding, machine tool dressing and measuring in-position of grinding wheel, modular grinding wheel flange, and the function of measuring the outline of the lens, which reduces the off-line workpiece and grinding wheel. The material removal rate is determined by the depth of cut and the feed rate. The mirror blank is usually a flat mirror, and the removal depth for the entire grinding phase amounts to a few tens of millimeters. In the initial stage of

grinding, it is usually necessary to use a larger cutting depth and feed rate in order to get the ideal surface as soon as possible (Mamalis et al. 2001, Jiang and Whitehouse 2012).

The subsurface damage layer is the mid-frequency waviness error in the surface profile caused by the vibration of grinding wheel and workpiece during the processing. Due to the limitation of equipment rigidity and accuracy, the larger grinding depth will produce larger grinding force and vibration amplitude, and the damage on the subsurface will be more serious. The measures to suppress the subsurface damage of the machine tool are as follows: the hydrostatic bearing pair is used to improve the precision and rigidity of the equipment, a smaller grinding depth is adopted in the refining stage, and the shape of the grinding wheel is precisely adjusted to control the radial runout of the grinding wheel.

Large-Diameter Aspheric Mirror Grinding Process Analysis

The development of large-diameter aspherical mirror milling machine aims to achieve high efficiency, high precision, and low subsurface damage processing of symmetrical aspherical mirrors. To achieve these goals, it is necessary to respond to these requirements in the grinding process planning and machine design (Scheiding et al. 2010).

High Efficiency

Efficient grinding means easy operation, adequate material removal, and convergence of surface accuracy. Conventional processing of large-diameter aspheric mirror usually includes roughing, grinding, contour measurement, compensation grinding, and other processes. Moreover, each process requires special equipment to complete. To achieve efficient machining, the machine will complete the above processes independently and sequentially, which saves the time for lens handling, secondary clamping, and alignment. In the rough grinding stage, the high-speed material removal rate is needed to achieve rapid prototyping of the lens-shaped surface. The effective material removal rate is determined by the grain form of the grinding wheel, the grinding depth, and the feed speed. To achieve the above parameters, we need a large diamond wheel, equipped with a separate wheel flange for grinding wheel installation of different stages. The grinding depth and feed rate are determined by the dynamic stiffness of the machine's motion shaft, which must have adequate driven power. However, the motor cannot choose too large; the reason is that the size of the corresponding components will also increase and the corresponding part size will increase, resulting in mass movement, reducing the machine's dynamic response. Due to factors such as machine motion axis error, grinding wheel grinding and slight temperature changes, the lens can not achieve the required precision for the first time. The compensation is used to improve accuracy, and the in-position measurement device should be equipped. Mechanical rigidity

depends on the structural form of the part and the accuracy of part manufacture and assembly. The complete heat treatment should be done for the parts material to obtain sufficient strength and stability.

High Precision

The characteristics of large-aperture aspheric mirror NC precision grinding machine are introducing CNC interpolation technology to the surface machining. Aspheric mirror formation principle is that complete high-efficiency grinding by controlling the grinding wheel in the processing space in accordance with the specified trajectory; the motion axis needs sufficient static and motion accuracy to achieve the required lens contour accuracy. Mechanical accuracy includes straightness, verticality, and torsion angle error. The use of hydrostatic bearing technology can obtain better mechanical accuracy than the rolling bearing. Motion accuracy includes positioning accuracy and repeats positioning accuracy. The current configuration is driven by a linear motor with ultraprecision grating line displacement sensor. Linear motor driving technology has no mechanical transmission deputy, which can eliminate the error of the motor rotating in the heart and twist. Due to the large moving mass, large-diameter aspheric surface grinding equipment need to use a large driving force flat linear motor. There is a large suction force between the primary coil and the second permanent magnet, up to about 10,000 N. The connection pieces should be sufficiently rigid, and a symmetrical arrangement is considered to counteract suction, which increases the driving characteristics. Grating line displacement sensor should be installed close to the main drive rail and be paralleled with the rail to reduce the Abbe error.

Low Subsurface Damage

Subsurface damage is the micro-breakage of the microstructure on the surface, which corresponds to the surface mid-frequency error. The reason for subsurface damage is the vibration between the grinding wheel and the workpiece in the brittle grinding mode, the pressing force generated during the grinding scrap peeling off, and the stress released after grinding. Corresponding equipment indicators are wheel shape accuracy, dynamic jump, rigidity, and accuracy of the axis. The corresponding process parameters are the depth of cutting. Subsurface damage layers can be completely suppressed using submicron cutting depths. However, the material removal rate in such grinding modes is extremely low, which is contradictory to the goal of efficient grinding. The subsurface damage layer can be reduced by using the micro-cutting depth under the premise of accurately controlling the shape accuracy of the grinding wheel and its beating. The subsurface damage layer can be reduced by using micron-level cutting depth in the grinding. Moreover, in compensation grinding stages, the spindle is equipped with online balancing device to reduce the impact of high-speed rotation of the wheel imbalance on spindle runout (Pei et al. 1999).

Machine Configuration Scheme

According to the above process requirements for the grinding stage of the large-diameter aspherical mirror, the analysis is done. Firstly, the interpolation modes are compared, and the XZC polar coordinate grinding mode is determined. Then, the shape and size of the grinding spindle grinding wheel are analyzed. The third part is the comprehensive consideration of processing space requirements.

Grinding Mode Selection

In many commercial aspheric mirror grinding equipment, the swing mode is used for the workpiece or spindle. This mode is more suitable for small-diameter aspherical mirror grinding; it can save processing space and increase processing freedom. For the large-diameter aspheric mirror, the size and quality of the wheel spindle and the lens are larger; it is hard to achieve the accuracy and rigidity of the demand. When the lens radius of curvature is large, the function of the device is relatively simple, only need to complete the grinding process. So using interpolation grinding mode is an economical and practical solution. For example, the Cranfield University OAGM2500 and Big Optix use the two interpolation modes shown in Fig. 11 (Leadbeater et al. 1989) and Fig. 12 (Shore et al. 2005), respectively.

In Fig. 11, the grinding mode prototype is a large gantry milling machine. For the lens diameter of 900 mm, the table trip needs to reach at least 900 × 900 mm, and the whole trip has to satisfy precision requirements. For the polar coordinate machining mode in Fig. 12, turntable tabletop diameter is 900 mm, and the X feed axis only needs 450 mm for achieving 900 mm lens grinding, which means a better trip efficiency. The machine in this chapter is XZC polar coordinate grinding mode as shown in Fig. 12.

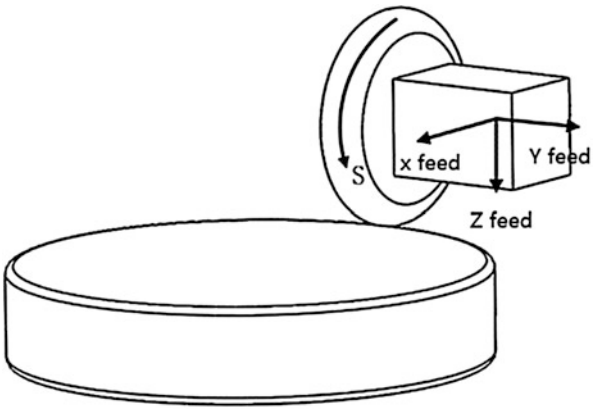

Fig. 11 XYZ linear interpolation

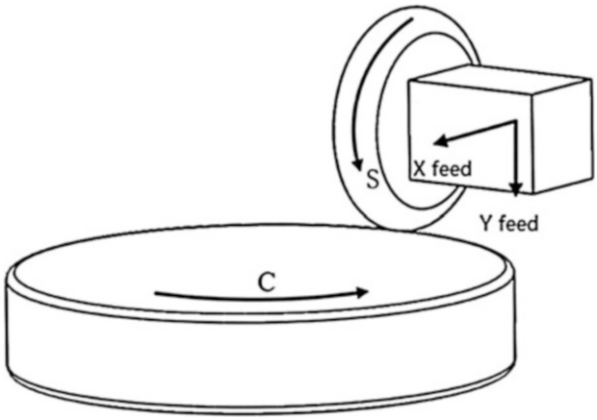

Fig. 12 XZC polar coordinate interpolation

Wheel Selection

Wheel Shape

Large-aperture aspheric mirror is usually hard and brittle ceramic materials, which needs to use the natural diamond wheel. However, the selection of wheel shape and particle size is important. The disk or cup shape is commonly used. The previous research introduces the comparison between the disk wheel and cup wheel. The ceramic material workpiece grinding wheel speed is usually 25–30 m/s. When the grinding speed is determined, the wheel radius of contact is inversely proportional to the rotational speed.

Hard and brittle material grinding line speed is 20–30 m/s, while the wheel diameter and speed are determined by the size of the workspace (Inasaki 1987). Small-diameter aspherical mirror grinding equipment usually uses small-size wheel, the wheel diameter is 50–150 mm, and the corresponding wheel speed can reach to 10,000 r/min, with hydrostatic axis system. In the large-diameter aspheric mirror grinding equipment, the machine workspace is very large, a larger-diameter wheel can be chosen with the size of 300–450 mm. The wear volume is large with large-size workpiece grinding wheel. Large-diameter grinding wheel can increase the effective grinding area and reduce the number of grinding wheel dressing and replacement. Grinding wheel diameter increases, its weight also increases accordingly; the requirement for the rigidity of the spindle is higher. In order to improve the strength of the wheel, more steel is used instead of aluminum, which leads to larger wheel weight (Gong et al. 2010). Therefore, the wheel spindle is usually the hydrostatic pressure spindle shaft system, the speed is 1700–2500 r/min to meet the requirements of linear speed (Fig. 13).

For the large-diameter aspheric mirror precision milling, the use of disk-shaped wheel can get higher speed and mass ratio. The disadvantage of a disk-shaped wheel is that it can only be used to grind a lens with a large radius of curvature. For a lens

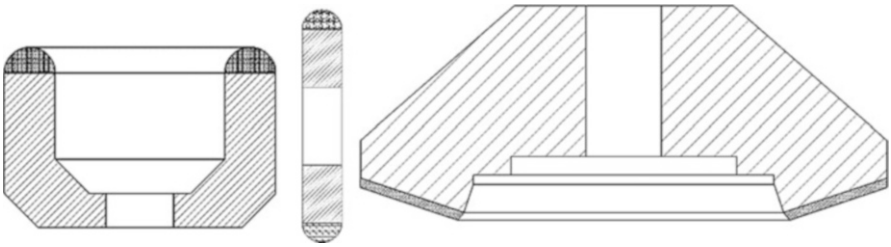

Fig. 13 Grinding wheel shape diagram

with a small radius of curvature, it will lead to the interferer. Disk-shaped lens wear occurs only in the radial direction of the wheel, so it will not cause imbalance.

For the wheel, it is necessary to balance the weight and speed of the wheel. For the spindle shaft system, the greater the weight of the wheel is, the greater its starting inertia should be. For grinding wheels 1, 2, and 3, wheel 3 achieves a better mass-to-diameter ratio while maintaining its strength. That is, sufficient grinding linear velocity can be achieved with a sufficient moment of inertia. The designed machine in this chapter uses a natural diamond disk-shaped circular grinding wheel with a diameter of 400 mm.

Wheel Particle Size and Binder

Grinding wheel particle size will affect the surface finishing and material removal rate (Chen and Rowe 1996). In the coarse grinding stage, a larger depth of cutting is used to ensure material removal rate. The workpiece surface finish and contour accuracy requirements are lower, you can choose coarse grinding wheel particles. The coarse grinding stage is a typical brittle removal mode, the binder should be copper or cast iron and even high-strength ceramic bonding agent to reduce the wear of wheel. In the semi-fine grinding stage, the roughness requirement is usually less than 0.5 μm, the contour accuracy requirement is less than 50 μm, the smaller grinding wheel particles can be selected, and the corresponding bonding agent should also be chosen. Due to the requirement of surface accuracy and the rigidity of the grinding wheel, steel wheelbase is selected to reduce the deformation of the grinding in the semi-fine grinding stage. In the fine grinding and compensating grinding phases, the roughness requirement is less than 0.3 μm, and the contour error requirement is in the order of microns. The smaller grinding wheel particle size is required, and the resin-bonded grinding wheel is selected.

Wheel Dynamic Balance

Wheel dynamic balance depends on material uniformity and circular beating (Hitchiner et al. 2016). The imbalance of the wheel shows vibration, which is the

main source of waviness error. The impact on the processing effect is to reduce the surface finish and increase the subsurface damage layer and even produce bite marks. During the grinding process, the wheel wear will cause unbalance. The continuous grinding force will cause the spindle to produce micro-deflection; it will also produce a certain amount of unbalance. Before the installation of the wheel, it is usually necessary to use the static balancer for mass balance. In the grinding process, a real-time dynamic balance needs to be carried out. The machine is balanced by Schmitt Balancing Systems (SBS)'s online dynamic balancer in the United States. The residual unbalance in the grinding process is less than 0.2 μm.

Wheel Dressing

The precision and sharpness of the grinding wheel are related to the cutting efficiency and the accuracy of grinding profile. The efficiency and the clamping adjustment determine the grinding dressing method. In the coarse grinding stage, the large particle grinder metal binder is used for the coarse grinding. For the secondary clamping, less demand on the repeat accuracy is required; off-line electrolytic dressing method is used. In the semi-fine and fine grinding stage, resin bonding wheel in-position dressing is used, the dressing device and process are provided by Xiamen University ultraprecision optical lens processing center.

Machine Structure Layout

Machine tool program will fully respond to the previous process and equipment requirements. In the program of the design process, the parts manufacturing and assembly process need to be weighed against the cost. The basic requirements of the whole structure layout are as follows:

(a) Work space with 900 mm aperture aspherical mirror in X/Z/C polar mode.
(b) Should have in-place measurement function and can complete the compensation grinding.
(c) Machining motion axes are supported by a hydrostatic bearing and are required to achieve micrometer-level motion straightness and positioning accuracy.
(d) With grinding wheel in-place trimming device.

From the basic requirements above, the basic travel parameters of the equipment can be determined. In the layout planning stage, the feasibility of the equipment manufacturing and assembly process and its corresponding costs should be measured. The selected solution is the mobile gantry layout as shown in Fig. 14, and the turntable is configured in the middle of the platform to realize polar coordinate mode is grinding. Operating space is relatively open, it is easy for loading and unloading parts. However, the equipment covers a large area, with heavy weight and hard

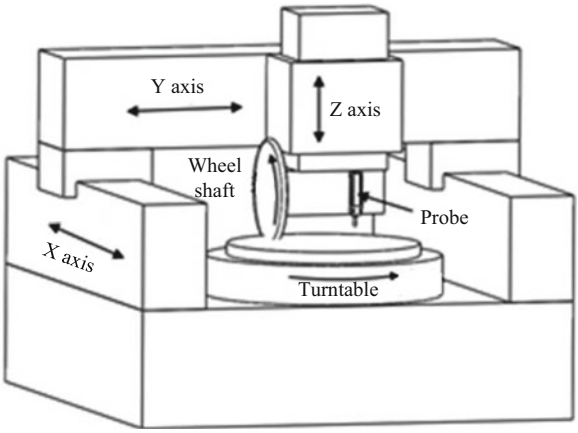

Fig. 14 Gantry mobile structure

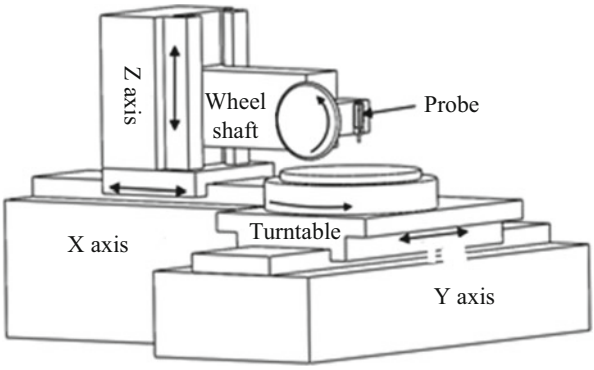

Fig. 15 Movable column structure

handling. The spans of gantry are large; the dual-drive technology should be used, which leads to higher manufacturing costs.

The surface grinder can also achieve aspheric mirror CNC grinding, the CNC system should have linear interpolation at least. Figure 15 shows the combination of the surface grinder and Tauren grinding machine, this plan has a compact structure and good manufacturability. The grinding force may increase the subsurface damage of lens or even cause the fragmentation.

This machine tool configuration selects a fixed beam gantry structure as shown in Fig. 16, including the XYZ linear motion axis, C rotary table shafting, and S wheel spindle, which all use hydrostatic bearings. The original size of natural granite material beam cross section is 1000 × 1000 mm, which has good stability and can avoid the common thermal residual stress deformation in casting. Forty-five degree inclined beam form is used to improve beam force situation. The oil groove is set at the bottom of the beam to deal with a hydraulic oil circulation problem. The static balance is equipped with Z-axis components to reduce the distortion, which is caused by the gravity of the beam itself and moving parts. XZC is used to realize

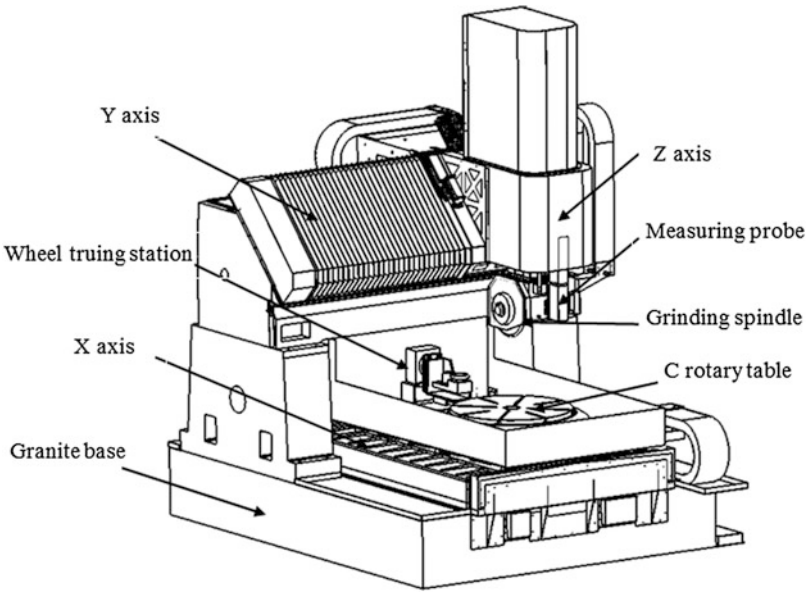

Fig. 16 Gantry inclined beam structure

the polar coordinate grinding of the symmetrical aspheric mirror. The independent measurement frame including displacement sensors and Y is used to realize in-position in grinding compensation. The wheel dresser is arranged on the right end of the X slide, which can realize resin-bonded diamond wheel dressing in-position in semi-fine and fine grinding stage.

Machine Tool Precision Estimation

The motion error of the grinding interpolation axis and the grinding wheel turning error are transmitted to the machined workpiece (Khan and Wuyi 2010). The straightness of the guide rail and the turning error of the spindle or turret usually transform into the shape error of the workpiece. Ultraprecision grinding belongs to the fixed abrasive processing technology, which needs to accurately determine the relative position between the wheel and the workpiece (Ferreira and Liu 1993). Grinding machine axis stroke can be determined based on the size of the workpiece, handling manufacturability and other auxiliary stroke. Moreover, the motion accuracy index can be estimated and designed using error estimation technology. The error estimation is the relationship between the grinder motion error and the shape error of the machined workpiece. The machining space error conditions can be set, and the shape error of the machined workpiece can be estimated through error estimation. When the workpiece shape error is determined, each movement error can be adjusted. In the actual machining of the workpiece, the workspace of a

linear axis will not reach to the extreme, or even not involved in the processing since high accuracy results in assembly difficulty and high cost. When estimating the error, the choice should meet the actual stroke demands or not count the axis of motion, which is not involved in the machining, to avoid high accuracy estimation.

In the error synthesis, the errors involved in the calculation of the definition equal must be confirmed at first, which means the same direction of the error value should be the same PV value or root-mean-square value (Okafor and Ertekin 2000). It may not be practical to adopt simple and additive methods because all individual error values may not be maximum at the same time. Vector sum can be used to express the synthetic error value of each error component, as shown in Eq. 8. However, the individual error components are independent of each other. In formula 8, P is usually 1.414, where e_i is the unidirectional error of the moving axis and all the e_i definitions must simultaneously be the peak-valley value or root-mean-square.

$$e_{\text{norm}} = \left[\sum_{i=1}^{n} |e_i|^P \right]^{\frac{1}{P}} \tag{8}$$

The maximum diameter of the workpiece is 900 mm. Considering the workpiece handling and grinding wheel dressing, X-axis total designed stroke is 1200 mm with XZC grinding mode, where the grinding wheel is only through the workpiece center and the actual effective stroke is 500 mm. Z-axis total stroke is 440 mm. Large-diameter aspheric mirror vector height is usually less than 100 mm, and the distance between the adopted 400 mm wheel and spindle bottom surface is 165 mm. So, the Z-axis actual effective grinding stroke is 140 mm. Stroke is the displacement error amplification factor from the pitch, yaw, and roll angle error. Meanwhile, too large stroke estimation will increase the difficulty of manufacturing and assembly and raise costs. Therefore, the effective working space of the grinder linear axis is (X) 500 × (Z) 140 mm.

According to the determined stroke, the error estimation method described in Eq. 8 is used to check the accuracy of each motion axis. The accuracy index of each axis and the final workpiece accuracy prediction are shown in Table 2. All the accuracy indicators are parameters within the valid workspace.

It can be seen from Table 2 that the theoretical prediction accuracy of the 900 mm aspheric mirror is 7.43 μm. In the actual grinding, in order to improve the contour accuracy, the compensation grinding also is used to reduce the impact of the interpolation axis error and grinding wheel rotation error on the grinding accuracy.

Grinding Vibration Analysis

The purpose of grinding vibration analysis is to determine the influence factors of grinding flutter so as to confirm the requirements of each component of the grinder and the selection method of processing parameters, which can reduce the impact of

Table 2 Checklist for machine tool precision of processing ring

Error source	Peak-valley value	
	X-axis direction (μm)	Z-axis direction (μm)
X-axis straightness	1	1
X-axis position precision	2	2
Z-axis straightness	0.5	0.5
Z-axis position precision	0.5	0.5
Wheel shape error	2	2
Wheel spindle runout	2	2
Wheel wear	1	1
Workpiece runout	2	2
Temperature fluctuations	1	1
Deformation caused by gravity and grinding forces	1	2
Residual sum of squares (RSS) of PV value	3.60	3.74
RSS of root-mean-square	6.91	7.43

chattering between the grinding wheel and the workpiece on the surface roughness and waviness (Furukawa et al. 1971). Compared with the single-point turning and multi-edge milling process, the wheel and the workpiece contact area force situation are more complicated in the grinding process. Vibrations in the grinding process include impact vibration, forced vibration, and self-excited vibration. Impact vibration is derived from the vibrations of the working environment or feed acceleration and deceleration during grinding. The cushioned foundation can be established to prevent external vibration from being transmitted to the equipment. Fierce feed acceleration and deceleration can be avoided by improving the stability of the feed system parts and improving the grinding path. The forced vibration is mainly caused by the imbalance of the grinding wheel, spindle or motor, which increases with speed and does not decrease with the grinding time. The forced vibration of the wheel can be eliminated by the online dynamic balance device. The main reason for the self-excited vibration is the regenerative effect between the grinding wheel and the workpiece, that is, the change of the workpiece and the grinding wheel surface in the grinding process. In grinding feed process, the cutting depth changes will result in cutting force changes and produce the corresponding vibration. The grinding wheel shape wear will also have a corresponding change in cutting force, and the vibration above can be measured by force or acceleration sensors, which can be suppressed by the method of increasing the active or passive damping (Wattanasakulpong et al. 2012) (Fig. 17).

In the past, all the research on grinding flutter analysis focused on the cylindrical, inner circle and plane grinding process (Yang et al. 2012). The cutting depth was taken as the input. Moreover, the grinder rigidity, flexibility, and regenerative effect between the grinding wheel and the workpiece were taken as the control variables. Moreover, the cutting force was taken as the output to determine the stability of the grinding system, equipment stiffness, and damping technology

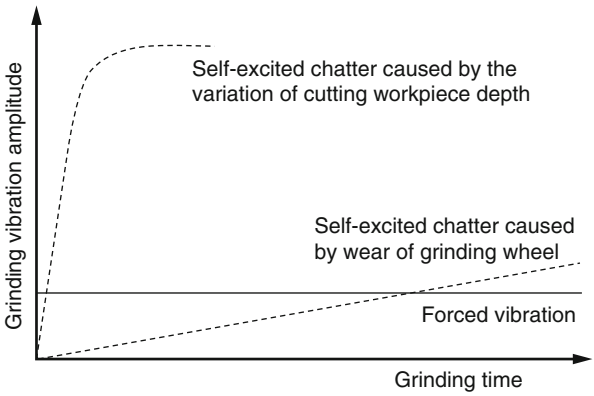

Fig. 17 Variation trend of grinding self-excited vibration amplitude

index. Also, it puts forward the improvement index of the equipment rigidity or damping. In aspherical mirror CNC grinding process, linear interpolation step changes constantly, and the change factors of corresponding cutting force are more complicated than the traditional grinding, which leads to more complex control technology.

According to this chapter of the grinding flutter model analysis, the rigidity and damping of each straight-line axis and the rotation axis will be proposed to provide the basis for the grinding equipment design and test.

Vibration Model

For the grinding mode shown in Fig. 18, the cutting forces can be divided into F_N and F_W, which, respectively, reflect the requirements of the rigidity of grinding wheel spindle, Z- and Y-axes. The weight of the turntable shafting and the X-axis components supporting workpiece are so great that the cutting forces' effect on them is negligible (Chang and Wang 2008). For any moment in the grinding process, the following conditions are satisfied: the grinding wheel cutting depth u_p is equal to the sum of the grinding wheel wear amount δ_s, the workpiece removal amount δ_w, the workpiece deformation amount Y_m, and the grinding wheel deformation amount Y_k. According to this relationship, the grinding flutter system is regarded as a linear time-invariant system, which can be expressed as a transfer function. Through the system stability criterion, the stiffness requirements of the grinder mechanical structure can be determined.

$$u_w = \delta_s + \delta_w + Y_m + Y_k \tag{9}$$

According to the brittleness removal mechanism, the grinding wheel normal cutting force is the main reason for indentation crack extension and the generation of residual subsurface damage layer (Oryński and Pawłowski 1999). As the grinding

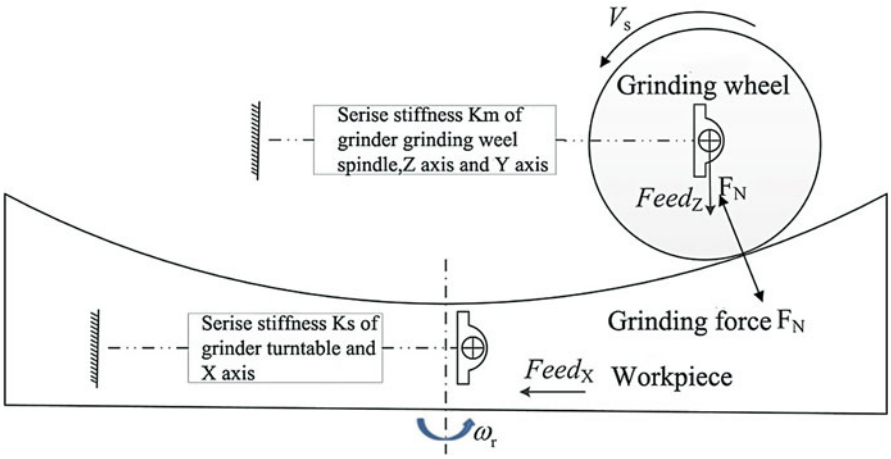

Fig. 18 Diagram of grinding wheel normal cutting force flutter model (Chang and Wang 2008)

time increases, the grinding wheel wear increases, which is the main cause for the grinding force variation. Owing to the micrometers or even tens of micrometers workpiece contour accuracy, the actual cutting depth is also changing. The workpiece regenerative effect is also one of the influencing factors causing flutter. Based on the analysis above, the closed-loop control principle of grinding wheel flutter vibration can be simplified as shown in Fig. 19.

The corresponding transfer function can be expressed as:

$$\frac{Z_W(S)}{K_W} \bullet \frac{1}{\mu_W e^{-\tau_W S} - 1} + \frac{Z_S(S)}{K_S} \bullet \frac{1}{\mu_S e^{-\tau_S S} - 1} - \frac{1}{K_c} = \frac{G_m(S)}{K_m} \tag{10}$$

The definition of the wheel contact length filter is given by Snoeys and Brown and corresponds to the fact that grinding wheel wear and cutting workpiece depth change do not result in a flutter at lower wheel speeds and cutting feed speed. The workpiece grinding contact area depth change filter Z_W can be expressed as:

$$Z_W(jw) = \begin{cases} 1 & \omega/2\pi < V_W/2l_C \\ 0 & \omega/2\pi > V_W/2l_C \end{cases} \tag{11}$$

For the wheel grinding contact area depth change filter, Z_S can be expressed as:

$$Z_S(jw) = \begin{cases} 1 & \omega/2\pi < V_S/2l_C \\ 0 & \omega/2\pi > V_S/2l_C \end{cases} \tag{12}$$

where ω is the grinding wheel and the unit is rad/s. V_W and V_S are the linear velocities of the workpiece and the grinding wheel. l_C is the cutting area length.

Grinding wheel contact at the grinding mode is shown in Fig. 18. It can be calculated according to Fig. 19; the contact length is equivalent to the wheel edge arc

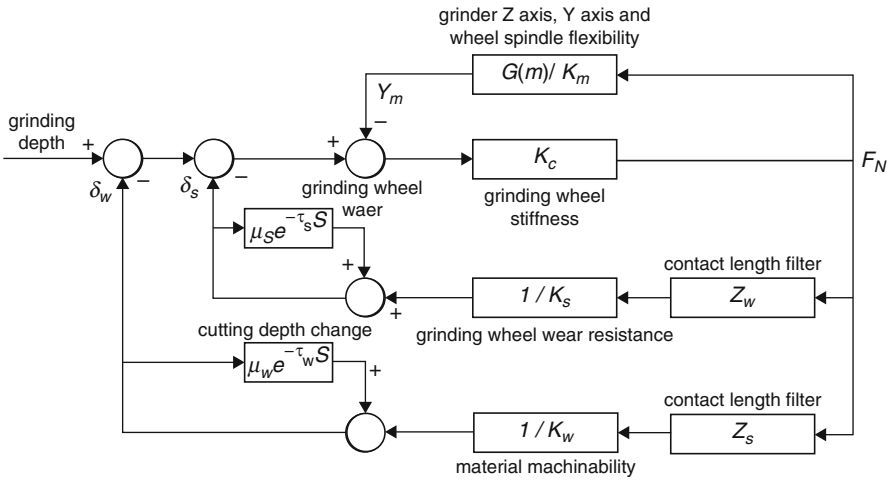

Fig. 19 Grinding wheel normal cutting force flutter control schematic

of the contact area; l_C expression about the wheel radius r_w and cutting depth D_c is as follows:

$$l_c = 2r_w Atn\left(\frac{\sqrt{{r_w}^2 - (r_w - D_c)^2}}{r_w - D_c}\right) \tag{13}$$

As can be seen from Eq. 13, for circular grinding wheel grinding aspheric mirror, grinding wheel grinding area contact length is proportional to the cutting depth.

Grinder Motion Axis Rigidity Distribution

According to the flutter conditions during grinding, the stiffness index of cutting depth and rotation speed can be determined, where K_m is the combined stiffness amount of the various motion axes in series with the grinding wheel spindle (Shore et al. 2005). For a series system as shown in Fig. 20, its total stiffness can be expressed as:

$$K_{\text{inseries}} = \left({K_1}^{-1} + {K_2}^{-1} + {K_3}^{-1}\right)^{-1} \tag{14}$$

The aspherical mirror grinding system consists of two subsystems: workpiece and grinding wheel. The workpiece subsystem consists of turntable components, X-axis, and fixture system; grinding wheel subsystem consists of grinding wheel, grinding wheel spindle, Z-axis, and Y-axis. According to the stiffness calculation

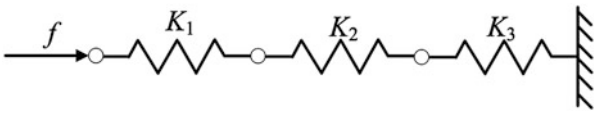

Fig. 20 Spring system in series

Table 3 Machine tool components' rigidity index

	Parts name	Parameters (N/μm)	Illustrations
$K_m = 300$ N/μm	Turntable	1000	
	X-axis	1000	
	Workpiece fixture	2000	
$K_c = 300$ N/μm	Grinding wheel spindle	400	
	Z-axis	1000	
	Y-axis	1000	
	Grinding wheel	20,000	Wheel body is aluminum, rigidity

method of the series system, the rigidity of grinder's each component and the rigidity of grinding wheel subsystem K_m and the workpiece subsystem K_c satisfy the following formula:

$$\begin{cases} \dfrac{1}{K_Z} + \dfrac{1}{K_Y} + \dfrac{1}{K_S} + \dfrac{1}{K_W} \geq \dfrac{1}{K_C} \\ \dfrac{1}{K_R} + \dfrac{1}{K_X} + \dfrac{1}{K_F} \geq \dfrac{1}{K_m} \end{cases} \tag{15}$$

According to the method of judging the flutter stability, the indexes of the grinder grinding wheel and the workpiece rigidity are, respectively, determined by Eq. 15. The rigidity index of each component can be determined as shown in Table 3:

This section focuses on the high efficiency, high precision, and low subsurface damage requirements of the hard and brittle aspheric mirror with the diameter of less than 1000 mm, and the machine tool adopts the fixed beam gantry structure to obtain enough working space. The X/Z/C polar coordinate processing mode is adopted to reduce redundant stroke damage on the rigidity of processing ring. Y motion axis and length gauge form a measurement framework, which is independent of processing ring. The grinding wheel dresser is equipped to reduce grinding wheel replacement time.

The error estimation method is adopted to check each motion axis accuracy of the machine tool, and the structural characteristics of each motion axis are introduced. The effect of static pressure film changes on the accuracy, which is caused by the kinematic pair bearing change, is also evaluated. According to the assembly static pressure requirements of the oil film thickness of static, kinematic pair, the structure and test methods for parts are given.

Conclusion

This chapter starts with the ultraprecision machining technology and analyzes the forward design of the ultraprecision machine tool. The analysis is carried out from the machining mechanism, the key components and parts technology, the basic requirements of the ultraprecision machine tool, the layout of the precision and ultraprecision structure, the machining process experiments, the error distribution, the linear motion axis accuracy index analysis, and other related aspects. According to the products on the ultraprecision machine tool market, several typical ultraprecision machine tool configurations are introduced, and the design of large-diameter aspheric ultraprecision CNC grinder is discussed in detail.

References

Bin L (2015) Large-diameter aspheric mirror precision CNC grinding technology. Xi'an Jiaotong University, Xi'an, China

Brinksmeier E, Mutlugünes Y, Klocke F et al (2010) Ultra-precision grinding. CIRP Ann Manuf Technol 59(2):652–671

Chang HC, Wang JJ (2008) A stochastic grinding force model considering random grit distribution. Int J Mach Tools Manuf 48(12–13):1335–1344

Chen X, Rowe WB (1996) Analysis and simulation of the grinding process. Part I: generation of the grinding wheel surface. Int J Mach Tools Manuf 36(8):871–882

Cheng X, Nakamoto K, Sugai M et al (2008) Development of ultra-precision machining system with unique wire EDM tool fabrication system for micro/nano-machining. CIRP Ann Manuf Technol 57(1):415–420

Cheung CF, Lee WB (2000) A multi-spectrum analysis of surface roughness formation in ultra-precision machining. Precis Eng 24(1):77–87

DeBra DB, Hesselink L, Binford T (1990) Ultra precision machining. Stanford University CA Department of Aeronautics and Astronautics, Stanford

Dornfeld D, Lee DE (2008) Machine design for precision manufacturing. Springer US, New York

Dornfeld D, Min S, Takeuchi Y (2006) Recent advances in mechanical micromachining. CIRP Ann Manuf Technol 55(2):745–768

Ferreira PM, Liu CR (1993) A method for estimating and compensating quasistatic errors of machine tools. J Eng Ind 115(1):149–159

Furukawa Y, Moronuki N (1988) Effect of material properties on ultra precise cutting processes. CIRP Ann Manuf Technol 37(1):113–116

Furukawa Y, Miyashita M, Shiozaki S (1971) Vibration analysis and work-rounding mechanism in centerless grinding. Int J Mach Tool Des Res 11(2):145–175

Gao W, Tano M, Araki T, Kiyono S, Park CH (2007) Measurement and compensation of error motions of a diamond turning machine. Precis Eng 31(3):310–316

Gong H, Fang FZ, Hu XT (2010) Kinematic view of tool life in rotary ultrasonic side milling of hard and brittle materials. Int J Mach Tools Manuf 50(3):303–307

Guangxian X, Xiangyun W (2010) Material structure, 2nd edn. Science Press, Beijing

Hitchiner MP, Marinescu ID, Uhlmann E et al (2016) Handbook of machining with grinding wheels. CRC Press, Boca Raton

Huang H, Yin L, Zhou L (2003) High speed grinding of silicon nitride with resin bond diamond wheels. J Mater Process Technol 141(3):329–336

Inasaki I (1987) Grinding of hard and brittle materials. CIRP Ann Manuf Technol 36(2):463–471

Jiang XJ, Whitehouse DJ (2012) Technological shifts in surface metrology. CIRP Ann Manuf Technol 61(2):815–836
Jianpu X (2015) Precision grinding and error compensation technology of aspheric optical components. Xi'an Jiaotong University, Xi'an, China
Khan AW, Wuyi C (2010) Systematic geometric error modeling for workspace volumetric calibration of a 5-axis turbine blade grinding machine. Chin J Aeronaut 23(5):604–615
Kim JD, Kim DS (1995) Theoretical analysis of micro-cutting characteristics in ultra-precision machining. J Mater Process Technol 49(3–4):387–398
Koenigsberger F, Tlusty J (2016) Machine tool structure. Elsevier, Oxford, UK
Komanduri R, Lucca DA, Tani Y (1997) Technological advances in fine abrasive processes. CIRP Ann Manuf Technol 46(2):545–596
Kong L (2010) Modeling of ultra-precision raster milling and characterization of optical freeform surfaces. Hong Kong Polytechnic University, Hong Kong, China
Kuriyagawa T, Saeki M, Syoji K (2002) Electrorheological fluid-assisted ultra-precision polishing for small three-dimensional parts. Precis Eng 26(4):370–380
Leadbeater PB, Clarke M, Wills-Moren WJ, Wilson TJ (1989) A unique machine for grinding large, off-axis optical components: the OAGM 2500. Precis Eng 11(4):191–196
Lee WB, Cheung CF, To S (1999) Materials induced vibration in ultra-precision machining. J Mater Process Technol 89:318–325
Lee WB, Cheung CF, Chiu WM et al (2000) An investigation of residual form error compensation in the ultra-precision machining of aspheric surfaces. J Mater Process Technol 99(1–3):129–134
Mamalis AG, Grabchenko AI, Horváth M, Mészáros I, Paulmier D (2001) Ultraprecision metal removal processing of mirror-surfaces. J Mater Process Technol 108(3):269–277
McKeown P, Corbett J (2004) Ultra precision machine tools//Autonome produktion. Springer, Berlin, pp 313–327
Okafor AC, Ertekin YM (2000) Derivation of machine tool error models and error compensation procedure for three axes vertical machining center using rigid body kinematics. Int J Mach Tools Manuf 40(8):1199–1213
Oryński F, Pawłowski W (1999) The influence of grinding process on forced vibration damping in headstock of grinding wheel of cylindrical grinder. Int J Mach Tools Manuf 39(2):229–235
Park CH, Song CK, Hwang J et al (2009) Development of an ultra precision machine tool for micromachining on large surfaces. Int J Precis Eng Manuf 10(4):85
Pei ZJ, Billingsley SR, Miura S (1999) Grinding induced subsurface cracks in silicon wafers. Int J Mach Tools Manuf 39(7):1103–1116
Ramesh R, Mannan MA, Poo AN (2000) Error compensation in machine tools – a review: part II: thermal errors. Int J Mach Tools Manuf 40(9):1257–1284
Rowe WB, Morgan MN, Qi HS et al (1993) The effect of deformation on the contact area in grinding. CIRP Ann Manuf Technol 42(1):409–412
Scheiding S, Damm C, Holota W et al (2010) Ultra-precisely manufactured mirror assemblies with well-defined reference structures//Modern Technologies in Space-and Ground-based Telescopes and Instrumentation. Int Soc Opt Photon 7739:773908
Shore P, Luo X, Jin T et al (2005) Grinding mode of the BOX ultra precision free-form grinder. Proc ASPE pp. 1–4
Shore P, Morantz P, Luo X, Tonnellier X, Collins R, Roberts A, MayMiller R, Read R (2005b) Big OptiX ultra precision grinding/measuring system. Proc SPIE 5965:241–248
Somiya (1984) Advanced technical ceramics. Academic, Tokyo
Taniguchi N (1983) Current status in, and future trends of, ultraprecision machining and ultrafine materials processing. CIRP Ann 32(2):573–582
Thompson R (2007) Manufacturing processes for design professionals. Thames & Hudson, New York
Wattanasakulpong N, Prusty BG, Kelly DW et al (2012) Free vibration analysis of layered functionally graded beams with experimental validation. Mater Des (1980–2015) 36:182–190

Xu HK, Jahanmir S, Ives LK (1996) Material removal and damage formation mechanisms in grinding silicon nitride. J Mater Res 11(7):1717–1724

Yang Y, Lin J, Xu S (2012) Surface grinding machine stability characteristics limited prediction. Mech Eng Res 2(2):114

Yuan J, Zhang F, Dai Y et al (2010) Development research of science and technologies in ultra-precision machining field. Jixie Gongcheng Xuebao (Chin J Mech Eng) 46(15):161–177

Zaghbani I, Songmene V (2009) Estimation of machine-tool dynamic parameters during machining operation through operational modal analysis. Int J Mach Tools Manuf 49(12–13):947–957

Zhang GP, Huang YM, Shi WH et al (2003) Predicting dynamic behaviours of a whole machine tool structure based on computer-aided engineering. Int J Mach Tools Manuf 43(7):699–706

Design of Tools, Grinding Wheels, and Precision Spindles

4

Huiying Zhao and Shuming Yang

Contents

Introduction 95
Rigid Removal Tool 95
Diamond Tool 95
Diamond Cutter Geometry and Structure 96
Diamond Material Selection and Orientation 96
Diamond Cutter Design 97
Cutter Head Geometry 97
Example of Diamond Turning Tool 97
Choice of Diamond Tool Crystal Surface of Rake and Rear Face 98
Diamond Tool's Wear (Wada et al. 1980) 99
Other Tools 100
Ceramic Tools 100
Polycrystalline Cubic Boron Nitride Tools 100
Diamond-Like Tools 100
Crystalline Diamond 101
Artificial Polycrystalline Diamond 101
CVD Diamond 101
Ultraprecision Grinding Wheel (Bin 2015) 101
Abrasive Particle Size and Sample Selection 101
Bond 102
Tissue and Concentration and Its Choice 103
Hardness and Its Choice 104
Wheel Strength 104
Wheel Shape and Size and Its Base Material 104
Selection of Ultraprecision Grinding Wheel 106

H. Zhao (✉)
School of Mechanical Engineering, Xi'an Jiaotong University, Xi'an, Shaanxi, China
e-mail: bjzhaohuiying@163.com

S. Yang (✉)
State Key Laboratory for Manufacturing Systems Engineering, Xi'an Jiaotong University, Xi'an, Shaanxi, China
e-mail: shuming.yang@mail.xjtu.edu.cn

Z. Jiang, S. Yang (eds.), *Precision Machines*, Precision Manufacturing,
https://doi.org/10.1007/978-981-13-0381-4_3

The Trimming of Ultra-Hard Abrasive Grinding Wheel 106
The Trimming of Ultra-Hard Abrasive Grinding Wheel 106
The Balance of Ultra-Hard Abrasive Grinding Wheel 107
Static Balance 107
Dynamic Balance 108
Flexible Tool 108
Ultraprecision Grinding and Polishing Tools 108
Grinding and Polishing Classification 109
Grinding and Polishing Abrasive 110
Ultraprecision Machine Tool Spindle Shaft System (Huan 2011) 115
Hydrostatic Spindle Shaft System 115
Hydrostatic Bearing Working Principle 115
Constant Pressure Oil Supply Hydrostatic Bearings Working Principle 116
Constant Flow of Oil Supply Hydrostatic Bearings Working Principle 117
Hydrostatic Bearing Throttling Method 118
Hole Restrictor 118
Capillary Restrictor 118
Film Feedback Throttle 119
The Key Technologies of Hydrostatic Bearing 119
Hydrostatic Bearing Structure 119
Hydrostatic Bearing Parameter Design 121
Gas Hydrostatic Spindle Shaft System 122
Gas Hydrostatic Bearing Working Principle 122
Hydrostatic Bearing Throttling Form 122
Porous Gas Hydrostatic Lubrication 123
Gas Hydrostatic Bearing Design 124
Effect of Porous Medium Permeability Φ on Static Performance 125
Supply Pressure *Pa* of the Impact 125
The Effect of the Average Film Thickness h_0 126
Influence of Bearing Length L 126
Effect of Porous Material Thickness 126
The Effects of Slippery Flow 126
Dual Cylinder Gas Hydrostatic Spindle Shaft Design 126
Conclusion 127
References 128

Abstract

This chapter focuses on process demands of ultraprecision machining technology, which contains cutting tools, grinding wheel, and ultraprecision spindle shafting. The key elements that should be emphasized in related stages are put forward. In particular, the classification of cutting tools' rigidity is introduced based on the generation of subsurface damage layer. The calculation and data are provided, and the design ideas and preliminary design schemes are presented.

Keywords

Cutting tools · Grinding wheel · Ultraprecision spindle shafting · Design theory

Introduction

Cutting tools and machine tools are the two main factors to achieve removal. Based on the needs of processing technology in the movement requirement of the tool, the machine tool can achieve the tool's trajectory and then achieve removal, and the cutting tools in contact with the workpiece can remove the workpiece material directly (Altintas 2012). At present, there are many methods for ultraprecision machining, and corresponding tools and machine tools have emerged (Yuan et al. 2012). Due to the increasing attention paid to the subsurface damage layer in the ultraprecision machining technology, research shows that the generation of subsurface damage is closely related to the removal rigidity properties of the tool (Suratwala et al. 2006, 2008). Therefore, according to the rigid classification of removal, this chapter can be divided into three types: rigid removal, flexible removal, and semiflexible removal. Turning tools, milling cutters, drills, etc. belong to the rigid removal tool; the grinding wheel belongs to the semiflexible removal tool; and grinding fluid, polishing fluid, etc. belong to the flexible removal tool.

Rigid Removal Tool

To achieve ultraprecision rigid removal of cutting, the tool should have the following properties (Kim and Burge 2010):

1. Extremely high hardness, extremely high wear resistance, and high elasticity modulus to ensure a long tool life and high dimensional durability.
2. Edge should be grinded to extremely sharp and extremely small edge radius ρ value, which can achieve ultrathin cutting thickness.
3. No defects in the blade and cutting-edge shape will be reflected on the processing surface in cutting, which can get ultrasmooth mirror.
4. Anti-adhesion, chemical affinity, and low coefficient of friction with the workpiece material, which can get excellent processing surface integrity.

The above technical requirements determine the performance requirements of the tool used in ultraprecision cutting. In order to meet the above technical requirements, the material selection of tool for ultraprecision machining becomes a major problem.

Diamond Tool

Natural single-crystal diamond, the hardest material known to man, has a series of excellent properties, such as high hardness, high wear resistance, great strength, good thermal conductivity, low friction coefficient with nonferrous metal, the ability to be grinded at extremely sharp edge, and so on (Wei et al. 1993). In 1954, the GE (General Electric) Company in the United States announced that H. Tracy Hall et al.

Table 1 Physical and mechanical properties of diamond

Hardness HV	6000–10,000 (variation with the crystal direction and temperature)
Bending strength	210–490 Mpa
Compressive strength	1500–2500 Mpa
Elastic modulus	9–10.5 × 10^{11} N/m^2
Thermal conductivity	(2–4) × 418.68 W/(m·K)
Specific heat capacity	0.516 J/(g·°C) (room temperature)
Start temperature of oxidation	900–1000 K
Start temperature of graphitization	1800 K (in inert gas)
Friction coefficient with aluminum alloy, brass	0.06–0.13 (at room temperature, variation with the crystal direction and temperature)

successfully synthesized diamond, polycrystalline diamond, which is now used in mass manufacturing of cutting tools in ultraprecision machining (Astakhov and Stanley 2015; Table 1).

In the ultraprecision cutting process, in order to process the machining surface with high dimensional accuracy, high precision, high quality, and no stress, the cutting technology demand is very strict.

Diamond Cutter Geometry and Structure

There are four diamond cutter head geometries, as shown in Fig. 1.

The first is a sharp edge, this tool is easy to install, but it must be regrinded immediately after wear.

The second is multi-row edge, and its installation is also convenient. This part should be regrinded after repeated use. Due to small assistant deflection angle χ_r', multi-row edge has smaller machining residual area than the sharp edge with the processing surface of good quality.

The third is a single linear edge. The longest linear edge reaches to 2–3 mm, but this tool's sharpening and installation are more difficult.

The fourth is arc edge. This tool is easy to install but more difficult to be grinded; its residual area is small.

Diamond Material Selection and Orientation

The quality of diamond tools first depends on the quality of the diamond material. The main problem during the use of diamond tools is that the tools' cutting performance varies greatly. Diamond tools often fail due to tipping and fragmentation, which are caused by the choice of tool orientation, grinding quality, and the diamond inherent defects.

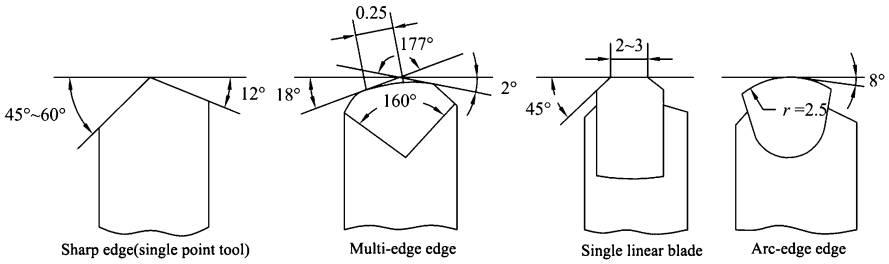

Fig. 1 Diamond tool head geometry

Due to the diamond crystal anisotropy, the properties of different crystal orientation vary greatly. When designing and manufacturing diamond tools, the crystal orientation must be the correct choice and the diamond raw material must be the crystal orientation. The diamond crystal orientation methods are artificial visual measurement orientation, X-ray crystal orientation, and laser crystal orientation (Sumiya et al. 1997).

Diamond Cutter Design

Single-crystal diamond tools are widely used for ultraprecision cutting, which generally requires the processing surface roughness Ra less than 10 nm and sometimes can reach the ultrasmooth surface whose roughness Ra is less than 0.8 nm. The diamond tool design is mainly to meet the above requirements.

The design of diamond cutting tools used for ultraprecision cutting has three main parts: the design and choice of the cutter head form, rake, and rear face of the design choices, determination of the tool structure, and the method of diamond fixed on the tool.

Cutter Head Geometry

Diamond cutting tools generally do not use the sharp knifepoint where main cutting edge and the side cutting edge intersect. Such knifepoint is not only easy to be tipped and worn, but also left machining marks in the processing surface, which increases surface roughness value. The use of transition edge between the main cutting edge and the side cutting edge of a diamond tool is to polish a machined surface, using linear edge as well as arc edge, which are also advantageous to obtain good machined surface quality (Davim and Mata 2005). Figure 2 shows different forms of diamond tool.

Example of Diamond Turning Tool

Figure 3 shows a general diamond turning tool that can be used to turn aluminum, copper, and brass. The turning angle adopts 45° as main tool angle, rake angle

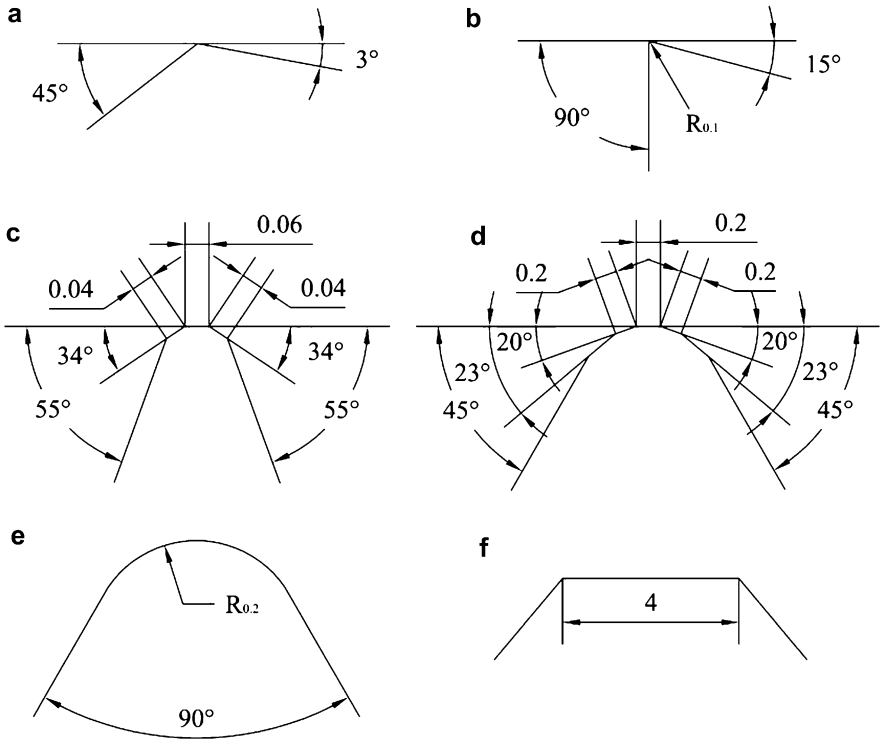

Fig. 2 Several different diamond tool head geometries

$\gamma_0 = 0^\circ$, and relief angle $\alpha_p = 5^\circ$. Using linear repair edge, whose length is 0.15 mm. This type of turning tool works well in the factory and can stably process the surface with Ra <0.02–0.005 μm.

Choice of Diamond Tool Crystal Surface of Rake and Rear Face

Due to the anisotropy of single-crystal diamond crystal, the performances in all directions are very different. Therefore, it is better to choose which crystal face in the rake and rear face of the diamond tool, which is an important issue in the design of diamond cutting tools (Yan et al. 2003).

Selecting (110) surface of the crystal as the rake or rear crystal surface is easier to grind sharp edge with high efficiency. Selecting (100) surface of the crystal as the rake or rear crystal surface, tools have wear resistance, high edge micro-strength and low friction coefficient with processed material, and it is not easy to produce microscopic tipping and easy to manufacture and grind.

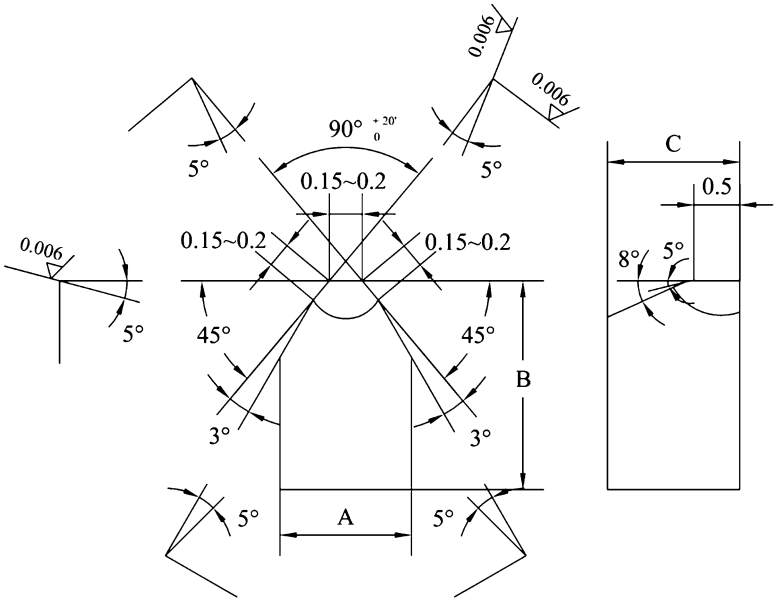

Fig. 3 A diamond turning tool for turning aluminum, copper, and brass

Diamond Tool's Wear (Wada et al. 1980)

Diamond Tool Wear Form

Diamond tool wear can be divided into mechanical wear, damage, and carbonation wear. Common wear forms are mechanical wear and damage; the carbonation wear is less common.

Mechanical Wear

After a long period of working, the diamond tool will appear slender and smooth wear band on the rake and rear face, and its edge will gradually become an arc with a smooth transition. As the machining continues, a larger arc will form, or a bevel will develop between the rake and rear face.

Tool's Damage

Diamond cutter damages are the following: crack, fracture, and cleavage.

For diamond tools, cleavage at the cutting edge is the main form of wear and tear, so the microscopic strength of the cutting edge is the main basis for the choice of crystal plane in tool design. Not being easy to produce cleavage damage is an important consideration for the choice of best crystal surface in diamond tool rake and rear face (Zhou et al. 2006).

Other Tools

With the increasing wide application of ultraprecision machining technology, new ultraprecision tool materials are emerging, such as ceramic tools, polycrystalline diamond tools, CVD diamond tools, and polycrystalline cubic boron nitride tools.

Ceramic Tools

The ceramic tool material is a composite ceramic sintered by adding borides (TiB_2, ZrB_2), carbide (TiC, SiC), and binder phase (Mo, Ni, Co) in $A1_2O_3$ or Si_3N_4. Its main raw materials, such as alumina and silicon nitride, are the most abundant elements in the crust, so the cost is low. Ceramic cutting tools are characterized by high hardness (2400–2800 HV), good wear resistance, high temperature performance, good affinity with the metal, good chemical stability, and low bending strength (0.5–1.5 GPa), and its cutting speed is of three to ten times higher than the carbide. With wide applicability, it is suitable for processing carbon steel, alloy steel, cast iron nickel-based alloys, silicon-aluminum alloy, and other materials, which are difficult to be processed. Common types of ceramic tools are alumina-based ceramic tools and silicon nitride-based ceramic tools (Brandt 1999).

Polycrystalline Cubic Boron Nitride Tools

Cubic boron nitride (CBN) is an allotrope of boron nitride (BN) with hardness second only to diamond. Polycrystalline cubic boron nitride (PCBN) is a polycrystalline material obtained by sintering fine CBN material under high temperature and high pressure. PCBN tool features high hardness (4700–5000 HV), wear resistance being 50 times that of cemented carbide, thermal stability being higher than diamond, up to 1400–1500 °C, and the cutting speed being three to five times that of carbide. It does not react with iron group metal at 1200–1300 °C but react easily with water at high temperature. It has low friction coefficient with steel, about 0.2–0.3, and it is suitable for ferrous metal dry cutting and other ultraprecision machining, whose life is several times of ceramic tool (Poulachon et al. 2001).

Diamond-Like Tools

Diamond-like tool materials are divided into four types: single crystalline diamond (SCD); artificial polycrystalline diamond (PCD) artificial polycrystalline diamond compact (PCD/CC) to choose carbide as the substrate, whose surface has 0.5-mm-thick polycrystalline diamond, same manufacturing method as PCD; and CVD diamond (CVDD) tool (Rosa et al. 2004).

Crystalline Diamond

Crystalline diamond (CD) is an allotropic carbon, and natural single-crystal diamond is expensive.

Artificial Polycrystalline Diamond

Artificial polycrystalline diamond (PCD) takes graphite as raw material, which is produced by high temperature and pressure sintering with catalyst. PCD tool has a very high durability, stable dimensional accuracy, and good workpiece surface roughness. It can process copper, aluminum, and other nonferrous metals and alloys, ceramics, composite materials, plastics, rubber, graphite, and other materials.

CVD Diamond

CVD diamond is a diamond grown by chemical vapor deposition at low pressure. CVD diamond tools have two forms: the first is to deposit a thin layer of less than 30 μm on a suitable substrate (tool), the second is to deposit a diamond layer of 1 mm thickness, then the thick film is cut into a certain size, and it is welded on the substrate for use.

Ultraprecision Grinding Wheel (Bin 2015)

Ultraprecision grinding is to process ferrous metals and hard and brittle materials with grinding wheel to obtain high shape accuracy and low surface roughness (Brinksmeier et al. 2010). Grinding wheel is the grinding tool formed by joint abrasive or powder with bond, which forms a certain shape with a certain intensity after using sintering, bonding, coating, and other methods (Stephenson et al. 2001). Among them, the grinding wheel formed by sintering is called the consolidation abrasive.

For the grinding wheel, it is necessary to balance the quality and speed of the grinding wheel. For the spindle shaft system, the greater the grinding wheel quality is, the greater the starting inertia should be. In other words, sufficient grinding linear velocity should be obtained with enough moment of inertia. In precision and ultraprecision grinding, in addition to corundum and carbide-based abrasives, super-abrasive is extensively used, which is determined by the requirements of precision and ultraprecision machining (Tian et al. 2011).

Abrasive Particle Size and Sample Selection

Abrasive material can be divided into two categories according to its granularity: abrasive and fine powder (Komanduri et al. 1997). And the granularity refers to the size of abrasive particles, which contains particle size and abrasive particle. The

abrasive particles are classified by the screening method, whose particle size number is expressed as the number of pores within 1 in. of the screen. For example, abrasive grains of 60 # indicate that it can pass a screen with 60 holes per inch, but not 70 holes per inch. Powder are classified by microscopically measuring, and their grain size is expressed as the actual size of the abrasive (W).

Grinding wheel particle size will affect the surface roughness and material removal rate. In the coarse grinding stage, a large depth of cutting is used to ensure material removal rate. The requirements of workpiece surface finish and contour accuracy are lower, so coarse grinding wheel particles can be chosen. The coarse grinding stage is the typical brittle removal mode; the bond should be copper or cast iron and even high-strength ceramic bonding agent to reduce the wear of the wheel. In the semi-fine grinding stage, the surface roughness is usually less than 0.5 μ, and the contour accuracy requirement is less than 50 μ. Therefore, the smaller grinding wheel particles can be selected, and the corresponding bonding agent has to be chosen as the resin bonding agent (Lin et al. 2007). Due to the surface accuracy and requirements of the grinding wheel itself rigidity, steel wheel base should be chosen at semi-fine grinding stage to reduce the deformation of the grinding wheel itself during grinding. In the grinding and compensating grinding stages, the roughness requirement is less than 0.3 μm and the contour error requirement is in the order of micrometers. A smaller grinding wheel particle size and a resin bond grinding wheel are required. The grain sizes for various grain sizes are shown in the following table (Table 2).

Bond

The function of the binder is to bind the abrasive together to form a certain shape of the grinding wheel. For grinding wheel in ultraprecision grinding, resin binder, ceramic binder, and metal binder are commonly used. The bond will affect the

Table 2 Abrasive grain size and particle size

Abrasive		Abrasive		Powder	
Granularity number	Particle size (μm)	Granularity number	Particle size (μm)	Granularity number	Particle size (μm)
14 #	1600–1250	70 #	250–200	W40	40–28
16 #	1250–1000	80 #	200–160	W28	28–20
20 #	1000–800	100 #	160–125	W20	20–14
24 #	800–630	120 #	125–100	W14	14–10
30 #	630–500	150 #	100–80	W10	10–7
36 #	500–400	180 #	80–63	W7	7–5
46 #	400–315	240 #	63–50	W5	5–3.5
60 #	315–250	280 #	50–40	W3.5	3.5–2.5

Abrasive's particle size larger than the 14 # and powder finer smaller than W3.5 are rarely used, which are not listed in the table

Table 3 Common bonds

Name	Code	Performance	Uses
Vitrified bond	V(A)	Water resistance, oil resistance, and acid and alkali corrosion resistance can maintain the correct geometry. Large porosity, high grinding rate, high strength, poor toughness, poor elasticity, poor vibration resistance, cannot afford lateral force	When grinding at V_{wheel} <35 m/s, this bond is most widely used, which can be made of a variety of abrasive tool, applying to form grinding and grinding thread, gear, crankshaft, etc.
Resin bond	B(S)	Strong and rich in elasticity, not afraid of impact, can work at high speed. Having friction polishing effect, but the solidity and heat resistance are poorer than the vitrified bond. Poor acid and alkali resistance, small porosity, easy to be plugged	When high-speed grinding at V_{wheel} >50 m/s, it can be made of thin grinding wheel millcourse and sharpening tool rake face. At high-precision grinding, cutting fluid alkali content should be <1.5% in wet grinding
Rubber bond	R(X)	Better elasticity than the resin bond, great strength. Small porosity, poor heat resistance, poor oil and acid resistance. Abrasive particles easily fall and have odor	Manufacture grinding wheel for grinding bearing channel, centerless grinding wheel, guide wheel, various thin slice grinding wheel for grooving and cutting, soft polishing grinding wheel, etc.
Metallic bond (bronze, nickel plated)	J	Good toughness, good mold ability, great strength, poor self-sharpening performance	Manufacturing all kinds of diamond abrasive tools, long service life

The code in the brackets is the old standard code

combination strength of grinding wheel, self-sharpening, chemical stability, and dressing methods (Ronald et al. 2009) (Table 3).

Tissue and Concentration and Its Choice

Abrasive content in ordinary grinding wheel is expressed by the tissue, which reflects the volume ratio relationship between the abrasive, bond, and stomata. The abrasive content of the superhard abrasive is expressed by concentration, which refers to the superhard abrasive weight contained in the abrasive layer per 1 cm^3 volume. The higher the concentration is, the higher the content can be (Webster and Tricard 2004). The relationship between concentration and abrasive content is shown in Table 4.

Concentration directly affects the grinding quality, efficiency, and processing costs. When choosing concentration, abrasive materials, particle size, bond, grinding methods, quality requirements and productivity, and other factors should be considered synthetically. Overall, the shape grinding, groove grinding, and plane grinding with wide contact surface should select high-quality concentration, semi-fine grinding

Table 4 Concentration values and abrasive content

Concentration code	Concentration/(%)	Abrasive content/(g·cm^{-3})	The occupied volume of abrasive in the abrasive layer/(%)
25	25	0.2233	6.25
50	50	0.4466	12.50
75	75	0.6699	18.75
100	100	0.8932	25.00
150	150	1.3398	37.50

(Malkin and Guo 2008). The fine grinding should select fine-grained, medium-quality concentration. The precision grinding and ultraprecision grinding of high-precision and low surface roughness use fine-grained, low-quality concentration, even less than 25%, which mainly considers the grinding wheel clogging heating problem.

Hardness and Its Choice

Ordinary grinding wheel hardness refers to the ease of abrasive particles falling off from the abrasive surface with the external force, low hardness abrasive is easy to fall off (de Oliveira and Dornfeld 1994). Superhard abrasive grinding wheels generally has higher hardness since superhard abrasive has high wear-resistant property, but it is more expensive. So, no hardness is in its mark. The common used hardness class of grinding wheel is shown in Table 5.

The general principle of choosing grinding wheel hardness is that when processing soft metal, in order to prevent the abrasive from falling off too early, hard grinding wheel is adopted. When processing hard metal, in order to timely make blunt abrasive particles fall off, exposing the new abrasive particles with sharp edges and corners (i.e., self-sharpening), soft grinding wheel is chosen. The former is because when grinding soft materials, the working abrasive particles of the grinding wheel wear very slowly and do not need to be separated too early; the latter is because the working abrasive particles of the grinding wheel wear out rapidly when grinding hard materials and need to be quickly updated.

Wheel Strength

Abrasive strength refers to the ability to resist its own fracture caused by centrifugal force for the abrasive tools in the high-speed rotation. All kinds of abrasive tools have the highest working linear velocity requirements.

Wheel Shape and Size and Its Base Material

According to the machine tool specifications and processing conditions, the shape and size of the abrasive tool are chosen; grinding wheel generally consists of

Table 5 Commonly used wheel hardness level

	Primary class	Soft			Medium soft		Medium		Medium hard			Hard	
Hardness grade	Secondary class	Soft 1	Soft 2	Soft 3	Medium soft 1	Medium soft 2	Medium 1	Medium 2	Medium hard 1	Medium hard 2	Medium hard 3	Hard 1	Hard 2
Code		G (R1)	H (R2)	J (R3)	K (ZR1)	L (ZR2)	M (Z1)	N (Z2)	P (ZY1)	Q (ZY2)	R (ZY3)	S (Y1)	T (Y2)

The code in the brackets is the old standard code; supersoft and superhard are not included; 1, 2, and 3 in table suggest the order of increasing hardness

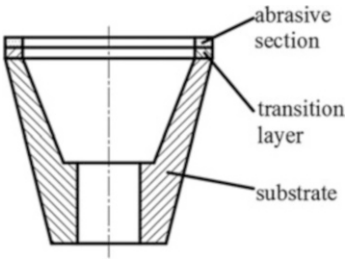

Fig. 4 Schematic diagram of grinding wheel

abrasive layer, the transition layer and the matrix. So, there are several aspects: wheel section shape, basic shape of the abrasive tool matrix, abrasive layer section shape, position of abrasive layer in the matrix, and so on (Hitchiner et al. 2016).

Grinding wheel structure diagram is shown in Fig. 4. The matrix material is related to the bonding agent; the metal-bonded abrasive tools usually use iron or copper alloy; resin-bonded abrasive tools use aluminum and aluminum alloy; ceramic-bonded abrasive tools usually use ceramic.

Selection of Ultraprecision Grinding Wheel

The selection principle of the grinding wheel used in ultraprecision grinding is easy to produce and maintain the micro-blade and its equal height. The particle size of the grinding wheel can be divided into two kinds, coarse-grained and fine-grained. The coarse-grained grinding wheel has been finely trimmed, and the tiny cutting function is the main one. The fine-grained grinding wheel after finishing, friction polishing effect between the semi-passive micro-edge under the appropriate pressure and the workpiece surface, is more significant; the higher-quality finished surface and grinding wheel durability can be obtained (Chen et al. 2010). The selection of ultraprecision grinding wheel is shown in Table 6.

The Trimming of Ultra-Hard Abrasive Grinding Wheel

Ultra-hard abrasive grinding wheel is mainly referred to diamond wheel and cubic boron nitride (CBN) wheel currently. It can be used to process difficult materials such as a variety of high hardness and high brittle materials. The accuracy of these processes is generally supposed to be high and the surface's require is low, these processes belong to the category of precision ultra-precision grinding.

The Trimming of Ultra-Hard Abrasive Grinding Wheel

The trimming of ultra-hard abrasive grinding wheel is an important problem in the use of the ultra-hard abrasive wheel (Sexton and Stone 1981). Trimming usually

Table 6 Ultraprecision grinding wheel selection

Grinding wheel						
Abrasive material	Particle number		Binder	Structure	Hardness	Processed material
White alundum (WA)	Rough 60–80	Fine 240~W7	Resin (B)	Density well-distributed	Medium light (K, L)	Hardened steel, 15Cr, 40 Cr, 9Mn2V, cast iron
Chrome alundum (PA)			Ceramic (V)	Small porosity	Soft (H, J)	Tool steel, 38 Cr Mo, Al
Brown alundum (PA)			Rubber (R)			
Green silicon carbide (GC)						Nonferrous metals

consists of truing and dressing, and it is a general term for shaping and sharpening. Truing is to achieve a certain degree of precision grinding wheel geometry. Dressing is to remove the binding agent between the abrasive particles, so that the abrasive particles protrude a certain height of the binding agent (generally about 1/3 of the abrasive grain size) and form enough cutting edge and chip space. The truing and dressing of the ordinary wheel are generally carried out in one step. The truing and dressing of the ultra-hard abrasive wheel are generally divided into two steps in succession. Sometimes, the truing and the dressing use different methods. There are many ways to make ultra-hard abrasive wheel dressing, which can be summarized into the following categories: turning method, grinding method, rolling method, jet method, electrical processing method, and ultrasonic vibration trimming method (Wegener et al. 2011).

The Balance of Ultra-Hard Abrasive Grinding Wheel

Ultra-hard abrasive grinding wheel grinding's stability and vibration can influence the grinding surface quality. Therefore, we must pay attention to the balance of the wheel. It not only affects the quality of grinding but also affects the accuracy of the grinding machine, which is also necessary for safety work. There are two types of wheel balance (Heying 2002):

Static Balance

It is also called torque balance, for the balance of the narrow wheel is in a plane balance. There are three ways to do static balance:

1. Static balance outside the machine. The use of static balance tool is by hand, but it is not convenient enough.
2. Onboard dynamic balance. Using dynamic balancing device on the wheel to complete automatic balance. Modern new grinder has dynamic balance device. The type consists of liquid, electrical, and pneumatic mechanical and so on. For the convenience of description, this kind of static balance under the working condition of grinding wheel is called dynamic balance.
3. Off-machine dynamic balance. Using a portable torque balancer, the wheels are dynamically balanced by the sensors on the instrument. The balance wheel on the wheel is manually adjusted. This method is more simple, quick, and easy than the machine outside static balance. And it gradually has wide range of applications.

Dynamic Balance

It is also called couple balance, which is used for the wide wheel and multi-wheel shaft balance.

Dynamic balance is generally carried out in the dynamic balancing machine; the instrument shows the unbalanced ends (left and right), phase and unbalance. In the manual adjustment on both sides of the wheel balance weight, after repeating for several times, the unbalance is adjusted within the allowable value.

As the super-abrasive abrasive wheel dressing is generally divided into trimming and dressing, the best use of artificial balance is after shaping. Grinding wheel will wear in the process of manufacturing, and the diameter will reduce. Therefore, there will be an imbalance to rebalance from time to time.

Flexible Tool

Ultraprecision Grinding and Polishing Tools

Grinding and polishing are the processing through which the abrasive rubs with the grinding tool and the workpiece or under the effect of mechanical, chemical, and other physical friction to obtain the required size and accuracy (Fig. 5).

Grinding and polishing are the oldest traditional process. Ancient stone, jade, bronze mirror, etc. which are created through grinding and polishing. Since ancient times, grinding and polishing have been the ultraprecision processing means, but its progress and development are slow. Until the 1950s, with the rapid development of the electronics industry, new life was given to the old art of grinding and polishing. Especially in recent years, the development of information technology and optical technology has not only increased the demand for optical components but also put forward high requirements on the quality and precision. Grinding and polishing, as the very important processing methods in optical processing, play an irreplaceable role (Shiou and Ciou 2008).

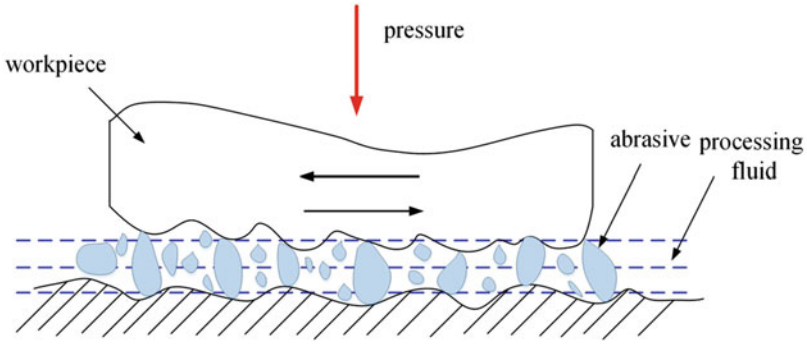

Fig. 5 Grinding and polishing process diagram

The processing of hard grinding tools is called grinding, the processing using soft grinding tools is called polishing.

Grinding and Polishing Classification

There are many ways for grinding operation. According to whether use working fluid in the grinding, it can be divided into two kinds of wet grinding and dry grinding. Wet grinding is a method in which a liquid abrasive (containing an abrasive in a working fluid) is placed between a workpiece and a grinding tool. Dry grinding is the abrasive embedded in the tool and wipes the excess residual abrasive. It is similar in operation to the wet milling method but with different grinding mechanisms. Whether grinding by manual operation, it can be divided into manual grinding or mechanical grinding. According to the surface classification of the workpiece, it can be divided into plane, outer surface, inner hole, sphere, thread, gear, noncircular surface, and other special surface grindings.

Grinding and Polishing Mechanism

For different grinding and polishing methods and different grinding and polishing materials, the processing mechanisms are different. Even with the same material and the same grinding and polishing methods, since grinding, polishing pressure, speed, and other processing parameters are different, the mechanism is not same (Lambropoulos et al. 1999).

The purposes of grinding and polishing are different, such as removing or reducing the processed metamorphic layer, obtaining the high dimensional accuracy, improving the position accuracy, and lowering the surface roughness Ra value to obtain the glossy surface, but the mechanisms of their removal of the surface layer are as follows:

1. **Mechanical micro-cutting effect**
   Abrasive edges will remove the material by mechanical extrusion and cutting action. Since the material removing process is accompanied by plastic damage

and brittle failure, the polished surface is left with varying degrees of processing metamorphic layer.

2. **The combined effect of mechanics and chemistry**
   In the mechanical grinding and polishing, the chemical role of the media is used or mixed workpiece with abrasive chemical liquid. This allows the surface to be machined and the surface chemically reactive with a polishing agent to produce a chemical reaction and remove the reaction product. This method not only can increase the grinding and polishing efficiency but also reduce or remove the processing of metamorphic layer.
3. **Chemical or electrochemical effects**
   In the grinding and polishing process without abrasive, the workpiece can be placed in chemical reagents by etching or electrolysis, to remove the surface of the material, so as to achieve the removal. The use of this processing method does not produce deterioration layer, but the accuracy is low.
4. **Other roles**
   The material of the workpiece is removed by using fluid energy or electrons, ion beams and other energy to achieve surface grinding and polishing.

   Several processing mechanisms described above, in different grinding and polishing objects or methods, due to grinding and polishing conditions are different; some just play a major role, and some play several functions at the same time.

Grinding and Polishing Abrasive

Abrasive properties directly affect the grinding and polishing effect. A large number of studies have conducted on experimental and test methods for abrasive properties and various properties of abrasive and its relationship with the grinding effect. The main function of mechanical micro-cutting abrasive should have the following five conditions (Shaw 1996):

1. The hardness is higher than the material being processed and can still maintain sufficient hardness at high temperature.
2. Abrasive deformation of abrasive itself should be small when grinding force is not easy to break.
3. In the grinding area, it will not melt or soften when the temperature rise.
4. The material to be processed should be chemically inactive, and the material will not be processed by chemical reaction and not be dissolved.
5. Abrasive cutting edge is easily broken after passivation, and the new cutting edge will form.

Grinding and Polishing Tools

Grinding and polishing tools are called lap tools; the main roles are to (1) keep abrasive and (2) keep the correct geometry and remake it on the workpiece. The first function requires the material of the research tool to be soft; the second one requires

the material to be hard. These two requirements are contradictory. A lot of materials can be made with lap tools, commonly used in the following categories (Jones 1977).

Cast Iron

Cast iron can meet the above conditions; it is the most widely used material. Cast iron is characterized by a hard ferrite matrix containing soft graphite; it can be buried abrasive. And the hard ferrite matrix can maintain the correct geometry.

Manual grinding requires the use of soft and fine cast iron, instead of using high hardness cast iron. In the thread grinding, the best tool uses the hardness of 140–200HB cast iron for manufacturing. Grinding plate uses the hardness of 150–180HB cast iron. Grinding plates for manual grinding are preferably made of pearlitic structure and have long willow-like cast iron with a hardness of about 140 HB on part of the crystal grain boundaries. If we use pure pearlite, graphite is a small state of co-integration. And if we use the hardness of 210HB cast iron grinding plate, the grinding effect is not good.

Steel

Grinding the holes with Φ8 mm or less, grinding tool is often made of low-carbon steel. And it is characterized by its high tensile strength and low cost.

Copper and Brass

In the past, the copper or brass is used for producing lap tools. But now they are replaced by cast iron. Because copper or brass is too soft and wear quickly, it is easy to lose the original geometry. It is mainly used for grinding hardened steel holes or cylindrical; and it is more applied in the gem grinding. Copper or brass, which is for the production of lap tools with hardness of 65HB, can get better grinding effect.

Soft Metal

In many cases, lapping is done by soft metals like lead and tin, and the lapping effect is good. Because these metals are very soft, the shape of the tool will vary with the shape of the workpiece. Therefore, in order to improve the accuracy of the workpiece geometry, it is more difficult. In order to ensure the machining accuracy of the workpiece, we must pay attention to the timely correction of the geometry of the lapping tool.

Plastic

With the development and progress of industry, more and more research tools made of plastic with various performance materials are used to grind various materials. In particular, the cemented carbide grinding, in order to save the diamond, diamond powder, and plastics, is often mixed to make lap tools for grinding.

In addition, the various materials can be used as tool material. Asphalt, wood, felt, leather, polyurethane, etc. can be used as grinding and polishing with lap tools.

Noncontact Grinding

Noncontact grinding is a grinding method that let the abrasive flow through the surface to be processed which the workpiece is not in contact with the grinding disk and noncontact state.

In the mechanical grinding process, the surface of the material will produce a large stress field, so that the surface has been processed to produce internal stress, lattice dislocations, cracks, and so on. Destruction units in the process directly affect the machining accuracy and surface quality of the workpiece. The material is composed of atoms, so the minimum unit of processing damage can also be atomic. If the grinding process in the cutting force of the stress field is particularly small and the added mechanical energy does not cause lattice dislocations and cracks on the surface of the workpiece and even causes the material to be processed on the basis of the elastic destruction of atomic units, you can get atomic-level accuracy and no defects in the surface.

Floating Grinding

Floating grinding using the dynamic pressure effect of sliding bearing principle, the grinding disk is easy to produce dynamic pressure effect shape. When the relative movement is existed between the workpiece and the grinding disk, due to the dynamic pressure effect, the workpiece will float, and then the workpiece is unlinked with the solid contact. Workpieces are machined by impact and scrubbing of the abrasive in the working fluid, which moves between the solid and workpiece.

Mechanochemical Grinding and Polishing

Mechanochemical grinding and polishing have two meanings. One is to change the workpiece edge corrosion grinding and polishing by adding abrasive in the etching solution. Another is polishing the workpiece surface by using the abrasive itself or between the abrasive and the chemical reaction (Kikuchi et al. 1992).

Grinding and polishing in the etching solution are to use the corrosive effect of the etching solution to reduce the metamorphic layer and improve processing efficiency.

In general, wear will occur when two objects rub against each other. When the workpiece is placed on an abrasive lapping tool, it is a representative method of friction and wear. In grinding and polishing in addition to friction and wear, the chemical reaction can promote its wear process. The practice is also different in different abrasive. It just needs to avoid or reduce the occurrence of friction and wear in the lubrication of the abrasive. Although they may seem different, they are actually two aspects of a problem.

The concept of mechanochemistry includes two aspects. The mechanical energy added in the compression, shearing, friction, and stretching of the solid material will induce changes in the physicochemical properties of the solid material. If it is placed in a different liquid or gas, a chemical reaction will occur, resulting in a variety of different phenomena. In powder processing, led by the mechanochemical role in lubrication, polymer materials and many other areas are actively studying.

Mechanochemical grinding is the role of mechanical energy on the basis of the workpiece and grinding fluid or abrasive chemical reaction to promote the grinding. That is the positive use of its chemical effects, such as its use in electronic components, Si, GaAs, GGG, or sapphire processing in the material removal process. Compared with mechanical grinding, mechanochemical grinding efficiency can not only be increased several times due to chemical effects but also can be processed without the surface of the degenerative layer.

Mechanochemical grinding can be divided into two categories. One is wet milling (solid- and liquid-phase reactions) that utilizes the chemical action of the slurry, and the other is dry milling which utilizes the chemical action of the abrasive itself (solid-phase reaction). In the former, an alkaline solution such as NaOH or KOH is used as a processing liquid for processing Si, an acidic solution is used as a processing liquid for processing GGG and sapphire. There is also a wet mechanochemical polishing of Si crystals by displacement of copper ions. In these wet mechanochemical grindings, the use of the chemical action of the working fluid not only increases the processing efficiency but also significantly reduces processing defects. An example of the latter is dry grinding of sapphire using a soft SiO_2 abrasive. Experiments show that dry milling is faster than aqueous wet milling. After the analysis of grinding debris confirmed that the workpiece and abrasive solid-phase reaction occurred, the processing surface does not process metamorphic layer. Experiments show that the use of soft abrasive dry grinding can also be used for quartz, Si, and other crystals.

Ultrasonic Grinding and Polishing

Ultrasonic grinding is a kind of processing method using free abrasive (grinding paste or grinding fluid) for cutting. The cutting function is generated by the vibration of the grinding tool, which transfers the shape of the grinding head (tool) to the workpiece.

The brittle material is not conducive to processing characteristics and, under the force of the crack in the material, will be extended, resulting in material fracture. Ultrasonic grinding uses the feature of brittle materials to promote material surface fracture and chip formation.

The principle of ultrasonic grinding is that a high-frequency generator generates an alternating current signal and then converts the electrical energy into mechanical energy through a piezoelectric ceramic ultrasonic transducer. The vibration frequency of the mechanical system is the same as the frequency of the AC signal. The resonant frequency of the ultrasonic grinding tool system is related to its mechanical structure and is generally selected in the range of f = 19–23 kHz. When the tool is worn, its resonant frequency changes, so the high-frequency generator must be automatically adjusted to the degree of wear of the tool, minimizing the power consumption of the entire vibration system at that frequency (Hocheng and Kuo 2002).

Ion Beam Polishing

Unlike conventional mechanical polishing methods, ion beam polishing uses charged high-energy atoms or ions (the mass of the ions is greater than the mass

of the atoms, and hence its kinetic energy is greater), which are directed to the workpiece by the ion gun under vacuum. When ions with very high energy strike the surface of the workpiece, the material is removed at the atomic level at the point of impact. The amount of material removed depends on the sputtering time of the ion beam at this point. Since ion beam polishing is to achieve material removal in the order of magnitude, the material removal rate is low. So before using this method, the workpiece should go through the traditional method of pre-polishing. After the use of ion beam polishing, surface profile of the workpiece (such as spherical, aspherical, and asymmetric free-form surface) can achieve very high-precision correction. Although ion beam polishing requires large capital equipment investment and high operating costs, it is still necessary to use ion beam polishing methods for some of the large optical surfaces that require special precision.

Compared with the traditional optical processing methods, ion beam polishing method has the following advantages:

1. It enables material-deterministic ultraprecision machining on the atomic scale.
2. It can achieve a complete correction of the surface shape error through a single machining process.
3. It is insensitive to the vibration of the external environment, temperature changes, and the stability of the loading card.
4. Since the ion beam polishing needs to be carried out in a vacuum space, it can be polished and coated in the same vacuum tank.
5. The workpiece edge will not collapse and warp.

Ion beam figuring (IBF) is generally seen as a shape polishing trimming process, rather than a uniform overall polishing process. The material is removed by the transfer of energy from a single ion (inert or reactive) bombardment to the surface (Cuomo et al. 1989).

Magnetic Fluid Polishing

Magnetic fluid polishing principle is using permanent magnet or electromagnet tools and then will be mixed with abrasive magnetic fluid adsorbed on the tool above the surface of the workpiece to be polished. As the magnetic fluid shape can be automatically changed with the shape of the workpiece, there are no strict requirements on the shape of the magnet tool. You can use a flat tool to adsorb magnetic fluid for polishing. You can also use the rod-shaped tools, one end of the adsorption of magnetic fluid to achieve the free-form surface polishing. Magnetic fluid polishing can get the high-quality processing surface (Kordonski and Jacobs 1996).

Airbag Polishing

Zeeko Company in Britain developed a successful processing of precision curved surface of the new method, which is airbag polishing. The working principle of airbag polishing is the following: the polishing tool is a rubber airbag with an abrasive film layer on the outside. When polishing, the tool airbag rotates to form a

polishing motion, and the workpiece performs relative feeding motion on the airbag polishing tool. The workpiece is generally three-axes feed motion, so that the entire surface of the workpiece can be polished. When going on polishing work, the tool bag also swings at the same time; swinging the center for the curvature of the center of the surface, the abrasive film layer wears uniformly. Due to the flexibility of the tool airbag, it can automatically adapt to the curved shape of the workpiece, so the same tool can be used to polish the surfaces of different shapes. This new surface finish method can obtain high-quality polished surfaces (Lee et al. 2010).

Ultraprecision Machine Tool Spindle Shaft System (Huan 2011)

Spindle shaft system is one of the core components of ultraprecision machine tools. At present, ultraprecision machine tools usually use the gas hydrostatic spindle shaft and hydrostatic spindle shaft system.

Hydrostatic Spindle Shaft System

Hydrostatic technology mainly refers to the hydrostatic bearing lubrication technology, including hydrostatic bearings, hydrostatic guide rail, hydrostatic nut screw pair, hydrostatic spline, and so on. Hydrostatic spindle supports use the form of hydrostatic bearing support technology. According to the principles of oil film pressure generated within the different bearings, fluid-lubricated bearings can be divided into hydrostatic bearings, hydrodynamic bearings, and hydrodynamic-hydrostatic bearings (Chen et al. 2012).

Hydrostatic bearings can get high rotary accuracy, hydrostatic bearings according to different classification methods that can be divided into the following categories:

1. According to the oil supply method, it can be divided into constant pressure oil supply and constant flow oil supply.
2. According to the bearing structure, it can be divided into radial hydrostatic bearings, hydrostatic thrust bearings, and radial thrust hydrostatic bearings.
3. According to whether there is back to the oil tank, it can be divided into circumferential oil tank return type and no circumferential return oil tank.

For details, please see Fig. 6.

Hydrostatic Bearing Working Principle

Hydrostatic bearings are mainly classified from the oil supply. Here are two ways to introduce oil pressure hydrostatic bearing working principle, and according to different principles, the advantages and disadvantages of both are introduced.

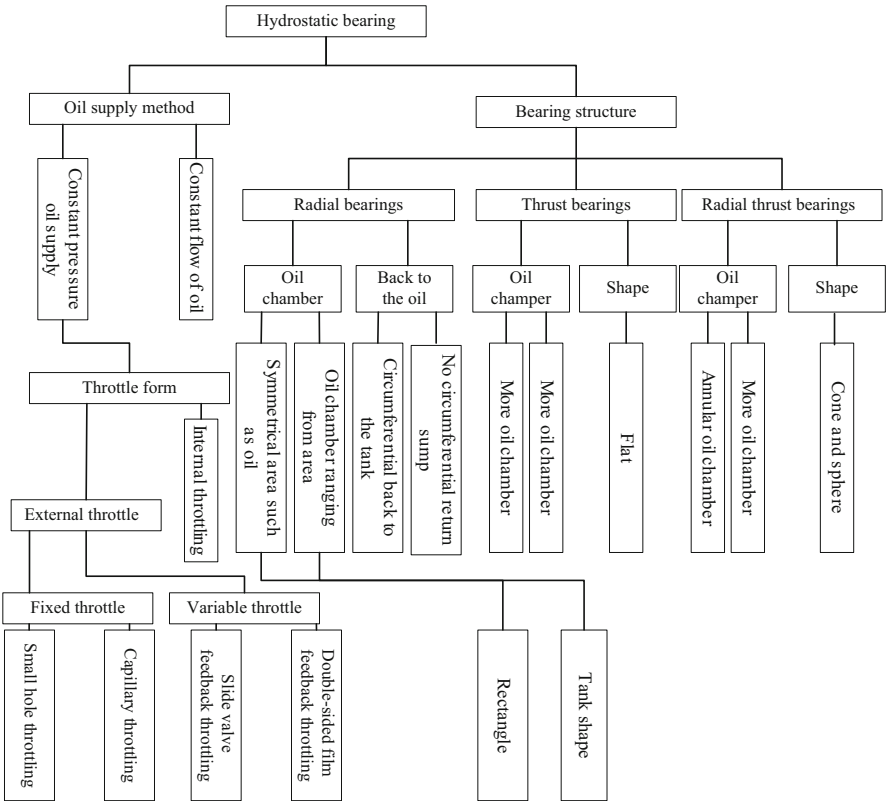

Fig. 6 Hydrostatic bearing classification

Constant Pressure Oil Supply Hydrostatic Bearings Working Principle

The hydrostatic pressure supplied from the constant pressure system of the hydraulic system is supplied from the external pressure oil through the compensating element and then from the oil supply pressure to the oil pressure and then from the oil pressure to the ambient pressure through the clearance between the oil seal surface and the journal. Theoretically, when the bearing is not affected by external force on the shaft, the journal and the bearing hole are concentric, and the clearances, flow rates, and pressures of the oil chambers are all equal, which is called design state. When the shaft is subjected to external force, the displacement of the journal and the average clearance, flow, and pressure of the oil chambers all change. At this moment, the vector of bearing external force and the oil film force of each oil chamber are balanced. Compensation components automatically adjust the pressure of the oil chamber, and the role of compensation flow and the compensation performance will affect the bearing capacity, film stiffness, and so on (Srinivasan 2013). Figure 7 is a schematic of the hydrostatic bearing for a constant pressure system.

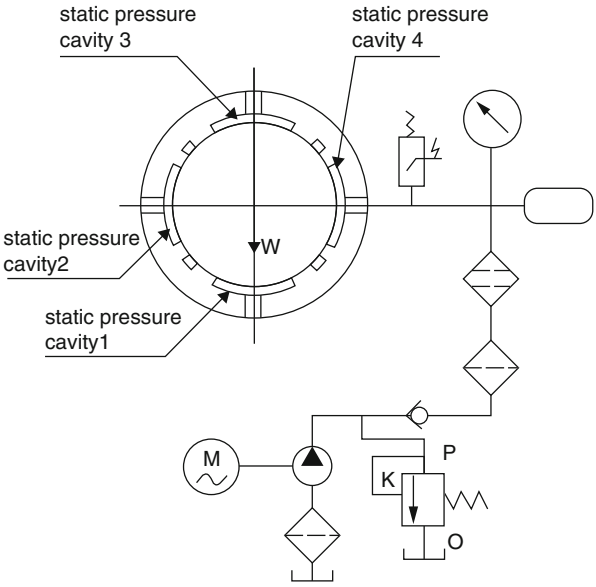

Fig. 7 Schematic diagram of hydrostatic bearing for constant pressure system

When the spindle is subjected to external loads W, the spindle moves to the direction of static pressure chamber 1 displacement e, and the pressure in the static pressure chamber 1 is reduced from h_0 to h_0–e. And then the oil flow resistance on the seal oil surface increases, and the flow from the static pressure chamber through the seal oil surface decreases. According to the continuous flow law, the flow from the oil supply system to the oil chamber 1 via the restrictor 1 is also reduced, so that the pressure drop $\triangle P$ across the restrictor 1 also decreases, so that the pressure $P_{R1} = P_s - \triangle P$ in the static pressure chamber 1 increases, that is, P_{R1} increases to P_{R1}.

On the other hand, the pressure $\triangle P$ of the pressure drop caused by flowing through the throttle 3 increases, so that the pressure $P_{R3} = P_s - \triangle P$ of the static pressure chamber 3 decreases, that is, P_{R3} decreases to P_{R3}. Suppose the effective bearing area of each oil chamber is A_e, then $A_e \times P_{R1}$ is the bearing capacity of the oil chamber 1, $A_e \times P_{R3}$ is the bearing capacity of the oil chamber 3, and the resultant force of the two is the bearing capacity of the hydrostatic bearing.

Constant Flow of Oil Supply Hydrostatic Bearings Working Principle

Constant flow oil supply is characterized by hydrostatic bearings, bearing four oil chambers are connected to a flow of the same pump, and the pump will be a constant flow of oil directly into the bearing oil chamber. Lubricating oil in the oil chamber is formed within the hydraulic force bearing capacity; the main shaft will float in the center of the bearing. Constant flow oil supply hydrostatic bearing oil pressure is the size of the pressure with the load changes. This is the kind of hydrostatic bearing for

oil supply, because each oil chamber of the bearing needs an oil pump with the same flow rate, which causes the complicated structure of the main shaft and increases the cost, which is not suitable for the main shaft structure of the finishing grinding machine. Therefore, this chapter uses constant pressure oil supply hydrostatic bearing work.

Hydrostatic Bearing Throttling Method

Compensating element in constant pressure of oil supply is called throttle, divided into fixed throttle and variable throttle. From the working principle of hydrostatic bearings, you can see that the throttle is a very important element in constant pressure oil supply hydrostatic bearings. It plays a role in automatically adjusting the pressure in the oil chamber, so that the constant pressure oil supply hydrostatic bearing has the corresponding film bearing capacity and oil film stiffness. Common fixed throttles include small orifice restrictors, capillary restrictors, spool throttles, membrane restrictors, etc. The fixed restrictor is simpler in construction than the variable restrictor. Fixed throttle suitable for light load or load changes little place; variable throttle should be used for heavy load or load changes in larger places (Jian 2010).

Hole Restrictor

Hole is d_0 full small and length $L_0 \rightarrow 0$ holes. Because of $L_0 \rightarrow 0$, the loss of energy due to viscous shear stress through the orifice is negligible. Therefore, here viscous fluid and ideal fluid flow are the same; you can directly reference the law of conservation of energy of the ideal fluid in the Bernoulli equation. Figure 8 shows a typical orifice choke (Mizumoto et al. 1996).

Capillary Restrictor

Figure 9 shows a schematic of a capillary choke. Assuming that the inner diameter of the pipe is dc and the length is Lc, the flow of the lubricating oil in the pipe diameter

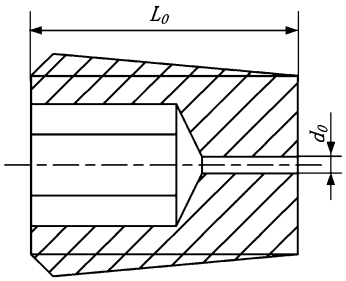

Fig. 8 Hole restrictor

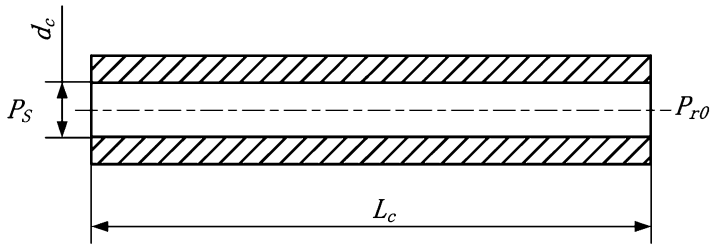

Fig. 9 Capillary restrictor

is laminar, and the cross section of the pipe is circular. Therefore, the viscous fluid pipe forms a concentric cylindrical flow and is an axisymmetric flow.

Flow rate of capillary cross section is calculated as:

$$Q = \frac{\pi \Delta P}{128 \eta L} d_c^4 \tag{1}$$

As can be seen from (1), the fluid flowing through the capillary creates a pressure drop, and the flow Q is proportional to the pressure drop $\triangle P$. Capillary tubes are made based on this feature of capillaries, which are commonly used as capillaries. Syringe needle size specifications, installation, and sealing are more difficult and more limited by the structure (Smith et al. 1986).

Film Feedback Throttle

Film feedback throttle, as shown in Fig. 10, directly uses the pressure feedback throttling principle to change the throttling gap by the elastic deformation of the film and play a feedback role. The advantages of thin film feedback throttles are (1) rapid response, (2) to allow larger bearing manufacturing tolerances, and (3) large bearing capacity. But the film feedback throttle processing is more complex, so improper adjustment of the film will vibrate (Jiang et al. 2013).

The Key Technologies of Hydrostatic Bearing

Hydrostatic Bearing Structure

Hydrostatic Radial Bearings

Figure 11 is a hydrostatic radial bearing structure. On the inner cylindrical surface of the bearing, there are four rectangular oil chambers 2 and a circumferential oil return groove 4 symmetrically, and the arc surface 5 between the oil chamber and the oil return groove is called a circumferential oil seal surface. Between the two ends of the bearing and the oil chamber arc, surface 1 is called

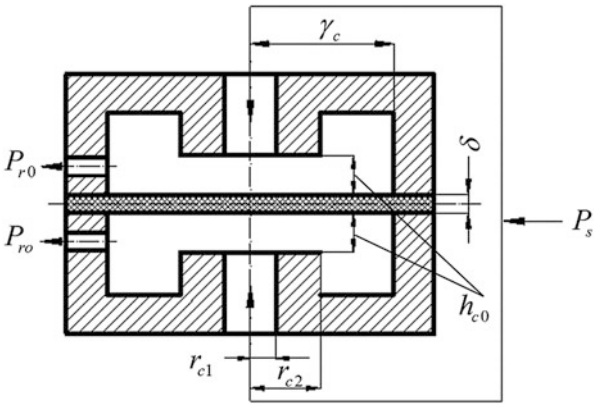

Fig. 10 Film feedback choke

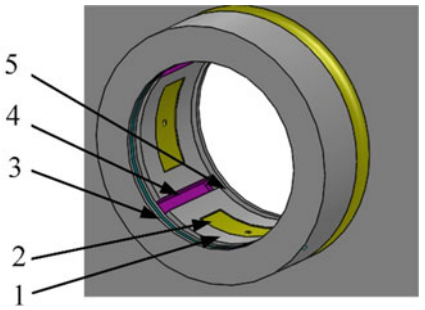

Fig. 11 Schematic diagram of hydrostatic radial bearings. (1) Axial sealing surface, (2) static pressure oil chamber, (3) circumferential sealing groove, (4) circumferential oil return groove, and (5) circumferential sealing surface

the axial seal surface. This structure and the widely used hydrostatic bearing structure are compared to an innovative point, that is, the design of the circumferential direction of the hydraulic oil seal groove 3 and the bearing structure as a whole, so that the entire hydrostatic shaft structure is simple. After the spindle is loaded into the bearing, there is an appropriate amount of clearance between the bearing seal face and the spindle. The size of this clearance directly affects the rigidity and accuracy of the spindle (Murphy and Wagner 1991).

Hydrostatic Thrust Bearings

Figure 12 shows the hydrostatic radial bearing structure. In the circumferential direction of the bearing face symmetrically distributed with six fan-shaped oil chambers 2 and the radial oil return groove 4. Oil chamber and the radial return groove 4 and the circumferential groove between the oil return groove 3 are called thrust bearing radial seal surface. Thrust bearings in pairs, by grinding the spindle shoulder to ensure oil film clearance, are adjusting the spindle axial movement, to ensure a small axial error and high axial stiffness (Lin 2000).

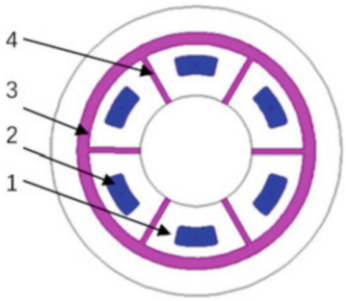

Fig. 12 Hydrostatic thrust bearing schematic. (1) Radial seal face, (2) static pressure oil chamber, (3) circumferential seal groove, and (4) radial oil return groove

Hydrostatic Bearing Parameter Design

Throttling Ratio β

Defining the hydraulic pressure supply station for the P_S and oil pressure for the P_R, throttle ratio is:

$$\beta = \frac{P_S}{P_R} \tag{2}$$

β has the best value for the maximum film stiffness as the objective function. The optimal throttling ratio is different for different throttling forms. For the small hole throttle, according to the production of practical experience, small hole aperture is too small and easy to block, but too large cannot play the purpose of improving the rigidity of the hydraulic oil. Through a series of experiments which obtained the maximum oil film stiffness through different oil supply pressures, the optimal ratio of the oil supply pressure P_R to the pressure P_S of the oil cavity was 1.71. This throttling ratio is used directly when calculating the oil chamber pressure in the following sections.

Bearing Clearance

Hydrostatic bearing design should first of all preset a film thickness h_0, known as the design gap. The vast majority of bearing performance and h_0 are directly related; it also directly affects the bearing parts of the machining accuracy. If h_0 is too small, it is easy to hold the shaft when the oil film breaks under heavy load, but if h_0 is too large, the lack of rigidity of the film cannot afford the required bearing capacity. Therefore, the calculation must be repeated checking h_0 and the bearing size, accounting oil film stiffness, load carrying capacity, flow, heat, and machining accuracy to determine the final h_0.

The Required Working Pressure for Bearing

The working pressure required for the bearing is that the oil supply pressure is set to P_s and the required flow at this supply pressure is set to Q_s. Raising the oil pressure can increase the bearing capacity but also increase the fixed throttle static pressure bearing stiffness. However, with the increase of the pressure of the oil supply, the flow of the bearing and the power consumption of the oil pump also increase correspondingly, causing the temperature of the bearing system to increase. Low

oil pressure, in addition to reducing the bearing capacity and stiffness, also adversely affects the dynamic performance of the bearing. Therefore, the choice of supply pressure principle is to meet the bearing maximum load capacity and stiffness under the conditions of the fuel supply device to minimize power consumption. It can also be conducive to reduce the bearing system temperature. Hole throttle device with the lubricating oil temperature is generally 50 °C, 50% of the two hydraulic oil supply pressure controls at 2.5 MPa or so.

Ultraprecision Hydraulic Hydrostatic Spindle Design

According to the technical requirements of the machine tool for the ultraprecision spindle shaft system, under the premise of the individual technical requirements described above, the design of the ultraprecision hydrostatic spindle shaft system is carried out.

According to the technical requirements of the machine tool for the ultra-precision spindle shafting, the design of the ultra-precision hydrostatic spindle shafting system is carried out under the premise of the individual technical requirements. The design requires consideration of the machining process and assembly accuracy of the parts, including the matching precision and contact accuracy between the parts, the position dimensional accuracy and the relative motion accuracy. Ultraprecision hydraulic hydrostatic spindle mainly includes built-in motor and shaft and so on. Figure 13 shows the assembly of the ultraprecision hydrostatic spindle.

Gas Hydrostatic Spindle Shaft System

Gas hydrostatic technology is the compressed air into the bearing through the throttle or guide gap, which forms the formation of a certain pressure and maintains a stable lubricating film. The theory was first proposed by G. Hirm in 1854. According to the different ways of hydrostatic bearing, the hydrostatic bearing can be divided into several forms, such as orifice throttling, slit throttling, surface throttling, and porous throttling (Chen et al. 2011).

Gas Hydrostatic Bearing Working Principle

Gas hydrostatic bearings use gas for lubrication and support loads to achieve ultraprecision machining. Gas hydrostatic bearings are high precision, low friction coefficient, low power consumption, no friction and wear, damping characteristics, and long service life (Ford et al. 1957).

Hydrostatic Bearing Throttling Form

The main methods of gas static pressure are throttling slit, orifice throttling, capillary throttling, surface throttling, and porous throttling. Gas hydrostatic throttling form

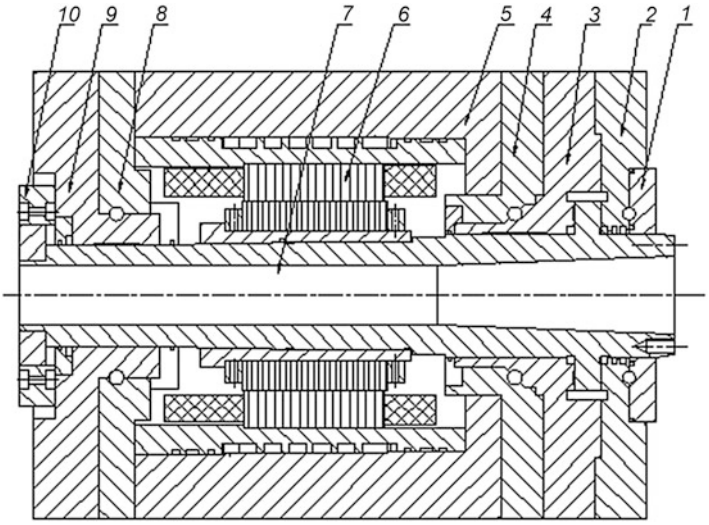

Fig. 13 Super-precision hydrostatic spindle assembly diagram. (1) Front cover, (2) thrust bearing, (3) front bearing, (4) front bearing transition sleeve, (5) sleeve, (6) Parker built-in motor, (7) spindle, (8) bearing transition sleeve, (9) rear bearing, and (10) encoder

and bearing pressure distribution have a great relationship; Fig. 14 is a common form of throttle pressure distribution. From the figure we can see that in several throttling forms, the pressure distribution obtained by porous throttling is the most uniform. The porous bearing surface can be used as a bearing composed of many tiny holes, so the pressure distribution in the gas film is uniform and the bearing capacity and rigidity are large. At the same time, the manufacture of porous materials is relatively simple, good damping, and stabile.

Porous Gas Hydrostatic Lubrication

Throttle Form

There are many types of porous, depending on the type of throttle that can be divided into full porous type, local porous type, porous throttle type, and so on. Three kinds of throttling structures are shown in Fig. 15. H and h in the figure are the thickness of the porous material and the thickness of the gas film, respectively; *Ps* and *Pa* are the gas supply pressure and the outlet pressure, respectively. Among them, the full porous throttling gas hydrostatic bearing has the advantages of simple structure, easy manufacture, and stable operation.

Porous Structural Material

Currently used for porous bearings are porous bronze, porous ceramics, porous graphite, and so on. Porous bronze and porous graphite are the most mature materials in the manufacturing technology at present. The comprehensive performance of

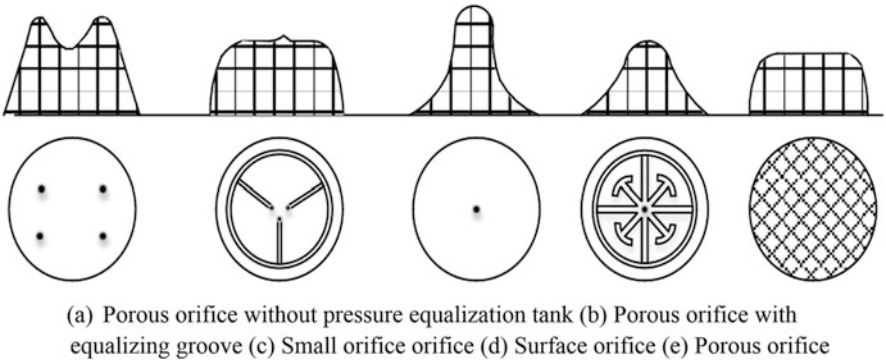

Fig. 14 Gas pressure distribution in different throttle modes. (**a**) Porous orifice without pressure equalization tank. (**b**) Porous orifice with equalizing groove. (**c**) Small orifice. (**d**) Surface orifice. (**e**) Porous orifice

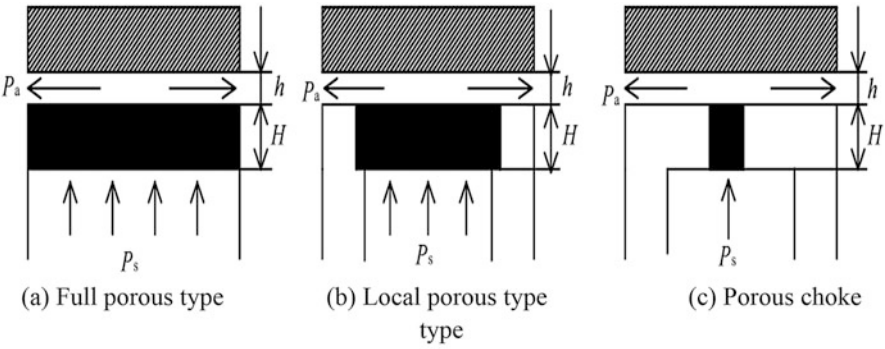

Fig. 15 Porous cutoff type. (**a**) Full porous type. (**b**) Local porous type. (**c**) Porous choke type

porous ceramics is better than the former two, but at present, it has not been widely used in China. Porous bronze is cheap, and its manufacturing process is simple, but its strength and hardness are poor. Porous graphite material itself has a certain degree of self-lubricating, post-processing more convenient and long service life. Therefore, considering all aspects of performance factors, porous graphite is ideal as a hydrostatic bearing surface material.

Gas Hydrostatic Bearing Design

For the hydrostatic spindle, the bearing capacity, stiffness, and stability of the gas film are directly related to the gas pressure distribution in the bearing gap. Relative to the orifice and other forms of throttle, porous gas pressure distribution of the bearings is more complicated. In addition to the anisotropy of the bearing, changes

in the pores and partial clogging in the process must also be considered. Therefore, when analyzing the pressure distribution inside the porous bearing and the gas film, related assumptions need to be made to establish a physical model that can meet the actual situation and at the same time facilitate theoretical analysis (Rowe 2013).

1. Gas flow inside the porous bearings to meet the hole model theory.
2. The flow of gas inside the porous material is mainly viscous flow, ignoring the influence of inertial flow and obeying Darcy's law.
3. The gas is compressible and satisfies the ideal equation of state.
4. Lubrication gas is isothermal and equal to viscosity flow.
5. At the interface between the porous material and the gas film, the internal pressure of the porous material is equal to the gas pressure on the surface of the bearing clearance.

Gas flow belongs to the field of fluid mechanics. Computational fluid dynamics is based on the three equations of continuous equation, momentum equation, and energy equation. In solving the gas pressure distribution of hydrostatic bearing, the continuous equation and momentum equation are mainly used. At the same time, we also need to solve the equation of state.

The optimal design of the ultraprecision gas static pressure spindle can achieve the rotation accuracy of 0.05 μm or more. The gas static pressure spindle has the advantages of high speed and high precision. Pneumatic hydrostatic spindle is used for porous throttle, with rigidity and easy processing characteristics. A variety of influencing factors should be considered when designing a porous ultraprecision spindle shafting.

Effect of Porous Medium Permeability Φ on Static Performance

At the same eccentricity, the permeability of porous media has a great influence on bearing performance. In order to achieve better throttling effect, the permeability can be taken in the order of 10^{-16}~10^{-14}, and when taking 10^{-15}, the best throttling effect can be achieved. If Φ is too small, the gas mass flow is very small, gas pressure drop through the porous medium is too large, the pressure in the film is too small, and of course, carrying capacity is small. If Φ is too large, the gas mass flow is large; the pressure drop on both sides of the bearing is very small; when the load changes, the pressure in the gas membrane changes little; and the carrying capacity drops. Therefore, for the use of porous materials for the throttle, the permeability should be selected on the order of 10^{-16} to 10^{-14}.

Supply Pressure *Pa* of the Impact

Gas pressure increases, the bearing capacity and static stiffness are increased, but the damping decreases.

The Effect of the Average Film Thickness h_0

The smaller the thickness of the film is, the larger the bearing capacity is, and the stiffness and damping increase at the same time. The best average film thickness h_0 should be less than 10 μm. Film thickness is mainly by the shaft and bearing with the guarantee; if the average film thickness h_0 less than 10 μm, the processing accuracy is very high, so in practice it is not desirable.

Influence of Bearing Length L

Carrying capacity and L are not directly proportional to the increase. Therefore, the actual design cannot blindly increase the bearing length method to increase the carrying capacity. Considering bearing processing technology and static performance factors, the general aspect ratio is L/D = 1.

Effect of Porous Material Thickness

In the case of the same permeability, the greater the thickness of the porous bearing, the smaller the mass flow bearing capacity, the smaller the carrying capacity. Bearing thickness is small, under the action of compressed gas, and easy to produce deformation and will also have an impact on the static performance. Therefore, in the bearing design, you should choose a suitable thickness.

The Effects of Slippery Flow

There is a radial flow at the interstices of the porous body and near the bearings, and slip flow occurs inside the bearing gap and adheres to the porous surface due to the continuity of the fluid. The influence of speed slip on the bearing stiffness is more complicated, which changes with the change of the film gap.

Dual Cylinder Gas Hydrostatic Spindle Shaft Design

Figure 16 shows the design of the ultraprecision body hydrostatic spindle shafting. The spindle shafting adopts a medium-shaped structure, that is, both ends of the spindle structure serve as a radial support, and both surfaces of the middle disk serve as a circumferential support. The medium-shaped spindle has the characteristics of high precision and high rigidity, but it is difficult to be processed and assembled. It is suitable for use as turning and grinding spindles for medium and large loads.

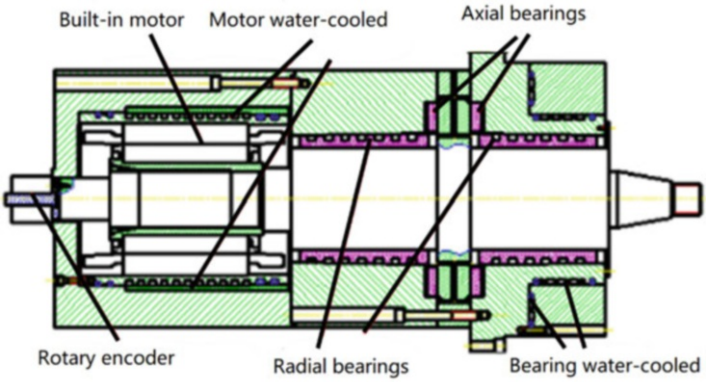

Fig. 16 Aerostatic spindle design

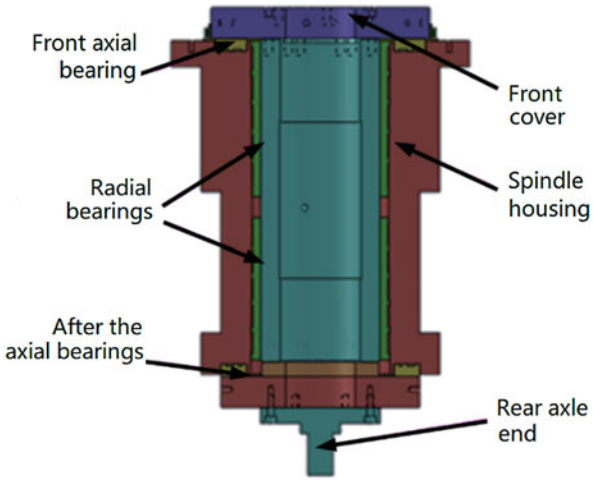

Fig. 17 Schematic diagram of the main shaft of the hydrostatic pressure shaft

Design of I-Shaped High Stiffness Gas Hydrostatic Spindle Shaft

The I-shaped spindle shaft is the axial support of the disk surfaces at both ends of the spindle, and the intermediate shaft serves as the radial shaft support structure. The appearance is shown in Figure 17. In I-shaped spindle, thrust surface can be designed larger and therefore has the advantage of large axial stiffness; I-shaped spindle, thrust plate, and rotor can be integrated design and processing and can be machined to a higher dynamic balancing accuracy.

Conclusion

This chapter according to the removal of the rigid classification can be divided into rigid removal tool, flexible removal tool, and semiflexible removal tool categories. Turning tools, milling cutters, drills, etc. belong to the rigid removal tool; the

grinding wheel belongs to the semiflexible removal tool; grinding fluid, polishing fluid, etc. belong to the flexible removal tool; this chapter describes the main technical content of various types of tools.

This chapter focuses on the diamond tool from the diamond tool design, material selection, and wear point of view. For ultraprecision grinding wheel, this chapter from the abrasive particle size and selection, binder, tissue and concentration and its selection, hardness and selection, the shape and size of the grinding wheel and its base material, the grinding of the super-abrasive grinding wheel, and the balance of the grinding wheel with the superhard abrasive are described. For flexible tools, this chapter describes various types of ultraprecision grinding and polishing tools.

This chapter elaborates the ultraprecision hydrostatic spindle shaft and ultra-precision gas static spindle shaft system and studies the related basic theory, design theory, and related influencing factors.

References

Altintas Y (2012) Manufacturing automation: metal cutting mechanics, machine tool vibrations, and CNC design. Cambridge University Press, Cambridge, UK

Astakhov VP, Stanley A (2015) Polycrystalline Diamond (PCD) tool material: emerging applications, problems, and possible solutions. Traditional machining processes. Springer, Berlin, pp 1–32

Bin L (2015) Large-diameter aspheric mirror precision CNC grinding technology. Xi'an Jiaotong University, Xi'an

Brandt G (1999) Ceramic cutting tools, state of the art and development trends. Mater Technol 14(1):17–22

Brinksmeier E et al (2010) Ultra-precision grinding. CIRP Ann Manuf Technol 59(2):652–671

Chen FJ et al (2010) Profile error compensation in ultra-precision grinding of aspheric surfaces with on-machine measurement. Int J Mach Tools Manuf 50(5):480–486

Chen D, Bonis M, Zhang F, Dong S (2011) Thermal error of a hydrostatic spindle. Precis Eng 35(3):512–520

Chen D, Fan J, Zhang F (2012) Dynamic and static characteristics of a hydrostatic spindle for machine tools. J Manuf Syst 31(1):26–33

Cuomo JJ, Rossnagel SM, Kaufman HR (1989) Handbook of ion beam processing technology. Noyes Publications, Park Ridge

Davim JP, Mata F (2005) Optimization of surface roughness on turning fibre-reinforced plastics (FRPs) with diamond cutting tools. Int J Adv Manuf Technol 26(4):319–323

de Oliveira JFG, Dornfeld DA (1994) Dimensional characterization of grinding wheel surface through acoustic emission. CIRP Ann Manuf Technol 43(1):291–294

Ford GWK, Harris DM, Pantall D (1957) Principles and applications of hydrodynamic-type gas bearings. Proc Inst Mech Eng 171(1):93–128

Heying LI (2002) Static and dynamic balancing of diamond grinding wheel. Diam Abras Eng 1:008

Hitchiner MP, Marinescu ID, Uhlmann E, Rowe WB, Inasaki I (2016) Handbook of machining with grinding wheels. CRC Press, Boca Raton

Hocheng H, Kuo KL (2002) Fundamental study of ultrasonic polishing of mold steel. Int J Mach Tools Manuf 42(1):7–13

Huan L (2011) Research on key issues of high precision hydrostatic spindle. Xi'an Jiaotong University, Xi'an

Jian TANG (2010) Study on load characteristic for hydrostatic bearing with different throttle methods. Mach Tool Hydraul 12:029

Jiang GY, Wang YQ, Yan XC (2013) Study on throttle methods for hydrostatic bearing. In: Applied mechanics and materials, vol 373. Trans Tech Publications, Switzerland, pp 2119–2123
Jones RA (1977) Optimization of computer controlled polishing. Appl Opt 16(1):218–224
Kikuchi M, Takahashi Y, Suga T, Suzuki S, Bando Y (1992) Mechanochemical polishing of silicon carbide single crystal with chromium (III) oxide abrasive. J Am Ceram Soc 75(1):189–194
Kim DW, Burge JH (2010) Rigid conformal polishing tool using non-linear visco-elastic effect. Opt Express 18(3):2242–2257
Komanduri R, Lucca DA, Tani Y (1997) Technological advances in fine abrasive processes. CIRP Ann 46(2):545–596
Kordonski WI, Jacobs SD (1996) Magnetorheological finishing. Int J Mod Phys B 10(23–24): 2837–2848
Lambropoulos JC, Jacobs SD, Ruckman J (1999) Material removal mechanisms from grinding to polishing. Ceram Trans 102:113–128
Lee H, Kim J, Kang H (2010) Airbag tool polishing for aspherical glass lens molds. J Mech Sci Technol 24(1):153–158
Lin JR (2000) Surface roughness effect on the dynamic stiffness and damping characteristics of compensated hydrostatic thrust bearings. Int J Mach Tools Manuf 40(11):1671–1689
Lin K-H, Peng S-F, Lin S-T (2007) Sintering parameters and wear performances of vitrified bond diamond grinding wheels. Int J Refract Met Hard Mater 25(1):25–31
Malkin S, Guo C (2008) Grinding technology: theory and application of machining with abrasives. Industrial Press, South Norwalk
Mizumoto H, Arii S, Kami Y, Goto K, Yamamoto T, Kawamoto M (1996) Active inherent restrictor for air-bearing spindles. Precis Eng 19(2–3):141–147
Murphy BT, Wagner MN (1991) Measurement of rotordynamic coefficients for a hydrostatic radial bearing. J Tribol 113(3):518–525
Poulachon G, Moisan A, Jawahir IS (2001) Tool-wear mechanisms in hard turning with polycrystalline cubic boron nitride tools. Wear 250.1(12):576–586
Ronald BA, Vijayaraghavan L, Krishnamurthy R (2009) Studies on the influence of grinding wheel bond material on the grindability of metal matrix composites. Mater Des 30(3):679–686
Rosa LG et al (2004) Evaluation of diamond tool behaviour for cutting stone materials. Ind Diam Rev 1:45–50
Rowe WB (2013) Hydrostatic and hybrid bearing design. Elsevier, Amsterdam
Sexton JS, Stone BJ (1981) The development of an Ultrahard abrasive grinding wheel which suppresses chatter. CIRP Ann Manuf Technol 30(1):215–218
Shaw MC (1996) Principles of abrasive processing, vol 3. Oxford University Press on Demand, Oxford
Shiou FJ, Ciou HS (2008) Ultra-precision surface finish of the hardened stainless mold steel using vibration-assisted ball polishing process. Int J Mach Tools Manuf 48(7–8):721–732
Smith RD, Fulton JL, Petersen RC, Kopriva AJ, Wright BW (1986) Performance of capillary restrictors in supercritical fluid chromatography. Anal Chem 58(9):2057–2064
Srinivasan V (2013) Analysis of static and dynamic load on hydrostatic bearing with variable viscosity and pressure. Indian J Sci Technol 6(6):4777–4782
Stephenson DJ, Veselovac D, Manley S, Corbett J (2001) Ultra-precision grinding of hard steels. Precis Eng 25(4):336–345
Sumiya H, Toda N, Satoh S (1997) Mechanical properties of synthetic type IIa diamond crystal. Diam Relat Mater 6(12):1841–1846
Suratwala T, Wong L, Miller P et al (2006) Sub-surface mechanical damage distributions during grinding of fused silica. J Non-Cryst Solids 352(52–54):5601–5617
Suratwala T, Steele R, Feit MD et al (2008) Effect of rogue particles on the sub-surface damage of fused silica during grinding/polishing. J Non-Cryst Solids 354(18):2023–2037
Tian Y, Zhang D, Shirinzadeh B (2011) Dynamic modelling of a flexure-based mechanism for ultra-precision grinding operation. Precis Eng 35(4):554–565
Wada R et al (1980) Wear characteristics of single crystal diamond tool. CIRP Ann Manuf Technol 29(1):47–52

Webster J, Tricard M (2004) Innovations in abrasive products for precision grinding. CIRP Ann Manuf Technol 53(2):597–617

Wegener K et al (2011) Conditioning and monitoring of grinding wheels. CIRP Ann Manuf Technol 60(2):757–777

Wei L et al (1993) Thermal conductivity of isotopically modified single crystal diamond. Phys Rev Lett 70(24):3764

Yan J, Katsuo S, Tamaki J'i (2003) Some observations on the wear of diamond tools in ultra-precision cutting of single-crystal silicon. Wear 255.7(12):1380–1387

Yuan J, Zhang F, Dai Y et al (2012) Development research of science and technologies in ultra-precision machining field. Jixie Gongcheng Xuebao (Chin J Mech Eng) 46(15):161–177

Zhou M, Ngoi BKA, Yusoff MN, Wang XJ (2006) Tool wear and surface finish in diamond cutting of optical glass. J Mater Process Technol 174(1–3):29–33

Design of Precision Linear Drives

5

Wanqun Chen and Yazhou Sun

Contents

Introduction 132
Key Factors to Improve the Precision of Linear Motion 132
Travel Accuracy 133
Positioning Accuracy 133
System Stiffness 134
Thermal Effects 135
Design Principles of the Precision Linear Drives 136
Types of Linear Motion Guides 138
Sliding Contact Linear Motion Bearing-Based Guides 139
Rolling Element Linear Motion Bearing-Based Guides 140
Hydrostatic or Aerostatic Linear Motion Bearing-Based Guides 140
Magnetic Linear Motion Bearing-Based Guides 142
Drive System 143
Ball Screw 143
Rack and Pinions 144
Linear Motor 144
Metrology and Sensor 145
Linear Encoder 146
Integrated Position Measuring with Linear Guides 147
A Case Study: Design of a Hydrostatic Guide 148
Structural Design of the Slide 148
Stiffness and Load Capacity Calculation of Hydrostatic Bearing 149
Influence of Constant-Pressure Oil Source Fluctuations on the Performance of Hydrostatic Slide 151
References 154

W. Chen · Y. Sun (✉)
Center for Precision Engineering, Harbin Institute of Technology, Harbin, People's Republic of China
e-mail: chwq@hit.edu.cn; sunyzh@hit.edu.cn

Z. Jiang, S. Yang (eds.), *Precision Machines*, Precision Manufacturing,
https://doi.org/10.1007/978-981-13-0381-4_4

Abstract

This chapter introduces the design of linear feed drive systems used in machine tools. The key factors to improve the precision of linear motion are summarized, and the design principle of the precision linear drives is given. The types of the linear motion guides and the drive systems commonly used in machine tools are described. Finally, a typical case on the design of hydrostatic slide is presented.

Keywords

Precision linear drives · Guideway design · Design principle

Introduction

Feed drives are usually employed to position the machine tool components installed with cutting tool and/or workpiece to the desired working location. The positioning accuracy and speed, hence, directly determine the quality and productivity of machine tools (Altintas et al. 2011). Generally, feed drives could be divided into two classes, including the linear and rotation ones. Thereinto, the linear drive elements are usually adopted in precision and ultra-precision machine tool.

Precision, as one key indicator of a linear drive system, is regarded as a combination of accuracy and repeatability. The former one refers to the discrepancy between the targeted position and actual position of a moving part. Therefore, positioning accuracy is the maximum deviation between the actual and targeted positions during each movement process. Repeatability relates to how precisely a linear motion system positions itself when repeatedly approaching a position from the same direction, which takes into the deviation of actual position from the targeted position account.

A linear drive system includes hardware and its controller. The hardware often consists of bearings, drives, guideways, and sensors, all of which have important influences on the working performance of the linear drive system. If the mechanical structures of the hardware are not reasonably designed, the precision of entire linear drive system is difficult to be ensured, despite the use of most-sophisticated motion controller. Reasonable design of the hardware, namely, mechanical component, is of significance for enabling the precise/ultra-precise movements.

For this reason, this chapter firstly discusses the key factors of the precision of linear motion. Secondly, the design principle of the linear drive system is given. Thirdly, the typical classes of hardware used in precision/ultra-precision machine tool are summarized; finally, a case of design and analysis of hydrostatic slide used for ultra-precision machining is provided.

Key Factors to Improve the Precision of Linear Motion

In order to improve the performances of linear drive system, the following factors should be considered.

Travel Accuracy

As shown in Fig. 1, a component has six degrees of freedom (DOFs), including three direction translating DOFs (*x*-, *y*-, and *z*-axis) and three rotating DOFs (*x*-axis rolling, *y*-axis yawing, and *z*-axis pitching). There are five possible types of way inaccuracy, corresponding to the five remaining DOFs (*y*- and *z*-axis translating; *x*-axis rolling, *y*-axis pitching, and *z*-axis yawing). For example, if this component is linearly moved along *x*-axis, three angular errors (*x*-axis rolling, *y*-axis pitching, and *z*-axis yawing) and horizontal and vertical straightness errors as well as *x*-axis position error may occur during the moving process. Additionally, there are interrelations between these errors (e.g., angular rotation produces a translational error at any point other than the center of rotation), it is worthwhile to carefully examine the effects of each type of error and its measurement method.

These motion errors highly depend on the quality of the traveling guidance system and the mounting surfaces. Linear motion systems typically conform to their mounting surfaces, so travel accuracy tends to vary with the manufacturing accuracy and the installation accuracy.

Positioning Accuracy

Positioning accuracy depends on the capabilities and tolerances of the drives used in the system. Currently, the usually used drives include electromechanical ball screw, hydraulic or pneumatic cylinder, electric linear motor, rack and pinion, etc. Ball screws have significant lead error or lead deviation within the ball screw or ball nut. The magnitude of error often depends on the manufacturing method used to generate the screw threads.

For forming threads via rolling, lead error can be induced primarily through the post process heat treatment. During the grinding process, due to the inherent machine inaccuracies, tool wear, or heating of the ball screw, lead error may be also formed. Grinding has been traditionally recognized as more accurate than

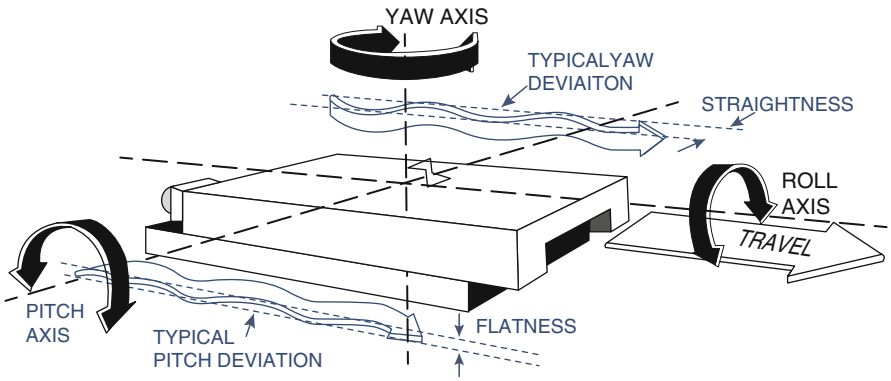

Fig. 1 Schematic diagram of the errors of a slide

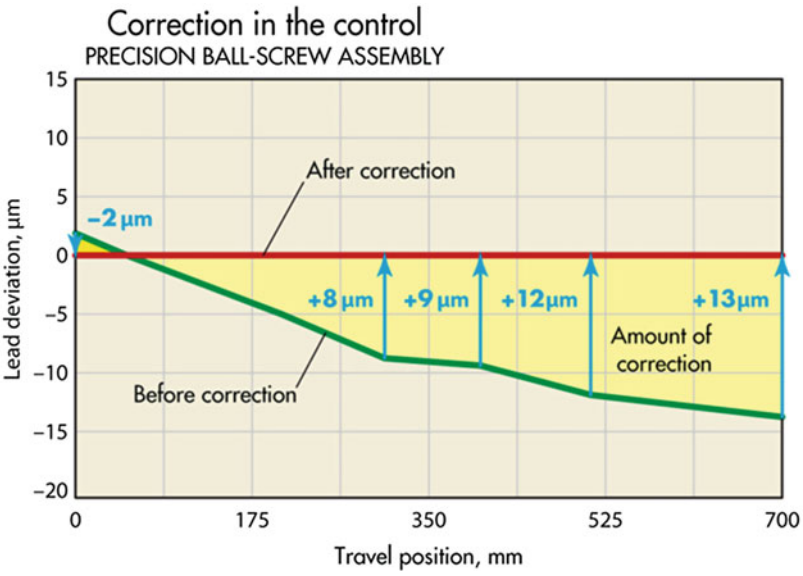

Fig. 2 This graph illustrates how electronic correction for ball screw lead error minimizes deviations across 700 mm of travel (http://www.machinedesign.com/motion-control/six-keys-more-precise-linear-motion)

rolling, but the gap is narrowing. Some Rexroth rolled screws deliver Class 5 or even Class 3 precision for travel (lead) deviation, with a maximum deviation of ±12 µm across travel distance of 300 mm. Electronic correction techniques capable of compensating lead errors across standard travel run can be also applied to further improve accuracy. The "Correction in the Control" graphic in Fig. 2 shows a corrected lead deviation of up to 13 µm over the travel distance of 700 mm.

Positioning accuracy can be also improved by imposing external feedback to the machine axis, which can be indirectly realized by using a rotary encoder or directly performed by using a linear scale. Positional feedback from sensor contributes to assist the servo drive to correct the final motion position.

System Stiffness

Precise or ultra-precision drive system requires higher system stiffness, which has extremely important influence on the practical precision. During the working state, any force or load imposed to the motion components along different directions, including downward, upward, or sideways, can cause deflection, seriously affecting the repeatability of the linear drive system. To eliminate such kind of deflection, highly experienced designers often improve the overall rigidity or stiffness of the linear guide block by introducing preload with oversized antifriction elements. The "Effects of Preload" graphic shows typical preload, using oversized rolling elements

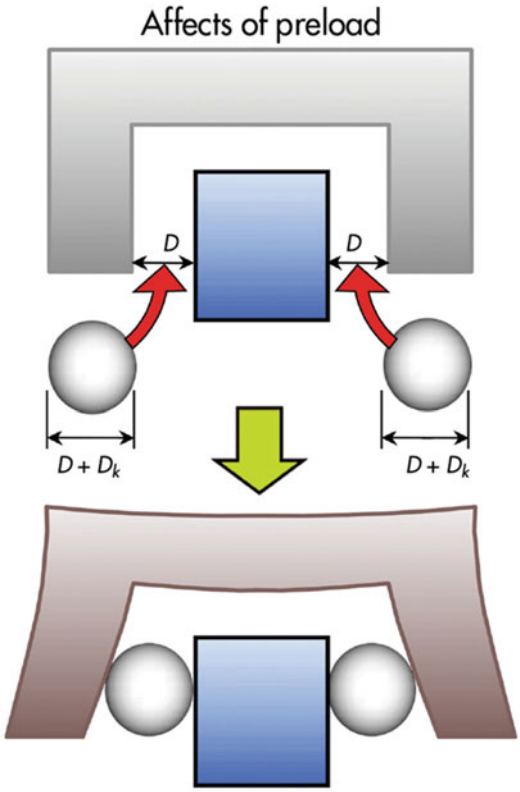

Fig. 3 One way to correct for elastic deflection is to preload linear guides with oversized antifriction components

(*Dk*) in the guide rail gap (diameter *D*), as given in Fig. 3. Linear guide manufacturers usually use widely varying levels of preload to minimize deflection.

In the precise/ultra-precision machine tool, higher system stiffness of the drive system can contribute to enhance the rigidity of the total machine tool. For the drive system, the system stiffness could be increased by reasonable adjusting the stiffness of its support bearings, ball nut unit, and the ball screw itself. For screw drive, the largest influential factor of its stiffness is its length. Generally, the longer the screw, the harder deflection compensation. The usually used compensation method includes imposing extra-preload or selecting a stiffer ball nut.

Thermal Effects

All linear motion components (motor, bearings and nut) will generate heat during working state, which should be considered in the design process to improve the performance of the drive system. Different temperatures could be exhibited at different positions of an axis, mainly depending on running time, dynamic cycle, and forces on each part. The nonuniform thermal temperature will induce the change

of the performance of the drive system. For instance, thermal effect may lead to nonuniform ball screw expansion and contraction, to eliminate this issue, the bearing could be floated within a pillow block. But this method will decrease the rigidity of the drive system. Additionally, thermoplastic deformation presents another challenge for engineers, as heat influences linear expansion of all components. Deformation could cause misalignment or displacement and lead to the formation of excess force on the bearings and nuts. Furthermore, this force will induce the generation of friction, which easily generates more heat. The higher rigidity also means the generation of more friction-induced heat, which will seriously affect the alignment, stiffness, and performance of device.

The good news is that designers can often offset or compensate for these thermal influences, with advances in drive and control electronics.

Design Principles of the Precision Linear Drives

The design principles of the precision linear drives can be summarized by analyzing the error sources of the linear drive system. Figure 4 illustrated a typical guideway in machine tool, which consists of a standard vee groove and a flat slideway. A number of common error sources could be clearly identified from Fig. 4 (Smith 2003).

Firstly, and most obviously, the drive axis is non-coincident with either the center of friction or the center of inertia. Driving through an axis non-coincident with the center of inertia will result in a torque perpendicular to the axis, which is proportional to the mass and the acceleration of the carriage and to the square of its offset. When a stable velocity is achieved, this effect is often ignored during the use of

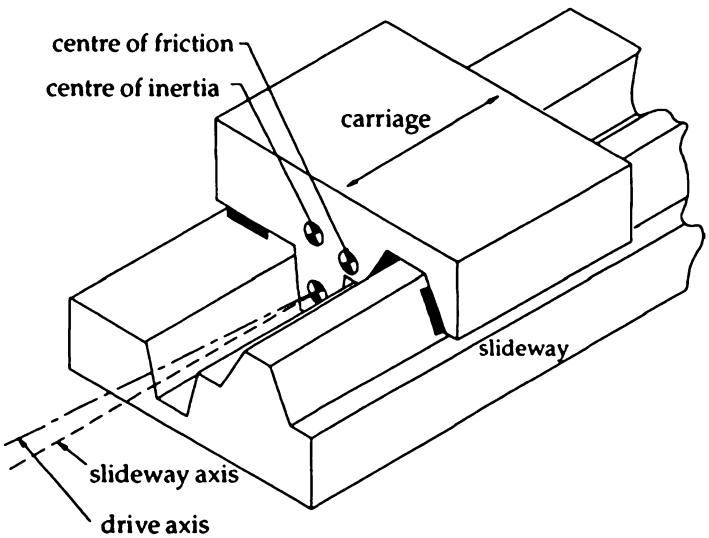

Fig. 4 A typical slideway geometry

continuously driven machinery. However, the performance of systems using stepper motors or involving discontinuous motion may be limited by this error. On the other hand, the varying moments, which are perpendicular to the drive axis, will be proportional to the frictional drag and the offset. Considering the fickle nature of friction, the magnitude is likely to be unpredictable, but the effect will be present even in the steady state. Therefore, *principle 1: ensure that the centers of inertia and friction are coincident with the drive axis*.

Figure 4 also shows that the axis of the drive is not parallel to that of the carriage motion. This may cause the carriage to twist, which must be prevented by imposing extra forces at parts of bearing pads. Although this may have only secondary effects on the straightness of a well-designed slideway, the increased and variable loads on bearing pads will increase internal stresses and may induce unnecessary wear. Variation of the forces may also shift the position of the center of friction. Therefore, *principle 2: in the design process, the drive and slideway axes should be ensured to be colinear.*

The main requirement in most slideway designs is for a reliable and robust system. However, for ultra-precision sideway, repeatability and linearity should be two critical parameters. However, the former one is easily limited by thermal stability and tribology of the mechanical components and bearings. As for linearity, considering that the friction forces between the carriage and slide may cause distortions of its structure, it will be influenced by the friction force. In designs that involve material contact, friction forces will vary with stick-slip-induced displacement and nonuniform abrasion or delamination of the bearing surface. Stick-slip may induce random errors into the motion and change the susceptibility of a bearing. Consequently, it is also unpredictable. Because the variations in frictional force are usually proportional to the normal force, a low friction coefficient, as found with hydrostatic bearings and some polymeric bearings under high load, is desirable. At high load, even low coefficients may cause significant force variation. Thus in most precision applications, some increase in friction coefficient will be tolerated in order to use a material with little tendency to stick-slip behavior. Therefore, *principle 3: optimize the tribological properties for the purpose of precision*.

Work done in maintaining carriage motion will create an equivalent amount of heat at the bearings that must eventually be extracted again. In many cases this simply involves allowing the heat to diffuse into a large thermal mass or into the environment. For many engineering applications, thermally induced errors are not highly significant. This is not the case in precision systems, where thermal loading, particularly if varying dynamically, can be a major error source. Apart from the direct frictional effects, thermal loads are commonly introduced by motor drives, machine coolants, and the flow of fluid in hydrostatic bearings. The problem of heat from motor drives can be dealt with by thermally and mechanically decoupling them to reduce conductive, convective, and radiative transfer. The heating effect of a fluid may be reduced by regulating its temperature at the input stage to be that of the room in which the instrument or machine is housed. In practice, close temperature regulation of fluids is far from simple, and control to better than 0.1 K can be very expensive. Another alternative that is becoming cheaper is to use low expansion

ceramics such as "Zerodur" for the structure. This approach assumes that thermal expansion causes the motion errors and often this is so. It will not, however, help if, for example, thermal effects cause softening of a polymeric bearing, since there will be no good conduction paths to take the heat away. Therefore, *principle 4: minimize the energy dissipated at or passed through the bearing interface*.

The purpose of any slide is to convey an object from one place to another. In doing so, the force distribution within the system will almost invariably alter. Stiffer slideway designs have reduced vibration sensitivity because the amplitude of motion is proportional to the square root of the ratio of the input energy to the stiffness at a given frequency. This becomes of primary importance in mechanisms having little internal damping. Therefore, *principle 5: make the transverse stiffness of the slideways bearing as high as possible to reduce its susceptibility to vibration and other perturbing forces*.

Kinematic analysis indicates that a single DOF translation can be modeled as five contact points suitably placed on the ways. Each of these will closely follow the slide geometry, including its errors. The motion error of the carriage will depend on how the paths of the individual pads interact, and we should attempt to place the pads so that the overall error is small. Therefore, *principle 6: optimize the kinematic design to minimize errors.*

Types of Linear Motion Guides

In machines, guideways help to guide the tool or workpiece along a predetermined path, usually either a straight line or a circle. Guideways, lubrication, and drive systems are discussed in the next section and form an important part of precision machines. There are basically two types of guideways – friction guideways and antifriction. Friction guideways were initially used but are now replaced by hydrostatic guideways in precision and ultra-precision machine tools. A guideway should be highly accurate, durable, and rigid. Machine tools require guideways for guiding the movement of the workpiece and for positional adjustment.

Linear motion guideways also known as linear motion bearings with mechanism to bear the load and to guide their linear motion simultaneously. The bearing type used in the linear motion guideways mainly contains sliding, rolling, and hydrostatic and aerostatic bearing. Table 1 shows the properties of the guideways with different bearings, and it can be noted that the guideway with hydrostatic and aerostatic bearing can reach a high straightness due to the non-contact form of movement.

Table 1 Properties of the guideway with different bearings

Slide bearing	Straightness μm/100 mm	Stiffness	Speed	Friction
Sliding	1–2	High	Medium	High
Rolling	1–2	Medium	High	Small
Hydrostatic	0.5–1	Medium	Medium	High
Aerostatic	0.1–0.5	Low	High	Very small

Therefore, hydrostatic and aerostatic bearing are widely used in the linear motion guideways for precision application.

The design of guideways for tables, saddles, and cross slides involves the following aspects:

- Shapes of the guiding elements and arrangements of their combinations
- Effect of material and working conditions upon the guiding accuracy (wear)
- Friction conditions and load-carrying capacity (roller bearings and lubrication)

According to Koenigsberger, a good guideway design is needed to satisfy the following requirements:

- Provision of an exact alignment of the guided parts in all positions and under the effect of the operational forces
- Provision of a means for compensating possible wear
- Ease of assembly and economy in manufacture (possibility of adjusting the alignment in order to allow for manufacturing tolerances)
- Freedom from restraint
- Necessary prevention of chip accumulation and ease of removal of any chips
- Effective lubrication must be possible

Sliding Contact Linear Motion Bearing-Based Guides

This type is the oldest, simplest, least expensive way, and it still has a wide range of applications. In general, all sliding contact bearings have greater friction coefficient than other types described hereunder, and, because of this, they are considered to be inferior to these guides for precise positioning applications. With lubricant forcibly maintained between two relatively moving objects, a relative speed helps to pull in lubricant, and, thereby, a thin film is formed, as shown in Fig. 5a.

Although numerous sliding contact linear motion bearings have been used for a long time, their positions are being quickly replaced by the rolling element linear motion bearings, as shown in Fig. 5b. This is because the sliding contact bearings

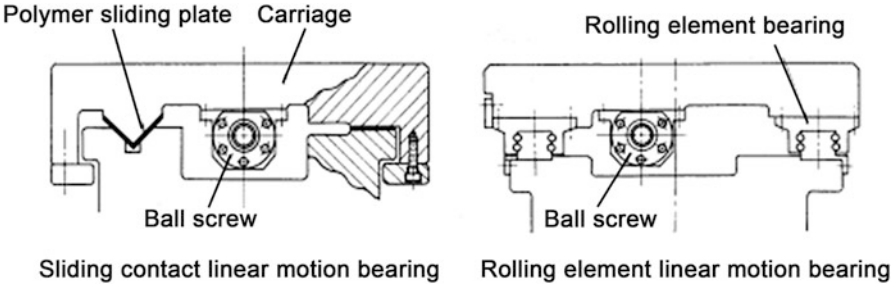

Fig. 5 Contact linear motion bearing

have the following disadvantages for today's needs for high-speed, high-precision, high-quality, and long-term maintenance-free operation.

- High friction and a large difference between their static and dynamic friction.
- It is hard to control positioning operation because variation of external loads and speeds largely affect the friction force.
- Poor positioning accuracy, particularly repeatability.
- It is not suitable for extremely low-speed or high-speed applications. Difficult to predict their life span.
- It is hard to predict their rigidity. Hence, it is difficult to achieve an optimum design for them.
- Frequent and periodical maintenance is required for them to maintain accuracy.
- Their quality largely depends on workmanship of scalping and clearance adjustment, etc.

Rolling Element Linear Motion Bearing-Based Guides

This type decreases friction utilizing rolling contact via rolling elements (balls, rollers, etc.) that are placed between two relatively moving objects. There are many specialized manufacturers, and each manufacturer provides a wide variety of products. Because of its superiority over the sliding contact linear motion bearings as described hereunder and because of its availability, this type has won the position as an essential component for the equipment that requires highly accurate positioning operation.

Recirculating and stationary roller-based guides are most widely used in present machine tool applications. The stationary rolling bearings tend to be used when the stroke of the slide is relatively short. The rolling elements can be steel balls, rollers, or needles, which are preloaded between two cages attached to stationary and moving parts of the guides. They have low friction, high load capacity, and stiffness, but with low structural damping. The recirculating roller-based guide has the advantage used in long stroke; however, the bearings circulating inside a linear guide can cause precision-reducing vibration as the bearings transition from "load-bearing" to "nonload-bearing" conditions. Some manufacturers optimize the bearings' transition-point geometry with specialized high-precision runner blocks to minimize vibrations. For example, Bosch Rexroth's high-precision ball rail uses a steel insert with relief zones that dampen ball-entry forces at the ends of the raceway. The result is consistent, extremely smooth motion as balls circulate in the bearing raceways. They can be supplied with integrated position sensors or racks to expedite the design and assembly of machine tool drives (Fig. 6).

Hydrostatic or Aerostatic Linear Motion Bearing-Based Guides

When extremely accurate and quiet operation must be attained, a guide without mechanical contact between its elements is often chosen. With pressurized fluid forcibly

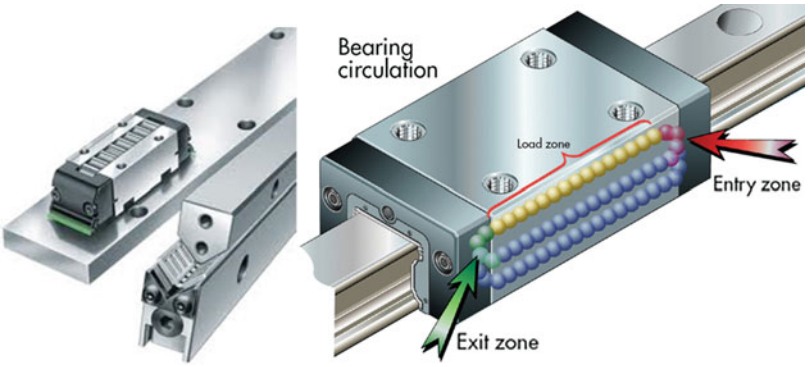

Fig. 6 Roller-based guides. (**a**) Stationary roller-based guide, (**b**) recirculating roller-based guide (https://www.ebatmus.com/ina_linear_rolling_bearings_and_linear_plain_bearings.html)

supplied between two relatively moving objects, one of them is kept floating by the fluid. Depending upon the fluid in use, it is classified in aerostatic and hydrostatic linear motion bearings. Although this type of guides is very advantageous for particular purposes, it is usually costly and difficult in manufacturing and requires expensive auxiliary apparatus. Yet, this type is widely used for ultra-precision machines.

Figure 7 illustrates the typical structure types of the aero/hydrostatic slide; they are dovetail rail guide, U-series rail guide, box-series rail guide, and T-series rail guide.

Throughout the machine tool industry, hydrostatic linear guides are considered the best technical solution for vibration damping at the point of system loading. The guides also carry heavy loads and can withstand contaminated environments. Rigidity can also be improved by increasing the oil pressure via a valve setting. In mechanical systems, higher preloads on the rolling elements are required to boost rigidity. Unfortunately, what also results is increased rolling friction and an exponential decrease in bearing life. Hydrostatic carriages, on the other hand, run on pressurized oil, so there is no increase in friction and no effect on the system's operating life. Friction is independent of load until the load limit is reached. Running accuracy partially depends on the straightness, accuracy, and rigidity of the structure to which the hydrostatic guide is mounted. System straightness is only achieved when the guideway is pressed against a controlled datum surface. Manufacturers supply mating-surface tolerance guidelines, as well as permissible height differences, deviations impair overall accuracy, affect the preload, and may even result in an inoperable system.

However, there was always a catch: most traditional hydrostatic guides are relatively expensive and time-consuming to mount and require a larger design envelope than conventional linear guides. For these reasons, they're infrequently specified.

Now, newer compact hydrostatic linear guides address old issues. Built to the dimensions of standard profiled rail linear guides, they fit within the same design space as typical recirculating bearing and guideway assemblies – to give engineers

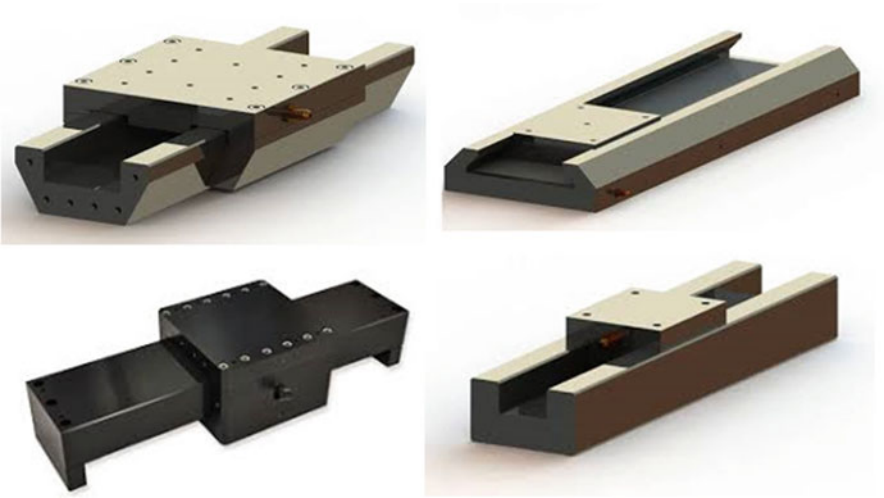

Fig. 7 Illustrates for topic aerostatic slide, (**a**) dovetail rail guide, (**b**) U-series rail guides, (**c**) box-series rail guides, (**d**) T-series rail guides (http://www.oavco.com/air-bearing-guide.html)

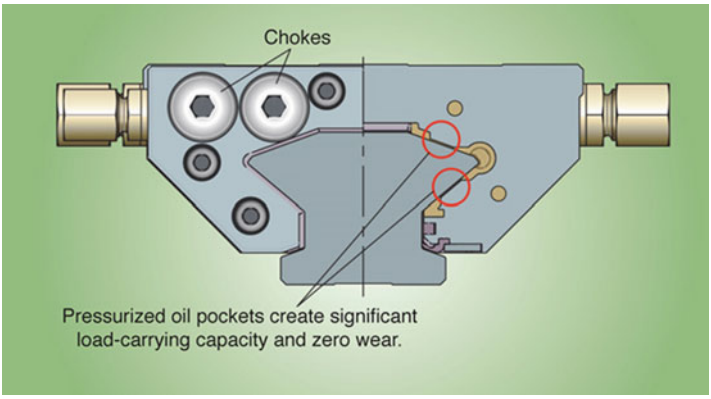

Fig. 8 Hydrostatic linear guiding for standard design spaces (http://www.machinedesign.com/linear-motion/hydrostatic-linear-guiding-standard-design-spaces)

and machine builders the benefit of unmatched damping without requiring installation compromises (http://www.oavco.com/air-bearing-guide.html) (Fig. 8).

Magnetic Linear Motion Bearing-Based Guides

By means of magnetic force, either repelling or attracting, one of the two relatively moving objects is kept afloat. The use of electromagnet makes it costly and ineffective in energy consumption. This type has very limited applications.

Drive System

Feed drives are either powered by linear motors directly or by rotary motors via ball screw and nut assembly.

Ball Screw

The drive by ball screw is the most widespread in the machine tool field for strokes not exceeding 4–5 m. The main characteristics which place it in such a favorable position are the high mechanical reduction provided maintaining a high efficiency and stiffness, as well as sufficient accuracy for existing machine tools. A ball screw is a mechanical device which transforms the rotary movement into linear movement. Its operation is similar to a leadscrew in which the sliding between the threads of the leadscrew and the nut has been replaced by the rolling of balls which are recirculated in the nut.

The common ball screw configuration consists of a ball screw coupled to a rotary servomotor either directly or via a belt to save the operate space. Figure 9 illustrates the two common ball screw configurations. The inherent gearing of a ball screw provides excellent dynamic stiffness, which makes ball screw configurations particularly suited to machining operations with high machining force, such as grinding, milling, and turning. However, although the rotary servomotors are capable of providing constant torque and high accelerations rates, when coupled to a ball screw, the drive can suffer from high friction, torsional flexing, and speed limitations (Moscrop 2008).

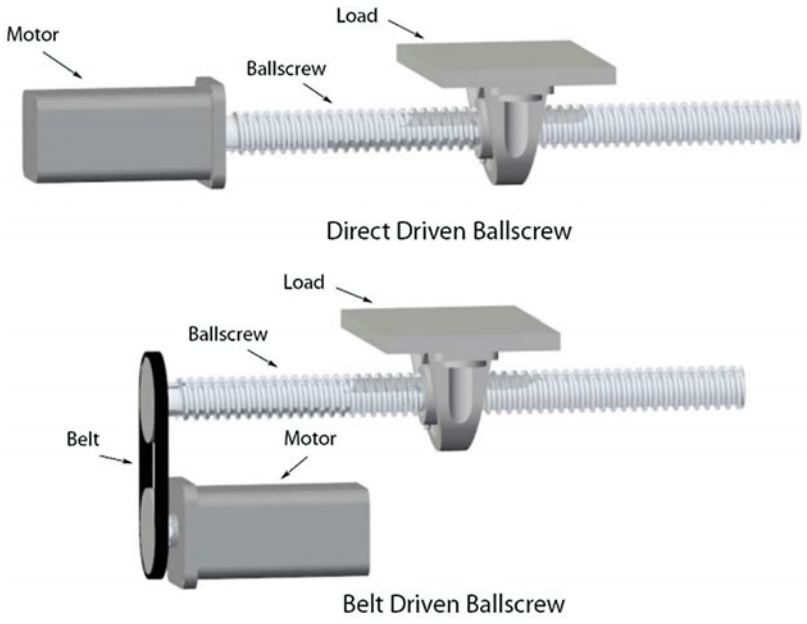

Fig. 9 Ball screw configurations (Moscrop 2008)

Rack and Pinions

The flexing and speed limitations of ball screw configurations make them unsuitable for machining operations where high-speed and long travels are required such as many power sawing operations. Modern sawing machines include plasma and laser cutters, which are characterized by very low machining force and long travels. In these machines, the mechanical transmission mechanism is usually a rack and pinion, as shown in Fig. 10, and the stroke of the slide can be greater than 4 or 5 m. In a rack and pinion drive, the servomotor is normally mounted very close to the pinion, to limit any torsional flexing. Although this drive configuration can provide much higher speeds and reduced flexing when compared to a ball screw drive, rack and pinions suffer from poor dynamic stiffness and increased backlash. Hence, rack and pinions are normally only used on machines with long travels and low cutting force.

The main advantage of the rack and pinion drive versus ball screw drive is that the characteristics do not depend on the slide stroke. The slide stroke does not limit either the maximum speed or the drive or affect the stiffness, unlike what occurs in case of the ball screw. In addition, it permits us to obtain high feed rates, and it is common to reach 120 m/min (Lacalle and Mentxaka 2008). On the other hand, the rack and pinion drive does not provide the high reduction that the ball screw can provide. In order to provide a greater reduction, pinions of as small a diameter as possible should be used, between 15 and 20 teeth. Therefore, a reducer should be used to obtain the same force and acceleration performance as the screw.

Linear Motor

In present, another important type of drive for machine tool slides is the linear motor. The main characteristic of the linear motor is the absence of mechanical elements of transmission of movements and/or forces. On eliminating these mechanical elements, wear and tear, gaps, lubrication requirements, and noise are also eliminated. Another important advantage is the absence of natural resonance frequencies of the drive. However, at the same time, the mechanical advantage is lost, such that the

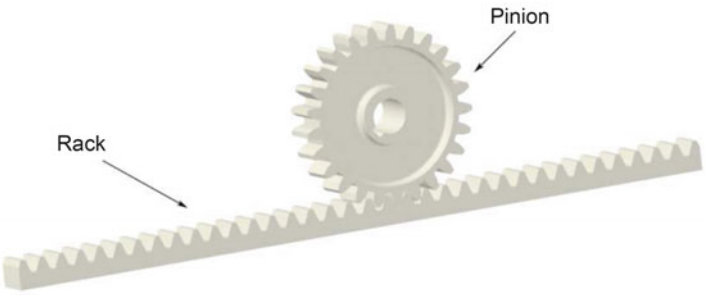

Fig. 10 Rack and pinion mechanism

Fig. 11 Linear motor (https://www.aerotech.com/Media.aspx?mId=12389)

force generated by the motor is directly the force exercised on the slide, and under no circumstances can it be higher.

The linear motor consists of a coil slide or primary and magnet plates as secondary, both on a linear basis. One of these is fixed on the moving part and the other on the fixed part.

Figure 11 illustrates two typical types of the linear motor, namely, "flat" and "U-channel" brushless linear servomotors. The "U-channel" type of linear motor has two parallel magnet tracks facing each other with the forcer between the plates. The forcer is supported in the magnet track by a bearing system. The forcers are ironless, which means there is no attractive force and no disturbance forces generated between forcer and magnet track. The ironless coil assembly has low mass, allowing for very high acceleration. Typically the coil winding is three phase, with brushless commutation. Increased performance can be achieved by adding air cooling to the motor. This linear motor design is better suited to reduced magnetic flux leakage due to the magnets facing each other and being housed in a U-shaped channel. This also minimizes the injury risks of fingers being trapped by powerful magnets. Due to the design of the magnet track, they can be added together to increase the length of travel, with the only limit to operating length being the length of cable management system, encoder length available, and the ability to machine large, flat structures.

When compared with a screw, the linear motor system does not introduce any backlash or positioning problems with the feedback device, as the linear slide bearing is its only friction point. As with all the other translation systems discussed, the positioning of the load in a screw system is made with a rotary encoder mounted on the motor. The controller never really closes a loop at the load. In a linear motor system, the encoder is at the load, reading actual load position.

Metrology and Sensor

A direct measuring system, free of external perturbations or noises, is always better than an indirect one. The latter needs part of geometrical parameters that may vary due to sources of error. A classic example of this principle is the use recommendation of linear encoders instead of encoders to measure the position of linear axes.

In Fig. 12 two measuring solutions are presented. The solution based on the encoder directly measures the angular position of the ball screw, placed on the

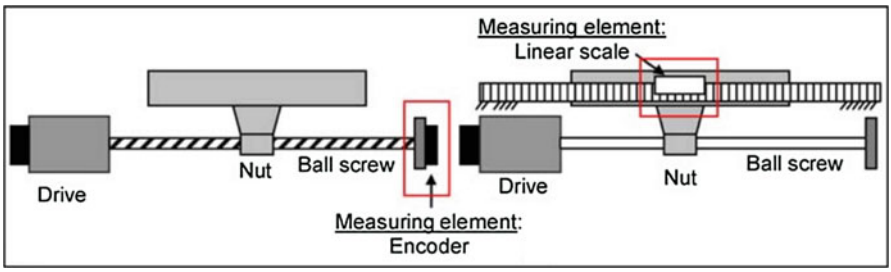

Fig. 12 Metrology type of the linear system. (**a**) Encoder-based measuring system. (**b**) Linear scale-based measuring system (Lacalle and Mentxaka 2008)

opposite side to the joint between the drive and the ball screw. Using this data, the position of the axis can be obtained for calculating the relationship between the linear axis motions with the ball screw rotation, which is defined by the ball screw lead. However, the measurement is affected by numerous sources of error. Thus, the encoder cannot detect the ball screw deformations due to thermal or load effects. On the other hand, the backlash of the ball nut is also not detected. In other words, the encoder cannot detect what happens in those elements placed after the drive system.

Contrarily, if a linear scale is installed between the table and the machine structure, the linear movement could be measured directly. This measurement is independent of the ball screw features (diameter and lead) and its deformations. Thus, it is again a more costly but very much precise solution. Linear guides provide accurate, high-capacity travel for a wide variety of machine types and processes. In the most demanding applications, linear position feedback is often needed in order to enable the tool, gripper, or workpiece to follow an exact path or reach a precise position. In these cases, designers can add a linear encoder to the motion system, or they can use a linear guide with an integrated measuring system.

Linear Encoder

Many precision linear encoders work by optical or photoelectric scanning. In short, a readhead tracks periodic graduations with just a few micrometers wide and outputs signals with small signal periods. The measuring standard is usually glass or steel (for large measuring lengths) bearing periodic graduations-marks on the carrier substrate. It's a contact-free mode of position tracking. Used with incremental grating periods between 4 and 40 μm, PRC (absolute) code image-scanning linear encoders work with light signal generation. Two gratings (on the scale and scanning reticle) move relative to each other. The scanning reticle's material is transparent, but the scale's material can be transparent or reflective. When the two pass each other, incident light modulates. If gaps in the gratings align, light passes through. If the lines of one grating coincide with gaps of the other, it blocks the light. Photovoltaic cells convert the variations in light intensity into electrical signals with a sinusoidal form (Fig. 13).

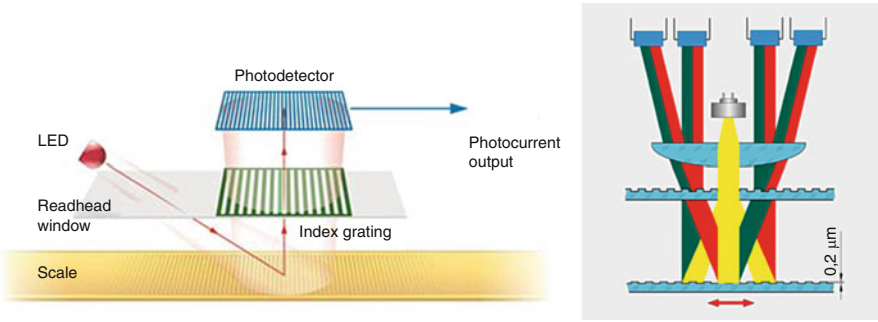

Fig. 13 Left: image-scanning linear encoder. Right: interferential encoders

Another option for graduations with grating periods of 8 µm and smaller is interferential scanning. This linear encoder mode of operation leverages diffraction and light interference. A step grating serves as the measuring standard, complete with lines 0.2 µm high on a reflective surface. In front of that is a scanning reticle-transparent grating with a period that matches that of the scale. When a light wave passes through the reticle, it diffracts into three partial waves with −1, 0, and 1 orders of roughly equal intensity. The scale diffracts the waves so luminous intensity concentrates in diffraction orders 1 and −1. These waves meet again at the reticle's phase grating where they diffract once more and interfere. This makes three waves that leave the scanning reticle at different angles. Photovoltaic cells then convert the alternating light intensity into electrical signal output. In interferential scanning, relative motion between reticle and scale causes the diffracted wave fronts to undergo a phase shift. When the grating moves by one period, the wave front of the first order moves one wavelength in the positive direction, and the wavelength of diffraction order −1 moves one wavelength in the negative. The two waves interfere with each other when exiting the grating, so shift is relative to each other by two wavelengths (for two signal periods from a move of just one grating period).

Integrated Position Measuring with Linear Guides

An integrated linear measuring system is very similar to a conventional linear encoder, but the former one mounts the scale onto the rail, and the readhead is mounted onto the carriage. The integrated measurement systems are often based on magnetic or inductive encoders, rather than optical versions, due to their low sensitivity to dust, debris, and liquid. They are also able to tolerate some variation in gap between the sensor and the scale, if the system undergoes shocks or vibrations. However, as the modern magnetic and inductive technologies can down the resolution to submicron level, the performance choosing integrated measuring systems over optical encoders will not be decreased.

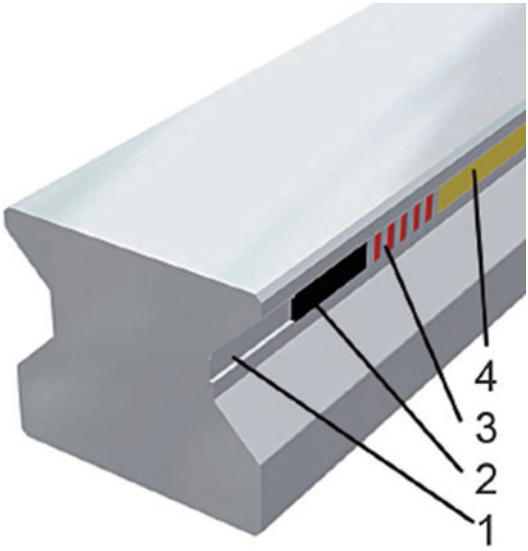

Fig. 14 The Schneeberger AMS system, the magnetic strip (2) is mounted into a ground slot (1) on the side of the rail. The strip is ground and magnetized (3), and then a protective cover (4) is welded to the rail (https://www.schneeberger.com/en/products/measuring-systems/)

The integrated measuring system includes the scale and the readhead. The scale is conventionally mounted in a groove on the side of the rail. The scale is protected by a laser-welded cover, which provides a dust-tight seal and prevent from water ingress (Fig. 14).

The readhead is typically mounted either inside or onto a housing, which sometimes also contains the encoder's electronics. The housing is mounted onto the end of the carriage, which increases the length of the carriage. Although this means that a slightly longer rail is needed in order to obtain the same travel distance, the lack of added width beyond the sides of the carriage means that an assembly with integrated measuring can fit in the same footprint as a standard assembly, so retrofits are generally easy, and no special provisions have to be made for added space.

A Case Study: Design of a Hydrostatic Guide

Structural Design of the Slide

A hydrostatic bearing guide is designed for ultra-precision machining; the structure of the slide is shown in Fig. 15. The oil film clearance is selected at 25 μm, the supply oil pressure is set to 1.5 MPa, the design stiffness of the slide is 730 N/μm, and the load capacity is 1500 N. The slide is driven by a permanent magnet ironless linear motor and detected by the linear encoder with 2 nm resolution.

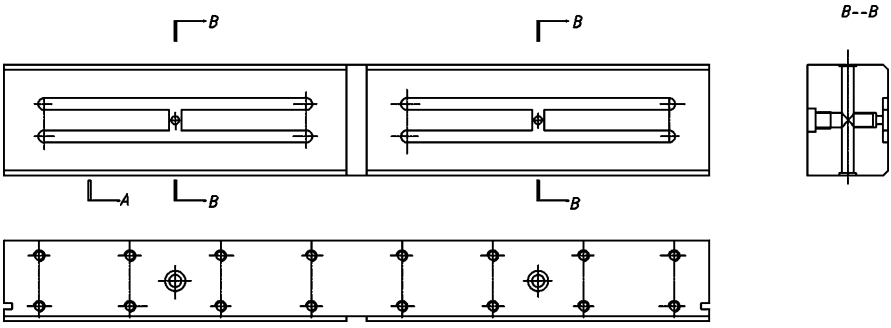

Fig. 15 The geometry structure of the slide

Fig. 16 Schematic of slide offset

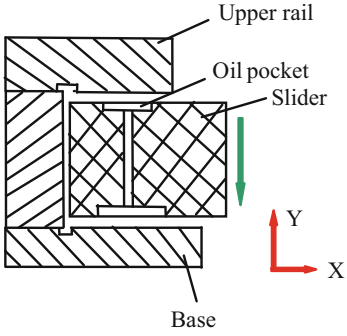

Stiffness and Load Capacity Calculation of Hydrostatic Bearing

Stiffness and load capacity are two important parameters, easily affected by many factors. As shown in Fig. 16, for a slider with an offset, oil film clearance change will lead to the change of guideway stiffness and carrying capacity. Therefore, slider offset must be considered. The relationship between stiffness and slider offset and the relationship between the carrying capacity of guideway and slider offset of the designed guideway are obtained using formulation about hydrostatic bearing.

The relationship curve of stiffness versus slider offset is shown in Fig. 17. It can be observed that the static stiffness tends to change with oil film clearance, the change of which should be caused by offset of slider. Under the same condition, as oil pressure increases, oil film stiffness will also increase. When the offset is about 0–5 μm, small stiffness decrease occurs slowly. When offset is 5–15 μm, differently, stiffness decreases greatly. Thus the offset should be less than 5 μm, in order to keep stiffness from changing largely.

The relationship curve of oil film carrying capacity and slider offset is shown in Fig. 18. Guideway carrying capacity increases as oil pressure increases. Carrying capacity increases significantly at the offset of less than 10 μm, and it increases slowly if the offset is larger than 10 μm. Therefore, the maximum displacement of

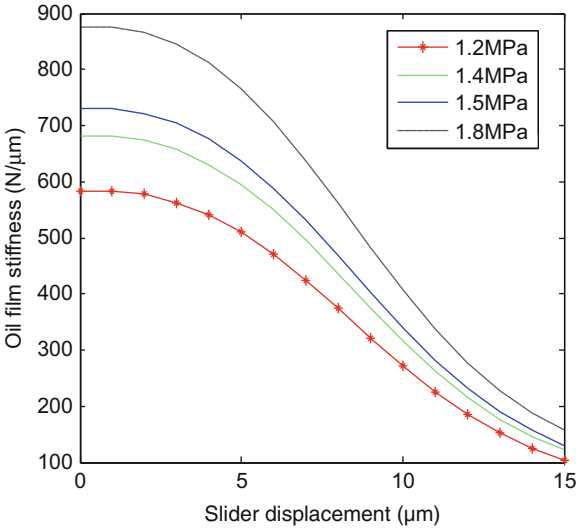

Fig. 17 The relationship between slider's displacement and guideway stiffness at different oil pressures

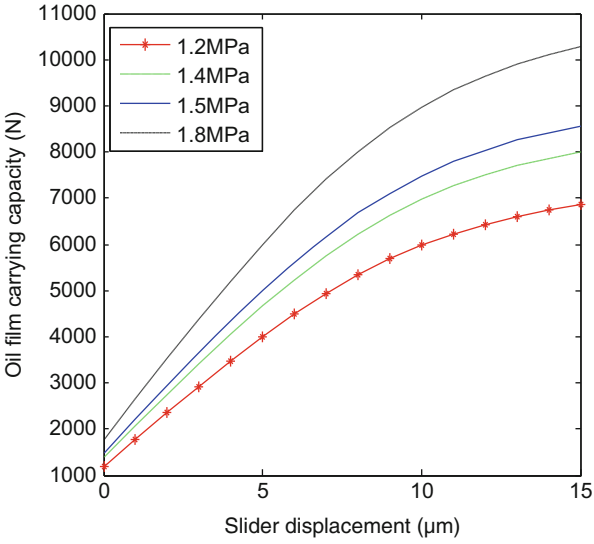

Fig. 18 The relationship between slider displacement and guideway carrying capacity

slider in the opposite direction of y-axis is 5 μm. As a result, the carrying capacity meets the demand and stiffness changes slightly. So the eccentricity rate is 0.2 because the designed oil film clearance is 25 μm, which agreed well with the existing range of orifice restriction.

The worktable is supported by hydrostatic slide, which is driven by a linear motor with excellent slow feeding performance. The hydrostatic slide system consists of oil tank, pump, check valve, motor, etc., as shown in Fig. 19. It is used to provide stable pressure, abundant flow rate, and clean working medium to the hydrostatic slide.

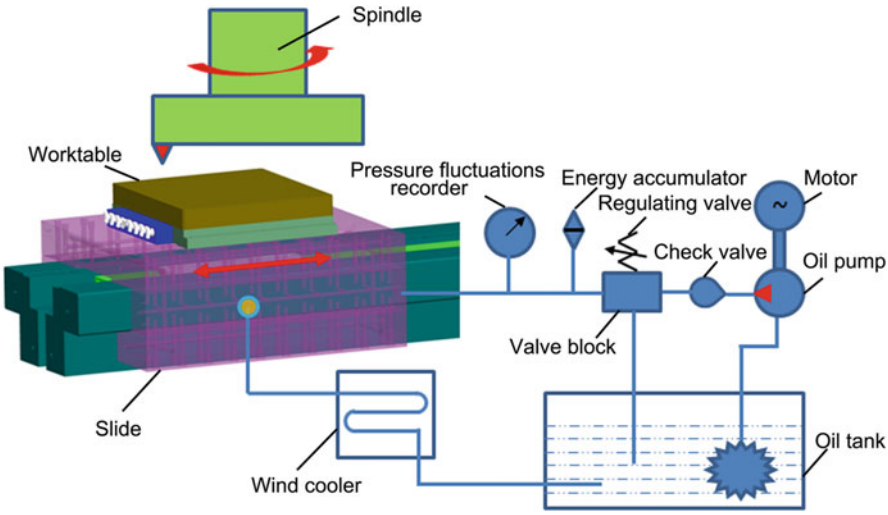

Fig. 19 Hydrostatic slide system

A prototyping hydrostatic slide is built, as shown in Fig. 20a. The specifications of the hydrostatic slide are shown as follows. The horizontal straightness of the *x*-axis is measured by the photoelectric autocollimator. Measured result shows that the straightness of the *x*-axis is less than 0.14 μm in 600 mm, as shown in Fig. 20b. The micro step response of the *x*-axis is shown in Fig. 20c, and the micro step could be with 30 nm resolution. In order to verify the stability of the low-speed performance of the slide system, the low-speed feeding experiment is carried out. Figure 20d shows the slide motion curve under the control commands 10 μm/s and 500 ms sampling period. It can be seen that the feed speed of the slide undulates within a range of ±0.1 μm/s, and the actual position coincides well with targeted position of feeding system, indicating that the low-speed stability of the control system is excellent.

Influence of Constant-Pressure Oil Source Fluctuations on the Performance of Hydrostatic Slide

In order to investigate the influence of oil pressure fluctuations on the surface generation, a pressure fluctuation recorder is used to record the pressure fluctuations of the slide (Chen et al. 2015). To identify that the oil pressure fluctuations are the only variable in the whole system, the experiment is carried out with the following conditions: the rotation speed of spindle is zero, the slide is fixed by the linear motor in the feed direction, and the oil supply system is working.

The testing results of the oil pressure fluctuations are shown in Fig. 21a. It can be found that though the constant pressure of the hydraulic oil supply system is set to 0.42 MPa, but the real oil supply pressure fluctuations (OSPF) reach up to several

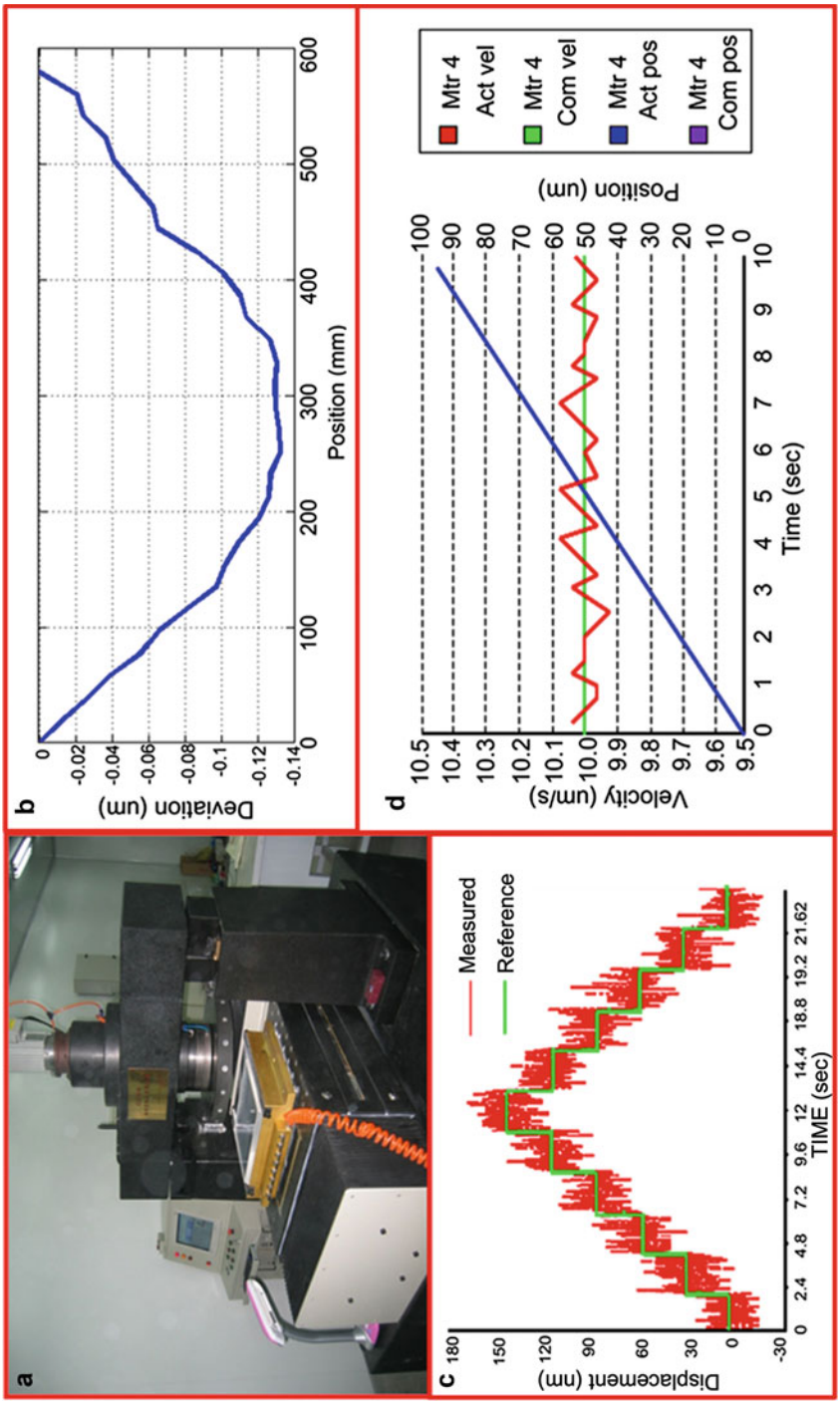

Fig. 20 The prototype and the test result

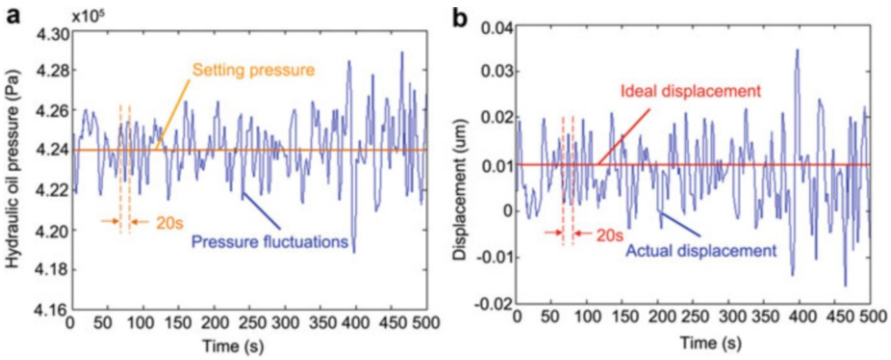

Fig. 21 The pressure fluctuations of the oil and the displacement of the slide

kPas, which is caused by the mechanical structure of the oil supply system. According to the hydrostatic principle, the relationship between the pressure fluctuations and the slide displacement can be obtained by Rowe (2012):

$$\bar{j} = \frac{W/C_W \cdot C_\alpha}{\mathrm{SA}_{b1} \cdot p_s} \tag{1}$$

and

$$e = \frac{h_0\left[\bar{j}\beta^2 + \beta(K_b - 1)\right]}{3(\beta - 1)(1 + K_b)} \tag{2}$$

where $\bar{j}$, W, C_W, C_α, and S denote the stiffness coefficient, load, diffusion loss coefficient, tilt loss coefficient, and the oil cavity equilibrium coefficient, respectively. A_{b1} denotes the effective area of the bearing, p_s denotes the oil supply pressure, e denotes the slide displacement under the pressure fluctuations, h_0 denotes the initial oil film clearance, β denotes the optimal throttling ratio, and K_b denotes the ratio of upper and lower bearing area.

From Eqs. (1 and 2), the slide displacement under the pressure fluctuations is obtained, as shown in Fig. 21b. It can be found that the displacement of the slide is around 10 nm, which is close to the amplitude of the mid-spatial frequency errors. The period of fluctuations is about 20 s, consistent with the OSPF.

The surface simulation, which considers the displacement of the worktable which is caused by the oil pressure fluctuations, is carried out. The 3D locus of the diamond cutting tool is given as follows:

$$\begin{cases} X = R\cos(2\pi\omega_z t) + v_f t \\ Y = R\sin(2\pi\omega_z t) \\ Z = h_0 + f(t) \end{cases} \tag{3}$$

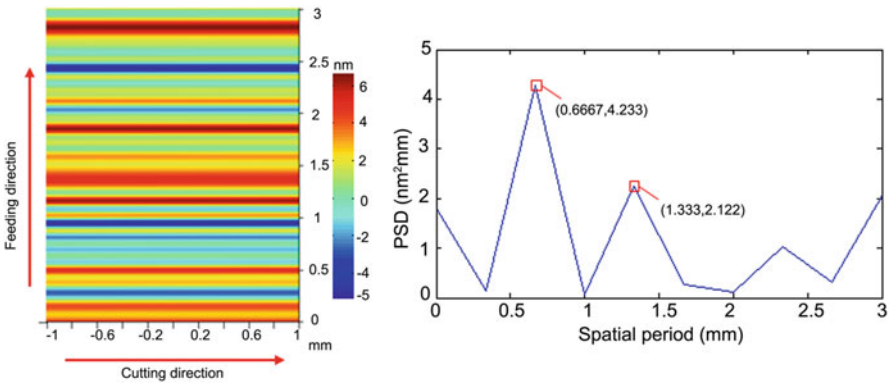

Fig. 22 The simulation result of the machined surface

where R denotes the radius of cutting tool locus, w_z denotes angular velocity component, v_f denotes the feed rate of machine table, h_0 denotes the desired cutting depth, and $f(t)$ denotes the displacement of the worktable caused by OSPF.

The simulation result of the machined surface is shown in Fig. 22, and its PSD analysis result shows that the waviness is mainly caused by the OSPF at 0.6–1.4 mm, which agrees well with the experiments' result. It demonstrates that the mid-spatial frequency errors in 0.5–1.5 mm on the machined surface are caused by the OSPF. Therefore, decreasing the OSPF will contribute to reduce the mid-spatial frequency errors of the optics.

Acknowledgments The authors gratefully acknowledge financial support of the National Natural Science Foundation of China (No.51505107), International Science and Technology Cooperation Program of China (No. 2015DFA70630), and Project (HIT.NSRIF.2017029) supported by Natural Scientific Research Innovation Foundation in Harbin Institute of Technology.

References

Altintas Y, Verl A, Brecher C, Uriarte L, Pritschow G (2011) Machine tool feed drives. CIRP Ann Manuf Technol 60(2):779–796

Chen W, Liang Y, Sun Y, An C, Chen G (2015) Investigation of the influence of constant pressure oil source fluctuations on ultra-precision machining. Proc Inst Mech Eng B J Eng Manuf 229(2):372–376

Lacalle NL, Mentxaka AL (2008) Machine tools for high performance machining. Springer Science & Business Media, Bilbao

Moscrop J (2008) Modelling, analysis and control of linear feed axes in precision machine tools. Doctoral thesis of University of Wollongong

Rowe WB (2012) Hydrostatic, aerostatic, and hybrid bearing design. Elsevier, Amsterdam

Smith ST (2003) Foundations of ultra-precision mechanism design, vol 2. CRC Press, Baton Rouge

Design of Precision Rotary Drives

6

Haitao Liu, Wenkun Xie, and Yazhou Sun

Contents

Introduction 156
Rotary Movement Error Analysis 157
Worm-Gear Drive 158
Roller Drive 160
Direct Drive 162
Rotary Motion Bearing 164
Measurement and Sensor 167
A Case Study: Design of a Hydrostatic Rotary Table 168
Scheme Design of the Rotary Table 168
Precision Design 169
Deformation Analysis of Critical Components Under the Action of Hydraulic Oil 169
References 170

Abstract

The performance of CNC machine tool is greatly dependent on the precision rotary drives. It is extremely significant to reasonably design the precision rotary drives used to ensure the optimal performance of the machine tool. This chapter first analyzes the errors of the single-coordinate rotary movement. Further, several commonly used transmission mechanisms in the design process of

H. Liu (✉)
Center for Precision Engineering, Harbin Institute of Technology, Harbin, People's Republic of China

School of Mechatronics Engineering, Harbin Institute of Technology, Harbin, People's Republic of China
e-mail: hthit@hit.edu.cn

W. Xie · Y. Sun
Center for Precision Engineering, Harbin Institute of Technology, Harbin, People's Republic of China
e-mail: xwk584523412@126.com; sunyzh@hit.edu.cn

Z. Jiang, S. Yang (eds.), *Precision Machines*, Precision Manufacturing,
https://doi.org/10.1007/978-981-13-0381-4_5

precision rotary feeding system of CNC machine tool are introduced. The characteristics and design methods of common transmission mechanisms, including worm-gear drive, roller drive, and direct drive, in the CNC machine tool rotary feeding mechanism are also summarized. Moreover, the measurement and sensor systems capable of ensuring the movement precision of circular feeding are briefly introduced. Finally, a design case of ultraprecision hydrostatic rotary table is presented to introduce the detailed design process of precision rotary drives. This chapter will contribute to provide technological guidelines to the optimal design of precision rotary drives.

Keywords

Precision rotary drives · Rotary feed mechanism · Design principle

Introduction

For CNC machine tool, in processing complicated shape surface, in order to improve the machining efficiency, ensure machining quality, and prevent interference, it commonly requires four- to five-axis linkage machining (Zhang et al. 2016). Except for the linear feed movements along X-, Y-, and Z-axis in Cartesian coordinate system, it also requires the rotary feeding movement along A-, B-, or C-axis of the rotary coordinate system, to enable the control of the control of the relative attitude between tool and workpiece.

The circular feed motion, in terms of motion decomposition, can be completed by the worktable where the workpiece is mounted, by the rotary shaft part on which the cutter is mounted, or by both. For example, CNC rotary table and CNC angle milling head are needed to provide high-precision indexing positioning function to multi-axis machining rotary axis. Moreover, they are also required to be able to directly serve as servo rotary axis and coordinate axis linkage, thereby achieving the low-speed and large load circular movement. The previous chapter has introduced the design of the linear feed drive system; this chapter will focus on the design of the circular feed drive system.

Like the linear feed driving system, the circular feed driving system is often required to have the characteristics of high precision and fast dynamic response. Circular feed motion can be realized by servo motor through mechanical transmission or directly driven by torque motor.

The circular feed drive with mechanical transformation, structurally, mainly consists of servo drive, mechanical drive, and angular displacement detection and feedback. Therefore, mechanical transmission is not only the key to achieve indexing positioning with high precision and low-speed high-torque rotary feed movement function key but also the important factor that could affect the rotating shaft positioning accuracy and repeat positioning accuracy. Its structural type also directly determines the structure layout of rotary feed mechanism in the machine tool and the dynamic and static performance of rotary feed mechanism.

As for direct drive, by directly connecting the rotor of the torque motor with the rotary unit, it could not only eliminate the intermediate driving link but also realize high-speed feeding of the rotary parts, thereby obtaining higher dynamic performance and positioning accuracy.

Overall, this chapter first briefly analyzes single-coordinate rotary motion error and then introduces the transmission ways and characteristics of several commonly used precision circular feed drives in CNC machine tools. Based on that, the key technologies in the design of rotary feed drives are introduced. Finally, a design case of ultraprecision hydrostatic rotary table is illustrated.

Rotary Movement Error Analysis

Figure 1 illustrates a rotary motion mechanism (such as rotary table) in the reference coordination frame O_0-$X_0Y_0Z_0$ of machine tool. When *C*-axis is rotated around *Z*-axis, there are six errors, including three movement errors (δ_x, δ_y, and δ_z) and three angle errors (ε_x, ε_y, ε_z). As shown in Fig. 1a, δ_x and δ_y are two *x*- and *y*-directional radial errors of *C*-axis rotary, while δ_z is the axial error for C-axis rotary motion. ε_x and ε_y represent the posture error of *C*-axis around *x*- and *y*-coordinates, and ε_z is the angle positioning error of *C*-axis rotation movement (Zhang et al. 2016; Zhang and Zhang 2016).

Under the coupled effects of the above six kinds of errors, the axis of the turntable will undergo position drift. As shown in Fig. 1b, the theoretical origin (*O*) will migrate to new origin (*O′*). The real *C*-axis will be not parallel or overlapped with the Z_0 axis, and it is also perpendicular to the *x*-*y* plane. In Fig.1b, an inverted tetrahedral cone consisting of eight dashed lines represents the possible position space of C-axis. The generation of angle error ε_z should be ascribed to the eccentric of drive mechanism (such as worm gear, etc.) and the misalignment between support

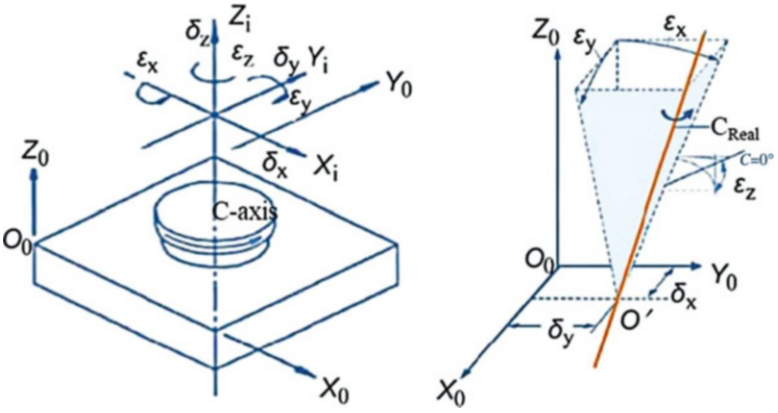

Fig. 1 Rotary motion error (Zhang et al. 2016; Zhang and Zhang 2016). (**a**) Elements of rotary motion errors (**b**) Spatial range of rotary motion error

and execution part (such as the outer diameter of the spindle and the spindle taper hole). As for other errors, they mainly consist of the predesigned tolerance of each part and the integrated assembly tolerance of turntable. For example, there is the misalignment between supporting holes of the front and rear bearings of the rotary shaft, the non-verticality between end faces and axis of front bearing, as well as the assembly and manufacturing clearances. All of them will be finally shown as the center deviation of tool or workpiece installed on the rotary table and the inclination of the center line of tool or workpiece.

Therefore, the reasonable design of bearing, transmission mechanism, and servo system is the key to ensure the high precision that the rotary movement requires, including rotation accuracy and positioning accuracy. The rotary accuracy is mainly dependent on the precision of the supporting bearing and its parts, while positioning accuracy mainly depends on servo accuracy, determined by transmission accuracy, shaft stiffness, feedback element accuracy, and other factors.

Worm-Gear Drive

Worm-gear transmission mechanism is one traditional indexing and circular feed transmission. As the back clearance is existed in worm gear and worm drive, thus, in the design of the rotary feed motion mechanism, it is the key to eliminate the influence of back clearance on the accuracy of circular motion trajectory. The commonly used side clearance adjustment methods for ordinary worm-gear and worm drive mechanisms cannot meet the requirements of high-precision rotary feed motion mechanism. Therefore, for the high-accuracy circular feed motion mechanism of CNC machine tool, the worm and worm-gear mechanisms are required with reliable and convenient clearance elimination function, mainly including double-pitch worm drive, double-section worm drive, and double-worm synchronous drive (Zhang et al. 2011, 2016).

Double-pitch worm drive: The tooth surfaces at the left and right sides of the worm have different pitches, P1 and P2. As shown in Fig. 2, due to the uniform pitch at the same side, normal meshing can be still ensured. For such kind of worm, its axial tooth thickness would increase or decrease proportionally along its axis from one end to the other end. Differently, the worm-gear meshed has equalling tooth thickness. Consequently, as the worm moves along the axis, theoretically, the side clearance between the worm and gear could be eliminated at a specific position of the worm.

In double-pitch worm transmission, the clearance can be adjusted by grinding adjustment ring, which has the advantages of accurate adjustment, convenient, and reliable. However, this method would reduce the worm tooth thickness, further decreasing the strength of the worm.

Double-section worm drive: In such kind of transmission, the worm consists of two segments, namely, the worm shaft and the hollow worm shaft. The sleeve could be axially moved from the hollow worm shaft to the worm shaft, as shown in Fig. 3. With the aid of the adjustment tab, the axial location of the hollow worm shaft could

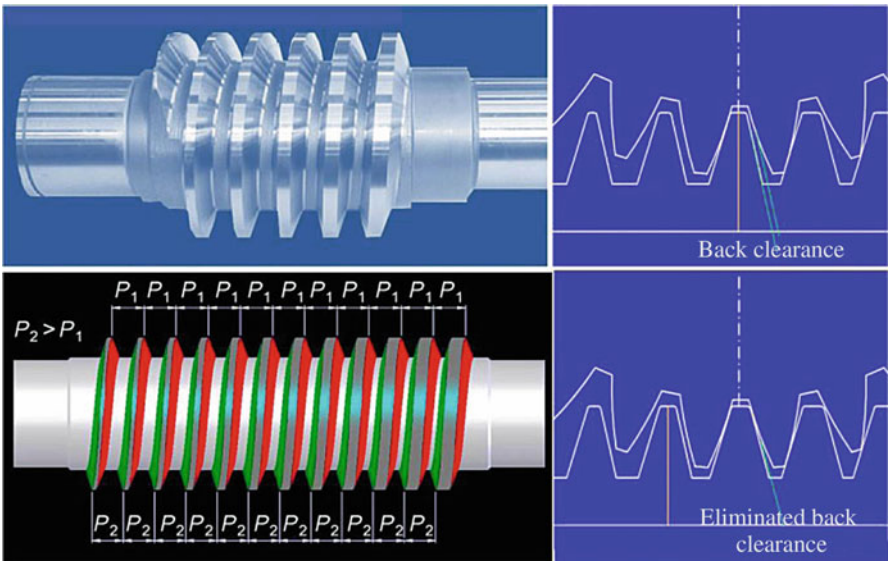

Fig. 2 Principle of double-pitch worm drive to eliminate back clearance (Zhang et al. 2016)

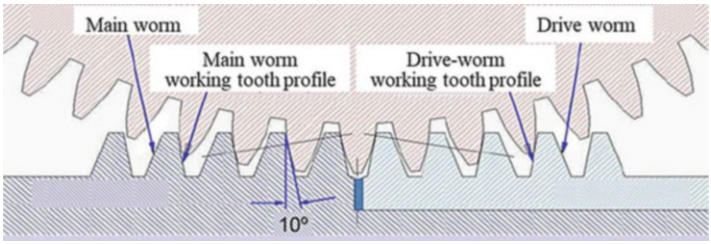

Fig. 3 Principle of double-section worm transmission to eliminate back clearance (Zhang et al. 2016)

be controlled, enabling the right-side tooth surface of worm shaft and the left-side tooth surface of hollow worm shaft to contact with the left- and right-side tooth surface of worm gear.

As a result, the acting tooth surface of the worm shaft will drive the worm gear to rotate clockwise, while that of the shallow worm drives the worm gear to rotate counterclockwise, thereby eliminating the gap between the worm and worm gear. This kind of transmission mechanism has the characteristics of simple clearance elimination and compact structure. Meanwhile, the non-acting tooth surface has a larger tooth shape angle than the acting tooth surface, possessing better transmission rigidity.

Double-worm synchronous drive: One worm shaft is installed at locations 0° and 180° of one worm gear, and they are connected by one differential gear

train, thereby keeping it no clearance in sync. Besides, two sets of worm and gear transmission mechanisms are employed in one circular feeding mechanism. By adjusting one worm shaft to move along the axial direction to drive the slight rotation of the rotary axis, consequently, the worm gear could come into contact with two different tooth faces during the rotation along the positive and negative directions, so as to adjust the reverse clearance of the rotation axis. By using such kind of method, although the gap could be easily eliminated, it requires higher transmission accuracy of the gear train. Otherwise, there will be back clearance formed. Additionally, two synchronous servo motors can be used to drive two worm gears; one of them can realize circular feed, and the other one can be used to eliminate back clearance.

Worm and worm-gear transmission, due to the advantages of large transmission ratio, compact structure, small impact load, smooth transmission, easy to self-lock, etc., is one of the commonly used transmission mechanisms in CNC turntable and double-swing angle CNC universal milling head. It is usually driven by servo motor. In the design of single-axis CNC turntable, there is less constraint on the layout of the serve motor. The circular feeding movement could be realized by special reducer drive worm and worm-gear pair (or even directly connected with the worm and worm-gear pair). Differently, for the design of the rotary axes of double-swing angle CNC universal milling head and biaxial CNC turntable, there are higher requirements for the flexibility and compactness. So it is needed to combine the worm and worm-gear transmission with other transmission mechanisms, including synchronous belt, gear, bevel gear, etc., thereby realizing the multistage transmission. Moreover, it is necessary to approximately set the transmission ratio at all levels and to adopt reasonable layout of servo motors, thereby ensuring the angle range of each functional part and the machining scope of workpiece. In the design process of multilevel transmission chain to realize the rotary feeding, the worm and worm-gear transmission mechanism is usually used as the last transmission link to directly transfer the torque to the workpiece or tool, for obtaining higher transmission rigidity.

Roller Drive

Roller drive, as one new type of seamless mechanical transmission mechanism, can be used to establish a new type of CNC rotary table. As shown in Fig. 4, the transmission mechanism consists of an input shaft with a globoidal CAM and a runner with a number of driven roller elements, which are arranged in a uniform radial direction on a circumference (Zhang et al. 2011, 2016; Muditha and Masaomi 2009).

As seen from Fig. 4, the table and the runner are fixed together. The CAM groove surface on the input shaft is linearly contacted and meshed with the outer ring surface of the driven roller element on the runner, thus driving the runner (i.e., the workbench) to rotate. The pillar end of the driven roller element is cold-pressed into the circumferentially distributed hole of the runner. Because of the needle roller bearing between them, its outer ring rotates in the meshing process. The sliding friction in the meshing process is transformed into rolling friction, which improves the

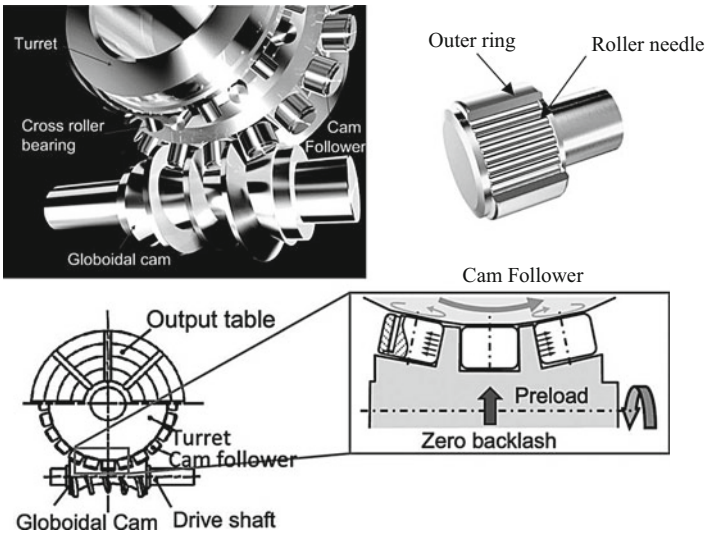

Fig. 4 Components and principle of roller drive mechanism (Muditha and Masaomi 2009)

transmission efficiency and significantly reduces the wear. The roller with cross configuration, which is installed between the runner and the shell, is treated as the support bearing to bear the axial and radial loading, to ensure its high rigidity and high precision of rotation. By adjusting the axis spacing between the input shaft (globoidal CAM) and output shaft (runner) spacing, the transmission clearance can be eliminated, and/or the preload could be applied.

The position accuracy, natural frequency, rotation error, and unbalance sensitivity of the roller-driven worktable were tested, and the comparative test results showed that the roller CAM-driven worktable has significantly higher static and dynamic performance than traditional worm- and gear-driven worktable. The roller CAM drive has no back clearance, and the rotation error is basically the same in the positive and negative direction and basically coincides with the static angle error curve. There is extremely slight jitter in the working process. Moreover, such kind of drive is not sensitive to the unbalanced mass, and the caused error is basically the same. The positioning accuracy is up to 10.6″, and the repeated positioning error is only 3.6″. Moreover, the regular error is exhibited, which could be compensated. In addition, there are higher natural frequencies of first and second order, but they have lower peak values. The test results of two workbenches with different drive forms are compared in Table 1 (Muditha and Masaomi 2009).

In the design field of rotary feed mechanism of CNC machine tool, the most representative roller CAM transmission mechanism is the RA-series precision drive unit technology by Japan's Sankyo Seisakusho Company. It has been successfully applied in many high-end functional parts (such as AB axis double-angle CNC universal head, B-axis, and NC rotary table) manufactured by Mazak, DMG Mori Seiki Co., etc.

Table 1 Summary of results (Muditha and Masaomi 2009)

		Worm gear	Roller gear cam
Frequency response (Hz)		270 Hz, 430 Hz	270 Hz, 430 Hz
Positioning accuracy and repeatability (arc/second)	Mean reversal value	32.8	2.7
	Repeatability of positioning *R*	34.5	3.6
	Accuracy *A*	38.6	10.6
Rotational fluctuation		Exist	Very small
Influence of unbalance mass		Influenced	Nil
Backlash		Exist	Nil

In addition, the rotary feeding mechanism of RIBROTRO EM series rotary table in FIBRO Company is also driven by roller CAM transmission mechanism. The difference is that in RIBROTRO EM CAM transmission mechanism, the CAM roller is axially arranged on the follower in circumferential direction. The CAM shaft can be decorated beneath the rotary follower, which is helpful to improve the radial compactness of the rotary feed mechanism. However, it also increases the length of the axial space of the rotary mechanism, while the radius of CAM shaft drive is decreased. Under the action of the same driving force, it will reduce the drive torque. Therefore, in the design process, the mechanisms' requirements for space and torque should be comprehensively considered.

Roller CAM transmission mechanism has higher accuracy and stiffness than worm-gear transmission mechanism. The transmission ratio could reach up to 40–160:1; thus, it has higher transmission torque. Moreover, such kind of transmission could be cooperated with three orthogonal axes, and it could provide large-torque rotary feed support for the heavy cutting of various materials (such as titanium alloy). This is also one important reason that the roller CAM is widely applied in the rotary feeding mechanisms of high-end CNC machine tool. However, although it has the above advantages, due to its higher manufacturing precision requirements and poor manufacturability, the roller CAM-driven worktable is usually of high cost. Consequently, the application of roller CAM transmission mechanism is, to a certain extent, limited.

Direct Drive

The rapid development of NC machine tool has put forward higher requirements for high-speed rotary feed mechanisms. In order to realize the high-speed drive of rotary feeding mechanism in functional parts, such as milling head, CNC rotary table, etc., the rotor of the torque motor is directly connected with the rotary units. It not only eliminates intermediate transmission link to realize high-speed feed of rotary parts but also has compact structure and small inertia to obtain high dynamic performance and positioning accuracy. Therefore, it has been widely used in a variety of

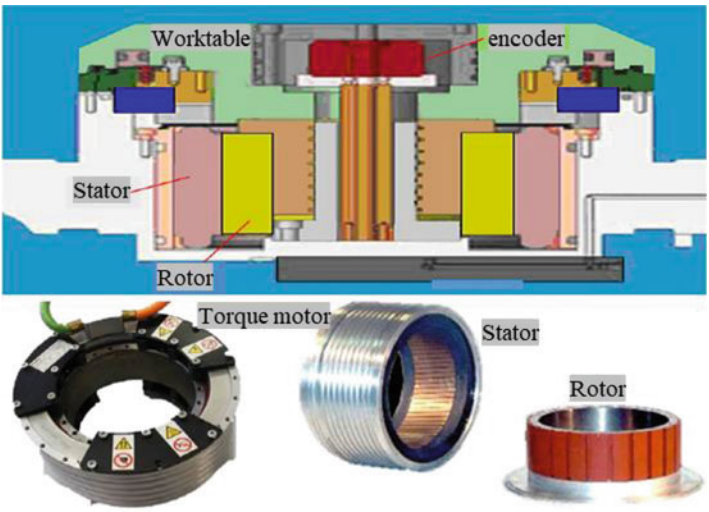

Fig. 5 Direct-driven worktable and torque motor (Zhang et al. 2016)

applications, including multi-axis linkage hybrid machining center, ultraprecision machine tools, special mechanical and electrical system, and precision measuring system. Figure 5 shows the structure and torque motor of direct-drive turntable (Zhang et al. 2016).

When the torque motor is applied to drive the rotary feeding mechanism to output, there is a large amount of heat generated in its coil, which has great influence on the performance of torque motor. So, the cooling system is one of the key design issues of the rotary feed mechanism using direct-drive technology.

The commonly used method is water-cooled cooling, where water jacket is contacted with the stator of the torque motor. The coil heat will be taken away by the heat exchange of recirculating cooling water. Using this method, on the one hand, the damage of the coil will be prevented, and the output of effective torque of the torque motor will be ensured. On the other hand, the designed water-cooling system also can effectively reduce the overall accuracy loss caused by the temperature rise. It has been proved that the torque of the torque motor with water-cooling system can be improved by 30–50%, compared with the torque motor with natural cooling (Zhang et al. 2011). In addition, the permanent magnet on the rotor of torque motor has strong adhesion capability; thus, the rotary feed mechanism is required to have good sealing properties.

The torque motor-driven rotary feed mechanism, restricted by structure and dimension of each functional unit, will suffer from limited rotary torque during rotary feed machining. Thus, direct drive is usually used in the rotary feed mechanisms of the functional parts of five-axis machine tool for finish machining, such as AC-axis double-pendulum angle CNC universal milling head and double-pendulum angle CNC rotary table. Figure 6 shows the structure of cradle-type AC-axis

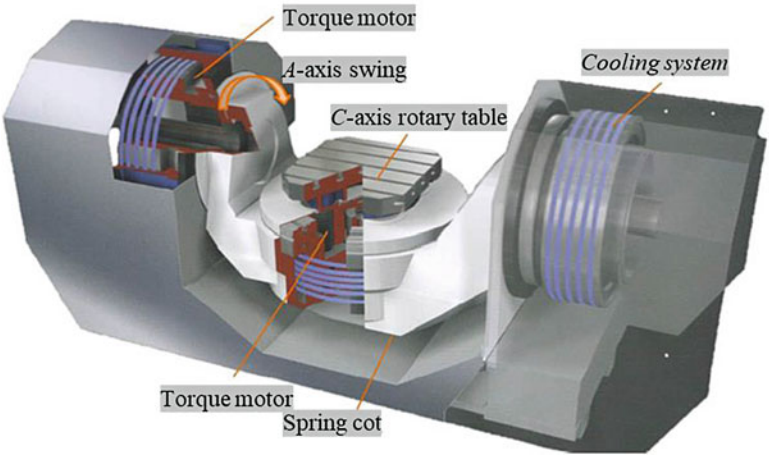

Fig. 6 Direct-drive cradle AC-axis double-pendulum working table (Zhang et al. 2016)

double-pendulum table in D500 vertical machining center by Japan Makino Company (Zhang et al. 2016).

The direct-drive rotary feed mechanism with large torque feed output can be also realized by the series or parallel connection of the torque motor. However, the serial arrangement structure has certain requirements for the axial space of the rotary feed unit. Therefore, in the design of the rotary feed mechanism of the CNC machine tool, direct drive could be used in the *B*-axis unit of the turning/milling compound machining center or the *C*-axis unit of the double-pendulum CNC universal milling head.

In the rotary feeding mechanism driven by parallel arrangement of torque motors, two torque motors are face-to-face or back-to-back arranged in axial direction. Due to its good symmetry, it is often used in the fork structure of the double-pendulum angle CNC universal milling head.

In addition, with the development of NC machine tool toward turning/milling compound machining, the rotary feed mechanism will be used to not only achieve the low-speed, high-torque milling feed but also realize the high-speed rotary turning. The torque motor, because of its high-speed characteristic, has become one of the most effective ways to achieve this function. It has exhibited obvious advantages than other methods.

Rotary Motion Bearing

The rotary movement precision is mainly determined by the precision of the supporting bearing and its parts. So, the supporting component is one of the key technological issues in the design of rotary transmission mechanisms. As the core component of rotary table, rotary table support should not only have high bearing

capacity but also have high turning precision, high anti-overturning ability, and high speed.

In the traditional rotary table, the table support generally adopts the combined configuration of multiple bearings (rolling bearings or sliding bearings, etc.) to bear the axial force and radial force. Due to the use of multiple bearings, it has various disadvantages, including complex structure, difficult-to-machine assembly, large volume, and low integration degree.

In the modern CNC machine tools, the rotary table bearing is often used, as shown in Fig. 5. High-precision cylindrical roller and bearings are used to bear radial force and axial force, making the structure of the rotary table simpler and more integrated. On the other hand, due to the direct use of turntable bearing, it is easier to optimize the structural parameters of the shaft system in the limited space, and rotary table has greater system stiffness. Meanwhile, the manufacturing of the table parts becomes much easier.

In high-precision manufacturing systems, such as ultraprecision machine tools and measuring equipment, hydrostatic or aerostatic bearings are widely used as the support for rotary motion. Compared with rolling contact bearings, due to the error-homogenized effect of hydrostatic oil film or gas film, hydrostatic or aerostatic bearings can achieve the rotary motion accuracy of submicron or even dozens of nanometers. Aerostatic bearing has small bearing capacity and low stiffness; thus, it is usually used as the support in ultraprecision measuring equipment. As for the hydrostatic bearing, because of its high load capacity, good damping, and high stiffness, it is widely used in ultraprecision machine tools.

Figure 7 shows the structural scheme of an ultraprecision direct-drive hydrostatic rotary table designed for meeting the overall requirements of an ultraprecision grinding machining of a large part (Wu 2013). The hydrostatic rotary table is directly driven by a large torque motor, and the angle encoder provides position, velocity, and acceleration feedbacks for closed-loop control. Other degrees of freedoms (DOFs) are constrained by hydrostatic bearings, including hydrostatic radial bearings and hydrostatic thrust bearings. Hydrostatic radial bearing is used to constrain two-straight-line movement in the horizontal plane, while hydrostatic thrust bearings are applied to constrain the vertical movement and rotation around the axis.

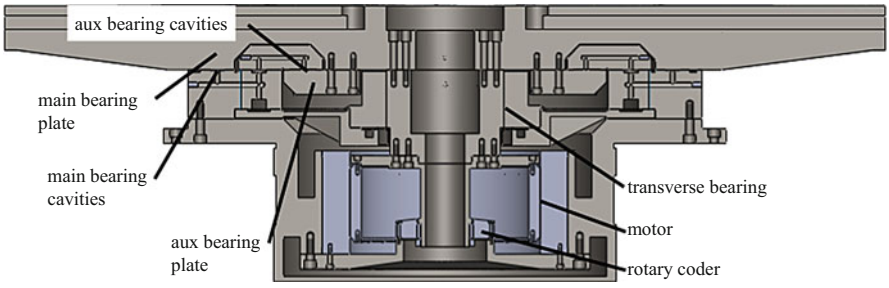

Fig. 7 One kind of structural scheme of an ultraprecision hydrostatic rotary table (Wu 2013)

In the hydrostatic thrust bearing, closed structure is adopted, the primary oil cavity ring is used to provide upward supporting force, and the secondary oil cavity ring is applied to provide the downward force. Under ideal conditions, the difference between the upward and downward forces is, namely, the predesigned rated support force, which is used to undertake the weight of all rotating parts in hydrostatic turntable and the weight of the loaded workpieces. The use of closed-thrust bearings is employed to obtain sufficient axial stiffness and angular stiffness.

In addition, Canadian scholars proposed a novel six-degrees-of-freedom (6-DOF) magnetic levitation turntable, as shown in Fig. 8 (Lu et al. 2015). The use of magnetic levitation can not only provide frictionless motion and achieve high-precision motion but also correct the six-axis motion error in real time. The six-DOF actuator consists of a circular Halbach magnet array, connected to the moving table's underside and a printed planar coil mounted on the stator. These forces are generated by the interaction of an electric current through a fixed coil with the magnetic field of a permanent magnet array.

In order to realize the complete noncontact motion feedback, one position measuring method of the 6-DOF worktable is proposed, which involves the use of four capacitance sensors and four optical encoders (ENC1, ENC2, ENC3, and ENC4).The optical encoder is installed, as shown in Fig. 8, where the grating is

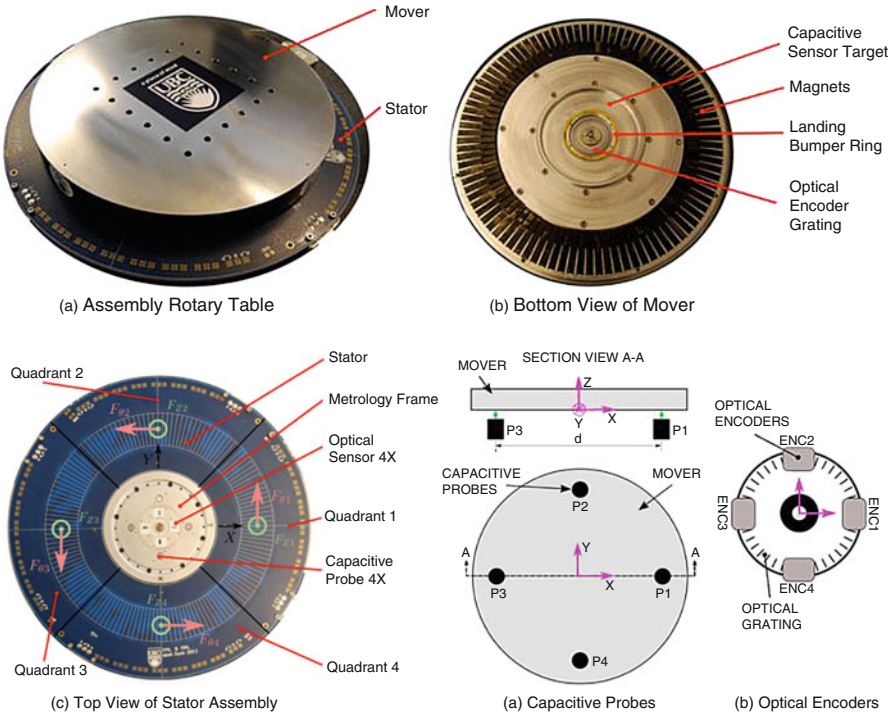

Fig. 8 Rotary table overview and sensor arrangement (Lu et al. 2015)

mounted on the worktable and the encoder head is mounted on the base. These encoders are applied to measure *X*-axis, *Y*-axis, and the rotation around the *Z*-axis. The alignment tolerance of the optical encoder allows the meter to undergo small movements in the direction that could not be measured by the optical encoder. The worktable is made, and the controller of each axis is designed. Movement has been demonstrated with a position resolution of 55 nm (RMS).

Measurement and Sensor

Advanced CNC machine tool feed drives, including linear and circular feed, often use position, speed, acceleration, and load sensors to improve their positioning accuracy and response bandwidth. The widely used measurement sensor systems include (1) position detection, (2) speed detection, (3) acceleration detection, and (4) current detection (Zhang et al. 2016).

Photoelectric angle encoder is one kind of sensor which converts the angle displacement of the rotating shaft into pulse or digital quantity by photoelectric conversion. It can be used for direct measurement and position feedback of circular feed mechanisms, such as rotary table, swing fork, and milling head. But it is more common for indirect displacement measurement and semi-closed-loop position feedback of linear feed of ball screw and nut pair.

Bearingless angle encoders have large apertures, and their gratings are made of different materials according to their diameters. For small, medium, and large sizes (up to 10 m), glass discs, steel drum, and steel bands are, respectively, used. In addition, the bearingless angle encoder can be integrated with the machine structure. For example, Heidenhain ERA 4200 bearingless angle encoder is integrated on the worktable of the machine tool, as shown in Fig. 9. At such case, the gate drum is a steel ring. There is a grating of 20 μm and reference points inscribed on its gold-plated surface. The grid drum rotates with the table, and the reading head is fixed on the substrate. During the working state, the relative angular displacements between grid drum and reading head are converted into electrical signals by using the principle of single-field imaging scanning. After focusing, the light source of the reading head has passed through the grating on the scanning mask. Then it is projected onto the graduated scale on the raster drum surface, forming the light signal with alternating light and dark. The optical signal, after reflecting through the window on scan mask, is projected onto the grid photoreceptor, producing four phase differences of 90° electrical signals. After high-frequency subdivision processing, up to 52,000 sinusoidal electrical signals can be emitted per revolution (Heidenhain 2013).

In order to track the movement of the table and improve its damping performance, the servo controller is needed to detect the speed of the feed drive. The commonly used method is to differentiate the value detected by the position encoder, thereby obtaining the corresponding speed value and then feeding it back to the speed.

Acceleration feedback is used in control algorithm for improving the dynamic performance of the machine tool structure and to check the real trajectory of the feed

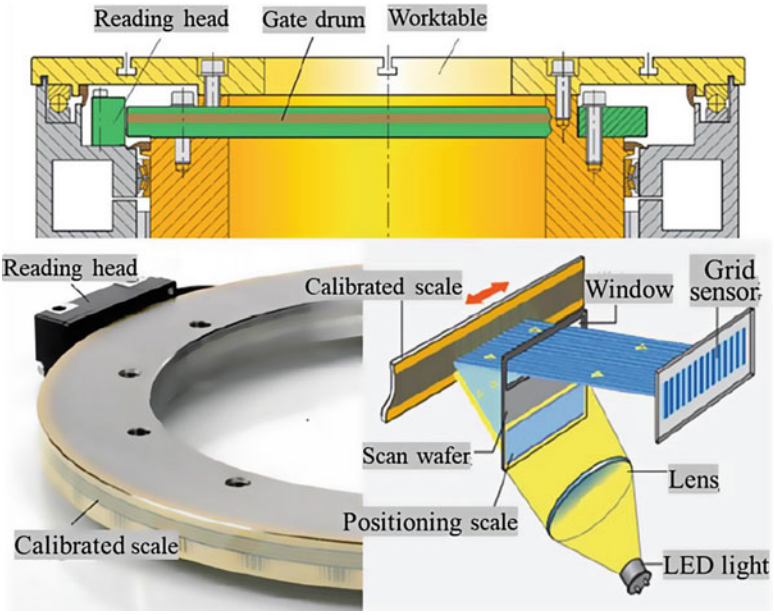

Fig. 9 Principle of bearingless angle encoder (Heidenhain 2013)

drive. The acceleration can be measured directly or by the second derivative of the measured value. The standard accelerometer based on piezoelectric crystals can be applied to measure the absolute acceleration of the moving parts, but it confuses the acceleration of the feed-driven rigid body with the vibration signal of the machine tool structure, which may not be beneficial to the improvement of the feed-driven control performance. Iron sensors based on electromagnetic induction are usually used to measure the relative motion acceleration of the feed driving components.

A Case Study: Design of a Hydrostatic Rotary Table

Scheme Design of the Rotary Table

As shown in Fig. 7, on the ultra-precision hydrostatic direct-drive tablethe, the outer ring is primary thrust bearing, while the inner ring is secondary thrust bearing. The primary and secondary thrust bearing faces are located at the same horizontal plane, which not only shortens the axial dimension but also reduces the processing difficulty of thrust plate. However, the connection mode of radial bearings increases the difficulty of machining and assembly, so the modified structure scheme is shown in Fig. 10 (Wu 2013).

According to the technical specifications of the turntable, one hydrostatic bearing is designed and calculated. Considering the manufacturing errors of actually

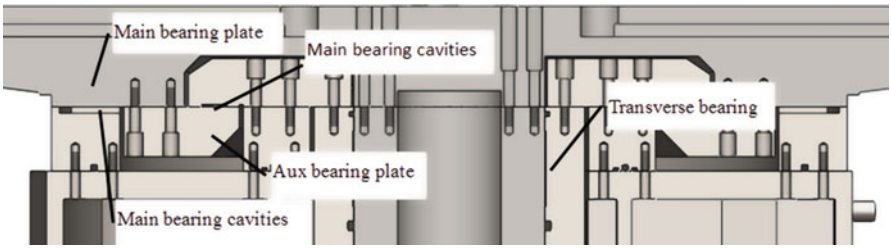

Fig. 10 Structure scheme of ultraprecision hydrostatic turntable after modification (Wu 2013)

processed bearing surfaces and bearing parts, the bearing capacity and stiffness indexes are predesigned to be approximately 25% higher than the technical requirements, so as to preliminarily determine the structural dimensions of hydrostatic bearings.

The drive and measurement feedback is closely related to the accuracy and dynamic response characteristics of the turntable. In the design scheme, the turntable is directly driven by Germany Siemens 1FW6 built-in torque motor with integrated cooling. The selected torque motor is to meet the requirements of electromechanical matching characteristics, that is, capacity matching and inertia matching principle. The RCN8000 high-precision angle encoder from Heidelberg, Germany, is applied to enable the measurement feedback. The feedback components are mainly selected according to the control mode and position accuracy of the turntable.

Precision Design

As mentioned above, the precision of rotary motion is mainly determined by the precision of the supporting bearing and various parts. For ultraprecision hydrostatic turntable, as shown in Fig. 10, based on the rotational motion error analysis, the main geometric error factors that affect the turntable accuracy include the perpendicularity error between the end faces of rotating shaft and radial bearing, and center axis, the main thrust plate flatness error, and the cylindricity errors of radial bearing hole and shaft. Those errors could directly affect the change of oil film clearance and further decrease the accuracy of turntable. Based on geometric error analysis and practical engineering experience, the geometric error of this case is limited to within 10% of the bearing clearance.

Deformation Analysis of Critical Components Under the Action of Hydraulic Oil

For hydrostatic thrust bearing, the thrust plate or the floating plate under the working condition will deform under the action of pressure oil, and the large deformation will affect the working oil film clearance. In addition, the number, distribution, and

preload of connecting bolts between parts will also affect the deformation of thrust plate or floating plate. Therefore, finite element method (FEM) was used to analyze the structural deformation, and the variation value of oil film clearance was obtained according to the deformation results, so as to recalculate the stiffness values of the bearing and to optimize the structure.

In addition, in the case of ultraprecision hydrostatic rotary table design, more attention should be paid to the control of hydraulic oil pressure fluctuations, the selection of the hydraulic oil with right viscosity, and the return of oil and other design points. These factors will also have an impact on the performance of ultraprecision hydrostatic rotary table.

Acknowledgments The authors gratefully acknowledge financial support of the National Science and Technology Special Program of China (No. 2011ZX04004-061).

References

Heidenhain (2013) Rotary encoders for highly dynamic servo drives[EB/OL]. 21 Mar 2013. https://www.heidenhain.us/wp-content/uploads/208922-2I__Encoders-for-Servo-Drives_en.pdf

Lu X, Dyck M, Altintas Y (2015) Magnetically levitated six degree of freedom rotary table. CIRP Ann Manuf Technol 64(1):353–356

Muditha D, Masaomi T (2009) High performance rotary table for machine tool application. Int J Automot Technol 30:343–347

Wu J D (2013) Design and analysis of an ultra-precision rotary table with a high diameter-length ratio. Master's thesis of Harbin Institute of Technology

Zhang BS, Zhang S (2016) Introduction on the geometric accuracy and measuring of machine tool. Mach Des Manuf Eng (in Chinese) 45(12):1–8

Zhang WB, Li Y, Gao XF, Yu CM (2011) Several transmission types of rotary feed mechanism of the numerical control machine tool. J Mech Transm (in Chinese) 35(5):76–80

Zhang S, Zhang BS, Wei HH (2016) The feed driving for the machine tool. Mach Des Manuf Eng (in Chinese) 45(8):1–10

Design, Development, and Analysis of a Hybrid Serial-Parallel Machine for Precision Polishing

7

Peng Xu, Chi Fai Cheung, Bing Li, Chunjin Wang, and Lai Ting Ho

Contents

Introduction 172
Conceptual Design of the Hybrid Serial-Parallel Precision Polishing Machine 173
Kinematic Analysis of the Serial-Parallel Mechanism 177
  Kinematic Analysis of the Parallel Mechanism 177
  Kinematic Analysis of the Serial Mechanism 185
Stiffness Model of the Parallel Mechanism 188
  Stiffness Model of the Leg Assembly 189
  Stiffness Model of the Drive Assembly 191
  Stiffness Model of the Guide Assembly 192
  Stiffness Performance Evaluation 195
Control System and Control Strategy 196
Prototype of the Hybrid Serial-Parallel Polishing Machine 199
Conclusion 203
References 204

P. Xu · C. F. Cheung (✉) · C. Wang · L. T. Ho
State Key Laboratory of Ultra-precision Machining Technology, Department of Industrial and Systems Engineering, The Hong Kong Polytechnic University, Hung Hom, Kowloon, Hong Kong
e-mail: penghit.xu@connect.polyu.hk; benny.cheung@polyu.edu.hk; chunjin.wang@polyu.edu.hk; lai.ting.ho@polyu.edu.hk

B. Li
School of Mechanical Engineering and Automation, Harbin Institute of Technology, Shenzhen, China

State Key Laboratory for Manufacturing Systems Engineering, Xi'an Jiaotong University, Xi'an, Shaanxi, China
e-mail: libing.sgs@hit.edu.cn

Z. Jiang, S. Yang (eds.), *Precision Machines*, Precision Manufacturing,
https://doi.org/10.1007/978-981-13-0381-4_20

Abstract

Mechanical polishing with abrasive slurry is a kind of finishing process that can reduce the surface roughness and improve the form accuracy effectively. In this chapter, the development of a serial-parallel machine for precision polishing of freefrom surface is presented. The topological structure of the machine is a six degrees-of-freedom (DOF) hybrid serial-parallel mechanism, including a three-DOF parallel mechanism, a two-DOF serial mechanism, and a functional extension limb providing a redundant DOF. The main features of the polishing machine are reflected in two aspects including the following: (1) the machine inherits the advantages of both serial mechanism and parallel mechanism, and (2) the rotation and translation motions between the polishing tool and the workpiece are decoupled. In this chapter, a systematic kinematics and stiffness analysis of the hybrid serial-parallel mechanism are performed. Afterward, the development of the polishing machine is explained. Finally, some preliminary experiments have been conducted on a saddle surface which aim to evaluate the performance and demonstrate the capability of the machine.

Keywords

Ultraprecision machining · Freefrom surface polishing · Hybrid serial-parallel mechanism · *Precessions* polishing process · Kinematics · Stiffness · Simulation · Mechanical design · Prototype development · Experimental evaluation

Introduction

Ultraprecision and defect-free freefrom surfaces are becoming more and more widely used in many high value-added products, such as advanced optical systems, biological engineering, precision molds, and aerospace applications. Abrasive polishing as one of the oldest manufacturing technologies is widely used to remove materials from the surface and improve its form accuracy. However, polishing of freefrom surfaces containing the features of non-rotational and non-translational symmetry is a great challenge. Nowadays, freefrom surfaces are still predominantly polished manually, which are very costly and time-consuming and heavily rely on the expertise and experience of the operator. To improve competitiveness, manufacturers have to continuously stringent the requirements on the form accuracy and surface quality as well as reduce the delivery times of the related products.

Computer-controlled polishing (CCP) with a small pitch tool is regarded as a breakthrough of modern optical machining techniques. Currently, there are many representative prior work in CCP, such as the stressed lap polishing (Martin et al. 1990; West et al. 1994), magnetorheological finishing (Kordonski and Golini 1999; Sidpara and Jain 2013), and ion beam polishing (Allen 1995). The material removal of the various CCP processes can be modeled and controlled precisely by the computer, so they are also known as the deterministic polishing processes. Making use of a compliant local-removal tooling system controlled by air pressure, Walker et al. (2003) proposed and developed a novel polishing technique, often referred to as

computer-controlled bonnet polishing (CCBP). Afterward, this polishing technique was successfully commercialized, and a series of Intelligent Robotic Polishers (IRP) were developed by the Zeeko Ltd. to hold the tooling systems (Walker et al. 2006). However, this polishing equipment is all constructed by using the serial mechanisms. Since all of the driving joints are connected in sequence, with the lower joints carrying the one above it, it leads to the accumulation of errors in each joint and limits the stiffness and dynamic performance of the whole machine.

A parallel mechanism is typically a closed-loop mechanism in which an end-effector is supported to a fixed base by several serial chains together. Due to their favorable characteristics in terms of higher precision, stiffness, and load-carrying capacity, parallel mechanisms are becoming more and more widely used in various fields, such as machine tool, flight simulators, medical robot, and so on. However, apart from the above merits, a fully parallel mechanism has a large number of links and passive joints, leading to several drawbacks, such as coupled motion, multiple singularities, and limited workspace. Parallel mechanisms with less than six DOF are classed as lower-mobility parallel mechanisms, having relatively simple structures and overcoming the shortcomings of the fully parallel mechanisms. To achieve a five-face machining, low-mobility parallel mechanisms can be integrated with corresponding serial mechanisms to form hybrid serial-parallel mechanisms, which can leverage the advantages of both parties.

As far as the polishing of a freefrom surface is concerned, the machine should be able to provide at least five-DOF motions to position the contact spot anywhere on the surface, as well as to orient the rotation axis of the tool with respect to the local normal directions. Various topological structures can be synthesized to configure the hybrid serial-parallel machine by using different theoretical approaches. Although several polishing machines with hybrid serial-parallel mechanisms have been developed (Brecher et al. 2006; Fan et al. 2015; Kakinuma et al. 2013; Liao et al. 2008; Lin et al. 2014; Lin et al. 2013), they are mainly originated from the corresponding milling machines by simply replacing the tooling system. Being a compliance machining technology, the material removal mechanism in polishing process is very different from that in the milling process. It not only depends on tool shape and the relative motion between the tool and the workpiece but also the velocity and pressure distribution on the contact area.

To overcome the defects of the existing polishing equipment and meet the requirements of precision polishing, it is necessary to analyze and improve the traditional polishing systems. In this chapter, the development of a novel serial-parallel polishing machine is presented, which is designed deliberately for polishing process by considering the process characteristics. After throughout kinematic analysis and stiffness analysis, a prototype of the polishing machine was developed and tested. The preliminary results justify its effectiveness for high precision polishing.

Conceptual Design of the Hybrid Serial-Parallel Precision Polishing Machine

One of the core techniques used in the conceptual design of the polishing machine is the *Precessions* polishing process (Walker et al. 2003), which is shown in Fig. 1. As the polishing tool moves toward the workpiece, a contact spot is generated. The

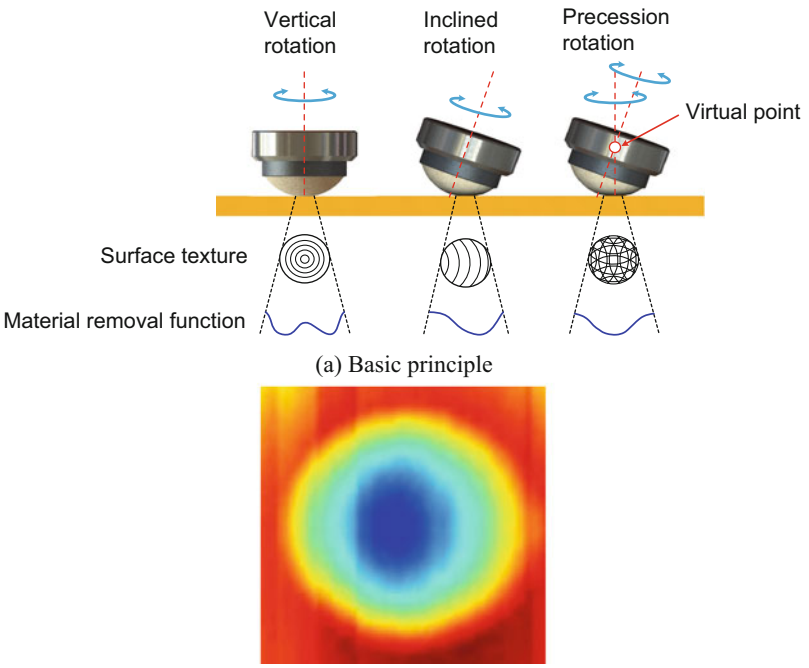

(a) Basic principle

(b) Gaussian-like material removal function

Fig. 1 *Precessions* polishing process

vertical rotation of the polishing tool shows a point with zero velocity at the center of the contact-spot, which is not effective to controlling form accuracy in polishing. To shift the tool tip with zero velocity outside the contact-spot, the compliant spherical-shaped polishing tool is obliquely pressed against the surface. Meanwhile, the axis of rotation of the tool is precessed in several discrete directions about the local normal direction to generate a Gaussian-like material removal function.

Motivated by this idea, a novel polishing machine with a hybrid serial-parallel mechanism is proposed as shown in Fig. 2 (Xu et al. 2017). It is well known that a wide range of orientation motion is difficult to be achieved by a parallel mechanism. In view of this, a serial mechanism, which consists of a rotating/tilting table, is used to orient the axis of polishing tool about two orthogonal rotational joints. Considering the characteristics of the *Precessions* polishing process, the curvature center of the spherical-shaped polishing tool is mounted to coincide with the virtual point intersected by the two axes of rotational joints. Serial mechanism provides two rotational DOF, leaving the parallel mechanism to provide three translational DOF. In addition, workpiece with axially symmetry is an important category of the polishing objects, which need the workpiece to achieve continuous full-circle rotation with respect to the polishing tool. As a result, parallel mechanism is required to provide three translational DOF and one rotational DOF, i.e., Schönflies motion. A variation of the traditional Delta parallel mechanism, which is a 3-$\underline{P}(SS)^2$ structure, is

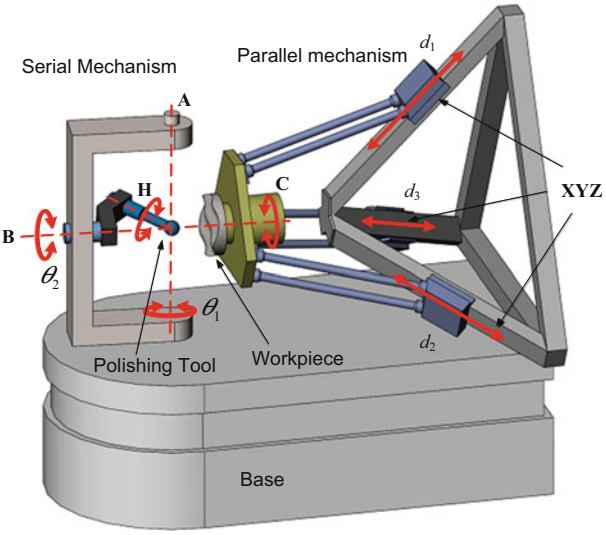

(a) Topological structure

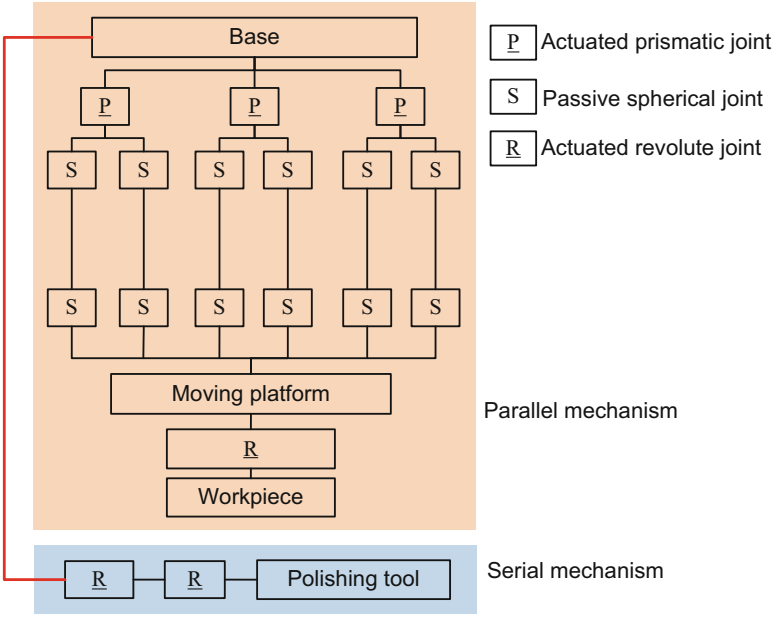

(b) Joint schematic

Fig. 2 Structure of the hybrid serial-parallel mechanism

adopted to achieve three translational DOF, and a redundant DOF is used to rotate the workpiece mounted on the moving platform. Here the notations of P, S, and $(SS)^2$ denote prismatic joint, spherical joint, and two S joints at either extremity of a spatial parallelogram, respectively. The underline indicates the actuated joint at the base frame.

Actuators in the serial mechanism enable tool axis to follow the local normal directions of the workpiece and impose the required inclination angles. Rotation of the spindle enables the polishing tool to create a material removal function. Actuators in the parallel mechanism realize the Schönflies motion that allows the workpiece to translate in all directions and rotate around an axis parallel to a fixed direction.

The characteristics of the design scheme are discussed. The rotational DOF in the five-face machining is implemented by the serial mechanism, while the parallel mechanism only provides three translational DOF, enabling the proposed design scheme to exhibit the merits of both parallel mechanism and serial mechanism. The identical design of each limb and symmetrical arrangement of the parallel mechanism reduce the design work and the manufacturing cost. Furthermore, the moving mass of the machine is greatly reduced by placing all the actuators on the machine base, which leads to a better dynamic performance. Since both ends of the leg in the parallel mechanism are spherical joints, they are only subjected to extension and compression force along the axis and thus have a high load-carrying capacity per unit weight. Three actuators in the parallel mechanism are arranged obliquely and intersected at a point in the space to form a tetrahedron structure, which can improve the rigidity and stability of the base and facilitate the modular design of the whole machine. At the same time, a flatter workspace can be achieved according to the geometric characteristics of the typical workpiece. This is particularly true for polishing optical components.

As the two rotational joints in the serial mechanism intersect at a point that is the curvature center of the polishing tool, any angular motions of the serial mechanism cause no translational motions. As a result, the translational and angular motions of the tool relative to the workpiece are decoupled during the synchronous motion. Translational motions are controlled by the parallel mechanism, and angular motions are determined solely by the serial mechanism, so that the rotational tool center point (RTCP) in the five-axis machining can be conveniently realized. These features in five-face machining greatly simplify its post-processor development.

This design scheme provides the capability to polish surfaces with various shapes, such as flat, aspherical, off-axis aspherical, and freefrom. Within the workspace, any tool path can be implemented. The redundant DOF can further improve the machining capacity, and it is also beneficial for the machine to carry out path planning in a larger range and adjust the power distribution of the servo motors in each limb. Since this design scheme is mainly used for polishing of small-diameter workpiece, the horizontal arrangement is favorable for the slurry to flow into the polishing contact area under the action of gravity, thereby improving the polishing efficiency and increasing the controllability of the polishing process.

As shown in Fig. 3, the produces to develop the precision polishing machine with serial-parallel mechanism are summarized, which shows that it is a long-term and complex system involving many disciplines and a wide range of knowledge (Merlet 1994). To facilitate the following studies and prototype development of the machine, the kinematic analysis and the stiffness analysis are undertaken.

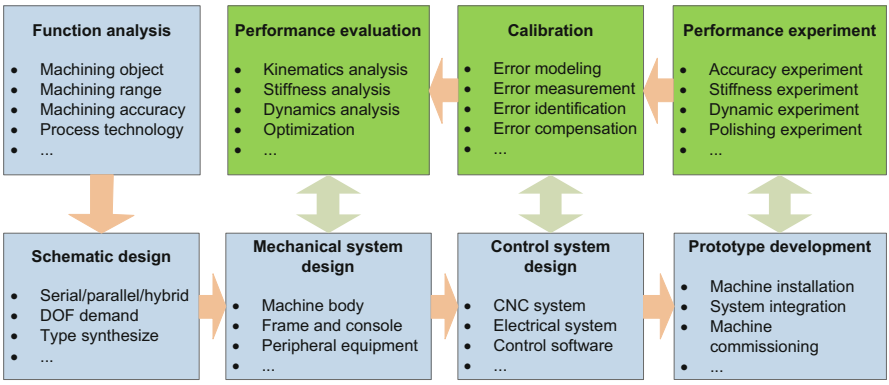

Fig. 3 Produces to develop the precision polishing machine

Kinematic Analysis of the Serial-Parallel Mechanism

Kinematic analysis aims to investigate the motion relationship between the inputs of actuators in joint space and the outputs of end-effector in operation space, which provides a foundation for the analysis, design, and control of the machine. In the proposed design scheme, the workpiece and the polishing tool are attached to the end-effectors individually. As a result, there are two kinematic chains including the closed workpiece chain from the base to the workpiece and the open tool chain from the base to the polishing tool. The two kinematic chains integrated together make up the whole kinematic chain. Considering the structural independence and the motion decoupling characteristics, the kinematics of parallel mechanism and serial mechanism can be analyzed separately with respect to the base.

Kinematic Analysis of the Parallel Mechanism

The original Delta mechanism proposed by Clavel (1990) has been extensively studied, and the methods of the relevant analysis are well filed. As one of its many variants, much less work has been reported for the linear Delta mechanism (Liu 2005; Liu et al. 2004). This section further studies and summarizes the class of interest, including mobility, position, velocity, workspace, and dexterity.

Mobility Analysis of the Parallel Mechanism

For the parallel mechanism, the first issue is to determine the mobility and the motion type of the end-effector. Serial mechanism has two orthogonally arranged rotational axes, and the mobility is easy to be understood. However, parallel mechanism has three coupled limbs, and the mobility is not obvious. As a result, it is the focus of the mobility analysis.

Parallel mechanism includes a fixed base, three 3-P(SS)^2 limbs, and a moving platform. In practical, a *R*UPUR limb is installed between the base and the moving platforms to transmit rotary motion from the base to the workpiece mounted on the moving platform. Since this limb provides an independent motion, it can be ignored in the following analysis without affecting the actuated motions. Each limb of the parallel mechanism contains 3 links, so that the entire mechanism contains 11 links including the fixed base and the moving platform. Each limb has 5 joints, including 1 prismatic joint and 4 spherical joints, resulting in a total of 15 joints for the whole mechanism. There are 13 DOF for each limb, resulting in 39 DOF for the whole mechanism. Applying the Grübler-Kutzbach formula, it has

$$M = \lambda(n - g - 1) + \sum_{i=1}^{g} f_i = 6(11 - 15 - 1) + 39 = 9, \tag{1}$$

where λ is the dimension of the task space, n is the link number, g is the joint number, and f_i represents the DOF of joint i.

Each (SS) leg has an idle DOF to rotate around the axis of the connecting leg itself. As a result, a total of six idle DOF are included in these nine DOF, so the parallel mechanism only has three DOF. To determine the type of the three DOF, it has been analyzed that the parallel mechanism constrains the rotation of the moving platform through the three-parallelogram mechanism (Yu et al. 2009). As a result, it leaves the parallel mechanism with three purely translational DOF.

Inverse Kinematic Analysis

The geometric parameters and the schematic diagram of the parallel mechanism are shown in Fig. 4, where the three guideways are inclined to form a tetrahedron in space. To facilitate analysis, the middle points between the two spherical joints for

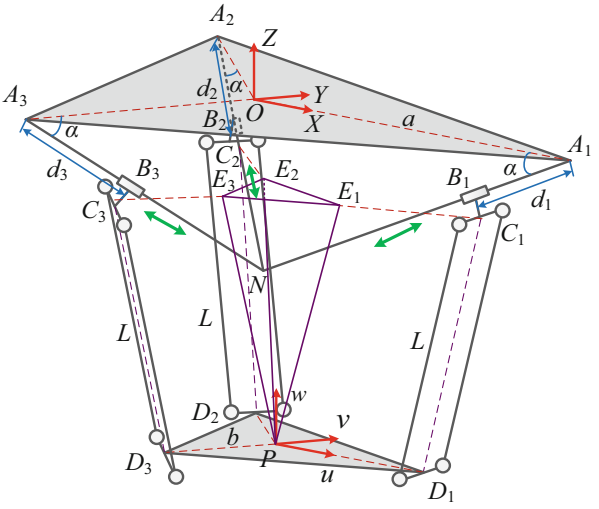

Fig. 4 Schematic diagram and geometric parameters of the three-DOF parallel mechanism

each of the three legs that are connected to the slider and the moving platform denote as C_i and D_i. A fixed coordinate system *O-XYZ* is put at the center of the fixed base $A_1A_2A_3$ with *Z*-axis vertical to the base and *X*-axis directing along OA_1. Another coordinate system *P-uvw* is put at the center of the moving platform $D_1D_2D_3$. Since the parallel mechanism has no rotational DOF, the *u*, *v*, and *w* axes are set to parallel with the *X*, *Y*, and *Z* axes, respectively. For the convince of formulation, related geometric parameters are given to describe the structure. Herein, $OA_i = a$, $A_iB_i = d_i$, $B_iC_i = c$, $PD_i = b$, and $C_iD_i = L$, for $i = 1, 2, 3$, and α is the inclination angle between OA_i and the actuated direction A_iN in the base.

Based on the determined structural parameters, the inverse kinematic solution is to calculate the positions of the three prismatic joints in the joint space with regard to the desired position of the moving platform. With the coordinate settings described above, the coordinates of the points A_i, B_i, and C_i in *O-XYZ* can be determined as

$$\begin{aligned} \boldsymbol{a}_i &= \begin{bmatrix} a\cos\eta_i \\ a\sin\eta_i \\ 0 \end{bmatrix}, \quad \boldsymbol{b}_i = \begin{bmatrix} (a - d_i\cos\alpha)\cos\eta_i \\ (a - d_i\cos\alpha)\sin\eta_i \\ -d_i\sin\alpha \end{bmatrix}, \quad \boldsymbol{c}_i \\ &= \begin{bmatrix} (a - d_i\cos\alpha + c\sin\alpha)\cos\eta_i \\ (a - d_i\cos\alpha + c\sin\alpha)\sin\eta_i \\ -d_i\sin\alpha - c\cos\alpha \end{bmatrix}, \end{aligned} \tag{2}$$

and the coordinate of the point D_i in *P-uvw* can be obtained as

$$\boldsymbol{d}_i^P = \begin{bmatrix} b\cos\eta_i \\ b\sin\eta_i \\ 0 \end{bmatrix}, \quad \eta_i = \frac{2\pi(i-1)}{3}, \tag{3}$$

where η_i is the direction angle of OA_i with respect to *X*-axis or PD_i with respect to *u*-axis.

Referring to Fig. 4, point $\boldsymbol{D}_i^P$ in *O-XYZ* can be described as

$$\boldsymbol{d}_i = \boldsymbol{P} + \mathbf{I}_3\boldsymbol{d}_i^P = \begin{bmatrix} b\cos\eta_i + x \\ b\sin\eta_i + y \\ z \end{bmatrix}, \tag{4}$$

where $P = [x, y, z]^{\mathrm{T}}$ is the position of moving platform and $\mathbf{I}_3$ is a unit matrix of order 3.

The distances between points D_i and C_i are always equal to the length of the leg. Hence, the following equations can be derived for the *i*th limb:

$$|\boldsymbol{d}_i - \boldsymbol{c}_i| = L \tag{5}$$

By substituting Eq. (2) and Eq. (4) into Eq. (5), one can write

$$(x - x_i)^2 + (y - y_i)^2 + (z - z_i)^2 = L^2, \tag{6}$$

where

$$x_i = -d_i \cos\alpha \cos\eta_i + R\cos\eta_i, \quad y_i = -d_i \cos\alpha \sin\eta_i + R\sin\eta_i,$$
$$z_i = -d_i \sin\alpha - c\cos\alpha, \quad R = a - b + c\sin\alpha.$$

Position d_i of the prismatic joints can be determined from Eq. (6) once the geometric parameters are given. According to Eq. (6), it should be noted that there are two solutions for each limb. As a result, eight solutions can be obtained for a certain position of the parallel mechanism as shown in Fig. 5. In this study, only the configuration shown in Fig. 5a is considered.

Forward Kinematic Analysis

When the parallel mechanism is in the control mode of jog or single limb, the position of the moving platform expressed in *O-XYZ* needs to be monitored in real time. As a result, the analysis of forward kinematic needs to be performed. The purpose of forward kinematic is used to determine the corresponding position of the point P when the positions of the actuated prismatic joints are known. However, the forward solution of the parallel mechanism is more complex than the inverse solution because of the close form constraints among the three limbs. The methods of analysis are mainly resorted to numerical method (Wampler et al. 1990), analytical method (Innocenti and Parenticastelli 1990), and geometric method (Tsai and Joshi 2000). Although numerical method can provide all the solutions, the computational cost is high, and there are many problems in practical application. As a result, a straightforward kinematic model is proposed here to

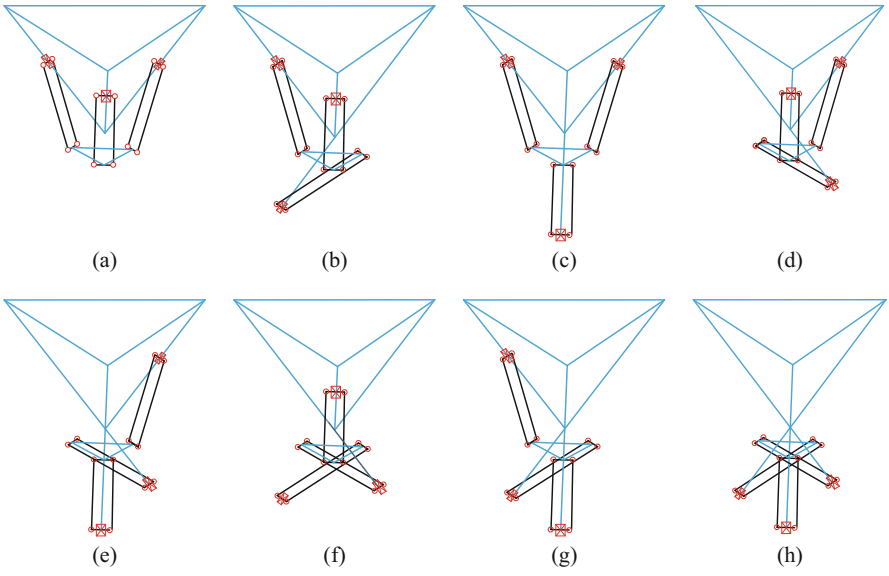

Fig. 5 Eight inverse kinematic solutions

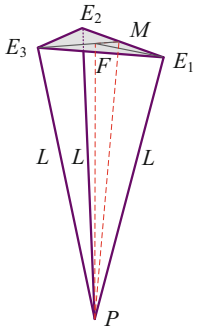

Fig. 6 Schematic of the forward model

solve the forward kinematic problems according to the geometrical characteristics, which is based on the spatial geometry and vector algebra.

As shown in Fig. 4, C_i can be moved to E_i along D_iP. Then, a tetrahedron is composed of points E_1, E_2, E_3, and P as shown in Fig. 6. Mathematically, the forward kinematic analysis is equivalent to determine the fourth point P of the tetrahedron when the other three points (E_1, E_2, E_3) are given.

In O-XYZ, point E_i and the center point of E_1E_2 denoted as M are

$$\boldsymbol{E}_i = \begin{bmatrix} (a - d_i\cos\alpha + c\sin\alpha - b)\cos\eta_i \\ (a - d_i\cos\alpha + c\sin\alpha - b)\sin\eta_i \\ -d_i\sin\alpha - c\cos\alpha \end{bmatrix}, \quad \boldsymbol{M} = \frac{\boldsymbol{E}_1 + \boldsymbol{E}_2}{2}. \tag{7}$$

The projection of point P on the plane constituted by E_i is denoted as F, and PM is perpendicular to E_1E_2 since PE_1E_2 is an isosceles triangle. Using the theorem of three perpendiculars, it can be found that FM is also perpendicular to E_1E_2. The same results can also be deduced by analyzing the other two edges. As a result, point F can be proven to be the circumcenter of $E_1E_2E_3$, and the position of F can be written as

$$\boldsymbol{F} = \boldsymbol{M} + \boldsymbol{MF}. \tag{8}$$

Hence, the vector $\boldsymbol{MF}$ becomes

$$\boldsymbol{MF} = |\boldsymbol{MF}|\boldsymbol{n}_{MF}, \tag{9}$$

where

$$|\boldsymbol{MF}| = \sqrt{|\boldsymbol{E}_1\boldsymbol{F}|^2 - |\boldsymbol{E}_1\boldsymbol{M}^2|},$$
$$|\boldsymbol{E}_1\boldsymbol{F}| = \frac{|\boldsymbol{E}_1\boldsymbol{E}_2||\boldsymbol{E}_2\boldsymbol{E}_3||\boldsymbol{E}_3\boldsymbol{E}_1|}{4S},$$
$$S = \sqrt{q(q - |\boldsymbol{E}_1\boldsymbol{E}_2|)(q - |\boldsymbol{E}_2\boldsymbol{E}_3|)(q - |\boldsymbol{E}_3\boldsymbol{E}_1|)},$$
$$q = \frac{1}{2}(|\boldsymbol{E}_1\boldsymbol{E}_2| + |\boldsymbol{E}_2\boldsymbol{E}_3| + |\boldsymbol{E}_3\boldsymbol{E}_1|),$$
$$\boldsymbol{n}_{MF} = \frac{\boldsymbol{E}_1\boldsymbol{E}_2 \times \boldsymbol{E}_2\boldsymbol{E}_3 \times \boldsymbol{E}_1\boldsymbol{E}_2}{|\boldsymbol{E}_1\boldsymbol{E}_2| \times |\boldsymbol{E}_2\boldsymbol{E}_3| \times |\boldsymbol{E}_1\boldsymbol{E}_2|}.$$

Once the position of point F is calculated, the position of point P expressed in O-XYZ can be obtained as

$$\boldsymbol{P} = \boldsymbol{F} + \boldsymbol{FP}, \tag{10}$$

where

$|\boldsymbol{FP}| = \sqrt{L^2 - |\boldsymbol{E_1F}|^2}$, $\boldsymbol{n}_{FP} = \frac{\boldsymbol{E_1E_2} \times \boldsymbol{E_2E_3}}{|\boldsymbol{E_1E_2}||\boldsymbol{E_2E_3}|}$.

The derivation process of the geometric method is very direct and concise as compared with the traditional algebraic method. It avoids the multiple solutions and can directly obtain the comprehension of the continuity of the motion in the workspace with a lower computational cost.

Velocity Analysis

The velocity analysis attempts to study the relationship between the velocity of the actuated prismatic joints in the joint space and the velocity of the reference point P in the operation space, which can be mapped by the Jacobian matrix. By differentiating Eq. (6) with respect to time, the relationship of velocities can be obtained as

$$\boldsymbol{J}^{inv}\dot{\boldsymbol{d}} = \boldsymbol{J}^{dir}\dot{\boldsymbol{X}}, \tag{11}$$

where $\dot{\boldsymbol{X}} = [\dot{x} \;\; \dot{y} \;\; \dot{z}]^{\mathrm{T}}$ is the output velocity of the moving platform and $\dot{\boldsymbol{d}} = \left[\dot{d}_1 \dot{d}_2 \dot{d}_3\right]^{\mathrm{T}}$ is the input velocity of the actuated joints.

The inverse Jacobian matrix $\boldsymbol{J}^{inv}$ can be expressed as

$$\boldsymbol{J}^{inv} = \mathrm{diag}(d_{11}, d_{22}, d_{33}), \tag{12}$$

where

$$\begin{aligned} d_{11} &= x\cos\alpha + z\sin\alpha - a\cos\alpha + b\cos\alpha + d_1, \\ d_{22} &= -\frac{1}{2}x\cos\alpha + \frac{\sqrt{3}}{2}y\cos\alpha + z\sin\alpha - a\cos\alpha + b\cos\alpha + d_2, \\ d_{33} &= -\frac{1}{2}x\cos\alpha - \frac{\sqrt{3}}{2}y\cos\alpha + z\sin\alpha - a\cos\alpha + b\cos\alpha + d_3, \end{aligned}$$

and $\boldsymbol{J}^{dir}$ is the direct Jacobian matrix expressed as

$$\boldsymbol{J}^{dir} = \begin{bmatrix} x_1 & y_1 & z_1 \\ x_2 & y_2 & z_2 \\ x_3 & y_3 & z_3 \end{bmatrix}, \tag{13}$$

where

$$x_1 = -a + d_1 \cos\alpha - c \sin\alpha + x + b,\ \ y_1 = y,\ \ z_1 = d_1 \sin\alpha + c \cos\alpha + z,$$

$$x_2 = \frac{1}{2} a - \frac{1}{2} d_2 \cos\alpha + \frac{1}{2} c \sin\alpha + x - \frac{1}{2} b,\ \ y_2 = -\frac{\sqrt{3}}{2} a + \frac{\sqrt{3}}{2} d_2 \cos\alpha - \frac{\sqrt{3}}{2} c \sin\alpha + y + \frac{\sqrt{3}}{2} b, z_2 = d_2 \sin\alpha + c \cos\alpha + z, x_3 = \frac{1}{2} a - \frac{1}{2} d_3 \cos\alpha + \frac{1}{2} c \sin\alpha + x - \frac{1}{2} b,\ \ y_3 = \frac{\sqrt{3}}{2} a - \frac{\sqrt{3}}{2} d_3 \cos\alpha + \frac{\sqrt{3}}{2} c \sin\alpha + y - \frac{\sqrt{3}}{2} b, z_3 = d_3 \sin\alpha + c \cos\alpha + z.$$

When the mechanism is not in a singular position, the following velocity relationship can be obtained from Eq. (11):

$$\dot{\boldsymbol{d}} = \boldsymbol{J}\dot{\boldsymbol{X}}, \tag{14}$$

where

$$\boldsymbol{J} = \boldsymbol{J}^{-inv}\boldsymbol{J}^{div} = \begin{bmatrix} \frac{x_1}{d_{11}} & \frac{y_1}{d_{11}} & \frac{z_1}{d_{11}} \\ \frac{x_2}{d_{22}} & \frac{y_2}{d_{22}} & \frac{z_2}{d_{22}} \\ \frac{x_3}{d_{33}} & \frac{y_3}{d_{33}} & \frac{z_3}{d_{33}} \end{bmatrix}_{3\times 3}$$

denotes the Jacobian matrix.

Reachable Workspace Analysis

The reachable workspace is an important factor that can reflect the working capacity of the machine. Compared with the serial mechanisms, parallel mechanisms generally have relatively small workspaces with irregular shapes. For the sake of simplicity, the reachable workspace of the parallel mechanism here is defined as a set of points that can be reached in the Cartesian space by the reference point P.

According to Eq. (6), the workspace of each limb can be regarded as a sphere surface with radii L when the prismatic joint moves to a given position. Assume that $d_{\min}$ and $d_{\max}$ are the minimum and maximum strokes of the prismatic joints; the workspace of each limb is a solid enveloped by these sphere surfaces. A set of structure parameters of the parallel mechanism are given in Table 1. As shown in Fig. 7, the workspace of the parallel mechanism can be generated geometrically by intersecting the three enveloping solids.

Table 1 Structural parameters of the parallel mechanism

Parameters	a	b	L	α	$d_{\min}$	$d_{\max}$
Value	300.63 mm	122.38 mm	370 mm	45°	−30 mm	170 mm

Another method, usually called discretization method (Bonev and Ryu 2001; Chablat et al. 2004), is also used to generate the workspace, and the produces are shown in Fig. 8. Firstly, an anticipated area is chosen which should be large enough to contain the reachable workspace. For convenience, it is usually a cylinder or a cubic area. With a height ranging from -100 mm to -500 mm and a radius of 300 mm, an anticipated area with a cylinder shape is selected as the search area. By dividing the cylinder with resolutions of $\Delta Z = 5$ mm, $\Delta R = 5$ mm, and $\Delta\theta = 3°$, a number of regularly arranged grids are then generated. By using the inverse kinematics, the active prismatic joint position d_i for each grid is determined and examined to see whether the gird is within the motion range. After checking all the grid points, the points that constitute the boundary of the workspace are plotted as shown in Fig. 9. From both the geometric method and the numerical method, it shows that the shape of the workspace is 120° symmetric about the Z-axis. This is consistent with the global reference frame and the symmetrical structure of the parallel mechanism.

Comparing with Figs. 7 and 9, it can be found that the reachable workspace obtained from both the geometric method and the discretization method is completely consistent with each other, which verifies the correctness of the results. It has been illustrated that the parallel mechanism possesses a fairly large workspace and an overall good continuity, and the workspace is triangular symmetrical about the center point, which is also consistent with the symmetrical architecture of the parallel mechanism.

Dexterity Analysis

According to literatures, various kinds of performance indices have been proposed to measure the singularity of mechanisms, such as manipulability (Yoshikawa 1985), dexterity (Gosselin and Angeles 1989, 1991), and motion/force transmissibility (Chen and Angeles 2007; Tsai and Lee 1994). Among these performance indices, the dexterity is defined by using the reciprocal of the condition number of the Jacobian matrix. Since the Jacobian matrix has the same units, the dexterity index η can be defined as

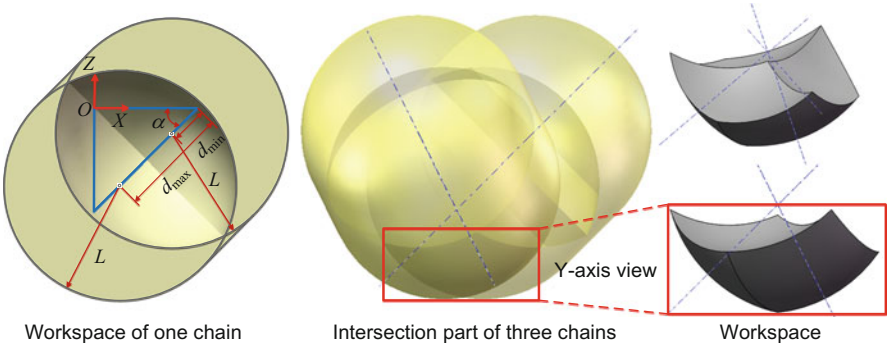

Fig. 7 Reachable workspace of the parallel mechanism generated with geometric method

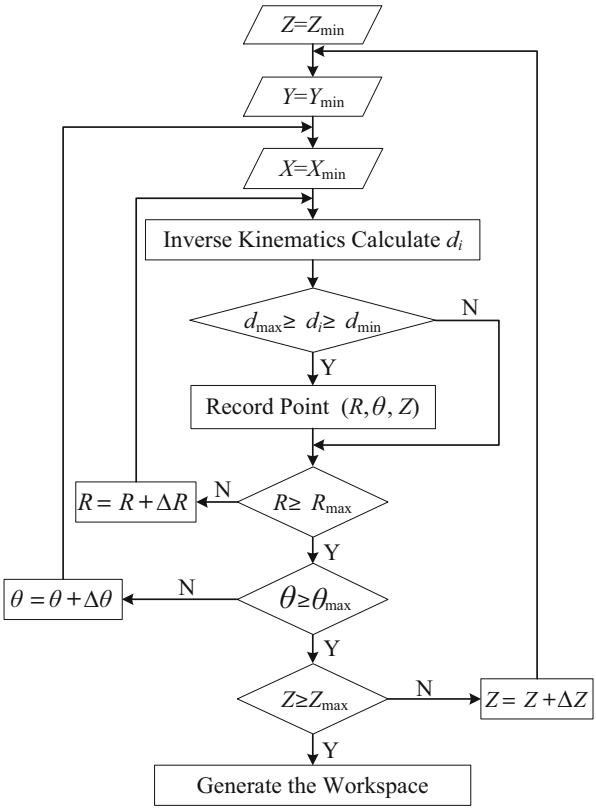

Fig. 8 Produces to generate the reachable workspace with discretization method

$$\eta = \frac{1}{\kappa}, \quad \kappa = \|\boldsymbol{J}\|\left\|\boldsymbol{J}^{-1}\right\|, \tag{15}$$

where $\|\cdot\|$ denotes the Frobenius norm or the Euclidian norm of a matrix.

Condition number η is a scalar ranging from 0 to 1. $\eta = 0$ means that the parallel mechanism is in its singular configuration, while $\eta = 1$ represents an isotropic configuration. As η is configuration dependent, the dexterity distributions in the workspace at different cross sections are shown in Fig. 10. The overall trend of η decreases as the moving platform far from the fixed base, and the overall trend of η also decreases as the moving platform moves away from the centerline.

Kinematic Analysis of the Serial Mechanism

Forward Kinematic Analysis

The structural parameters of the serial mechanism are shown in Fig. 11 with a fixed coordinate system *o-xyz* put at the center of the polishing tool. The *z*-axis points to

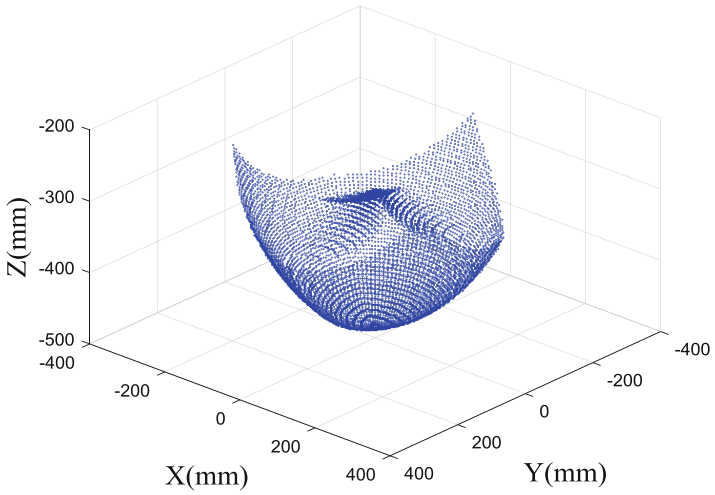

Fig. 9 Reachable workspace of the parallel mechanism generated with discretization method

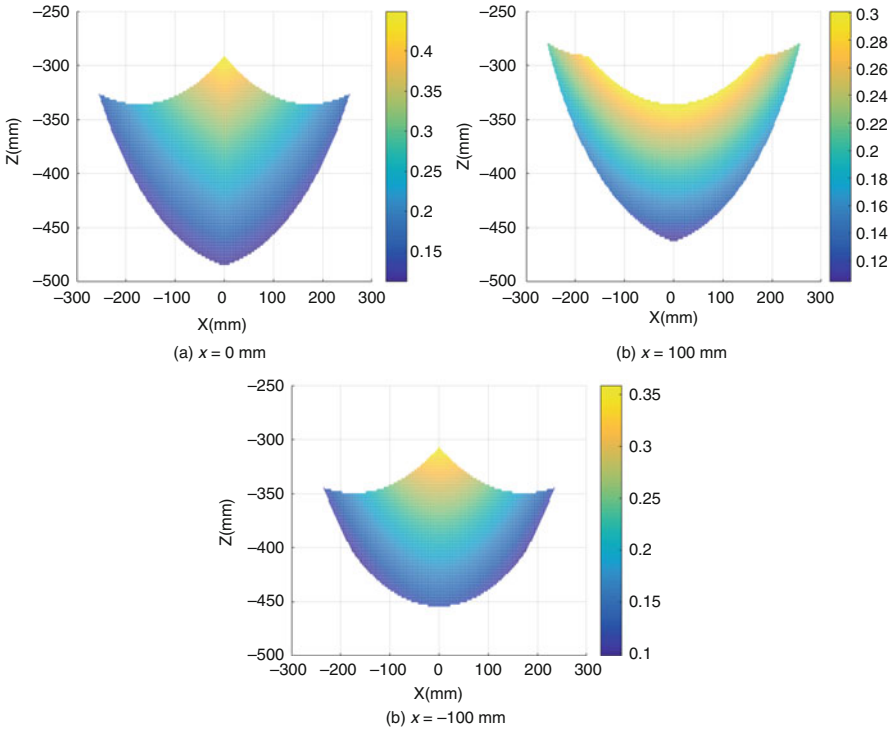

Fig. 10 Dexterity distribution on *O-YZ* plane in the workspace

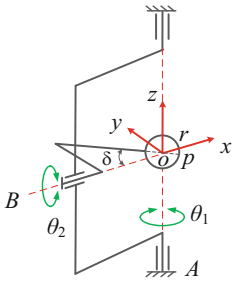

Fig. 11 Schematic diagram of the serial mechanism

the vertical joint axis, and the x-axis points to the initial direction of horizontal joint axis. The initial configuration of the serial-parallel mechanism is shown in Fig. 2a, where r is the radius of the tool head and δ is the angle between the x-axis and the tool axis. The rotation angles of vertical joint and horizontal joint are set as θ_1 and θ_2, respectively, and the tool tip is denoted as point p.

For the serial mechanism, the forward kinematic is to map the rotary joints position to the tool orientation represented by op. As shown in Fig. 11, it can be written as

$$\boldsymbol{p}_0 = [r\cos\delta - r\sin\delta 0]^{\mathrm{T}}, \ \boldsymbol{p}_a = [xyz]^{\mathrm{T}}, \tag{16}$$

and the coordinates of p_a should fulfill the constraint:

$$x^2 + y^2 + z^2 = r^2. \tag{17}$$

With the rotation of the two joints, it has the following relationship:

$$\boldsymbol{p}_a = \boldsymbol{R}_\theta \boldsymbol{p}_0, \tag{18}$$

where $\boldsymbol{R}_\theta$ is the rotation matrix expressed as

$$\boldsymbol{R}_\theta = \begin{bmatrix} \cos\theta_1 & -\sin\theta_1 & 0 \\ \sin\theta_1 & \cos\theta_1 & 0 \\ 0 & 0 & 1 \end{bmatrix} \begin{bmatrix} 1 & 0 & 0 \\ 0 & \cos\theta_2 & -\sin\theta_2 \\ 0 & \sin\theta_2 & \cos\theta_2 \end{bmatrix}.$$

Inverse Kinematic Analysis

When the orientation of op is given, the purpose of inverse kinematic is to find the actuator inputs θ_1 and θ_2. As shown in Fig. 12, the points of p_a and p_b projected on the o-xy plane are represented as c and d. The points of c and d projected on the x-axis are o_1 and e. Then, θ_1 and θ_2 can be derived as

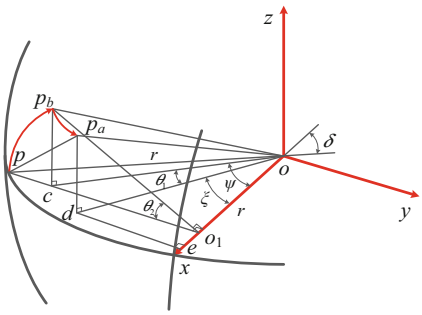

Fig. 12 Schematic for the inverse kinematics

$$\theta_2 = -\arcsin\frac{P_b c}{P_b o_1} = -\arcsin\frac{P_a d}{po\sin\delta} = -\arcsin\frac{z}{r\sin\delta},$$
$$\theta_1 = \psi - \xi = \arctan\frac{P_b c\cot\theta_2}{op\cos\delta} - \arctan\frac{de}{oe} = \arctan\left|\frac{z\cot\theta_2}{r\cos\delta}\right| - \arctan\left|\frac{y}{x}\right|, \tag{19}$$

where the signs of θ_1 and θ_2 can be chosen according to the actual need.

Workspace Analysis

Similar to the parallel mechanism, serial mechanism also requires a workspace analysis. Here, the workspace is defined as the set of all points where the tool tip p can reach in the Cartesian space. The constraints that affect the workspace of the serial mechanism mainly include the movement range of the driving joints.

In the initial position, the zero position of vertical joint makes the horizontal joint axis perpendicular to the parallel mechanism's moving platform, and the zero position of the horizontal axis makes the spindle axis horizontal to the fixed base. To avoid the interferences between the serial mechanism and the moving platform, the movement range of the vertical joint needs to be limited during the synchronous motion. According to the actual parameters of the polishing machine, the workspaces of the serial mechanism with $r = 20$ mm, $s = 767.42$ mm, $\delta = 45°$, $\theta_A \in [-90°, 90°]$, and $\theta_B \in [-180°, 180°]$ are obtained as shown in Fig. 13. The workspace is a discontinuous circular belt on a sphere due to the fact that the vertical joint cannot rotate over the entire circumference.

Stiffness Model of the Parallel Mechanism

Stiffness analysis is to establish the relationship between the forces exerted on the end-effector and its corresponding deformations. As one of the important requirements for precision machining equipment, stiffness performance is required to be analyzed and evaluated in the design stage. Due to the complexity of the parallel mechanism, the stiffness analysis mainly focuses on the parallel mechanism.

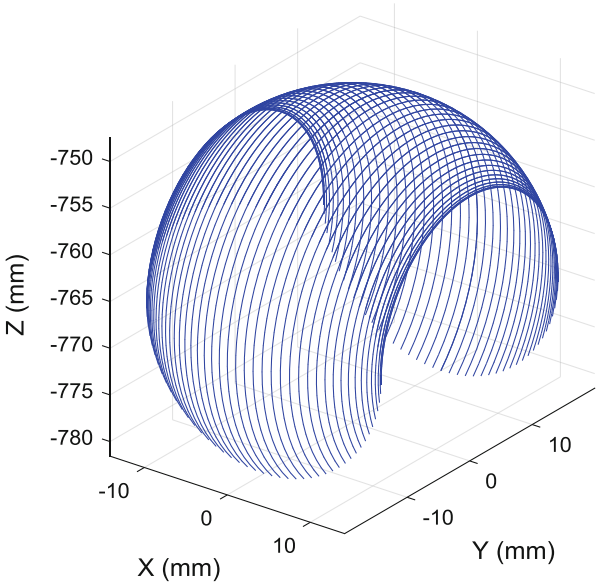

Fig. 13 Workspace of the serial mechanism

Let $[\boldsymbol{F}^{\mathrm{T}}, \boldsymbol{M}^{\mathrm{T}}]^{\mathrm{T}}$ denote as the external forces exerted on the end-effector and $[\boldsymbol{\Delta X}^{\mathrm{T}}, \boldsymbol{\Delta\Theta}^{\mathrm{T}}]^{\mathrm{T}}$ denote as the corresponding deformations caused by that force. $\boldsymbol{F} = [F_x, F_y, F_z]^{\mathrm{T}}$ and $\boldsymbol{M} = [M_x, M_y, M_z]^{\mathrm{T}}$. Similarly, $\boldsymbol{\Delta X} = [\Delta X_x, \Delta X_y, \Delta X_z]^{\mathrm{T}}$ and $\boldsymbol{\Delta\Theta} = [\Delta\theta_x, \Delta\theta_y, \Delta\theta_z]^{\mathrm{T}}$. Then, it has

$$\begin{bmatrix} \boldsymbol{F} \\ \boldsymbol{M} \end{bmatrix} = \boldsymbol{K} \begin{bmatrix} \boldsymbol{\Delta X} \\ \boldsymbol{\Delta\Theta} \end{bmatrix}, \quad \begin{bmatrix} \boldsymbol{\Delta X} \\ \boldsymbol{\Delta\Theta} \end{bmatrix} = \boldsymbol{C} \begin{bmatrix} \boldsymbol{F} \\ \boldsymbol{M} \end{bmatrix}, \tag{20}$$

where $\boldsymbol{K}$ and $\boldsymbol{C}$ denote the stiffness matrix and compliance matrix.

The parallel mechanism can be divided into several subassemblies, including moving platform assembly, leg assembly, drive assembly, guide assembly, and base assembly. By regarding the moving platform assembly and the base assembly as rigid bodies, the deformations of the end-effector caused by the leg assembly, drive assembly, and guide assembly are analyzed, respectively.

Stiffness Model of the Leg Assembly

This section derives the deformation of the end-effector, denoted by $\Delta\boldsymbol{X}_l$ (translational deformation) and $\Delta\boldsymbol{\Theta}_l$ (rotational deformation), caused by the deformation of leg assembly. Since both ends of the leg in the parallel mechanism are spherical joints, the leg assembly is only subjected to axis force and deformation. It is assumed that the axis force and deformation of the jth leg in the ith limb are f_{ij}^{l} and δ_{ij}^{l}; the following equations can be obtained according to the principle of virtual work:

$$\left[\boldsymbol{F}^{\mathrm{T}}\boldsymbol{M}^{\mathrm{T}}\right]\begin{bmatrix}\Delta\boldsymbol{X}_l\\ \Delta\boldsymbol{\Theta}_l\end{bmatrix}=\sum_{i=1}^{3}\sum_{j=1}^{2}f_{ij}^{l}\delta_{ij}^{l}. \tag{21}$$

In a matrix format,

$$\left[\boldsymbol{F}^{\mathrm{T}}\boldsymbol{M}^{\mathrm{T}}\right]\begin{bmatrix}\Delta\boldsymbol{X}_l\\ \Delta\boldsymbol{\Theta}_l\end{bmatrix}=\boldsymbol{F}_l^{\mathrm{T}}\Delta\boldsymbol{L}, \tag{22}$$

where $\boldsymbol{F}_l$ and $\Delta\boldsymbol{L}$ denote the force vector and deformation vector of the leg assembly.

The relationship of $\boldsymbol{F}_l$ and $\Delta\boldsymbol{L}$ can be derived according to Hooke's law:

$$\boldsymbol{F}_l=\mathrm{diag}\left(k_{ij}^{l}\right)\Delta\boldsymbol{L},\quad k_{ij}^{l}=\left(\frac{1}{k_{ij}^{\mathrm{le}}}+\frac{2}{k_{ij}^{\mathrm{j}}}\right)^{-1}, \tag{23}$$

where k_{ij}^{l} is the equivalent elastic coefficient of the jth leg assembly in the ith limb, $k_{ij}^{\mathrm{le}}=\pi d_l^2E_l/4l$ is the elastic coefficient of the leg, k_{ij}^{j} is the elastic coefficient of spherical joint, d_l is the diameter of the leg, and E_l is the elastic modulus of the leg.

As shown in Fig. 14, the force analysis shows that the external force and the reaction forces on the leg assembly can be formulated as

$$\begin{cases}\sum_{i=1}^{3}\left(f_{i1}^{l}+f_{i2}^{l}\right)\cdot\boldsymbol{l}_i=\boldsymbol{F}\\ \sum_{i=1}^{3}\left[f_{i1}^{l}(\boldsymbol{b}_{i1}\times\boldsymbol{l}_i)+f_{i2}^{l}(\boldsymbol{b}_{i2}\times\boldsymbol{l}_i)\right]=\boldsymbol{M}\end{cases}. \tag{24}$$

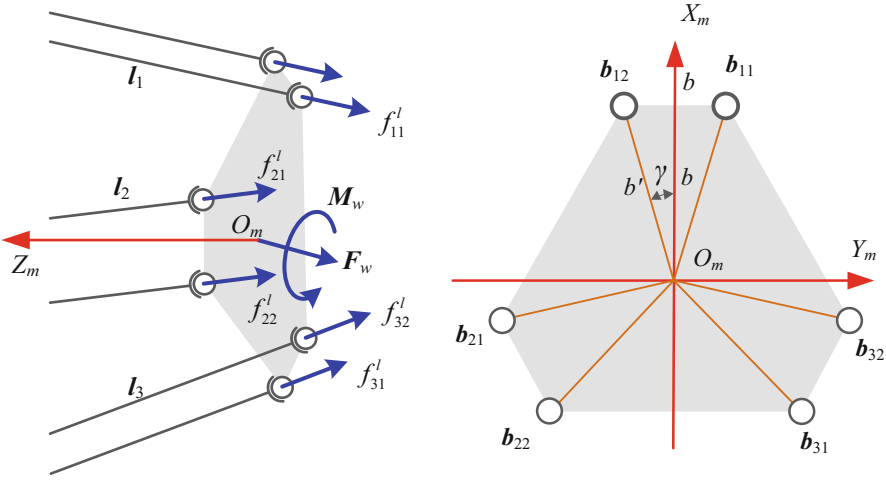

Fig. 14 Force analysis of the moving platform

In Eq. (24), $\boldsymbol{b}_{i1}$ and $\boldsymbol{b}_{i2}$ denote the vectors PD_{i1} and PD_{i2}, which can be determined as

$$\begin{aligned} \boldsymbol{b}_{i1} &= \begin{bmatrix} b' \sin(\eta_i - \gamma) \\ b' \cos(\eta_i - \gamma) \\ 0 \end{bmatrix}, \quad \boldsymbol{b}_{i2} = \begin{bmatrix} b' \sin(\eta_i + \gamma) \\ b' \cos(\eta_i + \gamma) \\ 0 \end{bmatrix}, \\ b' &= \sqrt{b^2 + (d/2)^2}, \quad \gamma = \arctan \frac{d/2}{b}, \end{aligned} \tag{25}$$

where d denotes the distance of the center line between two spherical joints in the ith limb.

Equation (24) can be rearranged as

$$\boldsymbol{J}_l \boldsymbol{F}_l = \begin{bmatrix} \boldsymbol{F} \\ \boldsymbol{M} \end{bmatrix}, \tag{26}$$

where

$$\boldsymbol{J}_l = [\boldsymbol{J}_{1l} \boldsymbol{J}_{2l} \boldsymbol{J}_{3l}], \quad \boldsymbol{J}_{il} = \begin{bmatrix} \boldsymbol{l}_i & \boldsymbol{l}_i \\ \boldsymbol{b}_{i1} \times \boldsymbol{l}_i & \boldsymbol{b}_{i2} \times \boldsymbol{l}_i \end{bmatrix}.$$

Thus,

$$\boldsymbol{F}_l = \boldsymbol{J}_l^{-1} \begin{bmatrix} \boldsymbol{F} \\ \boldsymbol{M} \end{bmatrix}. \tag{27}$$

Combining Eqs. (22), (23), and (27), the deformation of the end-effector caused by the deformation of the leg assembly can be derived as

$$\begin{bmatrix} \Delta \boldsymbol{X}_l \\ \Delta \boldsymbol{\Theta}_l \end{bmatrix} = \boldsymbol{C}_l \begin{bmatrix} \boldsymbol{F} \\ \boldsymbol{M} \end{bmatrix}, \quad \boldsymbol{C}_l = \boldsymbol{J}_l^{-\mathrm{T}} \left[\mathrm{diag}\left(k_{ij}^l \right) \right]^{-1} \boldsymbol{J}_l^{-1}, \tag{28}$$

where $\boldsymbol{C}_l$ is the corresponding compliance matrix.

Stiffness Model of the Drive Assembly

Each leg assembly is connected to a slider and actuated by a drive assembly. The deformation of the end-effector caused by the deformation of drive assembly is derived. The axis force exerted on the drive assembly results in an axial deformation of the assembly, which only causes the translational deformation $\Delta \boldsymbol{X}_d$ of the end-effector. Hence, the following equation can be obtained according to the principle of virtual work:

$$\boldsymbol{F}^{\mathrm{T}}\Delta\boldsymbol{X}_d = \sum_{i=1}^{3} f_i^d \delta_i^d, \tag{29}$$

where f_i^d is the force and δ_i^d is the deformation of the ith drive assembly.

In matrix format

$$\boldsymbol{F}^{\mathrm{T}}\Delta\boldsymbol{X}_d = \boldsymbol{F}_d^{\mathrm{T}}\Delta\boldsymbol{d}, \tag{30}$$

where $\boldsymbol{F}_d$ is the force vector and $\Delta\boldsymbol{d}$ is the deformation vector of the drive assembly.

Since each drive assembly contains a shaft, a bearing, a coupler, and a nut, the relationship of $\boldsymbol{F}_d$ and $\Delta\boldsymbol{d}$ can be calculated according to Hooke's law:

$$\boldsymbol{F}_d = \mathrm{diag}\left(k_i^d\right)\Delta\boldsymbol{d}, \quad k_i^d = \left(\frac{1}{k_i^{\mathrm{c}}} + \frac{1}{k_i^{\mathrm{b}}} + \frac{1}{k_i^{\mathrm{s}}} + \frac{1}{k_i^{\mathrm{n}}}\right)^{-1}, \tag{31}$$

where k_i^d is the equivalent elastic coefficient of the ith drive assembly and k_i^{c}, k_i^{b} ,k_i^{n}, and $k_i^{\mathrm{s}} = \pi d_s^2 E_s d_{\mathrm{m}}/4d_i(d_{\mathrm{m}} - d_i)$ are the elastic coefficients of coupler, bearing, nut, and screw, in which E_s, d_s, and $d_{\mathrm{m}} = d_{\max} - d_{\min}$ are the elastic modulus, diameter, and motion range of the screw.

According to the kinematic analysis, $\Delta\boldsymbol{X}_d$ and $\Delta\boldsymbol{d}$ can be mapped by using the Jacobian matrix:

$$\Delta\boldsymbol{X}_d = \boldsymbol{J}_d\Delta\boldsymbol{d}. \tag{32}$$

By substituting Eq. (32) into Eq. (30), it has

$$\left(\boldsymbol{F}_d^{\mathrm{T}} - \boldsymbol{F}^{\mathrm{T}}\boldsymbol{J}_d\right)\Delta\boldsymbol{d} = 0. \tag{33}$$

Apparently, the relationship of the driving force and the external force is

$$\boldsymbol{F}_d = \boldsymbol{J}_d^{\mathrm{T}}\boldsymbol{F}. \tag{34}$$

Combining Eq. (30), Eq. (32), and Eq. (34), the deformation of the end-effector caused by the deformation of drive assembly can be formulated as

$$\Delta\boldsymbol{X}_d = \boldsymbol{C}_d\boldsymbol{F}, \quad \boldsymbol{C}_d = \boldsymbol{J}_d\left[\mathrm{diag}\left(k_i^d\right)\right]^{-1}\boldsymbol{J}_d^{\mathrm{T}}, \tag{35}$$

where $\boldsymbol{C}_d$ is the corresponding compliance matrix.

Stiffness Model of the Guide Assembly

This section derives the deformation of the end-effector caused by the deformation of guide assembly. The linear guide assembly mainly consists of a rail, in

which a slider is supported by four rows of balls. The motion of the slider is derived by the drive assembly. A local coordinate system B_i-xyz is attached to the center point of the slider. The x-axis directs alone the screw, and the y-axis is vertical to the normal of rail. In B_i-xyz, let $[(\boldsymbol{f}_i^g)^{\mathrm{T}}, (\boldsymbol{m}_i^g)^{\mathrm{T}}]^{\mathrm{T}}$ denote as the force exerted on the ith guide and $[(\Delta\boldsymbol{x}_i^g)^{\mathrm{T}}, (\Delta\boldsymbol{\theta}_i^g)^{\mathrm{T}}]^{\mathrm{T}}$ denote as the deformation of the ith guide. Hence, the following equation can be obtained by using the principle of virtual work:

$$\left[\boldsymbol{F}^{\mathrm{T}}\boldsymbol{M}^{\mathrm{T}}\right]\begin{bmatrix}\Delta\boldsymbol{X}_g\\ \Delta\boldsymbol{\Theta}_g\end{bmatrix} = \sum_{i=1}^{3}\left[\left(\boldsymbol{f}_i^g\right)^{\mathrm{T}}\left(\boldsymbol{m}_i^g\right)^{\mathrm{T}}\right]\begin{bmatrix}\Delta\boldsymbol{x}_i^g\\ \Delta\boldsymbol{\theta}_i^g\end{bmatrix} \tag{36}$$

$$\boldsymbol{f}_i^g = \left[f_{xi}^g f_{yi}^g f_{zi}^g\right]^{\mathrm{T}},\ \ \boldsymbol{m}_i^g = \left[m_{xi}^g m_{yi}^g m_{zi}^g\right]^{\mathrm{T}},$$
$$\Delta\boldsymbol{x}_i^g = \left[\Delta x_{xi}^g \Delta x_{yi}^g \Delta x_{zi}^g\right]^{\mathrm{T}},\ \ \Delta\boldsymbol{\theta}_i^g = \left[\Delta\theta_{xi}^g \Delta\theta_{yi}^g \Delta\theta_{zi}^g\right]^{\mathrm{T}},$$

where $\Delta\boldsymbol{X}_g$ and $\Delta\boldsymbol{\Theta}_g$ are the translational deformation and the rotational deformation of the end-effector.

Besides, the relationship of $[(\boldsymbol{f}_i^g)^{\mathrm{T}}, (\boldsymbol{m}_i^g)^{\mathrm{T}}]^{\mathrm{T}}$ and $[(\Delta\boldsymbol{x}_i^g)^{\mathrm{T}}, (\Delta\boldsymbol{\theta}_i^g)^{\mathrm{T}}]^{\mathrm{T}}$ follows:

$$\begin{bmatrix}\boldsymbol{f}_i^g\\ \boldsymbol{m}_i^g\end{bmatrix} = \boldsymbol{k}_{gi}\begin{bmatrix}\Delta\boldsymbol{x}_i^g\\ \Delta\boldsymbol{\theta}_i^g\end{bmatrix},\ \ \boldsymbol{k}_{gi} = \mathrm{diag}\left(k_{fxi}^g k_{fyi}^g k_{fzi}^g k_{mxi}^g k_{myi}^g k_{mzi}^g\right), \tag{37}$$

where $\boldsymbol{k}_{gi}$ is the elastic coefficient of the guide assembly.

Hence, Eq. (36) can be rearranged as

$$\left[\boldsymbol{F}^{\mathrm{T}}\boldsymbol{M}^{\mathrm{T}}\right]\begin{bmatrix}\Delta\boldsymbol{X}_g\\ \Delta\boldsymbol{\Theta}_g\end{bmatrix} = \boldsymbol{F}_g^{\mathrm{T}}\Delta\boldsymbol{G}, \tag{38}$$

where

$$\boldsymbol{F}_g = \left[\left(\boldsymbol{f}_1^g\right)^{\mathrm{T}}\left(\boldsymbol{m}_1^g\right)^{\mathrm{T}}\left(\boldsymbol{f}_2^g\right)^{\mathrm{T}}\left(\boldsymbol{m}_2^g\right)^{\mathrm{T}}\left(\boldsymbol{f}_3^g\right)^{\mathrm{T}}\left(\boldsymbol{m}_3^g\right)^{\mathrm{T}}\right]^{\mathrm{T}},$$
$$\Delta\boldsymbol{G} = \left[\left(\Delta\boldsymbol{x}_1^g\right)^{\mathrm{T}}\left(\Delta\boldsymbol{\theta}_1^g\right)^{\mathrm{T}}\left(\Delta\boldsymbol{x}_2^g\right)^{\mathrm{T}}\left(\Delta\boldsymbol{\theta}_2^g\right)^{\mathrm{T}}\left(\Delta\boldsymbol{x}_3^g\right)^{\mathrm{T}}\left(\Delta\boldsymbol{\theta}_3^g\right)^{\mathrm{T}}\right]^{\mathrm{T}}.$$

According to Hooke's law, the relationship of $\boldsymbol{F}_g$ and $\boldsymbol{\Delta G}$ is

$$\boldsymbol{F}_g = \boldsymbol{k}_g\Delta\boldsymbol{G},\ \ \boldsymbol{k}_g = \mathrm{diag}\left(\boldsymbol{k}_{g1}\boldsymbol{k}_{g2}\boldsymbol{k}_{g3}\right). \tag{39}$$

According to the geometrical relationship of the parallel mechanism, the following relationship holds:

$$\boldsymbol{p} + \boldsymbol{b}_{ij} = \boldsymbol{a}_i + d_i\boldsymbol{u}_i + \boldsymbol{g}_{ij} + l\boldsymbol{l}_i, \tag{40}$$

where $\boldsymbol{g}_{ij}$ is the position vector of the jth spherical joint in the ith limb and $\boldsymbol{u}_i$ is the unit vector of the actuated prismatic joint.

The first-order approximation of Eq. (40) can be made:

$$\boldsymbol{p} + \Delta\boldsymbol{X}_g + \boldsymbol{b}_{ij} + \Delta\boldsymbol{\Theta}_g \times \boldsymbol{b}_{ij} = \boldsymbol{a}_i + d_i\boldsymbol{u}_i + \boldsymbol{g}_{ij} + \boldsymbol{R}_i\left[\Delta\boldsymbol{x}_{gi} + \Delta\boldsymbol{\theta}_{gi} \times \boldsymbol{g}_{ij}\right] + l\boldsymbol{l}_i + l\left(\Delta\boldsymbol{\Theta}_g \times \boldsymbol{l}_i\right), \tag{41}$$

where $\boldsymbol{R}_i$ is the transformation matrix of B_i-xyz relative to O-XYZ.

Subtracting Eq. (41) by Eq. (40) yields

$$\Delta\boldsymbol{X}_g + \Delta\boldsymbol{\Theta}_g \times \boldsymbol{b}_{ij} = \boldsymbol{R}_i\left[\Delta\boldsymbol{x}_{gi} + \Delta\boldsymbol{\theta}_{gi} \times \boldsymbol{g}_{ij}\right] + l\left(\Delta\boldsymbol{\Theta}_g \times \boldsymbol{l}_i\right). \tag{42}$$

Taking the dot product on both sides of Eq. (42) with $\boldsymbol{l}_i$ and assembling in matrix format yields

$$\left[\boldsymbol{l}_i^{\mathrm{T}}\left(\boldsymbol{b}_{ij} \times \boldsymbol{l}_i\right)^{\mathrm{T}}\right]\begin{bmatrix}\Delta\boldsymbol{X}_g \\ \Delta\boldsymbol{\Theta}_g\end{bmatrix} = \left[\left(\boldsymbol{R}_i^{\mathrm{T}}\boldsymbol{l}_i\right)^{\mathrm{T}}\left(\boldsymbol{g}_{ij} \times \left(\boldsymbol{R}_i^{\mathrm{T}}\boldsymbol{l}_i\right)\right)^{\mathrm{T}}\right]\begin{bmatrix}\Delta\boldsymbol{x}_{gi} \\ \Delta\boldsymbol{\theta}_{gi}\end{bmatrix}. \tag{43}$$

Assembling the three limbs in matrix format gets

$$\boldsymbol{A}_g\begin{bmatrix}\Delta\boldsymbol{X}_g \\ \Delta\boldsymbol{\Theta}_g\end{bmatrix} = \boldsymbol{B}_g\Delta\boldsymbol{G}, \tag{44}$$

where

$$\boldsymbol{A}_g = \left[\boldsymbol{A}_{1g}\boldsymbol{A}_{2g}\boldsymbol{A}_{3g}\right],\ \boldsymbol{A}_{ig} = \begin{bmatrix}\boldsymbol{l}_i & \boldsymbol{l}_i \\ \boldsymbol{b}_{i1} \times \boldsymbol{l}_i & \boldsymbol{b}_{i2} \times \boldsymbol{l}_i\end{bmatrix},$$

$$\boldsymbol{B}_g = \mathrm{diag}\left(\boldsymbol{B}_{1g}\boldsymbol{B}_{2g}\boldsymbol{B}_{3g}\right),\ \boldsymbol{B}_{ig} = \begin{bmatrix}\boldsymbol{R}_i^{\mathrm{T}}\boldsymbol{l}_i & \boldsymbol{R}_i^{\mathrm{T}}\boldsymbol{l}_i \\ \boldsymbol{g}_{i1} \times \left(\boldsymbol{R}_i^{\mathrm{T}}\boldsymbol{l}_i\right) & \boldsymbol{g}_{i2} \times \left(\boldsymbol{R}_i^{\mathrm{T}}\boldsymbol{l}_i\right)\end{bmatrix}^{\mathrm{T}}.$$

Then,

$$\begin{bmatrix}\Delta\boldsymbol{X}_g \\ \Delta\boldsymbol{\Theta}_g\end{bmatrix} = \boldsymbol{J}_g\Delta\boldsymbol{G}, \tag{45}$$

where

$$\boldsymbol{J}_g = \left(\boldsymbol{A}_g^{\mathrm{T}}\boldsymbol{A}_g\right)^{-1}\boldsymbol{A}_g^{\mathrm{T}}\boldsymbol{B}_g.$$

Combing Eqs. (38), (44), and (45), the deformation of the end-effector caused by the deformation of guide assembly can be formulated as

$$\begin{bmatrix} \Delta \boldsymbol{X}_g \\ \Delta \boldsymbol{\Theta}_g \end{bmatrix} = \boldsymbol{C}_g \begin{bmatrix} \boldsymbol{F} \\ \boldsymbol{M} \end{bmatrix}, \quad \boldsymbol{C}_g = \boldsymbol{J}_g \boldsymbol{k}_g^{-1} \boldsymbol{J}_g^{\mathrm{T}}, \tag{46}$$

where $\boldsymbol{C}_g$ is the corresponding compliance matrix.

Stiffness Performance Evaluation

It is assumed that the deformations are small and these deformations can be added directly according to the linear superposition principle:

$$\begin{bmatrix} \Delta \boldsymbol{X} \\ \Delta \boldsymbol{\Theta} \end{bmatrix} = \begin{bmatrix} \Delta \boldsymbol{X}_d \\ \Delta \boldsymbol{\Theta}_d \end{bmatrix} + \begin{bmatrix} \Delta \boldsymbol{X}_l \\ \Delta \boldsymbol{\Theta}_l \end{bmatrix} + \begin{bmatrix} \Delta \boldsymbol{X}_g \\ \Delta \boldsymbol{\Theta}_g \end{bmatrix}. \tag{47}$$

Substituting Eqs. (28), (35), and (46) into Eq. (47) leads to

$$\begin{bmatrix} \Delta \boldsymbol{X} \\ \Delta \boldsymbol{\Theta} \end{bmatrix} = \boldsymbol{C} \begin{bmatrix} \boldsymbol{F} \\ \boldsymbol{M} \end{bmatrix}, \quad \boldsymbol{C} = \left[\begin{bmatrix} \boldsymbol{C}_d & \boldsymbol{0}_{3\times 3} \\ \boldsymbol{0}_{3\times 3} & \boldsymbol{0}_{3\times 3} \end{bmatrix} + \boldsymbol{C}_l + \boldsymbol{C}_g \right]_{6\times 6}, \tag{48}$$

where $\boldsymbol{C}$ is the compliance matrix of the parallel mechanism.

Without considering the gravity force, the external force on the end-effector is only exerted by the serial mechanism, which can be denoted by a concentrated wrench $[\boldsymbol{F}^{\mathrm{T}}, \boldsymbol{M}^{\mathrm{T}}]^{\mathrm{T}}$. Due to the special design of the serial mechanism, the force is always directed along the local normal direction of the contact-spot. To ensure the stabilization of the polishing process, tool offset should be kept constant during the polishing process, resulting that the values of external forces at different positions are nearly the same.

For a flat surface or a curved surface with a small curvature, the force on the end-effector mainly directs along Z-axis, and the moment on the end-effector mainly directs around X-axis and Y-axis. In addition, the horizontally arranged parallel mechanism is also subject to the gravity force directing along X-axis. As a result, the translational stiffness along X-axis and Z-axis and the rotational stiffness around X-axis and Y-axis are the preferential directions that should be considered. Each diagonal element in the 6×6 compliance matrix denotes the amount of translation/rotations per unit force in the corresponding direction. By normalizing the rotational elements with the radius of the moving platform, normalized $\boldsymbol{C}_p$ can be extracted from the compliance matrix $\boldsymbol{C}$ with the same units:

$$\boldsymbol{\Delta X}_P = \boldsymbol{C}_P \boldsymbol{F}_P, \tag{49}$$

where

$$\boldsymbol{\Delta X}_P = \left[\Delta X_x \Delta X_z b \Delta \theta_x b \Delta \theta_y\right]^{\mathrm{T}}, \quad \boldsymbol{F}_P = \left[F_x F_z M_x / b M_y / b\right]^{\mathrm{T}},$$

$$\boldsymbol{C}_P = \begin{bmatrix} c_{11} & c_{13} & bc_{14} & bc_{15} \\ & c_{33} & bc_{34} & bc_{35} \\ & & b^2 c_{44} & bc_{45} \\ \text{sym} & & & b^2 c_{55} \end{bmatrix}.$$

Table 2 Stiffness parameters of the related components

Parameter	Value
k^j	585 N/μm
E^l	2×10^{11} N/μm^2
k^c	930 N/μm
k^b	601 N/μm
E^s	2×10^{11} N/μm^2
k^n	1730 N/μm
k^g_{fxi}	980 N/μm
k^g_{fyi}	430 N/μm
k^g_{fzi}	430 N/μm
k^g_{mxi}	24 MN m/rad
k^g_{myi}	20 MN m/rad
k^g_{mzi}	20 MN m/rad

The stiffness performance of the parallel mechanism can be evaluated by using the eigenvalue of $\boldsymbol{C}_p$:

$$\sigma = \lambda_{\max}(\boldsymbol{C}_P), \tag{50}$$

where $\lambda_{\max}(\boldsymbol{C}_p)$ represents the maximum eigenvalue of $\boldsymbol{C}_p$.

The stiffness parameters of the related components are listed in Table 2. The distributions of stiffness performance σ in the workspace are shown in Fig. 15. The results show that the stiffness performance exhibits a mirror symmetry characteristic in the *O*-*YZ* cross section. For a certain height along the *Z*-axis, the highest stiffness performance occurs at the center of the cross section and decreases when the parallel mechanism moves the boundary of the workspace. As a result, it is suggested to restrict the parallel mechanism to work in the sub-workspace that is located at the center of reachable workspace. Moreover, the stiffness performance increases along the *Z*-axis from the bottom to the top.

Control System and Control Strategy

Control system is one of the cores of the precision polishing machine. In this study, an industrial computer (IPC) combined with a programmable multi-axis controller (PMAC) is used to constitute an open-type CNC system, as shown in Fig. 16. This scheme shows a common applicability and has been widely used in industrial automation.

NC code generation for the CNC system is the basis to realize the automated polishing process. Computer-aided design (CAD) and computer-aided manufacturing (CAM) systems are used widely for the theoretical design as well as the manufacturing. However, commercial CAM systems developed for

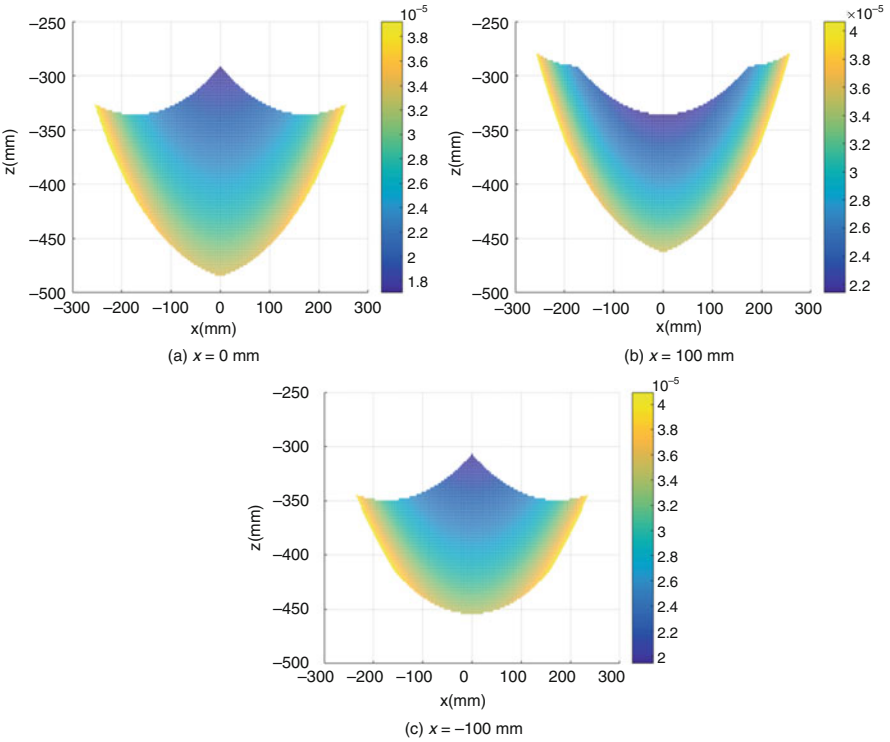

Fig. 15 Stiffness distribution on *O-YZ* plane in the workspace

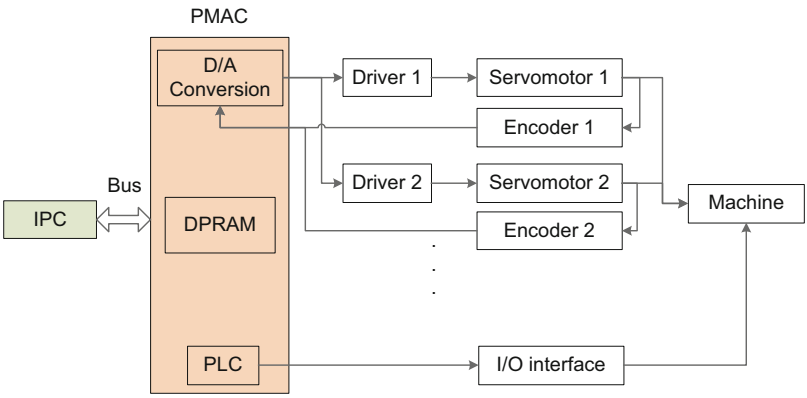

Fig. 16 Control system of the polishing machine

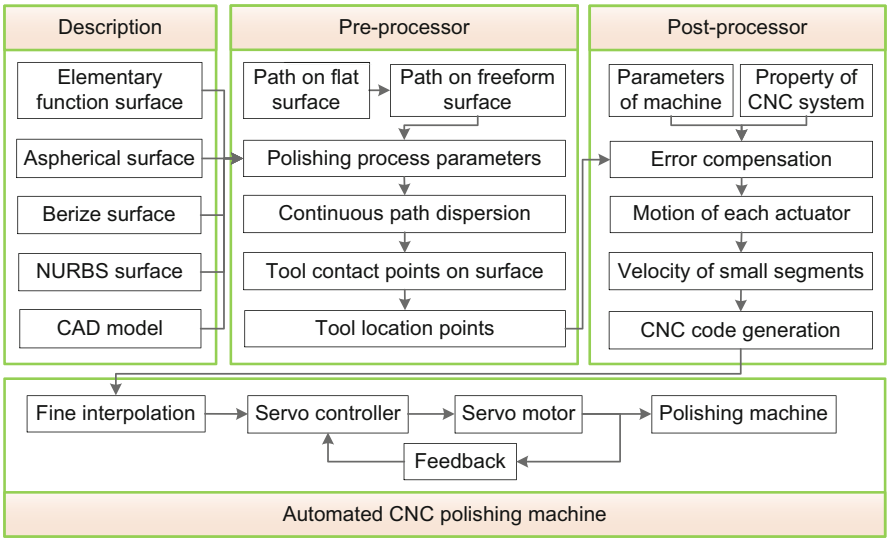

Fig. 17 Control strategy of the automated CNC polishing machine

the conventional milling machines cannot be directly used to generate the tool paths for polishing process. Although many CAM systems provide the post-processing modules, they are limited to the traditional serial machines and do not consider the topological structural and key parameters of the special machines such as serial-parallel ones. As a result, the hybrid serial-parallel polishing machine cannot be directly controlled by the general NC system without an appropriate pre-processing and post-processing strategy. Due to the unique motion in the *Precessions* polishing process, an off-line programming software is developed to realize the direct conversion of the surface information and polishing process parameters into the NC code.

As shown in Fig. 17, the control strategy of the polishing machine mainly contains the parts of surface description, pre-processor and post-processor. The specific processes are briefly explained as follows:

1. *Surface description*: The surfaces to be polished are described with different methods.
2. *Pre-processor*: According to the tool path planned on the plane surface and the mapping rules on the freefrom surface, the tool path on the curved surface can be obtained. By dispersing the continuous tool path according to the accuracy requirements, the tool contact points and tool location points in the workpiece frame are obtained.
3. *Post-processor*: The tool location points in the workpiece coordinate system are transformed into the motions of independent actuators by inverse kinematic models of parallel mechanism and serial mechanism.

4. CNC system: This performs fine interpolation of the NC program in the joint space and controls the machine to achieve the desired movement of the polishing tool relative to the workpiece.

To show the control strategy, a saddle surface as shown in Fig. 18a is selected to be polished by the developed machine. As an example, a raster polishing path is selected with 1 mm dwell point space and 2 mm trace space. The orientation of the polishing tool is determined by setting the precession angle as $\rho = 15^\circ$ and the inclination angle as $\phi = 0^\circ$. In the pre-processor, the tool location data which includes the orientation of the tool axis and the position of the tool center point are obtained are shown in Fig. 18b, which includes 1137 dwell points in total. In the post-processor, the position of each individual actuator with respect to the tool location data is calculated as shown in Fig. 19. According the characteristics of the general CNC system, these data can be directly transferred into the GM code for the polishing machine.

Prototype of the Hybrid Serial-Parallel Polishing Machine

According to the proposed design scheme, a detailed mechanical design of the hybrid serial-parallel polishing machine is performed. During the polishing process, continuous polishing slurry is required, and the spindle is water-cooled and air-sealed, so the machine also requires to design water circulation system and air circulation system. The CAD model of the machine is given as shown in Fig. 20, which mainly consists of a console, a control cabinet, a serial-parallel mechanism, and a coolant/slurry tank. Based on that, a prototype of the polishing machine is developed as shown in Fig. 21. To show the effectiveness of the developed machine, two polishing experiments are conducted on a flat surface and a saddle surface,

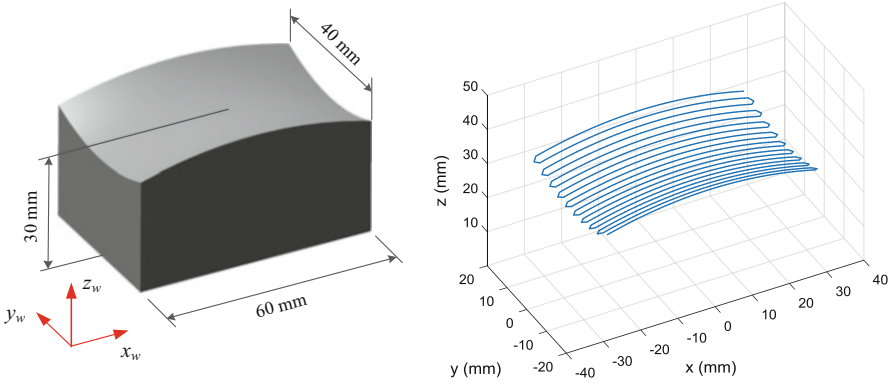

(a) Saddle surface (b) CAD model

Fig. 18 Test workpiece for polishing

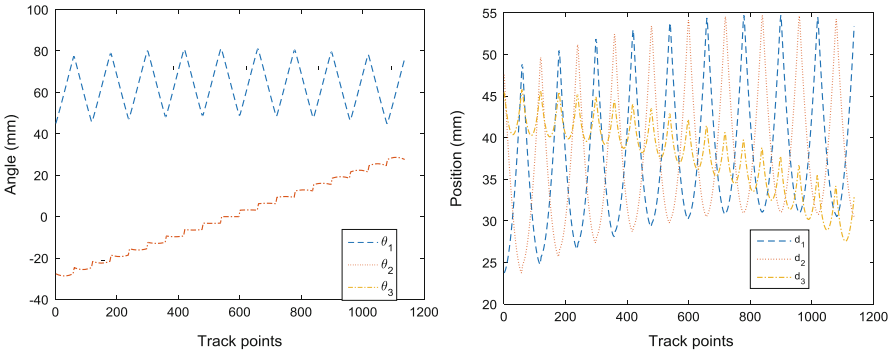

(a) Motionof the tworevolute joints inthe serial mechanism

(b) Motionof the three prismaticjoints inthe parallelmechanism

Fig. 19 Motion of the actuators in the hybrid serial-parallel polishing machine

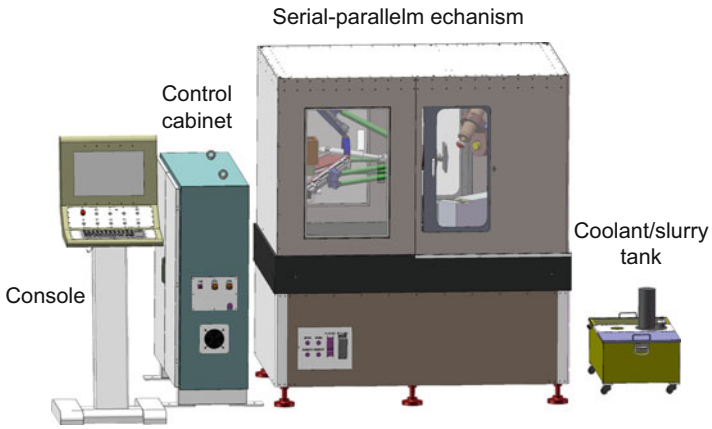

Fig. 20 Design of the polishing machine

Fig. 21 Prototype of the hybrid serial-parallel polishing machine

respectively. With the help of the developed automatic programming software, corresponding NC programs are generated. The surface roughness before and after polishing is measured by the Zygo Nexview white light interferometer.

Two groups of polishing experiments are carefully designed. The first set of experiments is conducted on a flat surface. A sample made of single crystal silicon (110) with a diameter of 50 mm is prepared. Table 3 gives the detail conditions of the polishing experiments. Firstly, rough polishing is executed two times using a R20 mm polishing tool. Then, four times of fine polishing is conducted using a R10 mm polishing tool. The total polishing time is about 68 min. The photographs of the sample before and after polishing are shown in Fig. 22. The experimental

Table 3 Polishing conditions for plane silicon surface

Conditions	1st	2nd
Slurry type	5 μm grit-size diamond paste	1 μm grit-size diamond paste
Radius of polishing tool (mm)	20	10
Tool offset (mm)	0.3	0.3
Inclination angle (deg)	15	15
Spindle speed (rpm)	2000	2000
Raster path pitch (mm)	0.5	0.4
Number of cycles	2	4
Polishing time of each cycle (min)	15	9.5

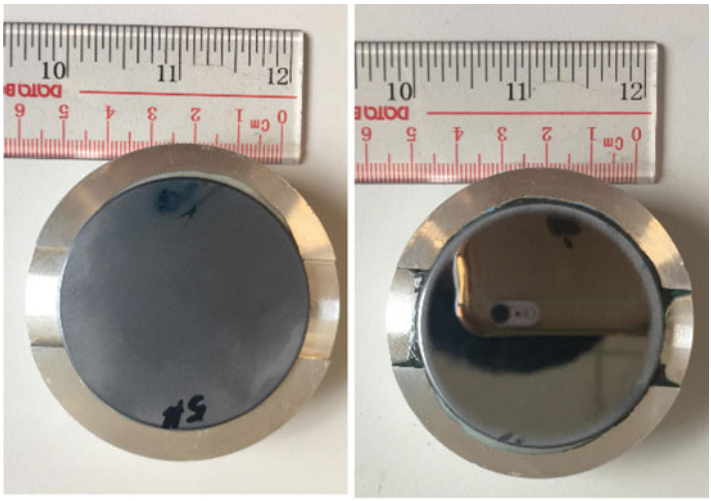

Fig. 22 Polishing experiment of the flat surface

results show that mirror-like surface is obtained after polishing. The measured results are shown in Fig. 23, which illustrate that the surface roughness is improved from arithmetic roughness Sa of 713 nm to Sa of 5 nm.

The second set of experiments is conducted on a saddle surface. A sample made of 304 stainless steels is manufactured, whose dimensions are shown in Fig. 18. Based on the polishing parameters listed in Table 4, a series of polishing experiment are conducted, and the total polishing time is about 86 min. The photographs of the sample before and after polishing are shown in Fig. 24. As shown in Fig. 25, it can be observed that the arithmetic surface roughness Sa is remarkably improved from 193 nm to 4 nm, indicating the effectiveness and practicality of the developed polishing machine.

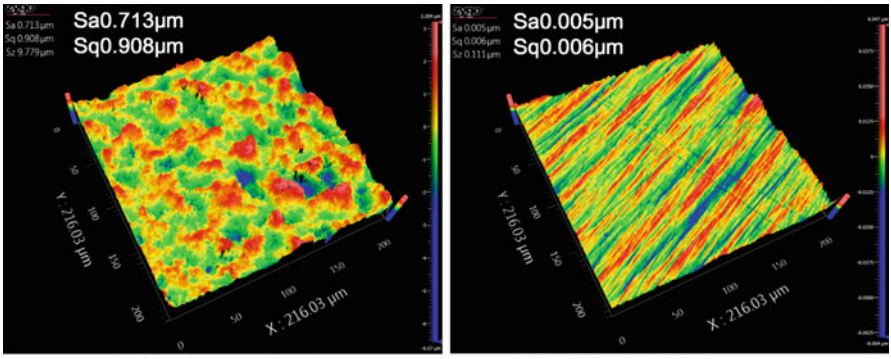

(a) Before polishing (c) After polishing

Fig. 23 Surface quality of the flat surface

Table 4 Polishing conditions for freefrom 304 stainless steel surfaces

Conditions	1st	2nd
Slurry type	5 μm grit-size diamond paste	1 μm grit-size diamond paste
Radius of polishing tool (mm)	10	10
Tool offset (mm)	0.3	0.3
Tilted angle (deg)	15	15
H-axis speed (rpm)	2000	2000
Raster path pitch (mm)	0.4	0.4
Number of cycles	2	2
Polishing time of each cycle (min)	21.5	21.5

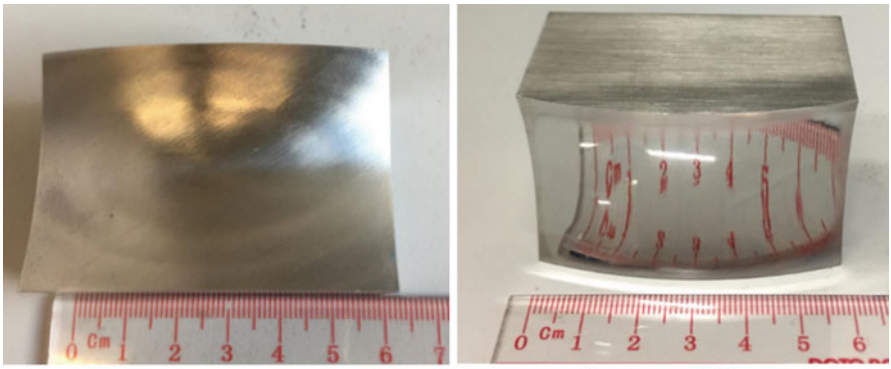

Fig. 24 Polishing experiment of the saddle surface

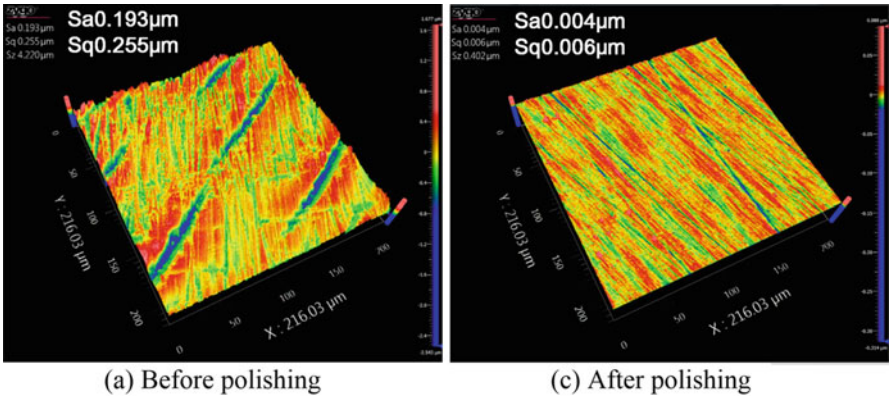

Fig. 25 Surface quality of the saddle surface

Conclusion

This chapter presents a newly developed hybrid serial-parallel polishing machine, which includes a two-DOF serial mechanism, a three-DOF parallel mechanism, and a functional extension limb providing a redundant rotation. An elastic spherical polishing head is adopted as the polishing tool. By installing its spherical center with the intersection point of the two rotation axes in the serial mechanism, the orientation and the position control of the polishing tool with respect to the workpiece are decoupled during the synchronized movements of all five actuators.

Considering the features reflected in the structural independence and motion decoupling, a detailed kinematic analysis of the polishing machine is conducted according to the structure of the machine. Owing to the complexity of the parallel

mechanism, stiffness performance of the parallel mechanism is also evaluated within the workspace. On the basis of these analysis and engineering practice, a physical prototype of the hybrid polishing machine tool was developed by completing the system integration and debugging work. A saddle surface finished with this machine is given as an example, and the experimental results show that the developed machine is able to perform freefrom surface polishing.

Acknowledgments The authors would like to express their sincere thanks to the Innovation and Technology Commission (ITC) of the Government of the Hong Kong Special Administrative Region (HKSAR) for the financial support of the research work under the project No. GHP/031/13SZ. The work was also supported a PhD studentship (project account code: RU98) from the Hong Kong Polytechnic University.

References

Allen LN (1995) Progress in ion figuring large optics. Proc SPIE – Int Soc Opt Eng 2428:237–247

Bonev IA, Ryu J (2001) A new approach to orientation workspace analysis of 6-DOF parallel manipulators. Mech Mach Theory 36:15–28

Brecher C, Lange S, Merz M, Niehaus F, Wenzel C, Winterschladen M (2006) NURBS based ultra-precision free-form machining. CIRP Ann-Manuf Techn 55:547–550

Chablat D, Wenger P, Majou F, Merlet JP (2004) An interval analysis based study for the design and the comparison of three-degrees-of-freedom parallel kinematic machines. Int J Robot Res 23:615–624

Chen C, Angeles J (2007) Generalized transmission index and transmission quality for spatial linkages. Mech Mach Theory 42:1225–1237

Clavel R (1990) Device for the movement and positioning of an element in space. US Patent

Fan C, Zhao GL, Zhao J, Zhang L, Sun LN (2015) Calibration of a parallel mechanism in a serial-parallel polishing machine tool based on genetic algorithm. Int J Adv Manuf Tech 81:27–37

Gosselin C, Angeles J (1989) The optimum kinematic design of a spherical 3-degree-of-freedom parallel manipulator. J Mech Transm-T Asme 111:202–207

Gosselin C, Angeles J (1991) A global performance index for the kinematic optimization of robotic anipulators. J Mech Design 113:220–226

Innocenti C, Parenticastelli V (1990) Direct position analysis of the Stewart platform. Mech Mach Theory 25:611–621

Kakinuma Y, Igarashi K, Katsura S, Aoyama T (2013) Development of 5-axis polishing machine capable of simultaneous trajectory, posture, and force control. CIRP Ann-Manuf Techn 62:379–382

Kordonski WI, Golini D (1999) Fundamentals of magnetorheological fluid utilization in high precision finishing. J Intel Mat Syst Str 10:683–689

Liao L, Xi FF, Liu KF (2008) Modeling and control of automated polishing/deburring process using a dual-purpose compliant toolhead. Int J Mach Tool Manu 48:1454–1463

Lin WY, Li B, Yang XJ, Zhang D (2013) Modelling and control of inverse dynamics for a 5-DOF parallel kinematic polishing machine. Int J Adv Robot Syst 10:1–21

Lin W, Xu P, Li B, Yang X (2014) Path planning of mechanical polishing process for freeform surface with a small polishing tool. Robot Biomim 1:1–15

Liu X-J (2005) Optimal kinematic design of a three translational DoFs parallel manipulator. Robotica 24:239

Liu XJ, Wang JS, Oh KK, Kim J (2004) A new approach to the design of a DELTA robot with a desired workspace. J Intell Robot Syst 39:209–225

Martin HM, Anderson DS, Angel JRP, Nagel RH, West SC, Young RS (1990) Progress in the stressed-lap polishing of a 1.8-M F/1 mirror. Proc SPIE – Int Soc Opt Eng 1236:682–690
Merlet JP (1994) Parallel manipulators – state-of-the-art and perspectives. Adv Robotics 8:589–596
Sidpara A, Jain VK (2013) Analysis of forces on the freeform surface in magnetorheological fluid based finishing process. Int J Mach Tool Manu 69:1–10
Tsai LW, Joshi S (2000) Kinematics and optimization of a spatial 3-UPU parallel manipulator. J Mech Design 122:439–446
Tsai MJ, Lee HW (1994) Generalized evaluation for the transmission performance of mechanisms. Mech Mach Theory 29:607–618
Walker DD, Brooks D, King A, Freeman R, Morton R, McCavana G, Kim SW (2003) The 'Precessions' tooling for polishing and figuring flat, spherical and aspheric surfaces. Opt Express 11:958–964
Walker DD, Freeman R, Morton R, McCavana G, Beaucamp A (2006) Use of the 'Precessions'(TM) process for prepolishing and correcting 2D & 2 1/2 D form. Opt Express 14:11787–11795
Wampler CW, Morgan AP, Sommese AJ (1990) Numerical continuation methods for solving polynomial systems arising in kinematics. J Mech Design 112:59–68
West SC et al (1994) Practical design and performance of the stressed-lap polishing tool. Appl Opt 33:8094–8100
Xu P, Cheung CF, Li B, Ho LT, Zhang JF (2017) Kinematics analysis of a hybrid manipulator for computer controlled ultra-precision freeform polishing. Robot Com-Int Manuf 44:44–56
Yoshikawa T (1985) Manipulability of robotic mechanisms. Int J Robot Res 4:3–9
Yu JJ, Dai JS, Zhao TS, Bi SS, Zong GH (2009) Mobility analysis of complex joints by means of screw theory. Robotica 27:915–927

Error Allocation in the Design of Precision Machines

8

Shanshan Chen and Guofeng Zhang

Contents

Introduction 208
Machine Design in Precision Engineering 209
Precision and Accuracy 209
Kinematic Chain in Precision Machine Design 210
Volumetric Errors of a Precision Machine 212
Geometry Error Involved in Precision Machine Design 213
Position-Dependent Source of Geometric Error 215
Position-Independent Source of Geometric Errors 217
Errors Induced by Thermal Deformation 217
Error Source Induced by Load 224
Conclusion 231
References 231

Abstract

Machining accuracy is an important index to evaluate the performance of a precision machine. However, the machining accuracy of parts is seriously limited by the designed machine's errors. Therefore, error allocation in precision machine design is the key element to produce the components with a closed tolerance. In this chapter, the main errors for the designed machine that affect the machining accuracy are introduced, which include machine tool geometric error, machine tool thermal deformation, and load-induced errors. Among them, the geometric error after the

S. Chen (✉)
School of Mechanical Engineering, Xi'an Jiaotong University, Xi'an, Shaanxi, China
e-mail: chenshanshan2009@163.com

G. Zhang
State Key Laboratory for Manufacturing Systems Engineering, School of Mechanical Engineering, Xi'an Jiaotong University, Xi'an, Shaanxi, China
e-mail: zgf0110@stu.xjtu.edu.cn

Z. Jiang, S. Yang (eds.), *Precision Machines*, Precision Manufacturing,
https://doi.org/10.1007/978-981-13-0381-4_26

assembly of the machine tool has the most direct impact on the machining accuracy, in which the position- and pose-related errors between each component transmit through kinematic chain and lead to the error combination. The essence of error allocation design is to use tolerance to limit the error of every part and finally ensure the overall output trajectory accuracy of the cutting tool. The deformation error caused by uneven temperature distribution is mainly caused by cutting process, friction behavior, and the surrounding environment, and it will further change the relative position of each part of the machine tool. Finally, load error under the action of force is introduced, which produces the elasticity or even structural deformation and further affects the relative position of the machine tool components. It shows that reasonable error allocation under the influence of multiple errors for the precision machine design is critical to ensure the machining precision.

Keywords

Machining accuracy · Error allocation · Machine design · Deformation

Introduction

In the last few decades, the demand for high-precision components has increased. These components have a wide range of industrial applications in space and aeronautics, optics, electronic devices, and medical and life sciences (Aurich et al. 2009). Ultraprecision machining technologies play an increasingly important role in the precision manufacturing field (Zhang et al. 2015). Ductile materials, such as aluminum, copper, and other metals, can be machined by single-point diamond turning (SPDT) or other deterministic ultraprecision machining technologies such as ultraprecision raster milling and tool servo machining. However, for difficult-to-machine materials, such as ceramics, silicon carbide, glass, and semiconductor materials, they are primarily machined by ultraprecision grinding technology (Brinksmeier et al. 2010; Zhao and Guo 2015).

A high-precision surface finish significantly improves the performance of the functional properties of precision components such as fatigue strength, frictional properties, and component life (Suto and Sata 1981; Hwang et al. 1999). In the modern industrialized world, the capability to design and fabricate the high-precision machines determines the level of manufacturing technologies and component's accuracy. Mechanical components are the basic elements for machine design, which can be assembled together to produce manufacturing instruments and machines for achieving a specific function, such as fabrication, monitoring and measurement, and so on. However, error involves in the whole process of machine design. In order to achieve the finial target accuracy, the error raised in each step of machine design should be controlled (including part manufacturing, assembling, and machine operation). Thus error allocation should be carried out to manage the various error sources to achieve acceptable levels.

Machine Design in Precision Engineering

Precision and Accuracy

In recent decades, the increasing demand for higher and higher precision components and products with good surface finish drives researchers to exploit new manufacturing technologies and design the new advanced machines with increased speed, high accuracy, and high reliability. These components have been used in high-resolution optical devices, biomedicine, and automotive goods and put forward an increasing need for design engineers to have a deep understanding of error resources and error allocation in the science of design.

Nowadays, ultrahigh-precision machining can achieve nanometer order of accuracy. At the same time, the improvement of machining accuracy also presents a challenge for measurement technologies. The measured revolution determines the upper limit for manufacturing technologies, and the measurement accuracy should be determined traceably. In recent years, precision manufacturing has been escalating to improve the characterization methods and exploit advanced equipment. The behavior of processed materials at the sub-nanometer level (atomic resolution) cannot be detected. The development of the existing machining approaches and new machine is illustrated as shown in Fig. 1 (Taniguchi 1994).

In machine design, the term accuracy refers to systematic errors of the machine system, which leads to the degree of agreement of actual measured index with targeted index (ideal value). As shown in Fig. 2, accuracy is one of the important performance indexes of NC machine tools, especially for the advanced machine tools with higher precision requirements. The accuracy of CNC machine tools can be

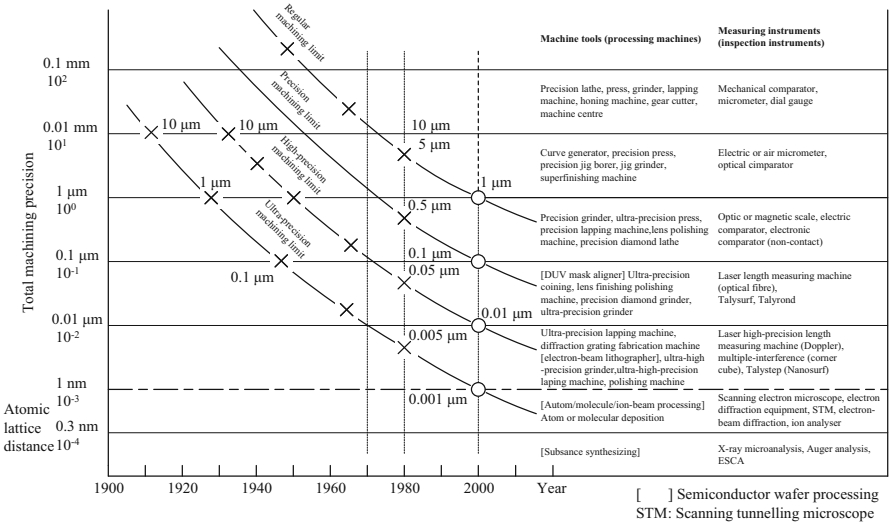

Fig. 1 Development of achievable accuracy (Taniguchi 1994)

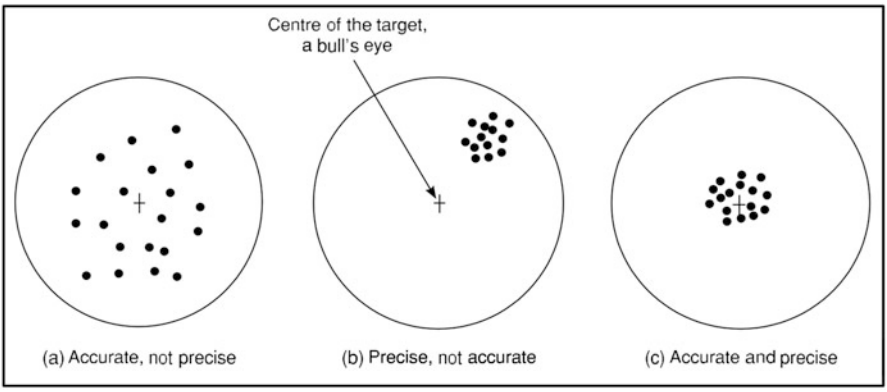

Fig. 2 The difference between the two items accuracy and precision (Ramesh et al. 2000)

improved through precision design and error compensation. However, the term precision is related to the degree to which the designed machine is capable of keeping the same level in repeated operations, which represents the repeatability of the process caused by random errors in the machine (Raju et al. 1976). Theoretically, it is impossible to eliminate the random error that results from synthetic of many micro errors, in which every single error does not play a determined role in the error calculation.

Kinematic Chain in Precision Machine Design

In the design of a precision machine tool, many parts are connected by a series of moving pairs to achieve relative motion between the tool and the workpiece. Under ideal conditions (no error), each moving pair of machine tools should have only 1 degree of freedom, as shown in Fig. 2. However, in the actual production process, from the manufacturing and installation of the machine tool to the normal operation of the machine tool, there will be a series of inevitable error elements, including CNC machine tool manufacturing and installation error, machine tool thermal deformation error, imperfect assembly, and errors caused by servo drive. These errors will lead to errors in the six degrees of freedom of stroke space of the motion pair, which can affect the relationship between the motion pairs in the machine tool kinematic chain and eventually results in the relative pose errors between the workpiece and the tool (Guo et al. 2019). As shown in Fig. 3, the motion precision of NC machine tool refers to the trajectory precision of the main moving parts of the machine tool in the operation state. It reflects the degree of conformity between the actual motion trajectory and the theoretical motion trajectory of the main parts such as the tool, the table, and the tool rest in the process of machining parts. The positioning and movement error of the machine tool is influenced by a series of imperfect dimension and manufacturing of each machine axis. The kinematic chain of axes is used to build up the error relationship between

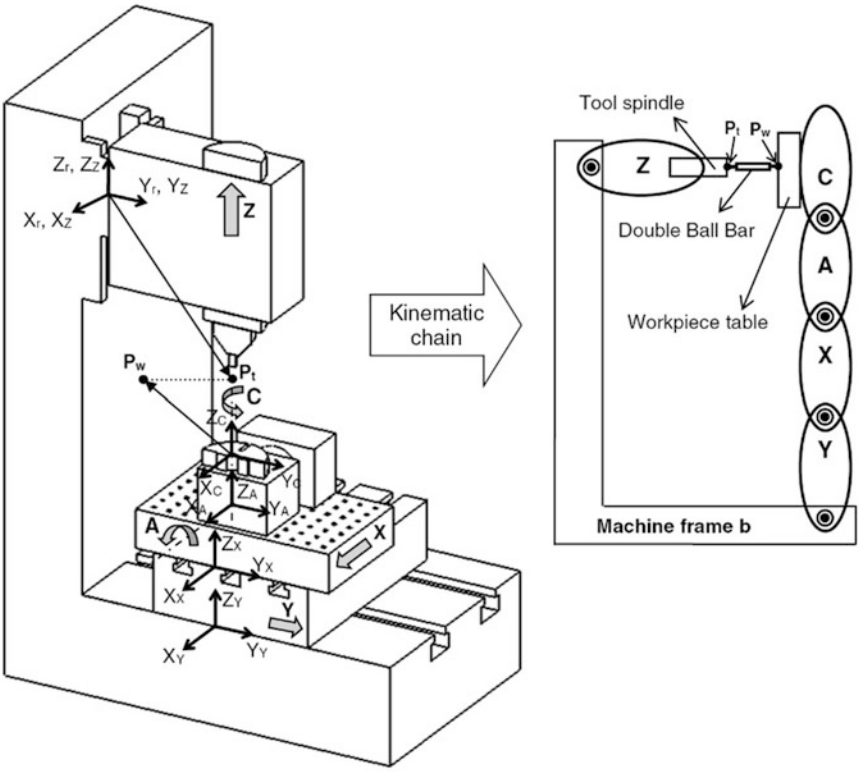

Fig. 3 Layout and kinematic chain of a typical machine tool (Lasemi et al. 2016)

allocation errors and locus error of the cutting tool acting on the surface of machined part according to reference coordinate system of the relative motion, as shown in Fig. 4.

The error allocation of the designed machine tool is the major contributor to the volumetric errors of machine performance, especially for geometric errors which lead to axis misalignment and angle positioning errors (Schwenke et al. 2008). Generally, the error resources related to the geometric error that need to be taken into consideration in machine element design; although advanced measurement devices can be used to detect geometric errors of the designed machine tool, it is very time-consuming and hard to know every single error involved in each machine element accurately (Lasemi et al. 2016). The quality of machine tool, to a large extent, is related to the output performance index such as the accuracy of the machined components. Therefore, it is necessary to look insight into error allocation in design step for a precision machine so as to reasonably allocate the precision index of instrument design to each element of a precision machine. The main objective of error allocation is to eliminate or reduce the influence of error sources on accuracy of machine tool.

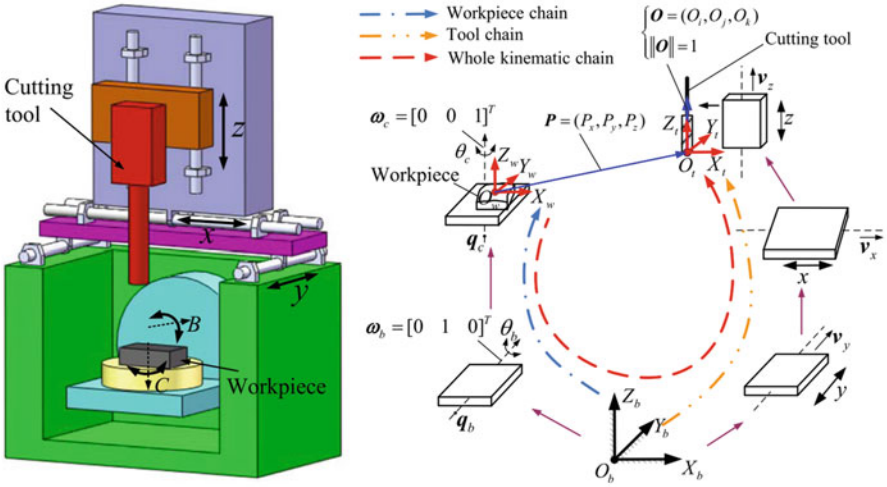

Fig. 4 Kinematic chain of movement transition (Yang et al. 2015)

Volumetric Errors of a Precision Machine

For the precision machine tool, the machining accuracy is largely determined by the deviation of the cutting tool from the desired position to produce a component with the specified tolerance (Ramesh et al. 2000). Generally, the machine is a system, which contains many elements; thus not only errors for the single part or mechanism should be studied, but also the comprehensive errors for the whole system should be researched to serve as the purpose of enhanced precision machine design. From the volumetric error, the general CNC machine tool is mainly composed of bed, column, spindle, and a variety of linear guides or rotating axes, in which every part is going to be an error element. There are many factors involved in the process of the final volumetric errors of a machine tool, which involved three main sources of errors, that is, geometric errors, thermally induced errors, and load-induced errors, as shown in Fig. 5. Of course, other errors such as machine tool assembly error, error of test equipment, tool wear, fixture error, and error of machine tool servo control and interpolation algorithm all contribute to the error sources.

From the property of error, it can be divided into quasi-static error and dynamic error. The so-called quasi-static error refers to the error that changes slowly with time and is related to the structure of the machine tool itself. It mainly includes geometric error, motion error when parts move at low speed, error caused by partial load of machine parts, thermal deformation error, etc. Dynamic error refers to the error caused by rotary motion error of spindle, machine vibration, and servo control performance of the machine. The dynamic error is more dependent on the working condition of machine tool. These errors will lead to changes in the relative position between the workpiece and the tool.

The inaccuracy of machine tool is the main source of workpiece error, so it is very important to control the integrated error of machine tool. CNC machine tool errors generally can be divided into three categories, geometric error, thermal error, and load error.

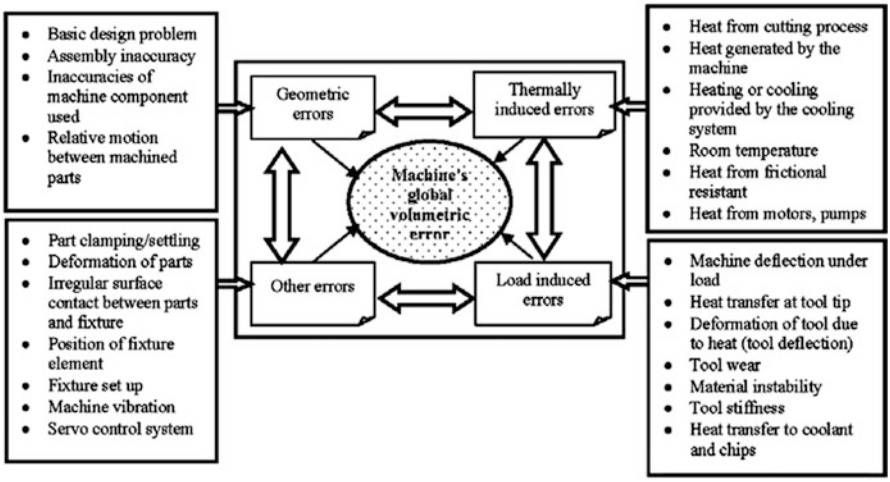

Fig. 5 Sources of machine tool errors (Ramesh et al. 2000)

Geometry Error Involved in Precision Machine Design

Geometric error of the machine tool is caused by the manufacturing and assembly defects of the machine tool itself. Geometric error is the category of quasi-static error in process of precision machine design, which relates to the errors generated when the machine operated under stable thermal environment and no-load condition. Each basic motion of a five-axis machine tool will produce six errors, the movement error along X, Y, and Z axis and the rotation error around X, Y, and Z axis. Therefore, there are three linear motion axes and two rotation axes in a five-axis machine tool, as shown in Fig. 6. The geometric error source of the machine tool mainly refers to the motion error of the moving parts for each axis and the relative pose error between the two axes, named position-dependent geometric errors (PDGEs) and position-independent geometric errors (PIGEs) (Lee and Yang 2013). Geometric error is the key factor that affects the machining accuracy of NC machine tool. In theory, the geometric error of the machine tool is deterministic, which affects the machining accuracy of the machine tool and can be measured and compensated (Shi et al. 2016). Therefore, extensive research has been conducted to analyze the effect of geometric error on CNC machine tools' performance.

In recent years, in the relevant academic field, the theory of spinor in robotics has been introduced into the modeling theory for developing the kinematic model of geometric error in five-axis CNC machine tool, by which the static geometric error in machining can be calculated. It provides a useful tool to analyze and improve error allocation in the design of precision machine to reduce error sensitivity of the geometric imprecision of the machine tool.

Undesirable machine geometric error in machine design results in the deviations between the actual and ideal geometric parameters and position of the machine tool.

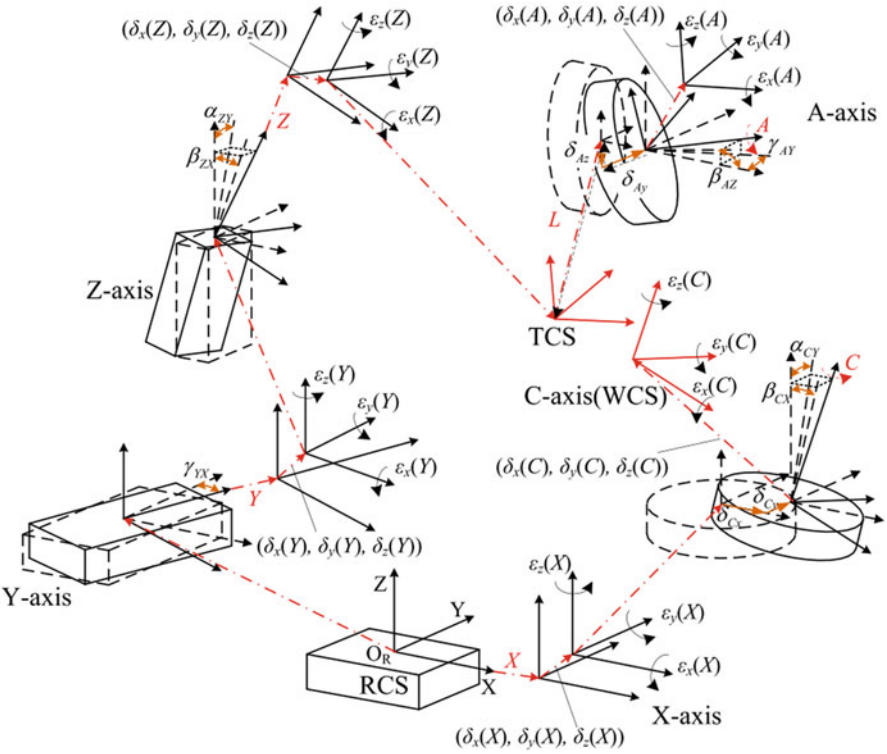

Fig. 6 Typical geometric errors of the machine tool (Ding et al. 2016)

In general, geometric error constitutes about 25–50% of the total machine error (Kreith and Goswami 2015). As mentioned above, there is a close relationship between the accuracy of the machine and various dimensional tolerance of each element, where the tolerance can be linear, angle, form, and position error (geometric quantities) or physical or chemical quantities. In precision machine design, a series of parts are needed to be designed fabricated and assembled. However, each element inevitably incurs certain deviations from ideal designed index. Those errors interact with each other and transmit one by one, resulting in a final accuracy for a designed precision machine (Schwenke et al. 2008). The assembly of these parts leads to the formation of a cumulative error, which will affect the accuracy of the machine operation and further the machine performance. Therefore, in the process of machine design and manufacturing, all the associated dimensional information as well as the relationship between the errors of these dimensions and the total error accumulation should be fully taken into account. In order to design a high-precision machine, the dimension and tolerance chain should be restrained. The role of the dimension and tolerance chain in the precision machine design can be summarized as follows:

1. The machine structure is analyzed, and the accuracy of parts is determined reasonably according to the prescribed performance indicators.

2. To provide the improvement tactics for the machine structure design, such as setting the necessary adjustment allowance and making the components have good assemblability and interchangeability.
3. The process error and accumulated error in the machining process are analyzed so as to determine the process size error and arrange the technological process reasonably. Finally the product is machined with high processing accuracy and economic efficiency.

Position-Dependent Source of Geometric Error

PDGEs are mainly represented by six pose errors generated by moving parts in a single motion axis during movement of the machine. Taking the translational X axis for an example, as shown in Fig. 7, the coordinate system $X_0 - xyz$ is a fixed coordinate system, which is established at the origin of the X axis coordinate. The direction of coordinate axis is consistent with the machine coordinate system; the coordinate system $X - xyz$ is used to describe the ideal motion of the X axis for the moving part in the error-free state. The origin is fixed at the reference point of the moving part at the X axis, which moved with the part. Due to the existence of errors, the actual position of the coordinate system $X - xyz$ is deviated and described by the coordinate system X'−xyz. There are six PDGEs in the coordinate system X'−xyz with respect to the coordinate system $X - xyz$, which include the positioning error $\delta_x(x)$; the straightness errors at Y axis direction $\delta_y(x)$ and Z axis direction $\delta_z(x)$, respectively; roll angle error $\varepsilon_x(x)$; yaw angle error $\varepsilon_y(x)$; and pitch angle error $\varepsilon_z(x)$, where δ_x, δ_y, and δ_z represent the position error and ε_x, ε_y, and ε_z represent the angular error around the respective axis of rotation. "x" in brackets indicates position of moving parts along the X axis (the positions of moving parts along the Y axis and the Z axis are represented by "y" and "z," respectively), that is, the above six PDGEs (as shown in Table 1) are functions of the X axis motion position of the machine tool. Therefore, PDGEs of the X axis can be calculated as:

$$\Delta(x) = \left[\delta_x(x) \;\; \delta_y(x) \;\; \delta_z(x) \;\; \varepsilon_x(x) \;\; \varepsilon_x(x) \;\; \varepsilon_x(x)\right]^T$$

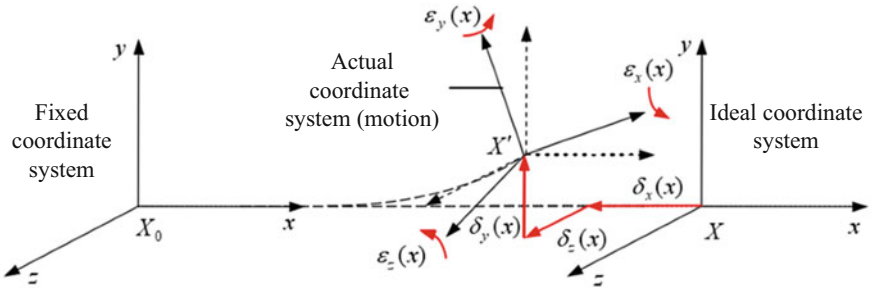

Fig. 7 PDGEs of translational axis X (Tian et al. 2014)

Table 1 List of PDGEs involved in kinematic chain of a precision machine (Lasemi et al. 2016)

Machine axis	Symbol of errors	Number of PDGEs	Number of error parameters
X	$\delta_x(x),\delta_y(x),\delta_z(x)\varepsilon_x(x),\varepsilon_y(x),\varepsilon_z(x)$	6	18
Y	$\delta_x(y),\delta_y(y),\delta_z(y)\varepsilon_x(y),\varepsilon_y(y),\varepsilon_z(y)$	6	18
Z	$\delta_x(z),\delta_y(z),\delta_z(z)\varepsilon_x(z),\varepsilon_y(z),\varepsilon_z(z)$	6	18
A	$\delta_x(\theta_A),\delta_y(\theta_A),\delta_z(\theta_A)$ $\varepsilon_x(\theta_A),\varepsilon_y(\theta_A),\varepsilon_z(\theta_A)$	6	18
C	$\delta_x(\theta_C),\delta_y(\theta_C),\delta_z(\theta_C)$ $\varepsilon_x(\theta_C),\varepsilon_y(\theta_C),\varepsilon_z(\theta_C)$	6	18

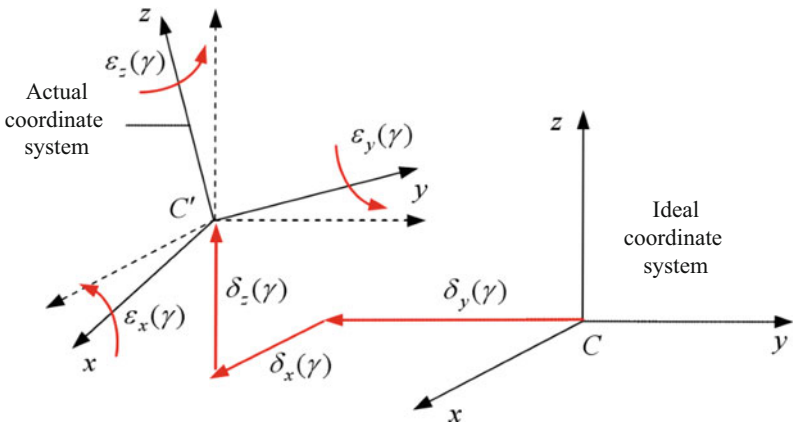

Fig. 8 PDGEs of rotational axis C (Tian et al. 2014)

Similarly, PDGEs of the Y axis and Z axis can be represented as:

$$\Delta(\mathrm{y}) = \left[\delta_x(\mathrm{y})\ \ \delta_y(\mathrm{y})\ \ \delta_z(y)\ \ \varepsilon_x(y)\ \ \varepsilon_x(y)\ \ \varepsilon_x(y)\right]^T$$

$$\Delta(\mathrm{z}) = \left[\delta_x(z)\ \ \delta_y(z)\ \ \delta_z(z)\ \ \varepsilon_x(z)\ \ \varepsilon_x(z)\ \ \varepsilon_x(z)\right]^T$$

For the rotation axis C, as shown in Fig. 8, C-xyz coordinate system is used to describe the ideal rotating movement without any errors; its origin is mounted on the reference point of moving part (at C axis) and moved with the part. C '−xyz coordinate system is used to describe the actual motion of the part. The six PDGEs with respect to C axis include two radial runout errors $\delta_x(\gamma)$ and $\delta_y(\gamma)$, one axial runout error $\delta_z(\gamma)$, two tilting errors $\varepsilon_x(\gamma)$ and $\varepsilon_y(\gamma)$, and one positioning error $\varepsilon_z(\gamma)$, where "γ" represents the position coordinates of the moving part at axis C (the position coordinates for axis A and axis B are expressed by "α" and "β," respectively). PDGE of C axis is derived as:

$$\Delta(\gamma) = \left[\delta_x(\gamma)\ \ \delta_y(\gamma)\ \ \delta_z(\gamma)\ \ \varepsilon_x(\gamma)\ \ \varepsilon_x(\gamma)\ \ \varepsilon_x(\gamma)\right]^T$$

Position-Independent Source of Geometric Errors

PIGEs mainly refer to the relative pose error between the two axes of machine tools, which is usually manifested as non-parallel, non-vertical, or non-intersecting between axes (listed in Table 2). It can be described as the relative position and attitude error between the fixed reference coordinate systems of adjacent moving parts. In the process of actual error modeling, most of PIGEs can be eliminated by properly setting the coordinate system of the machine tool. Similar to PDGEs, the PIGEs of each axis (e.g., X axis) can be expressed as:

$$\Delta_x = \left[\delta_{xx}(x)\ \ \delta_{xy}(x)\ \ \delta_{xz}(x)\ \ \varepsilon_{xx}(x)\ \ \varepsilon_{xy}(x)\ \ \varepsilon_{xz}(x)\right]^T$$

Errors Induced by Thermal Deformation

Under the actual working conditions of the CNC machine tool, the environmental temperature, the spindle rotation, the cutting parameters, and other factors result in some heat sources generation and generate a complex temperature field, which causes the thermal deformation of the various parts of the machine tool and results in the change in the relative position of the spindle end of the cutting tool and the table on which the workpiece is mounted. Ultimately, it results in machining errors in the part. The relative position of the spindle end and the table caused by the temperature variation is usually used as the basis for the evaluation of the thermal error of the CNC machine tool.

The research shows that the geometric error and the error caused by thermal deformation accounts for about 70% of the total error of the machine tool. In precision machining, the internal and external heat sources will generate a lot of heat, which cannot be completely absorbed by the cooling system. The residual heat

Table 2 List of PIGEs involved in kinematic chain of a precision machine (Lasemi et al. 2016)

Machine axis	Symbol of errors	Item description
Y	γ_{xy}	Angular error of Y axis around X_r axis
X	γ_{yx},	Angular error of X axis around Y axis
X	γ_{zx}	Angular error of X axis around Z axis
A	δ_{ya}	Translational error of A axis along Y_X axis
A	δ_{za}	Translational error of A axis along Z_X axis
A	γ_{ya}	Angular error of A axis around Y_X axis
A	γ_{za}	Angular error of A axis around Z_X axis
C	δ_{xc}	Translational error of C axis along X_A axis
C	δ_{yc}	Translational error of C axis along Y_A axis
C	γ_{xc}	Angular error of C axis around X_A axis
C	γ_{yc}	Angular error of C axis around Y_A axis

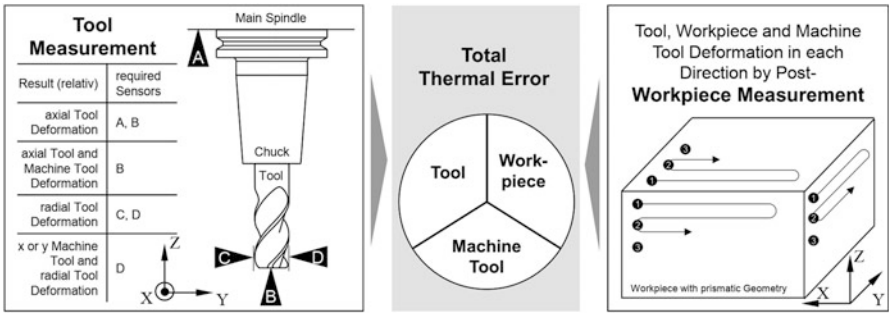

Fig. 9 Machine tool deformation caused by thermal errors (Putz et al. 2019)

will lead to the deformation of the parts of the machine tool, thereby reducing the machining accuracy, as shown in Fig. 9. Furthermore, the more precise the machine tool is, the more serious the thermal error will be (Kim and Chung 2005). When the influence of temperature change is very small, geometric error accounts for the main part of the error. Geometric error is relatively stable and easy to be compensated.

In the operation process, the machine tool temperature will be affected by the internal and external environment, resulting in temperature rise. The tool head structure will produce different degrees of thermal deformation, affecting the machining accuracy.

The heat source can be divided into two parts according to the source of internal heat source and external heat source. External heat source mainly refers to the external environment, sunlight, light, and external heating device. The internal heat source mainly refers to the heat generated by the motor, the cutting heat of the cutting tool, and the heat generated by the friction of the moving pair such as the bearing gear. The transmission parts, tools, and motors generate far more heat than other parts. Due to the narrow space between the coupling components within the tool head, the heat is generated but can't be taken away completely by the cooling system, which leads to high temperature in the head and breaks the temperature balance between head inside and outside. Different components may have different degrees of thermal deformation and eventually reduce the machining precision and generate manufacturing errors. These deformations will finally be reflected in the tip position of the cutting tool, resulting in a decrease in the machining accuracy. The interactions among different heat source elements result in complex degree of the machine tool deformation. Therefore, it is difficult to calculate the machining deviation by simply adding together all of the thermal errors generated by the individual element (Mayr et al. 2012). The influence of heat source on machine tool error is shown in Fig. 10.

Due to the different heat source intensity, distribution position, and action time as well as the different thermophysical parameters and heat dissipation conditions of each part of the machine tool, the temperature rise of each part is different, resulting

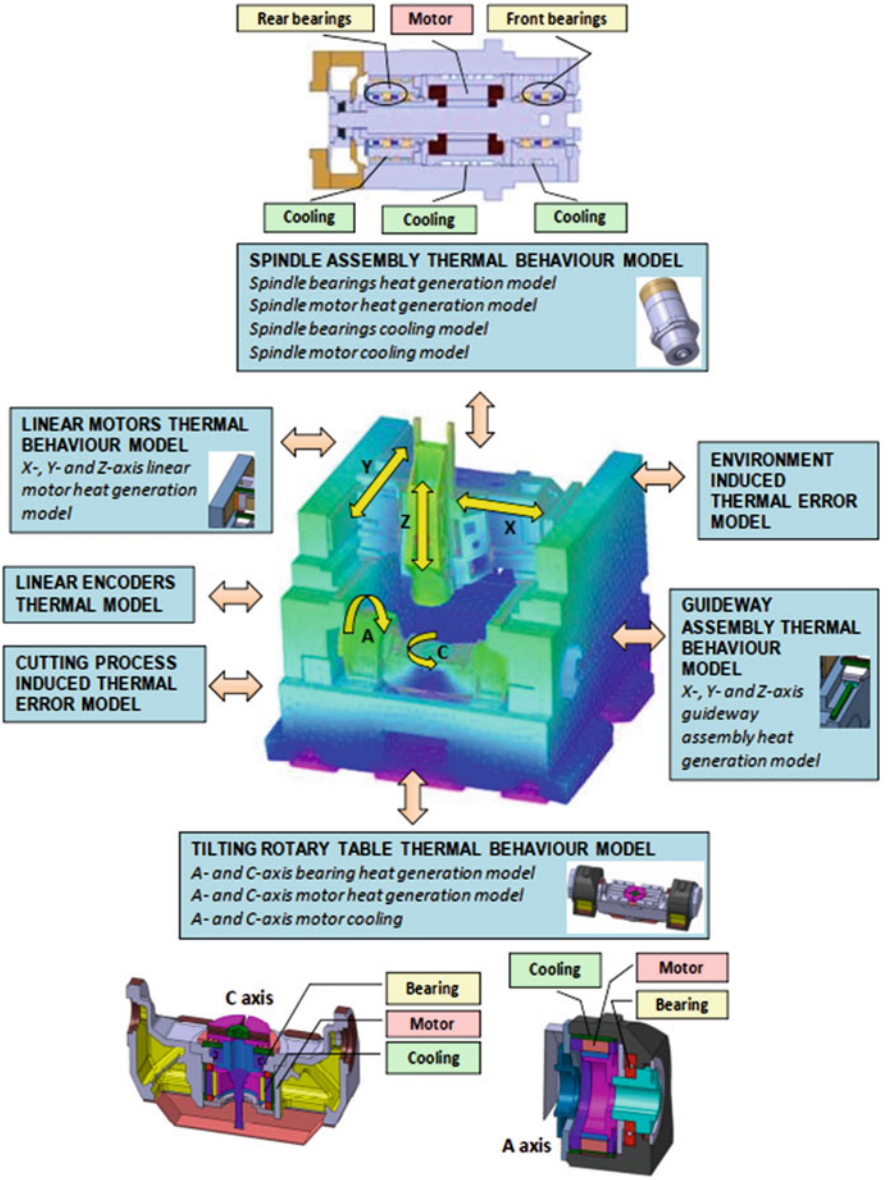

Fig. 10 The influence of thermal behavior on machine tool error (Turek et al. 2010)

in uneven distribution of thermal deformation and large thermal error. Therefore, additional heat sources can be used in the design of the machine tool to balance the temperature field, and the thermal deformation of the machine tool as a whole or parts tends to be consistent, reducing the thermal error.

At the same time, to reduce thermal deformation, we can optimize structural design so as to obtain reasonable machine tool structure design. For example, the structure and layout of large parts of the machine tool have a great impact on the thermal characteristics of the machining center. It is easy to produce torsional deformation if the single column is adopted. However, if the double-column symmetrical structure is adopted, only the translation in the vertical direction will be generated, which can be compensated easily. In addition, the machine tool elements, such as machine bed, columns, slide, gears, bearing, and so on, should be designed symmetrically so that the temperature rise of each part is even and the thermal error caused by thermal deformation will be reduced.

The main cause of thermal deformation of machine tool parts is the temperature gradient change caused by heat. Heat transfer is the basic theory of thermal deformation of machine tools. The heat transfer of machine tool is mainly composed of heat conduction, heat convection, and heat radiation (Putz et al. 2019).

Heat conduction is the main way of heat transfer of machine tool parts. From a macroscopic point of view, heat conduction is the process of energy diffusion from objects with higher temperature to objects with lower temperature. Therefore, if heat conduction occurs in the machine tool, there is a temperature difference between the parts or two parts in contact, and the heat transfer process follows the heat conduction law. The specific relationship is as follows:

$$q = \frac{\Phi}{A} = -\lambda \frac{\partial T}{\partial n}$$

where Φ is heat flux, heat pass unit area in unit time (W), A is the area perpendicular to the direction of heat flow (m^2), $\frac{\partial T}{\partial n}$ is the temperature gradient in the normal direction of area A, λ is thermal conductivity coefficient (W/(m · K)), and q is the heat flow density (W/m^2).

Thermal convection is the main form of heat exchange between machine tools and the surrounding environment. It is the transfer process of heat generated by air and the surface of machine tools and known as convection heat exchange. Thermal convection can be divided into natural convection and forced convection. For machine tool, the natural convection has static outer surface such as machine tool bed. The forced convection has cooling fan and cooling fluid. The corresponding equation can be derived according to Newton cooling theory:

$$q = hA\left(T_s - T_f\right)$$

where A is the area perpendicular to the direction of heat flow (m^2), h is the surface heat transfer coefficient (W/(m^2 · K)), ($T_s - T_f$) is the temperature difference of the object surface ($^{\circ}$C), and q is heat transfer by convection.

Thermal radiation means that an object has higher temperature than 0 K and carries out energy exchange by radiating electromagnetic waves. This process is bidirectional and the higher the temperature is, the larger the capacity of radiated heat will be. Heat transfer capacity can be calculated according to Stefan-Boltzmann law. The formula is derived as:

$$q = \varepsilon \delta A T^4$$

where A is the surface area of radiation (m^2), ε is the Stefan-Boltzmann radiation constant, T is the thermodynamic temperature of the black body (K), and δ is the emissivity of the surface and the actual surface of the object (gray body) $0 \ll \delta \leq 1$.

Figure 11 shows the map of heat transfer coefficient distribution on different machine tool elements. Heat source heating is the main reason for thermal deformation of machine tool generated by convection, radiation, and conduction. The combined effects of the internal and external heat source impose the heat transfer among the parts and components, which made the temperature of machine tools and parts rise and form unstable temperature field. It leads to the deformation of machine and the corresponding parts and eventually contributes to position deviation of the cutting tool from the target location, which affect machining accuracy of machine and surface quality of products.

The heat conduction process of machine tool is very complicated as it is limited by its own material, structure, and surrounding environment. The thermal inertia and heat capacity between the components are different, which leads to the huge complexity for form of the surface area of the thermal error distribution in the CNC machine tool. Generally, thermal error is greatly affected by its structure, for

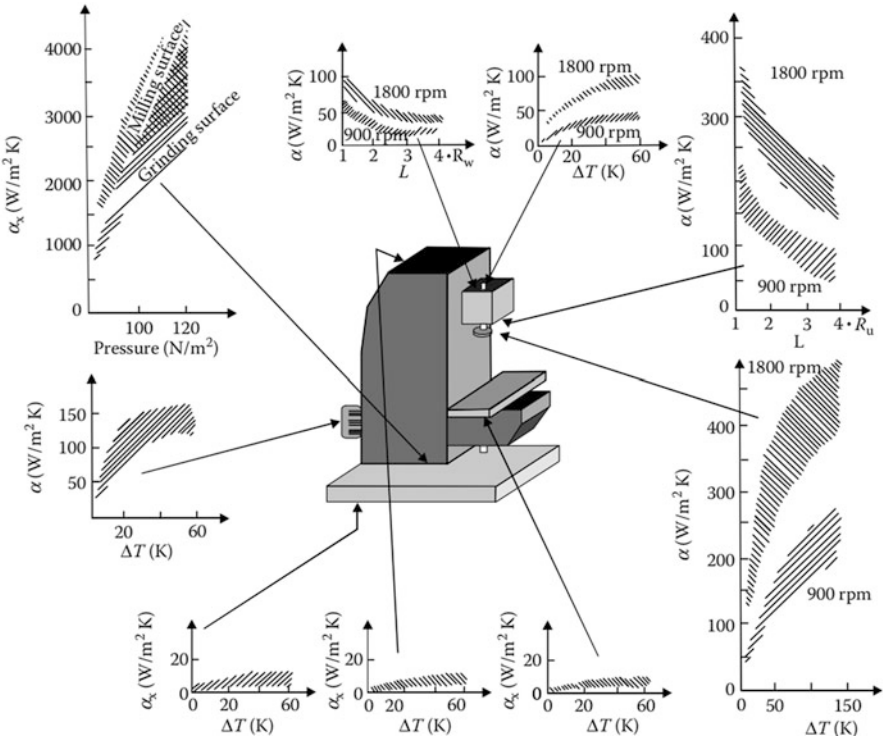

Fig. 11 Heat transfer coefficient distribution for different parts of the machine tool (Mekid 2008)

example, the machine tool spindle will appear a certain degree of warping Abbe error with the change of ambient temperature. In order to control and minimalize the thermal error, special structural and specific material design for precision CNC machine tools need to be conducted. Machine tool structure and material design aims at improvement of thermal-sensitive characteristics so that the machine tool is less affected by temperature interference, thereby reducing the thermal error of the machine tool.

The heat source of CNC machine tool mainly includes heat generated by spindle motor rotation, ambient temperature, friction heat generated between spindle and sleeve, and friction heat generated between each axis and guide rail. Among these thermal errors, the heat generated by rotational spindle and ambient temperature are the main sources of thermal deformation of spindle. The friction between the high-speed rotating spindle and the sleeve can produce considerable amounts of heat, whose distribution is determined by the shape geometry of the spindle and the ambient temperature. The heat mainly originates from the friction node and the power loss of the motor during motor rotation, bearing rotation, and guide friction and will finally contribute to the spindle elongation and bending changes. The research on thermal error mainly focuses on four aspects including the measurement of thermal error, the arrangement and selection of temperature measuring points, thermal error modeling, and thermal error compensation. High-precision measurement of temperature data is the prerequisite of thermal error modeling. The measurement of thermal error is the key step for thermal error compensation. To find out the sensitive points of thermal error of spindle, the temperature value of each point on spindle must be measured at the same time. Due to the limitation of experimental conditions, the data of the thermal error and temperature is measured when the spindle is under idle running and machining at a fixed or naturally variable ambient shop floor temperature (Mekid 2008). Due to the thermal error, the relative positions of the machine tool parts with respect to the reference position change over time with operating conditions, such as spindle rotational speed, as shown in Fig. 12. The power losses contribute to heating up and thermal deformation error, which is originated from drive system of the machine tool, such as spindle bearing, gear, motor, and so on, as shown in Fig. 13.

The thermal error modeling based on the thermal error data of machine tool is a key issue to relate each temperature-sensitive point to the respect thermal error, which serves as the purpose of analyzing its thermal performance at the precision machine design stage and can be exploited to optimize geometric structure design as well as error allocation design so as to minimize thermal errors. An accurate model provides a quantified interrelationship between power loss, heat distribution, thermal deformation, and relative position error of components consisted of machine tool. Due to many thermal processes and coupling interaction between each other for the whole machine structure elements, it is necessary to build a comprehensive model to take all those heat behaviors. The 3D finite element method (FEM) or the finite difference method (FDM) can be exploited as an advanced tool to calculate errors caused by

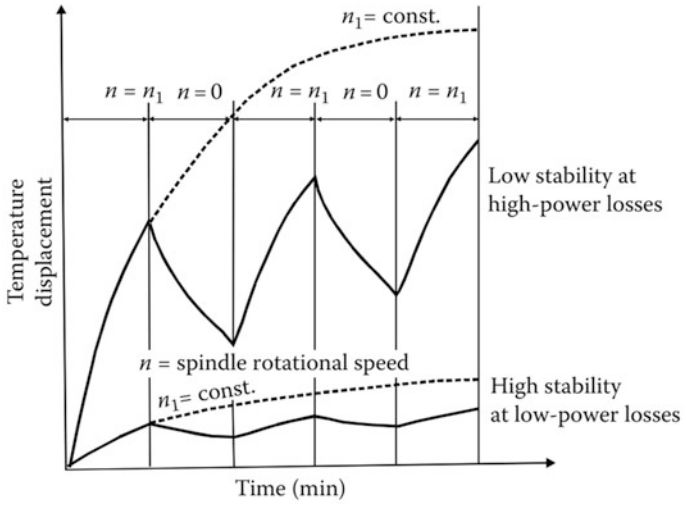

Fig. 12 Typical patterns of sharp heating changes of spindle bearings and corresponding spindle displacement at low and high machine tool thermal stability (Mekid 2008)

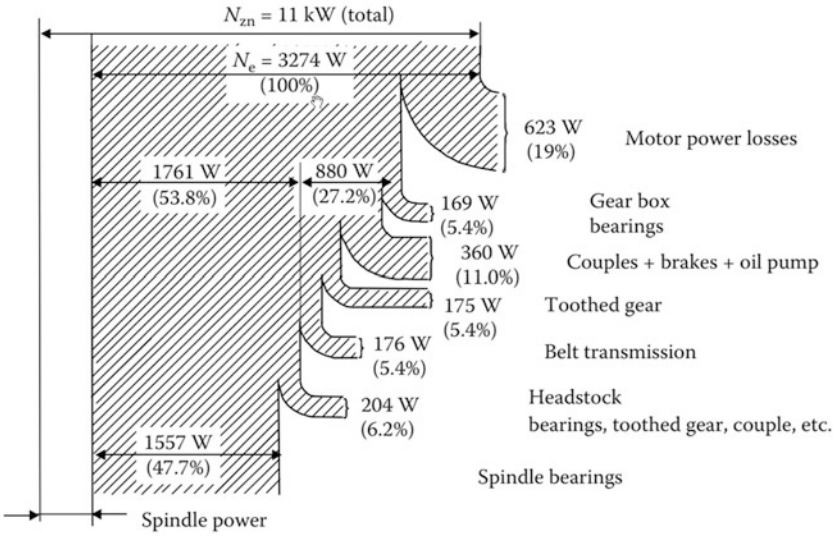

Fig. 13 Map of driver power losses for machine tool spindle (n = 1800 rpm) (Mekid 2008)

specified heat sources accurately to relate temperature field to thermal deformation error distributions under heat transfer conditions, as shown in Fig. 14. It provides a guideline for error allocation in machine tool design to minimize the influence of errors on machining accuracy.

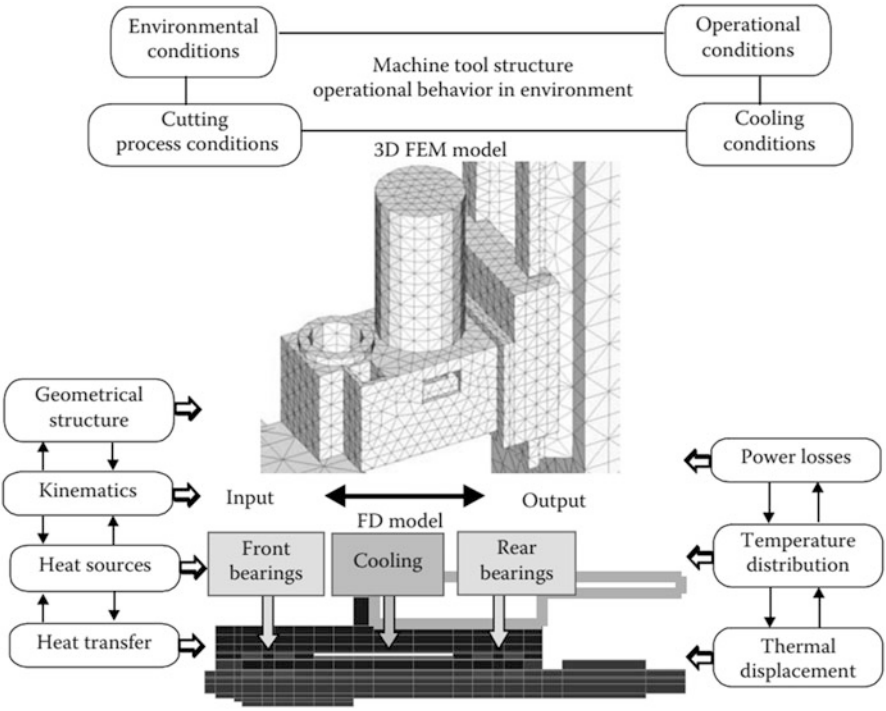

Fig. 14 3D finite element modeling of thermal and deformation distribution in machine tool (Mekid 2008)

Error Source Induced by Load

The machining accuracy is an important index to evaluate the design of machine tool. It is a key objective of machine tool design research to find out the weakness that affects machining accuracy. Load error known as stiffness error is mainly reflected in large or heavy machine tools, which stems from the machine tool itself gravity, the deformation of the machine tool caused by cutting force. Generally some standard blocks are installed on the machine tool column to determine the amount of structural deformation through online detection, and then error compensation is conducted. In machining, the cutting load results in the distortion of the process system, including machine tools, cutting tools, workpieces, and fixtures. This error causes the serious shape distortion of the processed parts, especially in machining thin-walled workpiece or using a slender tool. In the machining, the tolerance of machined surface is mainly determined by the static and dynamic behavior of the machine tool (Hamouda et al. 2016), and especially the tool vibration (originated from cutting force) deteriorates the quality of the machined surface most. There are two major types of vibration in grinding: forced and self-excited vibration (Biera et al. 1997; Liao and Shiang 1991;

Sexton and Stone 1981). In the cutting process (loading condition), CNC machine tool has a greater probability of falling into the unstable region, thus arousing vibration. It leads to the deterioration of the surface quality of the workpiece and the geometric shape error. Due to the existence of the loading force, the different positions of the load, the different shape and structure of each part, and the different constraints, various displacements errors such as tension, compression, bending, and torsion produce the relative position changes between the part and components related to the machining accuracy and inevitably lead to the deterioration of the machining accuracy of the machine tool as shown in Fig. 15. In the machine tool, supporting elements such as bearings and slideways mainly bear and transmit the load, and their elastic deformations caused by the force are relatively larger. The manufacturing error

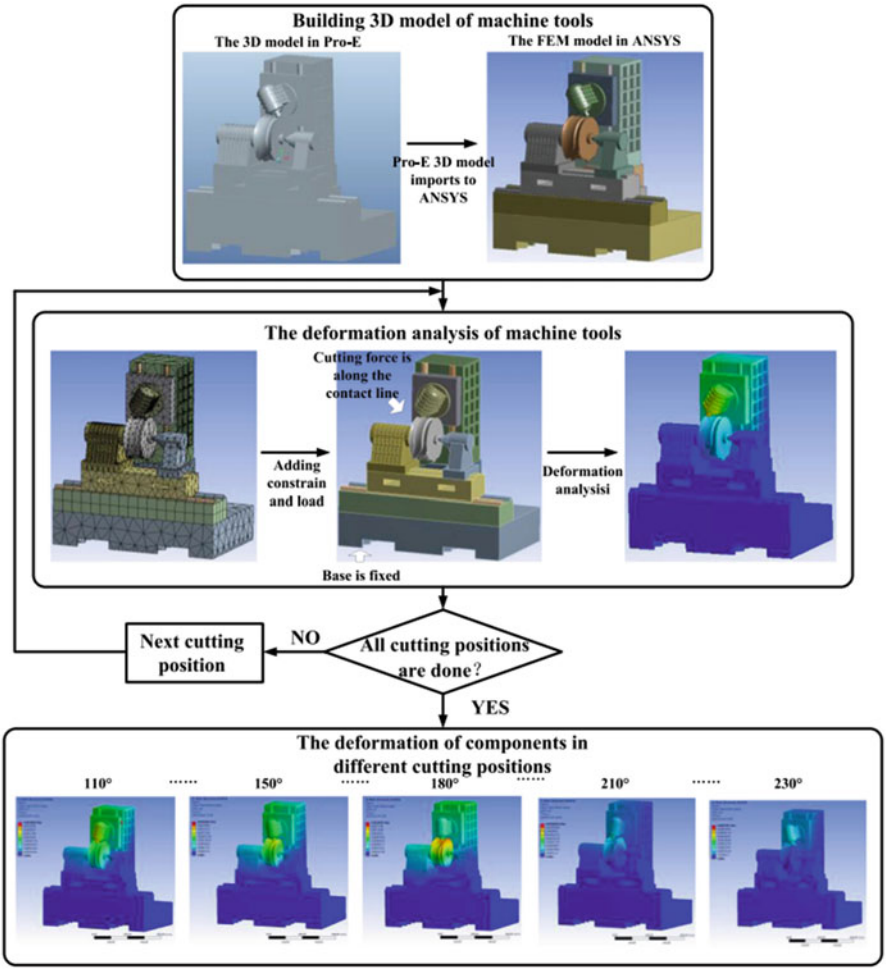

Fig. 15 Deformation error distribution of components under dynamic load (Zhao et al. 2016)

and elastic deformation of the supporting parts lead to the pose error of the parts connected with the supporting parts of the machine tool, which affects the machining accuracy of the machine tool. Therefore, robust error allocation optimization design first needs to solve the configuration error distribution of the parts connected to the supporting parts. Considering the elastic deformation of the supporting parts, it is essential to establish their error transformation matrices and obtain the error distribution among the connecting parts. Finite element method can be adopted to calculate the elastic deformation of supporting elements under different working conditions, and then the pose error distribution is obtained.

Currently, the emergence of virtual prototyping technology (VPT) brings designer and manufacturing technology into a new stage. The digital prototype model of the mechanical system is established through the systematic software platform. Through reasonable and multi-times simulation analysis, the error and deficiencies of machine design are found, and possible problems in use can be predicted. Finally, the machine performance is improved and optimized based on these output results. The appearance of VPT greatly reduces the cost and time, shortens the research and development cycle of physical prototype, and thus provides a new solution for machine tool design with large system scale, long manufacturing cycle, and high research cost. Using VPT to study the influence of dynamic load error and error allocation on the performance of expected designed machine tool can effectively improve the success rate of trial production and enhance accuracy of CNC machine tool. The advantages of VPT are illustrated in Fig. 16.

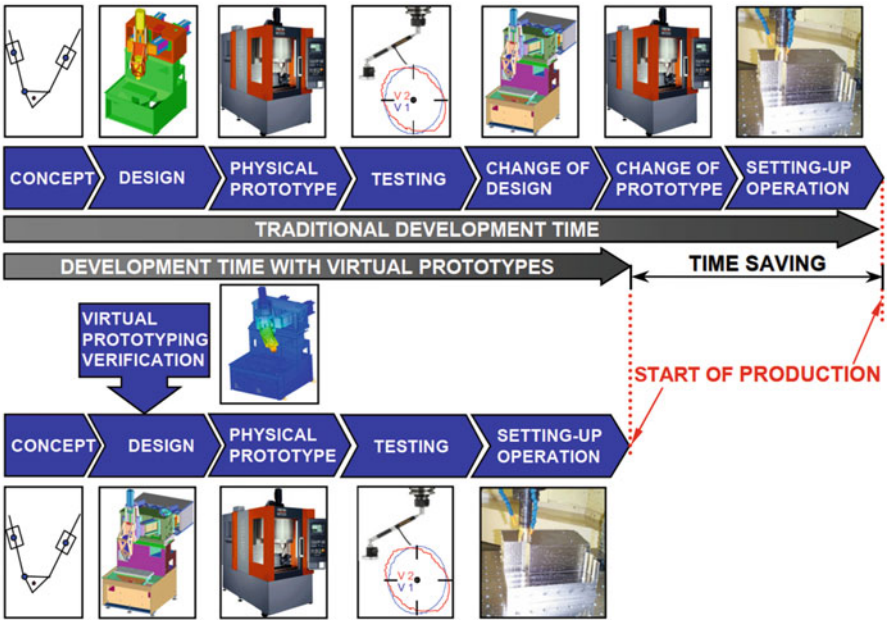

Fig. 16 The virtual prototyping technology for machine tool design (Altintas et al. 2005)

As the increasing improvement of the hardness and toughness of cutting tools, hard cutting has become a new trend in machining. Hard cutting (machine tools and tools) can solve the difficulties involving in machining hard materials with high material removal rate. At the same time, for hard cutting, it is unnecessary to conduct heat treatment for softening the surface of the workpiece before machining. However, in the process of hard cutting, great cutting force imposed on CNC machine tool will cause a certain degree of plastic and elastic deformation and lead to motion chain error of the machine tool.

At the same time, the load caused by cutting force is the major cause of machining error. Cutting force will directly lead to deformation of the machine tool process system and machining errors. It also increases the bearing's supporting and reaction force, aggravates the bearing's load condition and the bearing wear, produces thermal deformation, and leads to the reduction of processing accuracy, as shown in Fig. 17. The increase of cutting force will also aggravate the wear of the tool, making the tool lose the correct tooth shape faster. Therefore, in the precision machine design, the load (cutting force) intrigued the force deformation should be taken into account to improve machining performance.

Firstly, the design of intensity and stiffness must meet the performance requirements. Generally, parts strength is related to the parts stress, tensile, compression, bending, torsion, shear and static stress, and fatigue state under alternating stress. The machine design scheme is capable of preventing stress concentration, damage, or failure phenomenon on the body of component in accordance with the specified

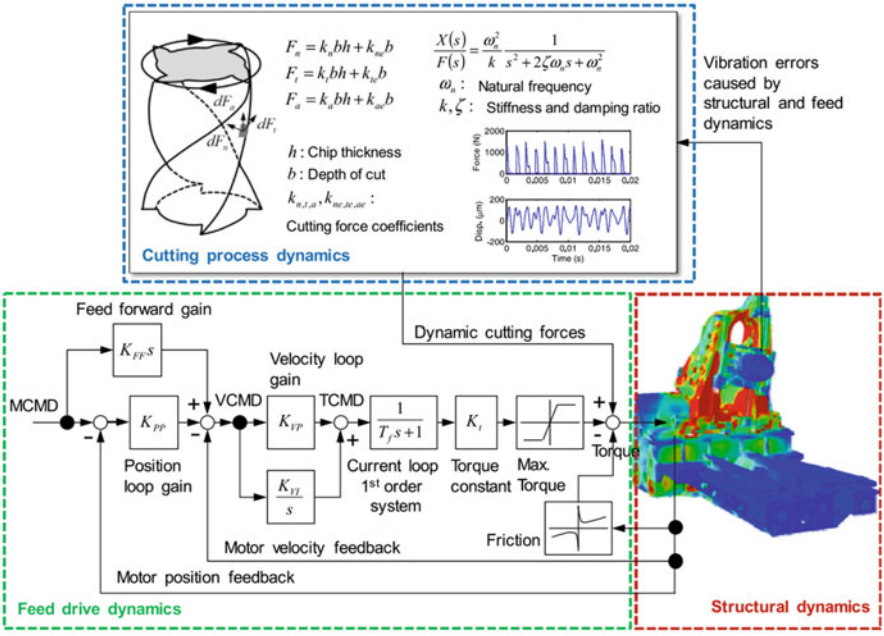

Fig. 17 Integrated error model considering dynamic cutting load (Lee et al. 2015)

materials. It needs to ensure that the maximum working stress for the structure design is less than the allowable stress of material. The stiffness index of component is the ability to resist deformation under external load, such as static, dynamic and thermal, etc. Of course, the application occasions and environments of different machines are not the same, and their emphases on stiffness index requirements are not the same. Therefore, when selecting design stiffness index, it is necessary to truly understand the working principle or weak link of the machine and put forward reasonable design index. Through the sensitivity analysis of the error, the sensitivity and influence degree of the deformation error of the machine tool caused by the load can be calculated. Then, error sensitivity coefficients are calculated and analyzed to identify the key errors that affect the machining accuracy. It provides an important theoretical basis for the design of high-precision machine tool, and the process of error sensitivity analysis is shown in Fig. 18. The error of each part accumulates into the overall space error of the machine tool, and the error elements of different parts have different influences on the overall error of the machine tool. By obtaining the sensitivity coefficient of each error element in the integrated error model, the influence degree of different error elements on the integrated error can be determined.

Therefore, the design of precision machine tool must consider the dynamic and static stiffness of the moving parts and the dynamic performance of the transmission chain. For NC machine tools with high precision requirements, the tool system should have high positioning accuracy and repeated positioning accuracy. Because many mechanical parts are involved in the kinematic chain of the machine tool, the relative motion transformation of different parts in the chain leads to the accumulation of the errors, which has a great influence on the distribution and form of errors. The effect of

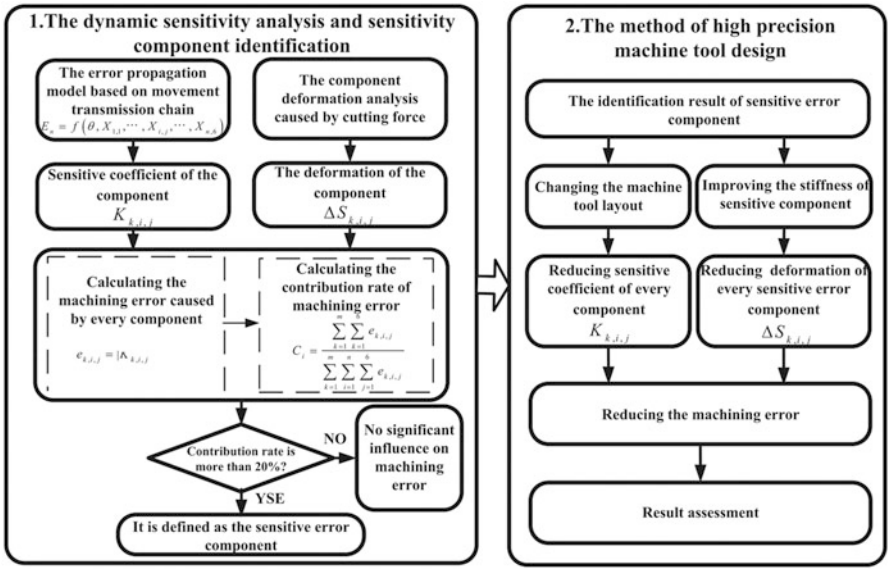

Fig. 18 The process of error sensitivity analysis (Zhao et al. 2016)

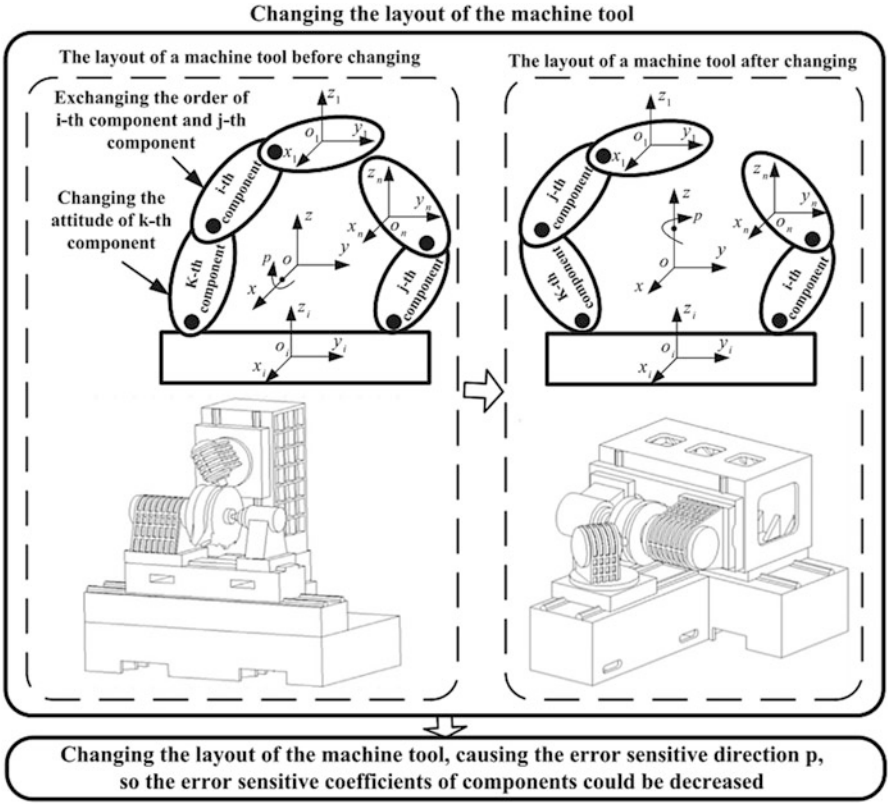

Fig. 19 Improved the layout of a machine tool to reduce the effect of error accumulation in the kinematic chain (Zhao et al. 2016)

error accumulation can be reduced by changing the machine layout, the component structure, and the length of error chain and tool chain, as shown in Fig. 19.

In order to ensure the machining accuracy, components with high stiffness should be designed to enhance the absolute stiffness of the machine tool, improve the load-carrying capacity of the large parts, and reduce the deformation caused by the load. The purpose of high stiffness design of machine tool base parts is to support accurate movement of moving parts and ensure the accuracy level of machine tool. The static stiffness of the machine tool is the ratio of the applied load to the deformation, which reflects the machine tool's resistance to deformation. For high rigidity design of machine tool base elements, it is necessary to accurately grasp the stress characteristics of base parts so as to reduce deformation errors and improve rigidity in precision machine design.

Referring to the structure and layout of machine kinematics and configuration, spindle used to hold the cutting tool or workpiece is the terminal element of the kinematic chain, which is one of the most key components of the machine. Its main functions are as below:

1. Undertakes the high-precision rotational movement of cutting tool or workpiece to improve machining accuracy
2. Provides the power and torque required for cutting within a certain speed range to ensure that the tool can efficiently remove excess material

In machine tool design, the spindle should meet the following conditions:

1. Bear the cutting force or forming force during processing.
2. Bear the additional force generated by the movement of moving parts.

After the preliminary design of the part, the manufacturing process and assembly process should be considered, and the corresponding geometric structure constraints should be added if necessary. For the precision machine, assembly error allocation and motion accuracy are important quality indicators. Assembly tolerance is the prerequisite of high motion for the machine tool, which should be designed according to the actual working conditions. As the main mechanical structure of the machine is assembled by the bed table, portal frame, guide rail, spindle box, spindle, screw, and other main parts, the assembly accuracy and movement accuracy of the whole machine are denoted as the deviation accuracy of the cutting tool relative to the table under static condition and trajectory deviation of cutting tool relative to the table at working. Therefore, in the stage of precision machine design, it is necessary to analyze the assembly accuracy and motion accuracy comprehensively, and tolerance analysis is the main method.

The main processing process is the control of machining allowance, the selection of machining datum, and the clamping and positioning of parts when they are processed. The positioning and clamping of the parts limit the freedom of the processing, and the corresponding clamping mechanism or device is used to ensure that the parts will not be affected by cutting load, inertial force load, and other factors in the process of manufacturing,

The elastic deformation (load error) of the cutting tool tip relative to the workpiece under machine tool operation should be calculated to provide data support for the static stiffness design of the whole machine. However, the displacement at the end of the actuator of the machine tool varies with the structural parameters of the actuator, the position parameters of the actuator, the external load of the mechanism, etc. Therefore, how to accurately describe the displacement vector at the end of the actuator is a key problem to realize the precise control of the mechanism action. Then, the static displacement vector model of mechanism for machine tool movement chain is established by considering the error of machine tool components and moving pairs.

The assembly quality of the designed precision machine is directly related to the error allocation design of parts. Error information, as the primary factor to ensure the rationality of mechanical structure design, must be taken into full consideration in the design stage to improve the feasibility of the design scheme. Improving the accuracy of machine parts is beneficial to enhance assembly accuracy. However, if the assembly accuracy is guaranteed by the machining accuracy of machine parts, it will bring obstacles to the processing of parts. Not only the manufacturing cost is high, but also the processing may not be done sometimes. Furthermore improper assembly method will also lead to low accuracy even if all parts meet the processing accuracy

requirements. Therefore, the quality of mechanical products and the requirements of operating accuracy ultimately rely on the assembly process, so the assembly quality of mechanical products determines the operating accuracy of mechanical products. The actual processing environment of the parts, the positioning in the assembly environment, and the deviation introduced by the fixture and other factors lead to the uncertainty of the assembly quality. Therefore, it is crucial to effectively improve the assembly accuracy of mechanical products through error allocation optimization.

Conclusion

The high-precision CNC machine tool has a complex mechanical structure, which is mainly composed of bed, column, slide plate, table, headstock, cutting tools, etc. They are combined together through different ways of connection, among which the moving parts can complete translation, rotation, linkage, and other movements. Each moving body will inevitably produce motion errors in the operation, and these errors will be transferred from one moving body to another within the machine tool kinematic chain. The "error marks" mainly originate from the deviation between the actual and ideal motion track of the tool, which will be reflected on the surface quality of machined workpiece and deteriorates the machining accuracy. The main errors in precision machine include machine tool geometric error, machine tool thermal deformation, and load errors. They lead to an integrated and complex error transfer process and a considerable challenge for error analysis and calculation. In order to improve machining precision, reasonably error allocation in the design stage should be carried out to reduce the error magnitude and accumulation in the error chain of the machine tool. Through analyzing the main error resources generated in the process of machine tool design, it is found that the optimization of the error allocation by structure design and tolerance design is critical to ensure the machining surface quality and improve the performance of the designed machine.

References

Altintas Y, Brecher C, Weck M, Witt S (2005) Virtual machine tool. CIRP Ann Manuf Technol 54(2):115–138

Aurich JC, Biermann D, Blum H, Brecher C, Carstensen C, Denkena B, Klocke F, Kröger M, Steinmann P, Weinert K (2009) Modelling and simulation of process machine interaction in grinding. Prod Eng 3(1):111–120

Biera J, Vinolas J, Nieto FJ (1997) Time-domain dynamic modelling of the external plunge grinding process. Int J Mach Tools Manuf 37(11):1555–1572

Brinksmeier E, Mutlugünes Y, Klocke F, Aurich JC, Shore P, Ohmori H (2010) Ultra-precision grinding. CIRP Ann Manuf Technol 59:652–671

Ding S, Huang XD, Yu CJ, Wang W (2016) Actual inverse kinematics for position-independent and position-dependent geometric error compensation of five-axis machine tools. Int J Mach Tools Manuf 111:55–62

Guo E, Ren N, Liu Z, Zheng X (2019) Influence of sensitive pose errors on tooth deviation of cylindrical gear in power skiving. Adv Mech Eng 11(4):1–12

Hamouda K, Bournine H, Tamarkin M, Babichev A, Saidi P, Amrou D (2016) Effect of the velocity of rotation in the process of vibration grinding on the surface state. Mater Sci 52(2):216–221
Hwang TW, Evens CJ, Malkin S (1999) High speed grinding of silicon nitride with electroplated diamond wheels, part 1: wear and wheel life. ASME J Manuf Sci Eng 121(1):32–41
Kim MS, Chung SC (2005) A systematic approach to design high-performance feed drive systems. Int J Mach Tools Manuf 45(12-13):1421–1435
Kreith FD, Goswami Y (2015) The CRC handbook of mechanical engineering: factors in precision engineering. CRC Press, New York
Lasemi A, Xue DY, Gu PH (2016) Accurate identification and compensation of geometric errors of 5-axis CNC machine tools using double ball bar. Meas Sci Technol 24:1–18
Lee KI, Yang SH (2013) Measurement and verification of position-independent geometric errors of a five-axis machine tool using a double ball-bar. Int J Mach Tools Manuf 70:45–52
Lee CH, Yang MY, Oh CW, Gim TW, Ha JY (2015) An integrated prediction model including the cutting process for virtual product development of machine tools. Int J Mach Tools Manuf 90:29–43
Liao YS, Shiang LC (1991) Computer simulation of self-excited and forced vibrations in the external cylindrical plunge grinding process. J Eng Ind 113:297–304
Mayr J, Jedrzejewski J, Uhlmann E, Donmez AM, Knapp W, Härtig F, Wendt K, Moriwaki T, Shore P, Schmitt R, Brecher C, Würz T, Wegener K (2012) Thermal issues in machine tools. CIRP Ann Manuf Technol 61(2):771–791
Mekid S (2008) Introduction to precision machine design and error assessment. CRC Press, Boca Raton, London, New York
Putz M, Regel J, Wenzel A, Bräunig M (2019) Thermal errors in milling: comparison of displacements of the machine tool, tool and workpiece. Procedia CIRP 82:389–394
Raju AS, Vaidyanathan S, Venkatesh VC (1976) Comparative performance of coated sandwich and conventional carbide tools. In: Proceeding of international conference on hard material tool technology, Pittsburgh, pp 144–156
Ramesh R, Mannan MA, Poo AN (2000) Error compensation in machine tools – a review part I: geometric, cutting-force induced and fixture dependent errors. Int J Mach Tools Manuf 40:1235–1256
Schwenke H, Knapp W, Haitjema H, Weckenmann A, Schmitt R, Delbressine F (2008) Geometric error measurement and compensation of machines-an update. CIRP Ann Manuf Technol 57:660–675
Sexton JS, Stone BJ (1981) The development of an ultra-hard abrasive grinding wheel which suppresses chatter. CIRP Ann Manuf Technol 30(1):215–218
Shi XL, Liu HL, Li H, Liu C, Tan GY (2016) Comprehensive error measurement and compensation method for equivalent cutting forces. Int J Adv Manuf Technol 85(1–4):149–156
Suto T, Sata T (1981) Simulation of grinding process based on wheel surface characteristics. Bull Jpn Soc Precision Eng 15(1):27–33
Taniguchi N (1994) The state of the art of nanotechnology for processing of ultraprecision and ultra fine products. Journal of the American Society of Precision Engineering 16(1):5–24
Tian WJ, Gao WG, Zhang DW, Huang T (2014) A general approach for error modelling of machine tools. Int J Mach Tools Manuf 79:17–23
Turek P, Jędrzejewski J, Modrzycki W (2010) Methods of machine tool error compensation. J Mach Eng 10(4):5–26
Yang JX, Mayer JRR, Altintas Y (2015) A position independent geometric errors identification and correction method for five–axis serial machines based on screw theory. Int J Mach Tools Manuf 95:52–66
Zhang SJ, To S, Wang SJ, Zhu ZW (2015) A review of surface roughness generation in ultra-precision machining. Int J Mach Tools Manuf 91:76–95
Zhao QL, Guo B (2015) Ultra-precision grinding of optical glasses using mono-layer nickel electroplated coarse-grained diamond wheels, part 2: investigation of profile and surface grinding. Precis Eng 39:67–78
Zhao LP, Chen HR, Yao YY, Diao GZ (2016) A new approach to improving the machining precision based on dynamic sensitivity analysis. Int J Mach Tools Manuf 102:9–21

Grinding and Dressing Tools for Precision Machines

9

Yunfeng Peng, Zhenzhong Wang, and Ping Yang

Contents

Introduction 234
Grinding Tools for Precision Machining 234
Superabrasives and Bonds 235
Bonds 236
Dressing Technologies for Conventional Wheels 237
Turning Dressing Method 238
Rolling Dressing Method 239
Grinding Dressing Method 240
Dressing Technologies for Superabrasive Wheels 242
Mechanical Dressing (Cup-Wheel Dressing) 243
Laser Dressing Technology 247
Electrical Discharge Dressing 252
Electrolytic in-Process Dressing (ELID) 258
Conclusion 261
References 261

Abstract

Grinding is a typical machining process which utilizes a grinding wheel consisting of abrasive grains held together with a binder material. The material removal action is done by the masses of tiny and sharp abrasives directly. Therefore, the good condition of grinding abrasives and wheel is very important to achieve good grinding performance. Thus, it is necessary to perform the conditioning (including both the dressing and truing processes) of grinding wheel. Generally, it is relatively simple to achieve the conditioning of conventional grinding wheel. But it is not the case for the superabrasive and wheels, which some novel dressing and truing methods and equipment are needed and

Y. Peng (✉) · Z. Wang · P. Yang
Xiamen University of China, Xiamen, China
e-mail: pengyf@xmu.edu.cn; Wangzhenzhong@xmu.edu.cn

Z. Jiang, S. Yang (eds.), *Precision Machines*, Precision Manufacturing,
https://doi.org/10.1007/978-981-13-0381-4_24

decisive for the high-quality conditioning of grinding wheel. In this chapter, the common abrasives and bonds used in a grinding process are roughly introduced to give a general background firstly. Then some typical conditioning methods and novel techniques for precision machining are presented, which are mechanical dressing (cup-wheel dressing), laser dressing (LD), electrical discharge dressing (EDD), and electrolytic in-process dressing (ELID), as this can provide an impressive basis for comprehension of the conditioning and preparation of a superabrasive grinding wheel in precision machining.

Keywords

Conditioning · Superabrasive wheel · Precision machining

Introduction

Grinding is one of the machining methods by using the abrasive grains to achieve high-efficiency and precision machining of mechanical components. The grinding process is achieved by a grinding wheel consisting of abrasive grains held together with special bonding material. The actual cutting points of abrasive grains act as micro-cutting tools interacting with the workpiece material. The spatial distribution and sharpness of abrasive grains over the wheel surface are very important for the grinding wheel to reach the machining results. But the morphology and shape of grinding wheel are prone to be wear and destroyed easily especially for some heavy-duty grinding operations (Marinescu et al. 2004). To keep the process capability, grinding wheel should be well prepared or conditioned prior to perform the grinding operation periodically during the course of grinding, which includes truing and dressing (Marinescu et al. 2004; Ding et al. 2017).

Grinding Tools for Precision Machining

The development and updating of the abrasive particles are very important in terms of precision grinding. If the cutting edge of the grinding wheel is easily worn and damaged, the grinding operation cannot continue without interruption. The development of diamond abrasive grains promotes the appearance of an ultrafine grinding wheel, which enables mirror grinding processing comparable to general lapping/polishing processing (Marinescu et al. 2004). Therefore, it is important to develop and popularize the super-hard abrasive (superabrasive) grains and its application widely.

The abrasive industry is largely based on five abrasive materials. There are three abrasive materials that are considered to be conventional abrasives, which are silicon carbide (SiC), aluminum oxide (alumina, Al_2O_3), and garnet (Marinescu et al. 2004). The other two, namely, diamond and cubic boron nitride (CBN), are

Table 1 Hardness of conventional abrasives and superabrasives (Marinescu et al. 2004)

Diamond	CBN	SiC	Alumina	Garnet
7000 kg mm^{-2}	4500 kg mm^{-2}	2700 kg mm^{-2}	2500 kg mm^{-2}	1400 kg mm^{-2}

termed superabrasives. There are dramatic differences in properties between conventional abrasives and superabrasives, of which the hardness on the Knoop scale is listed in Table 1.

There are many abrasive materials that can be used as cutting tools including both natural minerals and synthetic products. The used abrasives are characterized by high hardness, sharp edges, and good cutting ability. The choice of abrasive for a particular application general bases on their durability tests involving impact strength, fatigue compression strength, dynamic friability, and resistance to detachment under the influence of thermal stress (Marinescu et al. 2004; Guo et al. 2014). Hardness is the primary but not unique requirement of a good abrasive (Marinescu et al. 2004). The decision to employ a particular abrasive is based on various criteria relating to workpiece material, specified geometry, and removal conditions (Marinescu et al. 2004).

Superabrasives and Bonds

The term superabrasive usually defines two hardest abrasives, which are diamond and cubic boron nitride (CBN) (Marinescu et al. 2004). Diamond is the hardest known abrasive material. CBN is the second hardest after diamond. The abrasive composite layer on a superabrasive wheel is always limited within a thin rim or layer to reduce the usage amount of costly diamond or CBN, and this structure also helps to the design of very high-speed wheels used for high removal rates (Marinescu et al. 2004; Ding et al. 2017; Guo et al. 2014).

Diamond (Marinescu et al. 2004)

The shape of the diamond crystals can be octahedral, dodecahedral, or hexahedral. Diamond has very good cleavage parallel to the direction of the octahedron faces. Natural diamond grows mainly in an octahedral form that provides several sharp points optimal for single-point diamond tools. Natural diamond abrasives always have flaws, inclusions, and defects. Therefore, the diamond should be crushed and filtered to be bonded together into metal or electroplated bonds and form a grinding wheel before use.

Diamond holds a unique place in the abrasive industry. Being the hardest known material, diamond not only is the natural choice for grinding the hardest and most difficult materials but is also the only material that can effectively true and dress the superabrasive grinding wheels.

There are also many synthetic diamonds that can become a substitute for natural diamond. The variations of the diamond synthesis process have led to a large spectrum of different grain types, which have different friability characteristics and

a large range of applications. The synthetic diamond generally can be divided into monocrystalline or polycrystalline depending on the nucleation process and interaction between various grits that are growing within the melt. Synthetic diamond dominates wheel manufacture, but natural diamond is preferred for dressing tools and form rolls.

Cubic Boron Nitride (CBN) (Marinescu et al. 2004)

Cubic boron nitride (CBN) is an allotropic crystalline form of boron nitride almost matching the hardness of diamond. The popularity of CBN is due to its high hardness, thermal resistance, and the good chemical resistance to the ferrous alloys. CBN has no affinity for low carbon steels and has being widely employed for grinding high-speed steels. CBN has an excellent thermal stability. In addition, the boron oxide layer can create protects against further oxidation of the active layer of grinding wheel.

CBN grinding wheel can be employed to achieve the high rotating speed. But the affinity of CBN to water vapor can dissolve the protective oxide layer and creates the conditions for hydrolysis to take place with boric acid and ammonia as an output, which is sometimes thought to be a drawback to wet grinding. While in practice, wet grinding with CBN is much better than dry grinding.

Bonds

The primary function of a bond is to hold the abrasive grains as a firm whole body during the grinding process. The maximum grit retention capability is not synonymous with high performance since the bond should fulfill several functions: provide adequate grit retention to avoid the grain or bonding material will be lifted off too early (Marinescu et al. 2004). Grit friability and retention are the two most crucial factors for the grinding interface. Bond systems can be divided into two types. One is those holding a single layer of abrasive grain to a solid core hub, and the other is providing a consumable layer and many grains which is thick with the abrasive held within the bond. The latter may be produced as a monolithic structure from the bore to the outer diameter and mounted on a resilient flange and mandrel core (Marinescu et al. 2004). There are three major bond types used for all abrasives, which are (Marinescu et al. 2004):

1. **Resin Bonds**
   Resinoid diamond wheels contain a polycrystalline, low-strength, metal clad diamond grit, allowing efficient self-sharpening via partial fragmentation. An abundant supply of coolant, which is a prerequisite to achieve high grinding performance, makes the utilization of resin-bonded grinding wheels very efficient. A resin-bonded wheel will be weakened when being exposure to excessive heat.
2. **Vitreous Bonds**
   Vitreous bonds are essentially glasses made from the high-temperature sintering of powdered glass frits, clays, and chemical fluxes such as feldspar and borax.

Their attractions are their high-temperature stability, brittleness, rigidity, and ability to support high levels of porosity in the wheel structure. Vitrified alumina wheels represent nearly half of all conventional wheels and the great majority of precision high production grinding. Vitrified superabrasive technology, especially CBN, is the fastest growing sector of the precision grinding market. The nature of an abrasive depends on both the processing of the grit and the vitrification process.

3. **Sintered Metal Bonds**
   There are mainly two kinds of metal bonder used for the grinding wheels, of which one is the sintered metal bonder and the other is electroplated metal bonders. The sintered metal grinding can hold the blocky monocrystalline grit much more firmly than resin bonds. During sintering the metallic binder softens and wets the diamond grit. The excellent grit retention and the high abrasive wear resistance make the sintered metal-bonded grinding wheel much suitable for the machining of brittle materials such as glass and ceramics. One disadvantage of the sintered metal grinders is the poor capacity of self-sharpening. However, the self-sharpening of sintered metal-bonded wheel is only possible under high grinding forces. Compared with resin-bonded wheels, these high pressures are possible only with stable, stiff machine tools. A disadvantage of sintered metal bond wheels is the high sintering temperature necessary to melt the metallic phase, which leads to high manufacturing costs. Metal bonds can also be used in the dry grinding condition only in the case of small contact areas.

   As for the electroplated bonder, it is the most popular in the field of diamond grinding wheels. The diamond grains are buried by the electroplated metal within the outer rim of grinding wheel. The retention capability of grains is always poor for the electroplated diamond grinding wheel, and the diamond grains are easy to be pulled off from the electroplated metal layer. The main advantage of electroplated grinding wheel is that the electroplated grinder can rotate much faster than grinders using other bonders. Thus, the electroplated diamond grinding wheel dominates the usage of high-speed grinding and ultrahigh-speed grinding. Generally, the electroplated diamond grinding wheel doesn't need to be dressed during the grinding process because of the single-layer electroplating-bonded grains.

Dressing Technologies for Conventional Wheels

Grinding wheel should be well prepared to meet the requirement of high precision grinding before normal grinding operation (Marinescu et al. 2004; Ding et al. 2017; Guo et al. 2014). This process includes cleaning, truing, and dressing process (Marinescu et al. 2004; Ding et al. 2017; Chen et al. 2005). The cleaning operation represents the removal process of debris, worn layer, and loading at the wheel surface to recover the active grains' protrusion and distribution on the wheel surface (Marinescu et al. 2004). The truing process is the process of profiling the grinding wheel within the specified workpiece tolerances possible when the wear of the grinding wheel exceeds the allowable range (Marinescu et al. 2004). Truing must

always be performed if the wheel is rebalanced and must be performed after balancing during the course of general grinding process (Marinescu et al. 2004). Dressing aims to sharp the abrasive edges and restore the cutting efficiency of grinding wheel. Generally, a new wheel should be dressed to expose its machinability at the commencement of operation and be redressed at periodic intervals during the grinding process. The natural or synthetic diamonds are the basic component for the active cutting surface of a dressing tool. Commonly, the employed dressing techniques for conventional grinding wheel devices include turning, rolling, and grinding (Guo et al. 2010).

Turning Dressing Method

Truing method is the most commonly application method for grinding wheel dressing (Guo et al. 2010). It is performed by using a single diamond, diamond pen, diamond chip dressing tool, or abrasive block as the dressing tools to turn the grinding wheel (Marinescu et al. 2004). A layer of depth abrasive is removed from the outer radius surface during each pass of the dressing tool across the wheel face. This type of dressing motion is analogous to turning on a lathe (Chen et al. 2005). The dressing velocity equals the wheel speed, and the dressing tool cuts into the grinding wheel with a certain amount of dressing depth and moves along the axial direction of the grinding wheel with a certain dressing lead (Guo et al. 2010). The removed wheel radius each dressing time is called the thickness of the dressing layer.

Single-grain diamonds are generally ground and polished to a certain geometry. For different diameter grinding wheels, diamonds of different particle sizes should be used. The larger the size of the grinding wheel, the coarser the particle size, and the higher the hardness, also the larger the diamond should be selected (Guo et al. 2010).

The diamond chip dressing tool is sintered with small natural artificially arranged diamond particles. According to the particle size and its distribution of diamond particle in the dressing tool, diamond pens can be divided into different types of chain, layer, row, and powder (Guo et al. 2010). Because a strong bonding alloy is used as a binder, the diamond particles are not easy to detach or fall off from the dresser when dressing, which results that it needn't to be conditioned till the diamond chip dressing tool is used up. The dressing abrasive blocks usually have two types, of which one is silicon carbide and the other is boron carbide. The silicon carbide blocks are generally used to dress the diamond grinding wheel that has been previously roughly dressed or used for the tool sharpening. The hardness and particle size of dressing block are always 1–3 or 2–3 grades higher than the dressed grinding wheel (Chen et al. 2005; Guo et al. 2010). The boron carbide blocks are mainly used for the dressing of the tool sharpening wheel or the rough dressing of the internal grinding wheel.

The brittle abrasives can be effectively crushed by the hard diamond when being turning dressed; therefore, abrasives buried under the active bond layer are exposed, and/or new micro-blades are generated. The grinding wheel dressed by turning method can get much sharper edges, and the resulted abrasives can have a strong grinding ability and a long service life (Guo et al. 2010).

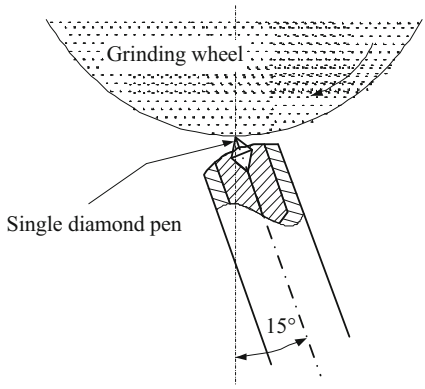

Fig. 1 Single diamond pen dressing (Guo et al. 2010)

The dressing operation by a diamond pen is a typical turning dressing method as illustrated in Fig. 1a. The dressing efficiency of single diamond pen is high. The dressing efficiency can be significantly improved for the grinding wheel surface with big shape error or being roughly dressed. The dressing tool is usually a mounted natural diamond (single-point) or a multipoint tool (cluster, nib, chisel, blade) consisting of one or more layers of diamonds set or impregnated in a metal binder (Guo et al. 2010). Single-point diamonds are usually tilted relative to the wheel with a drag angle of 10–15° as shown in Fig. 1. As being continuously used, it needs to adjust or reset the diamond pen to expose a new point edge when the exposed edge on a single-point diamond tool becomes more and more blunt.

In addition, if diamond pen is mounted higher than the wheel center, the nib of diamond pen is easy to insert into the wheel and generate unwanted vibration. Therefore, diamond pen should be mounted 1–2 mm lower than the grinding wheel center (Guo et al. 2010).

Rolling Dressing Method

Another dressing method which is especially used for generating profiles is rotary diamond dressing. A rotary diamond dressing tool consists of an axisymmetric body with diamond particles impregnated in a metal matrix or held by an electroplated metal coating on its outer surface (Marinescu et al. 2004). The rotatory roll has the same profile as that required on the workpiece, so the wheel is dressed with the reverse profile (Malkin and Guo 2008). The kinematic arrangement for traverse conditioning is similar to the external diameter grinding process, that the roller dresser contacts a strip of the rotating abrasive wheel and is traversed along its surface. Both cylindrical parts of the wheel/roller friction couple are in rotational movement with different rotational speeds. The peripheral speed of the grinding wheel, v_s, and that of the dresser, v_d, are illustrated in Fig. 2.

For most cases, the dressing roll is driven at a peripheral velocity v_r while being fed radially into the rotating wheel at an infeed velocity v_i corresponding to a depth

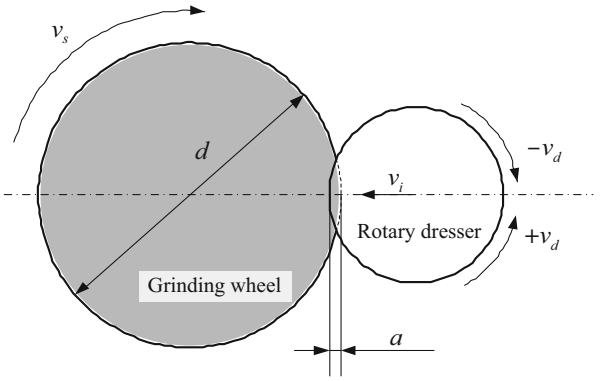

Fig. 2 Rotary diamond dressing of a grinding wheel (Malkin and Guo 2008)

per wheel revolution a_r (Fig. 2) (Malkin and Guo 2008). When the wheel speed equals the dressing wheel, the rotary diamond dressing then calls the rolling dressing method (Guo et al. 2010). Generally, the rolling wheel is driven by the grinding wheel and rotates at a low speed. During dressing, the rolling wheel applies about 3–5 Mpa pressure on the grinding wheel to smash or detach the dull abrasive on top of the active wheel layer (Guo et al. 2010).

The commonly used rolling wheels include metal roller, cemented carbide roller, and abrasive wheel (Guo et al. 2010). Metal rolling wheels are usually made of tool steel, alloy tool steel, or low carbon steel. They are mostly used for dressing grinding wheels in forming grinding, and steel rolling wheels can also be used to dress superabrasive grinding wheels. The grain size of abrasive roller should be finer than the wheel to be dressed, and the hardness should be at least two grades higher than the hardness of the processed wheel (Guo et al. 2010). The dressing of the superabrasive grinding wheel generally adopts a corundum or silicon carbide abrasive rolling wheel. When the abrasive rolling wheel and the super-hard abrasive grinding wheel are rolled each other, only the abrasive grains of the rolling wheel are broken, and the superabrasives of the grinding wheel are removed from the bonding agent, so that the grinding wheel is sharp (Marinescu et al. 2004; Guo et al. 2010).

For the rolling dressing, the rolling wheel crushes the abrasive grains of the grinding wheel or causes the abrasive grains to detach and fall off from wheel body. The cutting performance of the grinding wheel is better, and the cost is lower, but the workpiece surface to be ground is rough. In addition, the rolling wheel is easily wearied to lose accuracy, which result its service life is short. Therefore, this dressing method is mainly used for forming grinding with small batch size and low precision requirements (Guo et al. 2010).

Grinding Dressing Method

Grinding dressing belongs to the rotary diamond dressing. Different from the rolling dressing technique, the grinding wheel speed is not equal to that of the dressing wheel when dressing (Guo et al. 2010).

Grinding dressing adapts abrasive discs or diamond rollers to simulate the grinding process to dress the grinding wheel. With this arrangement, the rotary dresser appears to be in "grinding" of the cylindrical grinding wheel surface during the grinding dressing operation (Malkin and Guo 2008; Chen et al. 2005; Guo et al. 2010). The peripheral dresser velocity v_r may be in the same or opposite direction as the grinding wheel velocity at the dresser-wheel contact interface (Malkin and Guo 2008). The rotating grinding wheel is ground by the self-rotating motion and the axial movement of the grinding wheel or the diamond roller. As illustrated in Fig. 3, the dressing wheel breaks the abrasive grains on the grinding wheel surface with its sharp edges, and the dressing abrasive on the wheel circumferential surface then dresses the grinding wheel, so that the abrasive top on the working grinding wheel surface is smoothed. Prior to retracting the dressing tool, its infeed may be deliberately or unintentionally stopped (dwell), which is analogous to "spark-out" grinding with single-point dressing (Malkin and Guo 2008).

Other less-used profile dressing methods include diamond block dressing and crush dressing (Malkin and Guo 2008). With diamond block dressing, the rotating wheel is traversed along a fixed diamond impregnated block having the required workpiece profile. Crush dressing is a fast operation using a crushing roller to open a wheel, reduce grinding forces, and increase productivity. With crush dressing, the wheel is usually forced under pressure into a hardened steel or cemented carbide axisymmetric crush roll mounted on bearings. In order not to grind away the roll, the rotational speed of the wheel during crush dressing is slowed down to only a few percent of the normal wheel velocity. The crushing process is performed at intermediate values of peripheral roller speed and at relatively high contact pressures. Crush dressing is not a process used in precision grinding (Chen et al. 2005).

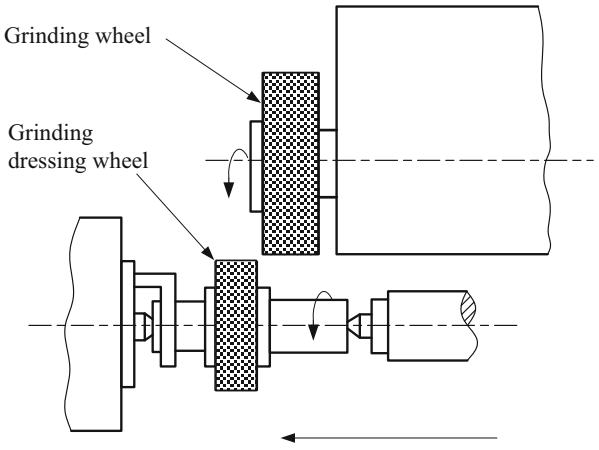

Fig. 3 SiC grinding wheel dressing wheel (Guo et al. 2010)

Dressing Technologies for Superabrasive Wheels

Superabrasive wheels are ultra-wear-resistant (Guo et al. 2014; Malkin and Guo 2008). Therefore, the truing and dressing of superabrasive wheels should be paid extra care and attention to gain a long wheel life and high process productivity (Guo et al. 2010). The truing and dressing of conventional abrasive grinding wheels can be carried out at the same time, but it is always not the case for bonding loose superabrasive grinding wheel (Marinescu et al. 2004). Truing and dressing can both be performed simultaneously in the same process for vitrified wheels or CBN grinding wheel, while it can be conducted separately for the bonded compact superabrasive grinding wheel, such as resin or metal bond diamond grinding wheel, etc., (Marinescu et al. 2004). The dressing quality of the grinding wheel heavily depends on the dressing tools and dressing conditions, which also has a direct impact on not only the surface shape of the grinding wheel and the sharpness of the cutting edge. The dressing result of grinding wheel then affects the wear of the grinding wheel, grinding force, and grinding temperature, which finally determines the surface integrity of the machined workpiece (Guo et al. 2010).

The superabrasive grinding wheel can still be trued by single crystal diamond pen, diamond roller, and grinding method (Guo et al. 2010). In addition, there is a soft steel grinding truing method, by which a soft steel roller is used to grinding dress the wheel and active abrasive. There are also many methods for dressing the superabrasive grinding wheel, such as free abrasive squeezing dressing (Chen et al. 2005), jet dressing (Cai et al. 2009), grinding dressing, electrolytic dressing (Rahman et al. 2009), etc.

The free abrasive extrusion dressing method injects the pressured mixtures of green silicon carbide or corundum abrasive grains into the narrow gap between the grinding and dressing wheel, of which the gap is about several tens of micrometers (Ding et al. 2017; Malkin and Guo 2008). The free abrasive particles are rolled between the grinding wheel and the dressing roller, so that the abrasive grains of the grinding wheel are exposed on the surface of the bonding agent to form a sharp cutting edge. The jet dressing method uses compressed air to spray abrasives, such as silicon carbide or corundum abrasive grains, onto the surface of a rotating superabrasives grinding wheel and thus removes the bonding agent between the abrasive grains to dress the grinding wheel (Ding et al. 2017). When dressing, the nozzle has an angle of inclination with respect to the grinding wheel. The silicon carbide or corundum grinding wheel can also be used for shaping and dressing. Electrolytic dressing is only suitable for dressing the metal bond superabrasive grinding wheel (Marinescu et al. 2004; Ding et al. 2017). The disadvantage of electrolytic dressing is that the bonding agent will locally dissolve and erode during the electrolysis process if the electrolysis parameters are not properly controlled; therefore, the bonding force is weakened, and the durability of the grinding wheel is then reduced (Marinescu et al. 2004).

In recent years, the high precision dressing technology of superabrasive grinding wheel has been greatly developed and widely applied except the conventional superabrasive wheel dressing methods, such as electric spark dressing, electrochemical dressing, contact discharge dressing, ELID online electrolytic dressing,

cup-shaped grinding wheel dressing, laser dressing techniques, etc. (Guo et al. 2010). However, because of the accuracy and efficiency, some dressing methods, such as jet pressure dressing, elastic dressing of abrasive belts, ultrasonic vibration dressing, etc., are rarely used in conditioning of diamond grinding wheels (Marinescu et al. 2004; Guo et al. 2010). The characteristics of existing dressing methods, which are based on dressing factors of abrasive grain state, shape accuracy, surface roughness, and dressing efficiency, are compared as shown in Table 2.

Hereafter, several dressing technologies for precision/ultra-precision grinding, such as mechanical dressing (mainly about the cup-wheel dressing method), laser dressing (LD), electrical discharge dressing (EDD), and electrolytic in-process dressing (ELID), are briefly introduced and compared.

Mechanical Dressing (Cup-Wheel Dressing)

Cup-wheel dressing technology was first put forward by Professor Katso Syoji at Tohoku University, Japan, who uses a GC (green silicon carbide grain) cup-wheel to dress the grinding wheel (Syoji 1993). During the process of cup-wheel dressing, the green silicon carbide grains fall off from the cup-wheel and form a direct impact to the diamond grits and binder of grinding wheel, and thus the grinding wheel is dressed (Syoji 1993). Cup-wheel dressing technique can realize the operations of both dressing and truing at the same time. But a special dressing device should be developed for the cup-wheel dressing method.

Table 2 Dressing method comparison of diamond grinding wheels (Guo et al. 2010)

Dressing types	Dressing accuracy	Surface roughness	Abrasive state	Dressing efficiency	Remarks
Single crystal diamond pen	Low	Large	Broken	High	None
Rotating diamond wheel	Low	Large	Broken	High	None
Wire electrical discharge dressing	Moderate	Moderate	Good	Moderate	Suitable for metal-bonded grinding wheel
Electrical chemical dress	Moderate	Moderate	Good	Moderate	Suitable for metal-bonded grinding wheel
Electrical discharge dressing	Moderate	Small	Good	Moderate	Suitable for metal-bonded grinding wheel
Electrolytic in-process dressing	High	Small	Good	Moderate	Suitable for metal-bonded grinding wheel
Cup-wheel dressing	High	Small	Good	Low	None
Laser dressing	High	Moderate	Good	Moderate	None

Dressing Characteristics of Cup-Wheel Dressing

Figure 4 schematically shows an illustration of GC cup-wheel dresser's structure (Syoji 1993). The end face is the cup-wheel's working part, which is driven to rotate by a speed regulating motor through a transmission belt wheel. The dresser can be set and fixed on the magnetic worktable of a machine tool, and the GC cup-wheel spindle should be vertical to the machine tool's worktable. In addition, the perpendicular of cup-wheel spindle to worktable can be adjusted and corrected by the regulating screw on the dresser and other related measuring instruments.

Principle of Cup-Wheel Dressing for Arc Diamond Wheel

With the cup-wheel dressing technology, the diamond grinding wheel can be dressing and truing simultaneously, and this can achieve a dressed wheel section with very high straightness (Guo et al. 2010; Syoji 1993). If this dressing characteristic can be effectively used, arbitrary convex sections can be dressed, and it is also easy to achieve high shape precision grinding wheel. On this basis, the principle of cup-wheel dressing for arc diamond wheel is shown in Fig. 5, of which the dresses arc diamond wheel only rotates and the self-rotating cup-wheel dresser swings and feeds to perform the dressing operations. In addition, the reciprocating motion is provided by the worktable of a machine tool.

Figure 6 is the geometric structure of a cup-wheel dresser for dressing an arc diamond wheel. The mutual relationship of different parts is (Guo et al. 2010):

①. The dresser should ensure the dressing accuracy of the arc radius R of the grinding wheel, that is, the swing center O_2 should be in the same plane with the rotation axis O_1 of the wheel. The distance between swing center O_2 and the dressed surface of the grinding wheel should equal to R.

②. During dressing, the reciprocating motion parameters should avoid geometrical interference. In order to realize the high precision dressing, the design accuracy of the dresser should be properly controlled, such as the end and radial runout of dressing wheel. Also the parallelism between the wheel end face and the dresser base should also be considered.

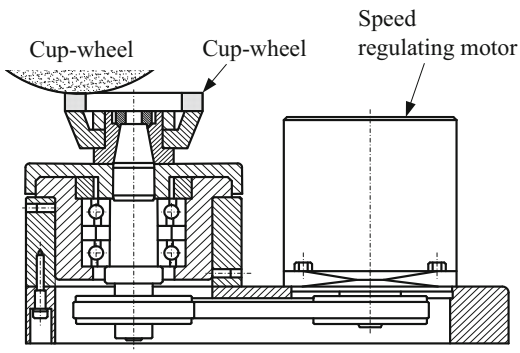

Fig. 4 Schematic illustration of GC cup-wheel dresser (Syoji 1993)

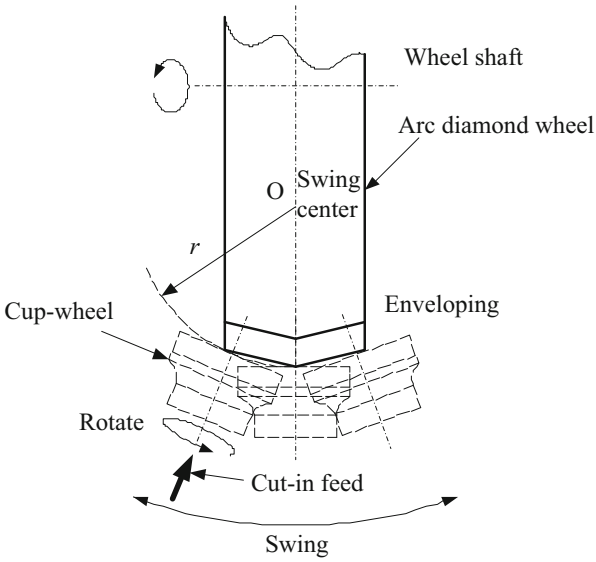

Fig. 5 Principle for dressing an arc diamond wheel (Syoji and Piao 1991)

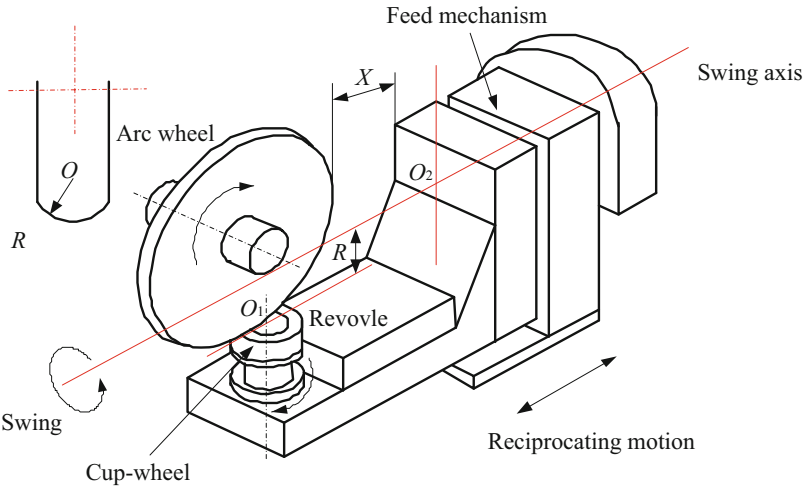

Fig. 6 Geometric structure of a cup-wheel dresser (Guo et al. 2003)

The structure of this cup-wheel dresser is much simple and easy to manufacture for industry. Furthermore, the dressing zero position is also can be directly determined. However, due to the horizontal arrangement between the dressing wheel and the diamond wheel, the contact arc length between the dressing wheel and the diamond wheel is short, and thus the surface error of the dressing wheel is an arc-shape distribution. According to the dressing principle of the cup-wheel dresser for

the arc wheel, the following two parameters of the dresser should be optimized to improve the dressing accuracy, which are (Guo et al. 2010):

①. Try to increase the contact arc length between the dressing wheel and the diamond wheel as far as possible, which helps to improve the dressing efficiency and obtain a good surface error distribution.
②. Design a reasonable dressing hysteresis rate. Since the cup-wheel dressing uses a linear enveloping method, for arc wheel dressing, the dressing hysteresis rate should be set reasonably, that is, controlling the dressing track points of forward dressing position and reverse dressing position not to coincide, which is conducive to improving dressing efficiency and accuracy.

Two-Axis Cup-Wheel Dresser (Guo et al. 2010)

The design of a cup-wheel dresser should take the dressing of both the flat and arc grinding wheel into consideration. Therefore, a two-axis control for the cup-wheel dresser is required. Here, an example of two-axis cup-wheel dresser is given.

As shown in Fig. 7, the specific structure scheme of the two-axis cup-wheel dresser for surface grinding machine is mainly composed of cup-wheel dressing unit, swing and control unit, dressing feed and control unit, inclination and control unit, single diamond pen dresser, and other parts.

The dressing experiment of a flat diamond wheel was carried out using the cup-wheel dresser developed. The cup-wheel is GC abrasive wheel with particle size of W63, and the dressed flat diamond grinding wheel is #600D91. The dressing speed of diamond grinding wheel V_s is 191 rpm, speed of GC cup grinding wheel V_w is 480 rpm, reciprocating speed provided by machine table V_x is 200 mm/min, amount of dressing feed is 0.02 mm, and total amount of Y-direction dressing is 2 mm. To examine dressing effect, a D91 flat diamond wheel was used to grind the optical glass with Φ100 mm in diameter, respectively, before and after dressing. The grinding speed of X-axis V_x is 4500 mm/min, the speed of Z-axis V_z is 120 mm/min, the dressing feed is 0.02 mm, and total amount of grinding is 0.1 mm. Figure 8 shows

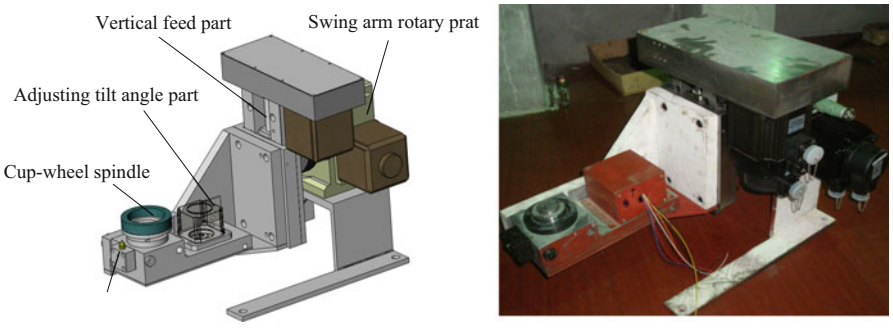

(a) Design of two-axis cup-wheel dresser (b) Dresser devices

Fig. 7 Two-axis cup-wheel dresser. (**a**) Design of two-axis cup-wheel dresser. (**b**) Dresser devices

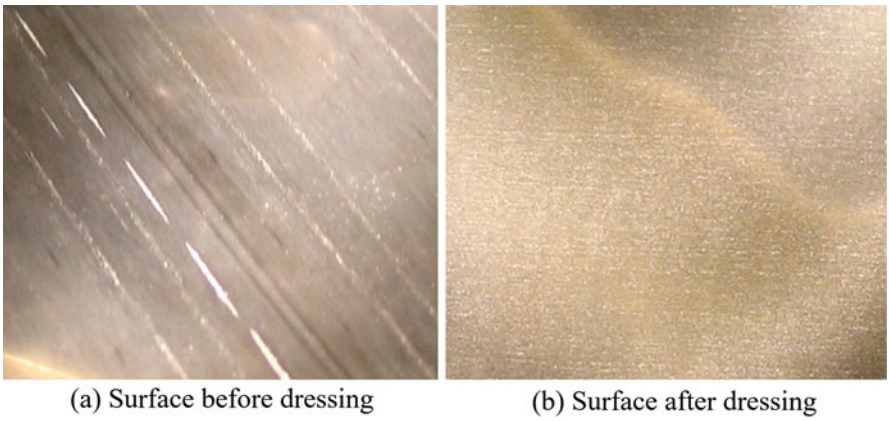

Fig. 8 Experiment of flat diamond wheel dressing (Guo et al. 2010). (**a**) Surface before dressing. (**b**) Surface after dressing

the enlarged comparison of grinding effect of diamond wheel before and after dressing. It can be seen intuitively that the grinding surface quality before dressing has many deep scratches and irregular distribution, which is obviously worse than the grinding quality of the dressed wheel by cup-wheel dressing. From a macroscopic view, the effectiveness and the improvement of grinding performance of the cup-wheel dressing device are verified.

Laser Dressing Technology

Principle of Laser Dressing Technology

Laser has many advantages, such as good monochromaticity, strong directivity, concentrated energy density, and good coherence. The energy of infrared photon acts on the solid matter and excites the electron to vibrate because of collision, therefore causing the temperature of the irradiated object getting rise, melting or vaporizing, and then changing the microstructure of the material (Ding et al. 2017). Thereby various processing effects are produced. Laser dressing technology was first proposed by Westkaemper in 1995 for the dressing and truing of resin-bonded CBN grinding wheels (Westkaemper 1995). Till now, laser dressing and laser-assisted dressing techniques have been intensively utilized for truing diamond wheels profiles and sharping the active abrasives on the dressed wheels' surface.

Figure 9 illustrates a basic principle of laser dressing (Hosokawa et al. 2006). Laser dressing uses an optical system to focus the laser beam into a very small spot on the surface of the grinding wheel, by which the material on the surface of the grinding wheel can be heat to melt or vaporize in a very short time. During the same laser action time, the laser power required to reach the melting point of the superabrasive material is several orders of magnitude higher than that of the binder

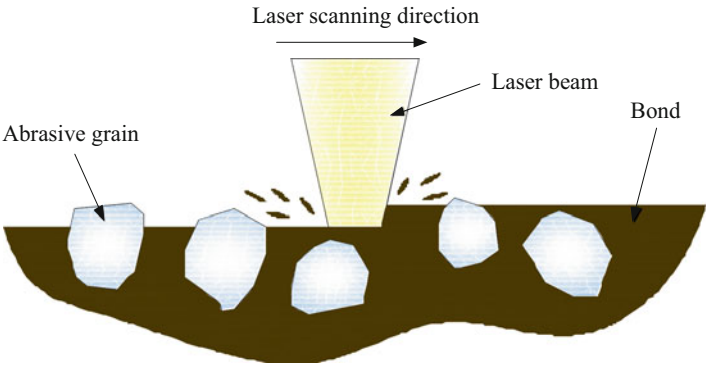

Fig. 9 Principle of laser dressing (Hosokawa et al. 2006)

material due to the large difference in physical properties between the superabrasive and the binder material (Ding et al. 2017). By controlling the laser processing parameters, it is possible to selectively remove the amount of the binder material without damaging the superabrasive grains, causing the abrasive grains to protrude, and forming a chip space on the surface of the grinding wheel, thereby achieving the sharpening purpose of superabrasive (Ding et al. 2017). When the superabrasive grinding wheel is dressed by laser, if the laser power density is high enough, the abrasive particles and bonding agent on the surface of the grinding wheel can be removed at the same time. By controlling the motion parameters of the grinding wheel, the grinding wheel can obtain its precise geometric shape and achieve the purpose of shape modification. In theory, the grinding wheel of various abrasives and bonding agents can be dressed by the laser action on the entire surface of the grinding wheel (Ding et al. 2017).

Generally, laser dressing has several advantages over conventional dressing techniques, such as no tool wear, good machinability of target materials, limited coolant pollution, high possibilities and flexibilities to create geometries with small dimensions or complex shapes, and ease to automation. However, appropriate selection and adjustment of laser dressing parameters and methodologies are essential for the protection of wheels from burning (Ding et al. 2017).

Figure 10 schematically illustrates an apparatus used for the radial dressing of bronze-bonded diamond wheels with a pulsed laser (Deng et al. 2014a). In this case, a compact pulsed Yb-doped fiber laser, whose distribution of the laser energy output is approximately Gaussian, was used to transmit the laser beam to the ablation head with a standard isolator fixed on a two-dimensional motorized translation stage. The beam strikes the grinding wheel surface perpendicularly, and a gas nozzle was used for auxiliary lateral blowing to remove any molten sputter produced in the laser-ablated area and to simultaneously cool the area, thereby reducing the layer of deteriorated diamond grains on the grinding wheel surface and the effect of thermal stress-induced cracking (Hosokawa et al. 2006).

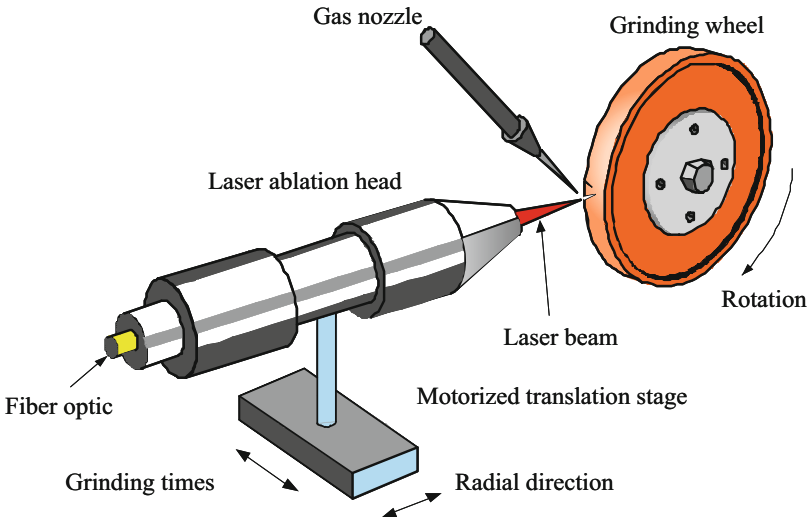

Fig. 10 A schematic of an apparatus used for pulsed laser dressing (Deng et al. 2014a)

Some Issues in Laser Dressing

The first issue worth mentioning about in laser dressing is the phase explosion. It is thought that phase explosion may take place during the laser dressing process of grinding wheel as shown in Fig. 11 (Cai et al. 2015). When the bond approaches the critical state of the phase explosion, the ablation depth is inconsistent and may form a negative effect on laser dressing. This ablation inconsistency might be explained as follows (Ding et al. 2017): When the phase explosion happens, the liquid internal pressure within the splashing bronze liquid will increase, resulting in a sudden violent outward ejection of liquid drops from the liquid surface. The rapid transfer of liquid mass results in a sudden rapid increase in ablation depth, which could lead to the blockage of the crater around the diamonds and reduces the chip space next to the diamonds. Therefore, the diamond protrusion height above the bond is insufficient to achieve the desired goal of dressing the bronze-bond grinding wheel (Deng et al. 2014b).

The second issue is the laser shooting directions in laser dressing. Generally, most of the laser truing or dressing operations directly shoot the laser beam on the wheel surface along the wheel's radial direction (Ding et al. 2017). This shooting strategy may result in several difficulties including not only (i) correct the contour error (e.g., roundness error), or obtain required dimension accuracy of the grinding wheel, but also (ii) properly control the laser ablation depth (Ding et al. 2017). To overcome these issues, Deng (Deng et al. 2014b) and Chen (Chen et al. 2015) presented an online tangential laser profiling method for coarse-grained bronze-bonded diamond wheels. As illustrated in Fig. 12, a laser beam, which is controlled by a multi-axis numerical control system, is set along in the tangential direction of the wheel working surface, by which the redundant diamond grains and bond located outside

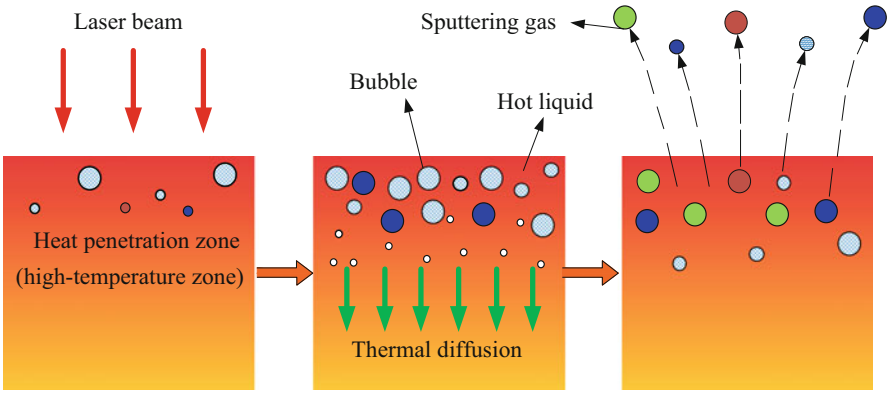

Fig. 11 Schematic diagram of phase explosion in laser dressing (Deng et al. 2014b)

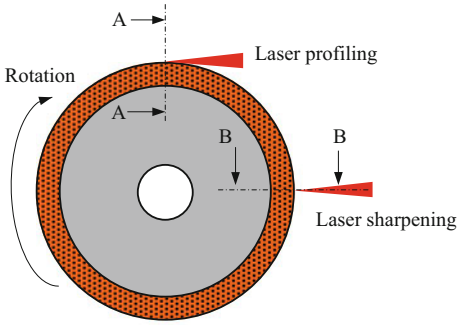

(a) action of laser beam projected from radial or tangential direction

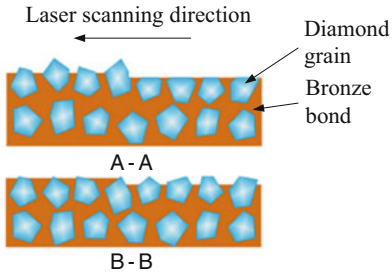

(b) wheel surface after laser dressing with different directions

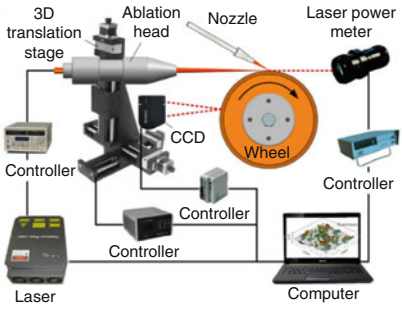

(c) online tangential laser profiling system

Fig. 12 Schematic of laser dressing of diamond wheels from radial or tangential directions (Deng et al. 2014b; Chen et al. 2015). (**a**) Aaction of laser beam projected from radial or tangential direction. (**b**) Wheel surface after laser dressing with different directions. (**c**) Online tangential laser profiling system

the specified profile of the grinding wheel then can be correctly removed. The grinding wheel can be fed forth and back to laser beam if the efficiency of laser ablation is found low until the desired profile accuracy is reached.

Laser-Mechanical Hybrid Dressing

The wear of diamond dresser is a big problem in mechanical dressing technology. By combining with laser-assisted dressing method, the wear of diamond dressers can be effectively reduced so as to achieve a desired contour of wheel surface in mechanical dressing. The method combining the mechanical diamond dresser and laser dressing is called the laser-mechanical hybrid dressing, which could have more superior dressing performances in terms of truing efficiency, accuracy, dresser wear, dressed wheel profiles, and specific forces, in comparison with conventional mechanical dressing method (e.g., single diamond dressing) (Zhang and Shin 2002). Figure 13a illustrates the principle of the laser-assisted truing and dressing method (Zhang and Shin 2002). A focused laser beam is set above a diamond dresser, of which the dresser is a little behind the focused laser spot along the axial direction of the wheel surface. With the heating of focused laser beam, the vitrified bond of the wheel is softened or even molten to facilitate the brittle vitrified bond material to be ductile removed by properly selecting the laser heating parameters and dressing conditions, which thereby the surface quality and the wear of dressing tools can be effectively improved. Figure 13b shows a conceptual thermal model of the laser-assisted truing and dressing process (Zhang and Shin 2002).

With the assistance of laser, a much deeper cut depth for laser-assisted dressing, which is apparently larger than that of conventional mechanical dressing, can be adopted because of the laser heating effect, which of course increases the dressing efficiency to achieve the required levels of out-of-roundness (Zhang and Shin 2002). Moreover, the wear rate of the diamond dresser in laser-assisted truing was shown to be much slower than that in mechanical truing (Ding et al. 2017).

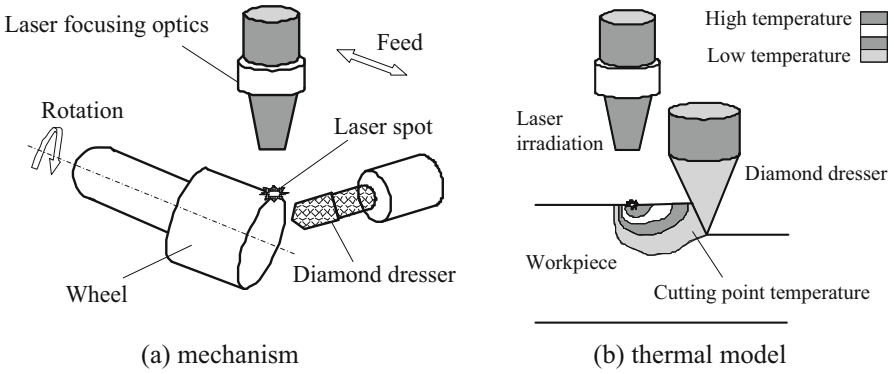

Fig. 13 Laser-assisted truing and dressing (Zhang and Shin 2002). (**a**) Mechanism. (**b**) Thermal model

Electrical Discharge Dressing

Electrical discharge dressing (EDD) is a precise, simple, and low-cost technology to true and dress metal-bonded diamond grinding wheels (Ding et al. 2017). This method was put forward by Suzuki et al. in 1987 (Suzuki et al. 1987). EDD uses the electrical and thermal erosion phenomenon of the pulse spark discharge occurring between the diamond grinding wheel and the tool electrode, and thereby the metal bond on the surface of the diamond grinding wheel is etched and washed away to achieve the purpose of shape modification and abrasive sharpening (Ding et al. 2017). Figure 14 schematically illustrates a setup of the electrical discharge dressing techniques (Guo et al. 2010). The EDD operation can be conducted at time when the grinding is in process, which is also called the online dressing. The grinding fluid can be directly used as the working fluid for dressing. In addition, the dressing force in EDD is small, and the small diameter and the extremely thin grinding wheel can also be dressed by EDD (Ding et al. 2017). EDD is suitable for the dressing of all grinding wheels with metal bond. If graphite powder is added to the bonding agent, it can also be used for resin and ceramic bond grinding wheel (Guo et al. 2010). For the time being, the EDD technique has been successfully applied to generate the precise form of metal bond diamond wheels using either the dies ink or wire electrical discharge machining (EDM) configuration (Zhang and Shin 2002; Suzuki et al. 1987; Kunieda et al. 2005).

Mechanism of Electrical Discharge Dressing

Generally, the electrical discharge dressing can be divided into contact EDD and noncontact EDD as illustrated in Fig. 15. The principle of noncontact electrical discharge dressing is schematically illustrated in Fig. 16 (Xu et al. 2012). Just like the electrical discharge machining, a voltage is applied between the tool electrode

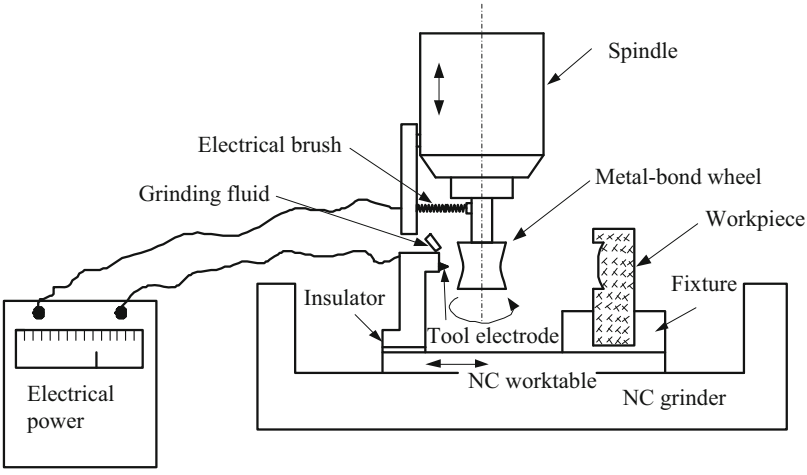

Fig. 14 Illustration of electrical discharge dressing (Guo et al. 2010)

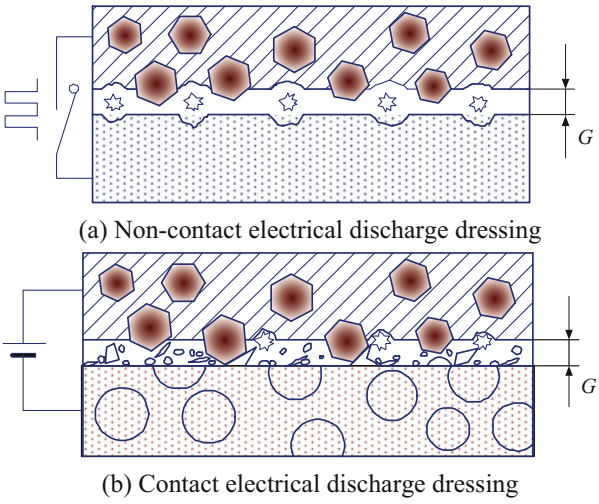

Fig. 15 Mechanism of electrical discharge dressing (Xu et al. 2012). (**a**) Noncontact electrical discharge dressing. (**b**) Contact electrical discharge dressing

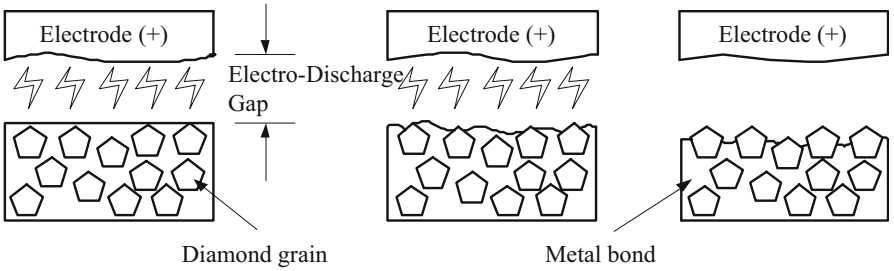

Fig. 16 The process involved in EDD a metal-bonded diamond grinding wheel (Xu et al. 2012)

and the grinding wheel that closely immersed inside a tank full of dielectric medium. When the electrodes approach to each other closely, the gap between them may be electrical arc breakdown, and an electric spark discharge then occurs to form a plasma channel between the cathode and the anode. Therefore, the molten and vaporized materials can be washed away off from the active surface of the grinding wheel by the dielectric fluid accompanying the collapses of the spark.

In EDD, the electrical discharge doesn't happen on the superabrasives and only occurs in the gap between the tool electrode and conductive metal bond among abrasives, therefore the metal bond surrounding abrasives is removed by amassed erosion, and the abrasives still stick to the grinding wheel surface (Ding et al. 2017). This selected removal process is of great importance for grinding since the dressing process has to provide the grinding wheel with sufficient grain protrusion and chip space, which is important for collecting ground chips and improving the cutting fluid transportation through the grinding zone (Weingartne et al. 2012). In addition, because diamonds are electric insulators, the EDD process can effectively remove electrically conductive bond materials and is little or even no thermal

damage to the diamond. Therefore, EDD process basically won't erode any diamond superabrasives.

The principle of contact electrical discharge dressing is illustrated in Fig. 15b. When the grinding wheel grinds the electrode, the metal bond is not in direct contact with the electrode, but is the chip generated at the tip of the diamond abrasive or the unformed chip of the unpeeled electrode and the grinding wheel (Weingartne et al. 2012). When the metal bond is close to the ring electrode at a certain degree, a pulse discharge occurs, and the metal bond is removed by hot melt and evaporation. Through several repeated fine pulse discharge, the grinding wheel binder is gradually removed, and the diamond grains protrude from the active surface of the grinding wheel to achieve the dressing effect.

For the noncontact discharge dressing mode, the gap between the grinding wheel and the electrode is maintained at a constant value by monitoring the discharge current. During the dressing process, part of the electrode is also consumed under the action of discharging together with the erosion of the metal bond. Therefore, appropriate electrode shape correction work must be adopted to ensure good dressing accuracy, and a pulse power source is usually used in the noncontact discharge dressing to make the discharge pulse to continuously occur (Guo et al. 2010).

The metal binder of grinding wheel removes by electrical discharge for both the contact EDD and noncontact EDD, while the main characteristic of contact discharge dressing is that the ring electrode is ground by the dressed grinding wheel. That is to say, the contact area between the grinding wheel and the electrode is large, and the gap between the working surface of the grinding wheel and the electrode keeps at a fixed value (Ding et al. 2017). In each grinding stroke, part of the electrode is consumed due to the discharge, so that the surface of the electrode can be kept smooth, which is favorable for maintaining the dressing precision (Guo et al. 2010).

In the contact discharge dressing, the particle size and the protrusion amount of the diamond abrasive grains determine the gap between the grinding wheel and the electrode. If the gap is too small, the short circuit is likely to occur, which reduces the number of discharges per unit time or stops the discharge; therefore, the abrasive grains are not easy to be sharpened to form enough blade edges. If the gap between the grinding wheel and the electrode is too large so that the discharge cannot occur, the penetration depth of the abrasive grains increases, and then the length of the chip becomes longer. That is to say, the contact discharge can be controlled by adjusting the grinding conditions (Guo et al. 2010).

Contact discharge dressing is a very efficient method for metal bond grinding wheels, but due to the periodicity of the discharge, the periodic discharge grooves are easy to be produced on the surface of the dressed grinding wheel, which may affect the accuracy of dressed grinding wheel (Guo et al. 2010). In order to evenly distribute the sharpened blade edges on the grinding wheel, the bipolar chip electrode assembly is used to insert into the resin bond cup wheel and form a mixed electrode as shown in Fig. 17 (Guo et al. 2010). The shedding abrasives from the mixed electrode of the cup-shaped grinding wheel can achieve the same dressing effect as a cup-shaped dresser. Moreover, the mixed electrode can disperse the

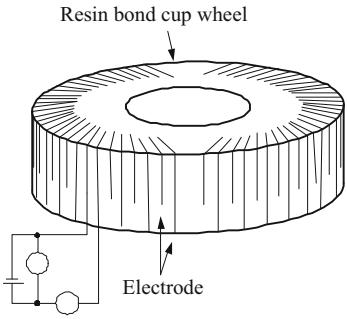

Fig. 17 Illustration of mixed electrode (Guo et al. 2010)

electrical discharge; thus, a good dressing surface of grinding wheel without discharge damage can be obtained (Guo et al. 2010).

The existing dressing methods for metal bond grinding wheel, such as electric spark dressing and ELID dressing methods, are based on the principle of electrical erosion between the electrodes and the metal bond of the grinding wheel by external power supply. Therefore, these two methods require special control devices to control and adjust the small gap between the grinding wheel and the electrode (Guo et al. 2010). Furthermore, electrolytic in-process dressing (ELID) even needs special electrolyte. By comparison, the contact EDD is relatively simple in view of the diamond dressing for application.

Principle of Dry Contact Electrical Discharge Dressing

Today, the green machining has become the mainstream in the manufacturing field. The dirty or poisonous liquid, such as grinding fluid and dielectric liquid, may be forbidden on the situation such as numerical control optical profile grinder (Xie and Tamaki 2006; Wang et al. 2006; Lu et al. 2015). Therefore, a dry electrical discharge assisted truing and dressing method emerges, which avoids the use of dielectric liquid and is free from the serious problems of electrolytic corrosion caused by electrolytic current flowing through water in conventional EDD (Wang et al. 2006).

Figure 18 schematically illustrates the dry contact electrical discharge dressing techniques (Malkin and Guo 2008; Guo et al. 2010). A ring electrode is placed on table and moves by the reciprocating machine table. The grinding wheel is set locating on the center line of the self-rotating electrode, on which a low open-circuit voltage E_i (switching regulator, unlimited current) was attached to the wheel and electrode without any coolant. The contact discharge between the metal bond and the electrode occurs when the metal bond grinding wheel grinds the electrode and causes the removal of part of the metal bond. Thereby contact discharge dressing occurs.

Figure 19 shows the dry electro-contact discharge dressing mechanism (Lu et al. 2015). Different from the mechanical dressing techniques, the dry electro-contact discharge uses an impulse electro-discharge to remove the metal bond of grinding wheel instead of any mechanical removal action (Fig. 19a; Lu et al. 2015). The spark discharge may occur between the approaching rolled-up chips and the metal bond when the nonconductive diamond grain comes into cutting the copper electrode,

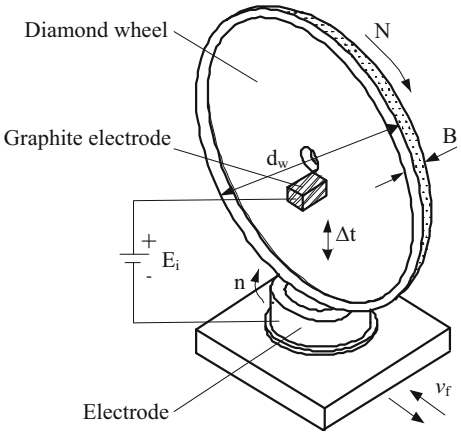

Fig. 18 Illustration of dry contact electrical discharge dressing (Malkin et al. 2008)

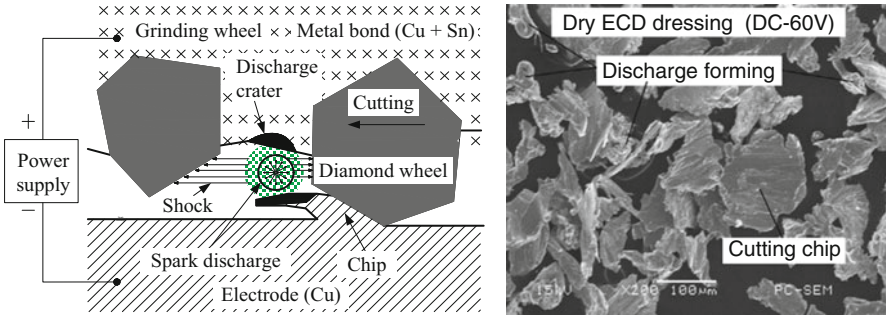

(a) Microremoval scheme (b) SEM photo of Cu chip

Fig. 19 Mechanism of dry electro-contact discharge dressing (Lu et al. 2015). (**a**) Microremoval scheme. (**b**) SEM photo of Cu chip

during which the metal bond is melted and thrown into a discharge crater; therefore, the diamond grains are gradually protruded from the wheel working surface (Lu et al. 2015). Meanwhile, the impulse discharge heat flow also shocked diamond grain edge, and some melted Cu chips by electrical discharge were formed in dry electro-contact discharge dressing as shown in Fig. 19b, and thus the uniform grain protrusion height in grinding might be formed (Lu et al. 2015).

Wire Electrical Discharge Dressing

Wire electrical discharge dressing (WEDD) is another fashion to the conventional EDD method, of which the electrode is replaced by a wire (Weingartner et al. 2012). Figure 20 shows an example of a metal-bonded grinding wheel being dressed by WEDD (Wegener et al. 2013). Different from other traditional electrical discharge dressing, the dressing tool wear of WEDD can be much simpler compensated by adjusting the wire feed speeds (Ding et al. 2017). Furthermore, WEDD is much more flexible to create different wheel profiles because the wire feed angle could be

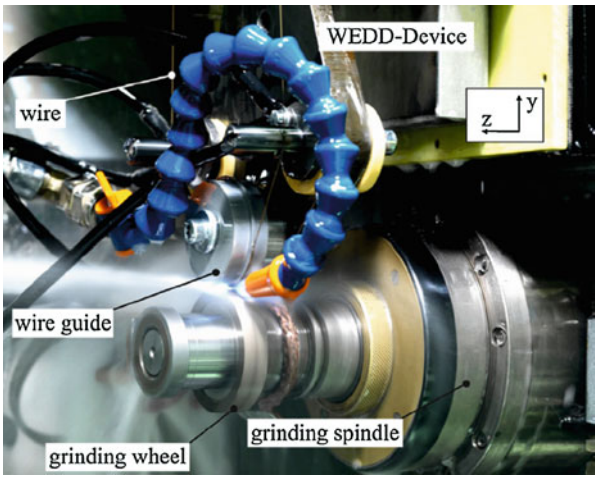

Fig. 20 WEDD device mounted inside a grinding machine (Wegener et al. 2013)

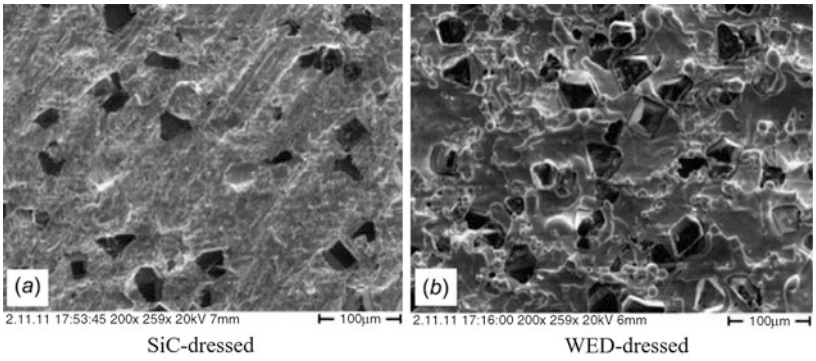

Fig. 21 SEM micrographs of the metal-bonded diamond wheels (Weingartner et al. 2012). (**a**) SiC-dressed. (**b**) WED-dressed

properly controlled according to the desired wheel shape. In addition, WEDD allows for the generation of more proper grinding wheel topographies compared to the SiC-dressed wheel surface, and also diamond abrasives are clearly more exposed in the WED-dressed wheel surface as displayed in Fig. 21 (Weingartner et al. 2012).

Electrical Discharge Dressing Combined with Electrochemical Machining

To increase the dressing efficiency and quality, there are many new EDD dressing methods emerging. The electrical discharge dressing combined with electrochemical machining (ECDM) is one of the proposed typical hybrid technologies that has been applied successfully on a centerless grinding machine (Ding et al. 2017). The principle of ECDM is schematic illustrated in Fig. 22 (Schopf et al. 2001). It can be seen that ECDM can realizes both the truing and dressing action of the diamond

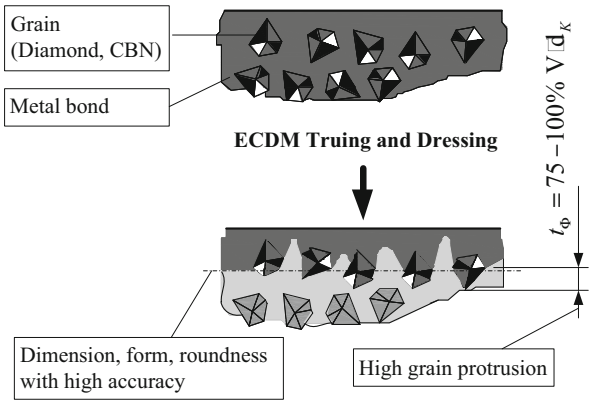

Fig. 22 Principle of the ECDM truing and dressing (Schopf et al. 2001)

grinding tools in just one step (Schopf et al. 2001). However, there are actually two different approaches in ECDM, namely, ECM and EDM. In ECDM, ECM dressing first anodic dissolves the bond layer and hence exposes a higher grain protrusion (Schopf et al. 2001; Kramer et al. 1999; Nebashi et al. 1998), and then EDM truing and dressing produces much smaller grain protrusion than the ECM process but it is of high macro-geometrical accuracy, which therefore is obviously very suitable for the dressing and truing of metal-bonded grinding wheels (Syoji et al. 1990).

Electrolytic in-Process Dressing (ELID)

Electrolytic in-process dressing (ELID) grinding was first proposed by the Japanese researcher Hitoshi Ohmori in 1990 (Ohmori and Nakagawa 1990). Electrolytic in-process dressing (ELID) grinding is an in situ dressing process that employs an electrolytic action to realize an in-process dressing of metal-bonded superabrasive wheel (Ohmori et al. 1996).

The basic principle of the electrolysis is schematically illustrated in Fig. 23. The metallic bond around the superabrasive grains is continuously dissolved and scraped away during the in-process electrolytic process, and thus new sharp abrasive grains expose on the newly active wheel surface (Deng et al. 2014b). One of the main advantages of ELID is that it can be conducted with the grinding process simultaneously; therefore, the ELID is helpful to improve the grinding and dressing efficiency, which certainly can maintain a high material removal rate and obtain a constant surface roughness at the same time. The ELID technique has been proved to suit the application for dressing the fine grain wheels, and it is efficiently to achieve very good surface quality and surface roughness, and especially, ELID can realize the ductile grinding removal of hard ceramics using a very small in cutting depth together with fine grain wheels, of which the failure of cracking can be effective avoided (Ding et al. 2017).

The ELID doesn't need to develop any special machine or devices, and it can be conducted on a conventional surface grinder (Ding et al. 2017). Furthermore, ELID

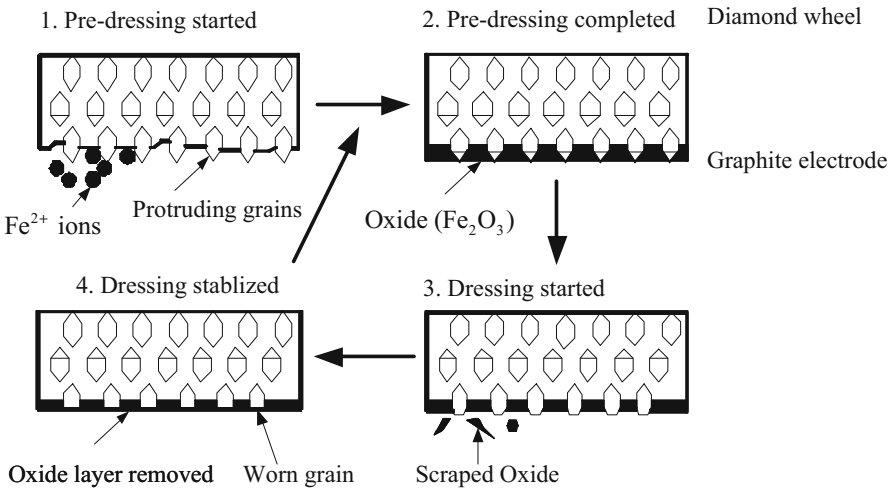

Fig. 23 Mechanism of ELID (Stephenson et al. 2001)

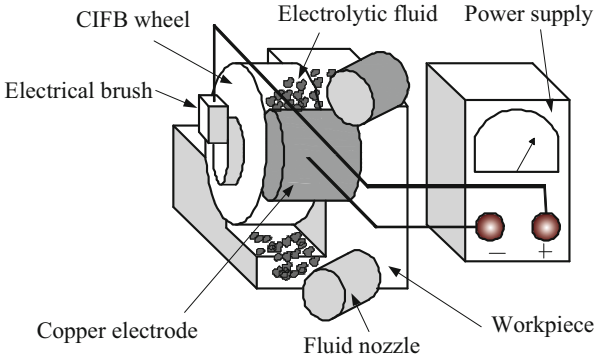

Fig. 24 Basic arrangement for ELID grinding (Malkin and Guo 2008)

can adopt the power sources from conventional electro-discharge or electrochemical machines and other ordinary grinding machines directly. Figure 24 schematically illustrates the basic arrangement of the ELID system that is suitable for any conventional surface grinding (Malkin and Guo 2008). An ELID system general includes a metal-bonded grinding wheel, a power source, and a high pH electrolytic coolant (Ding et al. 2017). The metal-bonded wheel is connected to the positive terminal of a power supply with a smooth brush contact, while the fixed electrode is connected to the negative pole. The electrode is made out of copper and must cover at least one sixth of the wheel's active surface and a width that is 2 mm wider than the wheel rim thickness. The gap between the wheel and the active surface of the electrode is usually set at 0.1–0.3 mm and can be adjusted by mechanical means as required (Malkin and Guo 2008).

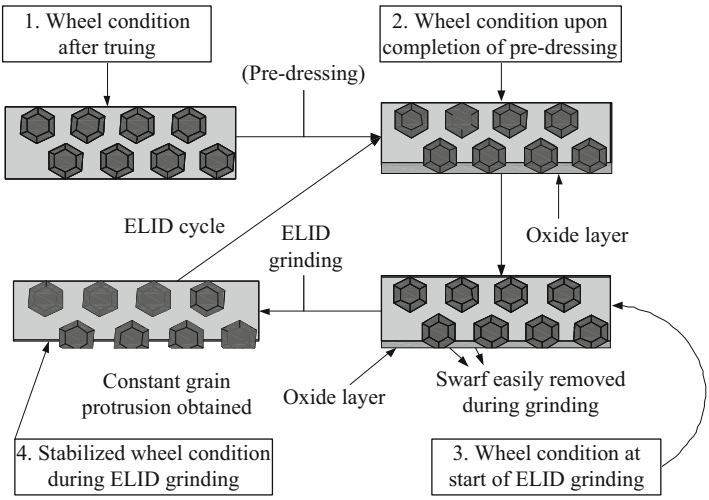

Fig. 25 Stages of ELID grinding (Ohmori et al. 1996)

In ELID grinding, the superabrasive wear rate is directly determined by grinding force, grinding conditions, and workpiece mechanical properties, and the removal rate of the metal bond depends on ELID parameters such as voltage, current, and the gap between the electrodes (Malkin and Guo 2008). While the removal of metal bond by electrolysis dissolution is carrying on together with the mechanical wear of superabrasives at the same time, thus it is important in ELID to ensure the balance between the removal rate of the metal bond and the wear rate of the superabrasive particles by proper regulating the grinding parameters (Chen and Li 2000).

When a direct current passes through the grinding fluid acting as an electrolyte between the fixed electrode and grinding wheel, the electrolysis phenomenon occurs, and then the metal-boned grinding wheel is dressed (Ding et al. 2017). Generally, the metal bond material at the metal-diamond interface dissolves fast, which means that the concentration of the diamond particles can facilitate the dissolution rate of the metal bond (Chen and Li 2000). The mechanism and various stages of the ELID grinding are displayed in Fig. 25, which can be classified as three stages, truing, dressing, and grinding/dressing, which are presented below (Ding et al. 2017; Malkin and Guo 2008):

(i) *Truing* is carried out to reduce the initial eccentricity below the average grain size of the wheel and to improve wheel straightness, especially when a new wheel is first used or reinstalled. Precision truing of a micrograin wheel is carried out to achieve a runout to a level comparable with, or less than that of, the average grain size of the wheel. During this stage, little or no coolant is supplied to prevent electrolysis and to obtain high truing precision. After truing, a pre-dressing operation is required prior to grinding.

(ii) *Pre-dressing* of the grinding wheel by electrolytic means aims to increase the protrusion of abrasive grains which is essential for proper grinding operation. The procedure is performed at low speed and takes about 10–30 min.
(iii) *Grinding* is performed simultaneously with continuous in-process dressing by electrolytic means.

According to the existing research and experiments, the electrolysis conditions of the last two processes may differ a little due to the changing of wheel-surface condition according to electrolysis (Ohmori et al. 1996).

Conclusion

Grinding techniques are very important to realize the high precision and efficient machining with massive of bonded hard abrasives. To achieve good grinding performance, the abrasives should keep the desired sharpness and the wheel be in good form accuracy. Thus, the conditioning process is necessary to be conducted intermittently to remove the thin outer rim of grinding wheel which is dull or blocked by the grinding chips. As a whole, there are many developed conditioning (dressing and truing) methods for the superabrasive and grinding wheels. For the novel and typical conditioning techniques for superabrasives and grinding wheel, there are cup-wheel dressing, laser dressing (LD), electrical discharge dressing (EDD), and electrolytic in-process dressing (ELID), which are introduced briefly in this chapter to give a general understanding of state of the art of these techniques. But these conditioning techniques all have clear advantages and disadvantages. For example, the conditioning techniques that can be online performed are generally achieved by energy-field assistance, which always have special requirements for the bond material and even are harmful to the environment. Especially, electrical discharge dressing (EDD) and electrolytic in-process dressing (ELID) are only suitable for conditioning of metal bond material grinding wheel and have no effect for the resin or vitrified bonded grinding wheel. In a word, to make the condition techniques much environment-friendly and widely technology-selective, the current conditioning methods still need to be further improved to meet the future requirement of precision grinding.

References

Cai LR, Jia Y, Hu DJ (2009) Dressing of metal-bonded Superabrasive Grinding wheels by means of mist-jetting electrical discharge Technology. J Mater Process Technol 209(2):779–784

Cai S, Chen GY, Zhou C, Deng H (2015) The mechanism and application of bronze-bond diamond Grinding wheel pulsed laser dressing based on phase explosion. Int J Adv Manuf Technol 80(9–12):1641–1653

Chen H, Li JC (2000) Anodic metal matrix removal rate in electrolytic in-process dressing I: two-dimensional modeling. J Appl Phys 87(6):3151–3158

Chen WK, Huang H, Yin L (2005) Loose abrasive truing and dressing of resin bond diamond cup wheels for Grinding Fiber optic connectors. J Mater Process Technol 159(2):229–239
Chen GY, Deng H, Zhou XC, Zhou C, He J, Cai S (2015) Online tangential laser profiling of coarse-grained bronze-bonded diamond wheels. Int J Adv Manuf Technol 79(9–12):1477–1482
Deng H, Chen GY, Zhou C, Li SC, Zhang MJ (2014a) Processing parameter optimization for the laser dressing of bronze-bonded diamond wheels. Appl Surf Sci 290:475–481
Deng H, Chen GY, Zhou C, Zhou XC, He J, Zhang Y (2014b) A theoretical and experimental study on the pulsed laser dressing of bronze-bonded diamond Grinding wheels. Appl Surf Sci 314:78–89
Ding WF, Li H, Zhang L et al (2017) Diamond wheel dressing: a comprehensive review. J Manuf Sci Eng 139(12). https://doi.org/10.1115/1.4037991
Guo YB, Zhang L, Xu YZ, Katso S (2003) Study on truing and dressing technology for arc-diamond wheel. Manuf Technol Mach Tool 4:38–40
Guo Y, Yang W, Wang Z (2010) Grinding Technology and Techniques. (in Chinese). National Defense Industry Press, Beijing
Guo Y, Yang P, Wang Z, Yang W (2014) Micro-nano manufacturing and precision measuring technology for advanced optics (in Chinese). National Defense Industry Press, Beijing
Hosokawa A, Ueda T, Yunoki T (2006) Laser dressing of metal bonded diamond wheel. CIRP Ann Manuf Technol 55(1):329–332
Kramer D, Rehsteiner F, Schumacher B (1999) ECD (electrochemical in-process controlled dressing), a new method for Grinding of modern high-performance cutting materials to highest quality. CIRP Ann Manuf Technol 48(1):265–268
Kunieda M, Lauwers B, Rajurkar KP, Schumacher BM (2005) Advancing EDM through fundamental insight into the process. CIRP Ann Manuf Technol 54(2):64–87
Lu YJ, Xie J, Si XH (2015) Study on micro-topographical removals of diamond grain and metal bond in dry electro-contact discharge dressing of coarse diamond Grinding wheel. Int J Mach Tool Manu 88:118–130
Malkin S, Guo C (2008) Grinding Technology: theory and applications of machining with abrasives. Industrial Press, New York
Marinescu ID, Rowe WB, Dimitrov B, Ohmori H (2004) Tribology of abrasive machining processes. William Andrew, New York
Nebashi N, Wakabayashi K, Yamada M, Masuzawa T (1998) In-process trueing/dressing of Grinding wheels by WEDG and ELID. Int J Electr Mach 3:33–38
Ohmori H, Nakagawa T (1990) Mirror surface Grinding of silicon wafers with electrolytic in-process dressing. Ann CIRP 39(1):329–332
Ohmori H, Takahashi I, Bandyopadhyay BP (1996) Ultra-precision Grinding of structural ceramics by electrolytic in-process dressing (ELID) grinding. J Mater Process Technol 57:272–277
Rahman M, Kumar AS, Biswas I (2009) A review of electrolytic in-process dressing (ELID) grinding. Key Eng Mater 404:45–59
Schopf M, Beltrami I, Boccadoro M, Kramer D (2001) ECDM (electro chemical discharge machining), a new method for trueing and dressing of metal bonded diamond Grinding tools. CIRP Ann Manuf Technol 50(1):125–128
Stephenson DJ, Veselovac D, Manley S, Corbett J (2001) Ultra-precision grinding of hard steels. Precis Eng 25:336–345
Suzuki K, Uematsu T, Nakagawa T (1987) On-machine truing/dressing of metal bond diamond Grinding wheels by electro-discharge machining. CIRP Ann Manuf Technol 36(1):115–118
Syoji K (1993) Ceramic bond diamond wheel dressing research (III): dressing principle of the cup-wheel. Diamond Abras Eng 1(73):6–11
Syoji K, Piao CG (1991) Studies on truing of diamond vitrified wheels – II: truing mechanism with cup-truer. J Jpn Soc Precis Eng 25(4):285–290
Syoji K, Zhou LB, Matsui S (1990) Studies on truing and dressing of diamond wheels – the measurement of protrusion height of abrasive grains by using a Stereopair and influence of protrusion height on Grinding performance. J Jpn Soc Precis Eng 24(2):124–129

Wang Y, Zhou XJ, Hu DJ (2006) An experimental investigation of dry-electrical discharge assisted truing and dressing of metal bonded diamond wheel. Int J Mach Tool Manu 46(3–4):333–342
Wegener K, Weingartner E, Blaser M (2013) In-process wire electrical discharge dressing (IWEDD) of metal bonded diamond wheels. CIRP Ann Manuf Technol 62(1):339–342
Weingartne E, Roth R, Kuster F, Boccadoro M, Fiebelkorn F (2012) Electrical discharge dressing and its influence on metal bonded diamond wheels. CIRP Ann Manuf Technol 61(1):183–186
Weingartner E, Wegener K, Kuster F (2012) Applying wire electrical discharge dressing (WEDD) to improve Grinding performance of metal bounded diamond wheels. Procedia CIRP 1:365–370
Westkaemper E (1995) Grinding assisted by Nd: YAG lasers. CIRP Ann Manuf Technol 44(1):317–320
Xie J, Tamaki J (2006) In-process evaluation of grit protrusion feature for fine diamond Grinding wheel by means of electro-contact discharge dressing. J Mater Process Technol 180(1–3):83–90
Xu MM, Li DD, Hu DJ, Jia Y (2012) Laminated manufacturing and milling electrical discharge dressing of metal-bonded diamond Grinding wheels. Proc Inst Mech Eng B 226(1):137–144
Zhang C, Shin YC (2002) A novel laser-assisted truing and dressing technique for vitrified CBN wheels. Int J Mach Tool Manu 42(7):825–835

Control Systems for Precision Machines

10

Bing Li

Contents

Introduction 266
Key Technology of Control System of Precision Machines 268
Technology of Precision Machines 268
Detection Sensor Technology 270
Information Processing Technology 272
Servo Drive Technology 273
Automatic Control Technology 275
System Software Technology 276
Common Control System of Precision Machines 278
Feed Motion Control System 278
Temperature Control System 282
Vibration Control System 283
Typical Examples of Control System of Precision Machines 285
Active Measurement System 285
Grating Scale Precision Control System 286
Conclusion 289
References 290

Abstract

The control system is a core component of precision machines. No matter the precision machines are used for manufacturing (e.g., turning, milling, grinding, lapping, polishing) or inspection of mechanical parts, the control system could significantly determine the performance of precision machines. In this chapter,

B. Li (✉)
School of Mechanical Engineering and Automation, Harbin Institute of Technology, Shenzhen, China

State Key Laboratory for Manufacturing Systems Engineering, Xi'an Jiaotong University, Xi'an, Shaanxi, China
e-mail: lb@xjtu.edu.cn

Z. Jiang, S. Yang (eds.), *Precision Machines*, Precision Manufacturing,
https://doi.org/10.1007/978-981-13-0381-4_13

the control system of precision machines is described in detail. Firstly, the development of control system used in the precision machines is briefly introduced and a definition is given. Secondly, some key technologies in the control system of precision machines are elaborated in detail, including precision machine technology, detection sensor technology, information processing technology, servo drive technology, automatic control technology, and system software technology. Thirdly, three common control systems of precision machines are introduced, such as feed motion control system, temperature control system, and vibration control system. Finally, two typical cases are applied in precision machine tool control, such as active measurement control system and grating scale precision control system.

Keywords

Precision machines · Control system · Sensor · Information processing · Serve drive · Motion control · Temperature control · Vibration control

Introduction

Since the invention of the steam engine in the early seventeenth century, with the continuous development of mechanical products, the control system of machines has become more and more automated and complicated. At the same time, with the introduction of research results in electronics, information, and other scientific fields, the mechanical control system has also changed from an early single open-loop control mechanism to a closed-loop control system with real-time monitoring and feedback functions (Fu et al. 2010). This not only improves the working efficiency of machines but also improves the rate of finished products of mechanical processing.

In a broad sense, mechanical control refers to the management and control of machines using related equipment. Generally speaking, the control power source mainly falls into electric, pneumatic, and hydraulic types (Wu 2009; Xiong 2012). The electric control is widely used in the field of precision mechanical control because of its high control accuracy, high compatibility with system, and easy control. In terms of controlled objects, the control system is divided into process control system and motion control system (Wang 2013). The former is mainly applied to the variable control of dynamic factors such as temperature, flow, and pressure in the production process, while the motion control system is the control of factors including speed and position, on mechanical actuating mechanism of production equipment. Therefore, control system of precision machines is the professional technology of mechanics, machines, electronics, material science, computer and signal processing, etc. It is an integrated system of motion control and process control of precision machines achieved by the operator's intentions (Dorf and Bishop 1998; Lei 2013).

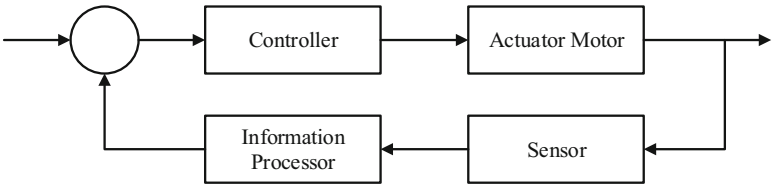

Fig. 1 Structure of simple control system

In order to fulfill the abovementioned control functions, the control system single circuit is generally composed of the controller and the corresponding sensor, information processor, and electric motor, as shown in Fig. 1.

Among them, the controller can be categorized into analog controller and numerical controller. The analog controller's hardware and circuit are more complex and less universal. Compared with the analog controller, the numerical controller is characterized by standardized hardware and circuit, and it can be controlled by software modification. In terms of algorithm, PID (proportional integral derivative) control algorithm is one of the most classical algorithms (Xu et al. 1995; Wang 2009), and PI (proportional integral) algorithm, the parameter adaptive PID, etc. are derived from PID to improve system performance. In addition, the hardware of the numerical controller generally uses PLC (programmable logic controller), and DSP (digital signal processor) can be used if the performance requirements are higher. With the development of digital industry, numerical controllers now account for the majority of controllers.

The actuator motor can be divided into drive motor and servomotor. The former is applied to the speed control system, and the latter is applied to the servo system (Hu 2013). In addition, the electric motor can be categorized as stepper motor, DC motor, and AC motor according to the working principle. AC motor is widely used as it is simple and easy to manufacture, and it doesn't need any mechanical commutator.

The power actuating device, according to the power supply type and the power supply required by the motor control, is categorized into motor type, electromagnetic type, power electronic type, and so on (Wang and Gu 2014). At present, the electronic power amplifier and the transformation device dominate, especially the position loop, speed loop, and current loop with both control and drive function and using power actuating device to form a system.

In the precision control system, physical parameters are mainly monitored, such as displacement, speed, and current. The corresponding high-precision detection sensor plays an important role in improving the accuracy of the system. The displacement detection element generally includes pulse transformer, linear grating sensor, resolver, inductosyn, and so on. Generally, speed detection elements include AC and DC tachogenerator, digital pulse-type speed sensors, rate gyroscope, and so on (Zhang et al. 2006). As the current signal is an analog variable signal, Hall current sensor is usually used for detecting.

Table 1 Classification of control system of precision machines

Classification source	Classification basis		Classification
Controller	Constituted by analog circuits		Analog control system
	Constituted by digital circuits		Numerical control system
Actuator motor	Controlled object	Rotating speed control	Speed control system
		Displacement control	Servo system
	Motor type	DC motor	DC transmission system
		AC motor	AC transmission system
Controlled parameters	Displacement		Servo motion control system
	Temperature		Temperature control system
	Vibration		Vibration control system

The control system of precision machines can be classified according to the characteristics of controller and actuator motor, as shown in Table 1.

Key Technology of Control System of Precision Machines

Technology of Precision Machines

Compared with the traditional mechanical products, technology of precision machines requires lightweight, small size, high accuracy, high strength and stiffness, and excellent dynamic performance. The stiffness of the machine can't be reduced while ensuring lightweight and small size. Moreover, the static and dynamic stiffness and thermal deformation should be taken into account, and the stiffness of the kinematic pair must be improved. Therefore, new composite and structures should be considered in the design. Modularized, standardized, and normalized design should be adopted to facilitate maintenance. In addition to taking full advantage of traditional mechanical technology, we must improve the precision machining technology, structural optimization design methods, dynamic design methods, virtual design methods, and so on; we must research and develop new composite to enable mechanical structures to reduce weight and volume and improve characteristic of quick response in control; we should research on high-precision guide rail, precision ball screw, and high-precision gear and bearing, to improve the accuracy and reliability of key components; we should also improve the design, manufacturing, and maintenance level of components by standardizing, serializing, and modularizing components. The key problems are:

1. Considering the small size and lightweight, we should research the thermal deformation and static and dynamic rigidity of mechanical parts.
2. We should improve the precision of key parts, including high-precision guide rail and precision ball screw, high-precision spindle bearing, and high-precision gear, to improve reliability and reduce cost.

3. We should improve the quality of cutting tools and lapping tools and improve material properties.
4. Ultraprecision machining and precision measurement technology.
5. Standardization, modularization, and standardization of parts to improve interchangeability and to ensure easy maintenance.
6. Friction, wear and lubrication technology.

CNC machine tool is taken as an example to illustrate the key technologies involved in precision machines. As a typical product of precision machines, CNC machine tool is mainly composed of CNC system, motion control system, position detection device, lathe body, and some auxiliary control units, as shown in Fig. 2. CNC motion control system and position detection device are the essential links between CNC system and machine structure, which to some extent determine the motion characteristics and accuracy of the machine tool. The motion control system comprises a servomotor, transmission mechanism, and servo driver and is connected with the actuating mechanism of machine tool. It controls the displacement and speed of the actuating mechanism according to the commands sent by the CNC system. The lathe body is the main body of CNC machine tool, composed by basic pieces (such as bed and base) of machine tool and various moving parts (such as workbench, bed saddle, and headstock). CNC machine tool is basically the same as the ordinary one, except that it has some special design and manufacture technology according to its own characteristics, such as the use of ball screw and rolling guide rail to replace sliding guide rail and various clearance eliminating mechanisms, in order to achieve the motion control of various motion control system and to bear the cutting force. Therefore, the lathe body must ensure a necessary geometric accuracy, enough stiffness, small thermal deformation, low frictional resistance, in order to guarantee the machining accuracy of the machine tool (Tan 2013; Liu et al. 2008).

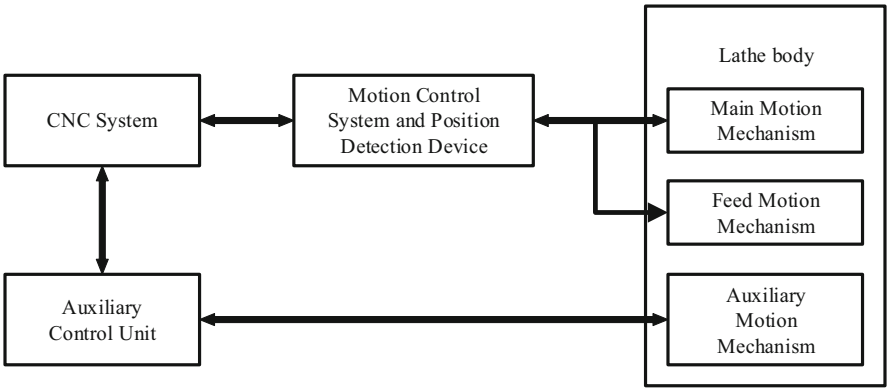

Fig. 2 The basic structure of CNC machine tool

Detection Sensor Technology

The sensor is a device or instrument that detects a signal by a certain law and converts the measured value (physical, chemical, and biological information) into another physical quantity (usually a power). It can not only convert non-electricity into electricity but also achieve an interconversion between power and non-power. The sensor is usually composed of the sensitive element, conversion element, and basic conversion circuit, as shown in Fig. 3.

According to the function, the sensor can be divided into internal information sensor that detects the internal state of mechanical system and external information sensor that detects the external environment. The internal information sensors include sensors that detect the position, speed, force, torque, temperature, and abnormal transformation. External information sensors include vision sensors, tactile sensors, force sensors, proximity sensors, angle sensors, and so on. Output signal can be classified as switch type, analog type, and digital type according to its nature.

A detection sensor refers to the detection sensor in mechatronic system, in which the sensor detects physical quantities such as temperature, velocity, pressure, flow, displacement, acceleration, force, and torque, as well as geometric parameters of the object. The accuracy of the detection parameters will directly affect the performance of precision machine products. Therefore, the detection sensor should be characterized by high precision, high reliability, and high sensitivity as well as other properties. The main performance indexes of the sensor are shown in Table 2. The main performance parameters of different sensors should be determined based on the actual needs.

Usually the sensor is a grand collection of light, machine, electricity, sound, information, and other technologies. Sensor mechanism, structural design, and manufacturing process of the components need to be carefully studied, and key problems need to be solved. With the rapid development of MEMS technology, precision machine has been encountering unprecedented challenges and opportunities. These technologies complement the constraints caused by mechanical manufacturing and push the development of precision machines to a higher level. There are also many problems in detection sensors: (1) The sensitivity and reliability of various sensitive materials and components need to be improved; (2) the sensor structure should be improved to develop a complex sensor integrating temperature, humidity, vision, and tactile detection; (3) online detection technology should be researched to improve the anti-jamming capability of the sensor and acquisition system; and (4) smart sensor should be researched and developed, so that it has functions of automatic diagnosis and automatic compensation.

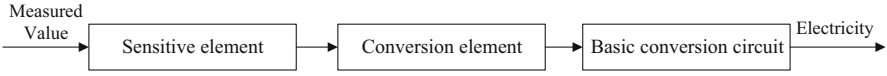

Fig. 3 The composition of sensor

Table 2 The sensor's main performance indexes

Item			Corresponding indexes	
Basic parameters	Range		Measurement range	The range of the measured value within the allowable error limit
			Range	The algebraic difference within upper and lower limits of the measurement range allowed by the sensor
			Overload capacity	The ability of the sensor to exceed its measurement range without causing a permanent change in the specified performance index
	Sensitivity		Sensitivity, resolution, threshold value, full scale output	
	Static precision		Accuracy, linearity, repeatability, hysteresis, sensitivity error	
	Dynamic characteristics	Frequency characteristics	Frequency characteristics, frequency response range, critical frequency	Time constant, inherent frequency, damping ratio, dynamic error
		Step characteristics	Overshoot, critical speed, adjustment time	
Environmental parameters	Temperature		Operating temperature range, temperature error, temperature drift, temperature coefficient, thermal hysteresis	
	Vibration shock		The ability to resist errors caused by vibration shock, including frequency, amplitude, and acceleration of each direction	
	Others		Anti-moisture, anti-dielectric corrosion, anti-electromagnetic interference ability, etc.	
Reliability			Working life, mean free error time, insurance period, fatigue properties, insulation resistance, withstand voltage	
Service conditions			Power supply, shape, weight, structural features, installation methods, etc.	
Price			Price, price performance ratio	

Information Processing Technology

Information processing technology refers to the technology of information input, conversion, computing, storage, and output by using electronic computers and external equipment. The computers herein include industrial personal computers, single chips, and programmable controllers. The computers and their external devices can increase their computing speed by upgrading integration in order to be embedded in the mechanical ontology; their reliability can be improved through self-diagnosis, self-recovery, and fault-tolerant technology; they can be more intelligent through artificial intelligence and expert system. Through the above measures, the computers are able to work in the harsh industrial environment in a long-term, safe, and reliable way. Interface technology is a key technology in information processing technology. In the mechatronic system, the connection between the computer and the peripheral devices (such as the actuating mechanism, the sensor, the mechanical body, the power source, the human-computer interaction equipment, etc.) is called the interface, and the function of interface is implemented by hardware circuit, as well as the corresponding interface software (driver). Usually the function of interface is achieved through the interface hardware and interface software. The function of the interface is to convert the input information of external device into the computer to a format acceptable to the computer or to convert the output information of the computer into a format that can be accepted by the peripheral device so that the transmission speed of the information between the computer and peripheral device matches each other, enabling the buffer of transmission information between the computer and peripheral devices as well as signal level conversion.

Information processing technology includes information input, transformation, operation, storage, and output technology. Information processing hardware includes input/output (I/O) devices, monitors, keyboards, computers, programmable controllers, microprocessors, numerical control devices, etc. Accurate and timely information processing will directly affect the quality and efficiency of precision machine products, thus becoming one of the key technologies of precision machine products. Information processing technology still needs to make improvement, such as reducing weight; improving processing speed, reliability, and anti-jamming capability, as well as standardization; improving operability; and facilitating maintenance. In-depth studies should be conducted in the following:

1. To improve the manufacturing process and level of large-scale integrated circuits, including microprocessor chips and application-specific integrated circuits, to ensure product reliability and reduce costs
2. To improve the conversion speed and reliability of I/O, A/D, and D/A
3. To develop high-speed processing technology, such as high-speed computing microprocessors and high-speed image processing technology
4. Communication and transmission technology, to formulate standardized communication protocols and networking, channel allocation, transmission rate, and other core technologies

5. To speed up the standardization of programmable controller, microprocessor, and memorizer and to improve the maintainability
6. To strengthen the information processing functions and to develop intelligent technology with self-diagnosis and unmanned operation and to achieve artificial intelligence and automation simulation and other cutting-edge technology on human interface device by using sound or image recognition and other means (Gao 2011)

Servo Drive Technology

Servo drive technology mainly refers to some technical issues related to actuating mechanism. The main ways of servo drive include electric, pneumatic, hydraulic types, etc. Hydraulic and pneumatic types mainly include pump, valve, oil (gas) cylinder, hydraulic (pneumatic) motor, their subsidiary liquid (gas) pressure components, etc. Motor drive mainly includes AC servomotor, DC servomotor, and stepper motor. In the electromechanical system, there are problems in various hydraulic and pneumatic components, such as function, reliability, standardization, weight reduction, and volume reduction. Electric drive still have problems in quick response and efficiency, requiring a larger motor torque and smaller rotary inertia of rotor to enable the motor to start and stop quickly.

In the control system of precision machines, the servo drive technology is an automatic control system where the position and speed of the mechanical moving parts are controlled variables. The static and dynamic performance of the servo system determines the movement precision, stability and reliability, and actuating efficiency of the mechanical system. The numerical control servo system is composed of servomotor, drive signal control conversion circuit, power electronic drive magnification module, current regulator, speed regulator, position regulator, and corresponding detection device (such as photoelectric pulse encoder G). The general structure of a servo system is shown in Fig. 4, which is a three-loop system: the outer is the position loop, middle is the speed loop, and inner is the current loop.

The position loop consists of a position regulating module, a positional detection, and a feedback element. The speed loop consists of a speed comparator, a speed detection device (such as a tachogenerator, a photoelectric pulse encoder, etc.), and a speed feedback. The current loop consists of a current regulator, a current feedback, and a current detection device. The power electronic drive device is composed of a

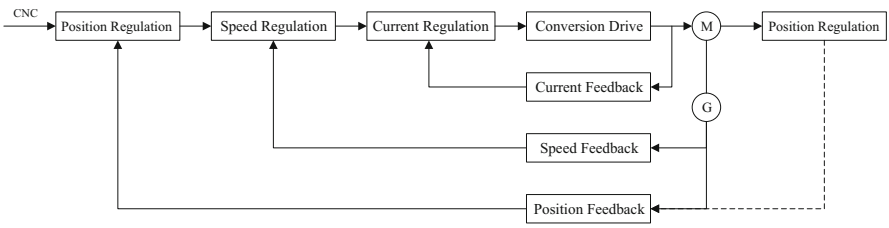

Fig. 4 Closed-loop servo system

drive signal generating circuit and a power amplifier. The position control mainly controls the position of each feed axis. It not only controls the movement speed and position precision of a single axis but also requires a good dynamic cooperation of the feed axis in the multi-axis linkage to ensure the movement precision of precision machines. The basic requirements of precision machines for servo drive are shown in Table 3.

A typical servo drive includes electric, pneumatic, and hydraulic types, and it's the way how actuating element movement actuates. The servo drive technology has a direct impact on the quality of the products. In the control system of precision machines, the electromechanical conversion components such as electric motors,

Table 3 The basic requirements of servo drive system for precision machines

Basic requirements	Explanation
High precision	The servo system precision refers to how accurately the output quantity can reproduce the input quantity. As a numerical control processing, contour machining has a more demanding requirement for positioning accuracy, which is generally allowed to range from 0.01 to 0.001 mm. Contour machining accuracy is also related with coordinated control of speed control and joint coordinates. In speed control, higher speed control accuracy has a stronger resistance to load disturbance and has a higher requirement for static and dynamic precision
Good stability	Stability means the system, in the given input or in external interference, after a short-term adjustment process, can achieve a new balance or restore to the original balance, requiring the servo system to have a strong anti-interference ability. Stability is a necessary condition to ensure the normal operation of CNC machine tools, and it has a direct impact on the accuracy and surface roughness of CNC processing
Quick response	Quick response is an important index of servo system's dynamic quality. In order to ensure the contour cutting shape accuracy and low processing surface roughness, the servo system must have a quick response to track command signals. On the one hand, it requires a short transition process time (motor from standstill to rated speed), generally less than 200 ms or even less than tens of milliseconds; on the other hand, it requires a small overshoot. These two requirements are often contradictory, so in practical applications, certain measures should be taken, and choice should be made according to processing requirements
Wide speed control range	Speed control range R_n refers to the ratio of maximum speed N_{max} and minimum speed N_{min} of the motor required by the production machine, which is usually expressed as:
	$R_n = \frac{N\max}{N\min}$
	where N_{max} and N_{min} generally refer to the rated load speed or actual load speed for a few machines with light load
	In the CNC machine tool, as the requirements for processing cutting tools, the processed workpiece materials and parts processing are different, the servo system needs a wide speed control range. At present, in the most advanced level, feed rate ranges within 0–240 m/min at a resolution of 1 μm, and steplessness is continuously adjustable
	For a typical CNC machine tool, it requires that the feed servo system can operate at a feed rate of 0–24 m/min

solenoid valves, hydraulic motors, and other actuating elements are required to have higher accuracy and higher reliability. The response speed is faster; DC servomotor requires a better control performance, with high resolution and high sensitivity, and a more stable speed and torque performance; AC speed control system requires frequency control, electronic inversion technology, vector transformation technology, and so on. In pneumatic and hydraulic systems, various components still need to improve their performance and reliability, to reduce weight and size and to be more standardized. In addition, the actuating elements should be smaller and lighter and have a higher output power, in order to improve the reliability and adaptability to the environment. Key technologies that need to be studied include (1) to improve the conversion accuracy, reliability, and quick response of electromechanical system; (2) to improve the performance of DC servomotor, such as high resolution and high sensitivity; (3) to improve the performance of AC speed control system, such as speed control of transducer, electronic inversion, and vector control technology; (4) to develop large, medium, and small inertia servomotors to improve their application performance; and (5) to develop pneumatic servo technology and micro-electromagnetic clutches and other products to better serve the precision machines system (Wen et al. 2003).

Automatic Control Technology

Automatic control refers to the use of control devices so that the controlled variables of controlled objects can change automatically according to a predetermined rule without human participation. The task of control system is to make some physical variables in production process or equipment remain constant or make them change by a certain law. Controlled objects and devices are connected in a certain way to form a completed and organic object to implement all kinds of complicated control tasks. The basic structure of a common series control system is shown in Fig. 5. Automatic control system usually consists of two parts, controller and controlled objects. The controlled objects refer to machines, devices, or production process which needs to be controlled in the system. Control signals calculated by controller control the controlled objects by a driver. The driver here can be considered as a

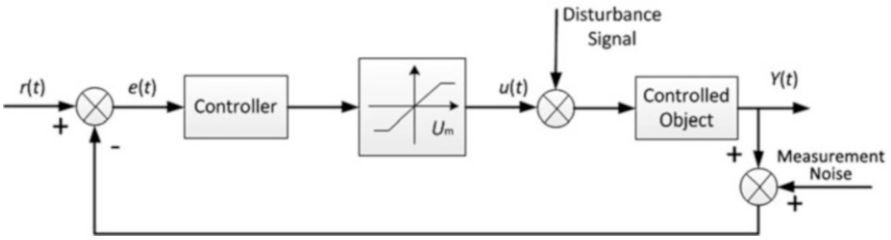

Fig. 5 The basic structure of typical control systems

saturated nonlinear link. In a control system, varieties of disturbance signals may exist, such as load disturbance, parameter variation of controlled objects, etc.

Automatic control system can be classified according to control system with or without the feedback element, the type of control system, quantity of control variables, change law of system, inherent dynamic characteristics of system, and control algorithms used by the system. All these are shown in Table 4.

The basic requirements for automatic control system are often expressed in performance indexes, which include three aspects: precision, stability margin, and response speed. Performance indexes are usually decided by the requirement of mechanical system. The requirement for performance indexes of a certain system should have a focus, for example, speed control system has a strict requirement for stability and steady-state accuracy, while tracking system expects a higher performance of rapidity. The proposal of performance indexes need foundations and should not be divorced from reality. If it demands a high response speed, then the energy provided to system and energy conversion system should be sufficient to ensure the moving parts can gain a higher acceleration; moving parts also need to bear the inertial load and centrifugal load generated during the process. Therefore, performance indexes of a system should be determined according to the practical application.

Automatic control technology includes high-precision positioning control, speed control, self-adaptive control, self-diagnosis, correcting, compensation, recovery, retrieval, and other technologies, which are critical in control system of precision machines. Among them, the most difficult points are engineering and practicability of modern control theory as well as construction of optimal control model, etc. With the advancement of industry 4.0, modern factories have higher and higher demands for automation, and the problems needed to be researched and solved include (1) multifunctional, completed CNC technology, and device, including multi-axis CNC, etc., (2) hierarchical control system, (3) intelligent control system, (4) simulation of complex control system, and (5) self-diagnosis monitoring and fault-tolerant technology, etc.

System Software Technology

Software is the key portion of control system as well as the soul of mechanical structure. Software structure is closely related and combined with hardware structure and functions of a control system. Software can be mainly classified as system software and application software. System software includes operating system, diagnostic system, development system, and information processing system. Usually, these softwares needn't be designed by users; they just need to know the basic principles and application methods. On the contrary, application software needs to be developed by users, so software design usually refers to design of application software. Control system requires the application software to be real time, pertinent, flexible, and universal. Modularized program and structured program are the two ways in the design of application software. Modularized program is to divide the

Table 4 Classification of automatic control system

Classification method	System type	System feature
System contains feedback element or not	Open-loop control system: the control system has no feedback channel between input and output. The effect of open-loop control system will not be affected by system output	It's difficult for the open-loop control system to implement a high-precision control. Typical application includes the positioning control system of stepper motor drive
	Closed-loop control system: the system provides output quantity for feeding back to the front link and joining control calculation	Controlled variables in system will affect output of controller and construct one or more closed loops
	Compound control: the system contains both feedback and feedforward control	Feedforward control is mainly used in eliminating system errors, improving control precision, and compensating all kinds of disturbances
Signal types in control system	Analog variable control system: all the signals in control system are time continuous functions, such as current, voltage, position, velocity, and temperature	
	Discrete control system: if there is at least one discrete signal in control system, it can be defined as discrete control system	Variable processed by computer is digital variable (discrete variable), so computer control system is a discrete control system or a numerical control system
Quantity of control variable	Single variable control system: control system has only a pair of input and output variable	Single variable control system is the research object of classical control theory
	Multivariable control system: control system has several pairs of input and output variable	Multivariable control system is the research object of modern control theory
Change law of system parameters	Time-invariant system: parameters of all the components constructing the system and parameters in system mathematical model do not change with time	Systems in practical engineering can often be simplified as time-invariant systems
	Time-varying system: parameters of components constructing the system vary with time, and certain coefficients in system mathematical model are function of time	Carrier rocket is an example of time-varying system, whose quality varies with time
Inherent dynamic characteristics of system	Linear system: mathematical model of system is linear differential equation or linear difference equation, whose control theory is the fundamental of automatic control theory	
	Nonlinear system: there are nonlinear components in system, or mathematical model of the system is nonlinear equation	

(*continued*)

Table 4 (continued)

Classification method	System type	System feature
Control methods used by system	In analog variable control system, controllers can be classified as "proportional differential(PD)," "proportional integral (PI)," "proportion integration differentiation(PID)," and other control methods	
	In computer control system, various kinds of intelligent control methods can be implemented conveniently. According to different control algorithms used by controllers, intelligent control system can be classified as fuzzy control system, optimal control system, neural network control system, expert control system, etc.	

whole program into several modules, and each module implements a certain function. Structured program is limited to a specified structure type and operating order, to facilitate searching and error correction.

Software development involves many core technologies such as procedure parameter application, real-time precision compensation, data algorithm processing, detection and compensation of system error, system fault diagnosis and processing, and Internet communication. Data sampling, servo control, interpolation motion of space trajectory, and multi-axis control should be implemented by internal program of control system. Software development should also take portability and maintainability into consideration. Modularized design represents the present main stream. For example, system software can be divided into procedure parameter application software, real-time precision compensation software, CAD/CAM and FMS software, etc. According to the object, programming language can be classified into object-oriented language, robot language, embedded system language, real-time control language, and the like. In addition, there are man-machine conversation programming technology and construction of special database, etc. As the globalized communication becomes more and more frequent, the demand for generalization and standardization of software is higher and higher as well.

Common Control System of Precision Machines

According to the different controlled objects, common control system of precision machines can be divided into feed motion control system, temperature control system, and vibration control system. This section will describe these three types of control system, respectively, and give a brief introduction to the active measurement and control system, a specific example used in precision grinding machine tool.

Feed Motion Control System

The composition principle of feed motion control system is shown in Fig. 6. The system consists of servo drive system (including speed control circuit and position

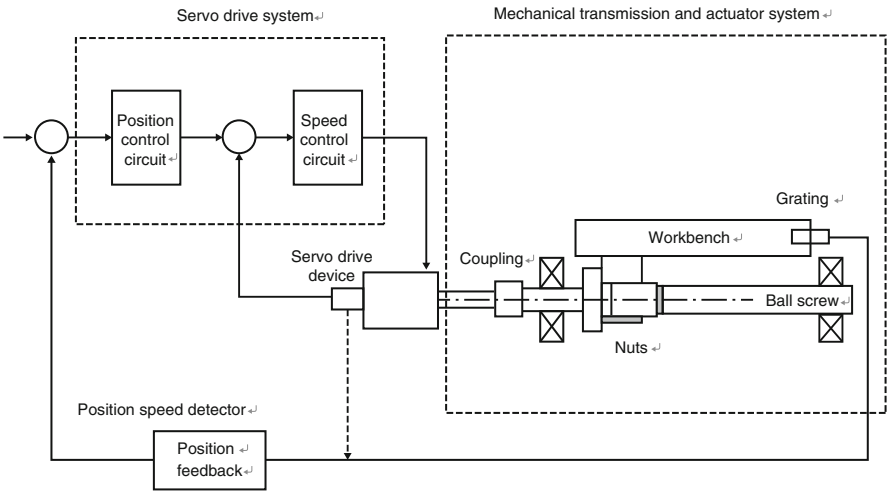

Fig. 6 Composition principle of a feed motion control system

control circuit), servo drive device, position detection device, mechanical transmission, and actuator system (Srinivasan and Tsao 1997). The drive device may be a DC servomotor, an AC servomotor, or a linear motor, and the position detection device is typically a linear measuring element such as an inductosyn or a grating scale.

The servo drive device and the transmission device will be described, respectively.

Servo Drive Device

The servo system is the actuating part of the feed motion control system, which receives various commands from the system and drives the controlled device movement. The servomotor is a key component of the servo system, which receives the feed command signal from the control system and converts it into angular displacement or linear displacement in order to drive the machine feed mechanism (Lin et al. 2011). The servomotor is divided into stepper motor, DC motor, AC motor, and linear motor. The motion control system of DC motor, AC motor, and linear motor will be introduced, respectively. The stepper motor will not be introduced due to its low accuracy.

DC Motor Motion Control System

DC motor is characterized by good starting, braking, and speed control, and it can easily achieve a smooth and stepless speed control in a wide range, so it is often used in occasions requiring a better speed control performance of servomotor. Linear motor is divided into electric excitation and permanent magnet excitation, in which permanent magnet motor dominates.

Permanent magnet DC servomotor has a wide range of speed control, a larger overload capacity, a larger torque output, and a higher mechanical strength.

Permanent magnet DC servomotor consists of a shell, stator pole, rotor hub group, rotor core, commutator electromechanical brush, and other components. The stator pole is permanent magnet and made of hard magnetic material, with a high remanence strength, as well as a high coercivity and good stability.

Permanent magnet DC servomotor can be divided into drive motor and servomotor, and there is no speed stabilizer for the DC drive motor. Servo DC motor with servo characteristics and quick response capability is often integrated with the feedback components, which include speed measuring motor, photoelectric encoder, as well as brake electromagnet embedded in the motor housing.

The working principle of DC servo is based on the law of electromagnetic force. Related to the electromagnetic torque are the two mutually independent variables of the main flux and armature current, which control the excitation current and armature current, respectively, and can easily control torque and speed. On the other hand, in terms of control, DC servo control is a single variable control system with a single input and a single output. The classic control theory is fully applicable to this system, so the DC servo system control is simple and has excellent speed control performance. However, considering the actual operation, DC servomotor introduces a mechanical commutation device. Commutator wears easily and needs regular maintenance. When the commutator is commutated, it produces sparks, thus limiting the maximum speed of the motor. Meanwhile, DC motor has the shortcomings including complex structure, manufacturing difficulties, overuse of steel materials and high manufacturing costs.

AC Motor Motion Control System

With the rapid development of the new high-power power electronic devices, new frequency conversion technology, modern control theory, and computer numerical control in practical applications, AC servo drive technology has made great progress, and AC motor began to be applied.

AC servomotor can be divided into asynchronous AC servomotor and synchronous AC servomotor. Among them, asynchronous AC servomotor has the advantages of strong structure, easy manufacture, and low cost; therefore, it has a good development prospect and represents the future direction of servo technology. However, the system uses a more complex vector transformation control compared with the synchronous AC servomotor, and the motor is facing low efficiency, serious heat, and other technical problems in the low-speed operation, so it has not been widely used. The technology of synchronous AC servomotor has become fully mature, with good low-speed performance, and can achieve flux weakening high-speed control, which makes it possible for synchronous AC servomotor to broaden the system speed range and adapt to the requirements of high-performance servo drive. Meanwhile, with the performance of a substantial increase and the continuous reduction of prices of permanent magnet materials, the synchronous AC servomotor will be more widely used in the field of industrial production automation. At present, it has become the mainstream of AC servo system.

Linear Motor Motion Control System

A linear motor is a power transmission device that directly converts electrical energy into linear motion mechanical energy. The working principle is similar as that of a rotating electric machine. Linear motors can also be divided into linear asynchronous motors, linear synchronous motors, linear DC motors, and special linear motors.

According to different excitation methods, linear asynchronous motor can be divided into permanent magnet linear motor and induction linear motor. Permanent magnet linear motor is better than induction linear motor in the unit area thrust, efficiency, controllability, and feed stability, but permanent magnet block process is complex and expensive. The presence of magnetism will bring a lot of inconvenience in the machine installation, operation, maintenance, chip removal, safety, and so on. There is no magnetism when the induction linear motor is not energized, so the induction linear motor is more convenient to install, operate, and maintain.

Transmission Device

The mechanical transmission device of the machine feed transmission system has two schemes, as shown in Figs. 7 and 8, respectively. Servomotor shown in Fig. 7 has a strong load capacity. Through the screw, it directly drives the workbench to feed, with a short transmission chain, high rigidity, and high transmission accuracy. It is the main form of modern CNC machine feed drive. The scheme shown in Fig. 8 has the following advantages:

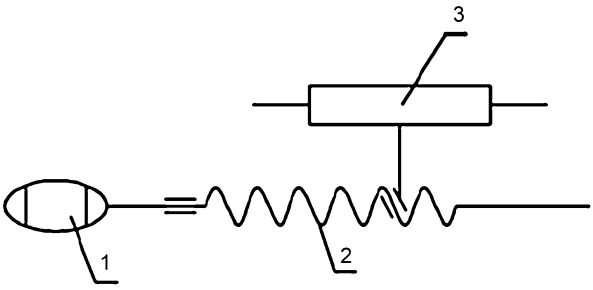

Fig. 7 Mechanical transmission device of direct drive

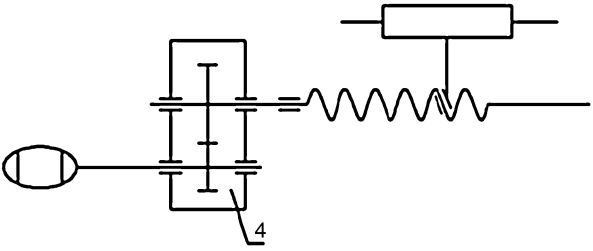

1. Servo motor 2.Ball screw nut pair 3.Workbench 4.Reducer

Fig. 8 Mechanical transmission device with reduction mechanism. (1) Servomotor, (2) ball screw nut pair, (3) workbench, and (4) reducer

(a) The scheme can refine the pulse equivalent, to ensure and improve the accuracy of the feed.
(b) The scheme can change the load torque applied to the motor shaft to achieve the best match with the motor output torque.
(c) The scheme can change the load inertia applied to the motor shaft to achieve the best match with the motor inertia.
(d) The scheme can improve the transmission damping and installation connections.

In general, the mechanical transmission device includes a guide rail for guiding and supporting the actuating part, a first to two stage gears or pulley drive couplings, a ball screw nut pair or a rack and pinion pair or a worm carrier pair and a support member thereof. The role of the gear pair or pulley pair of the transmission system is mainly to reduce the inertia of the feed system and obtain the required output mechanical characteristics by deceleration and also to match the required pulse equivalent for the open-loop system.

Temperature Control System

The temperature control system refers to the temperature control system of the machine tool spindle. The spindle rotates at a high speed in working condition, making a lot of heat and causing a higher temperature on the spindle. Once the spindle temperature exceeds the allowable range, it will result in the decrease of machining quality and even machine tool fault (Li et al. 2009).

Temperature Control System of Spindle Based on PLC

The working principle of the system is shown in Fig. 9. The infrared temperature sensor feedbacks the real-time temperature of the machine spindle to the input of PLC and compares it to the preset temperature. When the temperature of the machine spindle is too high, meaning the measured temperature is higher than the preset temperature, PLC issues a closed command to the relay through the parameter operation, and the control circuit closes the AC contactor, and then the cooling pump and fan motor enter the working state. When the cooling pump and fan motor begin to work, the temperature of the machine tool spindle will decrease. At this point, the infrared temperature sensor detects a temperature lower than the preset

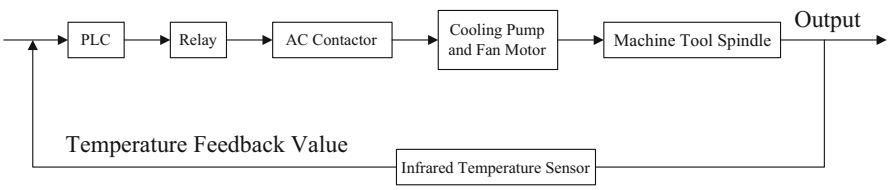

Fig. 9 Principle diagram of a temperature control system of machine tool spindle based on PLC

temperature of PLC, then the PLC control relay is disconnected, and the control circuit disconnects the AC contactor, so the cooling pump and fan motor stop working (Liang et al. 2015).

Temperature Control System of Spindle Based on Single-Chip Microcomputer

The working principle of the system is shown in Fig. 10. The system consists of single-chip microcomputer, relay, AC contactor, cooling pump, cooling fan, CNC machine tool spindle, spindle motor, and temperature sensor. When the specified temperature T_{i1} is compared with the feedback temperature t_{o1}, the error signal 1 is obtained to control the opening/closing of Relay 1, so as to turn on/off the cooling pump of CNC machine tool spindle; the error signal 2 is obtained after comparing the specified temperature T_{i2} with the feedback temperature t_{o2}, and then the opening/closing of Relay 2 is controlled to turn on/off the cooling fan of spindle motor, so as to control the temperature of spindle and spindle motor of CNC machine tools and to keep the temperature within the preset safe operation range.

Vibration Control System

Vibration control is an important branch in the field of vibration engineering. The vibration control can be classified as passivity-based control and activity-based control according to whether energy is needed. The former is also called passive control, and the latter is called active control.

Passive Control System

Passive control does not require external energy sources. Owing to its other advantages including simple structure, easy realization, good economy, and reliability, it has a wide application. Generally speaking, passive vibration control refers to passive damping design. The objective of all passive damping design is to maximize the absorption and dissipation of modal strain energy in the modes of interest. According to structures, passive damping system usually includes the following

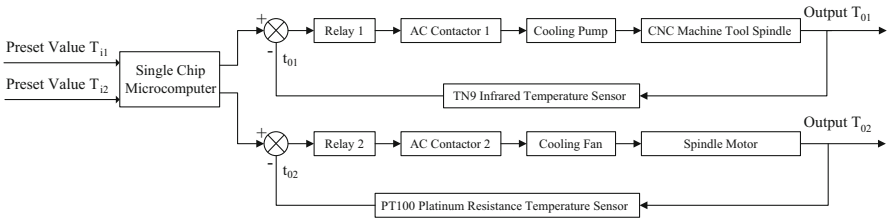

Fig. 10 Principle diagram of a temperature control system of machine tool spindle based on single-chip microcomputer

aspects: bar damper, damping hinge, mass tuned damper, unconstrained damping structure and constrained damping structure, etc. (Rivin 2003).

Active Control System

With the increasing demand for vibration characteristics, the limits of passive control become clearer. For example, when the passive vibration isolator isolates vibration of low external frequency, problems like excessive static deformation and instability will occur, resulting in serious problem of low vibration isolation, and the damping of the isolator cannot be changed once it is determined. Active vibration control technology is attracting more and more attention because of its potential advantages such as efficiency and adaptability.

Active vibration control means in vibration control process, according to the detected vibration signal and by control strategy and real-time computing, the actuator exerts certain influence on the controlled objects to suppress or eliminate the vibration (Wen 2014). Active vibration control can be classified as open-loop control and closed-loop control, and the block diagram is shown in Fig. 11.

Open-loop control is also called program control, as shown in Fig. 11a. The control rate is designed in advance, so it is independent of the vibration state of a controlled object. But the controller in closed-loop control works according to the vibration state of the controlled object as feedback information. At present, closed-loop control is the most widely used control method.

The vibration closed-loop control is shown in Fig. 11b. It is the real-time external control which makes the vibration meet the predetermined requirements based on the vibration state of the controlled object. Specifically speaking, the sensor mounted on a controlled object senses its vibration, and the sensor signals are adjusted, amplified, and transmitted to the controller, and then the controller implements the desired control law. The output is the actuating instructions of the actuator, and the actuator exerts directly or through the attached sub-system on the controlled object, which constitutes a closed-loop vibration control system.

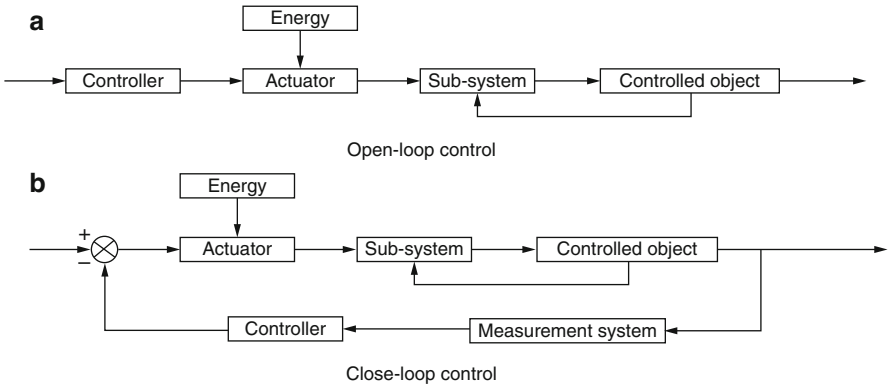

Fig. 11 Two active vibration control systems

Typical Examples of Control System of Precision Machines

Active Measurement System

Active measurement used in the precision grinding machining is an automatic measurement technique in machining processes of machine tools or other equipment, also known as online measurement. It refers to the measurement of size and roughness of the workpiece during the processing of the workpiece and the immediate adjustment of processing conditions according to the information obtained from the measurement, in order to ensure that the workpiece produced is qualified. Active measurement combines the measurement and machining process together to ensure the accuracy of the workpiece, improve the production efficiency, and prevent the waste from being produced. Active measurement is a positive method of measurement, so it's also called positive measurement.

The working principle of active measurement system is to constantly measure the size of workpiece by a measuring device during the internal and external circular grinding process and to transmit the size variations to the controller, and then the controller sends a signal, such as coarse grinding, fine grinding, polishing, and reaching target dimensions, to control the actions of the machine tool. Because the operator could measure the workpiece size accurately without downtime, the system can effectively reduce the labor intensity, improve the production efficiency, reduce the rejection rate, and ensure that the size of the workpiece is highly consistent. This system is especially suitable for large-scale assembly line work, such as the processing of auto parts and bearing parts, etc.

In the grinding process of the workpiece, the measuring device measures the workpiece in real time and delivers the measurement results to the controller. The controller sends out signals according to the preset signal points, to control the actions of the machine tool. Figure 12 shows the grinding process controlled by three signal points. First the grinding wheel fast feeds and enters into the coarse grinding stage, where P1 is the signal point from coarse grinding feed to fine grinding feed, P2 is the signal point from fine grinding feed to sparking out feed, and P3 is the tool

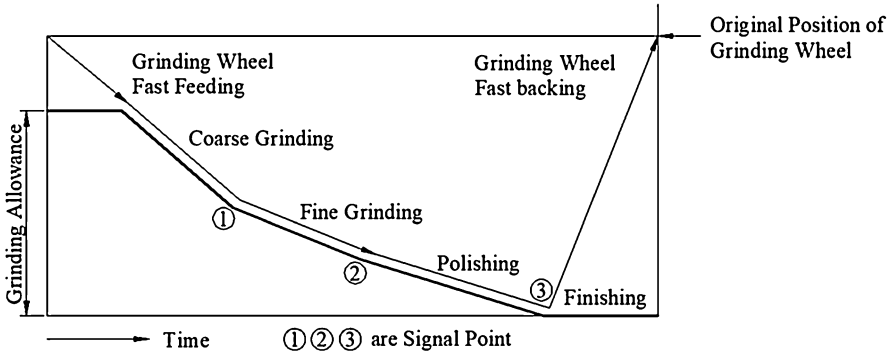

Fig. 12 Grinding process

retracting signal point of reaching target dimensions. The machine tool control system receives these three signals successively from the controller and performs different actions, respectively, completing a grinding cycle. For high-precision grinding, the dimension distribution of workpiece can be controlled at 2–3 μm. The control signal points can be increased from 3 to 4–6 points according to the different requirements of technique and dimensional accuracy.

The active measurement system mainly consists of three parts: measuring device, drive device, and controller. (1) The measuring device usually uses inductance sensors, commonly known as probes, which can change the size of the measured parameters into measuring voltage signals. It's the main part of the measuring instrument. In the process of workpiece grinding, two diamond probes of the device always contact the surface of the workpiece, and the variation of the workpiece diameter passes through the probe and the lever, so that the position of the magnetic core and inductance coil in the device is relatively displaced. Thus, the change of size can be converted to the change of inductance. According to the structural difference, the measuring device can be classified as single-point measuring device and double-point measuring device. The former can be used in end face positioning or in measuring larger diameter by combining two devices. The latter can measure the outer diameter, inner diameter, slot width, step width, etc. (2) Controller is an important part of active measurement system. It can collect the inductance signals detected by the measuring device. The inductance signals are phase-rectified, amplified, and displayed, sending coarse grinding, fine grinding, polishing, and reaching dimension signals to the grinding machine control system. The grinding machine control system controls the feed mechanism of the machine tool after receiving the signals and finishes the workpiece processing, so as to achieve the purpose of controlling the size of the workpiece. (3) The oil pressure drive device drives the measuring device to feed and retract. When the workpiece is installed, the grinding wheel fast feeds and the drive cylinder also drives the active measuring device into the measuring station at the same time. After grinding to reach target dimensions, the controller sends out a tool retracting signal, the grinding wheel retracts quickly, and the drive cylinder also drives the active measuring device to exit the measuring station, to facilitate operator to load and unload the workpiece (Wang and Gu 2004; Duan 2016).

Grating Scale Precision Control System

Grating Scale

The purpose of motion control is to implement an accurate control of the position of moving parts, and in most cases, closed-loop control is adopted; therefore, sensors that can accurately measure the position of the moving parts are indispensable in a completed closed-loop control system. At present, digital sensors are commonly used in CNC machine tools and robot control, such as linear and rotary photoelectric encoder, linear grating scale, magnetic railing ruler, resolver, etc. Among them, high-precision grating linear displacement sensor, a.k.a. grating scale, is an element for

precision measurement and position feedback detection. It is mainly used in precision or ultraprecision CNC machine tools and precision measuring equipment and plays an irreplaceable role in advanced manufacture as well as metrology and measurement. Grating linear displacement sensor is a priority selection for moving parts of positioning machines. Due to its high precision, high resolution, relatively low cost, dustproof and liquid-proof enclosed structure, it is widely used in mechanical machining and manufacturing as well as in coordinate measuring machine, robot, positioning device, and almost every application that requires motion control of position and speed. Take mechanical machining and manufacturing as an example, micrometer and submicron positioning have already been successfully applied in common and high-precision machining and measurement, while ultraprecision machining with positioning under submicron is mainly used in areas such as modern national defense and military, astronomy, and aerospace (Zhang et al. 2006; Israel et al. 2008; Hafeez et al. 2015).

Principle of Grating Scale

Take transmission grating as an example, when the stripes in indicative grating and scale grating form a small angle θ, and the two grating scales are placed with their grooved faces parallel, under the irradiation of light source, alternated dark and bright fringes are produced in the direction which is nearly perpendicular to the grating lines, that is called "moire fringes," as is shown in Fig. 13. Strictly speaking, moire fringes are arranged in a direction perpendicular to the bisector of the included angle between two grating lines. The distance between two bright stripes or two dark stripes is called width of moire fringe, denoted as W:

$$W = \omega/2^{*} \sin(\theta/2) = \omega/\theta$$

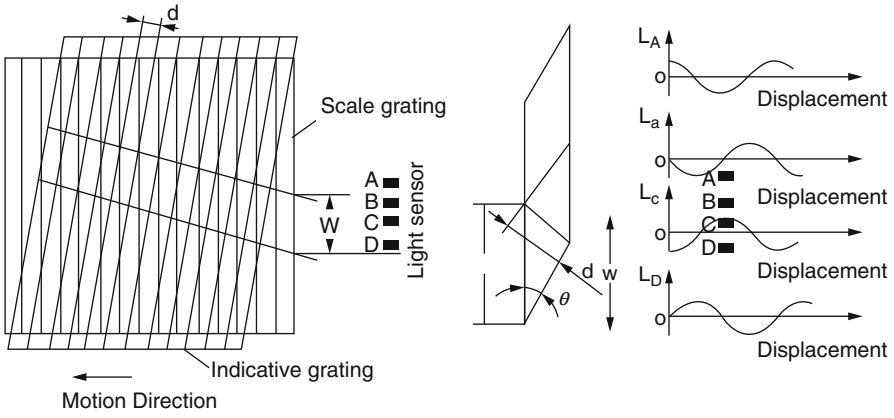

Fig. 13 Moire fringes

Measuring displacement by grating in essence is using grating pitch as a standard scale. Generally, it is difficult to fabricate grating scale with high resolution and the cost is expensive. To improve systemic resolution, subdividing moire fringes is required. Electronic subdivision is mostly used nowadays in system of grating scale sensors. When two grating plates coincide with a tiny angle, moire fringes will be produced in the direction approximately perpendicular to the grating lines. With the movement of grating plates, moire fringes fluctuate at the same time. By this means, measuring grating pitch can be transformed into counting the numbers of moire fringes.

Within a single width of moire fringes, electronic subdivision and direction judgment can be implemented by setting four photoelectric devices at certain intervals. For a grating scale of 0.02 mm grating pitch and 50 grating line pairs per mm, counting pulse with resolution of 5 μm can be obtained if four subdivisions is done. This has achieved a high precision in common industrial measurement and control. Because displacement is a vector, both direction and value should be tested, so at least two photoelectric signals with different phases are required. In order to eliminate common mode interference, DC component, and even harmonics, differential amplifier constituted by low-drift operational amplifier is usually adopted. Four photoelectric signals acquired by four photo sensors are transmitted to the input ends of the two differential amplifiers, from which two output signals will have a phase difference of $\pi/2$. To obtain the direction judgment and counting pulses, these two signals should be shaped as square wave with duty ratio 1:1. Then by comparing and discriminating the phase of the square wave, the movement direction of the grating scale can be obtained; by counting the square wave pulses, the displacement and velocity of the grating scale can be obtained.

Application of Grating Scale in Machine Tools

In precision CNC machine tools, grating scale is used as a position detection device to detect whether the actual displacement of linear axis in the machine tool is consistent with the issued instructions from the numerical control system. The critical elements that determine the machining accuracy of a CNC machine tool not only depend on its mechanical parts but also on the accuracy of its grating scale (i.e., resolution). Grating scale is generally constituted by "fixed scale," "movable scale" (grating reading head), and connecting cables. HEIDENHAIN (Germany), the first brand worldwide in the field of grating scale, plays an important role in the machining accuracy of CNC machine tool. FAGOR (Spain) grating scales are currently used in many of the world's manufacturers and definitely become the world's second brand. As a position detection device in CNC machine tool, grating scale "supervises" whether the linear axis moves accurately to the position required by instruction issued from the CNC system.

Grating linear displacement sensor with resolution less than 1 nm is mainly used in precision machining at atomic and molecular level. Take picometer grating resolution from SONY (Japan) company as an example, grating linear displacement sensor with resolution of 50 pm is mainly applied in semiconductor detection equipment, LCD lithography equipment, high-precision lathe, and spark erosion

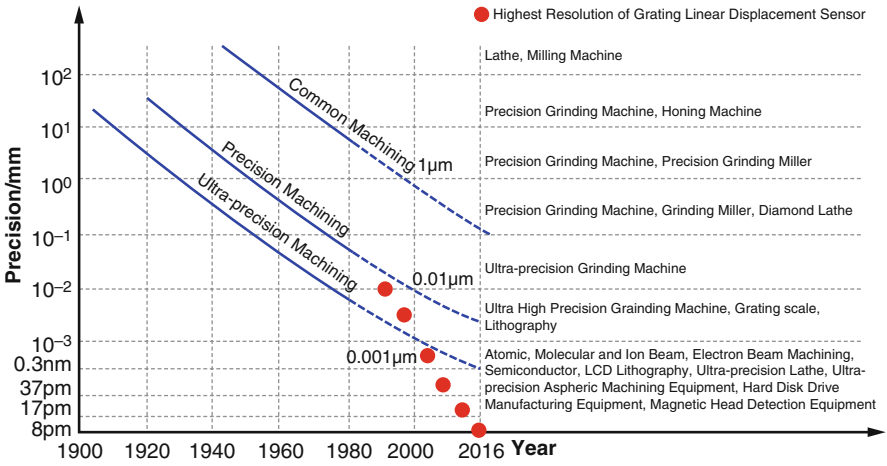

Fig. 14 Requirement of grating scale resolution and mechanical machining

equipment; grating linear displacement sensor with resolution of 31.25 pm is applied in hard disk drive manufacturing equipment and magnetic head detection equipment; grating linear displacement sensor with resolution of 17.25 pm is mainly applied in semiconductor lithography equipment, detector, disk cutting machine, aspheric machining equipment, and EB tracking equipment; ultraprecision lathe and aspheric machine tool developed by MOORE (USA) in 2016 adopt grating linear displacement sensor with resolution of 8.4 pm and 8 pm. The surface accuracy of some representative parts it machined is less than 0.1 μm, which can be used to produce reflectors of laser gyroscope in intercontinental cruise missiles and camera lens of unmanned plane to meet the strategic needs of national defense.

The requirement of mechanical machining accuracy and resolution of grating linear displacement sensor is shown in Fig. 14. From a worldwide perspective, as the resolution of grating linear displacement sensor improves, the machining accuracy develops rapidly in common machining, precision machining, and ultraprecision machining. Funded by China's national 12th 5-year plan in the field of advanced manufacturing technology, ultraprecision machining related to advanced manufacturing technology has also developed rapidly. However, manufacturing technology at subnanometer or picometer level has brought us new challenges.

Conclusion

This chapter first briefs on the development of control system of precision machines and then gives a definition of control system of precision machines. It also describes the common classification of control system of precision machines according to different classification criteria. Then, some key techniques in the control system of precision machines are elaborated in detail, including precision machine technology,

detection sensor technology, information processing technology, servo drive technology, automatic control technology, and system software technology. Finally, this chapter briefly introduces three common control systems of precision machines, such as feed motion control system, temperature control system, and vibration control system, as well as two typical cases applied in precision machine tool control, such as active measurement control system and grating scale precision control system.

References

Duan TS (2016) Development of digital mill processing active measuring instrument. J Mach Tool Hydraul 44(16):146–148

Fu SG, Zhang XZ, Ma EN (2010) Foundation of machinery manufacturing process, 3rd edn. Tsinghua University Press, Beijing

Gao ZY (2011) Mechanical and electrical control engineering. M. Tsinghua University Press, Beijing

Hafeez H, Ryu HY, An IS et al (2015) Dimensionally controlled complex 3D sub-micron pattern fabrication by single step dual diffuser lithography (DDL). J Microelectron Eng 143:25–30

Hu SS (2013) The principle of automatic control, 6th edn. Science Press, Beijing

Israel W, Tiemann I, Metz G et al (2008) An international length comparison at an industrial level using a photoelectric incremental encoder as transfer standard. J Precis Eng 32(1):1–6

Lei D (2013) Motion control system. Post & Telecom Press, Beijing

Li SY, Dai YF, Wang JM, Wu YL, etc. (2009) Precision and ultraprecision machine tool design philosophy and methodology. National University of Defense and Technology Press, Changsha

Liang ZY, Zhong PS, Liu K, Ge X (2015) Machine spindle temperature control system based on PLC. Manuf Technol Mach Tool 7:87–90

Lin S, Zhang CY, Chen SL (2011) Modern CNC machine tools. Chemical Industry Press, Beijing

Liu HY, Luo Z, Wong F (2008) Modern mechanical engineering automatic control. M. Science Press, Beijing

Dorf RC, Bishop RH (1998) Modern control systems. Addison-Wesley, Menlo Park

Rivin EI (2003) Passive vibration isolation. ASME, New York

Srinivasan K, Tsao TC (1997) Machine tool feed drives and their control – a survey of the state of the art. J Manuf Sci Eng 119:743–748

Tan X (2013) The foundation of mechanical engineering control. M. Tsinghua University Press, Beijing

Wang XS (2009) Precision mechanical motion control system. M. Science Press, Beijing

Wang XK (2013) Technology of Mechanical Manufacture. China Machine Press, Beijing

Wang HW, Gu MC (2004) Active measuring instrument in grinding process. J Tools Technol 38(3):65–67

Wang JH, Gu SS (2014) The principle of automatic control, 2nd edn. Tsinghua University Press, Beijing

Wen BC (2014) Machinery handbook (5th edn), monograph, Mechanical system vibration design and noise control. China Machine Press, Beijing

Wen BC, Zhou ZC, Han QK et al (2003) The important role of modern mechanical product design in the development of new products – also on the comprehensive design method of "dynamic optimization, intellectualization and visualization" for the overall quality of products. Aust J Mech Eng 39(10):43–52

Wu KG (2009) Mechanical equipment control technology. Higher Education Press, Beijing

Xiong LS (2012) Fundamental of mechanical manufacture technology. Huazhong University of Science and Technology (HUST) Press, Wuhan

Xu XH et al (1995) Electronic precision mechanical design. M. National Defense Industry Press, Beijing

Zhang SY, Gao LQ (2006) Modern control theory. Tsinghua University Press, Beijing

Zhang J, Lu ZH, Wang LJ (2006) Precision measurement of the refractive index of air with frequency combs. J Opt Lett 30(24):3314–3316

Robot-Based Precision Machines

11

J. P. Xi

Contents

Introduction 292
Composition of the Robotic Machine Tools 292
Manipulator 292
Composition and Classification of Manipulators 293
Accurate Machine Tools 294
Control System 297
Vision System 299
Application of Robot-Based Precision Machines 302
Turning Lathe 302
Additive Manufacture of Machine Tools 303
Thin-Wall Machine Tools 304
Accurate Polishing Robot Machine Tools 306
Research on Complex Surface Machining 307
Design Requirements of Flexible Polishing Tools 308
Polishing of Optical and Aspheric Surface 310
Conclusion 311
References 312

Abstract

Traditional processing methods depend on manual work, which is time-consuming and physically demanding, and results in relatively low production efficiency and machining accuracy. To improve from the current situation, a series of automatic processing technologies built on robots and mechanical equipment have emerged. Precision machining is realized by designed manipulators and other equipment. This chapter introduces a series of mechanical equipment, such as turning machines, thin-wall processing machines, and polishing machine, that are based on manipulators. Automatic equipment is composed of a mechanical

J. P. Xi (✉)
Zhongyuan University of Technology, Zhengzhou, China
e-mail: xjpyq2010@163.com

Z. Jiang, S. Yang (eds.), *Precision Machines*, Precision Manufacturing,
https://doi.org/10.1007/978-981-13-0381-4_27

structure and a control system. The mechanical part refers mainly to the structure of the manipulator, which is designed based on its functions in the machining process, whereas the control system includes primarily the visual system and feedback system. The precision of automatic machining is determined by the precise control of the manipulator. Automatic processing methods have higher precisions and productivities and have therefore replaced traditional processing methods. With the improvement of the level of industry, industrial robots have become more widely used.

Keywords

Manipulator · Precision machine tool · Control system · Polishing

Introduction

For a wide variety of machining operations, robotic machining centers have great advantages, such as a large range of operations, strong reorientation ability, and low cost. Among the many advantages of using robots in machining operations, the most important is the low cost, where the cost of a robot is lower than that of human labor within the same workspace. Most robots are used in machining operations where the cutting forces required are quite small, such as trimming, drilling, burring, grinding, milling, and polishing of composite parts and metal parts. In recent years, the rate of sale of industrial robots has been increasing, which indicates that industrial robots have become increasingly important in machining centers.

Based on precision, machining can generally be classified into three types: general, precision, and ultraprecision machining. However, with the development of production technologies, common machining technologies can no longer satisfy the evolving requirements of the industry. Therefore, domestic ultraprecision has been systematically developed for machining technology. Precision and ultra-precision machining, which can be accomplished via the comprehensive application of precision machine tools and robots, has replaced traditional manual processing, thus guaranteeing compliance with the requirements of precision machining and realizing the fulfillment of technological innovation. This development is of great significance to the innovation of production and processing technologies (Ren 2008; Zhu and Tian 2003).

Composition of the Robotic Machine Tools

Manipulator

Multidisciplinary integration is one of the fastest-growing fields in modern high-tech and is an important part of modern machinery manufacturing. In automatic production processes, the manipulator is a type of mechanical device used for grabbing and

moving workpieces. The industrial manipulator, on the other hand, a new form of technology in the field of modern automation control, is a mechanical device that can replace traditional manual labor by automatically transferring or operating objects (such as materials, workpieces, parts, or tools) according to a given program. Additionally, higher types of manipulators can be simulated to move like a human arm to perform more complex operations.

At present, because of its continuous development, the industrial manipulator has many advantages, such as automatic positioning, repeatable programming, multi-function, and multi-freedom. Using a manipulator improves the degree of automation, the rhythm, and the conditions of work in the production process, which reduces human labor and the occurrence of dangerous accidents.

Composition and Classification of Manipulators

A manipulator is generally composed of a hand, connecting gear, driving part, control unit, and other parts. Because manipulators are widely used for a variety of purposes, they are often classified in terms of their range of use, forms of motioning coordinates, and driving modes.

Manipulator Usage

① Special manipulator. This type of manipulator usually has a fixed program and no separate control system. It belongs to a machine or production line that automatically transfers objects or creates tools. Examples include the "blank feeding and unloading manipulator" and the "automatic turning lathe manipulator." The structure of this manipulator is simple and suitable for mass production.

② General manipulator (also known as industrial robot). This term refers to a control system with variable programs and separate drives. This kind of manipulator is not subordinate to another machine and can automatically transfer objects or operate certain tools.

The general manipulator can be classified as either the simple type or servo type, according to the way of positioning and control mode. The simple type performs point control only and is managed via the control type program. The servo type, on the other hand, can perform both point and continuous trajectory control, which are managed by the digital control type.

Manipulator Coordinates of Motion

① Rectangular coordinate manipulator. The arm can move along the X, Y, and Z axes of the rectangular coordinate system, that is, forward and backward, left and right, and up and down, respectively.

② Cylindrical coordinate manipulator. The arm can move along the X and Z axes of the rectangular coordinate system, that is, forward and backward, and up and down, respectively, and can also rotate around the Z-axis, that is, left and right rotation.

③ Spherical coordinate manipulator. The arm can move along the X axis of the rectangular coordinate system, that is, forward and backward, and can also rotate around the Y and Z axes, that is, up and down swing, and left and right rotation, respectively.
④ Multi-joint manipulator. The manipulator is divided into a large arm and a small arm. There are joints between the large and small arms, and between the large arm and body, that is, the small arm can swing up and down around the elbow, the large arm can swing around the shoulder (body) at a certain angle, and the entire arm can also rotate left and right.

Manipulator Driving System

① Hydraulically driven manipulator: driven by oil pressure
② Pneumatic manipulator: driven by compressed air
③ Electrically driven manipulator: directly driven by an electric motor
④ Mechanically driven manipulator: a driving mode transmits the power of the host machine to the manipulator via a cam, connecting rod, gear, intermittent mechanism, etc. (Peng 2006)

Accurate Machine Tools

Among machine tools, the most common industrial robot, which is used in almost all industrial automation, is the automatic feeding and unloading manipulator. The basic requirement of designing this manipulator is balance. When the manipulator grasps the material, stability is ensured in the process of movement. Certain requirements, such as the control of adjusting speed and setting of motion path, are necessary in designing its control system. After the material is clamped, balance is maintained, and the load control should be accurate. Some industrial manipulators are designed with a balance mechanism, which is a design method that allows two materials to be grasped at the same time. In this way, the efficiency of feeding and unloading will be relatively high, and the cost performance will also be high.

No matter which design method is adopted, there has to be a balance mechanism to ensure that balance is also maintained in the working state (Chen 2018; Zhao and Lv 2015; Wu et al. 2019).

The feeding and unloading manipulator is a special industrial manipulator, wherein the implementation of the program is generally fixed or allows only for simple modifications to the programming. Thus, the action of the manipulator is fixed. This type of manipulator can deliver only one or a limited number of items, because the program control system is relatively simple.

This manipulator, which utilizes a kind of feeding mechanism along with a material groove and slide, grabs an object (workpiece) from one position (material groove) and then carries it to another position. Its basic action is as follows: When it starts feeding, the manipulator takes the workpiece from the material groove to the designated station and puts it onto the station, and then the manipulator returns to its original position. When unloading, the manipulator takes down the workpiece from

the station and puts it into the material box. The working process for the feeding phase has some requirements for position and orientation, whereas the unloading phase generally has no strict requirements. Thus, the feeding phase is the key that determines the effectiveness of the manipulator.

To complete the above actions, the hand claw of the upper and lower material manipulator must reach two points (picking point – material groove; feeding point – processing station), which can be achieved by the arm of the manipulator. The claw must perform two actions (grasp material and drop material), which can be achieved by closing and opening the claw of the manipulator. The feeding requirements can generally be met by the wrist movement of the manipulator, the track should be: straight line down → straight line up → plane arc swing → straight line down.

Characteristics of the feeding and unloading manipulator:

① Adaptability to a variety of complex environments. The manipulator can perform tasks under conditions that may not be comfortable, healthy, or safe for human beings, such as noisy environments, high temperatures in workshops, and some dangerous operating environments.
② Capability for continuous work. There is a time limit for how long people can work. If this time limit is not implemented, the job and workforce will be prone to dangerous accidents. On the other hand, a manipulator can work continuously for a long time without any accidents. The stability is still relatively high, and the efficiency is basically unchanged, compared to that of human labor.
③ Accurate action for clamping and positioning. The working path of the manipulator is set by the program. The program executed once every cycle is completed, and the action is basically unchanged, compared to what humans do.
④ Wide applicability and high flexibility. These characteristics refer to the feasibility of designing the manipulator for a wide variety of jobs.

An automatic feeding and unloading manipulator is shown in Fig. 1. In dangerous processes and machinery, such as the punch press, the manipulator will replace the manual feeding and unloading (Li 2019; Tian 2016).

The robot is also widely used in the production and manufacture of pistons. The developmental trend for machining pistons is the use of automatic production lines with high efficiencies and flexibility. Key technologies include processing technology, tooling and logistics, automatic detection, automatic and comprehensive compensation, and processing integration. The technical requirements for the noncircular surface, ring groove, and pin hole of the piston group include the machining of the coarse and fine pin holes, coarse and fine turning ring grooves, and outer circle and top surface. In the past, the truss manipulator was used for its high efficiency and flexibility. Using robots for feeding, unloading, and logistics can simplify the auxiliary structure of logistics, and realize the efficient and flexible processing of pistons (Huang 2008).

Another typical example is the use of manipulators as a polishing head for polishing machine tools. Because of its flexibility and high precision, the manipulator is often used as a polishing head, as shown in Fig. 2, when complex surfaces and optical components are being machined.

Fig. 1 Automatic feeding and unloading manipulator

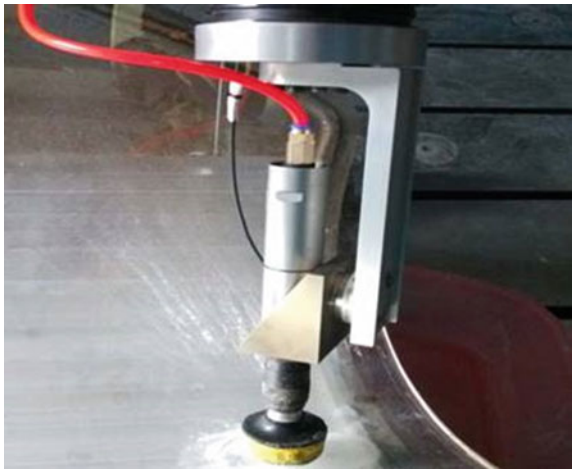

Fig. 2 Polishing head

In the process of machining, flexible polishing tools are used to produce high-quality polished surfaces. The end actuator of the manipulator is made to be able to rotate flexibly because complex surfaces may have multiple surfaces. Based on the change of the surface curvature during polishing, it may be necessary to flexibly rotate the polishing head and adjust the polishing angle. During polishing, the polishing tool is always rotating at a high speed. The contact material between the tool and surface of the work piece is mostly sandpaper, and thus this sandpaper wears out easily and has to be changed regularly. The manipulator is polishing the curved

surface, which is polished by the high-speed rotation of the polishing head and the friction between the sandpaper and the contact surface.

Control System

The control system, which plays a leading role in both ultraprecision machine tools and industrial manipulators, is a basis for determining whether these tools and equipment can accurately work in a designated position and are able to work continuously.

In the process of machining, maintaining the accuracies of ultraprecision machine tools high is very critical. The slide carriage is an important part of the machine tool because the vibration it generates is directly transmitted from the tool holder to the surface of the workpiece and affects the quality of machining. During this process, reducing the vibration amplitude of the slide carriage is necessary for improving the accuracy of linear motion, which is, in turn, of great significance to improving the surface quality of the workpiece.

The function of the actuator is useful in the process of designing the system. The actuator itself provides the proper control force for the controlled object. Because of the vibration during the movement of the slide carriage, two problems will need to be solved: the first is that the control accuracy of the actuator itself depends on the displacement, whereas the second is that the actuator and the slide carriage or guide rail should be movably connected, and that the slide carriage must be accurate. However, achieving precise control for the components at the same time is relatively difficult. Therefore, another design method can be used. Installing the actuator between the static guide rail and slide carriage is difficult, and thus the guide plate is installed on one side or both sides of the slide carriage, which is parallel to the static guide rail. The actuator is placed between the slide carriage and guide plate. Two actuators are required to control the lateral movement and rotation about the vertical axis of the slide carriage. The vibration signal of the slide carriage is measured by a sensor and is amplified and filtered by an amplifier and filter, respectively. The data are then transmitted to a computer, and the result is calculated by the computer using an algorithm and transmitted to the power supply of the actuator. The actuator can then control the vibration of the slide carriage (Wang 2002).

The control of machine temperature is one of the basic conditions that can actualize ultraprecision machining and keep the precision basically unchanged. According to the current theory on machine tools, one of the main reasons for the decline of machining accuracy is the change of temperature around the machine tools. Therefore, keeping the temperature constant around the machine tools during the process of machining is important. Through a comparison of several temperature systems, constant-temperature oil spray is found to be the most effective way of reducing the thermal deformation of machine tools and improving thermal stability and machining accuracy. The temperature control system can be designed using a fuzzy control system for a single-chip microcomputer, which mainly adopts the

structure of a single-chip microcomputer and uses delay pulses to trigger a bidirectional thyristor. Without the special contactor, the control process is relatively simple, and the transition time is short (Wang 2000).

In addition, specialized systems, such as distance detection systems, positioning systems, and servo systems, may be included in the setup. In a system designed for a manipulator, a programmable logic controller (PLC) is used mainly to control the industrial manipulator, with the control system designed based on the basic structure and workflow of the industrial manipulator (Han 2019; Jin 2019). The design uses the structure of a cylinder to drive the manipulator up and down and to perform in-plane rotation. The common working modes of the system can be divided into four: manual, single step, single cycle (semi-automatic), and continuous (fully automatic). The basic workflow of the manipulator is shown in Fig. 3 (Wang et al. 2019).

In this system, the main task is to control the cylinder using a solenoid valve and to complete the process of grasping using the manipulator. With an air compressor as the power source and compressed air as the working medium, energy and information are transmitted. The cost of this process is low. In the process of air pressure control, balancing the input and output pressures of the cylinder is necessary. Therefore, the system should employ feedback control of the air circuit, which includes three modules: air source processing, air load processing, and signal feedback processing. Air source processing involves air intake from the production room, and filtration and modulation of the voltage regulator. After treatment, the compressed gas is delivered to the cylinder and an empty load selection module. In air load processing, the empty load selection module, which is composed of pressure-regulating valves and switches, transmits the signal when the manipulator is loaded to the signal feedback processing device. The signal feedback processing module, on the other hand, consists of a cylinder, a main pneumatic control valve, and an OR valve. This module can input the feedback signal of the cylinder and the logic or valve signal of the empty load to the main pneumatic control valve until the input and output pressures of the cylinder reach a balance. The balance of the manipulator is also adjusted, especially in the case of no-load and load. Adjusting the different pressures is necessary to reach a state of force balance. The output pressure

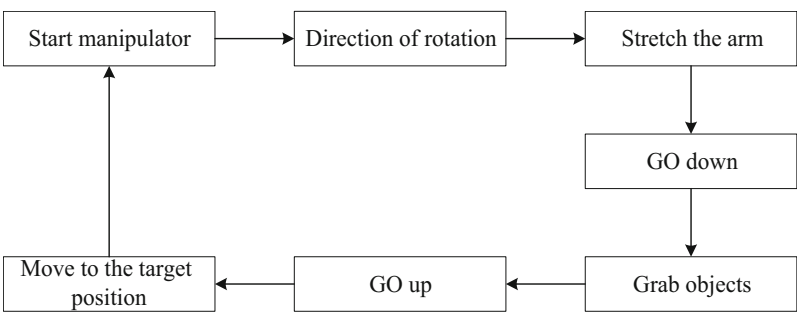

Fig. 3 Workflow of manipulator

of the main air control valve should be adjusted and controlled for the load end of the manipulator to become equal to the torque of the air cylinder. The cylinder can sense the change of the load end in real time, which allows balance of the manipulator to be enforced at any time (Ba et al. 2017; Zhou 2019).

Vision System

Vision is the main source of external information. Human beings sense the external world through their eyes, which transmit information to the brain to process the information, send out corresponding control signals, and complete a series of limb movements.

The vision system of a machine, on the other hand, uses a vision sensor to convert information from the surrounding environment into visual information and then transfers the converted information to the controller of the manipulator. Subsequently, the controller of the manipulator sends out commands that make the manipulator work flexibly, to better adapt to the surrounding environment. As industrial development progresses, the vision system is also being constantly applied to the direction of product processing, to better achieve full production automation. For example, a parallel sorting robot, together with some picking robots, was developed by Guangzhou CNC.

Machine vision has the following characteristics: fast processing of information, non-destructive testing, wide range of detection, and high accuracy (Li 2018). The core of an image sensor is either a charge-coupled device (CCD) unit or standard complementary metal-oxide semiconductor (CMOS) unit, which is similar to each other. Most sensors use CMOS units. Their basic principles and photosensitive materials are similar, but their processes for reading an image are different. With a CCD unit, data are transmitted in frame or line mode via the cooperation of synchronous and clock signals, and the reading speed is low. On the other hand, a CMOS unit reads the signal in a way similar to that used by dynamic random-access memory (DRAM), which uses a simple circuit and has a high reading speed. The quality of optical devices and resolution of visual camera determine the resolution of each pixel and the fine description of local features during imaging. To obtain three-dimensional information on an object, measuring its image is necessary. Image measuring technology involves computer recognition, the visual image, and other related fields. In image measuring technology, the required three-dimensional information can be obtained from the two-dimensional information of an image using a camera and the calibration of a coordinate system. The result of calibration and the stability of the algorithm are keys to the accuracy of the measurement.

The precision of the system can be controlled by visual feedback, that is, visual servo in machine vision. Visual servo is widely used in tracking rockets, automatic navigation, and other similar systems, and is able to solve the problem of low precision encountered with robots. Visual servo systems are divided based on the different types of information found in the feedback: position-based, image-based, and 2.5D-based visual servo systems.

A position-based visual servo system, which is also called a 3D visual servo system, takes the position of the end actuator as the feedback information. The system is adjusted by the controller according to the deviation between the actual and expected terminal position of the manipulator. The system chart is shown in Fig. 4. Because the signals of the input and feedback are spatial poses, designing the controller is easy. The pose of the object in the three-dimensional space is restored according to the measured image. However, system errors caused by camera calibration have a great impact on the control system. This type of setup is therefore not suitable for systems where these kinds of errors tend to be large.

Meanwhile, the image-based visual servo system takes the features of the image and extracts them from two dimensions as the feedback, which is also known as 2D visual servo. The system is directed by the controller according to the error between the features of the actual image and the expected features. The system chart is shown in Fig. 5. Designing a controller for this system is difficult, and therefore the Jacobi singularity, which is easy to enter into the control process, is used. Unlike with the position-based system, errors from camera calibration in an image-based visual servo system have little effect on the control system.

The 2.5D-based visual servo system is a combination of the 2D and 3D visual servo. This system, illustrated in Fig. 6, combines the advantages of the former two systems: like an image-based system, it is not sensitive to errors of camera calibration, and like a position-based system, it does not need to establish the Jacobi matrix. The 2.5D-based visual servo system also does not rely on spatial poses. However, the adaptive matrix of the image space has to be calculated in a complex process that requires large calculations. The least square method is often used to calculate this matrix. Additionally, the control system is sensitive to noises in the image.

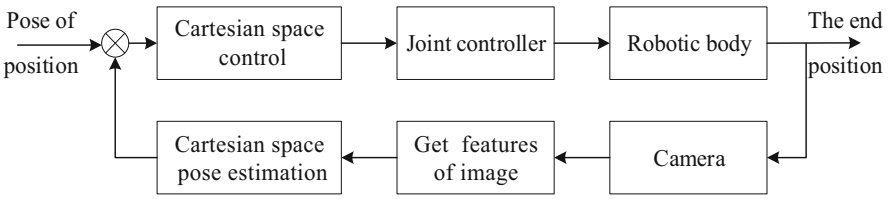

Fig. 4 Block diagram of position-based visual servo control system

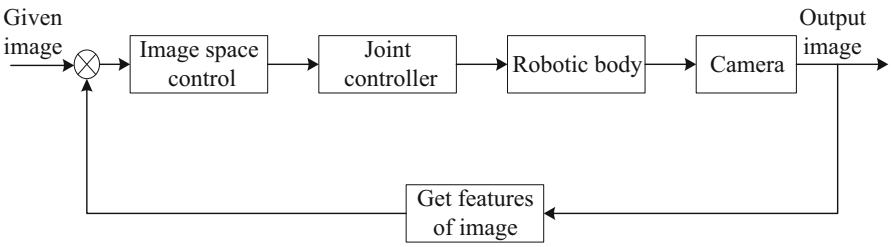

Fig. 5 Block diagram of image-based visual servo control system

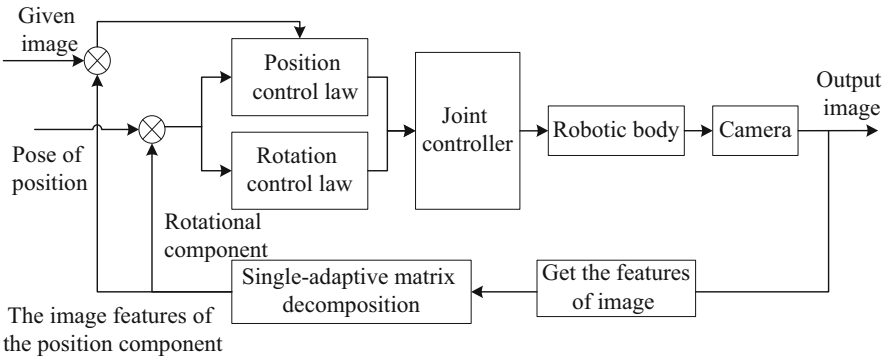

Fig. 6 Frame of 2.5D-based visual servo control system

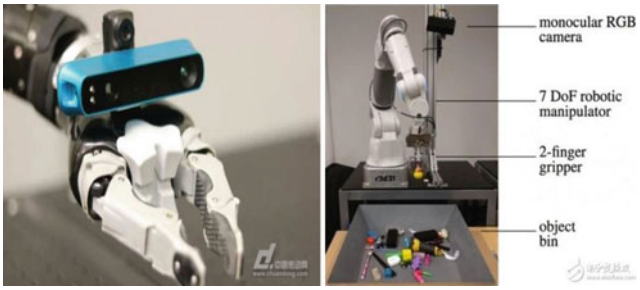

Fig. 7 Eye-in-hand (left) and eye-to-hand (right)

Classification of visual servo systems can also be based on the relative positions of the end actuator (manipulator) and visual sensor (eye). Under these criteria, a system can be classified as either an eye-in-hand or eye-to-hand system (Jin 2018), as shown in Fig. 7. Two different assembly forms are shown in the figure.

The difference between the two visual servo systems lies in the relative positions of the end actuator and visual sensor. In an eye-in-hand system, on the left in Fig. 7, the body of the manipulator is fixed together with the visual sensor, and thus the field of vision changes with the movement of the manipulator. As the manipulator moves toward the target, the positional error generated by the processing reduces. However, as the robot moves with the manipulator, the target object may appear to break away from the field of vision of the vision sensor during motion. On the other hand, in an eye-to-hand system, on the right in Fig. 7, the body of the manipulator is separated from the visual sensor. The camera is installed on the outside of the manipulator, hence the name "eye-to-hand." In this way, the visual sensor does not change its position with the movement of the manipulator, and the field of vision is fixed. The errors of the system would come mainly from errors in camera calibration. If the accuracy of calibration is high, the accuracies of positioning and grasping will also be high (Dang 2015).

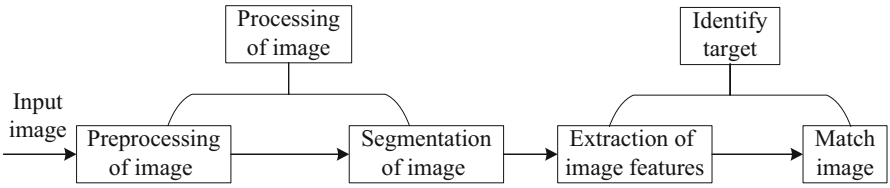

Fig. 8 Flow chart of image recognition

The principle of the machine vision recognition system is to transform detected image information into digital image information using a machine vision camera. The information of the digital image is transported to the signal processing system, which finally transforms it into a digital signal. The image processing system performs corresponding operations on the received image signal according to different algorithms and obtains effective features of the measured object. The system then controls the related equipment based on the results of independent discrimination. The process flow of the image recognition of a detected object is illustrated in Fig. 8.

In the process of image recognition, the input quality of the detected object will have a great impact on the accuracy of the process. In the image preprocessing stage, interfering information in the image can be eliminated, and the authenticity of the image can be restored. After image preprocessing, the detectability of the detected image is enhanced, and the amount of data is simplified for image processing (Miao 2019).

Application of Robot-Based Precision Machines

Turning Lathe

In turning machine tools, the robot is used mainly for the turning mechanism of a lathe tool, which is used for rotating workpieces and for performing hole processing, tapping, and other similar processes. The basic components of these machine tools generally include a spindle box, feed box, lead screw, light bar, slide box, lathe bed, knife rest, and tail stock. The rotating accuracy of the spindle in the spindle box determines the precision, an important factor in measuring the value of the machine tool.

The general tools of the machine can satisfy only the normal processing requirements and may be insufficient for more precise processing. Therefore, the application of robot research on machine tools is done to achieve high-precision processing. Based on the processing technology of the machine tools, an industrial robot is combined with cutting technology, with the general structure of the resulting cutting robot characterized by a large range of robotic motion and good flexibility. However, the robotic rigidity is poor, and the accuracy of the robotic motion is low. The poor rigidity is due to the rigidity of the connecting rod and joint and the overall layout of

the industrial robot. The main reason for this limitation is that the arm components of general cutting robots are thin, long, and suspended, making the rigidity relatively poor. The stiffness of the joints of a robot with many revolute joints can be improved by reducing the gap at the joints, increasing the pre-tightening force of the joints and the contact area.

In addition, during the turning process, another task performed by an industrial robot is to feed and unload the workpiece, a procedure that also requires high design requirements. Accurately clamping the workpiece into the processing device and removing it after processing is completed have to be taken into consideration and require the accurate design of the industrial robot (Wang et al. 1999).

A lathe manipulator is a mechanical device that is used for the automatic feeding and unloading of a computer numerical control (CNC) lathe. Following pre-written program instructions, its basic working principle is to grasp each of the workpieces from the stock bin one at a time and clamp it to the lathe for the turning process. The manipulator then transfers the processed workpiece to the finished stock bin. A set of double position claws, one of which is responsible for the loading, and the other responsible for the unloading, is installed on the manipulator. The manipulator takes out the rough parts from the stock bin and sends them to the lathe, and the process proceeds to the following steps:

① The manipulator takes down the finished parts in the lathe and starts the rotating cylinder to rotate 180°.
② The chip blowing device of the manipulator cleans the iron chips inside and outside of lathe.
③ The manipulator puts the rough parts into the lathe.
④ The manipulator exits the lathe, and the finished workpiece is transferred to the finished stock bin, thus completing the workflow.

The manipulator repeats the same action to the lathe for feeding and unloading, until the rough parts are processed in the stock bin.

Additive Manufacture of Machine Tools

Traditional machining processes have been unable to satisfy requirements for parts and other related tools to effectively shorten the cycle of the production in the sheet-metal forming process, thus limiting the reasonable use of these machine tools in small batch production and prototype manufacturing. Incremental sheet-metal forming (ISF) technology is widely used to counter this limitation. In incremental sheet-metal growth, the final shape is generated by the incremental feed of the hemispherical forming tool in the direction of the depth, wherein the motion is along the same level of the contour or in the form of a helix. This process is known as robot molding and is performed by industrial robots, as shown in Fig. 9. As shown in the figure, there are two manipulators in the processing process, and the two manipulators cooperate with each other to produce.

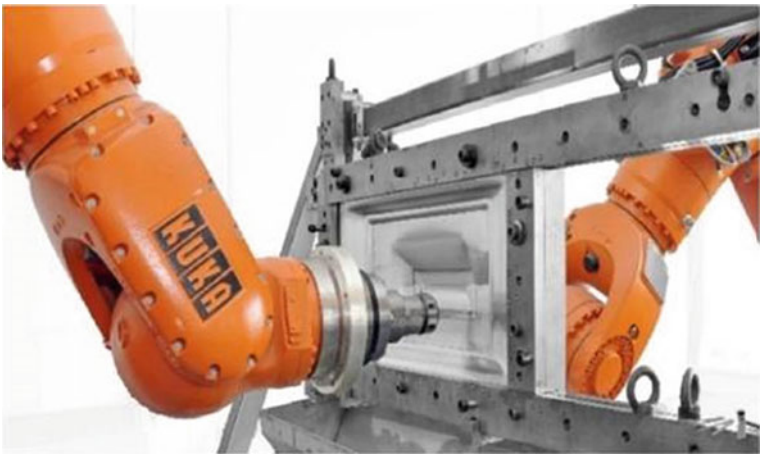

Fig. 9 Incremental sheet-metal forming device based on robot technology

An additional supporting tool whose motion is opposite to that of the forming tool can be installed on the second robot. The predefined gap and force are generated between two hemispherical tools. This locally substitutes a die to improve the accuracy of the formed part. To manufacture and design the forming process chain of the robot, some additional elements that make it possible to plan the path based on CAM and form the target geometry from the plane metal sheet need to be designed. The CAM system is used to determine the position where the metal surface should be touched. The robot then generates the processing steps, defines the process parameters, and so on. The extended geometry is produced by an incremental molding machine (Manns et al. 2018; Cai and Choi 2019). The applied CAM system determines the positions where the forming tool is contact with the metal surface. A post-processing step is required for robot program generation. All process parameters are defined in the step. The forming of the extended geometry is executed by the incremental forming machinery. The sheet metal is then unclamped, annealed, and cut down to the initial target geometry (Verl et al. 2019).

Thin-Wall Machine Tools

Thin-wall machining is unstable because producing deformation and flutter in the process of machining tends to be easy. Therefore, taking advantage of an industrial robot as an active and stable support for thin-wall machining is necessary to prevent the instability of machining flutter. Based on the feed motion of the machine tools, different end actuators, such as rubber roller and metal casting, can be used for support. For example, when a robot is used for machining thin-walled parts, a mobile rubber roller support on the robot provides not only support force but also additional damping to the components, effectively controlling the shape error to a minimum, and improving surface processing quality. Sometimes, to increase the rigidity of

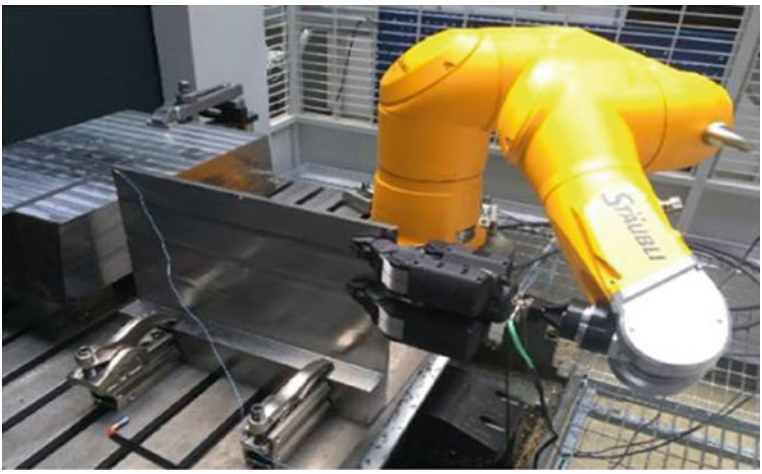

Fig. 10 Robot arm supported on thin wall

components, additional support is required, like shown in Fig. 10. Since both machine tools and robots are in motion during the process, there is a risk of collision between them. Therefore, the integration of the machine tool control and robot control needs to be established to achieve synchronous motion.

To satisfy the requirements of thin-wall machining, two methods are incorporated: the first is the passive method, which includes off-line process planning and optimization of machining systems, and the second is the design of a special workpiece holder, such as a plastic claw or a six-claw chuck, to hold flexible workpieces. Another way to avoid flutter is to determine the rotation speed of the spindle according to the structural mechanics of the machine tools, to provide a relatively large stability margin, and to improve productivity and material removal rate. Industrial robot manipulators can be used as an active steady rest in machining thin-walled workpieces to prevent machining chatter instability. Feedback control is applied to the robotic steady rest in contrast to the other more popular active control method where the cutting tool is controlled. The entire dynamic system is characterized by delay differential equations with time varying interactions between the tool side and work side dynamics. Semi-discretization, finite element modeling, and model reduction are applied to obtain a lower order plant model for the feedback control design (Esfandi and Tsao 2017).

In the machining of thin-walled workpieces, deformation and flutter can be reduced by stiffening the workpiece near the cutting position. A robot with a fast end actuator and feedback control is used to provide sufficient stable support for the workpiece. Because the rigidity and precision of the robot in the precision machining of thin-walled parts are not as good as those of machine tools, the robot is used to control the deformation and flutter, which can be fixed or time-varying at the contact position between the robot end actuator and the workpiece. The moving contact between the workpiece, manipulator, and tool will cause the system to change in

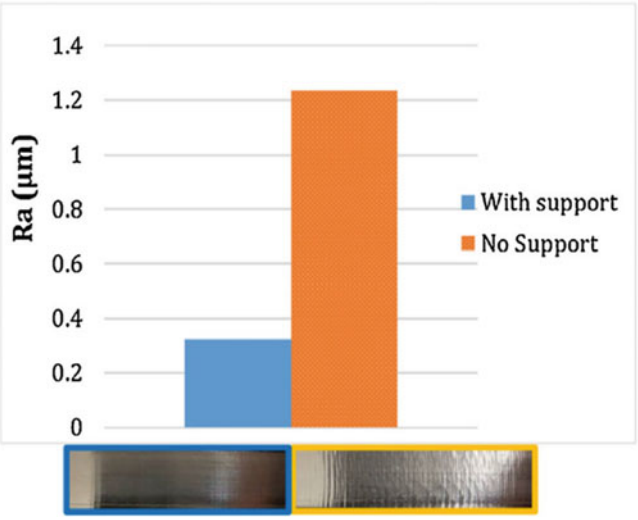

Fig. 11 Improvement in surface quality *Ra* with the support

time. Chatter problems experienced in the center of the part were eliminated, resulting in an improved surface quality. This is shown in Fig. 11. As can be seen from the figure, the support can improve surface quality. A dexterous hand can also be used as an additional support in order to increase the dynamic stiffness of the part as shown in Fig. 10 (Verl et al. 2019).

Accurate Polishing Robot Machine Tools

Requirements on the surface quality of machined parts are becoming higher with the development of manufacturing technology, and as a result, improvements on the grinding and polishing processes have become essential. Traditional grinding and polishing of parts are done by hand, resulting in relatively low efficiency, generally low surface quality, and unremarkable precision. To improve the process and remove these disadvantages, a robot-based automatic polishing system and some flexible polishing tools are therefore developed. This system can overcome the contradiction between the rigidity and flexibility of the robot, especially because the application on complex surfaces results in a good effect. General polishing methods can be divided into two categories: traditional polishing technology and non-traditional polishing technology. The former is mainly mechanical polishing, and the latter is primarily a number of special polishing methods, such as chemical polishing and laser polishing. Methods of mechanical polishing are usually studied in industrial manufacturing, and the development of mechanical automatic polishing systems is based mainly on CNC machine tools and industrial robots (Pu et al. 2018).

The following section introduces an automatic polishing system that makes use of an industrial robot. Some examples of this technology, in China, robot polishing technology has also been deeply studied. For example, the Chinese Academy of Sciences (CAS) has researched and manufactured a "five axis frame polishing robot system" with independent intellectual property rights. Subsequently, the Ningbo Institute of Engineering Materials of CAS has made progress in producing polishing robot technology based on force control, and has developed a force control polishing system for a stainless steel cup external wall robot (Liu 2015).

Free-form surface machining technology for mold and other industries is an interdisciplinary frontier for precision machining technology and automatic manufacturing technology and is an important sign of the increasing level of development of manufacturing technology. Precision forming of free-form surface is an important problem in mold manufacturing. The automation of grinding and polishing processes not only reduces the processing cost but also improves the surface quality of the die. The free-form surface machining process generally includes two parts: the rough machining of the shape, and the finishing of the free-form surface. After free-form surface machining, the surface must undergo grinding, polishing, and other finishing processes to obtain the expected surface machining quality, regardless of the type of machining method.

Industrial robots, especially in free-form surface machining, have advantages that other machining tools do not have, especially in relatively complex surface machining; some machining tools are not as easy to use in the process, which otherwise requires the flexibility of a robot to polish the surface. The flexibility of a robot is very suitable for automatic polishing.

Research on robot polishing involves mainly the robot body design and polishing technology. The robot body includes its kinematics, dynamics, and control, whereas the polishing process includes the process method and process law. Before the polishing process, the surface quality of the surface to be machined is detected and compared with the required surface-quality data. The machining path of the robot is planned, including the setting of the polishing path, polishing pressure, and process, according to the results of the comparison, and the data are transmitted to the controller to drive the robot for polishing. This process is repeated until the requirements are met (Ren et al. 2019; Wan et al. 2019; Xu et al. 2017).

Research on Complex Surface Machining

Compared to traditional equipment, an industrial robot is advantageous for processing complex surfaces. A complex surface is basically composed of many subsurfaces, with different curvatures, which require the flexibility of a robot. Research on the automatic lapping and polishing of complex surfaces is mainly being conducted on the manufacture of optical devices and molds. Industrial robots have

high flexibility and are low in cost, and thus are gradually drawing attention and interest for in-depth research. The automatic polishing system of a robot generally includes, among other components, industrial robots, controllers, force/torque six-dimensional sensors, flexible polishing tools, and air compressors (Denkena et al. 2013).

The basic process of automatic grinding and polishing is as follows. First, the path of the polishing process is planned using a CAD/CAM software. The robot controller drives the external moving axis and joint axis of the robot, and drives the grinding and polishing tool of the end actuator to begin processing. The rotary force of the grinding and polishing tool is generated by an air motor in the compressor, and the rotary speed is controlled by the pressure of an air pressure valve. When the flexible polishing tool exerts pressure on the surface of the machining workpiece, the force/torque sensor that is installed at the end of the robot detects the polishing pressure and transmits the real-time pressure value to the computer. The value of the force is analyzed and processed by the control system of the computer. The system transmits the processed command to the robot controller and adjusts the position of the tool. Real-time compensation of the pressure ensures that the polishing pressure is relatively constant throughout the reprocessing.

The functions of some accessory devices used in the process can be defined as follows (Tian et al. 2016; Klimchik et al. 2016):

① End polishing tool: This is the main working device, which completes the processing task.
② Information exchanger: As the network connection point, it is mainly responsible for the exchange of information between the computer, robot controller, and end force/torque sensor. Additionally, it transmits corrected instructions to the robot controller to control the position.
③ Lubrication system.

Design Requirements of Flexible Polishing Tools

Based on the characteristics of workpiece machining, a polishing tool should have the following features to produce a high-quality polishing surface (Gao 2016):

① The ability to adjust the position and pose independently in the process of machining complex curved surfaces according to the change of the surface curvature is necessary.
② The contact force between the polishing tool and surface of the workpiece should be stable, and the contact pressure between the polishing tool and surface of the workpiece can be monitored by force/torque sensors in real-time.
③ While polishing, the tool should be rotated at a high speed without any deviation. The design structure of the tool should therefore be symmetrical. Otherwise, the processed-surface quality of the part will be reduced.

④ The tool should be able to accommodate replacements. Because the polishing tool is directly in contact with the processed surface, the wear is relatively large, and the service life is relatively short. Therefore, it is necessary to frequently replace the tool.

The force/torque sensor, shown in Fig. 12, installed between the end-connecting flange of the robot and polishing tool, is the main device for detecting the sensing contact between the robot and the outside. This sensor can simultaneously measure all the force/torque information of three-dimensional spaces in the Cartesian coordinate system.

The essential condition for the automatic polishing of robots is the mode of the communication among the systems, that is, the information exchanges among the robots, force/torque sensors, and upper computers. The communication scheme, illustrated in Fig. 13, has two main working threads: communication engineering between the computer and robotic motion controller, and communication engineering between the computer and force/torque sensor (Hu 2015).

Fig. 12 Force/torque sensor

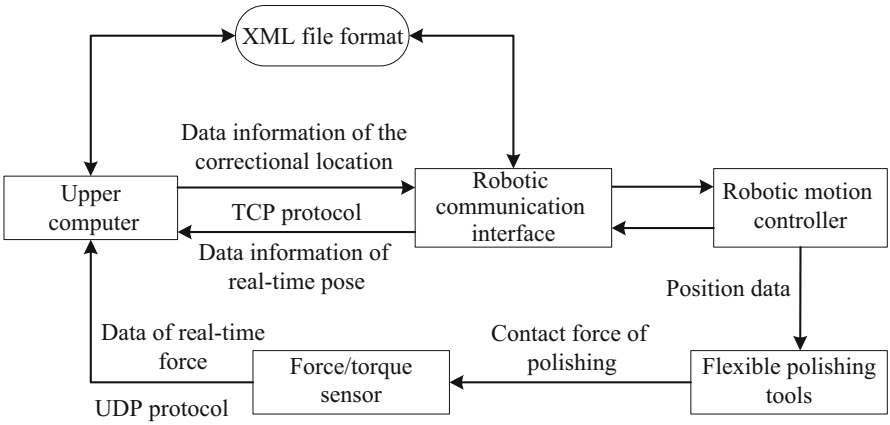

Fig. 13 System communication scheme

Polishing of Optical and Aspheric Surface

The traditional processing of optical components relies primarily on manual polishing, where experienced technicians use fixed pressure and speed to accomplish the polishing process. Although this method has a small investment and low cost, its efficiency is not high, and its reliability is poor. This method is based mainly on past methods that are not suitable for large-scale production.

To polish the concave surfaces of aspheric parts using an industrial robot, a polishing disc is connected to the end of the robot. The diameter of the polishing disc is much smaller than that of the largest surface of the optical work piece. The machining trajectory along the surface is well designed, and the error is controlled within the allowable range by controlling the time that the polishing disc stays at each point of the workpiece surface, the pressure at each polishing point, and the relative speed between the polishing disc and each point of the workpiece surface (Liu et al. 2018).

The process of using an industrial robot to polish and shape optical and aspheric surfaces is as follows (Wang et al. 2010):

① Plan the polishing path and corresponding control points.
② Calculate the position and direction of the polishing head when polishing the control point and convert it into the control point of the robot.
③ Calculate the moving speed through the control points and convert it into the moving speed of the robot.
④ The data from Steps ①–③ are formed into commands for the robot, and the process of polishing is finished according to the design requirements.

Before polishing, the parts that need to be processed should be manually clamped on the mechanism. Because the robot has a force sensor, it can use different forces at each point to ensure the uniformity of machining. The complete polishing process is visualized in Fig. 14.

In the process of polishing an aspheric surface, the materials are placed on the worktable, and then the aspheric surface is polished by the robot. After the polishing process, the results are tested, and the relevant parameters are compensated. According to the test results, computer-controlled optical surfaces (CCOS) technology is used to process the optical aspheric surface several times. The polishing operation of the robot is terminated when the parameters of the aspheric surface satisfy the technical requirements. Figure 15 shows a photograph of a form of numerically controlled (NC) machining of an aspheric surface by the FSGJ-2, which integrates CCOS technology, grinding, polishing, and other related technologies. As shown in Fig. 15, according to the quantitative measurement results of surface shape, CCOS technology polishes the optical aspheric surface with a relatively small grinding head controlled by computer. The amount of material removal is controlled by controlling the residence time of the grinding head on the workpiece surface and the relative pressure between the grinding head and the workpiece (Wang et al. 2018).

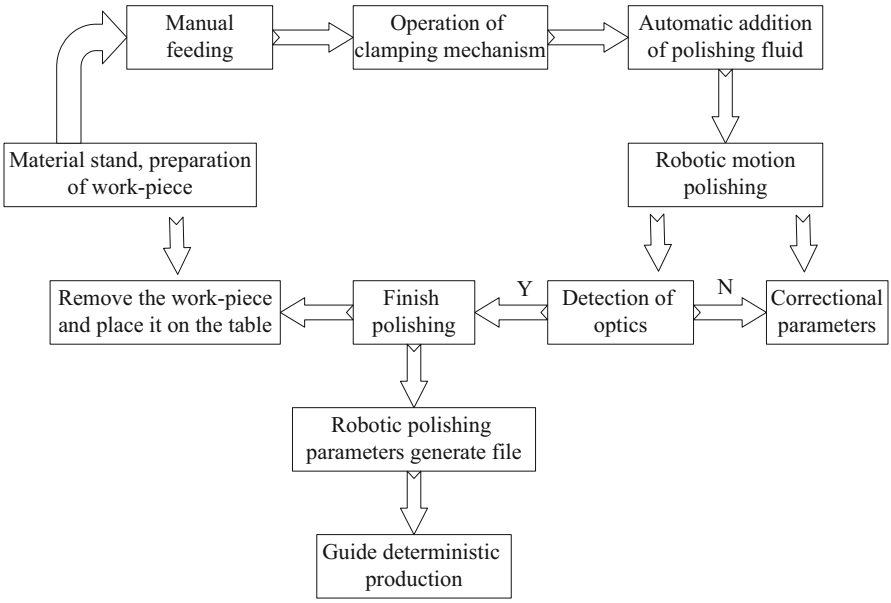

Fig. 14 Flowchart of robot polishing process

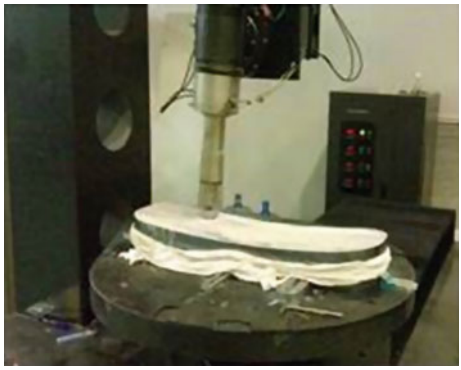

Fig. 15 Aspheric machining by FSGJ-2

Conclusion

This chapter explains the application of robots in precision machining. Unilateral application cannot satisfy the requirements of production and processing; however, with the deep development of mechanical and computer technology, the speeds of processing by industrial robots have been increased. The rapid development of the industry has influenced the constant innovation of industrial robots, which are applied in various industrial fields, especially in high-precision processing, which

require the production of robots characterized by high precision. This chapter describes the industrial robot and the different roles it plays in various aspects of processing, replacing traditional methods of processing and moving toward the direction of automatic production. The use of industrial robots is beneficial for improving the efficiency of processing and the surface quality of workpieces, and for realizing industrial automation and mechanical intelligence.

The design of the structure of the robot and its corresponding control system are described. Robots have been widely used in turning machines, additive manufacturing machines, thin-wall machine tools, and polishing machine tools. Detection technology, processing technology, and path planning have been applied to industrial robots in the process of machining and have contributed to the expansion of robot technology.

The main objective of robot manufacturing is to realize high-precision machining using a simple programmable control system. In polishing, the machining path of the robot is planned in detail using a control system, including the angle and direction between the polishing head and machining surface during the machining of complex surfaces. The data are precisely calculated by a computer and then transmitted to the robotic motion control system to achieve high-precision machining and improve the efficiency of the polishing machine. Robots also use their motion systems to control the working process of feeding and unloading of processed workpieces. The motion accuracy of a robot is best exhibited by its ability to ensure that work materials are accurately clamped from one position and placed on the worktable, thus replacing the corresponding traditional manual process.

However, many problems should be considered in robotic design, such as the rigidity of the robot design, and the selection and calculation of materials. The design has to ensure good rigidity and high flexibility. The problem with maintaining balance when a robot holds a workpiece and methods that can be used to make the robot achieve stable movement are also summarized in this paper. Robot machining processes may also involve some small errors, such as position deviation. The control system detects the corresponding data and compensates for the errors, making it more reliable than traditional manual methods. In actual processes, robots may encounter successive problems, which need to be resolved, requiring robotic technology to be developed further.

References

Ba XF, Li HH, Wang YH, Lu SW, Yan XQ (2017) Feedback control system design of the pneumatic balance assists manipulator. Hydraul Pneum (12):90–94.

Cai Y, Choi SH (2019) Deposition group-based toolpath planning for additive manufacturing with multiple robotic actuators. Procedia Manuf 34:584–593.

Chen J (2018) Key technology of the manipulator loading and unloading control system. Electron Technol Softw Eng (12):128.

Dang KP (2015) Research and application of the vision system in the coordinate robot system. Chongqing University.

Denkena B, Litwinski K, Schönherr M (2013) Innovative drive concept for machining robots. Procedia CIRP 9:67–72.
Esfandi N, Tsao TC (2017) Robot assisted machining of thin-walled structures. IFAC Pap OnLine 50(1):14594–14599.
Gao Q (2016) Research on key technologies of robot polishing of complex curved surface. Shenyang University of technology.
Han DX (2019) Design of manipulator system based on soft PLC. Autom Technol Appl 38(06):81–84.
Hu HJ (2015) Research and design of large aperture optical polishing robot system. Chongqing University Press, Chongqing.
Huang KQ (2008) Research and development of special manipulator for loading and unloading of coupling wire machine. Zhejiang University Press, Hangzhou.
Jin HL (2018) Research on spatial target grasping of manipulator based on vision. Shenyang University of Technology Press, Shenyang.
Jin W (2019) Design of industrial manipulator control system based on PLC. Digit Commun World (04):257.
Klimchik A, Ambiehl A, Garnier S, Furet B, Pashkevich A (2016) Experimental study of robotic-based machining. IFAC-Pap Online 49(12):174–179.
Li PY (2018) Design of manipulator target grabbing system based on active vision. Electr Technol (18):133–135.
Li J (2019) Design and research of automatic loading and unloading manipulator. Beijing University of Posts and Telecommunications Press, Beijing.
Liu GB (2015) Research on robot polishing technology of large complex curved surface. Shenyang University of Technology Press, Shenyang.
Liu HT, Li Y, Wang YH, Zhao Q, Mu JL (2018) Robot flexible polishing of concave surface of optical aspheric parts. New Technol New Technol (06):34–37.
Manns M, Morales J, Frohn P (2018) Additive manufacturing of silicon based PneuNets as soft robotic actuators. Procedia CIRP 72:328–333.
Miao P (2019) Research on the vision based manipulator work piece grabbing system. Tianjin University of Technology Press, Tianjin.
Peng LM (2006) Research on the manipulator for the loading and unloading of friction welded drill pipe. Coal Science Research Institute Press, Beijing.
Pu YS, Wang HJ, Jiang J, Yu LB (2018) Application of industrial robots in polishing process. Sci Technol Innov Guide 15(29):42–43.
Ren SX (2008) Application and research of the robot in the ultra-precision machining. Scientific Era (03):20–21.
Ren LJ, Zhang GP, Zhang L, Zhang Z, Huang YM (2019) Modelling and investigation of material removal profile for computer controlled ultra-precision polishing. Precis Eng 55:144–153.
Tian LH (2016) Design and research on the manipulator of punch loading and unloading. Qingdao University of Science and Technology.
Tian FJ, Lv C, Li ZG, Liu GB (2016) Modeling and control of robotic automatic polishing for curved surfaces. CIRP J Manuf Sci Technol 14:55–64.
Verl A, Valente A, Melkote S, Christian Brecher, Erdem Ozturk, Lutfi Taner Tunc (2019) Robots in machining. CIRP Ann, 68(2): 799–822.
Wan SL, Zhang XC, Wang W, Xu M, Jiang XQ (2019) Edge control in precision robotic polishing based on space-variant de-convolution. Precis Eng 55:110–118.
Wang JB (2000) Research on the constant temperature control system of oil in ultra-precision machine tools. Modular Mach Tools Autom Process Technol (12):20–22.
Wang JC (2002) Study on the vibration active control system of the slide of ultra-precision machine tool. Harbin University of Technology Press, Harbin.
Wang XY, Huang YM, Liu YC, Zhang GP, Jing WX, Dong LX (1999) Study on the structure of a new cutting robot. J Xi'an Univ Technol (01):35–38.

Wang J, Guo YB, Zhu R (2010) Robot flexible polishing technology of optical aspheric elements. J Xiamen Univ (NATURAL SCIENCE EDITION) 49(5):636–639.
Wang XK, Xue DL, Zhang XJ (2018) Common reference processing and inspection of large aperture aspheric system. Opt Precis Eng 26(4):743–748.
Wang JL, Liu RF, Li C (2019) Control mode and control system design of manipulator. Times Automot (06):109–110.
Wu X, Lin JB, Dong H, Yu L (2019) Design and development of the general control system for the loading and unloading manipulator. Comput Meas Control 27(07):70–73 + 78.
Xu P, Cheung CF, Li B, Ho LT, Zhang JF (2017) Kinematics analysis of a hybrid manipulator for computer controlled ultra-precision freeform polishing. Robot Comput Integr Manuf 44:44–56.
Zhao H, Lv QJ (2015) Motion analysis of loading and unloading based on 6-DOF manipulator. Sci Technol Innov Guide 12(14):3–7.
Zhou S (2019) Design of control system of pneumatic manipulator with magnetic card based on PLC. Nan Fang Agric Mach 50(11):32–33.
Zhu T, Tian DL (2003) Application and research of the micro robot technology in ultra-precision machining. Mech Eng (01):3–5.

Processing Techniques of Critical Components

12

Shanshan Chen

Contents

Introduction 316
Classifications of Traditional Processing Technology 316
Surface Generation Mechanism for Different Processing Techniques 317
Processing Techniques for Machining Hard and Brittle Materials 318
Processing Component with Microstructure Surface 322
Five-Axis Milling Sculpture Surface 327
Ultra-Precision Grinding (for Processing Hard and Brittle Materials) 328
Chip Formation Kinematics and Undeformed Chip Geometry 333
Wheel Truing, Dressing and Topography 334
Ultra-Precision Grinding of Freeform Surfaces 337
Theoretical Modeling of Scallop-Height in Ultra-Precision Grinding 338
Conclusion 350
References 350

Abstract

Critical components with complex structure (such as ultra-precision roller, reflective lenses, and engine blade) are the key element for advanced devices or equipment (roller machine, space telescope and engine, etc.), and they have high requirement for processing accuracy. With the increasing demand for components with complex and microsized structures, how to choose relevant processing techniques is becoming an essential task to fabricate those parts with a closed tolerance. In this chapter, main ultra-precision machining technology for manufacturing the critical components is introduced, which includes single point turning, five axis milling, microchiseling, micromilling, and ultra-precision grinding. The optimization of machining strategies considering kinematic constraints of machine tools can effectively improve the machining efficiency of

S. Chen (✉)
School of Mechanical Engineering, Xi'an Jiaotong University, Xi'an, Shaanxi, China
e-mail: chenshanshan2009@163.com

Z. Jiang, S. Yang (eds.), *Precision Machines*, Precision Manufacturing,
https://doi.org/10.1007/978-981-13-0381-4_28

critical parts. The machining strategy optimization considering the cutting force and machining errors of the process system can effectively improve the machining accuracy of the parts. At present, the manufacture of high-tech products requires the support of precision and ultra-precision processing technology; therefore, it is necessary to know the basic knowledge about the processing techniques so as to comprehensively understand and master this technology and better apply it to scientific research and critical components fabrication.

Keywords

Critical components · Processing accuracy · Machining · Errors

Introduction

In the last few decades, the demand for critical components with high-precision and form accuracy has been increasing. These components play an important role in many fields for human society and have been used in space and aeronautics, optics, electronic devices, and medical and life sciences, such as turbine blade, Hubble telescope lens, missile gyroscope, optical functional component, and so on. The quality of critical components determines the performance of the equipment. Therefore, the processing and shape accuracy of the critical components are strictly required in general. It promotes the production and development of ultra-precision machining technology. For ultra-precision machining technology, it is generally believed that the size and shape error of the processed part is less than a few tenths of a micron, and the surface roughness is between a few nanometers and a dozen nanometers. As an important part of modern manufacturing technology, ultra-precision machining technologies including single diamond turning, grinding, lapping, polishing have been widely used in national defense, aerospace, measurement and testing, biomedical, instruments, and other fields. At present, ultra-precision machining technologies play an increasingly important role in the precision processing of key components.

Classifications of Traditional Processing Technology

In machining, the cutting tool removes the excess material from the workpiece surface to produce the desired surface quality and specified geometrical shape. The tool geometry and characteristics are directly related to the machining accuracy and surface quality, as well as the mechanism of surface generation of the workpiece. According to the number of cutting edges, the machining process can be categorized as single point and multi-point tools, as shown in Fig. 1. Single point tool for turning, fly cutting, and planning utilizes only one cutting edge to remove surplus materials in the form of cutting chips along the tool path, which is widely employed in machining complex aspheric and freeform surface. Multipoint tool can be classed as defined tool

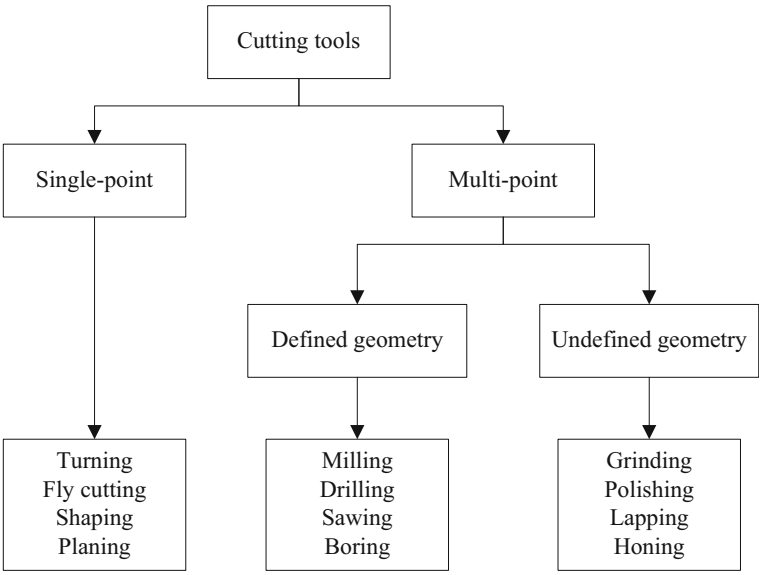

Fig. 1 Different cutting tools for surface generation in traditional machining

and undefined tool. The defined tool such as for milling, drilling, sawing, and boring, has deterministic cutting edges with a uniform shape and size as well as consistent space interval. The surface is generated by many separate and small cutting teeth which are mainly used to shape bore or cut flat surface. However, the undefined tool, such as for grinding, polishing, lapping, and honing, has randomly arranged cutting edges. Therefore, it is very difficult to describe the tool size and position. Usually, the statistical approach is employed to define the cutting tool geometry.

Surface Generation Mechanism for Different Processing Techniques

Different cutting tools generate diverse mechanisms of surface generation, as shown in Fig. 2. Single-point turning makes use of a tool with an arced nose to generate the required surface geometry. Face milling utilizes a tool with a limited number of cutting edges and rotates (main motion) while the workpiece implements the feed movement to generate the required surface profile resulting from the overlap of all cutting edges. However, grinding and polishing have great differences with regard to the surface generation as compared with turning and milling. The abrasive grains as the cutting tool are randomly oriented and distributed on the grinding wheel surface, but not all of them contribute to the final surface generation due to the different depths of their penetration. The surface generation is caused by the interference of neighboring active grain tips both in the peripheral and traverse directions. Polishing is a press control process which utilizes loose abrasives combined with a liquid to

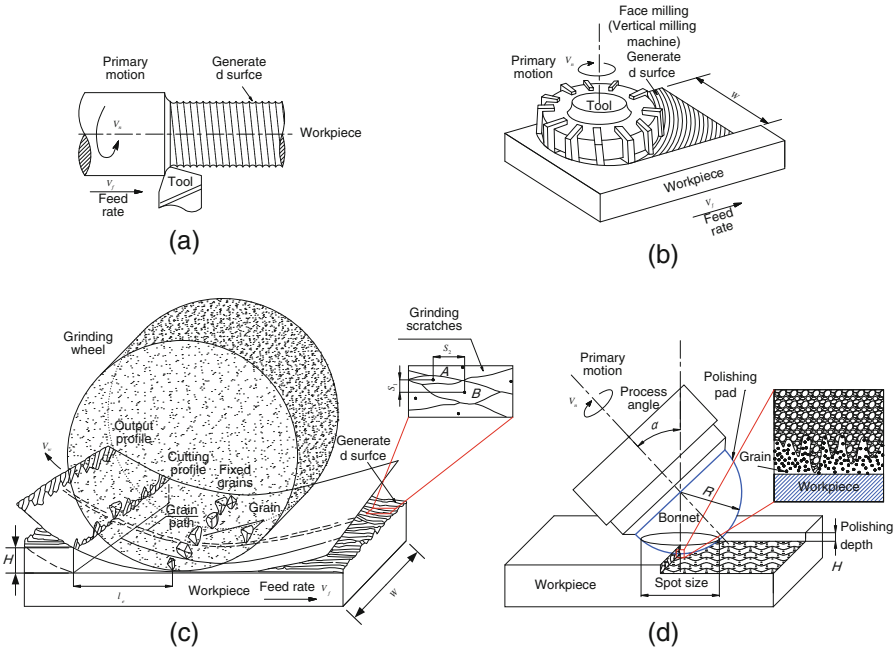

Fig. 2 Different surface generation mechanisms of different machining technologies: (**a**) single point turning, (**b**) face milling, (**c**) ultra-precision grinding, (**d**) ultra-precision polishing

remove undesired material (Cao and Cheung 2016; Beaucamp et al. 2014). Grinding, as a displacement control process, utilizes fixed abrasive grains to remove the volume of materials from the workpiece. Polishing may be employed for the post-grinding process to further improve the surface finish. However, the improvement of the form accuracy of the workpiece is limited and the polishing efficiency is low (O'Hara et al. 1993; Tsai and Huang 2006). As a result, optimization of the ultra-precision grinding to achieve good surface finish without the need for post polishing is becoming an essential objective.

Processing Techniques for Machining Hard and Brittle Materials

The major uniqueness of grinding is the grinding wheel. In grinding, synthetic or natural abrasives such as diamond, silicon carbide, cubic boron nitride, and aluminum oxide are utilized to grind the workpiece with high accuracy and high efficiency. The wheel is made of hard abrasive grains, bonds, and pores, as shown in Fig. 3. The abrasive grains are held by a bonding material and serve as the role of cutting edges. The pores can reduce the exclusion of grinding chips and grinding heat, which also affect abrasive grain spacing. Conventional precision grinding usually uses silicon carbide or aluminum oxide grit combined with a vitrified or

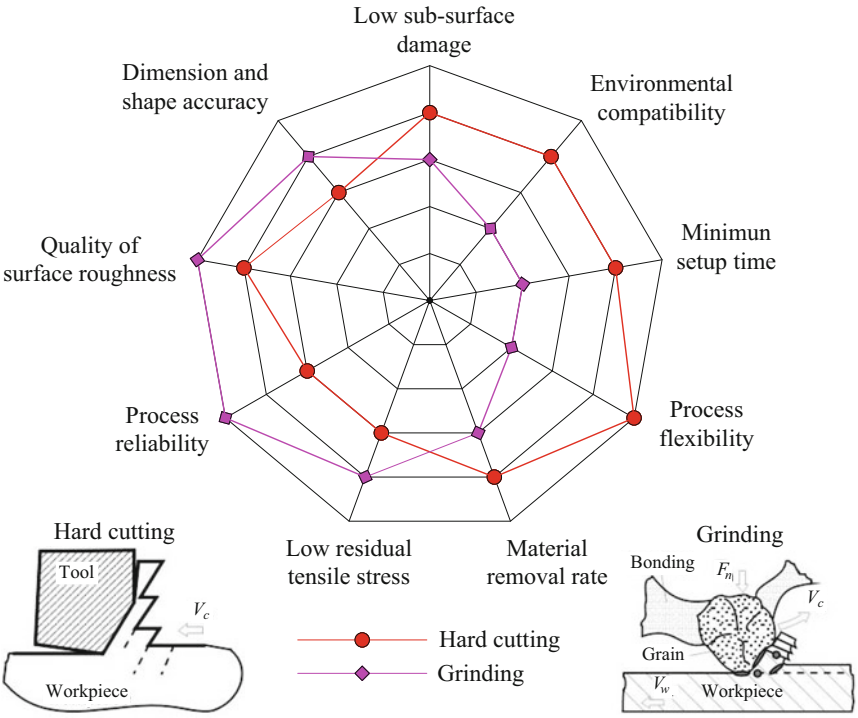

Fig. 3 Qualitative comparison of the capability of hard cutting and grinding technologies (Klocke et al. 2005)

resin bond. In ultra-precision grinding, the wheel is made of a superabrasive, such as diamond or cubic boron nitride (CBN) with metal vitrified or resin bonding material.

Figure 3 shows a qualitative comparison between cutting and grinding with the capability of machinability for difficult-to-machine materials (Klocke et al. 2005; Brinksmeier et al. 2001). It shows that grinding is more capable of machining hard and brittle materials in regard to machined surface quality with higher accuracy and flexibility, lower subsurface damage and higher material removal rate, etc. As a result, it has been widely used in the ultra-precision machining process to generate high-quality and functional components especially for optical manufacturing.

At present, grinding is one of the most important material processing technologies for realizing precision and ultra-precision machining (Gao et al. 2017). The primary motivations of grinding are both to realize material removal and obtain a good surface finish. Surface roughness is the most crucial indicator in evaluating the quality of ground surface and grinding performance and results from the interaction of the tool and machined material. A high-quality surface finish significantly improves the performance of the functional properties of precision components such as fatigue strength, frictional properties, and component life.

However, the quality of ground surface and grinding performance are affected by numerous factors involving the shapes of grains, their distribution and size in the grinding area, the material characteristics of the workpiece, and grinding process conditions. The complexity in the grinding process and its stochastic nature make it difficult to study the modeling of a grinding system in surface generation, surface topography, and dynamics analysis for surface generation in grinding (King and Hahn 1986; Susič and Grabec 2000; Aurich et al. 2009). The surface topography of machined surface depends on the various effects existing in the cutting area due to the behavior of active grits (Tönshoff et al. 1992; Setti et al. 2017).

Due to the random distribution of abrasive grains, different machining conditions, and the cumulative effect of various effects and interactions, it is irregular and complex to analyze the machined surface. The surface topography of the ground surface corresponds to the geometrical shape of the grinding tool. The effects are shown in Fig. 4. These factors are divided into three groups including the process parameters, abrasive tool features, and grinding process conditions.

Advanced engineering ceramic materials such as silicon carbide (SiC), alumina (Al_2O_3), zirconia (ZrO_2), silicon nitride (Si_3N_4), and tungsten carbide (WC) possess outstanding material properties of stiffness, structural stability, wear resistance, and chemical stability as compared to traditional metallic materials (Agarwal and Rao 2005). As a result, they have increasingly been applied in a wide range of applications in recent years. For example, it can be exploited for structural parts, space telescope lenses, automobile components, and X-ray mirrors, etc. However, these

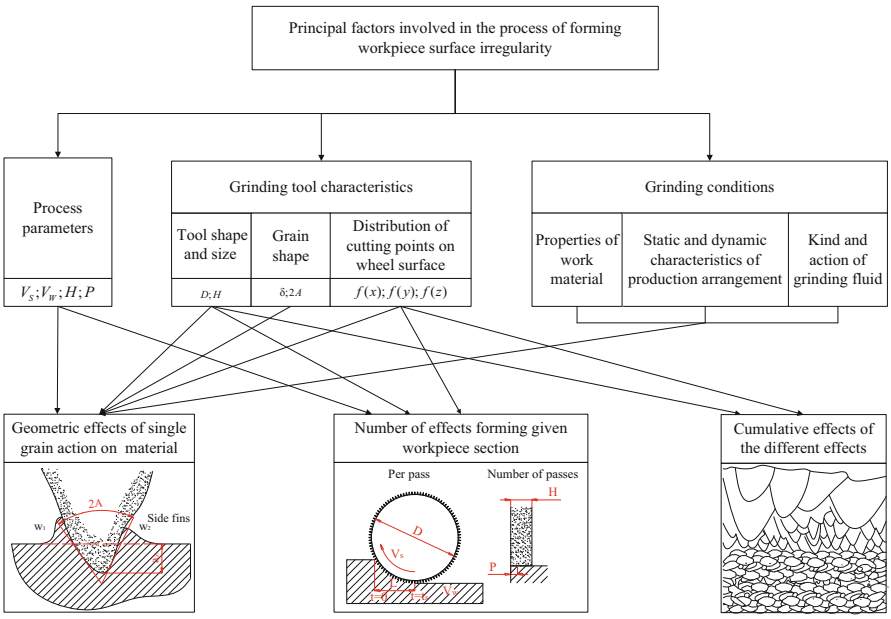

Fig. 4 Principal factors involved in the irregularity of workpiece surface

materials have difficulties being machined to a good surface finish due to their hardness and brittle features.

Grinding is the most commonly used machining operation to shape ceramic materials. In general, the surface generation in the machining of ceramic materials results from numerous cutting edges on the grinding wheel which penetrate into the workpiece to realize material removal. Compared with metallic parts, ceramic components do not reveal the macroscopic behavior of plastic deformation. Ceramics only exhibit ductile mode within a microlevel. As a result, the material removal and chip formation are different as compared to metallic materials (Khanov et al. 2014) in surface and subsurface generation. In ultra-precision grinding, the surface generation mechanism is also affected by the pre-existing flaws. With the increase of machining scale, the material removal is more susceptible to pre-existing defects and needs less energy, as shown in Fig. 5. Dislocation of grains and defects is conducive to chip formation (Taniguchi 1994).

Indention tests on ceramic material have been employed to study the propagation behavior of crack systems in the grinding. As shown in Fig. 6, plastic deformation is found near the surface. Three main crack systems appear from the plastic region: median, radial, and lateral cracks. Median cracks can degrade the part strength, lateral cracks extend to the surface, and bridged radial cracks may induce potential chip formation taking into account material removal.

The size of the indenter radius has insignificant effect on ductile material regardless of pressures, which will not induce cracks. However, for brittle materials, the radius of indenter tip produces remarkable influence on crack propagation. The larger radius leads to cone crack, but small tip radius can produce both median crack and lateral crack under high load, as shown in Fig. 7.

In grinding, the wheel is characterized by a large number of grains with negative rake angles and small depths of cut. Due to the high hardness of ceramic materials, diamond is almost the exclusively used grain material in ultra-precision grinding.

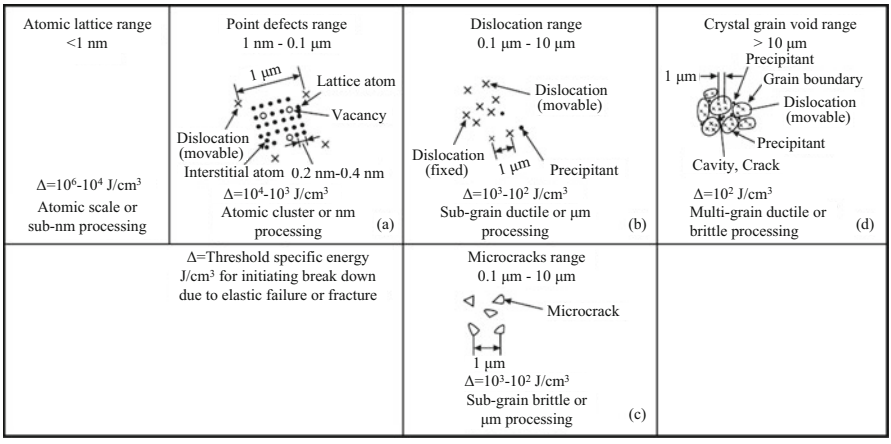

Fig. 5 The influence of preexisting flaws on removal mode in different scale

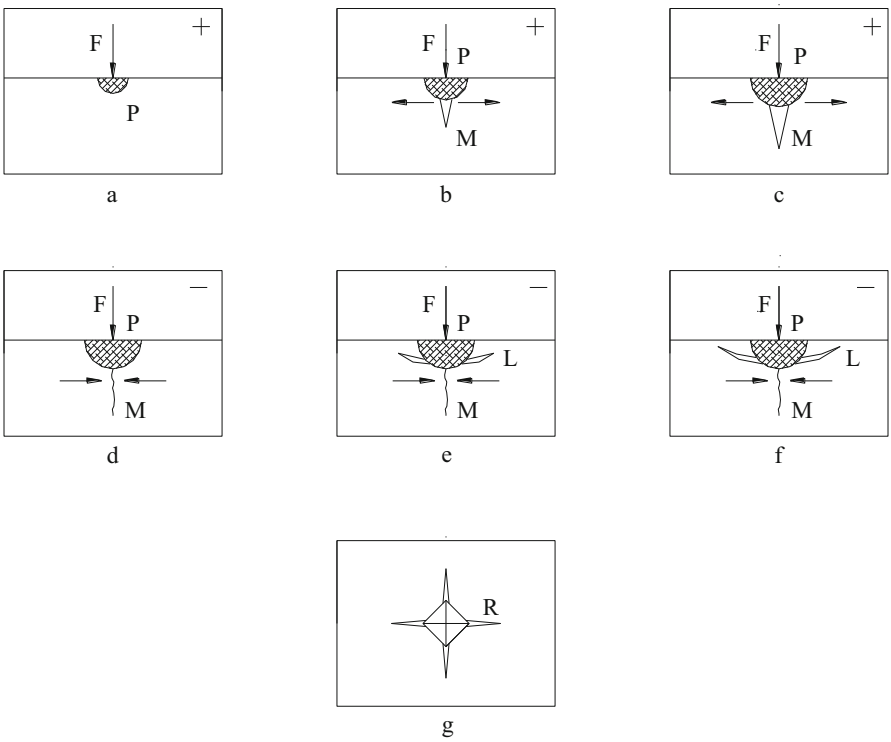

Fig. 6 Mechanisms of crack formation under punctual load

The material removal mechanism on these brittle-hard materials is governed by two modes, that is, brittle and ductile regime. As the diamond grain penetrates into the workpiece, the response of the machined material experiences elastic and plastic deformation, after which chips are formed; if the depth of cut exceeds the critical value of brittle-to-ductile transition, cracks are induced and the surface is generated by the extension of cracks as shown in Fig. 8. In order to achieve a good surface finish, ductile regime is preferable in the grinding process.

A brittle-to-ductile transition is possible for all materials, regardless of their characteristics, such as hardness and brittleness, if the depth of cut is small enough (Ngoi and Sreejith 2000). Plasticity becomes the predominant regime for surface formation and material removal when the depth of cut of grinding is lower than the critical depth of cut.

Processing Component with Microstructure Surface

Microstructure surface refers to the surface with a specific microtopological structure, which has important applications in biological, optical, mechanical, and other fields. For example, microgroove surface can control cell migration (Miyoshi et al.

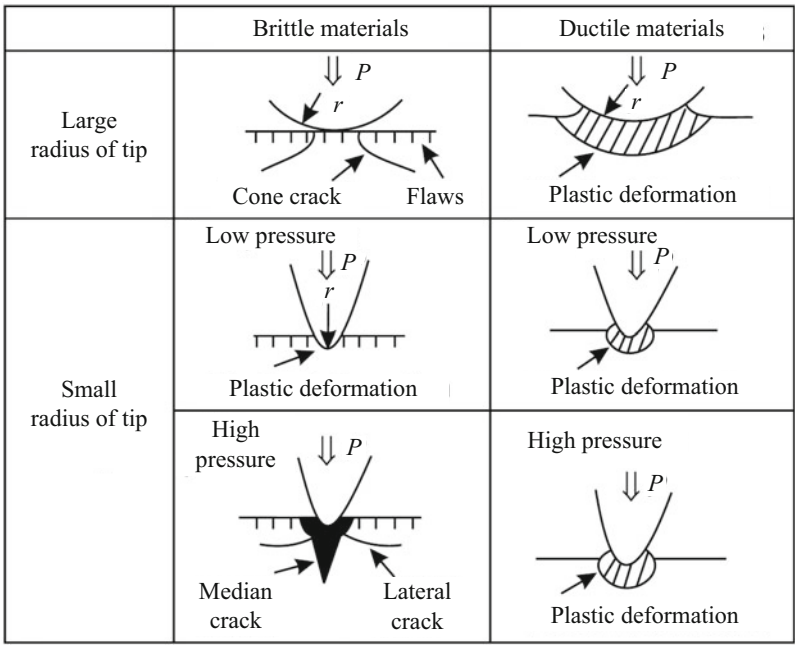

Fig. 7 The influence of indenter geometry and loads on ductile and brittle materials (Inasaki 1987; Lawn and Wilshaw 1975)

2010), microlens and pyramid array can be used for liquid crystal display lighting (Liu et al. 2013; Tsai et al. 2012), and mushroom microstructure surface can produce super adsorption (Carbone et al. 2011). There are many processing technologies for microstructure surface, including mechanical, chemical, and biological processing. Single point diamond cutting technology or FST, STS, fly cutting can be used to machine microstructure surface for nonferrous metals, as shown in Fig. 9. According to the machining mechanism and feature, it can be divided into three categories: removal machining, combined machining, and deformation machining. Removal machining, also known as the division processing such as the traditional turning, milling, grinding, lapping, and polishing, removes a part of the material from the workpiece. Combined processing utilizes physical and chemical methods to combine different materials together. According to the combining mechanism and method, it is divided into attachment, injection, and connection. Deformation processing is known as flow machining, which exploits force, heat, molecular transport, and other means to change the workpiece shape and size.

With the development of optical devices towards microminiaturization, the application of ultra-precision machining technology in microoptical components is increasing. Ultra-precision machining technology mainly includes ultra-precision turning, milling, grinding, and polishing, among which turning is the most widely used technology in the processing of complex curved surface optical elements and microlens array. It is mainly used for processing infrared crystal, nonferrous metal,

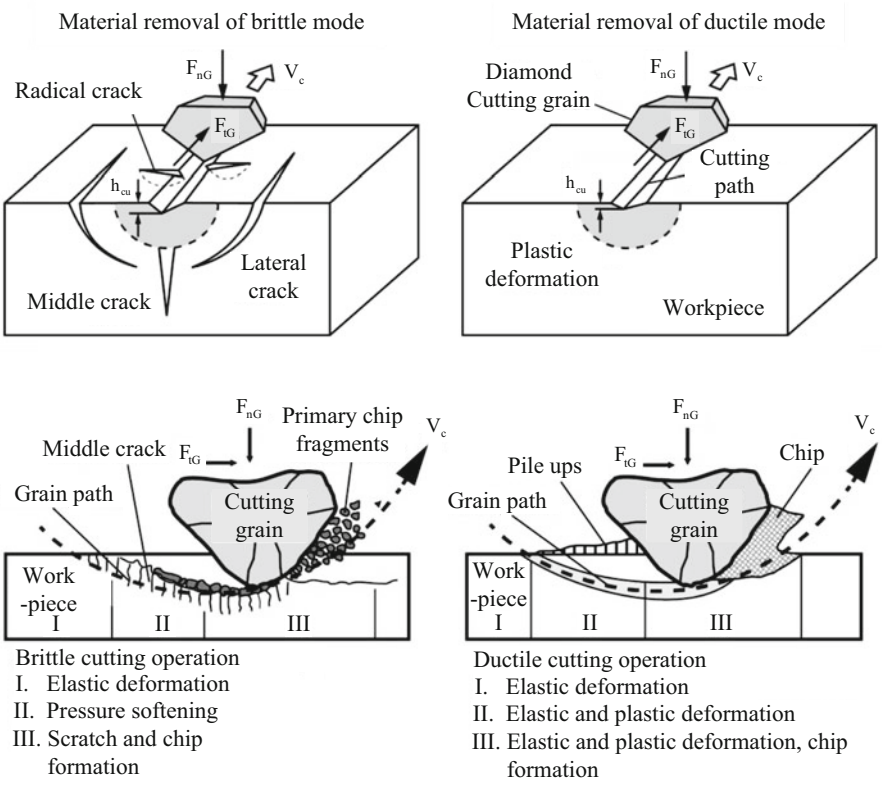

Fig. 8 Material removal mechanisms on brittle-ductile materials (Heike et al. 2017)

part of the laser crystal and optical materials, and capable of processing complex surface or special structure surface, such as high order aspheric, diffraction optical element, and diffraction hybrid optical element. SPDP can fabricate microlens array, precision die mold, micropyramid array, free-form surface with rotational symmetry feature. The advantages of single point diamond turning technology are as follows: it can be formed in one time, the surface quality is high, the surface roughness can reach nanometer level, the processing efficiency is high, and the processing cost is low.

Roller is the critical component for microstructure molding to fabricate optical thin film, which includes spherical microstructures, Fresnel microstructures, prismatic microstructures, and cylindrical microstructures, etc. Fresnel diffraction structure is a typical rotationally symmetric complex surface. Compared with aspheric lens with the same function, Fresnel lens has the advantages of small size, light mass, and low manufacturing cost. Figure 10 shows the processing method of micro-Fresnel lens array by adopting diamond turning.

The research on automatic tool change and tool alignment during microstructure array processing has been carried out by using the force sensor integrated in the fast tool servo system (Fig. 11a, b). Because of the long processing time of the roller

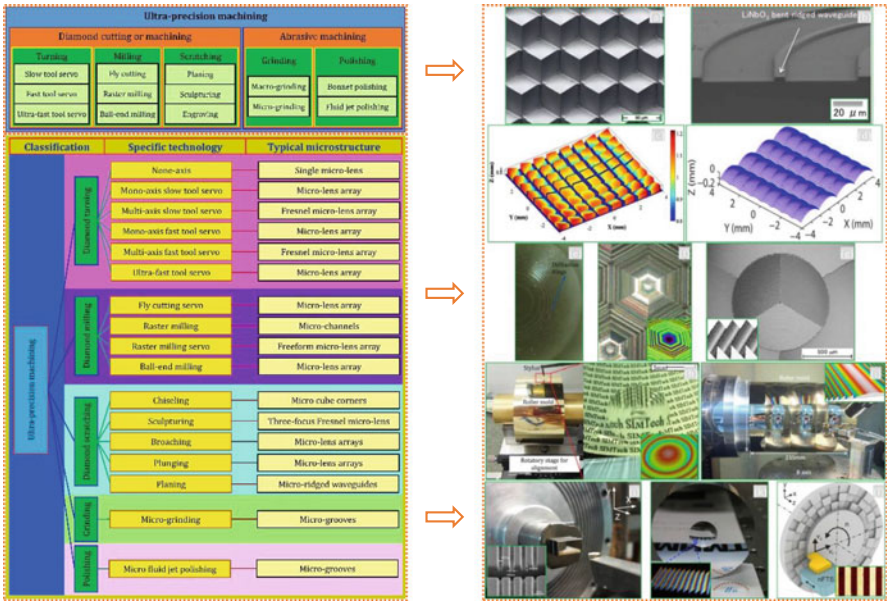

Fig. 9 Ultra precision machining techniques and microstructures (Zhang et al. 2019)

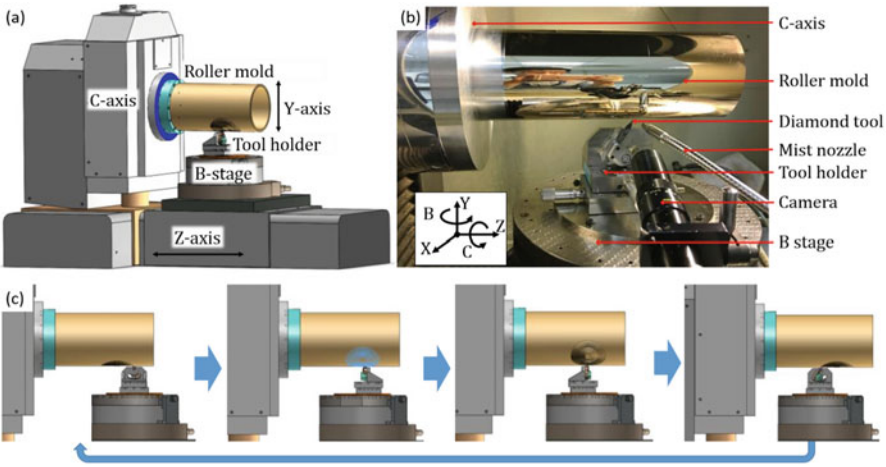

Fig. 10 Ultra precision machining Fresnel lenses on a roller mold for processing of functional optical film (Zhang et al. 2018)

surface microstructure array, the diamond cutter needs to carry on the reciprocating cutting continuously, and the cutter will inevitably wear or even be damaged. Therefore, it is of great significance to study the automatic cutter replacement in the cutting process.

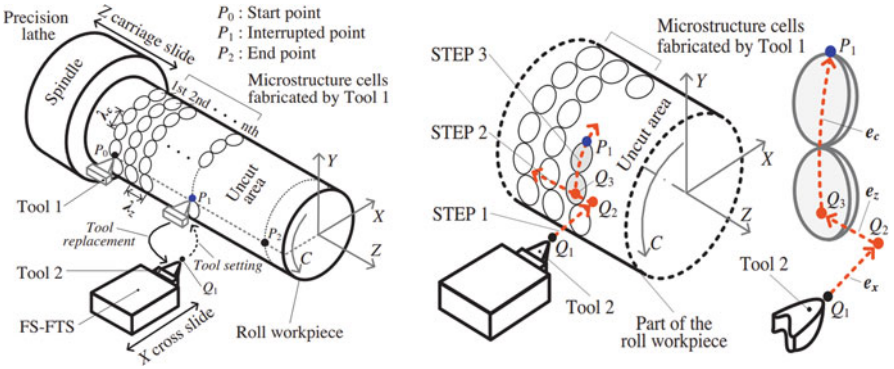

(a) Automatic tool change (b) tool setting

Fig. 11 Microstructural array processing system with powerful sensors (Chen et al. 2015). (**a**) Automatic tool change (**b**) tool setting

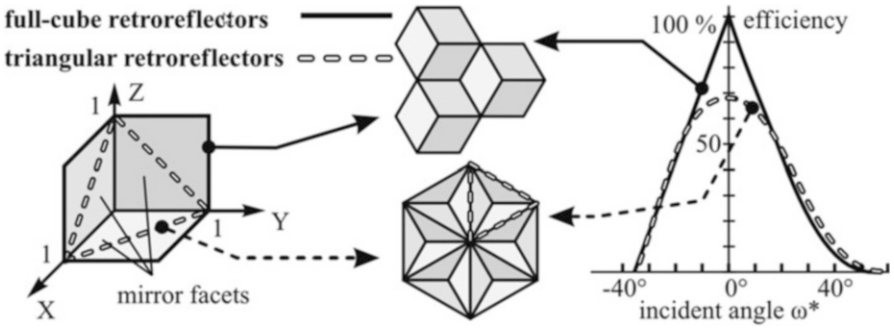

Fig. 12 A comparison for reflectivity between hexagonal and triangular aperture (Eckard 1971)

Microhexagonal structure is capable of lowering parallel displacement of reflected light, which provides a convenient way to embed it to the equipment with small size. Compared with the triangular structure which can only reach at approximately 66%, microhexagonal structure can provide a very high efficiency (approximately 100%) at 0° incidence, as shown in Fig. 12 (Eckard 1971).

Due to the processing limitation of concaves with sharp edges by employing turning or milling, Diamond Micro Chiseling (DMC) is developed. DMC as a new processing technology mainly aims to generate prismatic microstructure with high accuracy, in which a very sharp tool is essential to generate expected prismatic cavities, as shown in Fig. 13. The tool radius of DMC is about 200 nm ~ 300 nm, but the tool of the general turning is a round nose and the radius is about 1 ~ 12 um. In DMC process, at least five axes are required to rotate the tool with respect to workpiece position (three linear sliding axes and two rotational axes), as shown in Fig. 14.

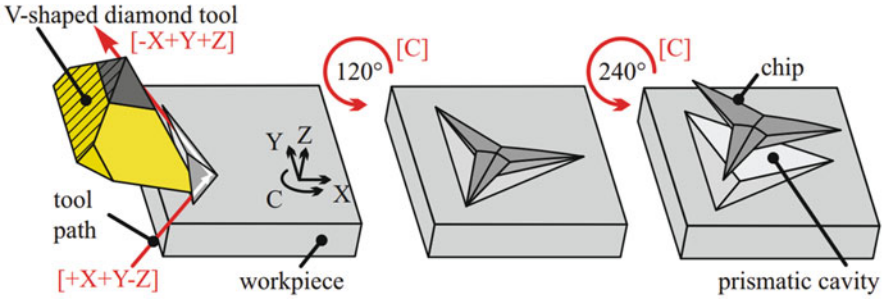

Fig. 13 Illustration of Diamond Micro Chiseling process (Eckard 1971)

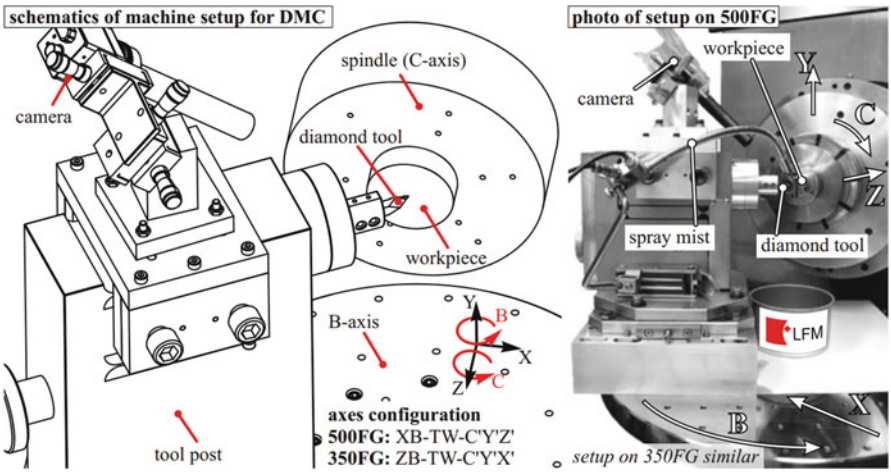

Fig. 14 Schematics of machine tool layout for DMC (Eckard 1971)

Five-Axis Milling Sculpture Surface

Due to the complicated geometric structure of the critical parts and the narrow feasible space of the cutter shaft, the tool with large length-diameter ratio must be used for processing. Under the action of cutting force in the process of machining, the relatively weak rigid tool is prone to deform and vibrate, which will greatly reduce the machining accuracy and efficiency of relevant parts. Due to the thin wall and long cantilever, the deformation and vibration of the workpiece caused by cutting force and the stress release after material removal are the key factors affecting the machining accuracy, as shown in Fig. 15.

In the finishing process, the effective cutting radius of the tool is reduced due to the wear of the back face. Compared with the three-axis machining, five-axis

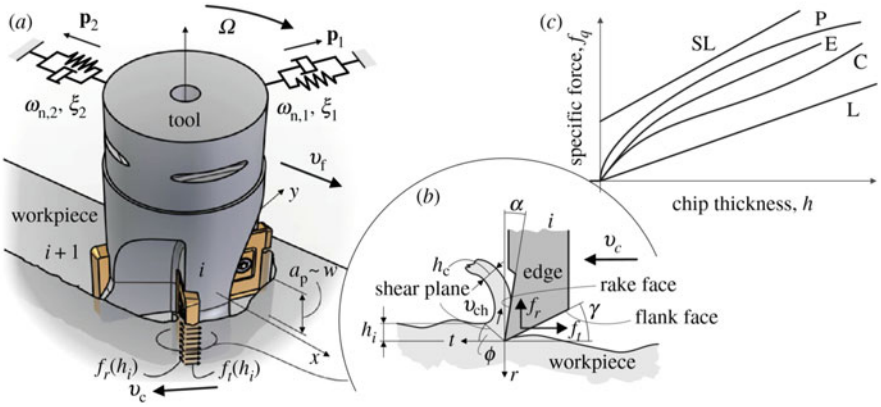

Fig. 15 Schematic of five-axis milling operation (Dombovari and Stepan 2015)

machining uses two additional rotational degrees of freedom, resulting in a more complicated relative motion relationship between the tool and the workpiece. However, it is capable of processing complex surfaces with high machining efficiency and surface quality, especially for machining aircraft engine turbine blades, turbine runner, and marine propeller parts, as shown in Fig. 16.

Microminiaturization technology characterized by small scale and complex structure has a strong application background in aerospace, defense technology, biomedical, emerging electronic products, and other fields and has been widely used in medical devices, automobiles, electronic/information equipment and other aspects. Micromilling technology has its unique advantages in the processing of microparts with small scale and 3D complex structure. The size range of micromilling parts ranges from 0.1 mm to 10 mm, and the processing feature size ranges generally between 0.01 mm and 1 mm. Therefore, the tool used in micromilling is very small in size, and generally its diameter is less than 1 mm, which puts forward higher requirements on the performance of the tool, as shown in Fig. 17. Compared with traditional milling, micromilling shows different cutting characteristics, such as scale effect and minimum cutting thickness. The scale effect and the minimum cutting thickness will lead to different cutting mechanisms and different degrees of tool wear and machining defects.

Ultra-Precision Grinding (for Processing Hard and Brittle Materials)

As a material removal process, grinding has a long history ever since the Stone Age. At that time, prehistoric man used a piece of stone to sharpen their cutting tools by rubbing them against each other. In the twelfth century, China first fabricated a true grinding tool by using crushed seal shells bonded to soft rubber. At present, the grinding process is one of the key manufacturing operations in industrialized

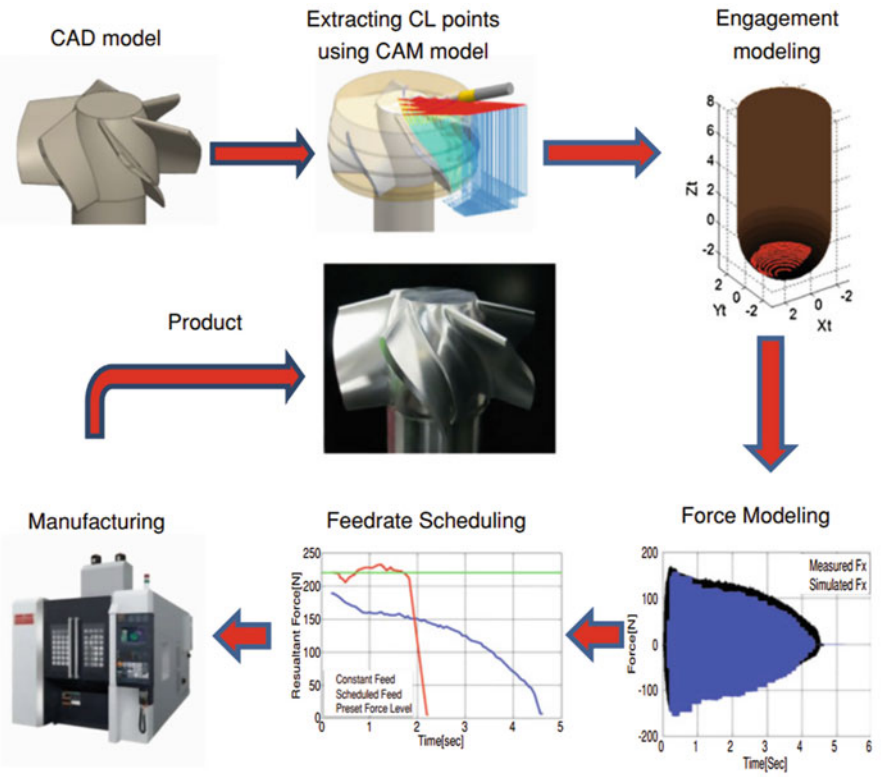

Fig. 16 Illustration of sculptured surfaces milling process (Dombovari and Stepan 2015)

countries and plays an increasingly important role in precision manufacturing and ultra-precision machining. Grinding accounts for about 20% ~ 25% of the cost of production (Marius 2016). In general, the grinding is considered to be one of the final processes for the production of the components so as to achieve high accuracy and smooth surfaces.

Nowadays, grinding is the primary machining process to shape hard and brittle materials so as to achieve microcrack-free and smooth surface, in the process of which the material is removed by plastic flow (ductile mode). In order to maximize ductile grinding, both the grain size and material removal rate should be very small and the protrusion height of abrasive grains must be small enough as shown in Fig. 18.

With the advancement in ultra-precision machine tool, it is possible to machine the hard and brittle materials in a full ductile model to realize mirror-like surface finish. Figure 19 shows a typical ultra-precision grinding machine, whose workpiece spindle is equipped with an ultra-high-resolution air bearing and high loop stiffness and damping in the axial direction to alleviate vibration and motion errors. The ground surface is generated by the continuous movement of the tool tip profile along

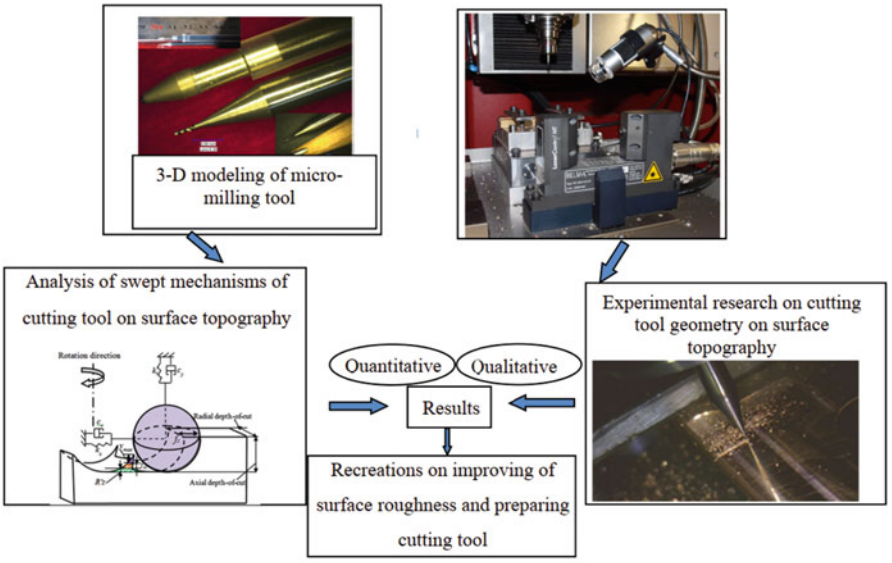

Fig. 17 surface generation mechanism of micromilling process (Shi et al. 2017)

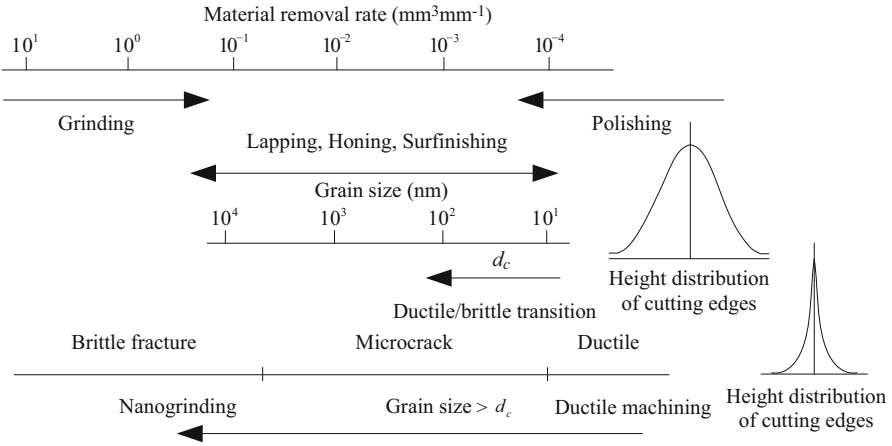

Fig. 18 Conventional abrasive machining versus nano-grinding (Miyashita 1989)

the traverse direction. It is clear that the tool, cutting parameters, wheel geometry, abrasives distribution, and relative engagement of the tool and the workpiece have significant influence on the surface finish.

In grinding, the material is removed in the form of chip formation which is similar to that of other conventional machining processes such as turning, milling, and drilling. At a finer scale, the machine tool geometry and its engagement with the workpiece for turning, milling, or drilling are well defined. However, it has a

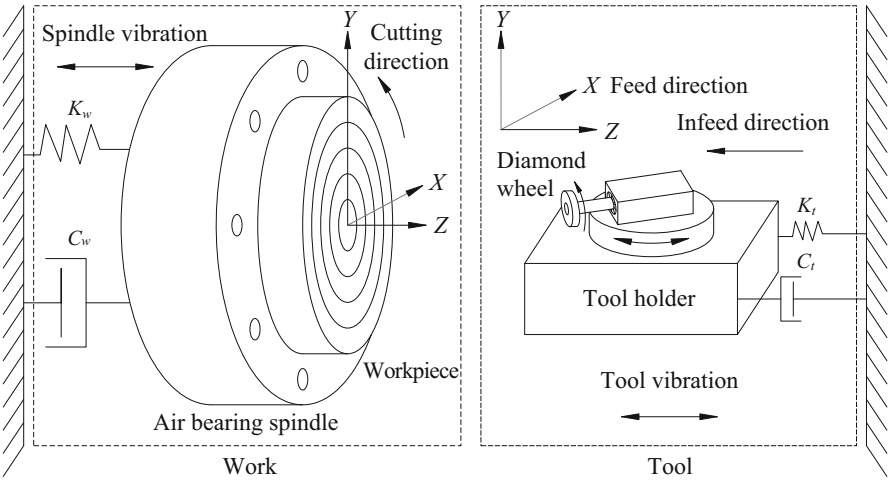

Fig. 19 Schematic of the ultra-precision grinding apparatus

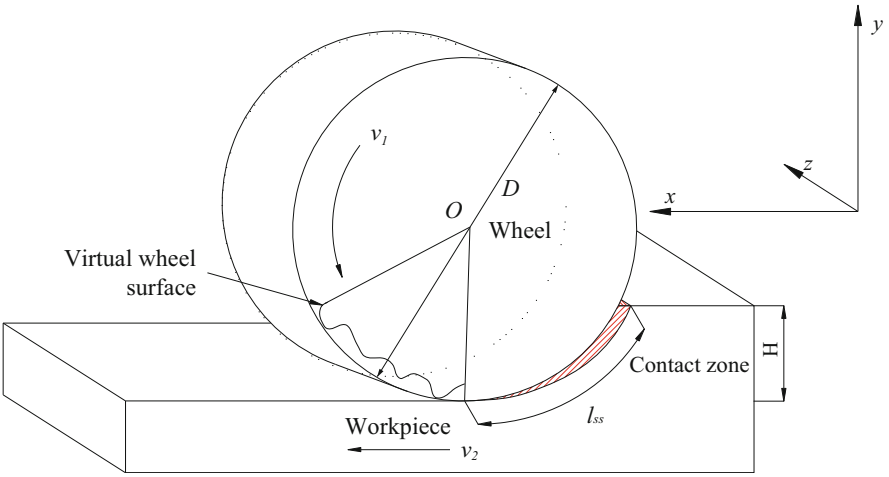

Fig. 20 Schematic illustration of surface grinding

multitude of undefined cutting edges with random positions, sizes, and orientations which make it a great challenge to describe the cutting tool geometry for grinding.

The surface grinding geometry is shown in Fig. 20. The grinding wheel rotates and penetrates into the workpiece at a feed speed, which results in a dynamic contact area where the cutting actions occur. In order to analyze the surface generation geometry, the abrasive cutting path needs to be defined, as shown in Fig. 21.

Neglecting the horizontal feed motions of the workpiece as well as the deformations, the arc length of the static contact zone can be derived as:

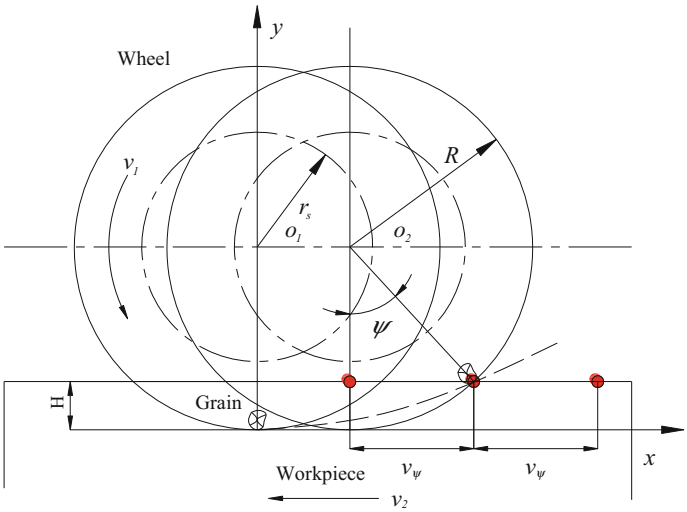

Fig. 21 Schematic illustration of abrasive grain motion

$$l_{ss} = \frac{D\theta}{2} \tag{1}$$

$$\theta = \cos^{-1}\left(1 - \frac{2H}{D}\right) \tag{2}$$

Due to $2H << D$, θ can be approximately expressed as:

$$\cos\theta = 1 - \frac{\theta^2}{2} \tag{3}$$

Combining those two equations, the arc length is derived as:

$$l_{ss} = \sqrt{HD} \tag{4}$$

For a grain, the relative trajectory can be expressed as:

$$x = R\sin\psi \pm v_\psi \tag{5}$$

$$y = R(1 - \sin\psi) \tag{6}$$

$$v_\psi = \frac{v_2\psi}{2\pi v_1} = \frac{v_2 R}{v_1}\psi \tag{7}$$

$$dx = R\left(\cos\psi \pm \frac{v_2}{60v_1}\right)d\psi \tag{8}$$

$$dy = R\sin\psi d\psi \tag{9}$$

$$dl_{ss} = \sqrt{dx^2 + dy^2} = R\sqrt{1 \pm \cos\psi + \left(\frac{v_2}{v_1}\right)^2}\, d\psi \tag{10}$$

Due to the extreme small depth of cut for ultra-precision grinding, ψ is very small, so $\cos\psi \approx 1$

$$dl_{ss} = R\left(1 \pm \frac{v_2}{v_1}\right)^2 d\psi \tag{11}$$

$$l_{ss} = \int_0^{\psi} R\left(1 \pm \frac{v_2}{v_1}\right) d\psi = R\left(1 \pm \frac{v_2}{v_1}\right)\psi \tag{12}$$

Chip Formation Kinematics and Undeformed Chip Geometry

The workpiece material is removed by numerous abrasive grains along a defined path, and chip formation is the result of successive actions of multiactive grits. Due to the fact that abrasive grains are uniformly distributed, the cutting points for active grains are not equally spaced apart and the penetration heights are not equal. As a result, the undeformed chip thickness is generally calculated from an "average" condition for the grain space and the penetrated height. Figure 22 shows the kinematics of an individual abrasive grain in surface grinding. Grain 1 travels along the cutting pathBA, and the wheel center is moved from O_1 to O_2. At the same time, the next grain passes along the path $FB'A'$ to generate the cutting chip$FB'A'AF$. In this process, the thickness for the chip is changed from 0 up to a maximum value h_m and then to 0 again.

The maximum undeformed chip thickness plays an important role in the grinding, which is directly related to the material removal rate and surface quality as well as

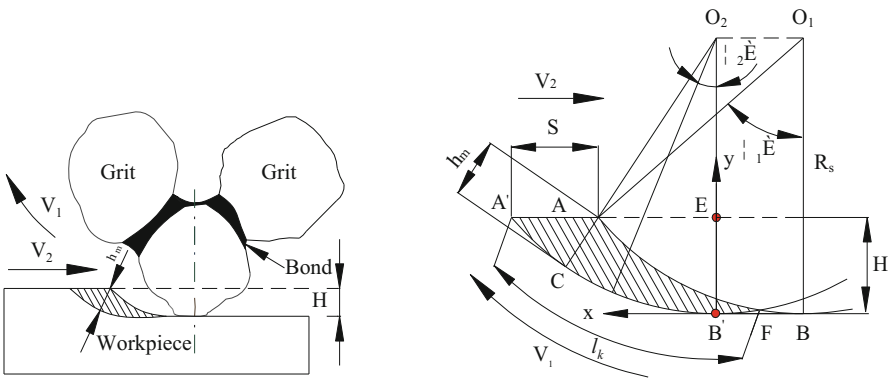

Fig. 22 Undeformed chip geometry for surface grinding

the specific grinding energy. According to the geometrical relationship for continuous motion, the maximum undeformed chip thickness h_m can be calculated as:

$$h_m = R_s - \sqrt{\left[{R_s}^2 + S^2 - 2SR_s\sqrt{(1 - \cos^2\theta_1)}\right]} \tag{13}$$

$$\cos\theta_1 = 1 - \frac{H}{R_s} \tag{14}$$

Combined with Eq. (15) and Eq. (16)

$$h_m = R_s\left(1 - \sqrt{\left[1 - \frac{4S}{R_s}\left(1 - \frac{H}{2R_s}\right)\sqrt{\frac{H}{2R_s}} - \frac{S^2}{{R_s}^2}\right]}\right) \tag{15}$$

Due to $\frac{2H}{R_s} << 1$

$$h_m = 2S\sqrt{\frac{H}{2R_s}} - \frac{S^2}{2R_s} \tag{16}$$

An alternative method to determine h_m is based on the material removal rate (MRR), in units of time and volume, and the number of cutting chips produced is equal to the MRR.

$$V_c(CbV_1) = HV_2b \tag{17}$$

$$V_c = h_a b_c l_k \tag{18}$$

The average width b_c is assumed to be proportional to h_m

$$b_c = ah_a \tag{19}$$

$$h_m = \sqrt{\left[\frac{4}{Ca}\left(\frac{V_2}{V_1}\right)\left(\frac{H}{2R}\right)^{1/2}\right]} \tag{20}$$

Wheel Truing, Dressing and Topography

In grinding, the process force, high temperature, and serious friction caused by the relative motion between the wheel and the workpiece result in the wear of the wheel and grain. It can change machinability and accuracy of the wheel, resulting in the deterioration of the surface quality and profile error of the machined component.

The wheel wear is the result of material loss on the wheel surface, which can be classified into abrasive wheel wear, adhesive wear, tribo-chemical wear, surface disruptions, and diffusion as shown in Fig. 23. For the abrasive grain wear, the

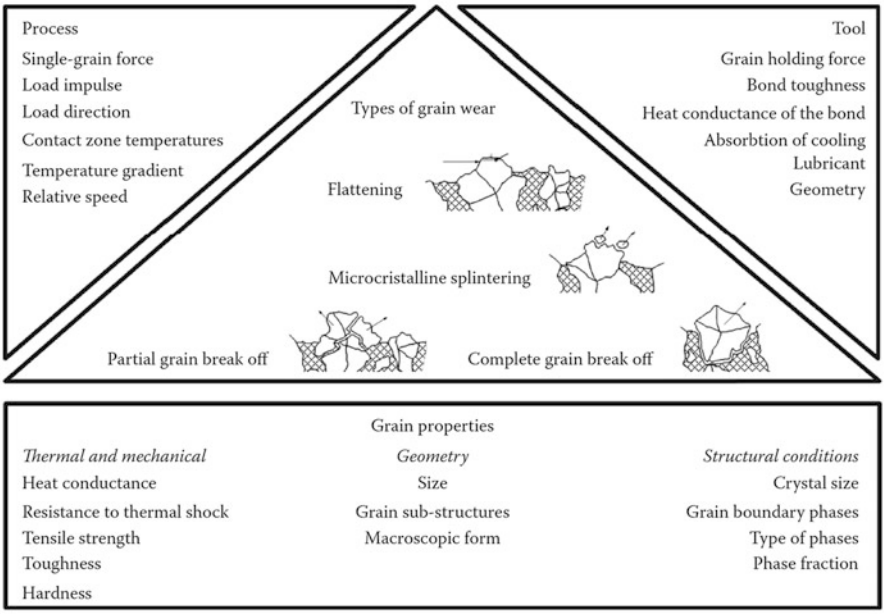

Fig. 23 The type of abrasive wear (Marinescu et al. 2016)

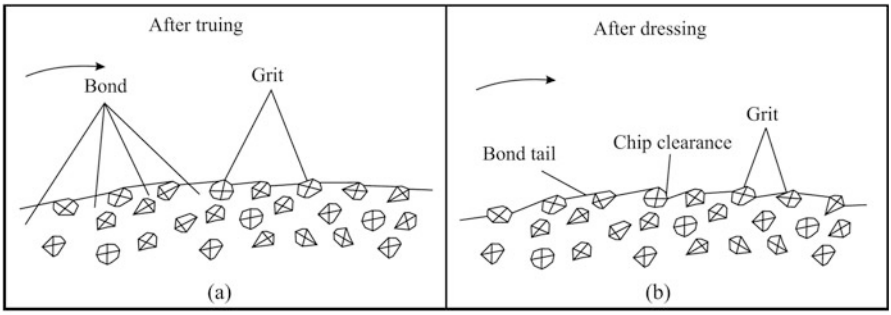

Fig. 24 Different grinding wheel topographies (**a**) after truing and (**b**) after dressing (Metzger 1986)

wear type is divided into: flattening (attribution wear), microcrystalline splintering, and partial and complete grain breakout (Yang and Yu 2012; Nadolny 2015). The mechanism and type of grinding tool wear are related to process variables, chemical and mechanical characteristics of the tool, composition and structure of the wheel.

Wheel topography condition plays an important role in the kinematic interaction between the grains and workpiece, which affects the surface generation process. In order to minimize run-out of the grinding wheel, truing is essential to carry out. The truing is to shape the profile of the grinding wheel to a particular shape, as shown in Fig. 24. The

main purpose of the dressing is to remove the dull abrasive grains to improve the cutting preference.

In ultra-precision grinding, diamond dressers are commonly used, such as single point diamond, synthetic needle diamond and multipoint diamond. Figure 25 shows three distinct single point diamond dressing processes, feed, and stationary and rotary dressing according to the different forms of relative motions. Dressing parameters such as diamond size, dressing depth, overlap ratio, scarf angle, and feed rate will affect the wheel topography generation, resulting in the fracture of abrasive grains and produce or expose sharp grits, as shown in Fig. 26.

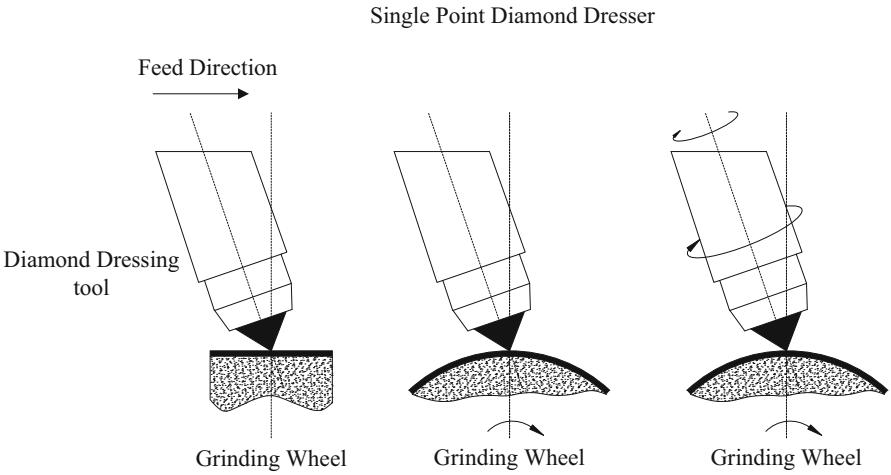

Fig. 25 The type of single point dressing operations for the grinding wheel

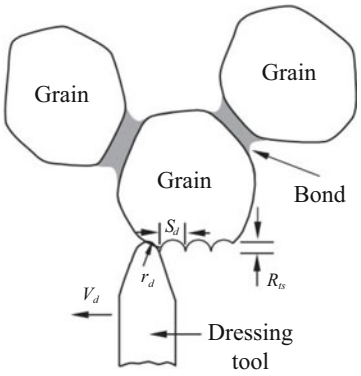

Fig. 26 Surface generation of the wheel under the dressing tool (Marinescu et al. 2016)

Ultra-Precision Grinding of Freeform Surfaces

With the increasing demand of optical and photonic manufacturing industries, many types of high-resolution and compact optical components are widely used in digital cameras, solar concentrators, aspectual illumination systems, and collimators. Freeform surfaces can reduce wave front error of optical elements and are the units of high-performance optical system. However, the complex curvature variation of freeform surface causes great challenges to its machining. Among various ultra-precision machining processes such as single point diamond turning (SPDT), diamond milling, fly cutting, microchiseling, and ultra-precision diamond grinding, grinding operation is more efficient and accurate than other machining processes in machining optical components made of hard and brittle materials. Tool path as a critical factor directly determines the form error and surface quality in ultra-precision grinding of freeform surfaces. In conventional tool path planning, the constant angle method is widely used in machining freeform surfaces, which results in nonuniform scallop-height and degraded surface quality of the machined surfaces. A theoretical scallop-height model was developed to relate the residual height and diverse curvature radius. Hence, a novel tool path generation method is necessary to achieve uniform scallop-height in ultra-precision grinding of freeform surfaces. Moreover, the iterative closest point (ICP) matching method is needed to determine the surface form error between the measured surface and the designed surface. Hence, an optimized tool path generator is verified, which allow the realization of the achievement of uniform scallop-height in ultra-precision grinding of freeform surfaces.

In machining of freeform surfaces, the CNC system controls sequential cutting points of the machine tool over the workpiece by an interpolation algorithm and tool trajectory. The tool path generation is vital for determining the surface quality and machining efficiency, which attracts a lot of research attention. For a three axes machine tool, the tool path generally evolves as an Achimedean spiral from the outmost area to the rotational center, in which a series of interaction points on the spiral are represented by a polar coordinate system according to the rotational angle and feed speed. In conventional machining, the constant angle tool path generation strategy is widely used in machining complex surfaces, resulting in nonuniform surface scallop-height. The outer area of the machined surface is coarser than that of central region of the surface due to a lager arc-length on outer area. Someone studied the influence of two different tool path generation strategies based on constant rotational angle and constant arc-length, respectively. It is found that constant arc-length was a preferable method to achieve the higher form accuracy (Chen et al. 2019).

For machining freeform surfaces, the variation of surface curvature can lead to different scallop-heights and produce form errors. As a result, it is vital to develop a new tool path generation strategy to achieve constant scallop-height. The relationship between the curvature and scallop-height is needed for analyzing theoretically and a new control strategy for the tool path with variable path interval is necessary, which can be used to achieve uniform scallop-height in ultra-precision grinding of freeform surfaces.

Theoretical Modeling of Scallop-Height in Ultra-Precision Grinding

In ultra-precision grinding, the rotational workpiece traverses across the high-speed spinning wheel to remove redundant materials and create desired surfaces by changing the tool position with respect to the part and feed speed, as shown in Fig. 27a. The ground surface generation mechanism is directly related to the tool path, and the grinding wheel moves in an Archimedes spiral in X-Y plane with respect to the workpiece, as shown in Fig. 27b.

In ultra-precision grinding of freeform surfaces, the tool trajectory is a spiral around the rotational center of the workpiece, and the scallop height on the workpiece surface between two adjacent paths is principally determined by the rotational speed of the workpiece, feed speed and curvature radius of the machined surface. The surface curvature variation results in the difference of the contact point between the wheel and the workpiece, which causes the difference of the scallop height on the ground surface. Figure 28 shows the different geometric relationships among flat surface, convex, and concave surface machining. For grinding flat surface, the tool path interval is easy to be determined, which keeps uniform spacing. However, for machining convex and concave surfaces, the calculation is more complex and the interval spacing is changeable according to the curvature radius.

For a given allowable tolerance for the scallop height in machining flat surface, the path interval can be determined according to the geometric relation as shown in Fig. 28) as follows:

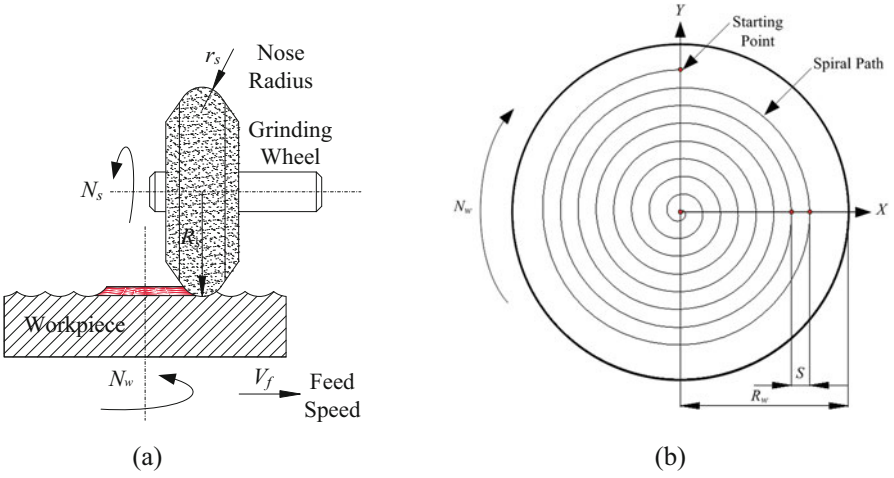

Fig. 27 Schematic of surface generation in grinding operation

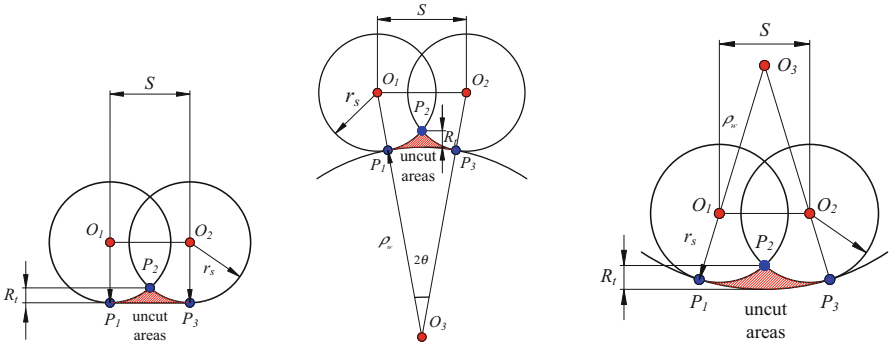

Fig. 28 Scallop height generation in ultra-precision grinding (**a**) flat surface (**b**) convex surface (**c**) concave surface

$$r_s{}^2 = \left(\frac{S}{2}\right)^2 + (r_s - R_t)^2 \tag{21}$$

$$S = \sqrt{r_s{}^2 - (r_s - R_t)^2} \tag{22}$$

where r_s is the nose radius of the grinding wheel.

S is the path interval.

In machining convex surface, the path interval can be derived as:

$$S = \frac{\rho_w}{(\rho_w + R_t)(\rho_w + r_s)} \sqrt{2\left[(\rho_w + r_s)^2 + r_s{}^2\right](\rho_w + R_t)^2 - \left[(\rho_w + r_s)^2 - r_s{}^2\right]^2 - (\rho_w + R_t)^4} \tag{23}$$

where ρ_w is the curvature radius.

S is the path interval.

R_t is the scallopheight.

In machining concave surface, the path interval can be obtained as follows:

$$S = \frac{\rho_w}{(\rho_w - R_t)(\rho_w + r_s)} \sqrt{2\left[(\rho_w + r_s)^2 + r_s{}^2\right](\rho_w - R_t)^2 - \left[(\rho_w + r_s)^2 - r_s{}^2\right]^2 - (\rho_w - R_t)^4} \tag{24}$$

According to the geometric relationship between the machining curved surface and workpiece as shown in Fig. 28b, the circle for scallop-height in machining convex surface can be derived as:

$$[x - (\rho_w + r_s)\cos\theta]^2 + [y - (\rho_w + r_s)\sin\theta]^2 = r_s{}^2 \tag{25}$$

where $\cos\theta = \frac{\sqrt{{\rho_w}^2 - \left(\frac{S}{2}\right)}}{\rho_w}$, $\sin\theta = \frac{S}{2\rho_w}$, $S = \frac{V_f}{N_w}$,.

To obtain the maximum scallop-height, y equals to 0, the intersecting point can be expressed as:

$$\left[x - \left(\frac{\rho_w + r_s}{\rho_w}\right)\sqrt{{\rho_w}^2 - \left(\frac{S^2}{2}\right)}\right]^2 + \left[(\rho_w + r_s)\sqrt{{\rho_w}^2 - \left(\frac{S^2}{2}\right)}\right]^2 = {r_s}^2 \tag{26}$$

$$x = \left(\frac{\rho_w + r_s}{\rho_w}\right)\sqrt{{\rho_w}^2 - \left(\frac{S^2}{2}\right)} - \sqrt{{r_s}^2 - \left(\frac{(\rho_w + r_s)S}{2\rho_w}\right)^2} \tag{27}$$

Since $R_t = x - \rho_w$, $S = \frac{V_f}{N_w}$ the scallop-height R_t can be determined as:

$$R_t = (\rho_w + r_s)\sqrt{1 - \left(\frac{{V_f}^2}{2\rho_w {N_w}^2}\right)} - \sqrt{{r_s}^2 - \left(\frac{(\rho_w + r_s)V_f}{2\rho_w N_w}\right)^2} - \rho_w \tag{28}$$

Feed speed (V_f) for machining convex surface can be calculated as:

$$V_f = \frac{\rho_w N_w}{(\rho_w + R_t)(\rho_w + r_s)}\sqrt{2\left[(\rho_w + r_s)^2 + {r_s}^2\right](\rho_w + R_t)^2 - \left[(\rho_w + r_s)^2 - {r_s}^2\right]^2 - (\rho_w + R_t)^4} \tag{29}$$

In the same way, for concave surface as shown in Fig. 28b, the scallop-height R_t can be determined as:

$$R_t = \rho_w - (\rho_w - r_s)\sqrt{1 - \left(\frac{{V_f}^2}{2\rho_w {N_w}^2}\right)^2} - \sqrt{{r_s}^2 - \left(\frac{(\rho_w - r_s)V_f}{2\rho_w N_w}\right)^2} \tag{30}$$

Feed speed (V_f) for machining concave surface can be calculated as:

$$V_f = \frac{\rho_w N_w}{(\rho_w - R_t)(\rho_w + r_s)}\sqrt{2\left[(\rho_w + r_s)^2 + {r_s}^2\right](\rho_w - R_t)^2 - \left[(\rho_w + r_s)^2 - {r_s}^2\right]^2 - (\rho_w - R_t)^4} \tag{31}$$

In order to obtain uniform scallop-height, the feed speed for the allowable residual error can be determined according to the Eq. (28) and Eq. (30) under different surface curvatures of the freeform surface in different contact points.

It is due to the fact that the different curvatures of the freeform surface with respect to the different types of surfaces (convex, flat, and concave surface) pose a significant difference in scallop-height. Figure 29 describes the influence of

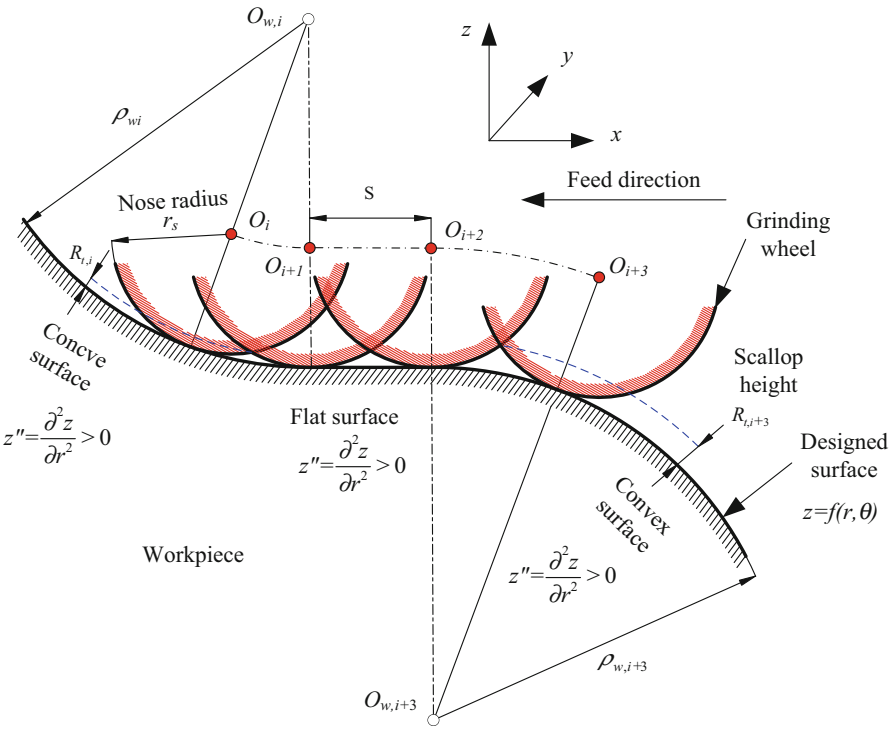

Fig. 29 Computation of the scallop height and discrimination of concave, flat, and convex surface in machining

curvature variation on scallop-height. Under the constant feed speed, the scallop height is different, which is determined by the curvature. In order to discriminate the three different surfaces, the second partial derivative of the designed surface $z = f(r, \theta)$ in different radical sections can be calculated as shown in Fig. 23.

$$z'' = f''(r,\theta) = \frac{\partial^2 z}{\partial r^2} \tag{32}$$

For convex surface, $z'' = \frac{\partial^2 z}{\partial r^2} < 0$, the flat surface $z'' = \frac{\partial^2 z}{\partial r^2} = 0$, for concave surface $z'' = \frac{\partial^2 z}{\partial r^2} > 0$.

According to the Eq. (29) and Eq. (31), the variable feed speed can be calculated. Figure 30 shows the flow chart of the algorithm for realizing the uniform scallop-height in ultra-precision grinding freeform surfaces.

The machining freeform surfaces are performed on an ultra-precision grinding machine (Moore Nanotech 450UPL). The grinding machine uses a rotational Table (B axis) to hold the wheel spindle and the workpiece is mounted on an air bearing. The workpiece spindle rotates and feeds over a high-speed spinning wheel to remove excess materials and shape the desired form, as shown in Fig. 31. In the

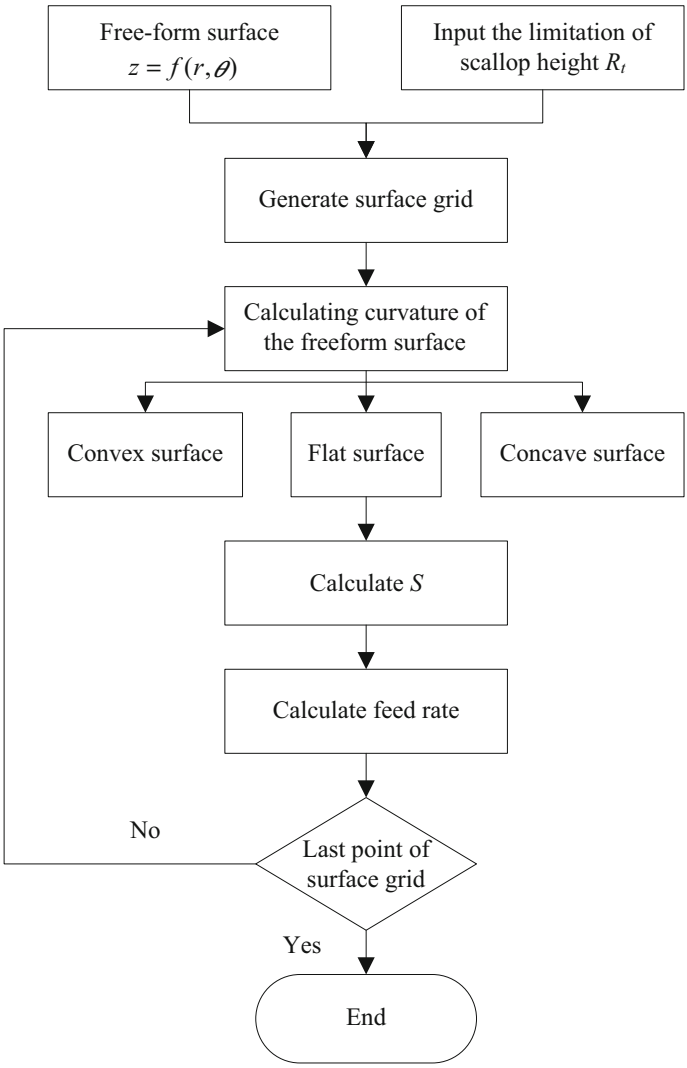

Fig. 30 Flow chart of the tool path generation for realizing the uniform scallop-height machining

ultra-precision grinding experiments, tungsten carbide (WC) is used as the workpiece material, which is widely used in the fabrication of the optical mold and the machining conditions are summarized in Table 1. In order to avoid the disturbance of the original surface topography of the workpiece, all workpieces are processed through two steps of rough and fine grinding before grinding experiment, and then the grinding wheel is dressed before machining each workpiece so as to reduce the impact of grinding wheel wear. The noncontact Zygo Laser Interferometer Profiler is used to measure the ground surface topography.

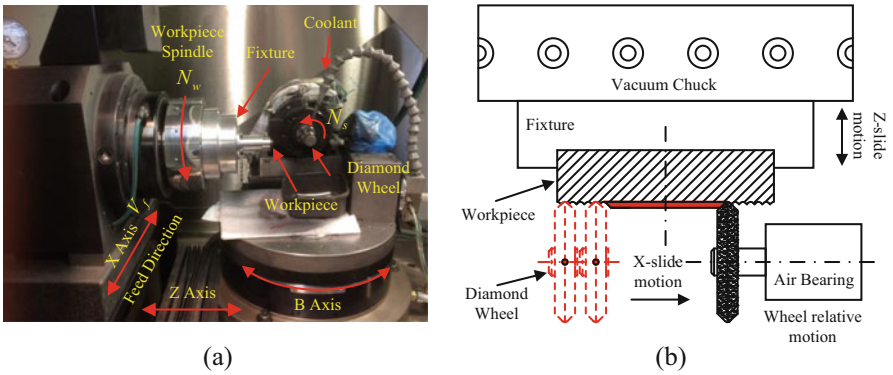

Fig. 31 Experimental setup for the ultra-precision grinding machine in experiments (**a**) schematic diagram of the grinding machine (**b**) layout of the grinding wheel and workpiece

Table 1 Grinding wheel and experimental conditions

Grinding Wheel	Resin bonded diamond wheel Grain size: 500-grit Diameter: 18 mm Thickness: 5 mm Nose radius: 0.5 mm Concentration:100% Structural number: 7
Speed of the grinding wheel (N_s) (RPM)	40,000
Speed of the workpiece (N_w)(RPM)	200
Feed rate (V_f) (mm per min)	5
Depth of cut (H) (μm)	10
Coolant	CLAIRSOL 330

In this experiment, two types of sinusoidal surface are machined, and they are annular sinusoidal surface and single sinusoidal surface. In cartesian coordinate system, they can be expressed in Eq.(13) and Eq.(14) respectively. According to Eq.(33) and Eq.(34) and setting $A = 50\mu m$, $\lambda = 3\text{mm}$ and $\varphi = 90^\circ$, the simulated sinusoidal surfaces are shown in Fig. 32a and b.

$$z = f(x, y) = A \sin\left(\frac{2\pi x}{\lambda} + \varphi\right) \tag{33}$$

$$z = f(x, y) = A \sin\left(\frac{2\pi\sqrt{x^2 + y^2}}{\lambda} + \varphi\right) \tag{34}$$

where A is the amplitude of sinusoidal surface, λ is the wave length of sinusoidal surface, φ is phase angle.

The allowable scallop height is setting at 1 μm and 2 μm for single sinusoidal surface and annular sinusoidal surface, respectively. The grinding wheel nose radius

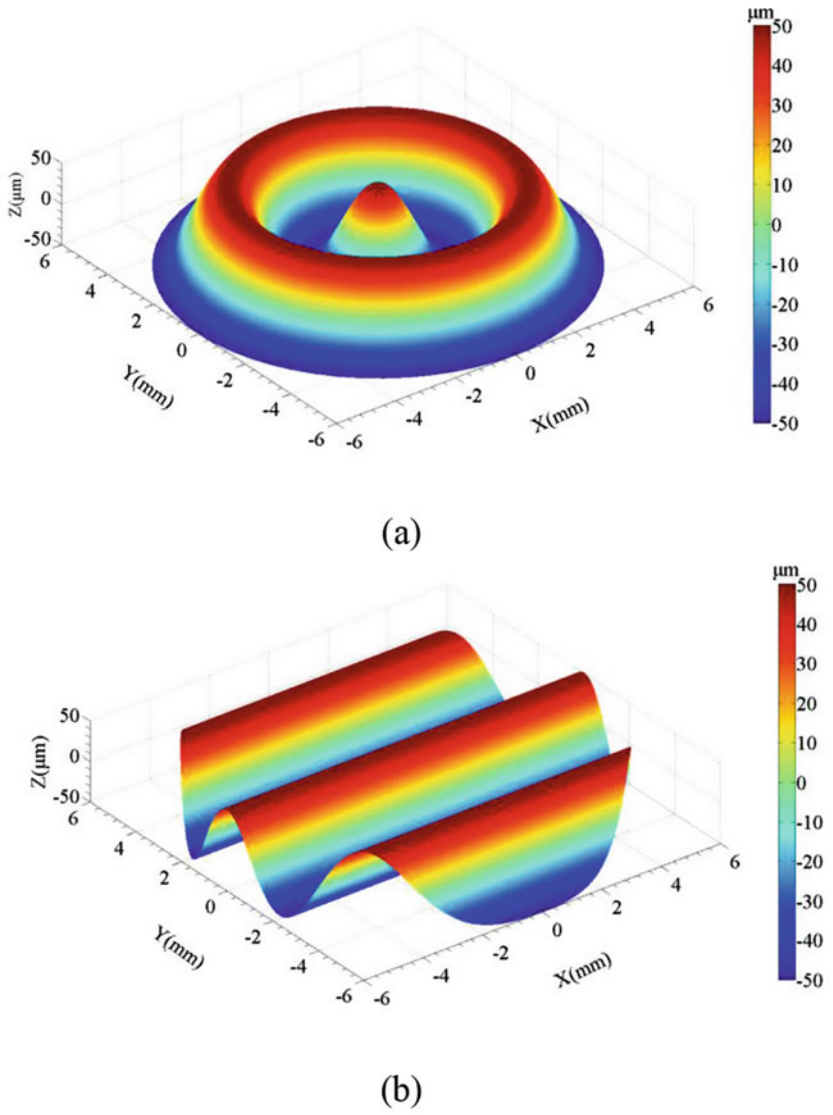

Fig. 32 Simulated sinusoidal surfaces (**a**) annular sinusoidal surface and (**b**) single sinusoidal surface

is 0.5 mm. According to Eq.(33) and Eq.(34), the tool path can be determined and Fig. 33 shows the estimated 3D tool path for machining the two sinusoidal surfaces. In order to observe the tool path clearly, the tool path intervals are enlarged.

The machined sinusoidal surfaces were measured by using a non-contact laser interferometer profiler apparatus. Figure 34 shows the sinusoidal surfaces machined by three-axis ultra-precision grinding machine. The result shows that the form error

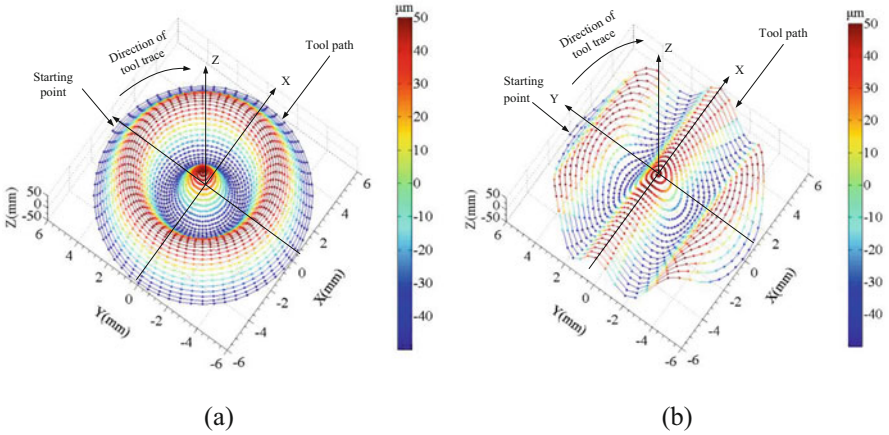

Fig. 33 Simulated tool path sinusoidal surfaces (**a**) annular sinusoidal surface and (**b**) single sinusoidal surface ($N_w = 200$ rpm, $N_s = 40{,}000$ rpm, $H = 10$ μm)

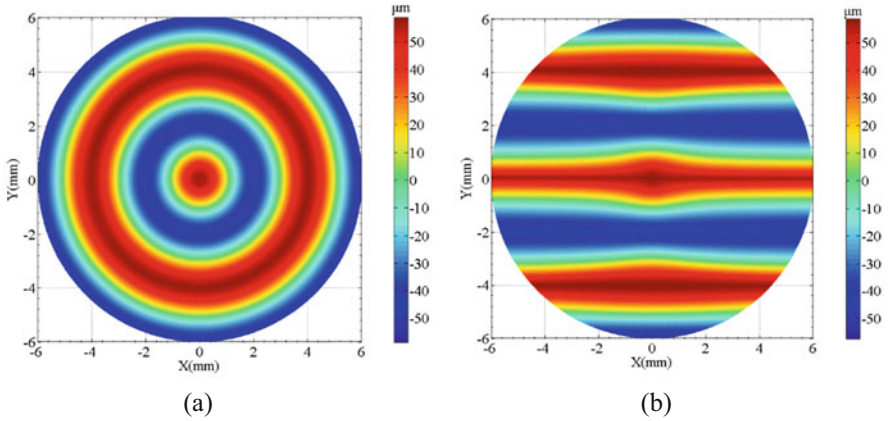

Fig. 34 Measured surfaces (**a**) annular sinusoidal surface and (**b**) single sinusoidal surface ($N_w = 200$ rpm, $N_s = 40{,}000$ rpm, $H = 10$ μm)

is larger for machining nonrotational symmetric surface than that for rotational symmetric surface, which may be caused by the machine dynamics errors. For rotational symmetric surface, the cross section profiles at different angular positions are the same. However, the cross section profile of the surface is related to the angular position for the nonrotational symmetric surface, which is susceptible to the tool motion control errors in machining.

The form accuracy in machining freeform surfaces is an important indicator to determine the functional performance in ultra-precision grinding. The deviation of whole ground surface and distribution of the form errors should be verified to evaluate machining performance. The main purpose of the surface matching

between the measured surface and the designed surface is to make the two surfaces as close as possible. In order to improve the matching accuracy, it is necessary to continuously iterate and adjust again and again to find the optimal spatial position of the measured surface.

There are two parts in the matching process. One part is the translation operation, which can be represented by the matrix $T(t_x, t_y, t_z)$; the other part is the rotation process, which can be represented by the matrix$R(\alpha, \beta, \gamma)$. The whole transformation calculation process is

$$M = T\left(t_x, t_y, t_z\right) \cdot R(\alpha, \beta, \gamma) \tag{35}$$

The translation matric can be expressed as:

$$T\left(t_x, t_y, t_z\right) = \begin{bmatrix} 1 & 0 & 0 & t_x \\ 0 & 1 & 0 & t_y \\ 0 & 0 & 1 & t_z \\ 0 & 0 & 0 & 1 \end{bmatrix} \tag{36}$$

where, t_x, t_y, and t_z represent translational transformation in x, y, and z direction.

Rotation transformation matrix can be expressed as:

$$\begin{aligned} R(\alpha, \beta, \gamma) &= R_z(\gamma) \cdot R_y(\beta) R_x(\alpha) \\ &= \begin{bmatrix} \cos\gamma\cos\beta & \cos\gamma\sin\beta\sin\alpha - \sin\gamma\cos\alpha & \sin\gamma\sin\alpha + \cos\gamma\sin\beta\cos\alpha & 0 \\ \sin\gamma\cos\beta & \cos\gamma\cos\alpha + \sin\gamma\sin\beta\sin\alpha & \sin\gamma\sin\beta\cos\alpha - \cos\gamma\sin\alpha & 0 \\ -\sin\beta & \cos\beta\sin\alpha & \cos\beta\cos\alpha & 0 \\ 0 & 0 & 0 & 1 \end{bmatrix} \end{aligned} \tag{37}$$

where α, β, and γ represent the rotation angle of the measured surface around x, y, and z axis.

According to Eq. (36)–Eq. (37), the spatial coordinate transformation matrix can be expressed as:

$$M = \begin{bmatrix} \cos\gamma\cos\beta & \cos\gamma\sin\beta\sin\alpha - \sin\gamma\cos\alpha & \sin\gamma\sin\alpha + \cos\gamma\sin\beta\cos\alpha & t_x \\ \sin\gamma\cos\beta & \cos\gamma\cos\alpha + \sin\gamma\sin\beta\sin\alpha & \sin\gamma\sin\beta\cos\alpha - \cos\gamma\sin\alpha & t_y \\ -\sin\beta & \cos\beta\sin\alpha & \cos\beta\cos\alpha & t_x \\ 0 & 0 & 0 & 1 \end{bmatrix} \tag{38}$$

In Eq. (38), there are six parameters need to be solved, rotation angle α, β, and γ and the translation distance t_x, t_y, and t_z. In order to figure out these six unknown parameters, the transformation matrix can satisfy the following equation:

$$\min\left[F_j(T)\right] = \min\left[\sum_{i=1}^{i=m}\left|T_j Q_{ij} - P_{ij}\right|^2\right] \tag{39}$$

where $Q_{ij} = [x_{ij}, y_{ij}, z_{ij}, 1]^T$Is the point on the measured surface, $P_{ij} = \left[x'_{ij}, y'_{ij}, z'_{ij}, 1\right]^T$ is the closest point to the measured surface on the designed surface, j is the number of iterations.

Substitute the data points of the measured surface into Eq. (19), then take partial derivative and set it equal to 0

$$\frac{\partial}{\partial T}\left[F_j(T)\right] = 2\sum_{i=1}^{i=m}\left[\left|T_j Q_{ij} - P_{ij}\right|\frac{\partial}{\partial T}\left(\left|T_j Q_{ij} - P_{ij}\right|\right)\right] = 0 \tag{40}$$

In order to further verify the deviation between the designed sinusoidal surfaces and measured surfaces quantitatively, the matching of the simulated surface and the measured surface is conducted, in which the measured points for surface and the data for the design surface are transferred into the same coordinate system by a spatial rotation and translation. Figure 35 shows the evaluated matching errors for the machining of different sinusoidal surface and larger errors for machining single sinusoidal surface.

It is found that the scallop-height is uneven in the conventional tool path control method, which is resulted from the influence of the changed curvature of workpiece surface. On the relatively flat area, the scallop-height is about 1 μm. However, on the area with small curvature radius, surface scallop-height is larger, and the scallop-height increased to 2.5 μm, as shown in Fig. 36.

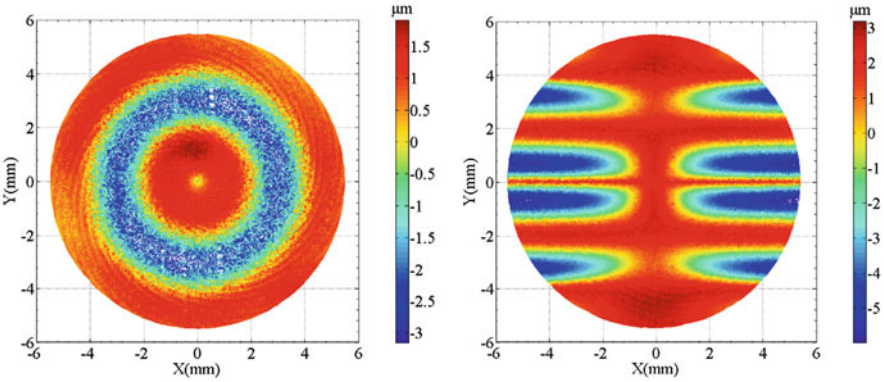

(a) (b)

Fig. 35 Matching error map for machining (**a**) annular sinusoidal surface and (**b**) single sinusoidal surface ($N_w = 200$ rpm, $N_s = 40{,}000$ rpm, $H = 10$ μm)

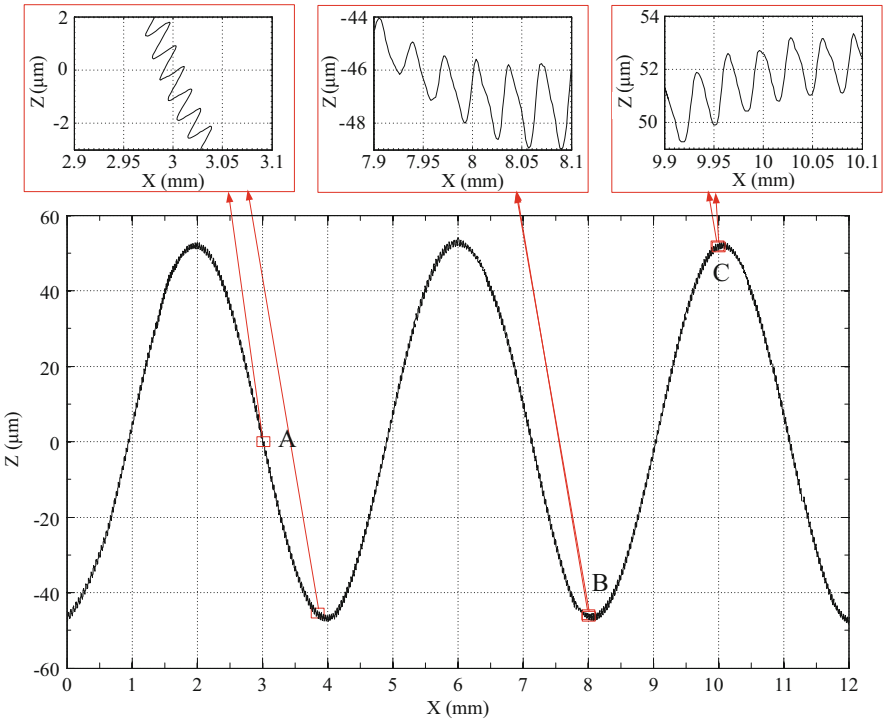

Fig. 36 Scallop height for cross section profiles generated in machining annular sinusoidal surface by adopting control strategy of constant feed speed ($N_w = 200$ rpm, $N_s = 40{,}000$ rpm, $H = 10$ μm, $V_f = 5$ mm/min)

Figure 37 shows the measured cross section profiles of sinusoidal surface and scallop-height is about 1 μm in grinding annular sinusoidal surface and single sinusoidal surface (X = 0). The scallop-height both for annular sinusoidal surface and single sinusoidal surface are kept uniform approximately. At the same time, the peaks on the maximum of the central sinusoid cause the tool setting error.

Table 2 shows a comparison of the arithmetic roughness of the two types of freeform surface with respect to different areas corresponding to the Fig. 10. Each workpiece is machined for 3 times and then the average value for *PV* value is calculated. It is found that the *PV* value approximately keep uniform in machining those two freeform surfaces, respectively, and the matching error for machining single sinusoidal surface in terms of root-mean-square value (*RMS is 0.182* μm) is significantly larger than that of machining annual sinusoidal surface (i.e., *RMS* = 0.108 μm*)*.

The model predicted results for the machined surfaces agree well with that of the experimental results. For machining freeform surface that is more complex and has a

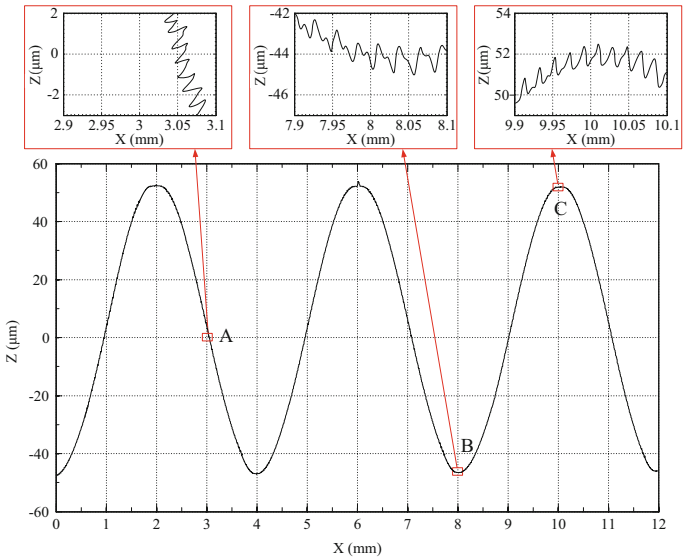

(a)

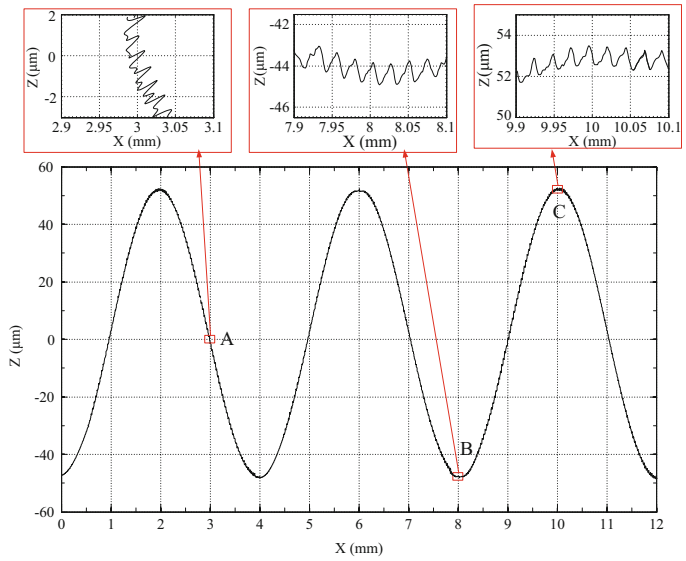

(b)

Fig. 37 Measured cross section profiles by adopting control strategy of uniform scallop height method (**a**) annular sinusoidal surface and (**b**) single sinusoidal surface (N_w = 200 rpm, N_s = 40,000 rpm, H = 10 μm)

Table 2 Machining results for the arithmetic roughness *Ra* and the root mean squared value (RMS) of matching errors

Surface type	*PV* value (μm)			*Root-mean-square value RMS*(μm)
	A	B	C	
Annular sinusoidal surface	1.19	1.21	1.26	0.108
Single sinusoidal surface	1.22	1.17	1.24	0.182

strong correlation to the curvature of the surface, the scallop height is significantly different from machining flat surface, the changing curvature radius of freeform surface leads to the ununiformed scallop height in grinding. The larger curvature radius the freeform has, the higher scallop height the machined surface embraces. This model provides an effect way to overcome the uneven surface residual height by changing the feed speed of the grinding wheel. In addition, the surface form errors for machining nonrotational symmetric surface are larger than that of rotational symmetric surface.

Conclusion

At present, critical components usually have complex surface structure and closed tolerance. The functions and performance of the critical components directly determine the capabilities of the whole device. Therefore, it is vital to choose the suitable processing technique for fabricating those components with high accuracy and low cost. With the increasing demand for high quality and precision components, ultra-precision machining technologies have been widely explored in processing the critical components because they can machine surfaces with high form accuracy and good surface finish. The ultra-precision machining technologies mainly include diamond turning, micromilling, and diamond grinding, which are the most widely used processing techniques in industry manufacture. Turning and milling are suitable to shape ductile materials, while grinding is more available to cut hard and brittle materials. Currently, due to the higher stiffness, structural stability, wear resistance, and chemical stability as compared to traditional metallic materials, advanced engineering ceramic has been more and more applied as the ideal material for the critical components. Therefore, ultra precision grinding is more and more employed to machine the critical parts, especially for optical manufacturing. However, the grinding process is more complex than turning and milling, which imposes great challenge to analyze and control the machine tools to achieve expected accuracy.

References

Agarwal S, Rao PV (2005) A probabilistic approach to predict surface roughness in ceramic grinding. Int J Mach Tools Manuf 45(6):609–616

Aurich JC, Biermann D, Blum H, Brecher C, Carstensen C, Denkena B, Klocke F, Kröger M, Steinmann P, Weinert K (2009) Modelling and simulation of process machine interaction in grinding. Prod Eng Res Dev 3(1):111–120

Beaucamp A, Namba Y, Messelink W, Walker D, Charlton P, Freeman R (2014) Surface integrity of fluid Jet polished Tungsten Carbide. CIRP Ann Manuf Technol 13:377–381
Brinksmeier E, Rickens K, Grimme D (2001) Duktiler materialabtrag beim schleifen sprödharter werkstoffe. Jahrbuch Schleifen Honen Läppen und Polieren 60:50–67
Cao ZC, Cheung CF (2016) Multi-scale modelling and simulation of material removal characteristics in computer-controlled bonnet polishing. Int J Mech Sci 106:147–156
Carbone G, Pierro E, Gorb SN (2011) Origin of the superior adhesive performance of mushroom-shaped microstructured surfaces. Soft Matter 7(12):5545–5552
Chen YL, Wang S, Shimizu Y, Ito S, Gao W, Ju BF (2015) An in-process measurement method for repair of defective microstructures by using a fast tool servo with a force sensor. Precis Eng 39:134–142
Chen SS, Cheung CF, Zhang FH, Ho LT, Zhao CY (2019) Theoretical and experimental investigation of tool path control strategy for uniform surface generation in ultra-precision grinding. The International Journal of Advanced Manufacturing Technology 103(9–12):4307–4315
Dombovari Z, Stepan G (2015) On the bistable zone of milling processes. Philos Trans R Soc A Math Phys Eng Sci 373:1–17
Eckard HD (1971) Simple model of corner reflector phenomena. Appl Opt 10:1559–1566
Gao H, Wang X, Guo DM, Chen YC (2017) Research progress on ultra-precision machining technologies for soft-brittle crystal materials. Front Mech Eng 12(1):77–88
Heike KF, Taghi T, Bahman A (2017) Material removal mechanism in ultrasonic-assisted grinding of Al2O3 by single-grain scratch test. Int J Adv Manuf Technol 91(9–12):2949–2962
Inasaki I (1987) Grinding of hard and brittle materials. CIRP Ann-Manuf Technol 36(2):463–471
Khanov AM, Muratov KR, Muratov RA, Gashev EA (2014) Abrasive finishing of brittle materials. Russian Engineering Research, 34(11):730–733
King RI, Hahn RS (1986) Handbook of modern grinding technology. Springer, New York
Klocke F, Brinksmeier E, Weinert K (2005) Capability profile of hard cutting and grinding processes. CIRP Ann-Manuf Technol 54(2):557–580
Lawn BR, Wilshaw R (1975) Indentation fracture: principles and applications. J Mater Sci 10:1049–1081
Liu CF, Pan CT, Chen YC, Liu ZH, Wu CJ (2013) Design and fabrication of double-sided optical film for OLED lighting. Opt Commun 291:349–358
Marinescu ID, Hitchiner MP, Uhlmann E, Rowe WB, Inasaki I (2016) Handbook of machining with grinding wheels. CRC Press, Boca Raton
Marius W (2016) Eco-efficiency of Grinding Processes and Systems. TU Braunschweig, Braunschweig, Germany. Springer
Metzger JL (1986) Superabrasive grinding. Butterworth & Co (Publishers) Ltd, London
Miyashita M (1989) Brittle/ductile machining. In: Fifth international seminar on precision engineering, Monterey
Miyoshi H, Ju J, Lee SM, Cho DJ, Ko JS, Yamagata Y, Adachi T (2010) Control of highly migratory cells by microstructured surface based on transient change in cell behavior. Biomaterials 31(33):8539–8545
Nadolny K (2015) Wear phenomena of grinding wheels with sol–gel alumina abrasive grains and glass–ceramic vitrified bond during internal cylindrical traverse grinding of 100Cr6 steel. Int J Adv Manuf Technol 77(1):83–98
Ngoi BKA, Sreejith PS (2000) Ductile regime finish machining-a review. Int J Adv Manuf Technol 16(8):547–550
O'Hara A, Hannah JR, Underwood I, Vass DG, Holwill RJ (1993) Mirror quality and efficiency improvements of reflective spatial light modulators by the use of dielectric coatings and chemical-mechanical polishing. Appl Opt 32(28):5549–5556
Setti D, Ghosh S, Rao PV (2017) A method for prediction of active grits count in surface grinding. Wear 382–383:71–77
Shi ZY, Liu ZQ, Li YC, Qiao Y (2017) Swept mechanism of micro-milling tool geometry effect on machined oxygen free high conductivity copper (OFHC) surface roughness. Materials 10(120):1–20

Singal RK, Singal M, Singal R (2008) Fundamentals of machining and machine tools. I. K. International Pvt Ltd, New Delhi

Susič E, Grabec I (2000) Characterization of the grinding process by acoustic emission. Int J Mach Tools Manuf 40(2):225–238

Taniguchi N (1994) The state of the art of nanotechnology for processing of ultraprecision and ultra fine products. J Am Soc Precis Eng 16(1):5–24

Tönshoff HK, Peters J, Inasaki I, Paul T (1992) Modelling and simulation of grinding process. CIRP Ann Manuf Technol 41(2):677–688

Tsai M, Huang J (2006) Efficient automatic polishing process with a new compliant abrasive tool. Int J Adv Manuf Technol 30(9):817–827

Tsai JZ, Chang RS, Li TY (2012) LED backlight module by a light guide-diffusive component with tetrahedron reflector array. J Disp Technol 8(6):321–328

Yang ZS, Yu ZH (2012) Grinding wheel wear monitoring based on wavelet analysis and support vector machine. Int J Adv Manuf Technol 62(1):107–121

Zhang XQ, Huang R, Liu K, Kumar AS, Shan XC (2018) Rotating-tool diamond turning of Fresnel lenses on a roller mold for manufacturing of functional optical film. Precis Eng 51:445–457

Zhang SJ, Zhou YP, Zhang HJ, Xiong ZW, Suet T (2019) Advances in ultra-precision machining of micro-structured functional surfaces and their typical applications. Int J Mach Tools Manuf 142:16–41

Zhou M, Zhang HJ, Chen SJ (2010) Study on diamond cutting of nonrationally symmetric microstructured surfaces with fast tool servo. Mater Manuf Process 25(6):488–494

Assembly Techniques of Precision Machines 13

Bin Li

Contents

Introduction 354
Measurement for the Precision Machine 355
Accuracy Test Methods for the Precision Machine's Part 355
Linear Motion Accuracy Measurement Methods 356
Rotary Motion Accuracy Measurement Methods 356
Precision Machine Assembly Cases 357
Polishing Spindle Assembly Case 357
Large Aspheric Mirror Grinding Machine Assembly Case 366
Conclusion 373
References 374

Abstract

Precision machine assembly process is thought to be simple, as the assembly process is carried out according to the drawing; however, the actual assembly is complicated. Precision machine assembly process is not only the combination of the parts but also the testing, modification, and debugging of mechanical system. In order to achieve the specified kinematic accuracy or functionality, the machine part should satisfy its dimensional, surface texture, and physical specifications, and the assembly process should be carried out according to the design demands. After the original assembly, the modification should be implemented according to the accuracy, stiffness, and damping test, as well as the auxiliary device. The assembly process for precision machine is firstly concluded and analyzed. The measurement methods for the workpiece and kinematic motion error are introduced thereafter, as well as the part modification methods. At last, the aerostatic spindle and rotary table, the larger aspheric mirror grinding machine UAG900's assembly process were introduced.

B. Li (✉)
College of Mechatronic Engineering, Zhongyuan University of Technology, Zheng zhou, China
e-mail: libin_zzti@zut.edu.cn

Z. Jiang, S. Yang (eds.), *Precision Machines*, Precision Manufacturing,
https://doi.org/10.1007/978-981-13-0381-4_29

Keywords

Precision machine assembly · Aerostatic bearings · Large aspheric grinding machine

Introduction

Compared with the design and analysis process of the precision machine, there are rare literatures for the precision machine assembly. The assembly for precision machines is generally implemented with the requirements of the designer, and finished by workers. However, the worker's description capability is rather poor to convert their experience into the words, and many important assembly procedures have not been written down to be as reference. Many assembly process might be recorded by the word description, video or voice record; the worker's personal experience and skill cannot be recorded, which causes the loss of many precision machine assembly method. Therefore, many smart designs could not achieve their final process accuracy.

In order to improve the assembly technique, many standards have been published to specify the assembly process. The first generation of precision machine was generally assembly by human hands, including the part modification. For the aerostatic spindle, the air gap between the shaft and the housing bore is less than 20 μm, and the gap uniformity should be controlled under 2 μm. Otherwise, the spindle unbalance would generate and cause the vibration of the spindle. It is impossible to satisfy the accuracy specification using the machine tools; the human hands could only be used. In order to using the honing process, the shaft shape was designed to be spherical, the shaft was roughly turned, and then the felt plate was used to hone the shaft. The housing bore was honed using the shaft. The workers need to control the air gap by adjusting the face screw. The first-generation single diamond turning machine has begun the era of the modern precision machine. The assembly is vital for the development of precision machine (Brian Rowe 2012; Abele et al. 2010; Tu et al. 1998).

For many large machine tools, module assembly method is necessary. The heavy weight would complicate the shifting process. For example, the large aspheric grinding machine OAGM 2500 consists of three axes and a basement with a total weight of more than 100 t, which is divided into several parts to facilitate the shipping and assembly (Leadbeater et al. 1989).

The assembly procedure should be considered firstly during the design stage, and the designer should prepare the feasible fixture tool to assist the assembly. Measurement measures and corresponding measuring device should also be considered, as the test results will determine whether the part or the assembly is qualified.

During the original assembly stage, the motors and sensors would also be equipped. However, the drive system would not be connected with the motors, but be tested dependently. After the original assembly, the actual assembly will be carried out. The measuring device will be used to test the linear and rotary motion accuracy. Then the precision machine's drive system would be conditioned to obtain

the optimized parameters. Since the assembly is finished, the machining process test would also be implemented to check whether the final process specifications are achieved.

Measurement for the Precision Machine

The workers should be very skilled; however, the human sense is not stable enough. The measurement instruments are needed to determine the errors numerically, and the modification will be carried out based on the measured results. The machine accuracy test is the vital measure to justify whether the assembly is qualified. The precision machine tool kinematic motion error could be classified into linear and rotary motions, and the relative positional error between each axis. To determine assembly accuracy of the machine tool, the part's accuracy should firstly be tested, and then the assembly should be carried out as all the parts' accuracy was satisfied. After assembly, the kinematic motion accuracy of the machine and unit should also be tested, as it will influence the final machining accuracy. Meanwhile, the machining test experiment should also be carried out, and the workpiece should be tested to justify the efficiency, accuracy, and stability requirements. As a result, the measurement technique is the basis of the precision machine assembly. The part and assembly's accuracy measurement methods and device will be introduced and concluded in this section (Whitehouse 1994; Muralikrishnan and Raja 2009).

Accuracy Test Methods for the Precision Machine's Part

Many items should be measured for the precision machine's part; however, this section focuses on the geometric errors. Nearly all kinds of the geometric errors, including the form and position errors and the size variations, could be measured. Coordinate Measuring Machine (CMM) was the first choice for the part measurement. The most precise CMM is the metrology type, and its volume uncertainty could be controlled under 0.5 μpm which is sufficient for most parts despite of the geometry and accuracy requirements. In order to guarantee the CMM's measurement accuracy, the environment temperature should be controlled, and the vibration should be isolated. The part should be cleaned and placed in the measurement laboratory to obtain the consistent temperature.

CMM is generally used to measure the parts with complicated geometry. The cylindrical parts are generally measured by the cylindricity measuring instrument. The instrument could achieve the measurement of the roundness, flatness, cylindricity, straightness, squareness, etc. It consists of aerostatic rotary table, Z and X axis, and the probe is arranged at the end of the Z ram. Comparing with the CMM, the cylindricity measuring instrument could sample more points of the part, and the equipped software could visualize the part surface using the sampled data. The rotary table's runout is less than 0.05 μm, which is sufficient for most cylindrical part.

In addition to the above two multifunction instruments, there are also many precision instruments, for example, outside diameter dial indicator, inside diameter dial indicator, dial gauge, gauge blocks, autocollimator, level gauge. There should be sufficient measurement instruments to numerically identify the error of the part (Morris and Langari 2012).

Linear Motion Accuracy Measurement Methods

For the linear motion, straightness and positioning accuracy are the two most important test items. Dial gauge and straightedge are generally combined to test the straightness of the linear guideways. The dial gauge could be mechanical leveler indicator or inductance meter, or even the capacitance micrometer; the selection is based on the straightness specification and the straightedge's characteristic. The material is the vital influence factors of its accuracy. The straightedge would be made of the granite, steel, and ceramic. The ceramic is the most stable, and it has the highest accuracy; however, its manufacturing process is the most complicated. In order to measuring the straightness precisely, the straightedge should be parallel to the guideways, otherwise, there would be abbe error. The straightness of the straightedge itself could be controlled under 50 μm. To further reduce the measurement uncertainty, the reverse method is generally used to eliminate the systemic error. Comparing with the laser interferometer, the straightedge method is not sensitive to the environment condition variation, including the vibration and temperature, thus the straightedge is the first choice thought the measurement result needs be further processed. As the straightedge length is generally less than 1000 mm, the piecing method is applied to expand the measuring range.

Compared with the straightedge measurement method, laser interferometer has a longer measuring range; however, it is easily affected by the environment temperature variation and vibrations. And the straightness measurement adjustment procedure is very complicated, and the measuring uncertainty is higher.

Rotary Motion Accuracy Measurement Methods

Items for the rotary motion accuracy consist of the axial runout, radial runout, and angle positioning error. The rotary units were classified into rotary table and spindle, according to the length and diameter ratio. Generally, the rotary table has low speed and high angel positioning accuracy.

The axial and radial runout can be measured by combining the standard bar or ball with the dial gauge. The bar or sphere was placed at the center, and the offset should be as small as possible to eliminate the system error. The bar would be fixed using the fixture, and the sphere is fixed using plasticizers rather than the magnate foundation as it would disturb the dial gauge readings.

For the angle positioning measurement, the modern instrument is angle encoder which is generally fastened at the end of the spindle or rotary table. The encoder is

generally used as the feedback sensor. The additional device is needed for angle measurement. Laser interferometer could be used; however, the additional reflective mirror is needed (Marsh 2007).

Precision Machine Assembly Cases

In this section, the large aspheric mirror grinding machine and large aerostatic table for the fast polishing machine assembly cases are introduced. The fluid film lubricated bearings will be widely adopted in the future precision and ultraprecision machines, which involved aerostatic and hydrostatic supporting bearings, respectively. The cases firstly introduced the vital part accuracy specifications and manufacturing process, and the assembly procedure was described (Li 2015; Fan 2014).

Polishing Spindle Assembly Case

With the development of the major optical projects, the demands of large plane optical components are dramatically increasing in major optical industries and emerging high-tech fields, such as defense weapon systems, aerospace technology, and astronomical detecting. The traditional polishing process cannot meet the demands. In order to fast polish process of large plane optics, the polishing spindle assembly of the large plane optics ultraprecision polishing machine KPJ1700 (polishing pad diameter being 1710 mm) is developed based on the design criteria of high precision, high stiffness, and high stability. The systematic theory and application research focuses on scheme design, areostatic bearings design static and dynamic characteristics analysis, and fabricating and assembling processes of the key parts and components.

In order to analyze the influence of processing parameters on the polishing quality, the analysis of the fast polishing theory is carried out, focusing on the analysis of polishing process and dressing process. According to the scheme of polishing machine tool KPJ1700, the technical targets of polishing spindle are achieved through the analysis of the machine tool's motion error. With high precision, high load capacity, and high stability as its design criterion, the overall design scheme that uses aerostatic bearings for polishing spindle assembly is proposed. The design of the aerostatic bearings is based on the theoretical analysis, simulation, and test of load capacity for the porous aerostatic bearing. The direct drive system with high precision angle encoder is designed with the aim of controlling the speed accurately and stably. Using ANSYS Workbench finite element analysis (FEA) software, statics and modal simulation analysis is implemented on the key components of polishing spindle system; the structures of polishing spindle and its parts are optimized; and stiffness, accuracy, and stability is also promoted.

Vital Part Machining Process

The polishing spindle consists of the aerostatic bearings, drive system, polishing pad, etc. The aerostatic bearing's performance would directly influence the polishing spindle's accuracy. The design and process of the spindle unit determines the performance of the aerostatic bearings, the process of the vital part should satisfy the design specification, and the process procedure should be designed properly to guarantee the accuracy stability of the part. As the size and weight of the spindle unit is very large, suitable assembly process should be designed to achieve the accuracy stability of the aerostatic bearings.

Housing Machining Process of the Polishing Spindle

The structure of the polishing spindle housing is illustrated as below; it is the basement of the polishing spindle unit. In order to guarantee the running stability and accuracy of the polishing spindle, the structure and material should have good performance of vibration reduction and accuracy stability. The high strength radial rib structure is adopted to guarantee the structural stability. In order to guarantee that the radial and axial runout of the polishing spindle is less than 2 μm, the contact surface between the housing and bed should be scrapped to obtain high-level flatness, and the granite surface should have a flatness of less than 5 μm after fine grinding process (Fig. 1).

1. **Material selection**
   Housing is the basement of the polishing spindle unit, which will be connected with the bed through the housing, and the granite block will be pasted onto the surface of the housing. The granite block will stand the effect of the high pressure air as well as the load of the other parts. In order to achieve the accuracy stability, the nodular cast iron QT500-7 was selected for its excellent performance of vibration elimination. Further, the QT500-7 cast iron's strength is very high, and the machinability is also very outstanding. The inside sphere structure could eliminate crack characteristic induced by the slice granite. As a result, the QT500-7 has both the strength of the steel and the characteristic of the vibration attenuation, wear, and corrosion resistant.

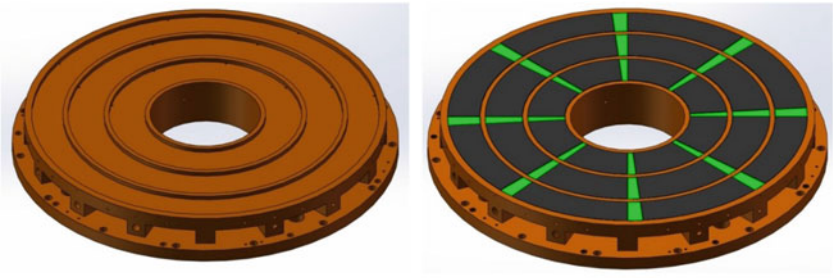

Fig. 1 Housing of polishing spindle

2. **Machining procedure for the housing**
   The housing is made of cast iron. To guarantee the machining quality and accuracy stability, the cutting depth during the machining process is much smaller than the conventional process to avoid excessive stress. The heat treatment is also carried out with more steps. The main machining procedure is listed as below (Table 1).

Static Pressure Plate Machining Process of the Polishing Spindle

As the load support of the aerostatic bearing, the static pressure plate is the rotor part of the polishing spindle unit; its structure is shown in Fig. 2. To guarantee the 10 μm air gap thickness of the aerostatic bearing, the flatness specification of the top load surface and bottom static pressure surface should be less than 5 μm, and the parallelism should be better than 10 μm. Meanwhile, to reduce the weight of the

Table 1 Main machining process for the housing

No.	Process name	Procedure
1	Casting	Blank, QT500
2	Heat treatment	Artificial aging two times, inside stress elimination
3	Rough turning	
4	Aging	
5	Fine turning	Fine turning of the top and bottom surface, inside cylinder
6	Granite paste	
7	Rough grinding	
8	Fine grinding	Fine grinding of the granite surface
9	Honing	Honing of the top surface and inner cylinder bore
10	Scrapping	Scrapping the contact surface between the housing and bed

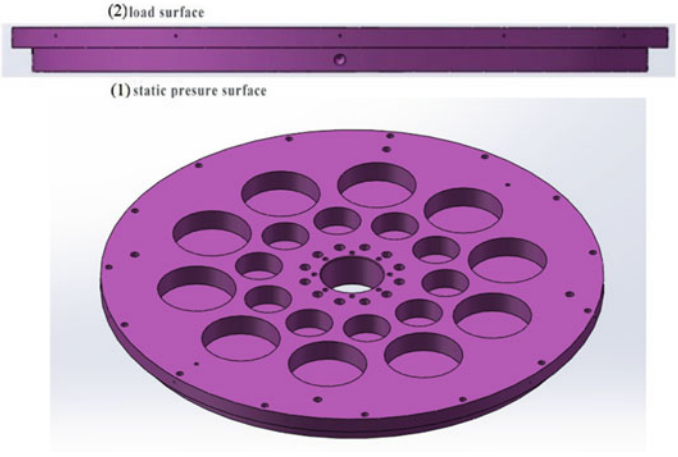

Fig. 2 Structure illustration of the upper aerostatic pad

static pressure, many blind holes are made on the top surface of the plate. The simulation is carried out to check the strength.

1. **Material selection**
   Static pressure plate is used as the rotor of the aerostatic bearings, and it will withstand the effect of the high pressure air, as well as the weight of the polishing pad and the pressure of the polishing process. Due to the humid working environment of spindle, the corrosion resistant measures should be taken to prevent the porous granite material from being corroded and blocked. The static pressure plate material is generally a forged blank made of 38CrMoAl or 40Cr. As the static pressure plate has a diameter of 1600 mm, the blank made of the 38CrMoAl was very hard to obtain, and it is not suitable for the large sized part. As a result, the 40Cr material was adopted, which has sufficient toughness, could bear high load, and has good wear resistance. It is generally used to transmit torque and load, and it also has corrosion-resistant capability.
2. **Machining procedure**
   The main machining process is listed as below (Table 2).

   The photo of the plate grinding and after-grinding is illustrated in Fig. 3.

Machining Process of the Shaft for Polishing Spindle

Shaft was the vital part for the radial aerostatic bearings, and its form accuracy would influence the radial aerostatic bearings' performance greatly. In order to guarantee the uniformity of the air gap, the cylindricity of the shaft outside cylinder should be less than 1 μm, and the squareness between the upper and lower surface toward the outside cylinder should be less than 5 μm.

Table 2 Main machining process for static pressure plate

No	Procedure	Notes
1	Forging	Blank, 40Cr
2	Rough turning	Normal size turning process according to the process drawings, blunt edge
3	Temper T235	
4	Fine turning	Fine turning of the upper and lower surface, 0.7–0.8 mm chipping allowance for each side
5	Quench	HRC55–60
6	Deep freezing treatment	
7	Rough grinding	Rough grinding of upper and lower surface, 0.3–0.4 mm chipping allowance for each side
8	Qualitative analysis in oil	
9	Fine grinding	Ra 0.8 μm, and no chipping allowance
11	Honing	Honing to the size that satisfies the air gap requirements

(a)Upper static pressure plate grinding (b) upper static pressure plate surface after grinding

Fig. 3 Fine grinding process of the upper static pressure plate

1. **Material selection**
   The shaft will connect the upper and lower static pressure plate. It will withstand the load of the high pressure air, as well as the transmitted torque from the torque motor and stress from the lower static pressure plate. The force distribution is very complicated, and the shaft has the same performance specifications with the upper and lower static pressure plate. However, because the size of the shaft is quite small, 38CrMoAl is selected to forge the blank. The material's mechanical property is more excellent than 40Cr. Its wear resistance and fatigue strength is very reliable. Meanwhile, its corrosion capability is also excellent to satisfy the performance requirement of the shaft.
2. **Machining procedure**
   In order to guarantee the size and accuracy stability of the shaft, multi-procedure and heat treatment are applied to the shaft machining process. The vital procedure is listed as below (Table 3).

Assembly and Test of the Polishing Spindle Unit

Assembly Process of the Polishing Spindle Unit

The aerostatic bearings are adopted for the polishing spindle, and its assembly process would influence the performance greatly. As the polishing spindle unit's size and weight is too large, the assembly process needs special fixture. The polishing spindle unit consists of three parts, the granite polishing pad, aerostatic bearings, and drive and feedback system. The structure is shown below. The aerostatic bearings are the most important unit that guarantees the accuracy. In order to secure the assembly and test, three procedures are scheduled (Fig. 4).

Assembly of the Aerostatic Bearings

The assembly of the aerostatic bearings is from the top to the bottom, as the developed aerostatic bearings' size and weight is extremely large, the diameter of the upper static pressure plate is 1600 mm, while the weight is more than 1200 kg,

Table 3 Main machining procedure of the shaft

No	Procedure	Notes
1	Forge	Blank, 38CrMoAl
2	Normalizing	
3	Rough turning	Normal size according to the drawing demands, blunt edge
4	Temper T235	
5	Grinding of two end faces	Ra 0.4
6	Aging treatment	
7	Fine turning	Fine turning of lower face and the hole
8	Inner hole boring	
9	Quenching	HRC55–60
11	Deep freezing treatment	
12	Rough grinding of outer cylinder	Chipping allowance in diameter, face grinding with 0.3–0.4 mm feeding
13	Stability in oil	
14	Outer cylinder fine grinding	No chipping allowance after grinding of outer cylinder
15	Face grinding	No chipping allowance after grinding of two end faces

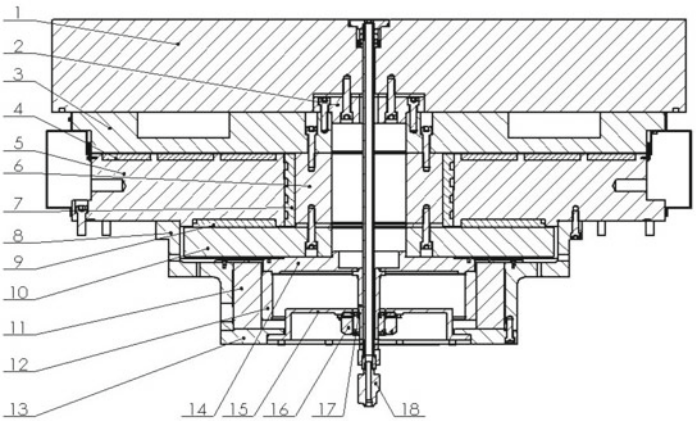

1-Polishing Pad；2-Central shaft；3-Upper static pressure plate；4-Axial porous restritors(upper)；5-Housing；6-Shaft；7-Radial restrictors；8-Torque motor housing；9-Axial porous restrictors(lower)；10-Lower static pressure plate；11-Torque motor stator；12-Torque motor rotor；13-Stator connection plate；14-Rotor connection plate；15-Encoder installation plate；16-Rotary encoder; 17-Encoder connection shaft；18-Rotary connector

Fig. 4 Illustration of the polishing spindle configuration

the assembly and the test procedure are very difficult. Assembly steps are shown below.

1. Check the accuracy of the parts. Make sure that the flatness of the upper and lower static pressure plate should be less than 5 μm.
2. Invert the upper static pressure plate onto the level surface, connect the upper pressure plate with the shaft, and adjust their concentricity within 3 μm.
3. Connect the part 6 and 3 with the housing 5, hone the inner cylinder with the housing 5, the clearance is 10 μm.
4. Connect lower static pressure plate 10 with part 3, 5, 6 through the screws, and hone the lower static pressure plate housing 5's flat, the clearance is 10 μm.
5. Let the pressure air flow through the porous bearings, rotate the housing 3 with hands, and if the rotary motion is very loose, the aerostatic bearings' assembly is excellent. The aerostatic bearing after assembly is shown below (Fig. 5).

Assembly of the Drive System and Feedback Encoder

After the assembly of the aerostatic bearings, the drive system and encoder feedback unit should be installed.

1. Install the torque motor onto the housing 8 and 5, and use the dial gauge to align the housing 8 and 5 until the concentricity is below 5 μm.
2. Connect the rotor connection plate 14 with the torque motor rotor 12.
3. Assemble the torque motor rotor 11 and stator 12 together according to the install guide, noting that the keeping frame should not be uninstalled, as shown.
4. Release the torque motor keeping frame and connect the stator plate 13 with the motor stator 11.
5. Install the encoder shaft 17 onto the rotor connection plate 14. Use the dial gauge to align their concentricity to be less than 5 μm.
6. Install the encoder installation plate 15 on the stator connection plate 15. Use the dial gauge to align the concentricity to be less than 5 μm.
7. Fasten the screw onto the shaft to fix the encoder (Figs. 6 and 7).

Fig. 5 Picture of the aerostatic bearings after assembly

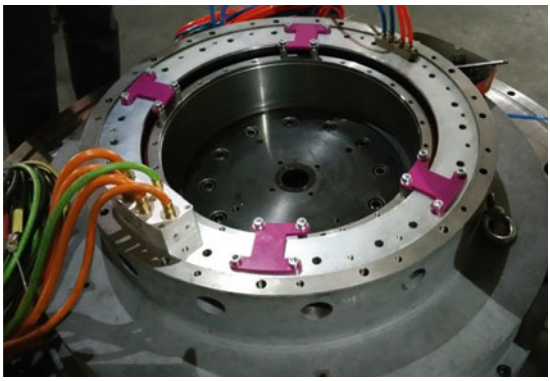

Fig. 6 Torque motor assembly process

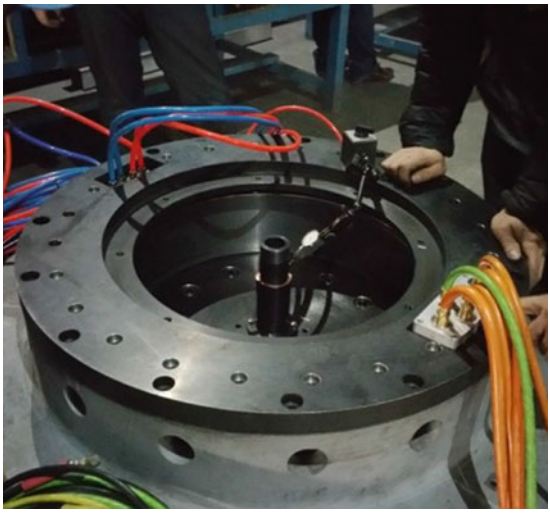

Fig. 7 Alignment process of the encoder and haft

Installation of the Granite Polishing Pad and Accessory

The final polishing accuracy of the flat is determined by the rotary table top surface, which should possess high flatness and stability. The granite material was selected as the polish base pad, and the polyurethane pad would be spliced onto it. As the granite pad needs to be kept flat for the whole surface, no connection holes are allowed on the top. Its connection screws are arranged at the back surface. The granite assembly should be implemented inversely. The assembly process is described as below.

1. Invert the unit. Place it levelly.
2. Connect the central shaft 2 with the static pressure plate 3.

3. Assemble the polishing pad 1 with upper static pressure plate 3, and align their concentricity to be less than 5 μm.
4. Install the polishing fluid pipe and rotary connector; the assembly after installation is shown in Fig. 8.

Connection with the Machine Bed

The rotary table is installed onto the machine bed, and the connection of the gas, electronic, and fluid pipe is then finished; the final assembly is shown below. As the rotary table is designed as the module, it could be installed onto the machine bed through the screw holes on the lower plate. In order to satisfy the positional accuracy of the rotary table relative to the other axes, the installation surface of the machine bed has to be scraped (Fig. 9).

Test of the Polishing Spindle Unit

In order to guarantee working stability of the polishing spindle of aerostatic bearings, the following procedure should be carried out before the normal machining process.

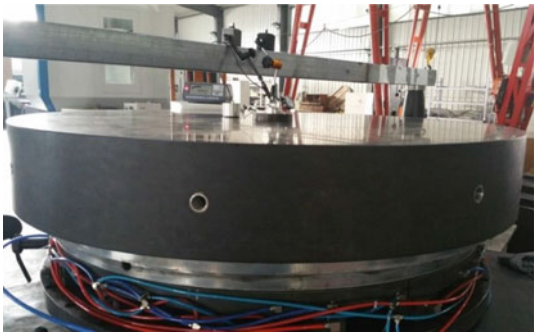

Fig. 8 Polishing spindle after installation

Fig. 9 Polishing spindle connected with machine bed

Supply Air Pressure Conditioning

The air pressure is the critical parameter that affects the performance of aerostatic bearings. Too much pressure will deform the static pressure plate, which will affect the uniformity of the air gap, as well as accuracy and stiffness of the bearing. Otherwise, the clearance of the floating bearing would be too small, some contact will be generated, and the bearings' life and performance would also be reduced. According to the design specifications, the air supply pressure should be 0.5 MPa. As the axial aerostatic bearings were divided into three parts, and their air supply systems are also independent. The test of the air pressure is debugged dependently to make the air bearings work stably. The ideal state is that the rotary table could be rotated easily by hands, and the friction force is quite small.

Drive System Parameters Debug

The polishing spindle is driven by the torque motor. The parameters of the motor drive system would greatly influence the characteristics of the machine start-stop and rotation. As a result, after the mechanical assembly, the drive systems' parameters should be optimized to meet the actual drive requirements of the polishing spindle. The running stability is vital.

The Machining Running Status Test

Based on the finished mechanical assembly and electronic test, the machining process test should be carried out.

1. Start the air supply system, and adjust the air pressure.
2. Rotate the table with hands; the table should be rotated easily. The friction force is very small.
3. Set four points averagely around the table with a diameter of 1600 mm. Put the dial gauge on the set four points, and start/stop the air supply system two times. Check the uniformity of the air gap.
4. Measure the radial and axial runout of the table.
5. Start the torque motor drive, and set the rotary speed with 1 rpm. Check the running stability of the table.
6. Put 100 kg workpiece onto the center of the table, and check the running accuracy and stability.
7. Put 100 kg workpiece 500 mm off the center of the table, and check the running accuracy and stability of the table.
8. Test if the air supply system will break down, and if the polishing spindle will stop immediately.
9. Run the machine continuously for 24 h, and check the stability of the rotary table.

Large Aspheric Mirror Grinding Machine Assembly Case

The module design scheme was adopted for the unit of UAG900, and the unit was assembled and tested independently. After the assembly of the dependent

component, the connection surfaces will be scrapped to adjust the relative position accuracy of part. The assembly quality was determined by the part measurement and fabrication accuracy. Considering the transmitting, manufacturing efficiency, and the cost during the assembly process, the final fine process for the hydrostatic bearings' part is scrapping. In order to finish scraping, the factors are to be considered during the part design stage include the strength, measuring datum, and feasibility.

X Axis Component

The assembly datum of the X axis component is bed basement. Its load bearing surface and side direction surface will be honed by hands. As the side direction slot is very narrow, the perpendicularity cannot be measured with the state of being placed horizontally. The basement should be placed perpendicularly to make the level gauge measurement possible.

The structure of the X axis slide is T type, as shown in Fig. 10, which causes the inconvenience of the large flat manufacturing and test. During the assembly process, if the X slide main body and guideway is integrated, the side oil film is just 0.04–0.05 mm, during the alignment of the side guideways, the X slide carriage would collate the granite base. The X slide carriage is disassembled; the fitting assembly of the load and direction hydrostatic guideway pairs has to be carried out independently, as shown in Fig. 10; and the X slide carriage consists of the slide main body and the guideway bar.

The measurement of the depth H_1 and H_2 is carried out using the comparison method, the standard block sets that are nearest to the measured size are used as the datum, and dial gauge are used for the measurement. The measurement procedure is shown as Fig. 11.

As shown above, assuming that the standard block sets size is H_o, and the dial gauge reading variation is ΔH, the measured size H_1 could be expressed as below.

$$H_1 = H_0 \pm \Delta H$$

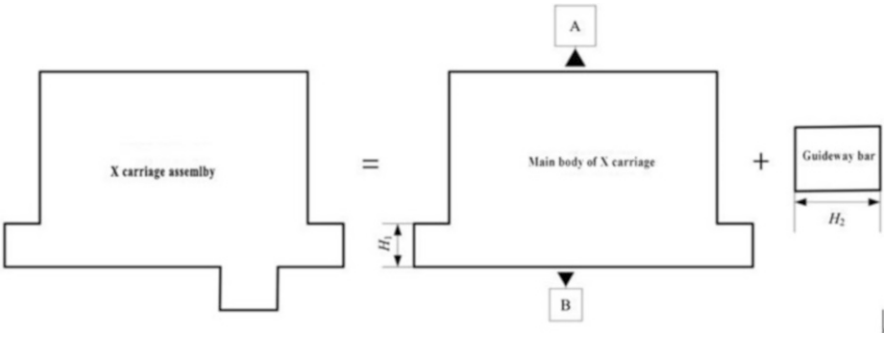

Fig. 10 Illustration of the X axis slide carriage

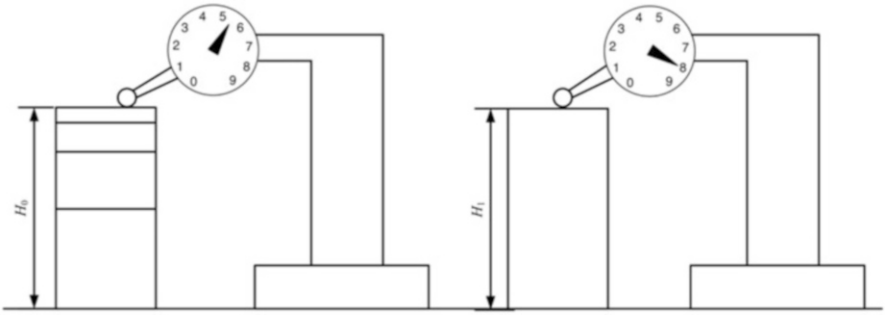

Fig. 11 Illustration of the comparison measurement method

In the above expression, the symbols adopt the plus if the dial gauge rotates clockwise, and the symbols adopt the minus if the dial gauge rotates counterclockwise.

The comparison measurement method is used for the assembly size measurement of the hydrostatic oil film, and the oil film size range is 0.04–0.05 mm. According to the variation by the comparison method, the scraping value could be determined directly. This method could be applied to the bore and shaft size measurement as well.

Y Axis Component

In order to facilitate the manufacturing and assembly, the 45° oblique beam structure is adopted for the Y axis carriage, and the special fixture is prepared as shown in Figs. 12 and 13. The manufacturing datum is the two side surface of the Y axis carriage, and this structure could be used to guarantee the perpendicularity between the Z axis and XY axes. As the Y axis hydrostatic guideways are assembly, the slide carriage and its units are placed on the datum table, the datum A and B surfaces are firstly scrapped, the hydrostatic guideway pairs' size H_1 and H_2 are measured by comparison method with the datum D, and scrapping processes are applied to guarantee the assembly size. The horizontal size H_2 is also measured using the comparison method, as illustrated in Fig. 11.

Z Axis Component

The Z axis is the closed loop box structure. The hydrostatic supports are arranged on the four surfaces of the 300 × 300 mm rectangle (Fig. 14). The U shape frame is selected as the measurement datum for the inside rectangle. The designed structure for the Z axis frame is shown in Fig. 15. Datum A and B are scrapped to the specified accuracy, by using the comparison measurement method, and the size H_1 and H_2 could be measured by taking the surface A and B as the datum. The flatness and parallelism of the inner surface could also be measured by the datum A and B. The size of the Z axis ram could also be measured using the same comparison method as shown below.

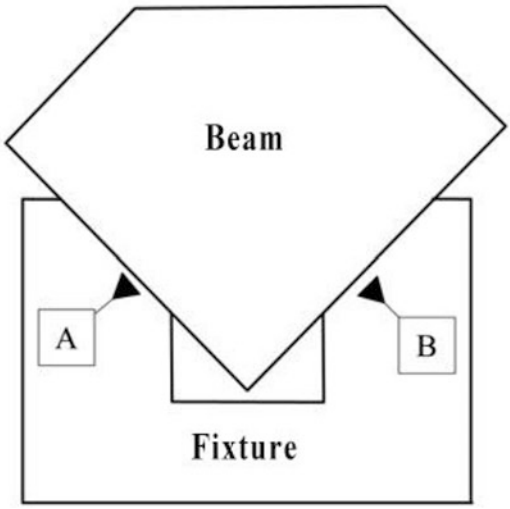

Fig. 12 Illustration of the beam fixture

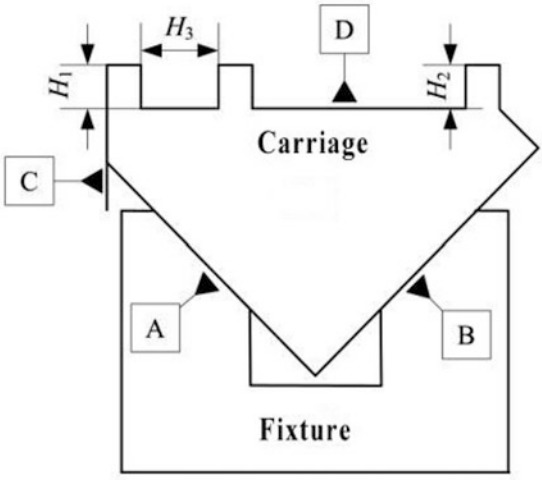

Fig. 13 Measurement of Y axis carriage

Rotary Table Component

The shaft diameter of the rotary table is 300 mm, and its material is 40Cr. The hardness is hardened to be HRC55–56 before fine grinding process using the quenching method. The fine outer cylinder grinding process is used to guarantee the radial size tolerance and cylindricity. The axial static pressure plate size is up to 900 mm. As the hydrostatic oil could lubricate the part, the corrosion problem could be neglected. The nodular cast iron material is selected for the upper and lower static

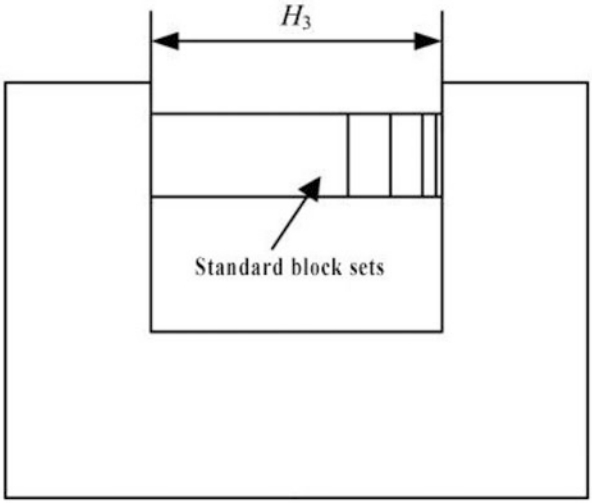

Fig. 14 Illustration of the horizontal standard block measurement method

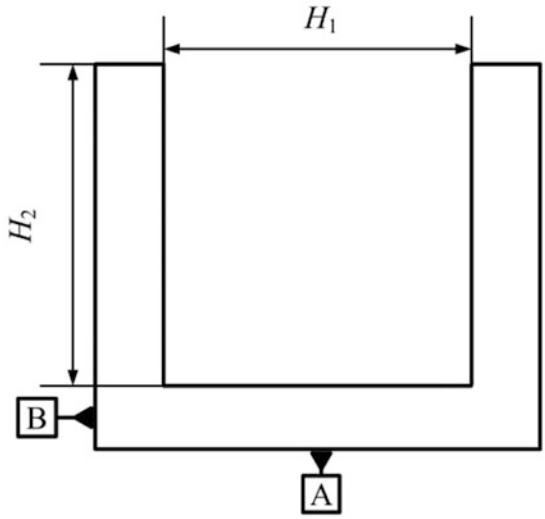

Fig. 15 Illustration of the U type frame datum for Z axis

pressure plate which would also ease the lapping process. The outer diameter of the housing is up to 1000 mm. Considering the cost and its difference with the shaft material, 45# steal is selected as the housing material. Its hardness is up to HRC35 before fine grinding. Fine grinding of the inner bore and end face are finished using vertical grinding machine. The outer diameter of the shaft and the inner bore of the sleeve are measured by the external and internal micrometers, respectively. The comparison datum for the internal micrometer is the outer diameter size of the shaft.

Fig. 16 Illustration of the rotary table component

The axial and radial runout of the rotary table could be measured using the standard sphere combined with the dial gauge. As the table rotates slowly, the inductive dial gauge could measure the axial and radial runout. Before the measurement, the standard sphere should be placed at the center of the table as near as possible (Fig. 16).

UAG900 Whole Machine Debugging

After the independent assembly and debug of the four components, the whole machine installation and gas-electronic test would be carried out, as well as the assistant component test. The main task of the whole machine assembly is to adjust the relative position accuracy between each axis. The gas-electronic assembly will be carried crossly.

During the debugging of the workpiece kinematic coordinate system, the X axis component is firstly assembled, the electronic system should also be installed and debugged, and the contact surface between the X axis and rotary table will be measured to guarantee the parallelism between the X axis and rotary table surface. Although the hydrostatic design provides the supply oil pressure of each pad, the supply oil pressure needs to be adjusted to be adaptive to the working conditioning. Before electronic debugging, the temperature of the cooling fluid for the stator of the linear motor should be adjusted. The hydrostatic station and cool fluid machine should be interlocked with the linear motor, which means that if hydrostatic station and cool fluid machine do not work, the linear motor will not move.

The double linear motors for the X axis share the same driver; however, they will be arranged with 12 mm distance in the X direction. The phase of the two motors should be adjusted during the debug process. After the dependent debug of the X axis, the debug of rotary table will start. The outside additional assistant component consists of the torque motor cooling system, pressure oil supply system, and oil active return system, all of which should interlock with the torque motor. After the assembly of the rotary table component, the oil pressure should be adjusted for the X axis hydrostatic bearings. After the assembly and debug of the X axis and rotary table, the reciprocating velocity of X axis and rotary speed of the rotary table were set to be 3 m/min and 60 r/min, the servo drive system parameters will be optimized

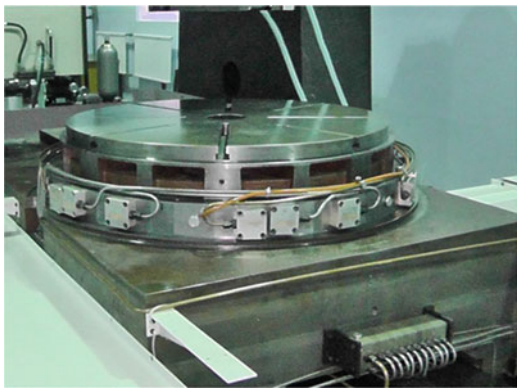

Fig. 17 Picture of the X axis and rotary table after assembly

to be the best status. The picture of X axis and rotary table after assembly and debug is shown in Fig. 17.

The same T type double linear motors drive system are adopted for Y axis component, the assistant unit hydraulic station and cooling system also interlocks with the drive motor, and the relative position between the primary coil and second magnetic plate should be adjusted several times to obtain the best drive parameters. After the debug of Z axis, the perpendicularity between X axis and Z axis should be adjusted. Taking the top surface of rotary table as the datum, the perpendicularity of the Z axis will be adjusted by scrapping one side of the assembly surface in front of the Y axis slide carriage. Using the standard squarebox as the datum, the squarebox is moved and aligned along the X axis, the adjustment method is to use the screw to make the beam rotate slightly around Z axis.

As the Z axis component is assembled on the front surface of the Z axis slide carriage, the static counterbalance weight is installed at the back of the beam, and oil supply pressure needs to be adjusted again according to the load variation. Using the squarebox as the datum to test the perpendicularity between the Z and X axes. As the perpendicularity was measured, scrapping and fastening method will be used to adjust the gesture of Z axis. The additional component of Z axis consists of the hydraulic station and oil active return system. They should interlock with each other. The linear velocity of the Y and Z axes are set to be 3 m/min, and their parameters would be optimized. The picture of the Y and Z axes is illustrated in Fig. 18, as well as the grinding wheel spindle.

The volume positional error of the grinding wheel spindle is measured using the standard bar as the datum, and the standard bar is adjusted to be concentric with the spindle. The Y axis will be moved to test the parallelism, and the grinding wheel spindle assembly will be adjusted thereafter. Perpendicularity between the length gauge and rotary table top surface will be measured using its side face as the datum. The Z axis will be moved to align the adjustment.

Other additional assistant components of UAG900 are listed: the grinding wheel dressing station, protect component, cooling fluid supply unit, hydraulic oil

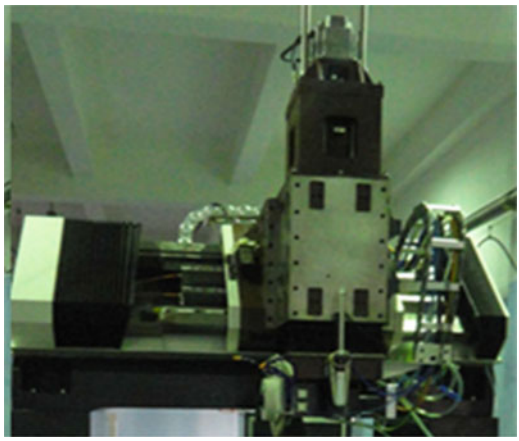

Fig. 18 Assembly picture of the Y and Z axes

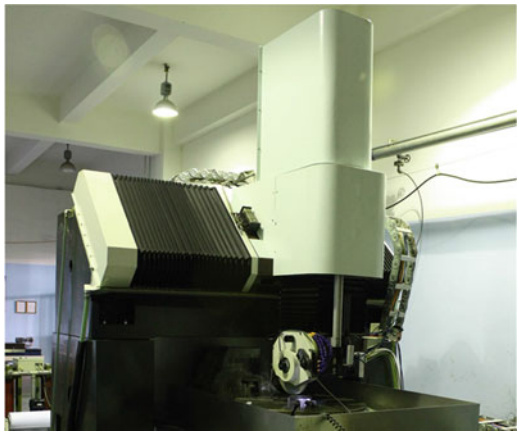

Fig. 19 Picture of the UAG900 whole machine

temperature control unit, grinding fluid filtering system, spindle gas sealing unit, etc. The whole machine after assembly was shown below (Fig. 19).

Conclusion

This chapter gives a fundamental description of the precision machine assembly process. The actual assembly process is complicated. The real assembly process is the best teacher rather than the book. However, the assembly process and examples listed in the book would benefit readers slightly. The part measurement is firstly described as the part quality that is critical for the whole machine assembly, and if the part quality is not valid, the assembly process is infeasible, and the specified accuracy and capability could not be achieved. Finally, the large aerostatic rotary

table and large aspheric grinding machine assembly processes are given and described.

References

Abele E, Altintas Y, Brecher C (2010) Machine tool spindle units. CIRP Ann Manuf Technol 59:781–802

Brian Rowe W (2012) Hydrostatic, aerostatic, and hybrid bearing design, 1st edn. Butterworth-Heinemann Press, Oxford

Fan Z (2014) Study on polishing spindle of ultra-precision fast polishing machine for large plane optics. Xi'an Jiaotong University, Xi'an

Leadbeater PB, Clarke M, Wills-Moren WJ, Wilson TJ (1989) A unique machine for grinding large, off-axis optical components: the OAGM 2500. J Precis Eng 11:191–196

Li B (2015) Study on the ultra-precision CNC grinding technology for large aperture aspheric mirrors. Xi'an Jiaotong University, Xi'an

Marsh ER (2007) Precision spindle metrology, 1st edn. DEStech Publications, Lancaster

Morris AS, Langari R (2012) Measurement and instrumentation: theory and application, 1st edn. Academic, Waltham

Muralikrishnan B, Raja J (2009) Computational surface and roundness metrology, 1st edn. Springer-Verlag London, London

Tu JF, Corless M, Gehrich MJ, Shih AJ (1998) Experimental study of a precision, hydrodynamic wheel spindle for submicron cylindrical grinding. J Precis Eng 22(1):43–57

Whitehouse DJ (1994) Handbook of surface and nanometrology, 1st edn. Institute of Physics Publishing, Bristol/Philadelphia

Electric-Magnetic-Mechanical Coupling in Precision Machines

14

Dongxu Ren

Contents

Introduction 376
Influence of Electrical Parameters on Precision Machine 378
Influence of Magnetic Parameters on Precision Machine 379
Impact of Mechanical Parameters on Precision Machines 381
Influence of Static Force Parameters on Precision Machine 381
Influence of Dynamic Force Parameters on Precision Machine 385
Influence of Vibration Parameters Toward Precision Machine 386
Influence of Electro-Magnetic-Mechanical Coupling on Precision Machine 389
Magnetic-Machine Coupling 389
Electric-Mechanical Coupling 391
Electro-Magnetic-Mechanical Coupling 394
Conclusion 397
References 397

Abstract

In this chapter, the electric-magnetic-mechanical coupling methods and related research progress of precision machine tools are discussed. The electromagnetic machine complex of guideway and spindle and the influence of electromagnetic machine parameters on precision machining equipment are discussed respectively based on the key functional parts of precision machine tools. Then, the electromagnetic coupling, motor coupling, and magnetic machine coupling are analyzed respectively to study the coupling of three technical directions, and the method involves the finite element analysis method and electromagnetic machine test method of electromagnetic machine. Based on a specific machining process example, this chapter discusses the theoretical analysis of the influence of three parameters of electromagnetic machine on precision machining machine tools. Finally, the summary analysis of this chapter needs to study the systematic

D. Ren (✉)
Zhongyuan University of Technology, Zhengzhou, China
e-mail: rendongxu313@zut.edu.cn

Z. Jiang, S. Yang (eds.), *Precision Machines*, Precision Manufacturing,
https://doi.org/10.1007/978-981-13-0381-4_31

theoretical system of the coupling of three directions of electromagnetic machine on the accuracy and reliability of machine tools, so as to promote the development of precision or ultra-precision machining equipment and supply machining process basic theory.

Keywords

Electric-Magnetic-Mechanical coupling · Precision machines · Machine accuracy and reliability · Motors and sensors

Introduction

With the development of modern design methods of precision machine tools and their key functional components, the demand for precision and precision reliability of precision machine tools has gradually increased. The difficulty of industrial design and the quality of customer requirements are further increased. Knowledge of the electro-magnetic-mechanical coupling has to be considered. The three main bodies of precision machine tools include precision linear motion, precision rotary motion, and precision reference. All three research directions involve electric-magnetic coupling and electric-mechanical coupling, electric-magnetic-mechanical coupling. Similarly, each kind of coupling is reflected on the key functional components of precision machine tools. In the end, it is necessary to carry out analysis of key functional components of precision machine tools and their complete machines in conjunction with electromagnetic machine coupling to assess the accuracy and reliability of precision machine.

That is, (1) in addition to the non-rotating electric field generated by the static charge, the changing magnetic field also generates the vortex electric field; (2) the changing electric field generates the vortex electric field just like the conducting current. That is to say, the changing electric field and magnetic field are not isolated from each other. They are related to each other and excited to form a unified electromagnetic field.

Precision machine is a complex electric-magnetic-mechanical coupling product which is coupled with mechanical structure, servo system, and cutting process (Qiang and Wu 2014). Coupling multi-rigid body simulation, coupling finite element simulation, coupling flexible multi-body system simulation, rigid flexible coupling characteristics, linear coupling physical characteristics, spatial target pose coupling, multi-physical field coupling characteristics, complex structure configuration model coupling, structure tool system machining process coupling modeling, and other technologies are used to realize the optimization analysis and design of machine tools, so as to improve the static processing and dynamic performance of precision machine.

This chapter uses a precision machine tool as an example to describe the electromagnetic field theory, as shown in Fig. 1, and explains the impact on the accuracy of the precision machine from three aspects of electricity, magnetism, and

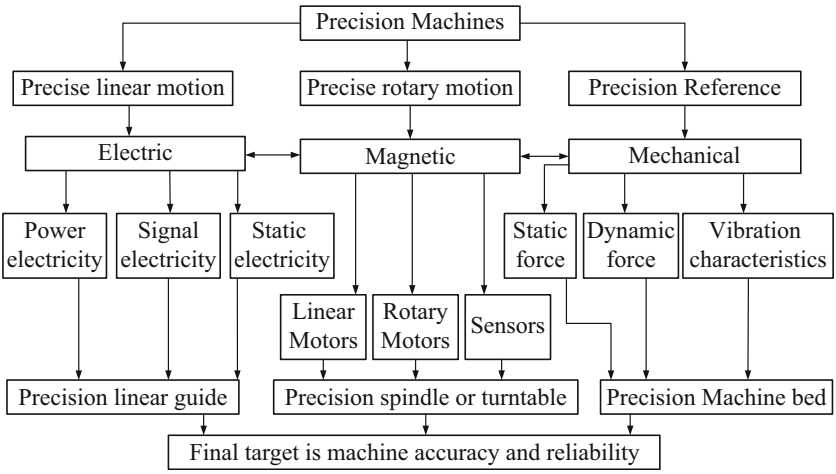

Fig. 1 Contents and goals of electro-magnetic-mechanical coupling in precision machine tools

machine, including power supply system, signal transmission, and electrostatic interference applications. The system includes linear motor, rotary motor and lead screw, linear guide system, and linear magnetic or optical linear displacement sensor. The rotation system includes a rotating motor, precision bearings, and angular displacement sensors. The mechanical system includes the mechanical characteristics of precision machines such as static force, dynamic force, and vibration characteristics. It is necessary to discuss the definition of coupling, the method of coupling, and the impact on typical coupling components of precision machines based on the above three factors of electromagnetic-mechanical coupling. The top-down and bottom-up analysis methods are used, combined with multi-element coupling and recombination methods to analyze the influence of electric-magnetic-mechanical coupling on accuracy of precision machines.

Macroscopically speaking, coupling is the result of the superposition of multiple factors to be solved and the interaction of various elements and the joint action of stroke; as for the electric magnetic mechanical coupling in precision machines studied in this chapter, it can be simply called multi-field coupling, such as the superposition of electric field, magnetic field, and spatial field of mechanical structure. Of course, it can also be explained by simple weighted average value. The ultimate goal is the machining accuracy and accuracy reliability of precision machine tools. There are many details involved here, such as the mechanical structure under the static and dynamic classification, which can be affected by driving force, static force characteristics, static force characteristics, static positioning accuracy, repeated accuracy, dynamic positioning accuracy, and other indicators. Then, it is necessary to optimize the mechanical structure design according to the indicators, such as the impact of indicators such as environmental requirements, space requirements, working condition requirements, working foundation requirements, and working condition monitoring. In addition to the electromagnetic effects

described in this chapter, physical fields such as temperature, gravity, humidity, and pressure fields must be considered. It can be seen that it is more helpful to understand such complex parameters by using the weighted average to explain the impact of each parameter on precision machine tools and processing technology.

In the expression of a precise linear or rotary motor, energy coupling is used to represent a better understanding of electromagnetic-mechanical coupling, such as the influence of three parameters of motor power control, electric energy, magnetic energy, and electromagnetic absorption force on the positioning accuracy of precision machine tools, which is also more feasible to help scholars to understand. In combination with precision machine tools, precision bearing characteristics, such as bearing accuracy, rotation speed, positioning accuracy, etc., must be taken into account. It is also the product of the combination of energy coupling and mechanical structure dynamic characteristics, from a macro perspective. In other words, such expression is also conducive to better understanding of scholars.

However, in the actual design and optimization of unit components and the whole equipment, the coupling data of electric-magnetic-mechanical is more realistic. For example, the finite element simulation design and optimization techniques are commonly used in modern design methods, which require specific data onto the three elements of electric-magnetic-mechanical coupling or similar data that can be analyzed for true values or parameters after simulation coupling. Therefore, the tests paved the way for subsequent testing and verification. The test and verification data are decoupled reversely, and the numerical values of the three elements of electric-magnetic-mechanical are calculated reversely, so as to optimize the finite element mathematical model. The idea of iteration is applied to continue the three element coupling finite element simulation and analysis, and the optimization algorithm is applied repeatedly to realize the coupling of precision machine tools and the rationality of processing technology joint research work.

Influence of Electrical Parameters on Precision Machine

The basic concept of Maxwell's electromagnetic field theory includes two main contents. That is, (1) in addition to the non-rotating electric field generated by the static charge, the changing magnetic field also generates the vortex electric field; (2) the changing electric field generates the vortex electric field just like the conducting current. That is to say, the changing electric field and magnetic field are not isolated from each other. They are related to each other and excited to form a unified electromagnetic field.

Most machine tool applications operate on industrial computer numerical controllers (CNC). These kinds of controllers are settled for three cascaded closed loops: current, speed, and position loop, from the internal to the external loop, respectively. Ghislain REMY (Remy et al. 2006) proposed to design resonant controllers of the current control loop by using the inversion principle of the Causal Ordering Graph (COG) representation of a PMLSM model. Ingo Schaarschmidt (Schaarschmidt et al. 2019) studied implementation of the machine tool-specific current and voltage

control characteristics in multi-physics simulation of electrochemical precision machining.

Electrical parameters include the power supply, signal, and control power of precision machinery; electrical parameters include power supply stability, control system stability, trigger pulse stability, anti-interference ability, pulse trigger reliability, electromagnetic interference impact on control system, etc. The stability of the power supply includes the nonlinear oscillation of the power supply and the sustainability of the power supply. Aiming at the stability of the power supply, the research on the multi-electromechanical system stabilizer using chaos optimization algorithm.

The parameters such as the bandwidth and power limitation of the sensors such as the encoder and the signal-to-noise ratio of the encoder are the basis of the undistorted and reliable signal transmission of the sensors used in the precision machine tool, the main guarantee for the precision machine tool to improve the mechanical parameter information acquisition and control, as well as one of the ways to accurately establish the electromechanical coupling and improve the precision and reliability of the precision machine (Huo et al. 2010).

Influence of Magnetic Parameters on Precision Machine

Magnetic field coupling refers to the phenomenon that the coil current changes and an induced electromotive force is generated in adjacent coils. The most helpful example to understand magnetic field coupling is transformer. The working principle of transformer is to realize energy transfer through magnetic field coupling between two coils.

The related magnetic parameters of precision machine tools mainly exist on two functional parts: linear motor driven by linear guide rail and spindle motor driven by rotating shaft. The displacement sensor on the precision machine tool also realizes the precise displacement measurement based on the magnetic moire fringe magnetic coupling effect. The sensor is composed of the excitation coil and the induction coil. In order to improve the displacement accuracy, the structure of the sensor is further optimized based on the measurement error that can be traced back to the source, so as to realize the error compensation and parameter identification of the magnetic grating displacement sensor (Zhong et al. 2019).

The harm in magnetic field coupling to precision machining is magnetic field coupling with electromagnetic interference. The frequency control system is anti-electromagnetic interference, and the electric drive has electromagnetic interference, which affects the ultra-precision machining.

Magnetic assisted ultra-precision machining, such as magnetic grinding, magnetorheological polishing, magnetic assisted electrochemical machining, magnetic particle jet machining, and magnetic floating body polishing, is another application of the magnetic coupling principle. For example, magnetic assisted EDM can help improve the machining stability and can realize the relevant EDM

process with high-efficiency and high-quality machining surface to meet the needs of ultra-precision machining (Lin and Lee 2008).

The dynamic analysis of the motor with mechanical and electrical interaction is carried out. As shown in Figs. 2 and 3, the dynamic behavior of BLDC motor when considering the air gap changed caused by the translation movement of rotor relative to the stator, kinetic energy, and potential energy. Rayleigh dissipation function and magnetic energy are expressed by rotor displacement and stator current. Hyungbin Im (Im et al. 2011) uses Lagrange's equation to derive a governing equation that is completely coupled between mechanical displacement and current and analyzes the mechanical and electromagnetic interactions of the motor due to changes in the air gap between the stator and rotor.

The motor thrust force has lots of harmonic components due to the nonlinearity of drive circuit and motor itself in the linear motor feed drive system. What is more,

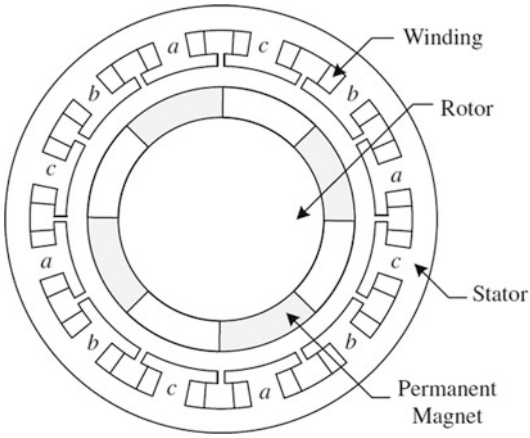

Fig. 2 The mechanical structure three-phase BLDC motor (Im et al. 2011)

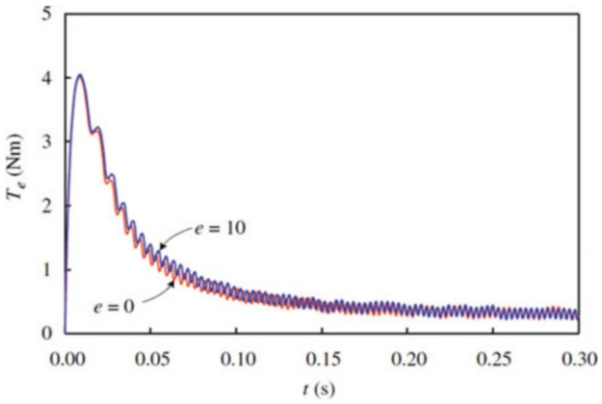

Fig. 3 Time responses of the electromagnetic torque when e = 0 and 10 mm (Im et al. 2011)

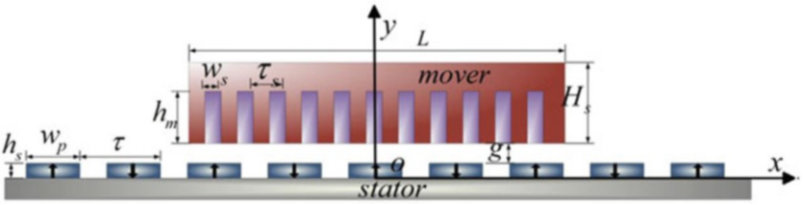

Fig. 4 The 2-D analytical model of the air-gap magnetic field (Yang et al. 2017)

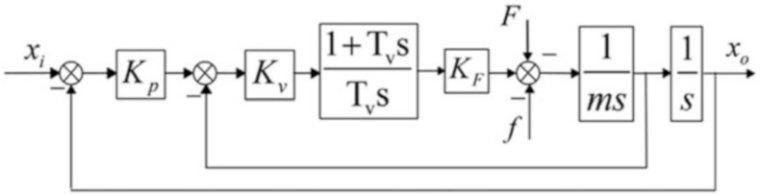

Fig. 5 Control model of linear motor feed drive system (Yang et al. 2017)

these thrust force harmonics may vary from the position, velocity, acceleration, and load in the motion process, which affects the displacement fluctuation of the feed drive system for precision machines (Yang et al. 2017). In order to analyze the influence of the change of thrust spectrum on the displacement fluctuation of the feed drive system, a control model of the linear motor feed drive system was established, as shown in Figs. 4 and 5.

The mutual inductance of the primary and secondary windings of the transformer will change according to the relative position relative to the core. The relative movement between the inductive sensor (encoder head) and the measurement scales in the measurement direction will periodically change the mutual inductance of each coil and generate two sinusoidal 90° phase-shift signals (sin and COS). In contrast to the magnetic system, the hysteresis of the material is completely suppressed. The deviation between the error and the ideal sine wave shape (harmonic content) is only 0.1%. As shown in Fig. 6, this allows high interpolation (subdivision level) in digital signals in the measurement encoder or subsequent electronic devices (CNC, etc.) (AMOSIN® – Measuring Principle 2019).

Impact of Mechanical Parameters on Precision Machines

Influence of Static Force Parameters on Precision Machine

The influence of static force parameters on precision machine tools mainly evaluates the machine tool's static accuracy, which refers to the accuracy of the machine tool's geometric accuracy, motion accuracy, transmission accuracy, positioning accuracy, and other detection under no-load conditions.

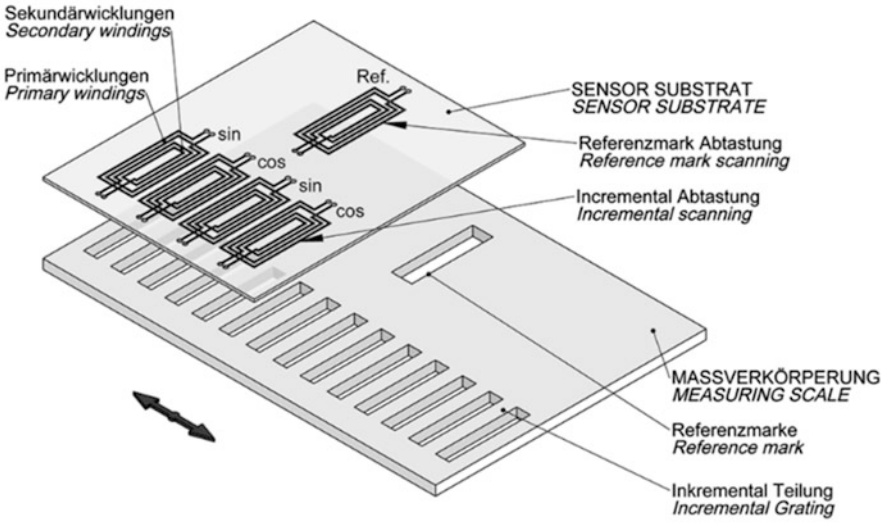

Fig. 6 Measuring Principle of mutual inductance for linear encoder (AMOSIN® – Measuring Principle 2019)

Through the research on the process chain of high-precision components with micron level characteristics, three workpiece classifications and micro production process chain (MPPC) model are defined. Finally, according to the condition of precision machine tool and environment, the guide of machining high precision parts with micro-scale feature in process chain is given (Uhlmann et al. 2016).

Geometric Accuracy

The geometric accuracy of the machine tool refers to the geometric accuracy of the working surface of some basic parts of the machine tool. It refers to the accuracy of the machine tool, when it is not moving (such as the spindle is not rotating and the table is not moving) or the speed of movement is low. It specifies the relative position tolerance between the main parts and components that determine the machining accuracy and between the motion tracks of these parts and components. For example, the flatness of the bed rail, the flatness of the work surface, the rotation accuracy of the spindle, the direction of movement of the tool slider, and the parallelism of the axis of the spindle must be considered. The shape of the surface of the workpiece processed on the machine tool is determined by the relative motion trajectory between the tool and the workpiece, and the tool and the workpiece are directly driven by the implement of the machine tool, so the geometric accuracy of the machine tool is the most basic condition to ensure the machining accuracy.

Aerostatic spindles are widely applied in precision and ultra-precision machine tools because of advantages such as lower heat generation, lower wear and friction, lower noise levels, less contamination, and higher precision. Chen (Chen et al. 2015) studies a novel dynamic modeling method for aerostatic spindle based on pressure

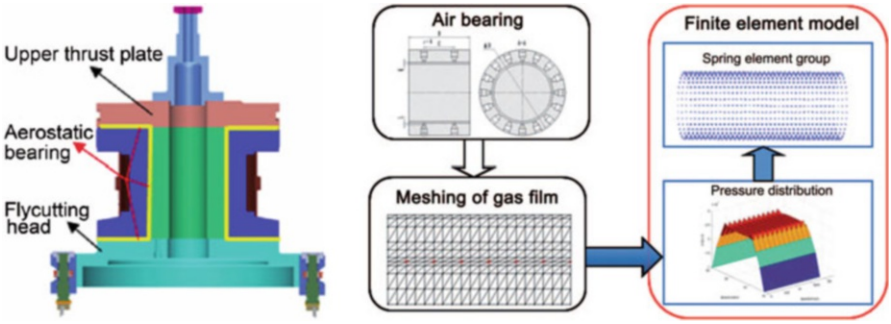

Fig. 7 Structure and outline of the dynamic modeling approach of the aerostatic spindle (Chen et al. 2015)

distribution as shown in Fig. 7, which is more efficient and reliable than traditional modeling methods for the precision machines.

Air bearing spindle is used in the ultra-precision drum lathe, which requires high movement accuracy and thermal stability. In order to improve the bearing capacity and stiffness of air bearing spindle, an air bearing spindle with high bearing capacity is proposed. Wu (Wu et al. 2015) uses FLUENT software, a three-dimensional simulation model of aerostatic spindle with orifice and feed chamber is established, and its load characteristics are analyzed. When the eccentricity is in the range of 0.2–0.3 and the air supply pressure is 0.6 MPa, the bearing capacity and stiffness are 9499.4 n and 2813.1 n/μm, respectively. Through a set of loading experiments, the feasibility and accuracy of the three-dimensional simulation method for calculating the loading characteristics of hydrostatic spindle is proved.

Aerostatic guideways are often used in machines requiring very high motion accuracy such as precision machines. T.Onat Ekinci (Ekinci et al. 2009) investigates the relationship between the motion errors of the axis' carriage and the guideways' geometric errors both mathematically and experimentally. As shown in Fig. 8, the analytical model uses bearings location and stiffness, guideway geometry, and static equilibrium to produce a model in matrix form. Validation experiments are conducted on a machine axis moving on aerostatic guideways with and without preload.

To diagnose the unbalance of aerostatic guideways, Chen (Chen et al. 2014) uses displacement and acceleration sensors to measure the vibration signals of the unbalance of the aerostatic guideways caused by the gas fluctuation, and the frequency characteristics for the unbalance of aerostatic guideways have been extracted from the measured signals by power spectral density.

Static Transmission Accuracy and Positioning Accuracy

The transmission accuracy of a machine tool refers to the relative movement accuracy between the two end pieces of the transmission chain in the machine tool. This error is called the transmission error of the transmission chain. For example, when turning a thread on a lathe, each time the spindle rotates, the

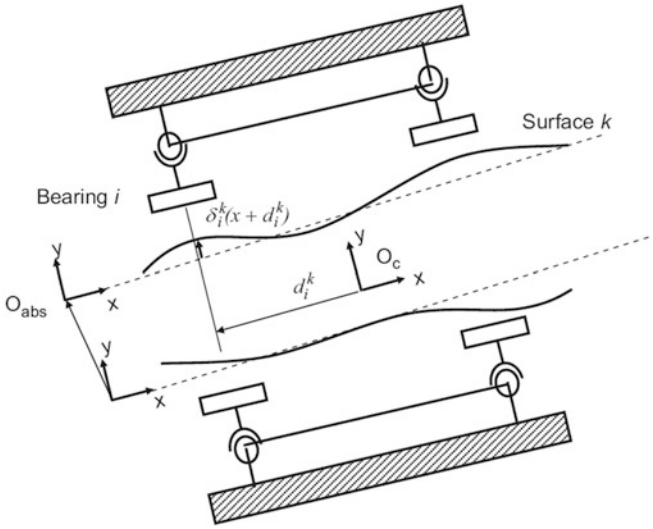

Fig. 8 Definition of air bearing location and guideways' geometric errors (Ekinci et al. 2009)

movement of the tool post should be equal to the lead of the thread. However, in fact, due to errors in gears, screws, and bearings in the transmission chain between the main shaft and the tool post, there is an error between the actual travel distance of the tool post and the required travel distance. This error will directly cause the workpiece pitches error. In order to ensure the machining accuracy of the workpiece, not only the necessary geometric accuracy of the machine tool is required, but also the higher transmission accuracy of the internal transmission chain is required.

The positioning accuracy of the machine tool refers to the accuracy of the actual position of the main parts of the machine tool at the end of the movement. The error between the actual position and the expected position is called a positioning error. For machine tools that determine the positioning of moving parts mainly by trial cutting and measuring the size of the workpiece, for example, ordinary machine tools such as horizontal lathes and universal lifting table milling machines do not require high positioning accuracy. However, for machine tools that rely on measuring devices, positioning devices of machine tools, and automatic control systems to determine the positioning position of moving parts, such as various automated machine tools, CNC machine tools, coordinate measuring machines, etc., they all have high requirements for positioning accuracy. The geometric accuracy, transmission accuracy, and positioning accuracy of a machine tool are usually measured without cutting loads and when the machine tool is not moving or the speed of the movement is low, so it is generally called the machine tool's static accuracy. The static accuracy is mainly determined by the manufacturing accuracy of the main parts and components on the machine tool, such as the main shaft and its bearings, screw nuts, gears, and bed, and their assembly accuracy.

Grating linear displacement sensor is the first choice for positioning the moving parts of mechanical equipment. It has high precision, high resolution, and relatively low price. Combined with the closed structure, it is used for dustproof and liquid proof, which makes it not only widely used in the field of machining and manufacturing but also can be used in the mark setting measuring machine, robot, positioning device, and every application requiring position and speed motion control. The positioning accuracy of micron and submicron has been widely used in general machining detection and precision machining detection in the field of precision ultra-precision machining (Fujimori et al. 2012). And the ultra-precision machining of positioning below submicron is used in the field of modern national defense, military, astronomy, and aerospace.

With the improvement of precision mechanical positioning accuracy, the resolution of grating linear displacement sensor is mainly used in the precision machining of atomic and molecular level below 1 nm (Tamiya et al. 2018; Lu et al. 2016). The commercial displacement sensor products such as Sony Magnescale company in Japan and Heidenhain company in Germany reach the picometer resolution grating, and its measurement benchmark includes a grating ruler of solid substrate, which is less affected by environmental fluctuations, and can provide the high-resolution stability. In order to reduce the accuracy drift caused by temperature factors, the ruler blank can be made by materials with small thermal expansion coefficient. It is mainly used in the precision machining fields such as semiconductor testing equipment, LCD photolithography equipment, high-precision lathe, EDM equipment, etc. Similarly, the ultra-precision lathe and aspheric machining machine developed by Moore company of the United States all adopt the grating interference position with picometer resolution, and the surface accuracy of the typical parts processed by the sensor is less than 0.1 μm. On the basis of precise displacement sensor, precise guide rail such as aerostatic guide rail and hydrostatic guide rail is also needed to realize precise machining.

Influence of Dynamic Force Parameters on Precision Machine

Static accuracy can only reflect the machining accuracy of the machine tool to a certain extent, for a series of factors will affect the machining accuracy in the actual working state of the machine tool. For example, machine parts and components will elastically deform due to cutting and clamping forces. In the machine tool, heat sources (such as heat from electric motors, hydraulic transmissions, friction and heat from bearings, gears, etc.) and environmental temperature changes under the influence of the machine tool, parts, and components will be thermally deformed. When the moving parts of the machine tool move at the working speed, the movement accuracy is improved due to the influence of the oil film between the relative sliding surfaces and other factors.

It is also different from the accuracy measured at low speed. All of these will cause the static accuracy of the machine tool to change, affecting the machining

accuracy of the workpiece. The accuracy of the machine tool under the working conditions of external load, temperature rise, and vibration is called the dynamic accuracy of the machine tool. In addition to the close relationship between dynamic accuracy and static accuracy, it is also largely determined by the stiffness, vibration resistance, and thermal stability of the machine tool. At present, in general, the comprehensive dynamic accuracy of a machine tool is evaluated by the accuracy of the workpiece processed by cutting, which is called the working accuracy of the machine tool. Working accuracy is a comprehensive reflection of the influence of various factors on machining accuracy.

Through the compensation function of the compensator to the feed system of the precision machine tool, the system error can be reduced, and the machining accuracy can be improved. Some structural parameters of the precision machine tool are often used to simulate and analyze the model with Matlab/Simulink, and the dynamic force parameters of the precision machine tool can be improved through the feed compensation.

To improve the spindle motion error of magnetic bearings in diamond turning, the methods can be determined, which include adjusting dynamic balance, reducing the harmonic effect of the working face, and improving the electronic error compensation. The optimization of the spindle motion error improves the dynamic characteristics of precision machine tools, which can significantly improve the turning flatness and surface roughness of ductile materials (Khanfir et al. 2005a).

Influence of Vibration Parameters Toward Precision Machine

Internal Vibration of the Machine

The relative vibration between tool and workpiece will significantly affect the performance of precision machine. Kim (Kim et al. 2014) developed a model to predict the vibration transfer from two main excitation sources (ground vibration and fluid carrying capacity) toward tool and workpiece relative positions through the mechanical and control systems of precision machinery as shown in Figs. 9 and 10. The frequency response function obtained from the finite element analysis of a machine is used to create a matrix of transmissibility defining the dynamic behavior of an electromechanical system. The validity of the developed model can be verified by comparing the measured relative vibration with the results calculated from the measured excitation.

For the coupling system of ultra-precision machining, ultra-precision machining requires high surface quality of optical elements, and its spindle must be well balanced. A coupling system of main shaft and frame based on flexible connection is proposed, which provides high rigidity through operation state, while the setting state allows the main shaft to vibrate along a degree of freedom, enhancing the vibration caused by imbalance (Foremny et al. 2016; Brandenburg et al. 2000).

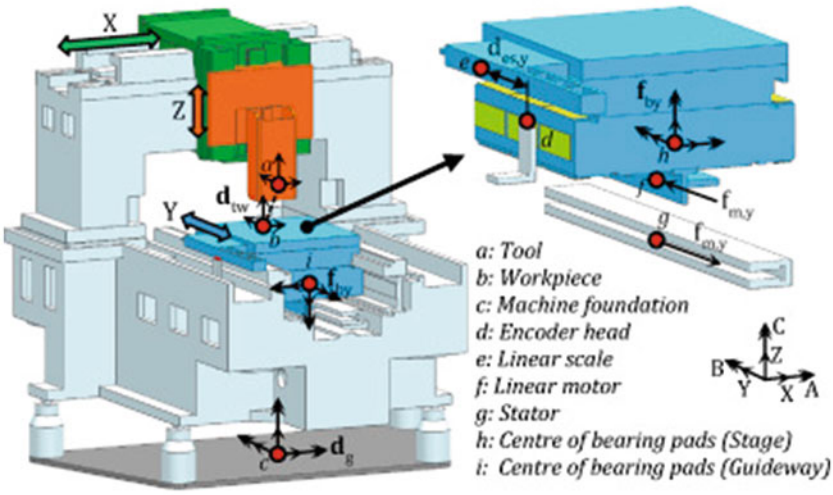

Fig. 9 Test precision machine and primary vibration sources (Kim et al. 2014)

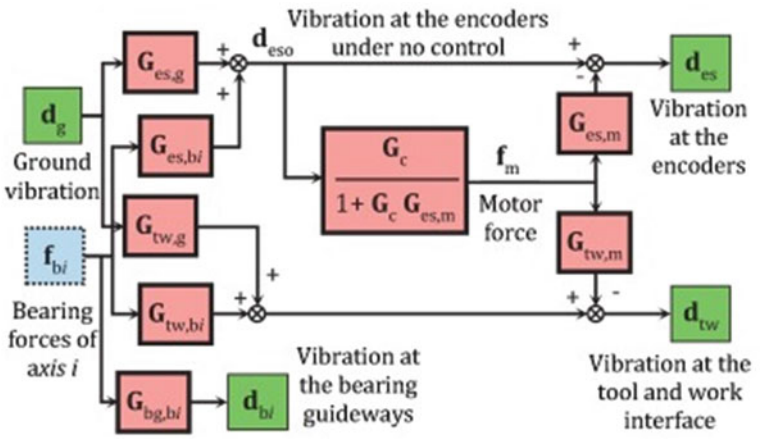

Fig. 10 Generalized diagram of the vibration transmission model (Kim et al. 2014)

External Vibration of the Machine

Due to the complex and dynamic working conditions of precision machine tools, fuzzy PID control is generally used to compromise the vibration disturbance of machine tools.

Ultra-precision manufacturing (UPM) machines are used to manufacture and measure complex parts with micron level features and nanometer level tolerance/surface finish. Vibration isolation system must be used to reduce the random vibration of the machine away from ground excitation and airborne interference. In the design of vibration isolation system, the vibration of UPM machine must be reduced; otherwise

the strict precision requirements of the machine cannot be met. UPM machines may vibrate due to external excitation (mainly from the ground (DeBra 1992; Rivin 1995, 2006; Kim et al. 2014)), or their vibration may be caused by airborne interference, for example, inertia response caused by moving machine components (Subrahmanyan and Trumper 2000; Jones and Ulsoy 1999). Based on the restrictive assumption of modal damping for isolated motors, Jihyun Lee (Lee and Okwudire 2016) studies the effect of mode coupling on the residual vibration of UPM machines with non-proportional (NP) damping, which is more realistic than modal damping as shown in Figs. 11 and 12. It is shown that although NP damping changes the vibration characteristics of the

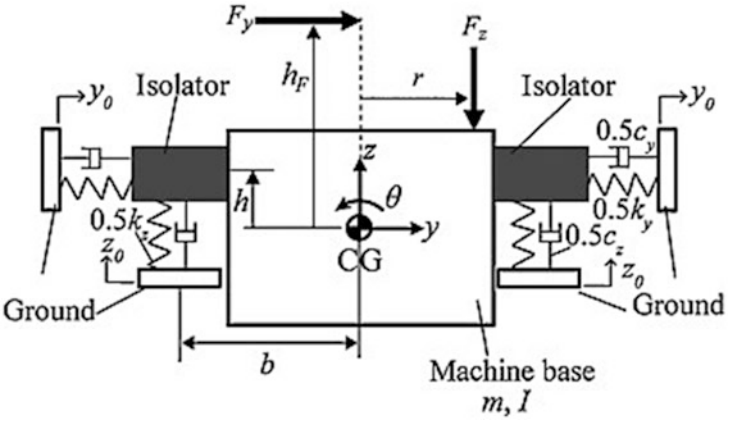

Fig. 11 Planar model of an isolated machine (Lee and Okwudire 2016)

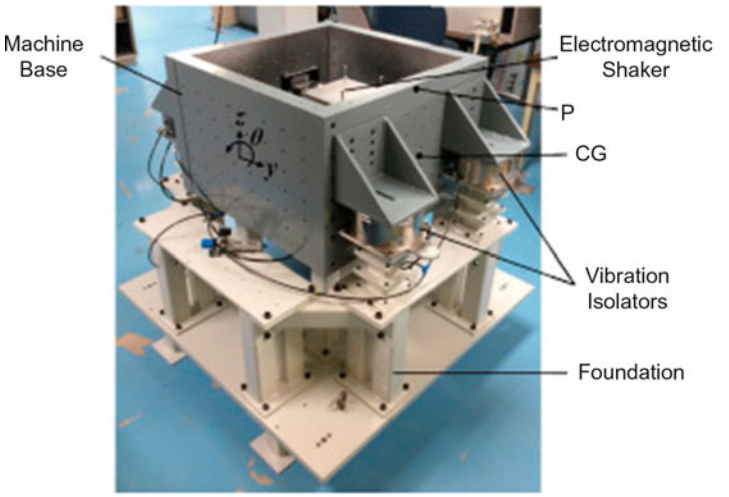

Fig. 12 Reconfigurable UPM machine base prototype used for simulations and experiments (Lee and Okwudire 2016)

machine compared with modal damping, modal coupling still provides sufficient opportunity to reduce residual vibration and transmissibility. It is verified that the residual vibration could be reduced by 40% and the transmissivity is reduced by 50%.

Influence of Electro-Magnetic-Mechanical Coupling on Precision Machine

The essence of coupling is that multiple factors interact with each other. Electrical-magnetic-mechanical coupling consists of the electrical, magnetic, mechanical, and other factors which affect each other. For example, the changing electric field will generate a magnetic field, and the changing magnetic field will turn into an electric field. The magnetic field and the electric field complement each other, and the mutual influence is electromagnetic coupling.

In precision machining, the optimization design of electromagnetic coupling driven by linear motor, using analysis model and finite element simulation, optimization design guide structure, and magnet configuration have been applied to the high precision cutting (Denkena et al. 2016). The design and manufacture of high-precision aerostatic guideway made of glass material (Lai et al. 2019), metal material (Chen et al. 2018a), marble material (Yao et al. 2016) can achieve the guideway precision with linearity better than 0.1 μ m through the coupling of linear motor and different types of guideways. In addition to the guide rail material, the guide rail media affects the linear accuracy and rigidity, such as gas (Chen et al. 2017), liquid (Liu et al. 2019), and other factors, among which the aerostatic guide rail has high accuracy and rigidity and the relative aerostatic guide rail has low accuracy and high rigidity. In the precision machining equipment and process design, the machining object and material removal rate are the main parameters to be considered, as well as the electromagnetic characteristics of the motor itself (Gannel 2019).

Coupling methods include multi-field coupling, energy coupling, data coupling, tag coupling, control coupling, external coupling, public coupling, and content coupling.

Magnetic-Machine Coupling

Magnetic-Machine Coupling of the Giant Magnetostrictive Actuator

A giant magnetostrictive actuator presents advantages such as large strain, high precision, and quick response, which can be used in the precision machines. Zhen Yu (Yu et al. 2018) studies on the magnetic-machine coupling characteristics of giant magnetostrictive actuator based on the free energy hysteresis characteristics; the nonlinear magnetic-mechanical coupling model under the weak form solution is deduced from the basic electromagnetic and mechanical theories. Based on the distribution law, the axial magnetic field simulation is carried out to analyze the output displacement characteristics of the giant magnetostrictive actuator under preload in Fig. 13.

In order to further improve the control accuracy of precision machine tools, the inherent relationship between the output and input of the actuator must be

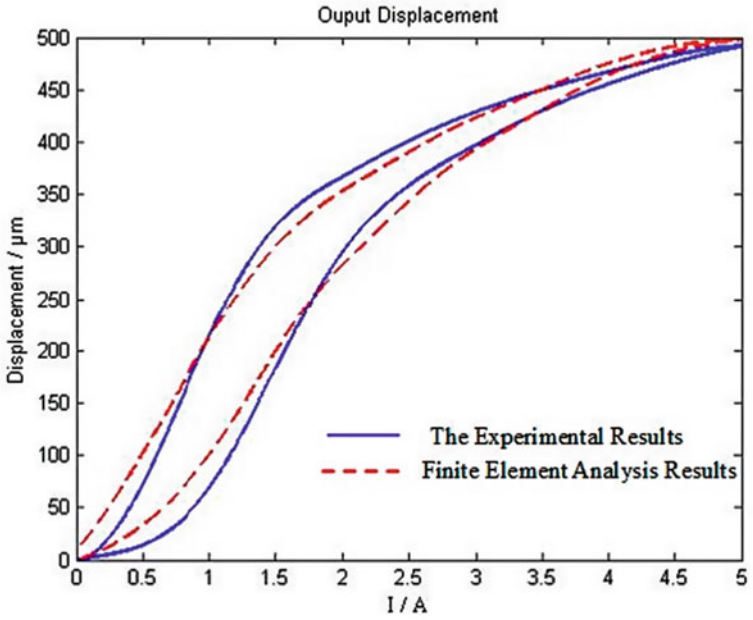

Fig. 13 Comparing the experimental hysteresis with the finite element analysis hysteresis (Yu et al. 2018)

determined. In this way, the inherent nonlinearity and hysteresis of the giant magnetostrictive material need to be further developed. Because of its strong coupling characteristics, nonlinear problems are very complicated, which makes modeling very difficult. Guo (Guo et al. 2015) studied and proposed a new Hammerstein model to simulate the rate-dependent hysteresis nonlinearity of GMA and only designed a 2 DOF (DOF is an abbreviation for degrees of freedom) control system. Zhang (Zhang et al. 2015) proposed a new type of adaptive filter to simulate rate-dependent hysteresis nonlinearity in giant magnetostrictive actuators. The proposed generalized playback operator adaptive filter can describe rate-dependent hysteresis characteristics, including different single-frequency input signals and multi-frequency composite input signals. AE Clark (1980) proposed a linear piezoelectric constitutive equation for large magnetostrictive actuators, which accurately describes the magneto-mechanical coupling relationship of large magnetostrictive materials. Azoum (Azoum et al. 2004) established a three-dimensional generalized finite element model based on the coupled constitutive equations of giant magnetostrictive actuators and simulated electromagnetic coils.

Magnetic-Machine Coupling of Spindle

In order to improve the machining accuracy of the magnetic levitation spindle unit installed on elastic structures such as machine tools and reduce the impact of

machine tool vibration on the spindle machining accuracy, Song (Song et al. 2010) studied a complex magnetic levitation electromechanical coupling system. The genetic algorithm was used to optimize the design variables of the coupling system; with the objective function and constraints, the optimal PID control parameters that meet the static and dynamic machining accuracy of the magnetic levitation spindle are obtained, and the machining accuracy of the magnetic levitation spindle unit is improved. On the basis of the dynamic model of planar parallel mechanism and magnetic control motorized spindle coupling system, the transient responses of the magnetic control motorized spindle under the action of the impulse, step, ramp, and simple harmonic excitation are analyzed, respectively, in two cases that the planar parallel machine tool is rigid and elastic, and the systematic evaluation of the dynamic performances of the coupling system is made (Song and Song 2011).

In air motorized spindle, the motor eccentricity between the stator and the rotor is inevitably introduced during the manufacturing process, which directly affects the machining results of workpiece surface, and this phenomenon is particularly unwanted in machining. However, little attention has been paid to the motor eccentricity of air motorized spindle. Wu (Wu et al. 2018) presented a new integrated electromechanical coupling method for estimating unbalanced force in air motorized spindle, and the effects of motor rotor eccentricity on surface topography in ultra-precision processes are analyzed as shown in Fig. 14.

By optimizing the dynamic performance of the spindle with magnetic bearings, there are two coupling factors to improve the waviness of ultra-precision turning effects. The first one is the dynamic balance of tilt motion; the second is to actively compensate the spindle motion. The final adjustment reveals an effective solution to reduce the disturbance of the rotating body by performing the seventh harmonic electronic compensation. It is verified that the evolution of the surface pattern is closely related to the dynamic motion of the main axis on the scale of several nanometers, so it may be greatly attenuated by using the active compensation (Khanfir et al. 2005b).

Wavelet transform and power spectral density are used to extract the unbalance characteristics of the spindle system, and two methods are used to calculate the frequency information of the spindle system. The relationship between the modal information of the spindle and the error frequency and power spectral density of the workpiece surface processed by wavelet transform comparison, and the signal characteristics of the waviness consistent with the unbalance frequency of the spindle are obtained. Thus, it can identify the main shaft unbalance error caused by the fluctuation (Chen et al. 2013).

Electric-Mechanical Coupling

Electric-mechanical coupling consists of the dynamic sensitivity analysis and geometric error parameters.

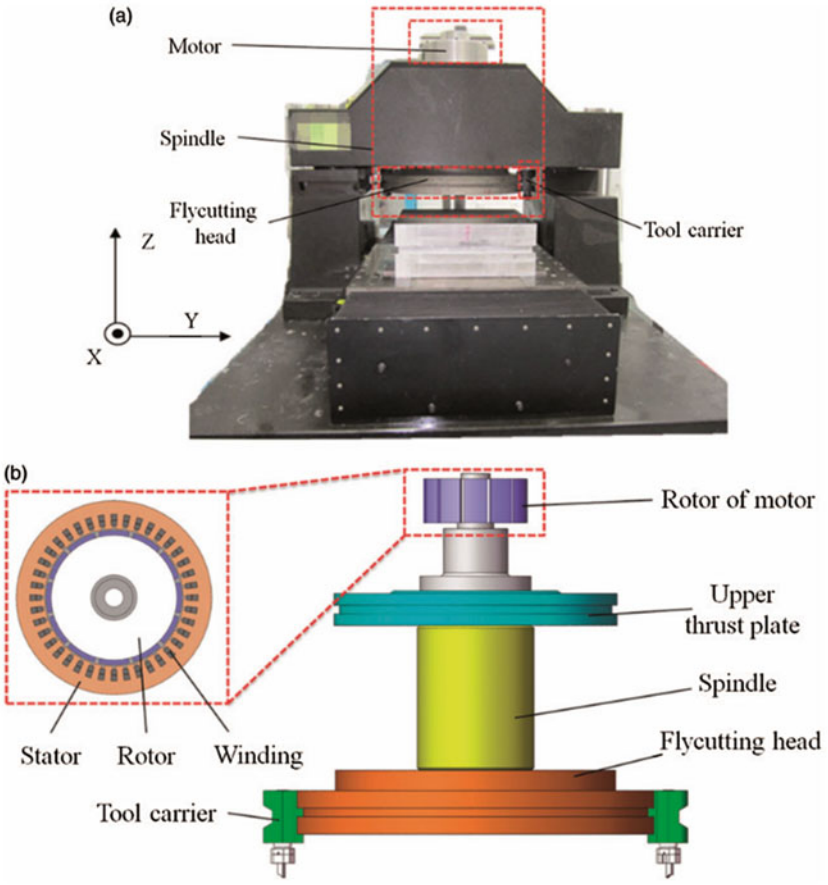

Fig. 14 Magnetic-machine coupling structure of the ultra-precision crystal machining tool (**a**) and its spindle (**b**) (Wu et al. 2018)

Liping Zhao (Zhao et al. 2016) proposed a new method to improve machining accuracy based on dynamic sensitivity analysis. The motion transfer chain of machine tool is analyzed, and the error propagation model is established. The model can be used to calculate the error sensitivity coefficient of each component. Secondly, the deformation of each component is obtained according to the finite element analysis. Combined with the error-sensitive coefficient and deformation, the sensitive error components of the machine tool are determined. Thirdly, according to the sensitive error component, the layout of the machine tool is modified, which not only increases the stiffness of the sensitive error component and reduces the machining error of the machine tool but also changes the layout of the machine tool according to the results of dynamic sensitivity

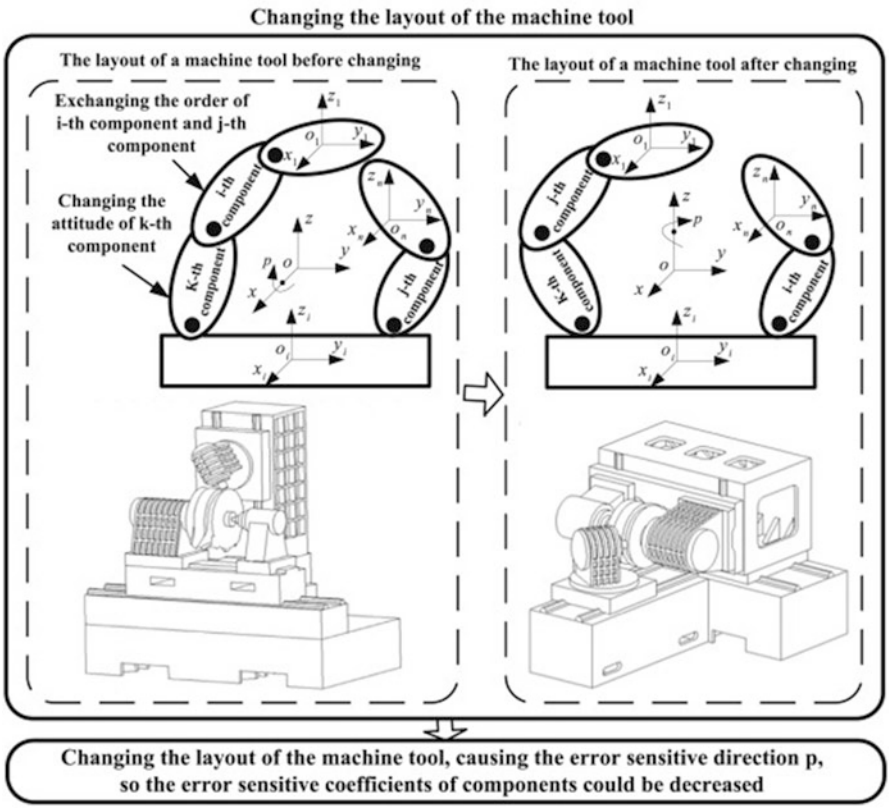

Fig. 15 Changed layout of a machine tool to decrease the error-sensitive coefficients of components (Zhao et al. 2016)

analysis. It can provide a new method to improve the machining accuracy as shown in Fig. 15.

Geometric error parameters are very important for the machining accuracy of five axis machine tools. Dongju Chen (Chen et al. 2018b) measured and determined the relative position error parameters and perpendicularity error of the non-orthogonal five axis machine tool. The error parameters related to the position of the translation axis are measured by the laser interferometer. According to its identification method, the rotary axis is measured in the axial, radial, and tangential measurement modes by using a double ball bar. After compensation, the machining accuracy is improved by 84.2% on average. The validity of the measurement and recognition method and the compensation method is verified in Fig. 16.

A new mathematical model can accurately calculate the magnification of the bridge type amplification mechanism. Using the elastic beam theory and Castigliano's second theorem, Quan Zhang (Zhang et al. 2020) established a

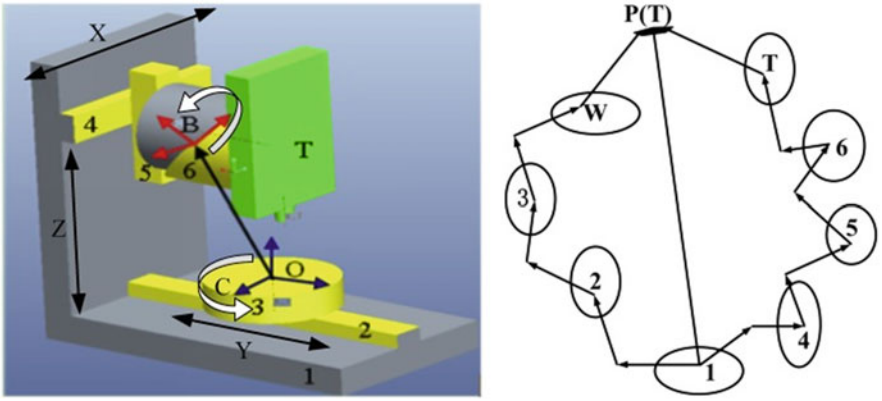

Fig. 16 DMU60P and topological structure of machining center with 5-axis (Chen et al. 2018b)

mathematical model considering the deformation of input beam, output beam, connecting beam, and flexible hinge. A decoupled XY precise positioning platform is studied. Considering the influence of the loading force on the amplification mechanism, the displacement magnification model of the positioning platform is established, and the results are further verified by the finite element simulation.

Electro-Magnetic-Mechanical Coupling

Electric magnetic mechanical coupling mainly includes finite element method and test method. Electromagnetic coupling, also known as mutual inductance coupling, is due to mutual inductance between two circuits, which makes the current change of one circuit affect the other circuit through mutual inductance. The changing electric field will produce a magnetic field, and the changing magnetic field will become an electric field. The magnetic field and the electric field are complementary, and the mutual influence is called electromagnetic coupling. Electromagnetic coupling is usually generated by the mechanical and electrical drive of machine tools, and then the two parts are related to the mechanical drive of machine tools, so as to realize the electric magnetic mechanical coupling.

Mustapha Zaouia (Zaouia and Benamrouche 2012) proposed an electromagnetic mechanical model based on the finite element and macro element technology and analyzed and studied the dynamic characteristics of the linear switched reluctance stepping motor (LSRSM), as shown in Figs. 17 and 18. After the finite element method based on node is used to solve the nonlinear electromagnetic equation of different material characteristics of the control motor, the equation firstly calculates the magnetic force through the Maxwell stress tensor, and then through the modified magnetic flux distribution, it is coupled to the moving parts of the mechanical

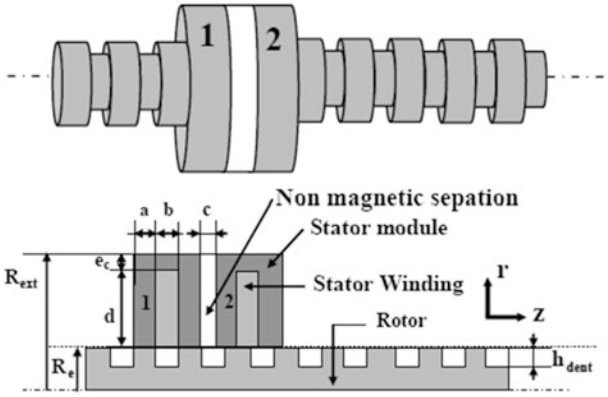

Fig. 17 LSRSM structure (Zaouia and Benamrouche 2012)

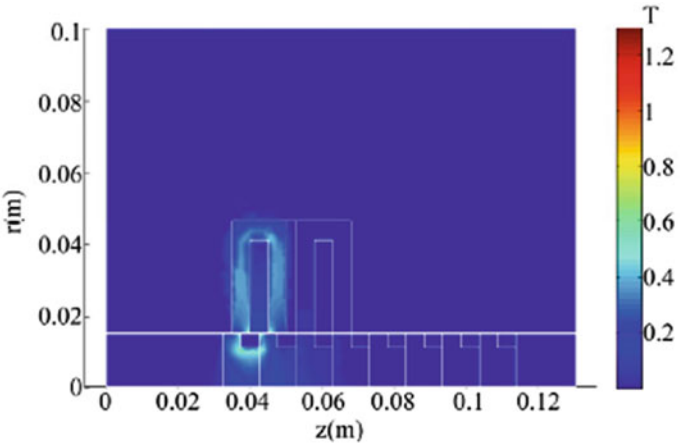

Fig. 18 Magnetic flux density in the LSRSM for NcI = 300 At (Zaouia and Benamrouche 2012)

equation. Because of the high precision of the moving parts of the stepping motor and the small air gap, comparing with other motion technologies, the macro element technology could ensure the motion simulation.

The machining of titanium alloy, especially in ultra-precision machining, involves many parameters. W.S. Yip (Yip and To 2018) uses magnetic field, and prodsi of SPDT machining parts is 2.39 higher than that of ordinary SPDT, which shows that the proposed machining technology improves the product sustainability. As shown in Figs. 19 and 20, the proposed processing technology provides a solid way to improve the productivity and accuracy level of titanium alloy parts and promotes sustainable ultra-precision manufacturing.

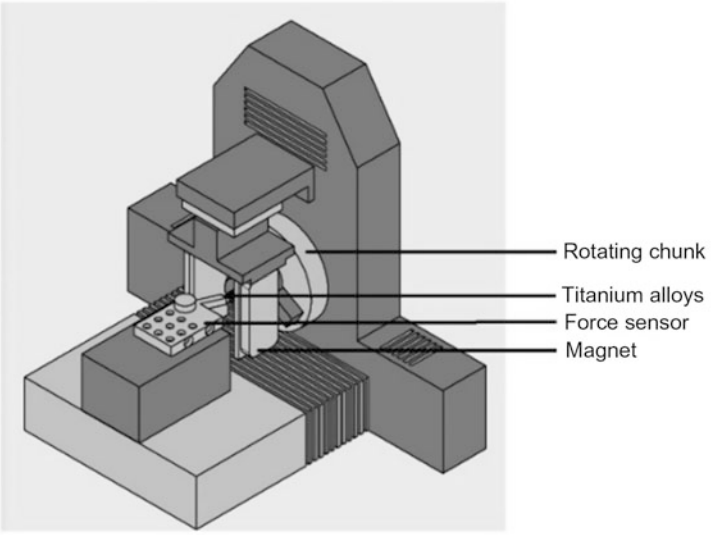

Fig. 19 Experimental setup of proposed machining technology (Yip and To 2018)

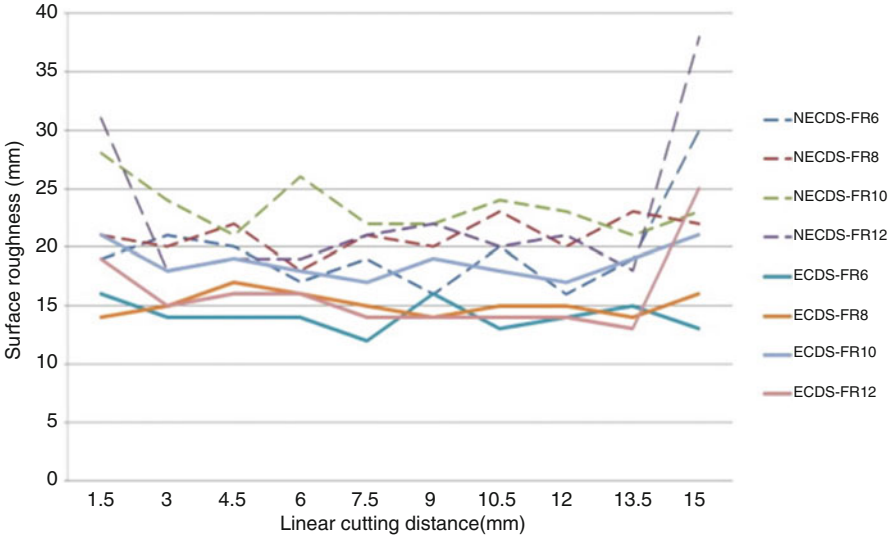

Fig. 20 Surface roughness of NECDS and ECDS against the linear cutting distance (Yip and To 2018)

Conclusion

In this section, the electric-magnetic-mechanical coupling of precision machine tool is described. Firstly, the main components of precision machine tool are analyzed, including guide rail, spindle, bed, and related adjustable mechanism. These individual components are composed of motor, precision guiding mechanism, and control unit. The precise coupling of these functional components determines the actual machining accuracy and reliability. This section discusses the influence of electromagnetic machine parameters on precision machining equipment and then analyzes electromagnetic coupling, motor coupling, and magnetic machine coupling, respectively. The future research direction is mainly focused on the unit functional components such as precision spindle electromagnetic machine coupling or precision guide rail electromagnetic machine coupling. The research coupling methods are mainly divided into electromagnetic machine finite element analysis method and electrical machine finite element analysis method. The magnetic machine test method, which is related to the influence of three parameters of electromagnetic machine on precision machining machine tools, is not perfect. Current research is based on a specific machining process. Through the summary and analysis of this section, it is necessary to establish a systematic theory of the influence of electromagnetic machine parameters toward the accuracy and reliability of machine tools, and it is also the basic theory of the development of precision ultra-precision machining equipment and processing technology.

References

AMOSIN® – Measuring Principle (2019) http://www.amo-gmbh.com/en/fundamentals/measuring-principle/

Azoum K, Besbes M, Bouillault F (2004) 3D FEM of magnetostriction phenomena using coupled constitutive laws. Int J Appl Electromagn Mech 19(1–4):367–371

Brandenburg G, Bruckl S, Dormann J, Heinzl J, Schmidt C (2000) Comparative investigation of rotary and linear motor feed drive systems for high precision machine tools. In 6th international workshop on advanced motion control. Proceedings (Cat. No. 00TH8494). IEEE, pp 384–389

Chen D, Fan J, Zhang F (2013) Extraction the unbalance features of spindle system using wavelet transform and power spectral density. Measurement 46(3):1279–1290

Chen D, Bian Y, Fan J (2014) Experiments and identification of the unbalance of aerostatic guideways on the micro-scale. Sensors 14(3):4416–4427

Chen W, Liang Y, Sun Y, Bai Q, An C (2015) A novel dynamic modeling method for aerostatic spindle based on pressure distribution. J Vib Control 21(16):3339–3347

Chen D, Han J, Huo C, Fan J, Cheng Q (2017) Effect of gas slip on the behavior of the aerostatic guideway. Ind Lubr Tribol. https://doi.org/10.1108/ILT-03-2016-0071

Chen D, Han J, Cui X, Fan J (2018a) Identification and evaluation for the dynamic signals caused by pressure fluctuation of aerostatic slider. Ind Lubr Tribol. https://doi.org/10.1108/ILT-11-2016-0271

Chen D, Zhang S, Pan R, Fan J (2018b) An identifying method with considering coupling relationship of geometric errors parameters of machine tools. J Manuf Process 36:535–549

Clark AE (1980) Magnetostrictive rare earth-Fe2 compounds. Handb Ferromagn Mater 1:531–589
DeBra DB (1992) Vibration isolation of precision machine tools and instruments. CIRP Ann 41(2):711–718
Denkena B, Dahlmann D, Krueger R (2016) Design and optimisation of an electromagnetic linear guide for ultra-precision high performance cutting. Procedia CIRP 46:147–150
Ekinci TO, Mayer JRR, Cloutier GM (2009) Investigation of accuracy of aerostatic guideways. Int J Mach Tools Manuf 49(6):478–487
Foremny E, Schenck C, Kuhfuss B (2016) Coupling system for ultra precision machining. J Mech Eng Autom 6(6):301–306
Fujimori T, Taniguchi K, Ellis C, Aoyama T, Yamazaki K (2012) A study on error compensation on high precision machine tool system using a 2D laser holographic scale system. J Adv Mech Des Syst Manuf 6(6):999–1014
Gannel LV (2019) Determination of stiffness of the Guideways of linear electric drive. Russ Electr Eng 90(7):538–542
Guo Y, Mao J, Zhou K (2015) Rate-dependent modeling and H robust control of GMA based on Hammerstein model with Preisach operator. IEEE Trans Control Syst Technol 23(6):2432–2439
Huo D, Cheng K, Wardle F (2010) Design of a five-axis ultra-precision micro-milling machine – ultramill. Part 1: holistic design approach, design considerations and specifications. Int J Adv Manuf Technol 47(9–12):867–877
Im H, Yoo HH, Chung J (2011) Dynamic analysis of a BLDC motor with mechanical and electromagnetic interaction due to air gap variation. J Sound Vib 330(8):1680–1691
Jones SD, Ulsoy AG (1999) An approach to control input shaping with application to coordinate measuring machines
Khanfir H, Bonis M, Revel P (2005a) Improving flatness in ultraprecision machining by attenuating spindle motion errors. Int J Mach Tools Manuf 45(7–8):841–848
Khanfir H, Bonis M, Revel P (2005b) Improving waviness in ultra precision turning by optimizing the dynamic behavior of a spindle with magnetic bearings. Int J Mach Tool Manu 45(7–8):841–848
Kim CJ, Oh JS, Park CH (2014) Modelling vibration transmission in the mechanical and control system of a precision machine. CIRP Ann 63(1):349–352
Lai T, Peng X, Guo M, Tie G, Guan C, Liu J et al (2019) Design and manufacture of high accurate aerostatic guideway with glass material. Int J Precis Eng Manuf. https://doi.org/10.1007/s12541-019-00081-5
Lee J, Okwudire CE (2016) Reduction of vibrations of passively-isolated ultra-precision manufacturing machines using mode coupling. Precis Eng 43:164–177
Lin YC, Lee HS (2008) Machining characteristics of magnetic force-assisted EDM. Int J Mach Tools Manuf 48(11):1179–1186
Liu C, Hu J, Hu Q (2019) Preview control of hydrostatic Guideway for Ultraprecision CNC machine tools. Iran J Sci Technol Trans Mech Eng 43(1):749–759
Lu Z, Wei P, Wang C, Jing J, Tan J, Zhao X (2016) Two-degree-of-freedom displacement measurement system based on double diffraction gratings. Meas Sci Technol 27(7):074012
Qiang L, Wu W (2014) Research progress in coupled modeling and analysis technology of CNC machine tools. Aerosp Manuf Technol 460(16):8–11
Remy G, Gomand J, Barre PJ, Hautier JP (2006) New current control loop with resonant controllers by using the causal ordering graph- application to machine tools. WSEAS Trans Syst 5(1):233–239
Rivin EI (1995) Vibration isolation of precision equipment. Precis Eng 17(1):41–56
Rivin EI (2006) Vibration isolation of precision objects. Sound Vib 40(7):12–20
Schaarschmidt I, Hackert-Oschätzchen M, Meichsner G, Zinecker M, Schubert A (2019) Implementation of the machine tool-specific current and voltage control characteristics in multi-physics simulation of electrochemical precision machining. Procedia CIRP 82:237–242
Song F, Song B (2011) Transient response analysis of planar parallel mechanism and magnetic control motorized spindle coupling system. In: Proceedings of the 30th Chinese control conference, pp 3872–3877. IEEE

Song F, Liu H, Song B, Feng H (2010) Dynamic optimization of PID control parameters of complex magnetic suspension electromechanical coupling system. In 2010 8th world congress on intelligent control and automation, pp 3435–3440. IEEE

Subrahmanyan PK, Trumper DL (2000) Synthesis of passive vibration isolation mounts for machine tools-a control systems paradigm. In: Proceedings of the 2000 American control conference. ACC (IEEE cat. No. 00CH36334), vol. 4. IEEE, pp 2886–2891

Tamiya H, Taniguchi K, Yamazaki K, Aoyama H (2018) Detection principle and verification of non-contact displacement meter with pico-meter resolution. J Adv Mech Des Syst Manufact 12(5):JAMDSM0107-JAMDSM0107

Uhlmann E, Mullany B, Biermann D, Rajurkar KP, Hausotte T, Brinksmeier E (2016) Process chains for high-precision components with micro-scale features. CIRP Ann Manuf Technol 65(2):549–572

Wu D, Wang B, Luo X, Qiao Z (2015) Design and analysis of aerostatic spindle with high load characteristics for large ultra-precision drum lathe. Proc Inst Mech Eng J Eng Tribol 229(12):1425–1434

Wu Q, Sun Y, Chen W, Chen G, Bai Q, Zhang Q (2018) Effect of motor rotor eccentricity on aerostatic spindle vibration in machining processes. Proc Inst Mech Eng C J Mech Eng Sci 232(7):1331–1342

Yang X, Lu D, Ma C, Zhang J, Zhao W (2017) Analysis on the multi-dimensional spectrum of the thrust force for the linear motor feed drive system in machine tools. Mech Syst Signal Process 82:68–79

Yao H, Li Z, Zhao X, Sun T, Dobrovolskyi G, Li G (2016) Modeling of kinematics errors and alignment method of a swing arm ultra-precision diamond turning machine. Int J Adv Manuf Technol 87(1–4):165–176

Yip WS, To S (2018) Sustainable manufacturing of ultra-precision machining of titanium alloys using a magnetic field and its sustainability assessment. Sustain Mater Technol 16:38–46

Yu Z, Wang T, Zhou M (2018) Study on the magnetic-machine coupling characteristics of Giant Magnetostrictive actuator based on the free energy hysteresis characteristics. Sensors 18(9):3070

Zaouia M, Benamrouche N (2012) Numerical modeling of the coupled electromagnetic and mechanical phenomena of linear stepping motors

Zhang Z, Ma Y, Guo Y (2015) A novel nonlinear adaptive filter for modeling of rate-dependent hysteresis in giant magnetostrictive actuators. In: 2015 IEEE international conference on mechatronics and automation (ICMA), pp 670–675. IEEE

Zhang Q, Zhao J, Peng Y, Pu H, Yang Y (2020) A novel amplification ratio model of a decoupled XY precision positioning stage combined with elastic beam theory and Castigliano's second theorem considering the exact loading force. Mech Syst Signal Process 136:106473

Zhao L, Chen H, Yao Y, Diao G (2016) A new approach to improving the machining precision based on dynamic sensitivity analysis. Int J Mach Tools Manuf 102:9–21

Zhong Z, Wu L, Mou C (2019) Measurement principle and structure optimization of two-dimensional time grating displacement sensor. In: Ninth international symposium on precision mechanical measurements, vol 11343. International Society for Optics and Photonics, p 1134329

Processing and Manufacturing Technology of Special Sensors

15

Qiulin Tan

Contents

Introduction 402
Ceramic MEMS Device Processing and Manufacturing Methods 404
L/HTCC Micro-assembly Technology 405
Heterogeneous Material Co-firing Technology 413
Co-firing of Heterogeneous Substrate Materials 414
Electronic Paste Heterogeneous Co-firing 416
Integration of Multiple Processing Technologies 417
C-MEMS High-Temperature Device 419
Langasite Device Processing and Manufacturing Methods 421
High Temperature Forming Mechanism 423
Wet Etching Mechanism 423
Dry Etching Mechanism 425
Bonding Mechanism 426
LGS Device Sealed Cavity Manufacturing Technology 427
Wet Etching Process 427
Inductively Coupled Plasma (ICP) Etching Process 428
Surface Polishing and Bonding Process 429
LGS Device Surface Graphic Manufacturing Technology 429
SAW Temperature and Pressure Integrated Devices 431
Conclusion 432
References 433

Q. Tan (✉)
Key Laboratory of Instrumentation Science and Dynamic Measurement, Ministry of Education, North University of China, Taiyuan, China

Science and Technology on Electronic Test and Measurement Laboratory, North University of China, Taiyuan, China
e-mail: tanqiulin@nuc.edu.cn

Z. Jiang, S. Yang (eds.), *Precision Machines*, Precision Manufacturing,
https://doi.org/10.1007/978-981-13-0381-4_23

Abstract

At present, the development of aerospace technology is changing with each passing day, which has greatly promoted the scientific and technological progress of human society. Among them, spacecrafts play an important role. For aerospace, industrial metallurgy, and other fields and for the testing requirements of various parameters in special environments such as high temperature, high rotation, and small space, traditional silicon-based sensors have problems such as PN junction failure, solder joint dropout, and ohmic contact failure in ultrahigh-temperature environments, so this chapter takes ceramic MEMS devices and langasite devices as examples to introduce the processing and manufacturing methods for special sensors suitable for harsh environments such as high temperature and high rotation, to realize the preparation of devices and parameter testing in special environments. Among them, ceramic MEMS device processing and manufacturing methods include L/HTCC (low-/high-temperature co-fired ceramic) micro-assembly technology, heterogeneous material co-firing technology, integration of multiple processing technologies, etc.; langasite device processing and manufacturing methods include wet etching, inductively coupled plasma etching, bonding, surface graphic manufacturing, and other technologies. From the aspects of mechanism, common equipment, and process, the processing methods of each special sensor are elaborated. Through the abovementioned processing and manufacturing methods, the preparation of special sensors is realized, the test of the sensors in special application environments is completed, and the working ability in harsh environments is verified.

Keywords

Ceramic MEMS devices · Langasite devices · L/HTCC micro-assembly technology · Heterogeneous material co-firing technology · Integration of multiple processing technologies · Wet etching · Inductively coupled plasma etching · Bonding · Surface graphic manufacturing

Introduction

Exploring space has always been a dream that mankind has pursued for a long time, and the development of aerospace technology has promoted the progress of mankind to the universe. Among them, spacecraft play a key role. The United States has successively issued IHPTET plans, VAATE plans, etc. for aviation engines; in China's 13th 5-year national science and technology innovation plan, aeroengine and gas turbine "two aircraft" are listed as major science and technology special projects, making them become key problems in the aerospace field together with aerospace aircraft and hypersonic aircraft projects.

The aerospace vehicle is often accompanied by harsh environments such as high temperature and high rotation, especially for key parts such as hypersonic aircraft surfaces, aeroengines, and gas turbines. The local temperature even exceeds 800 °C. However, in situ real-time acquisition of parameters such as temperature, pressure, and vibration in harsh environments is of great significance for material selection, structural design, and protective measures of spacecraft (George et al. 2005; Jatlaoui et al. 2011). For example, when the spacecraft is running at high speed, the surface skin is rubbed against the atmosphere, generating a lot of heat. The temperature, aerodynamic load, and vibration test of the skin surface are essential for skin structure design and protection measures (Zhao et al. 2009); aircraft engine combustion chamber temperature is over 800 °C, and the working pressure is greater than 1.2 MPa. Combustion chamber internal temperature and pressure parameters real-time monitoring is of great significance to the material selection and failure analysis (Anonymous 2017); aerospace engine turbine blades with ultrahigh temperature, strong turbulence, and severe vibration environment, vulnerable to damage or even generate crack, directly decide the quality of the aerospace engine performance, so the turbine blades, such as temperature, pressure, and vibration parameters of real time monitoring in situ for space is especially important to the safe operation of the engine (Sabol et al. 2009).

However, traditional silicon-based testing technology is difficult to achieve accurate real-time monitoring of various parameters in the above harsh environment (Jatlaoui et al. 2007, 2008a, b, 2009; Scott and Peroulis 2009). On one hand, traditional sensors usually take silicon as the base, and silicon material higher than 500 °C will appear as plastic deformation. So silicon sensors cannot meet the requirements of ultrahigh-temperature application (Diem et al. 1995).On the other hand, the traditional wired sensor has problems such as aging at high temperature, ohmic contact failure, etc., and the active sensor has insufficient endurance, which are not suitable for working under high-temperature and high-rotation environment.

Therefore, the current multiparameter test technology for temperature, pressure, and vibration in critical environments such as high temperature and high rotation has become one of the main bottlenecks restricting the development of spacecraft. There is an urgent need for substrate material selection, test sensitivity mechanism, device structure, manufacturing process, packaging, and other aspects to break through the traditional restrictions and to develop new special sensors to achieve real-time in situ accurate testing of multiple parameters in harsh environments.

Special sensors refer to sensors with new structures, new functions, etc., which are manufactured by new principles, new technologies, new materials, and new processes. They are used for multiparameter real-time in situ accurate measurement under high-temperature, high-pressure, high-rotation, and other harsh environments.

First of all, in the selection of materials, materials are required to have good high-temperature stability, chemical stability, and other characteristics (Yanjie et al. 2018). On the one hand, raw ceramics are flexible materials. Compared with silicon-based materials, raw ceramics have the advantages of high-temperature resistance, high electrical insulation performance, low dielectric constant and dielectric loss, high thermal conductivity, good chemical stability, close to the thermal expansion

coefficient of components, etc. and are very suitable for application in harsh environments such as high temperature and high rotation. On the other hand, langasite (LGS) is one kind of hard and brittle materials. LGS crystal has good high-temperature stability and chemical stability, and its electromechanical coupling coefficient is two to three times of quartz. It can achieve remote wireless passive monitoring and be suitable for high-temperature and high-rotation environment parameters test (Zhang and Yu 2011).

Secondly, the sensor components are required to be able to work normally under the environment of high-speed rotation. Wireless passive sensor can effectively avoid the problems of ohmic contact failure of wired sensor and insufficient battery life of active sensor in harsh environment. Therefore, the wireless passive sensor components based on high-temperature-resistant materials have significant advantages in testing various parameters in harsh environments such as high temperature, high rotation, and vibration. At present, wireless passive sensing technology is mainly divided into three categories: LC resonance mutual inductance coupling technology, surface acoustic wave (SAW) technology, and microwave telemetry technology. The LC resonant wireless passive sensor adopts near-field coupling technology, which can realize fast reading and energy coupling of test data in a harsh environment, and has a simple and reliable structure (Ren et al. 2012; Rodriguez and Jia 2011; Tan et al. 2017a); wireless passive sensor based on the principle of surface acoustic wave testing has simple structure, small volume, high Q value, and good stability and can realize long-distance, multiparameter wireless passive monitoring (Cheng et al. 2011, 2012; Ren et al. 2011); the microwave-based sensor has the advantages of long transmission distance and strong anti-metal interference, which can be dynamically monitored to realize real-time data processing (Liu and Tong 2015). Since the preparation process of the chip-type microwave sensor is substantially similar with the LC resonance-type sensor. Therefore, this chapter mainly takes the preparation process of LC sensor and SAW sensor as examples.

Finally, due to the special application environment of special sensors, typical structure requires miniaturization and integration. Therefore, it is very important to realize the miniaturization and integrated manufacturing of sensors through controllable micro-machining technology. This chapter introduces the technology of wireless passive special sensor processing and manufacturing suitable for high-temperature and high-rotation and other harsh environments, taking typical high-temperature-resistant materials such as ceramic and LGS as is depicted in Fig. 1.

Ceramic MEMS Device Processing and Manufacturing Methods

The ceramic MEMS devices are mainly based on flexible low-/high-temperature co-fired ceramic (L/HTCC) raw ceramic tape and integrate the manufacturing process of MEMS micromechanical structure. By means of micro-assembly and sintering technology, it forms highly integrated electronic circuits in three-dimensional space. The flexible L/HTCC raw porcelain belt is easy to realize

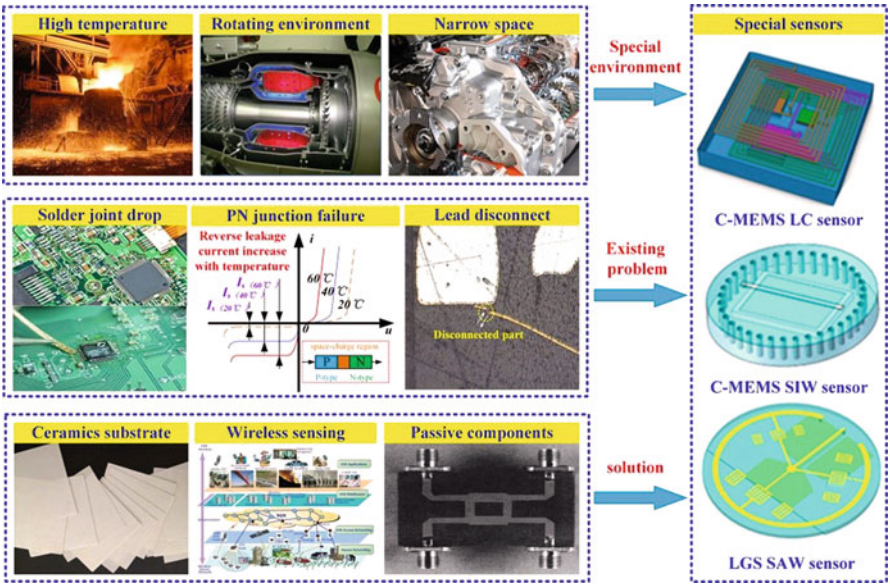

Fig. 1 Special sensor application background

multilayer wiring, and each layer of circuit is connected through an interconnection through the hole, ensuring the integrated density of the device prepared from this. In addition, the flexible substrate is easier to form cavity, beam, microchannel, and other micromechanical structure, compared with the hard substrate, more conducive to the control of processing accuracy. In addition, sintered L/HTCC-based devices can realize self-packaging. Ceramic substrates with high-temperature resistance and good corrosion performance can form good self-protection for the circuit encapsulated in them, thus further reducing the volume of devices and enhancing the reliability of devices under special circumstances. The wireless passive devices formed by C-MEMS and LC coupling RF sensing and signal reading technology can realize multiparameter wireless telemetry in special environment and have great application prospects in aerospace, industrial manufacturing, metallurgy, mining, and other fields.

L/HTCC Micro-assembly Technology

The C-MEMS wireless passive sensor mainly involves the microstructure cavity, beam structure, microchannel structure, and curved surface structure. It integrates a single or several different microstructures on the same substrate through the L/HTCC micro-assembly process and combines with LC coupling resonance loop to realize parameter detection of different functions. L/HTCC micro-assembly process mainly includes raw porcelain with cutting, filling, silk screen printing,

lamination, laminating, sintering molding, and so on, according to the need to implement the function of the device, corresponding to the micromechanical structure design, by adjusting the preparation process, thus forming a ceramic substrate of cavity, the beam structure, the microchannel structure, and surface structure and microstructure.

Porcelain Belt Punching Process

The punching process of raw porcelain belt is mainly to cut the L/HTCC flexible raw porcelain belt formed by convection to form the structure of through-hole, cavity, beam, and microchannel with different shapes and sizes. As shown in Fig. 2, the through-hole structure is mainly used for interlayer interconnection of multilayer circuit and lamination positioning of L/HTCC substrate. For interconnect vias, a reserved via is formed at a corresponding location on each layer of the flexible ceramic substrate for filling the paste to achieve a three-dimensional integrated interconnection, depending on the design requirements of the interlayer interconnection of the device circuitry. Multilayer electronic circuit. For the positioning hole, the positioning hole of the corresponding size must be reserved according to the state of the laminating mold to ensure that the positional deviation of each layer structure does not occur during the lamination process. Common cavity structures mainly include quadrilateral cavities, hexagonal cavities, and circular cavities. They are similar to the through-hole structure, and the cavity of a specified size and shape is cut by laser at a specified position, combined with self-encapsulation technology of L/HTCC, which can form a closed cavity structure.

Typical beam structures include single cantilever beam, double cantilever beam, double end beam, double island five beam, double end four beam, four side beam,

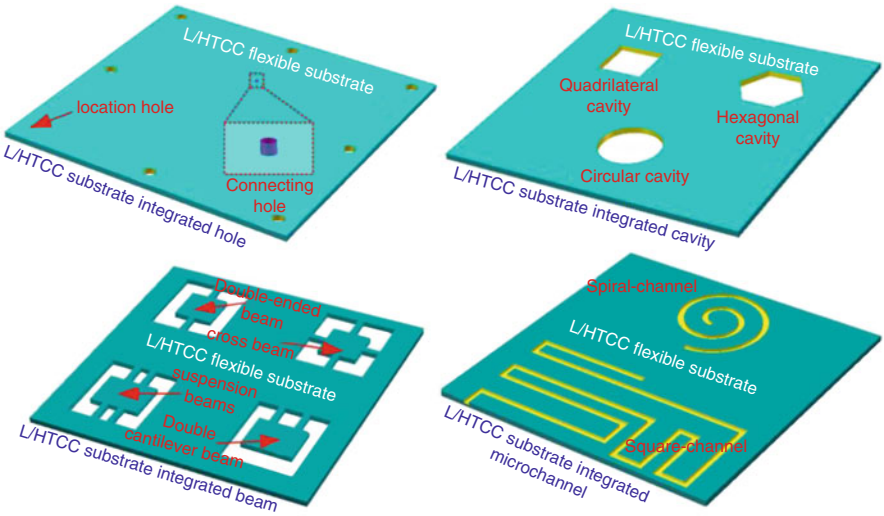

Fig. 2 L/HTCC substrate microstructure

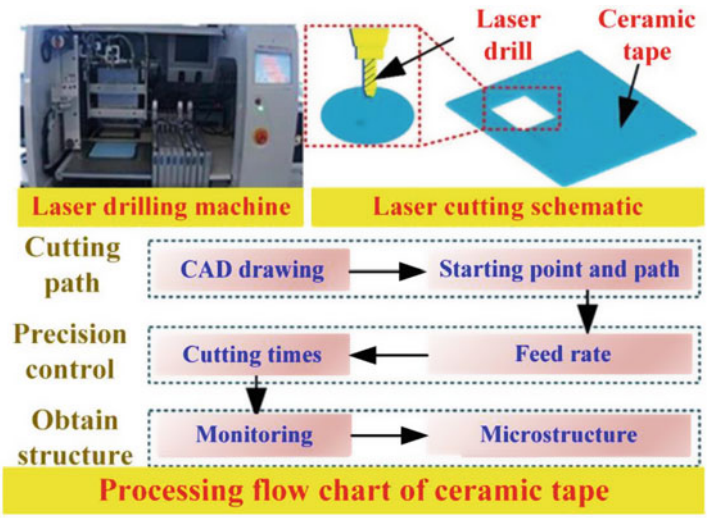

Fig. 3 L/HTCC substrate punching process

and eight side beam. Different from the punching technology of through-hole and cavity structure, only when the beam and the substrate form a whole, its microstructure is effective; therefore, the beam structure needs to be removed in reverse. Figure 2 shows the L/HTCC substrate with integrated through-hole, cavity, beam structure, and microchannel, and the raw porcelain belt laser punching machine and its cutting schematic diagram as shown in Fig. 3.

At present, micron ceramic microstructure can be achieved by mechanical punching or laser punching, and machining precision can be controlled by controlling cutting times and feed quantity. However, to meet the higher precision and size of micro devices requirements, automation equipment is difficult to finish at present stage, for example, in the microchannel structure processing, if can be implemented in single layer ceramic substrate arbitrarily deep punching, makes the size of microchannel is not limited to raw porcelain thickness, will greatly improve the ceramic base microchannel processing and application ability.

Filling and Screen Printing Process

The filling process is mainly set up for the interconnection of circuits between multilayer L/HTCC substrates. According to the device circuit design, interlayer interconnection through-hole is cut at the corresponding position of each layer of substrates through the punching process. However, it is impossible to achieve circuit interconnection only through the through-hole, only in the through-hole filled with the corresponding electronic paste, in order to ensure the formation of current path in the insulation medium. Figure 4 shows the filling equipment and filling diagram of L/HTCC microhole.

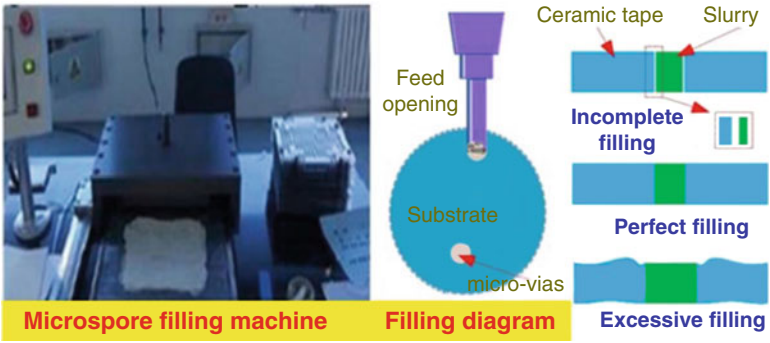

Fig. 4 Filling process and its coordination

Generally, there are three different situations in the filling process. When the filling slurry is insufficient, the gap filling is formed. At this time, the connecting through-hole and the slurry cannot be fully fitted, resulting in slurry falling off and filling failure in the subsequent process. When the slurry is overfilled, the through-hole cannot fully accommodate the slurry. In the subsequent lamination and lamination processes, the slurry is squeezed by the outside world, and the connected through-hole wall is subjected to uneven stress from the slurry, resulting in the destruction of the flexible substrate structure and the weakening of mechanical properties. When the slurry is filled with the interconnecting through-hole, a complete filling is formed, which is an ideal filling condition. The slurry can completely fit the through-hole substrate without excessive extrusion on the through-hole wall and damaging the structure of raw porcelain belt.

Screen printing in L/HTCC process is a simple process in which electronic metal paste is formed on the base material through screen printing plate. According to the designed circuit layout, the screen printing plate is prepared, and the mesh of the screen printing plate can print the slurry to ceramic substrate. During printing, the pulp is put into one end of the screen printing plate, and a scraper is used to apply certain pressure on the pulp part of the screen printing plate. At the same time, the scraper moves toward the other end of the screen printing plate at a constant speed. During the movement, the electronic pulp is squeezed by the scraper from the layout holes to the substrate, as shown in Fig. 5. Due to the limitations of sintering process, different substrate materials need to choose corresponding electronic pastes for printing. For example, LTCC ceramic substrate can be co-fired with silver pastes, while HTCC ceramic substrate can be co-fired with platinum, tungsten, and other electronic pastes. Screen-printing technology has the advantages of low-cost, simple method and, through the automatic screen printing machine, can accurately control circuit part printing precision, thus forming electronic components or circuit design, such as planar spiral inductor and a parallel plate capacitor; fork refers to the capacity as well as passive components such as integrated circuit, the circuit design of different functions such as gate. As shown in Fig. 5, it is a fully automatic screen printing machine.

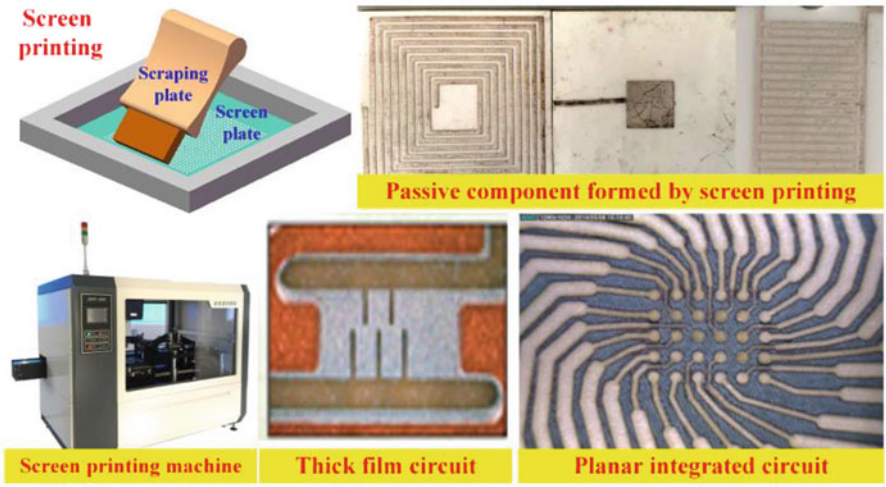

Fig. 5 Screen printing technology

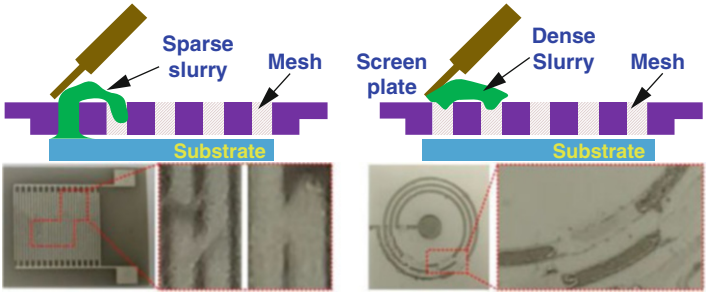

Fig. 6 Effect of paste consistency on silk screen

Currently, the common equipment repetition accuracy is 10 μm, the screen size is 550 × 550 × 25 mm, and the maximum scraper pressure is 300 N.

Limited by the screen printing plate manufacturing process, screen printing can achieve the minimum printing line width of 50 μm, for the smaller size of the circuit pattern, through the screen printing technology to achieve the metallization of ceramic substrate will become very difficult. In addition, due to the fluidity of the paste itself, the circuit pattern printed on the substrate surface will spread, resulting in the actual printing size larger than the design size. For narrow wire, the fluidity of the paste may lead to short circuit of adjacent wire. Therefore, the consistency of the paste is important for screen printing. As shown in Fig. 6, the thick slurry cannot pass through the screen mesh, thus it is unable to complete the substrate metallization; However, if the slurry is too thin, the short circuit or open circuit of adjacent conductors will be caused by the fluidity.

Lamination Process

Lamination process is an important part of the interconnection between the layers of the electronic circuits of the C-MEMS devices, the self-packaging of the devices, and the microstructure forming. After the perforation process, filling process, and screen printing process, the sequence superposition of printed circuit patterns and microstructure flexible ceramic raw ceramic tape layers was carried out. The circuit patterns of different raw porcelain belt layers are connected to each other through filled connection holes to ensure that the whole circuit pattern forms a path and is highly integrated in the three-dimensional space, as shown in Fig. 7. Interconnection layer 1, interconnection layer 2, and interconnection layer 3 are connected to each other through sequential lamination.

Lamination technology can realize the self-encapsulation of device circuit while realizing the interconnection of different substrate circuits. In Fig. 7, interconnection layer 3, as the top metallized ceramic layer, is extremely vulnerable to corrosion by high temperature, corrosion, and other harsh environments. In the long run, the circuit part will fail, resulting in device damage. L/HTCC material has a good anticorrosion performance, covering a layer of substrate above the top layer of metallized ceramic. Through lamination process, the circuit part is completely encapsulated in the substrate, so as to avoid damage to the device by the external environment. In addition, since L/HTCC raw porcelain belt itself is flexible, changing the laminated mold can change the base material forming. By designing the surface laminated mold and laminating the base material, the surface device blank sample can be obtained.

Lamination process is an important step in the preparation of C-MEMS devices. Therefore, the process and precision errors in the lamination process will reduce the yield of devices. As the circuit part first, printing with a raw porcelain layer is covered for the preparation of microstructure flexible ceramic raw porcelain layer, in order to prevent subsequent laminated microstructure has been damaged by the high pressure in the process, need to fill microstructure by sacrifice layer materials, as shown in Fig. 8, and filling process are similar, too big a sacrifice layer materials will squeeze the edge of microstructure, its mechanical performance degradation, while the sacrifice layer materials is too small will be caused by a lack of bearing capacity,

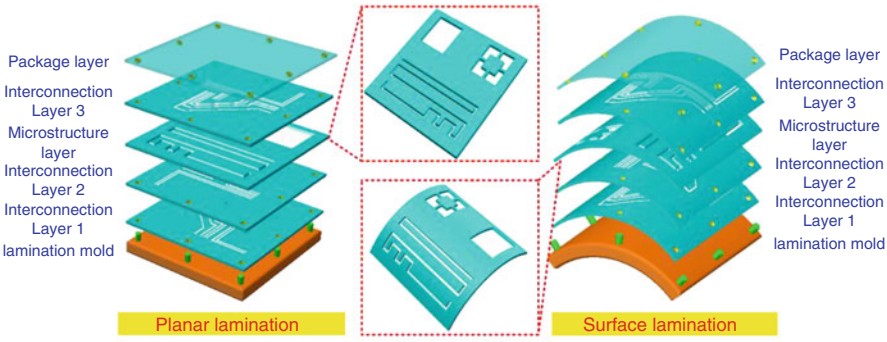

Fig. 7 Lamination process of L/HTCC substrate

causes in the process of laminated microstructure to collapse. In addition, laminated positioning accuracy also affects device performance. Interlayer circuit connection hole size is small, so even a small positioning error will lead to interlayer circuit connection break. Figure 8 shows a fully automatic laminating machine with a maximum number of lamination layers of 80 and a maximum stack thickness of 5 mm. The lamination accuracy can be controlled within 10 μm.

Lamination and Sintering Process

Lamination is one of the key technologies in the L/HTCC micro-group process. Appropriate lamination conditions can make each raw ceramic layer physically interconnected, and then through the sintering process, the layers of the green porcelain strip and the electronic paste are completely viscous. The principle of bonding the raw ceramic is shown in Fig. 9. The raw ceramic is composed of ceramic particles, glass components, and organic components, wherein the organic components are mainly binders. During the lamination process, the raw ceramic is physically bonded together under a certain temperature and pressure, the organic components become plastic, and the ceramic particles and the glass components of the respective layers are diffused and aggregated together with the applied pressure. The setting of the lamination conditions also affects the performance of the device or microstructure. Excessive pressure can cause the microstructure to collapse, while too little pressure can't compress the layers of the raw ceramic strip, resulting in the separation of the layers of raw ceramic, as shown in Fig. 10. It is a laminator with a maximum applied pressure of 5000 Psi, a maximum

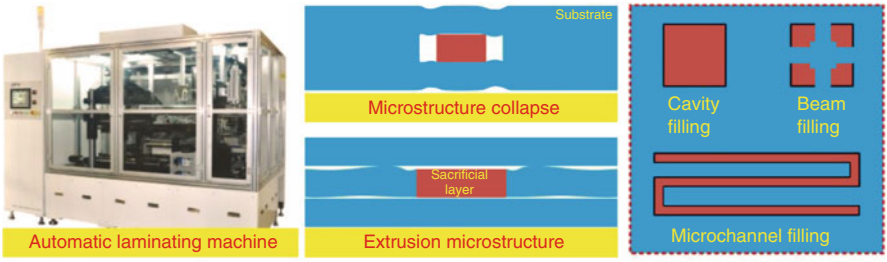

Fig. 8 Fully automatic laminating machine and sacrificial layer filling

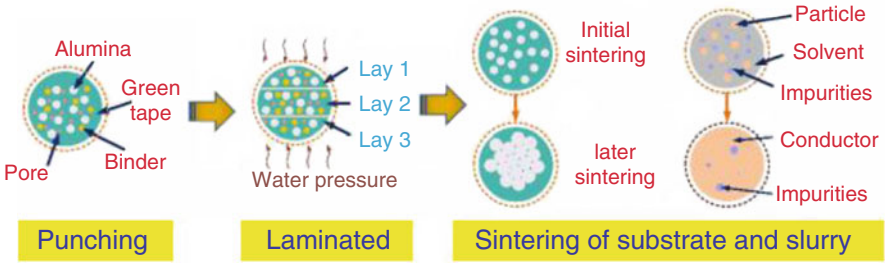

Fig. 9 Interlayer adhesion mechanism of L/HTCC

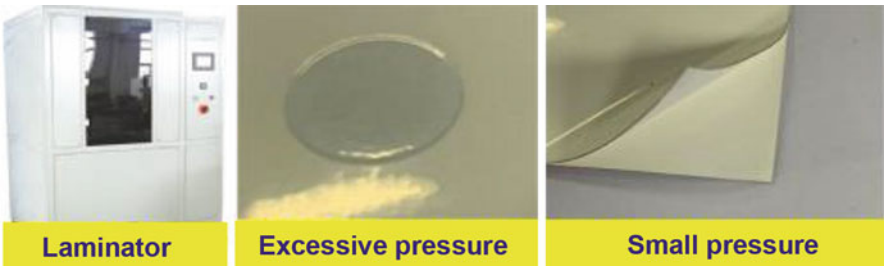

Fig. 10 L/HTCC laminator and its influencing factors

pressure control accuracy of ±50 Psi, a maximum application temperature of 85 °C, and a temperature control accuracy of ±3 °C.

After lamination, the device is sintered at a high temperature, the filled sacrificial layer is burned together with the organic matter in the ceramic sheet to become a gas discharge, and the glass component is melted, so that the ceramic particles are bonded together, and at the same time, the glass composition in the metal paste and the organic binder volatilizes, and the metal particles gradually expand to form a conductor. In the sintering process, it is necessary to explore and grasp the temperature curve, so that the timing of the rubber discharge is consistent with the high-temperature evaporation of the carbon film. The final purpose of the sintering is to turn the laminated raw ceramic into a dense whole and perfect the solid phase. During the sintering process, the melting of the glass components plays a crucial role in the viscous flow of all the components in the raw sheets.

The discharge of the sacrificial layer is related to the high-temperature change characteristics of the green porcelain strip. The green porcelain strip exhibits a loose porous surface state during the debinding process, and when the glass phase in the green belt is completely melted, the green ceramic sheet begins to become dense; therefore, the sacrificial layer needs to be completely discharged at the critical point where the green tape is completely dense. The sacrificial layer volatilizes prematurely, the flexible ceramic layer on the microstructure will collapse, and the sacrificial layer will evaporate too late, the ceramic layer will be dense, and the sacrificial layer will not be discharged. This leads to cracks in the microstructure and even breaks up, as shown in Fig. 11. Therefore, in the sintering process, by adopting a suitable sintering process curve, it is necessary to ensure that the sacrificial layer is fully volatilized before the ceramic sheet becomes dense, and at the same time, the sacrificial layer is prevented from being volatilized too quickly, so that the flexible microstructure cannot be self-supporting to collapse. The equipment shown in Fig. 10 is a LTCC raw belt sintering furnace with a maximum sintering temperature of 1050 °C, a maximum heating rate of 30 °C/min, and a temperature control accuracy of ±3 °C.

For the curved structure, it is necessary to pay attention to the placement of the device during the sintering process and horizontally. Because the curved shape is warped and suspended on both sides, the curvature of the sample will gradually change or even become flat under the influence of gravity during the sintering

Fig. 11 L/HTCC sintering furnace and sintering influencing factors

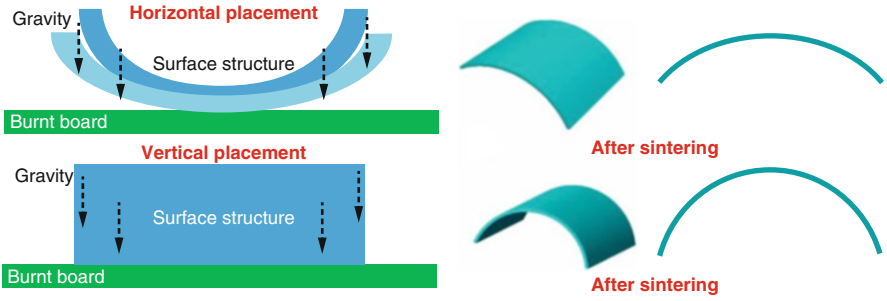

Fig. 12 Influence of placement mode on sintering

process. In response to this problem, the effect of gravity on the surface can be reduced by placing it vertically, as shown in Fig. 12.

Based on the above preparation technology, a C-MEMS device with integrated temperature, pressure, and vibration parameters was prepared, as shown in Fig. 13. In the device, three independent LC-sensitive loops interact with the test antenna through the near-field coupling, respectively. When external factors cause the sensitive capacitance to change, the resonant frequency of the corresponding sensitive loop drifts, thereby detecting the change of the external environment. In the layout design of the sensor, the overlap between the coils is avoided, which is beneficial to weaken the electromagnetic interference between different resonant signals. The final sensor has a test temperature of 20–800 °C and a temperature response sensitivity of 9.13 kHz/°C. After testing, the current vibration signal period is 1.89 s, and the pressure response sensitivity is 13.6 kHz/kPa.

Heterogeneous Material Co-firing Technology

In many special application environments, a single base material or electronic metal paste is difficult to meet the test requirements. For example, during the high-temperature test, the sensitivity of the sensor is not high enough because the

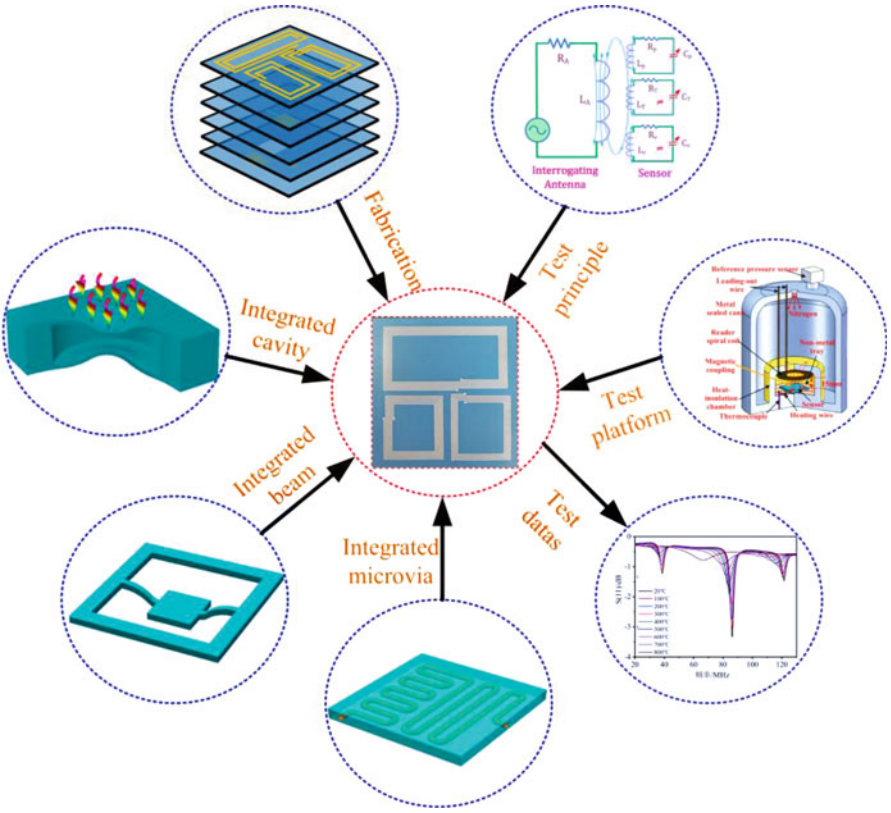

Fig. 13 C-MEMS devices with integrated temperature, pressure, and vibration parameters

dielectric constant of the L/HTCC substrate itself changes slowly with temperature. If a high-temperature substrate whose partial dielectric constant changes rapidly with temperature can be co-fired with the L/HTCC substrate, the high-temperature test problem can be solved, and high-sensitivity sensing can be realized. Heterogeneous sintering of electronic paste is also a very important technology. For example, in the ultrahigh-temperature test, the thermocouple pair composed of different electronic pastes is tested for temperature. Therefore, the co-firing technology of heterogeneous materials plays a very important role in the testing of special environmental parameters.

Co-firing of Heterogeneous Substrate Materials

The co-firing of the heterogeneous substrate material is a combination of two or more base materials having different compositional compositions by micro-assembly and sintering processes to make them self-contained. Due to the different thermal and mechanical properties of different materials, in the sintering process, as

the temperature increases gradually, the heterogeneous materials may be warped and deformed. In order to avoid the above situation, it is necessary to study the sintering mechanism of the heterogeneous material. Combining thermal material analysis and sintering kinetics analysis, the sintering kinetics model of heterogeneous co-firing was established to provide a basis for the optimization of multi-material heterogeneous co-firing system. The composition and microstructure of the co-firing interface of heterogeneous materials were studied. The interface behavior during the co-firing process of the material is combined with the electrical-mechanical performance test to study the influence mechanism of the interface properties of the heterogeneous material on the mechanical and electrical properties of the L/HTCC ceramic MEMS device. The specific heterogeneous material co-firing research process is shown in Fig. 14.

The biggest difficulty in co-firing of heterogeneous ceramic materials lies in the different heat shrinkage rates and shrinkage directions of different materials. For the same ceramic material, it is only necessary to face the same surface of each layer of substrate in one direction during lamination, so that it can be guaranteed. During the sintering process, the green tape shrinks in the same direction without arching or cracking. For heterogeneous materials, different shrinkage rates result in different rates of shrinkage and shrinkage of the foreigner strip, resulting in shear stress in the horizontal direction, resulting in tearing of the substrate. In addition, if the heterogeneous layer material shrinks in the opposite direction, the critical surfaces of the two materials will generate vertical stress, causing the substrate to swell and rupture. Figure 15 shows the situation after the zirconia green tape is laminated and sintered with the alumina green tape. After lamination, the heterogeneous layer is physically bonded, and the substrate appears to have formed a whole, but after the sintering process, due to the different heat shrinkage rate and shrinkage direction, the aluminum oxide layer is completely separated from the zirconia layer, and the heterogeneous layer is broken due to the existence of shear stress, as shown in Fig. 15.

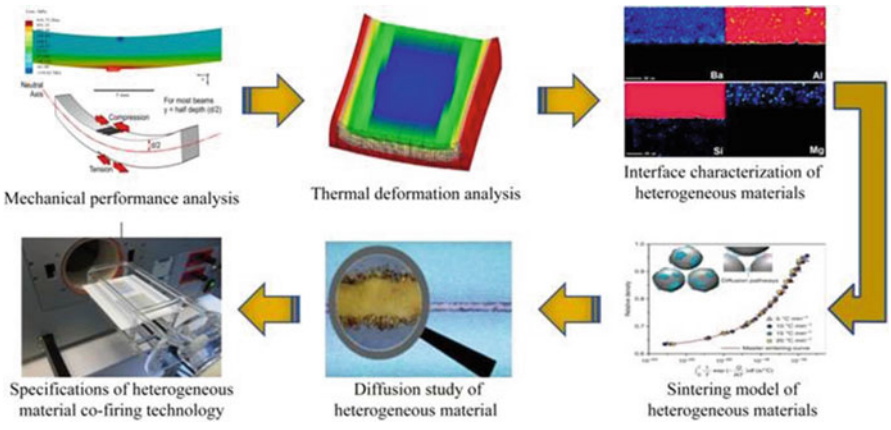

Fig. 14 Study on heterogeneous co-firing mechanism

Fig. 15 Co-firing of alumina and zirconia

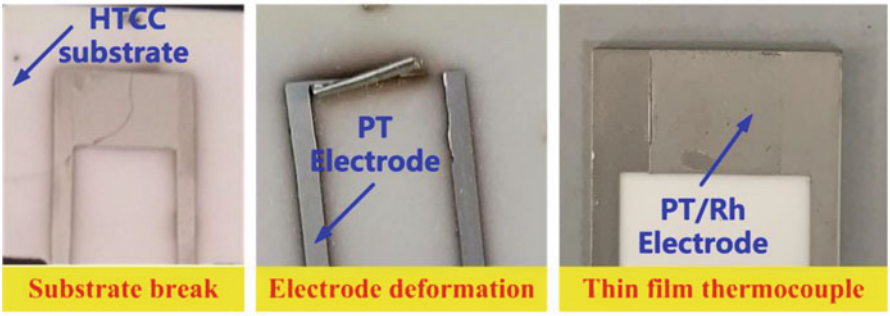

Fig. 16 Heterogeneous co-fired electronic paste

Electronic Paste Heterogeneous Co-firing

The heterogeneous slurry is formed on the surface of the medium by screen printing. Due to the different thermodynamic properties of the different slurry and the substrate medium, the substrate may even rupture during the sintering process, as shown in Fig. 16. Different pastes are in contact with each other by a silk screen process, and after high-temperature sintering, different thermal stresses cause the heterogeneous electrodes to fall off, causing the device to fail.

In the sintering process, on the one hand, the sintering process curve should be adjusted to ensure that the chemical changes between different slurries and between the slurry and the substrate can be carried out slowly and stably, preventing excessive chemical reactions and reducing the mechanical properties of the materials. Slowing the sintering rate of the substrate or slurry during the debinding process, the organic matter discharged through the block causes the metal electrode to warp or even fall off; on the other hand, it can be offset by the external physical pressure to offset the high temperature between different materials. Thermal stress plays an important role in the preparation of sensors, as shown in Fig. 17, since the weight of the base material itself is much larger than that of the electronic paste, in the sintering process, the electronic paste may be placed facing the burning plate and the substrate facing upward, using the substrate itself.

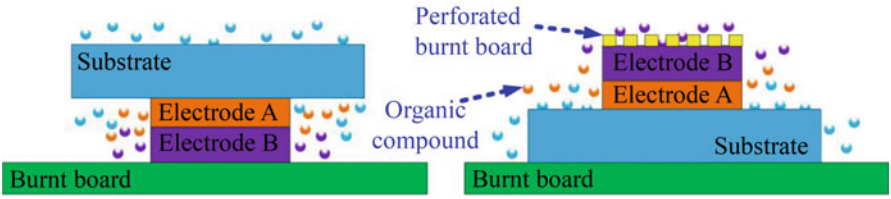

Fig. 17 Heterogeneous co-firing placement

Fig. 18 Plate for heterogeneous co-firing

The weight is used to offset the thermal stress between the different electrodes. It should be noted that when placed in this way, the setter is to be polished, as shown in Fig. 18, to prevent the metal paste and the setter during the sintering process. Bonding results in damage to the circuit structure. Generally, in order to ensure the metal electrode and the debinding of the substrate, the substrate is placed facing the burning plate downward and the metal electrode upward, and at the same time, the metal electrode and the substrate material are pressed by the hole-bearing plate. This can offset the thermal stress from different materials due to the difference in thermodynamic properties while ensuring that the metal paste is fully degreased.

Integration of Multiple Processing Technologies

L/HTCC process technology can realize the preparation of ceramic-based devices, screen printing technology reduces the cost of ceramic metallization, and the sintering process can achieve complete bonding of metal circuits and ceramic substrates. However, for some metal or heterogeneous substrates with low melting point or poor matching ability with ceramic substrates, bonding cannot be achieved by sintering process. Therefore, only a combination of various MEMS processing technologies can solve the above problems.

In the special test environment, traditional silicon-based integrated circuit components are prone to failure. Various types of gate circuits composed of ceramic-based

diodes and transistors can replace silicon-based circuit components, solving the problem that silicon-based devices cannot achieve normal operation and operation under special environments. However, in the preparation process of the transistor, due to the limitation of the material itself, the heterogeneous material cannot be formed by the sintering process, and the photolithography sputtering process can avoid the erosion of the material by the high temperature and achieve the bonding of different materials. This part takes ceramic-based transistors as an example to illustrate the C-MEMS devices formed by the combination of L/HTCC process and photolithography and sputtering processes.

The ceramic-based film diode needs to integrate different metal materials and semiconductor materials on the ceramic substrate. Due to the characteristics of the semiconductor material and the thickness of the metal layer, it cannot be formed by screen printing and high-temperature sintering. The ceramic-based thin film diode structure is shown in Fig. 19. The ideal barrier height of Schottky diode is the difference between the metal and semiconductor work function, but the actual barrier height is not only related to the preparation material but also affected by the preparation conditions and process. Although the alumina ceramic sheet has a high hardness, it is brittle and brittle when the thickness is thin, so care must be taken during cleaning. In addition, the cleanliness and roughness of the substrate have a great influence on the workability of the semiconductor device. When cleaning, a plurality of ceramic sheets was placed in a petri dish. Figure 20 is a surface top view of a mirror-polished 96% Al_2O_3 ceramic observed by SEM. It can be seen that even with mirror polishing, there are many micropores of about 2–3 μm on the surface of alumina, which is three orders of magnitude larger than that of standard polished

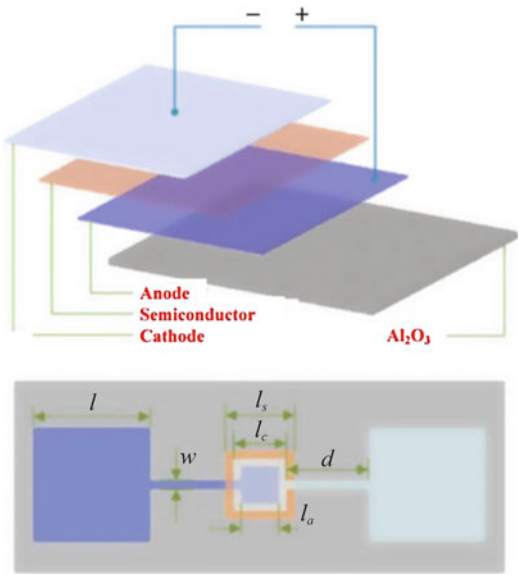

Fig. 19 Ceramic-based thin film diode structure

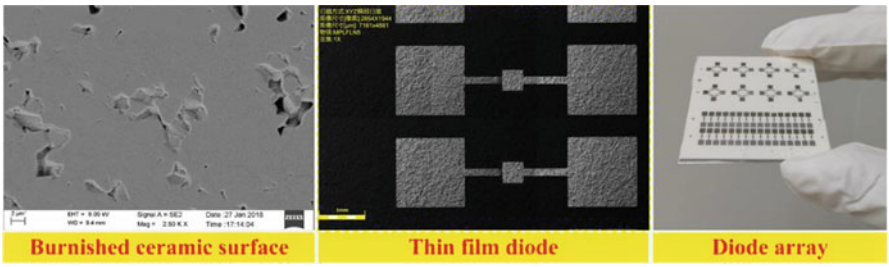

Fig. 20 Ceramic-based thin film diode

silicon wafers and silicon carbide. This is also one of the challenges in fabricating MEMS devices on high-temperature-resistant alumina ceramics.

C-MEMS High-Temperature Device

Based on the above process and manufacturing technology, C-MEMS high-temperature devices were fabricated and tested at high temperature to confirm that the C-MEMS devices based on the above manufacturing process can meet the parameter testing requirements in special environments.

C-MEMS devices with integrated microstructures and circuits: Based on the L/HTCC process, an LC wireless passive temperature-pressure dual-parameter sensor is designed and fabricated (Ji et al. 2018; Li et al. 2014; Lu et al. 2018; Qiulin et al. 2018; Tan et al. 2015, 2017b, 2018).

The sensor compensates the temperature drift of the pressure signal through the temperature-sensitive unit to achieve accurate calibration and measurement of the sensor. The sensor structure and test results are shown in Fig. 21. The sensor pressure-sensitive film thickness is 100 μm, so the sensor pressure response sensitivity is higher. The temperature-sensitive loop does not overlap spatially with the pressure-sensitive loop, which greatly facilitates weakening crosstalk between the coils. The sensor temperature response sensitivity is 11.33 kHz/°C, and the pressure response sensitivity at room temperature is 73.59 kHz/kPa. At 1100 °C, the pressure response sensitivity increases to 92.98 kHz/kPa.

Heterogeneous substrate co-fired C-MEMS devices: The LTCC/ferroelectric ceramic heterogeneous co-fired LC wireless passive temperature sensor enables longer test distances and higher sensitivity temperature tests. On the basis of the L/HTCC ceramic micro-assembly process, the ferroelectric ceramic is filled into the LTCC substrate. Since the dielectric constant of the ferroelectric ceramic changes with temperature, when the external temperature changes, the capacitance in the sensor LC circuit changes, causing the sensor resonance frequency to change. Figure 22 shows the structure of a LTCC-based temperature sensor filled with ferroelectric ceramics. By adjusting the sintering process, the ferroelectric ceramics and the LTCC substrate are completely bonded. The two materials permeate each

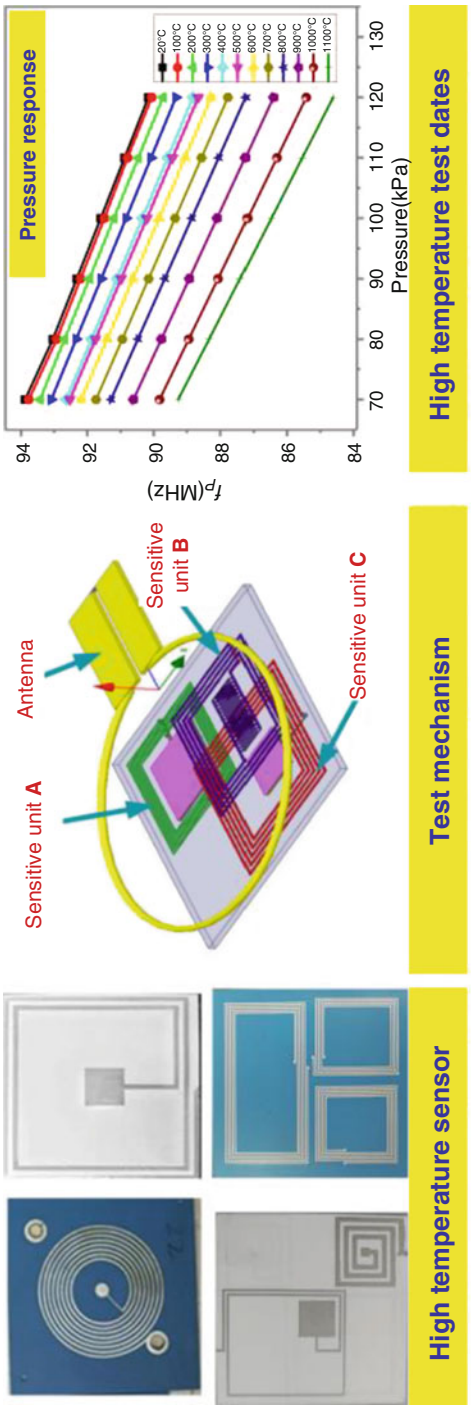

Fig. 21 Passive ceramic-based LC sensor

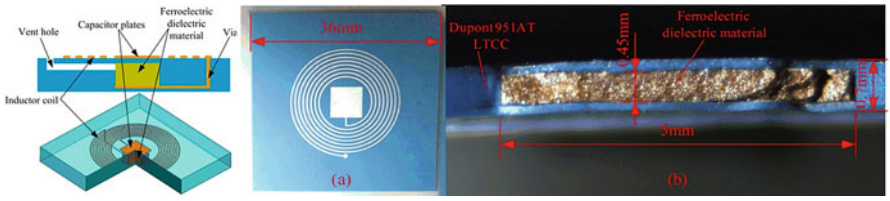

Fig. 22 LC temperature sensor for co-firing of heterogeneous substrates

other, and there is no deformation or crack due to different materials. The heterogeneous co-fired C-MEMS device finally achieved a 700 °C high-temperature test, and the sensor frequency sensitivity was 12.14 KHz/°C over the entire test range (Tan et al. 2014).

Heterogeneous slurry co-fired C-MEMS devices: The heat flow sensor structure formed by co-firing platinum and platinum rhodium paste is composed of thermocouple, distributed on the top and bottom of the ceramic substrate. The sensor structure is shown in Fig. 23 (Lyu et al. 2018). Low thermal conductivity insulators are used to create temperature differences, which increase the electromotive force output and increase sensitivity. The Pt electrode and the Pt/Rh electrode were well connected after sintering at 1350 °C, and the thickness and width of the thermocouple electrode were 22.59 μm and 195.71 μm, respectively. The test results show that the sensor's maximum electromotive force output is as high as 6.74 mv and the temperature sensitivity is about 8.9 μV/°C, which has high sensitivity in a given heat flow range.

C-MEMS devices combined with photolithography and sputtering processes: The Pt/a-IGZO/Al diode was successfully fabricated on Al_2O_3 substrate and tested by I-V at 20–400 °C (Guo et al. 2019). The diode can work stably at 21–400 °C. At the same time, a thin film transistor suitable for up to 250 °C was fabricated on an alumina ceramic substrate using MEMS technology, and a thin film transistor based on a ceramic material is shown in Fig. 23. The test results show that the device has good electron mobility and stability, the mobility μsat decreases from 263.1 (293 K) to 250.3 (523 K), and the subthreshold swing SS increases with temperature, increased from 83.4 mV/dec to 136.4 mV/dec, and on this basis, digital logic circuits such as inverters, NAND gates, and AND gates that can operate at higher temperatures are designed and tested (Fig. 24).

Langasite Device Processing and Manufacturing Methods

Langasite (LGS) devices are mainly based on hard and brittle materials, such as platinum (Pt), rhodium (Rh), iridium (Ir), and PtIr, TiN, WC, and other composite materials which are commonly used at high temperatures as electrode materials (Hornsteiner et al. 1998). This kind of device is mainly manufactured by hot pressing

Fig. 23 Heterogeneous slurry co-fired ceramic-based heat flow sensor

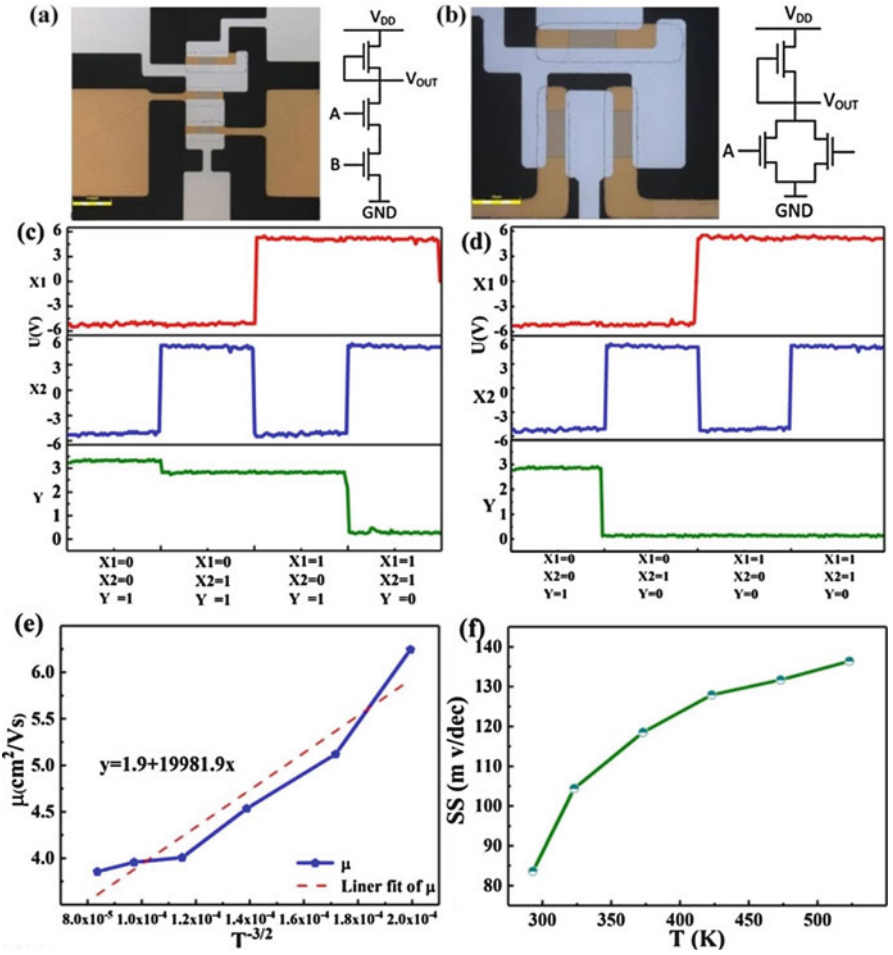

Fig. 24 Ceramic-based thin film transistor structure

process in high temperature, mainly involving the manufacturing process including etching, polishing, bonding, and other technologies.

High Temperature Forming Mechanism

Wet Etching Mechanism

Wet etching refers to the process of systematically removing materials by immersing solid materials in liquid. Its removal rate can be adjusted by temperature. It is easy to control the shape and thickness of the film. Wet etching can be divided into two categories: isotropic etching and anisotropic etching. Isotropic etching refers to the

removal of materials in all directions at the same speed. Most etchants belong to this category. Anisotropic etching is a process in which etchants remove materials at different speeds according to the exposed crystal plane (Gaura and Newman 2006).

Wet chemical etching of $La_3Ga_5SiO_{14}$ is usually carried out in a mixed solution of HCL and HF. The specific process is as follows: Firstly, $La_3Ga_5SiO_{14}$ reacts with HCL.

$$La_3Ga_5SiO_{14} + HCl + H_2 \rightarrow SiO_2 + (LaCl_3 + H_2O) + GaCl_3 \quad (1)$$

Then, hydrofluoric acid removes silicon oxide.

$$SiO_2 + 6HF \rightarrow H_2SiF_6 + 2H_2O \quad (2)$$

Therefore, the total reaction equation is obtained by etching langasite in the mixed solution of HCL and HF, as shown in Fig. 25.

$$La_3Ga_5SiO_{14} + HCl + HF + H_2O \rightarrow H_2SiF_6 + (LaCl_3 + 7H_2O) + GaCl_3 \quad (3)$$

The effects of hydrofluoric acid and hydrochloric acid solutions with different concentrations on corrosion rate and roughness were studied. The results show that the combined corrosion rate of hydrofluoric acid and hydrochloric acid can reach about 60 mm/h when HF accounts for 10% of the solution, and the batch microfabrication can be realized. At this time, the roughness is about 200 nm, which still meets the design requirements. In addition, the mixed solution of hydrofluoric acid

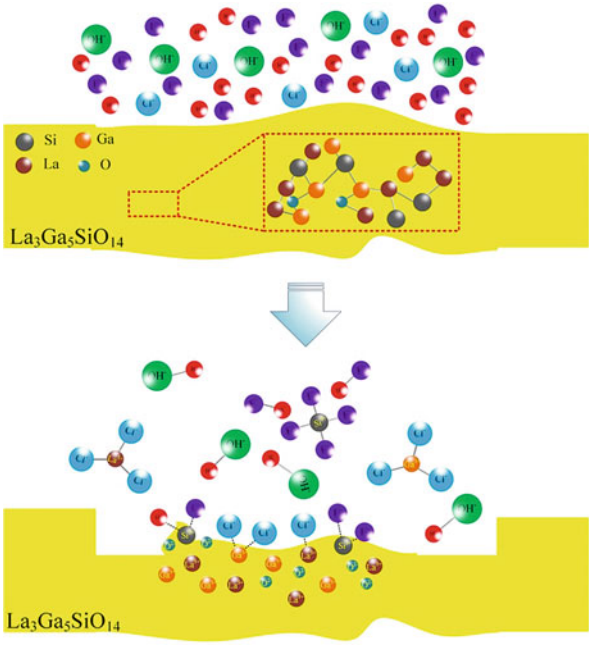

Fig. 25 Wet etching schematic of LGS

and hydrochloric acid can achieve isotropic corrosion of $La_3Ga_5SiO_{14}$, which helps to reduce the roughness of the device (Ansorge et al. 2011).

Dry Etching Mechanism

Dry etching refers to the removal of materials by chemical reaction between a low-pressure gas and the base (Gaura and Newman 2006). Inductively coupled plasma etch (ICPE) is the result of the interaction of chemical and physical processes. Its basic principle is that the RF generated by ICP RF power supply is output to the ring coupling coil under vacuum and low pressure. A high-density plasma is produced by coupling glow discharge of coil etched gas in a certain proportion. The plasma bombards the substrate surface under RF (radio frequency) of the lower electrode. The chemical bond of the semiconductor material in the pattern area of the substrate is interrupted, and the volatile substance is formed with the etched gas, which is separated from the substrate in the form of gas and extracted from the vacuum pipeline. Figure 26 shows an Oxford instruments ICP CVD.

Dry etching of $La_3Ga_5SiO_{14}$ is usually done by Cl2/Ar ICP. As the rate of vapor phase corrosion increases linearly with the increase of chlorine content in plasma (from 20% to 70%), it is inferred that Cl2 is chemically corroded to the material. Physical sputtering of $La_3Ga_5SiO_{14}$ and corrosion residues is caused by Ar gas (Giehl et al. 2003). The reaction equation is described as follows (Cho et al. 2007).

$$La_3Ga_5SiO_{14} + 13Cl_2 \rightarrow 3LaCl_3 + 3GaCl_3 + 2GaCl_2 + SiCl_4 + 7O_2 \quad (4)$$

In the process of Cl_2/Ar ICP discharge, the etching rate of single crystal $La_3Ga_5SiO_{14}$ wafer is affected by plasma composition, plasma source power, and radio frequency chuck power. The maximum corrosion rate can reach 160 nm/min at relatively high source power (~1000 w) or high Cl_2 content. In most cases, the surface roughness of etched $La_3Ga_5SiO_{14}$ is similar to or even better than that of non-etched wafers.

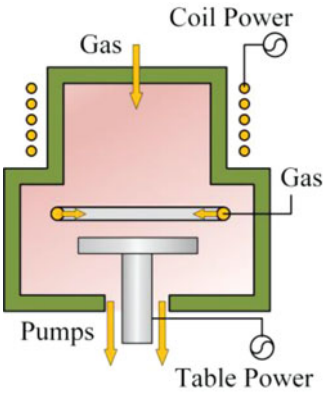

Fig. 26 Oxford instruments ICP CVD

Bonding Mechanism

Bonding refers to the process of making patterns on the substrates of several materials and contacting them closely to form a complex structure (Gaura and Newman 2006). The most commonly used wafer bonding types in microstructural fabrication can be divided into three categories: direct bonding, anodic bonding, and interlayer bonding. Among them, direct bonding is most commonly used. Direct bonding refers to the direct contact of wafers .There is no intermediate layer, adherence of smooth surfaces, and some form of thermal cycle after contact to improve bonding strength. The highest annealing temperature is below 450 °C or above 800 °C (Schmidt 1998).

Direct bonding consists of three steps: surface preparation, pre-bonding, and permanent bonding. The first step is surface preparation. The process is to clean two wafers to make their surfaces smooth enough to form a hydrated surface. The second step is pre-bonding. In a clean environment, two wafer surfaces are contacted and pressed together by gentle pressure at a central point to form a bond between OH bases on the relative surface. The contact points are bound by the surface gravity of two water-bearing surfaces. The contact waves start from this point and sweep across the wafer surface to make them close to each other on the whole surface. The third step permanent bonding is to heat the wafer and expel water molecules from the system to form strong bonds. The usual annealing temperature is between room temperature and 1200 °C.

According to the above direct bonding process, the LGS bonding process is as shown in Fig. 27, firstly performing hydrophilic treatment, so that the surface of the substrate adheres to the -OH group, and then pre-bonding, so that the two surfaces are in close contact, and finally the high-temperature annealing is performed to achieve permanent bonding.

Among them, the pre-bonding and high-temperature bonding process is completed in the temperature-pressure integrated controllable loading vacuum hot-pressing furnace independently developed by North University of China, as shown in Fig. 28. The furnace can also be used for pressure sintering of various ceramics and nano-materials. The high-temperature furnace device heats the LGS substrate through an electrode and adjusts the heating rate by controlling the power.

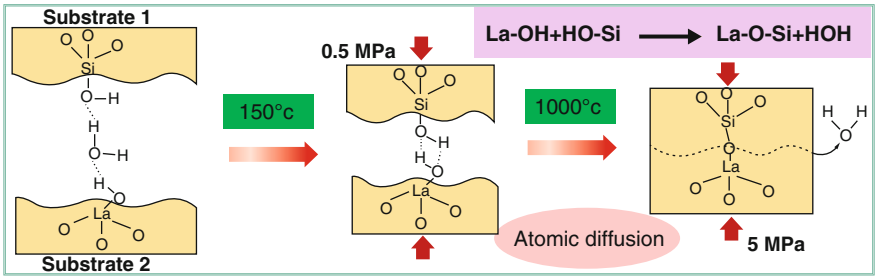

Fig. 27 Inductively coupled plasma etching of LGS

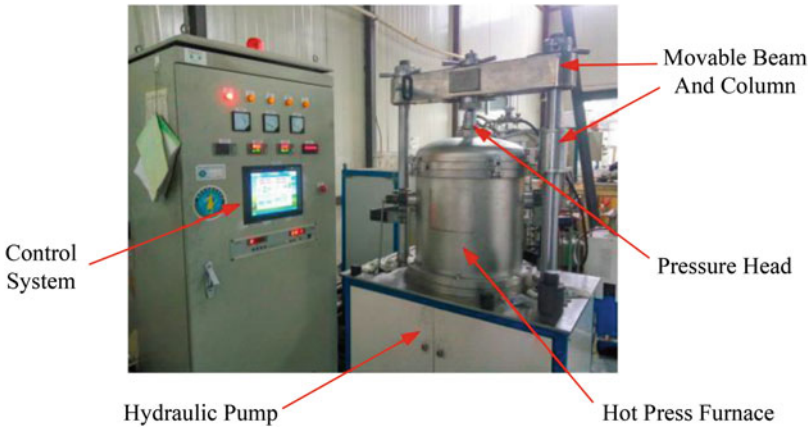

Fig. 28 The temperature-pressure integrated controllable loading vacuum hot-pressing furnace (Li et al. 2017)

Pressure is applied to the workpiece by a hydraulic pump and pressure head displacement control system. In addition, in order to ensure the verticality, a column connection is also provided on the table and the movable beam of the hot press furnace. Most importantly, the hot press furnace can provide a vacuum environment for the substrate bonding to form a vacuum-sealed cavity, which is beneficial to improve the performance of the sensor device.

LGS Device Sealed Cavity Manufacturing Technology

The formation of LGS sealed cavity is a key problem that SAW multiparameter sensor needs to solve urgently in harsh environments such as high temperature, high rotation, and high pressure. First, the etching of the LGS cavity can be achieved by two methods: wet etching and inductively coupled plasma (ICP) etching, followed by surface polishing and bonding to complete cavity fabrication.

Wet Etching Process

The specific process steps of wet etching are shown in Fig. 29:

1. First, the gallium silicate lanthanide wafer was cleaned with acetone, isopropyl alcohol, and a mixed solution of H_2O_2 and H_2SO_4 and heated at 150 °C for 20 min to remove the organic matter remaining on the surface of the gallium silicate.
2. SU-8 photoresist was spin coated onto the surface of the gallium silicate germanium wafer. Among them, the thickness of the photoresist is 200 μm, which prevents the adhesion problem caused by the passage of acidic molecules through

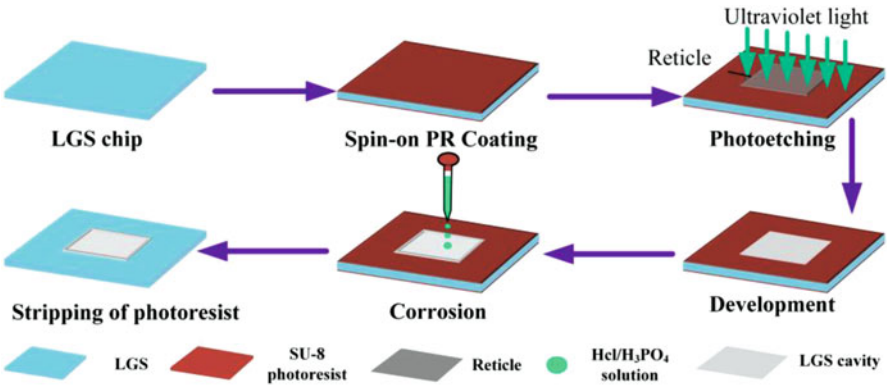

Fig. 29 Wet etching process flow chart of LGS

the photoresist. In order to solve the problem of poor adhesion of the photoresist to the edge of gallium silicate, an HDMS layer is deposited on the surface of the gallium silicate wafer to enhance the adhesion of the photoresist.

3. Place a reticle, perform photolithography, develop, and clean it with deionized water.
4. Prepare a mixed solution of hydrochloric acid and hydrofluoric acid (HCl:HF: $H_2O = 1:1:2$), and heat to 80 °C. The LPS coated with photoresist is etched. This acid mixture makes the surface of LGS smooth and has a faster corrosion rate; HF can dissolve the SiO_2 formed by the reaction, maintaining the surface flatness of the LGS wafer. The temperature in the reaction tank has an important influence on the corrosion rate.
5. After the gallium silicate ruthenium is etched for a period of time, it is cleaned by deionization, then the SU-8 photoresist is peeled off, the corrosion effect is observed by a microscope, repeated tests are performed to determine the optimal etching time of the LGS, and finally the obtained LGS cavity is required.

Inductively Coupled Plasma (ICP) Etching Process

Using inductively coupled plasma (ICP) etching, as shown in Fig. 30, the substrate is cleaned with deionized water, alcohol, and acetone to remove dust, oil, and organic matter from the surface of the piezoelectric substrate; using silicon dioxide as a hard mask material, the LGS wafer with a mask is placed in a plasma etching zone, and ions in the gas in the reaction chamber are bombarded by the flat pressure of the reaction chamber to form a damaged layer.

Thereby, the free reactive groups in the plasma are accelerated on the surface thereof, and the ion bombardment reflects the anisotropy of the dry etching, and the reaction of the free radicals is well suppressed due to the deposition of the sidewalls. The LGS cavity is etched by continuously adjusting the process chamber pressure, the upper RF source power, the lower RF source power, the helium back pressure, and the flow rate. Due to the unique combination of physical and chemical reactions

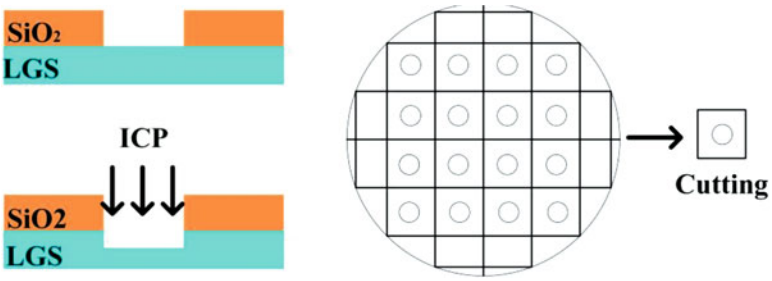

Fig. 30 Plasma etching process of LGS

of dry etching, the size and shape of the pattern can be precisely controlled under the interaction of anisotropic and isotropic.

Surface Polishing and Bonding Process

The three-dimensional structure of the LGS with the sealed cavity is realized by bonding with the etched LGS cavity. Prior to bonding, the pre-bonded LGS substrate is first surface-polished to reduce the surface roughness of the substrate, followed by a hydrophilic surface treatment including wet cleaning and plasma treatment. The LGS substrate was wet-cleaned with acetone, alcohol, piranha solution (SPM), standard cleaning solution No. 1 (SC1), diluted hydrofluoric acid solution, and deionized water. Subsequent surface activation of the LGS substrate by oxygen plasma can also achieve the purpose of eliminating wafer surface contamination and further reducing surface roughness.

After the above surface treatment, direct pre-bonding is performed by using the polished surfaces of the two LGS substrates, as shown in Fig. 31a. The pre-bonded sample is fixed in a graphite mold and then placed in a sleeve and fixed in a sintering furnace to pressurize the upper and lower surfaces in the vertical direction, and the whole is subjected to a heating experiment to achieve permanent bonding of the sample, thereby obtaining a sealed LGS cavity. In the pre-bonding process, the -OH groups of the two bonding faces are bonded, and in a high-temperature environment, water molecules between the two bonding faces are ejected to form a permanent bond. As shown in Fig. 31b, a sealed cavity is formed.

LGS Device Surface Graphic Manufacturing Technology

Integrated design of SAW multiparameter resonator/antenna is based on LGS piezoelectric material. The three-dimensional structure of LGS with sealed cavity is realized by inductively coupled plasma etching technology and bonding process, the back-receiving antenna is fabricated by screen printing process, and the electrode surface acoustic wave resonator is fabricated by ion plating process. Figure 32 is a

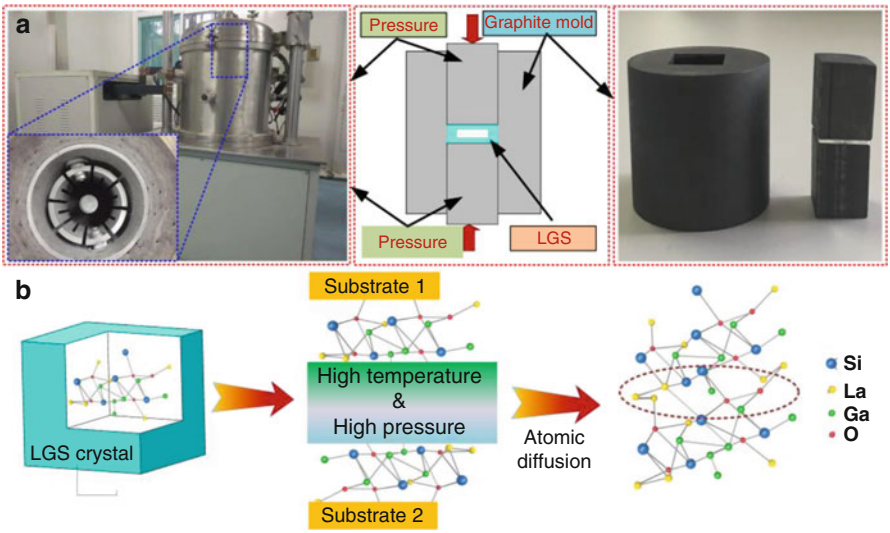

Fig. 31 (**a**) Bonding process of LGS cavity; (**b**) schematic diagram of atomic diffusion

process flow diagram of the SAW multiparameter resonator/antenna integrated fabrication. This method is applicable to the manufacture of all surface acoustic wave sensors. The specific steps are as follows:

1. Experimental preparation and pretreatment: The base piezoelectric material used in the experiment was washed with freshly prepared piranha solution for 15 min, ultrasonically washed with ethanol for 5 min, and ultrasonically cleaned with acetone for 5 min. Finally, the surface of the deionized water is ultrasonically cleaned for 5 min to clean the surface, which can effectively remove the adhesion of organic substances (such as grease) on the surface of the piezoelectric substrate and enhance metal adhesion in subsequent metal sputtering.
2. The fabrication of the cavity: the manufacture of the LGS sealed cavity by wet etching and plasma etching combined with bonding process.
3. Mask electrode fabrication: A photoresist is coated on the surface of the piezoelectric material, and a mask having an electrode pattern is overlaid on the surface of the photoresist and exposed to ultraviolet light. After the exposed photoresist is subjected to development processing, a mask pattern window is formed on the photoresist.
4. Fabrication of the antenna: The screen printing process was carried out by using a platinum-rhodium paste to realize the antenna printing on the lower surface of the piezoelectric material and placed in a muffle furnace at a low temperature of 100 °C for low-temperature sintering.
5. Lead connection: The through hole is filled with platinum paste to realize the electrical connection between the antenna and the SAW sensor, and the whole device is placed in a high-temperature sintering furnace to be sintered according to a specific heating curve.

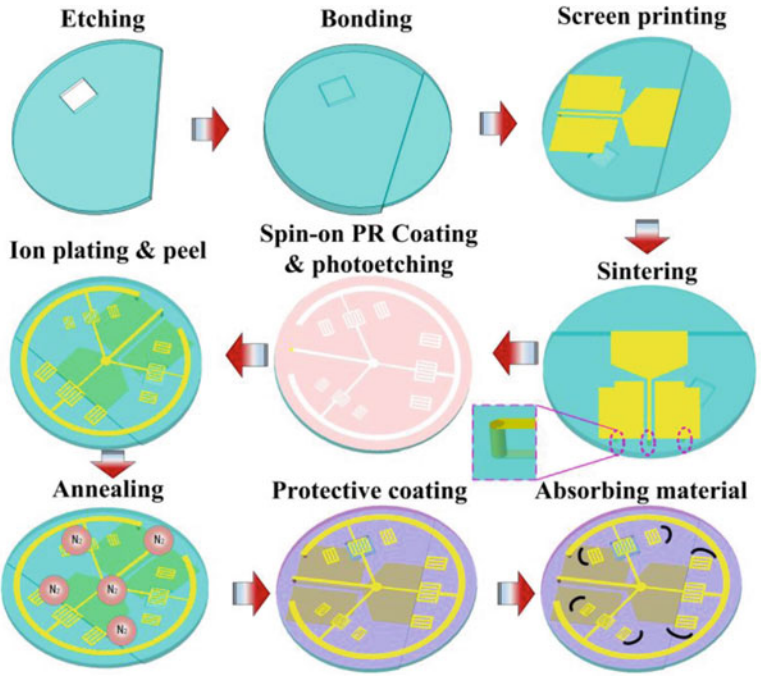

Fig. 32 Integrated multiparameter SAW sensor/antenna integrated manufacturing process

6. Fabrication of surface electrode: The metallization of the surface acoustic wave sensor platinum-ruthenium electrode is realized by ion plating process, and the ion plating device is developed in acetone to obtain a complete metallized electrode.
7. Annealing treatment: The surface acoustic wave device is treated by annealing. First, rapid annealing is performed in an N2 atmosphere to form an ohmic contact between the electrode and the substrate material, thereby improving the electrical performance of the electrode. Then, the device is placed in a high-temperature furnace for conventional annealing, and the electrode is aged to improve the stability of the electrode in a high-temperature environment.
8. A protective layer film and an absorbing material are applied to the surface of the LGS.

SAW Temperature and Pressure Integrated Devices

The lithium niobate-based SAW temperature and pressure integrated sensor based on the above process are shown in Fig. 33. Among them, the temperature sensor can measure 25–325 °C. The resonance frequency decreases with the increase of temperature, showing a negative temperature change trend. The temperature sensitivity

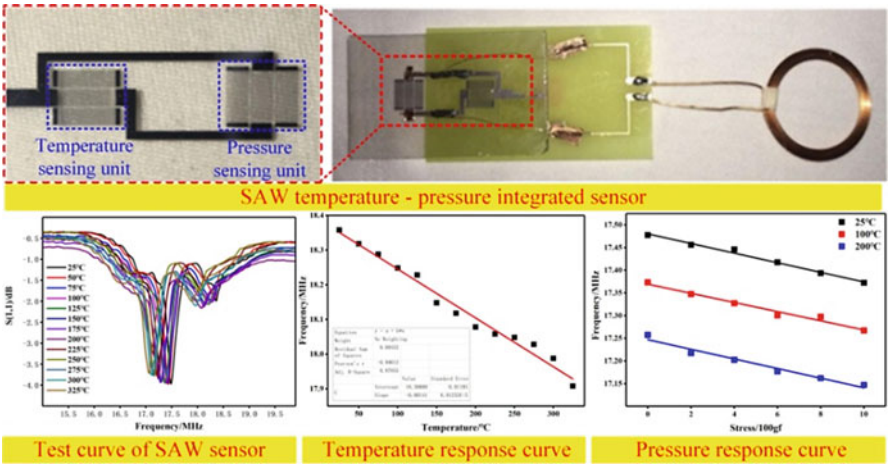

Fig. 33 SAW temperature and pressure integrated device

of the temperature resonator is 1.41 KHz/°C, and the temperature sensitivity of the pressure resonator is 1.34 KHz/°C. The test range of the pressure sensor is 0–1000 gf, and the maximum sensitivity of the pressure at 25–200 °C is 10.6 KHz/100 gf.

Conclusion

This chapter introduces the flexible material processing and manufacturing technology represented by C-MEMS devices and the hard and brittle material processing and manufacturing technology represented by LGS devices. C- MEMS devices can be fabricated by a mature L/HTCC micro-assembly process. Combined with heterogeneous co-firing and traditional MEMS processes, multifunctional integrated devices can be fabricated. However, compared to conventional silicon devices, the miniaturization process of C-MEMS devices still needs to be improved. LGS devices currently have processing techniques such as wet etching, inductively coupled plasma etching, bonding, etc. Although LGS devices can be processed, how to process high-precision, miniaturized, and integrated devices still faces serious challenges. For example, in the process of wet etching, how to configure the solution ratio so that the corrosion rate can be controlled and the surface roughness can be reduced to realize the balance between work efficiency and finished product quality is one of the difficulties; in inductively coupled plasma etching, it is also a difficult problem that how to control the composition of the etching gas, the power of the plasma source, and the power of the RF chuck to realize the precise etching of the langasite micro-/nano-structure, and in the bonding process, how to eliminate the voids formed during the high-temperature annealing is also an urgent problem to be solved.

References

Anonymous (2017) 33rd AIAA aerodynamic measurement technology and ground testing conference, 2017. In: 33rd AIAA aerodynamic measurement technology and ground testing conference, 2017, June 5, 2017–June 9, 2017. American Institute of Aeronautics and Astronautics, AIAA, Denver

Ansorge E, Schmidt B, Sauerwald J, Fritze H (2011) Langasite for microelectromechanical systems. Phys Status Solidi 208:377–389

Cheng H, Ebadi S, Ren X, Yusuf Y, Xun G (2011) A compact wireless passive sensing mechanism based on a seamlessly integrated resonator/antenna. In: IEEE international symposium on antennas & propagation

Cheng H, Ebadi S, Xun G (2012) A low-profile wireless passive temperature sensor using resonator/antenna integration up to 1000 celsius. IEEE Antennas Wirel Propag Lett 11:369–372

Cho H, Lee DM, Hwang S, Lee BW, Shim KB, Pearton SJ (2007) Post-CMP dry etching for the removal of the nanoscale subsurface damage layer from a single crystal $La_3Ga_5SiO_{14}$ for a high quality wide band SAW filter device. J Ceram Process Res 8:98–102

Diem B, Rey P, Renard S, Bosson SV, Bono H, Michel F, Delaye MT, Delapierre G (1995) SOI 'SIMOX'; from bulk to surface micromachining, a new age for silicon sensors and actuators. Sensors Actuators A Phys 46:8–16

Gaura E, Robert N (2006) Artificial Intelligence techniques for microsensors identification and compensation. Smart MEMS and Sensor Systems. pp 305–368

George T, Son KA, Powers RA, Castillo LYD, Okojie R (2005) Harsh environment micro-technologies for NASA and terrestrial applications. In: SENSORS, 2005 IEEE, p 6

Giehl AR, Kessler M, Grosse A, Herhammer N, Fouckhardt H (2003) Deep reactive ion etching of GaSb in Cl_2/Ar-plasma discharges using single-layer soft mask technologies. J Micromech Microeng 13:238

Guo Q, Lu F, Tan Q, Zhou T, Xiong J, Zhang W (2019) Al2O3-based a-IGZO Schottky diodes for temperature sensing. Sensors 19:224

Hornsteiner J, Born E, Fischerauer G, Riha E (1998) Surface acoustic wave sensors for high-temperature applications. In: IEEE international frequency control symposium

Jatlaoui MM, Pons P, Aubert H (2007) Radio frequency pressure transducer. In: 37th European microwave conference, EUMC, October 9, 2007–October 12, 2007. IEEE Computer Society, Munich, pp 736–739

Jatlaoui MM, Chebila F, Pons P, Aubert H (2008a) Pressure sensing approach based on electromagnetic transduction principle. In: 2008 Asia Pacific microwave conference, APMC 2008, December 16, 2008–December 20, 2008. Institute of Electrical and Electronics Engineering of Computer Society, Hong Kong

Jatlaoui MM, Pons P, Aubert H (2008b) Pressure micro-sensor based on radio-frequency transducer. In: International microwave symposium digest

Jatlaoui MM, Chebila F, Pons P, Aubert H (2009) New micro-sensors identification techniques based on reconfigurable multi-band scatterers. In: Asia Pacific microwave conference 2009, APMC 2009, December 7, 2009–December 10, 2009. IEEE Computer Society, Singapore, pp 968–971

Jatlaoui MM, Chebila F, Pons P, Aubert H (2011) Working principle description of the wireless passive EM transduction pressure sensor. Eur Phys J-Appl Phys 56:13702

Ji Y, Tan Q, Wang H, Lv W, Dong H, Xiong J (2018) A novel surface LC wireless passive temperature sensor applied in ultra-high temperature measurement. IEEE Sensors J 18:105–112

Li C, Tan Q, Zhang W, Xue C, Li Y, Xiong J (2014) Microfabrication of a novel ceramic pressure sensor with high sensitivity based on low-temperature co-fired ceramic (LTCC) technology. Micromachines 5:396–407

Li W, Liang T, Chen Y, Jia P, Xiong J, Hong Y, Lei C, Yao Z, Qi L, Liu W (2017) Interface characteristics of Sapphire direct bonding for high-temperature applications. Sensors 17:2080

Liu C, Tong F (2015) An SIW resonator sensor for liquid permittivity measurements at C band. IEEE Microw Wirel Components Lett 25:751–753

Lu F, Wang H, Guo Y, Tan Q, Zhang W, Xiong J (2018) Microwave backscatter- based wireless temperature sensor fabricated by an alumina-backed au slot radiation patch. Sensors 18:242

Lyu W, Ji Y, Zhang T, Liu G, Xiong J, Tan Q (2018) A novel ceramic-based heat flux sensor applied for harsh heat flux measurement. In: 17th IEEE SENSORS conference, SENSORS 2018, October 28, 2018–October 31, 2018. Institute of Electrical and Electronics Engineers Inc., New Delhi, Defence R and D Organisation (DRDO); et al.; Government of India, Department of Science and Technology; IEEE; IEEE Gujarat Section; IEEE Sensors Council

Qiulin T, Fei L, Yaohui J, Haixing W, Wendong Z, Jijun X (2018) LC temperature- pressure sensor based on HTCC with temperature compensation algorithm for extreme 1100°C applications. Sensors Actuators A Phys 280:437–446

Ren X, Ebadi S, Cheng H, Chen Y, Xun G (2011) Wireless resonant frequency detection of SiCN ceramic resonator for sensor applications. pp 1856–1859

Ren X, Ebadi S, Xun G (2012) A single-antenna wireless passive temperature sensing mechanism using a dielectrically-loaded resonator. In: IEEE international symposium on antennas & propagation

Rodriguez RI, Jia Y (2011) A wireless inductive-capacitive (LC) sensor for rotating component temperature monitoring. Int J Smart Sens Intell Syst 4:325–337

Sabol, Stephen M, Ramesh S, Anand A. Kulkarni (2009) Apparatus and method of monitoring operating parameters of a gas turbine. U.S. Patent No. 7,582,359. 1 Sep. 2009

Schmidt MA (1998) Wafer-to-wafer bonding for microstructure formation. Proc IEEE 86: 1575–1585

Scott S, Peroulis D (2009) A capacitively-loaded MEMS slot element for wireless temperature sensing of up to 300C. In: 2009 IEEE MTT-S international microwave symposium, IMS 2009, June 7, 2009–June 12, 2009. Institute of Electrical and Electronics Engineers, Boston, pp 1161–1164

Tan Q, Luo T, Xiong J, Kang H, Ji X, Zhang Y, Yang M, Wang X, Xue C, Liu J, Zhang W (2014) A harsh environment-oriented wireless passive temperature sensor realized by LTCC technology. Sensors 14:4154–4166

Tan Q, Wei T, Chen X, Tao L, Wu G, Chen L, Xiong J (2015) Antenna-resonator integrated wireless passive temperature sensor based on low-temperature co-fired ceramic for harsh environment. Sensors Actuators A Phys 236:299–308

Tan Q, Luo T, Wei T, Liu J, Lin L, Xiong J (2017a) A wireless passive pressure and temperature sensor via a dual LC resonant circuit in harsh environments. J Microelectromech Syst 26: 351–356

Tan Q, Tao L, Wei T, Liu J, Xiong J (2017b) A wireless passive pressure and temperature sensor via a dual LC resonant circuit in harsh environments. J Microelectromech Syst 26(2):351–356

Tan Q, Wen L, Ji Y, Song RJ, Fei L, Dong H, Zhang W, Xiong J (2018) A LC wireless passive temperature-pressure-humidity (TPH) sensor integrated on LTCC ceramic for harsh monitoring. Sensors Actuators B Chem 270:433

Yanjie G, Fei L, Lei Z, Helei D, Qiulin T, Jijun X (2018) Properties of ceramic substrate materials for high-temperature pressure sensors for operation above 1000°C. Adv Mater Sci Eng 2018:1–6

Zhang S, Yu F (2011) Piezoelectric materials for high temperature sensor. J Am Ceram Soc 94:3153–3170

Zhao Y, Kim SH, Yuan L, Bo P, Wu X, Tentzeris M, Parapolymerou J, Allen MG (2009) A micromachined airflow sensor based on RF evanescent-mode cavity resonator. In: International microwave symposium digest

Environmental Control and Compensation of Precision Machining

16

Bing Li

Contents

Introduction 436
Effects and Control of Thermal Environment 436
The Impact of Thermal Environment 436
Control of Thermal Environment 440
Effect and Suppression of Vibration 440
Effect of Vibration Interference 440
Suppression of Vibration Interference 441
Vibration-Isolating Elements 442
New Developments in Vibration Isolators 444
Airflow and Air Pressure 445
Airflow 445
Air Pressure 447
Other Environmental Factors 448
Electrostatic Field 448
Cleanliness 450
Reference 457

Abstract

In order to meet the requirements of precision machining and ultraprecision machining, and to make the processing accuracy achieve the micron or even sub-micro level, the external environment must be strictly controlled. The external environment refers to the entire external environment that must be controlled, except for the operational experience and technical level of workers and the process system of precision

B. Li (✉)
School of Mechanical Engineering and Automation, Harbin Institute of Technology, Shenzhen, China

State Key Laboratory for Manufacturing Systems Engineering, Xi'an Jiaotong University, Xi'an, Shaanxi, China
e-mail: lb@xjtu.edu.cn

Z. Jiang, S. Yang (eds.), *Precision Machines*, Precision Manufacturing,
https://doi.org/10.1007/978-981-13-0381-4_12

machining and ultraprecision machining. The external environment includes thermal environment, vibration environment, air and air pressure environment, electromagnetic environment, cleanliness, and so on. Different methods of precision machining and ultraprecision machining require different levels of control on different external environments. The external supporting environment that precision machining and ultraprecision machining require to control is only the environment within a local scope, such as indoor environment or the local scope of the processing region. With the continuing accuracy improvement of precision machining and ultraprecision machining, the requirements of the external environment are becoming more and more comprehensive and demanding.

Keywords

Environmental control · Environmental compensation · Thermal environment · Vibration · Air environment

Introduction

Because the environmental impacts in machining workshops are complicated and diversiform (Choat 1972; Manning 1976), each type of influencing factor should be deeply studied. And the requirement of environmental control is listed in Table 1 (Shinno and Hashizume 2002).

In this section, the effects and control of these elements will be analyzed one after the other.

Effects and Control of Thermal Environment

The Impact of Thermal Environment

Temperature

The machining precision of precision machining and ultraprecision machining is closely related with the thermal environment. The major quantities that should be controlled in the thermal environment are temperature and humidity.

Table 1 External environment and control requirements

External supporting environment	Control requirements	External supporting environment	Control requirements
Thermal environment	Temperature, humidity, surface thermal radiation, etc.	Electrostatic environment	Static electricity, electromagnetic waves, radiation, etc.
Vibration environment	Frequency, acceleration, displacement, micro-vibration, etc.	Cleanliness environment	Number of dust particles
Air environment	Cleanliness, airflow velocity, pressure, harmful gas, etc.		

When environment temperature changes, it will first affect the accuracy of equipment machining. For example, the bed of a planning machine is 10 m long and 0.8 m high. When the temperature changes of 1 °C, the thermal deformation of the guide rail will reach up to 0.19 mm. In addition, uneven temperature distribution will also affect the accuracy of the machining equipment. Take a lathe installed near the window, for example. Due to the local exposure to the sun, a temperature difference of 10 °C on two opposite sides of the lathe will be produced, and the lathe deformation can reach up to 0.14 mm/m (Kuznetsov 2015). The deformation starts when the sun rises and peaks at 11 o'clock.

The temperature change not only affects the accuracy of the lathe but also leads to expansion and contraction of the workpiece. For example, when machining the 70 mm × 1650 mm screws with a common precision CNC milling machine, the accumulated error of the workpiece machined in morning 7:30–9:00 and the workpiece machined in afternoon 2:00–3:30 can reach up to 85 μm. However, under constant temperature conditions, the error can be reduced to 40 μm. Therefore, machining and measuring under strictly controlled constant temperature is one of the most important conditions in precision machining and ultraprecision machining.

Length precision measurement is an important guarantee for quiet and ultraprecision machining. Precision measurement of length can be conducted normally only under certain conditions, and temperature is one important condition. Every object will change its size under internal or external temperature imbalance. Therefore, it does not make any sense to specify the exact length of an object without specifying the temperature conditions.

20 °C is an international standard temperature for the measurement of length. The greater the difference between the values of the linear expansion coefficient of the two objects subjected to the length comparison is, the more precisely the temperature of the two objects is required to be equal to 20 °C. Otherwise, the measurement error will occur, which is:

$$\Delta L = L[\alpha_1(\theta_1 - 20) - \alpha_2(\theta_2 - 20)] \tag{1}$$

where L is the length of the measured part (mm).

$\alpha_1$is the linear expansion coefficient of the measuring tool (1/°C).
$\theta_1$is the temperature of the measuring tool (°C).
$\alpha_2$is the linear expansion coefficient of the workpiece (1/°C).
$\theta_2$is the temperature of the workpiece (°C).

It can be inferred, when the temperature of the measuring tool is the same as that of the workpiece, there is:

$$\Delta L = L(\alpha_1 - \alpha_2)(\theta - 20) \tag{2}$$

The above equation means that if the measurement error $\Delta L = 0$, then $\alpha_1 = \alpha_2$ or $\theta = 20^{\circ}$C. We cannot manufacture a corresponding length standard ruler for workpiece built by different materials, so standard temperature control is even more

important (Jędrzejewski and Modrzycki 1997). It determines the precision limit that can be achieved by precision machining and ultraprecision machining. Therefore, machining and measuring under strictly controlled constant temperature is one of the most important conditions in precision machining and ultraprecision machining.

The constant temperature conditions are mainly measured by two standards. One is the constant temperature cardinal number, which refers to the average temperature of the air. Another is the constant temperature precision, which refers to the allowable deviation value compared to the average temperature. As the machining and assembling often take up a very large space, it's too difficult to maintain constant temperature. Particularly, the atmospheric temperature varies greatly in different geographical locations or in difficult seasons of the same geographical location. Therefore, defining the constant temperature cardinal number in a uniform standard without taking regional or seasonal differences into consideration will greatly increase investment and waste energy. As a result, lots of precision machining and ultraprecision machining workshops adjust the temperature in different seasons. Except for some occasions with special precision requirements, the general occasions of precision machining and ultraprecision machining mainly require that the temperature fluctuations and constant temperature are within a small temperature difference. So, in proper occasions, it is beneficial to adjust the constant temperature cardinal number in different seasons.

Constant temperature accuracy mainly depends on the different accuracy requirement and process requirement of precision machining and ultraprecision machining. Generally speaking, the higher machining accuracy requires a more rigid temperature fluctuation range. The accuracy of constant temperature has four levels: 0.2, 0.5, 1, and 2, which indicate four different accuracy levels: ±0.2 °C, ±0.5 °C, ±1 °C, and ± 2 °C。 For jig boring machines that should be adjusted and calibrated at Level 1, the accuracy of constant temperature should be ±1 °C; for miniature high-precision rolling bearings that should be assembled and adjusted, the accuracy of constant temperature should be ±0.5 °C.

With the development of modern industrial technology and continuous advancement of precision machining and ultraprecision machining technology, the requirements for constant temperature accuracy are getting higher and higher.

For example, during the production of components of large-scale integrated circuit, the lithography exposure process requires that the difference of coefficient of thermal expansion between mask materials and silicon wafers should decrease, because the temperature of silicon wafers with the diameter of 100 mm rises by 1 °C and the linear expansion will increase by 0.24 μm, which is not allowed (Wernsing et al. 2014). Therefore, the accuracy of constant temperature should be ±0.1 °C. At present, a constant temperature environment of ±0.01 °C has emerged, and many special measures are required to maintain it. For example, the entire equipment is immersed in a constant temperature oil tank, a constant temperature hood is added in the machining region, and a local environment of relatively high constant temperature accuracy is created based on the common constant temperature accuracy. During the manufacturing of integrated circuits, the accuracy of constant temperature in

some areas of the mask aligner (which uses the most cutting-edge manufacturing technologies) should be even up to ±0.001 °C.

Humidity

Precision machining and ultraprecision machining also have requirements on the relative humidity of the environment. The relative humidity refers to the ratio of partial pressure of water vapor in the air to saturated water vapor in the same temperature (Mcclure and Thal-Larsen 1970). It reflects the degree to which the water vapor in the moist air is nearly saturated. If the value of relative humidity is small, it indicates that the air is far from saturation and that the air is drier and has a stronger ability to absorb water vapor. On the contrary, if the value of relative humidity is large, it indicates that the air is close to saturation and that the air is more humid and has a weaker ability to absorb water vapor.

Excessive humidity can cause many factors that are detrimental to precision machining and ultraprecision machining. When the relative humidity exceeds 50%, lathes and equipment will be corroded and mildew will appear on the optical lens, which will severely affect the performance of the instrument and equipment. When relative humidity exceeds 55%, it will cause condensation on the cooling water pipe. If it occurs in the circuit system of the precision device, it will become a hidden danger of accidents. Figure 1 is a commonly used humidity measuring device; it is usually made up with humidity sensor, data acquisition card, and cable.

In the practical production, the low relative humidity is not conducive to precision machining and ultraprecision machining. When relative humidity is less than 30%, some materials are so dry that they become brittle and flammable; the dust can be more easily adsorbed on the surface of the object due to the effect of electrostatic force; some semiconductor devices are prone to breakdown. In general, the relative humidity should be controlled between 35% and 45%.

Fig. 1 Humidity measuring device

Control of Thermal Environment

The heat converted from energy consumption and the heat sent out from the operator's body during the process of precision machining and ultraprecision machining are the major internal factors that influence the constant temperature environment, while the heat transfer produced due to the difference of outdoor temperature and indoor temperature is the main external factor that influences the constant temperature environment. These major factors influence the constant humidity in a similar way. Therefore, the constant temperature control and constant humidity control of the clean room should be carried out at any time. Air-conditioning system is the critical facility to solve this problem.

There is a lot of air treatment equipment in air-conditioning system, including air heating equipment, cooling equipment, humidifying equipment, and dehumidifying equipment. In addition to the electric air heater and the equipment using solid hygroscopic agent, most air-conditioning system is heat and humidity exchange equipment for air and other media. Water, water vapor, liquid hygroscopic agent, and refrigerant can all be used as the media of heat and humidity exchange. Temperature control and humidity control can be realized through direct contact or surface heat and humidity exchange method.

Effect and Suppression of Vibration

Effect of Vibration Interference

The precision machining and ultraprecision machining put forward higher requirements for vibration environment, and the restrictions have become stricter than ever before. The internal and external vibration interference of the process system generate unnecessary relative movement between machining and machined objects; thus the required machining precision and surface quality of the workpiece cannot be achieved. For example, in the precision grinding, the vibration interference will produce a polygonal contour shape, so the machining precision will be affected and the surface roughness will not meet the requirements, either. In order to ensure that the surface roughness is less than Ra0.01 μm, the amplitude during grinding should be 1~2 μm. Thus, the amplitude caused by external vibration interference and the amplitude of idling machines should be much less than 1 μm.

The quality of precision machining and ultraprecision machining depends not only on the amplitude of vibration interference but also on the frequency of vibration interference. Some high-frequency vibration can be filtered by process system, but the vibration interference less than 70 Hz has a strong impact on the surface quality of machining. Therefore, the amplitude of lower-frequency vibration should be controlled below 0.125 μm, while the amplitude of higher-frequency vibration should be controlled below 0.25 μm. Especially, the electron microscopes that can magnify things to 100 million times and deep submicron semiconductor processing

equipment are sensitive to micro-vibration interference. Thus, it is important to control the vibration interference.

Generally, micro-vibration (also known as background vibration) can affect precision machining and ultraprecision machining. Its vibration acceleration is 2×10^{-2} m/s^2, vibration amplitude is less than 5 μm, and its frequency is 0.5~70 Hz. Vibration mainly comes from three aspects:

1. Natural vibration source: Earthquakes, waves, micro-movement, and wind.
2. Indoor vibration source: Vibration caused by the equipment operation (such as imbalance of the rotary parts, insufficient stiffness of parts or components, and so on), vibration caused by people walking in the production area, vibration caused by material handling, and vibration generated by auxiliary facilities.
3. Outdoor vibration source: Vibration generated by production, transportation, construction, and so on.

These micro-vibration sources spread to the precision machining and ultraprecision machining areas in different ways and exert an influence thereafter. So we should first recognize the major vibration sources, analyze the possible routes of transmission, and take proactive measures of prevention and isolation, so as to eliminate the impact of vibration interference and meet the environmental requirements of precision machining and ultraprecision machining.

Suppression of Vibration Interference

In order to ensure the normal operation of precision machining and ultraprecision machining, the effective measures should be taken to eliminate the impact of vibration interference, mainly through the method of vibration isolation.

External vibration interference is often independent and uncontrollable, such as the vibration interference generated by transportation, construction, and so on, especially the vibration interference generated by natural micro-movement, wind, etc. We should take a variety of measures to isolate vibration interference and to prevent them from spreading to the process system.

The most basic vibration isolation method is to keep away from the vibration sources. The railway, road, and other vibration sources outside the machining area should be investigated first. The machining area should keep a certain distance from these vibration sources. In the construction layout, try to keep the power room, air-conditioning machine room, and other facilities far away from machining area, so that the equipment sensitive to vibration are not affected.

The vibration isolation measures of precision machining and ultraprecision machining are usually multilevel. First of all, the clean room or even the entire workshop should be built on a good foundation of vibration isolation. On the basis of this foundation, the elastic materials or vibration-isolating elements should be installed, so as to isolate the vibration interference better.

Vibration-Isolating Elements

According to the principles of vibration isolation described above, most vibration isolation methods used in engineering are realized by installing the elastic supports between the machine tools and the foundation. These elastic elements include vibration-isolating pad and vibration isolator. Both of them have enough stiffness and can produce a restoring force that is proportional to vibration displacement. They also have damping and can produce a damping force that is proportional to vibration velocity. If the vector sum of these two forces that are applied to the mounting base gets smaller and the inertia force caused by equipment vibration partially offsets the external vibration and interference, the goal of actively isolating vibration is achieved. Well-designed elastic supports can absorb most of the interference caused by external vibration.

Vibration-Isolating Pad

The simplest vibration isolation method is to select an appropriate elastic material as vibration-isolating pad. Firstly, select proper parameters (such as elastic material type, thickness) based on allowable load, dynamic coefficient of elasticity, and interference frequency; secondly, select the cross-sectional area and the number of pads based on the total mass of machine tool equipment (Debra 1992).

Common elastic materials used to produce vibration-isolating pad include soft rubber, medium hard rubber, foam rubber, microporous ebonite, natural soft wood, soft wood board, felt, fiberglass, foamed plastic, etc. (Ghanadan 2014). They do not have uniform shape and size and can be cut and connected depending upon the situation. Figure 2 is a common rubber isolation pad. Usually a machine tool is equipped with six to eight such vibration isolation pads according to the size.

Vibration Isolator

Vibration isolator is an elastic element that has a specific shape and can absorb vibration. Common vibration isolators include spring vibration isolator, rubber

Fig. 2 Vibration-isolating pad

vibration isolator, spring and rubber composite vibration isolator, and air-spring vibration isolator (Lee and Cheung 1999).

1. Spring vibration isolator: It consists of one or more same metal springs, locking blocks, bolts, covers, etc. Metal springs are the most important elastic vibration-isolating elements among them. Since the springs can offer reliable performance and have high loading capacity, huge amount of compression under dead load, and low natural frequency, they have been used in many applications.
2. Rubber vibration isolator: It consists of oilproof vibration-isolating rubber, inner and outer metal ring, protection cover, and other parts. Vibration-isolating rubber is the most important elastic vibration-isolating element among them. Compared to metal springs, it has lower loading capacity, amount of compression under dead load, and natural frequency. However, it has bigger damping force and can isolate high-frequency components. Additionally, it is not only cost-effective and easy to install and replace but also can offer better isolation performance. Thus, it has been used widely.
3. Spring and rubber composite vibration isolator: It consists of metal springs, vibration-isolating rubber, locking blocks, metal rings, protection cover, and other parts. Metal springs and vibration-isolating rubber are the most important elastic vibration-isolating elements among them. It has high loading capacity and low natural frequency as spring vibration isolator and can offer bigger damping force as rubber vibration isolator. Its springs and rubber can be arranged in series and parallel. The rubber is used to wrap the metal rings or inserted into the springs in order to isolate the high-frequency components that may be transferred to the springs. If the rubber vibration isolator cannot meet the requirements and the spring vibration isolator cannot offer enough damping force, it is proper to use spring and rubber composite vibration isolator.
4. Air-spring vibration isolator: It consists of air, rubber, cover, and other parts. Air and rubber are the most important elastic vibration-isolating elements among them. Its natural frequency can be as low as possible and remains unchanged when its natural frequency changes. The height of some air-spring vibration isolators can be adjusted by injecting air. These isolators can isolate high-frequency components effectively; thus they are very suitable to prevent micro-vibration, especially for precision machining and ultraprecision machining equipment. But it is complex and expensive (Zhang et al. 2013).

Active Controller

For a vibration system of one degree of freedom with mass m, damping coefficient C, stiffness k, and external force F (caused by vibration interference), its motion equation is:

$$\mathrm{m}\ddot{x} + C\dot{x} + kx = F \tag{3}$$

This equation shows all forces of the vibration and the relationship between these forces. The first term on the left of the equation is the product of mass and velocity, which represents the inertia force; the second term is the product of damping coefficient and velocity, which represents the damping force; the third term is the

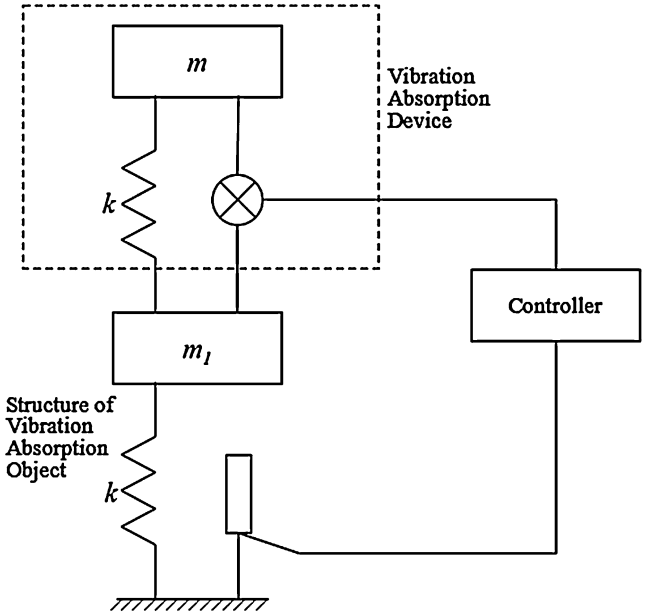

Fig. 3 An example of active control using compensation mass

product of stiffness and displacement, which represents the elastic force. The sum of all forces in the left equals to the external force caused by vibration interference. Thus, whether the vibration can be controlled will depend on if all of these forces can be controlled. This is how active control works.

Figure 3 shows an example of active control using compensation mass. It gets information about controlled quantity through displacement sensors, and special-purpose controllers use this information to send control signals that drive actuators to produce additional control force to absorb vibration.

As the ultraprecision machining requires higher accuracy, even the best passive vibration isolator cannot meet the vibration isolation requirements, so the active vibration isolation system will be the best choice. Currently, there are some high-performance active vibration isolators which can offer active vibration isolation of 6 degree of freedom, including active vibration isolation platform and active vibration isolator, such as TMC's statics series vibration isolation platforms and vibration isolators and Meiritz's maps series vibration isolation platforms and vibration isolators.

New Developments in Vibration Isolators

Dual-Chamber Air Spring

The air spring mentioned previously has a single chamber which has high non-linearity and poor vibration isolation performance. Thus, the single-chamber air

spring has been replaced with dual-chamber air springs gradually. Now, dual-chamber air-spring vibration isolators have been used widely in precision machining and optical fabrication.

Suspension (Pendulum)

Suspend the equipment by using steel cable to connect air-spring vibration isolators or other vibration isolators, so that the vibration isolators can isolate vibration transversely. The transverse natural frequency of suspended vibration isolator basically depends on the length of steel cable. Please note that these suspended vibration isolators have been used widely in aerospace and astronomy.

Negative Stiffness System

Negative stiffness system is a newly developed vibration isolator that can adjust the natural frequency of system by changing the system stiffness.

Airflow and Air Pressure

Airflow

The airflow has two major functions in the environment of precision machining: on the one hand, the dust in the environment needs to be discharged as quickly and effectively as possible, and on the other hand, the temperature and humidity in the machining environment should remain stable. Therefore, there are generally two major forms of airflow, which are turbulent flow and laminar flow (Noh et al. 2005).

Turbulent Flow

The turbulent flow discharges the indoor dust through the constant flow of the air, and it mainly uses the clean air to dilute dust load in the environment. To be specific, the purified air is first sent into the room from the ceiling and then discharged from the ground or the wall near the ground for filtering circulation. The direction of airflow is consistent with the direction of the dust's gravity. As the airflow has different directions, it is called turbulent flow, as shown in Fig. 4.

In order to maintain the level of Class 1000, the air needs to be changed more than 60 to 70 times per hour. At the same time, in order to avoid blowing dust on the surface, the airflow velocity should be controlled below 0.2 m/s. At present, the turbulent flow is limited by the layout of the air inlet and the outlet and can only maintain a cleanliness level of 1000–100,000. However, construction and operation costs are low, so it is widely used.

Laminar Flow

Laminar flow means that the indoor airflows are almost parallel, flowing in one direction at a uniform speed to avoid the vortex. The speed of airflow is generally referred to as 0.45 m/s, according to American 209B Standard. The minimum wind

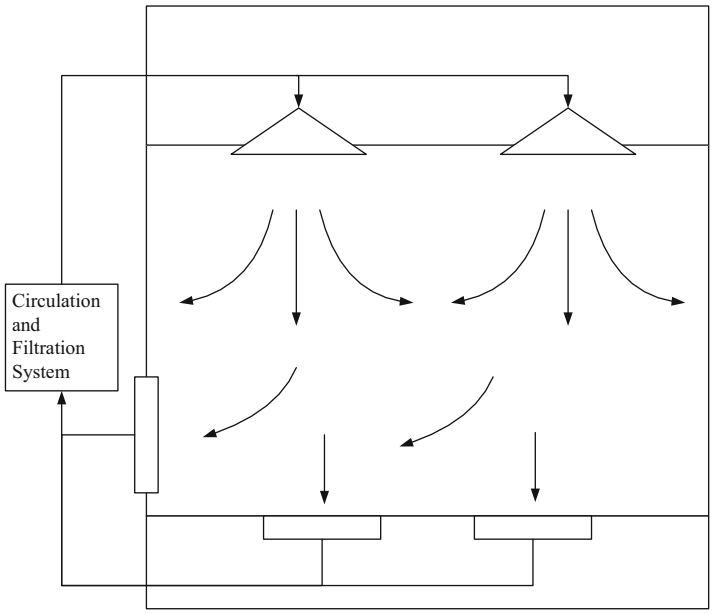

Fig. 4 Turbulent flow

speeds required by pollution control under different circumstances are listed in Table 2.

The purified air in laminar flow can remove the dust and control the temperature in the work zone, so the cleanliness can reach Class 100 or higher, and generally the system can meet the requirements for machining environment after activating for 1 ~ 2 minutes. However, its construction and operation costs are higher.

According to the direction of airflow, laminar flow can be classified as vertical laminar flow and horizontal laminar flow.

1. Vertical laminar flow: The vertical laminar flow is characterized by intensive arrangement of air inlets on the ceiling while dense installation of air outlets on the ground, so the entire operating space is filled with purified air, which flows at a uniform speed in order to quickly discharge the indoor dust, as shown in Fig. 5.
2. Horizontal laminar flow: The horizontal laminar flow is characterized by intensive arrangement of air inlets on one wall while installation of air inlet on the opposite wall, so the air flows horizontally into the operating space, in order to accomplish the purpose of removing dust and controlling the temperature, as shown in Fig. 6. As the direction of airflow is inconsistent with the direction of dust settling, the wind speed is generally faster than the vertical laminar flow, so as to reduce the influence of dust settling. In addition, the cleanliness is decreased from top to bottom and gradually along the airflow direction under the horizontal laminar flow, which should be taken into consideration in equipment machining and installation.

Table 2 Minimum wind speed

	Minimum wind speed/(m/s)	Condition
Vertical laminar flow	0.12	No one or very few people in or out, no obvious heat source
	0.3	General condition of no obvious heat source
	0.5	There are people and obvious heat source
Horizontal laminar flow	0.3	No one or very few people in or out
	0.35	General condition
	0.5	People are frequently in and out

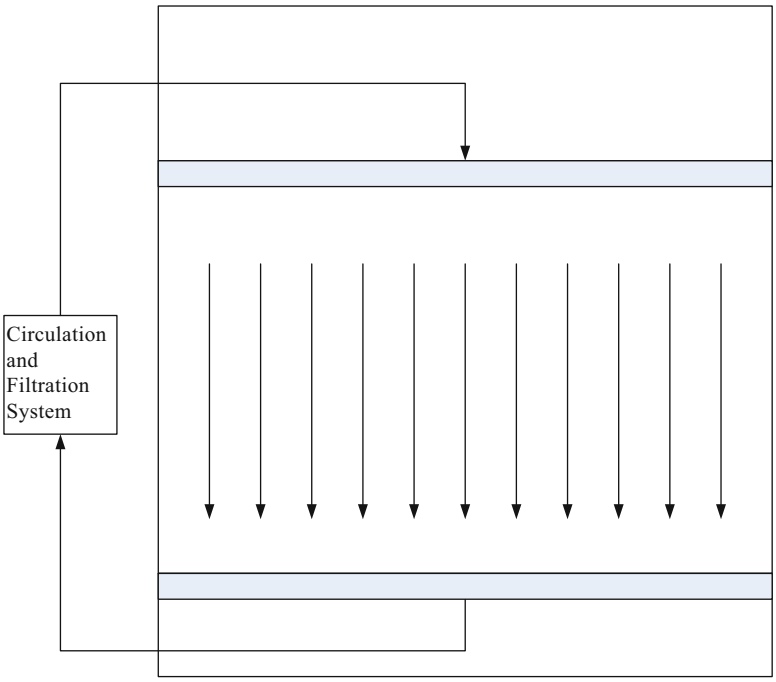

Fig. 5 Vertical laminar flow

Air Pressure

The infiltration of external air accounts for an important reason of machining environmental pollution. In order to ensure the stability of indoor environment and to prevent air infiltration from the outside, it is necessary to maintain a certain positive pressure in the indoor environment. When the air output is greater than the exhaust air rate, the positive pressure is achieved, and the larger value of positive pressure increases the energy loss. Therefore, the value of indoor positive pressure should be maintained within a reasonable range. According to different applications,

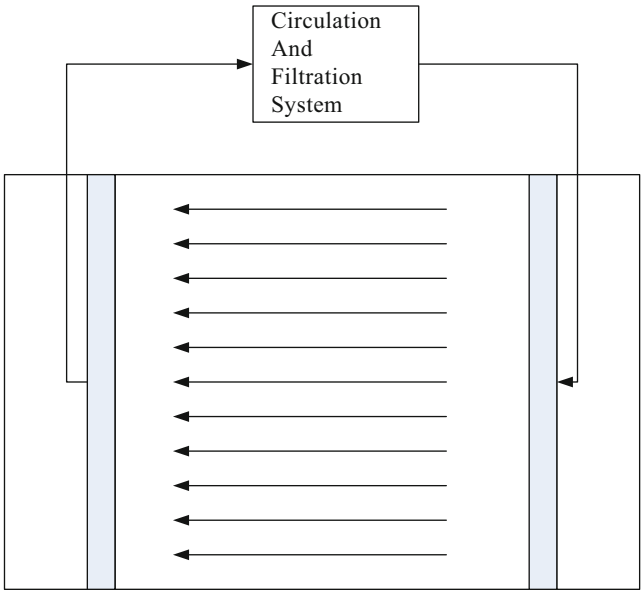

Fig. 6 Horizontal laminar flow

Table 3 Required pressure difference

Applications	Minimum pressure difference/Pa
Clean room of different levels	4.9
Clean room and quasi-clean room	9.8
Clean room and general studio	14.7

the required pressure difference values are listed in Table 3 (van den Brink and Schijndel 2012).

As the dust amount in the purifier increases in the long operational process, the purifier's resistance also increases, resulting in the change of indoor pressure environment. The commonly used pressure difference control method is to install a pressure regulating device, such as the excess pressure valve or electric airflow regulating valve of differential pressure type.

Other Environmental Factors

Electrostatic Field

Precision machining and ultraprecision machining have a demanding requirement for the electrostatic environment. Because in the clean room, there are a lot of high-resistivity materials which can easily generate and accumulate static electricity, such as plastic floor, nylon wall, polyester work clothes, etc. There are also a large number

of actions and opportunities which may generate and gather static electricity, such as operations in machining process including stirring, bonding, grinding, spraying, cleaning, etc.; the operators' various actions can also cause friction between objects and friction between airflow and pipe or equipment. Moreover, the relatively dry humidity also has an adverse influence on the electrostatic environment (Feng et al. 2008).

A large amount of static electricity generated and accumulated may also lead to the following accidents:

1. Due to the electrostatic discharge, people may get electric shock and generate involuntary movements, which lead to accidents or even the secondary injury such as electric shock, bruises, and fall damages.
2. Electrostatic discharge leads to the breakdown of components, especially for the components which are quite sensitive to electrostatic discharge; the damage rate is extremely high.
3. The light of electrostatic discharge can result in abnormal photosensitivity of the films. The heat generated may ignite the flammables and cause explosion. The electromagnetic waves generated will interfere with the devices so that they may make the wrong actions.
4. The force generated by static electricity can absorb dust particles onto the surface, resulting in product pollution, dust blocking, and other production accidents.

To reduce static electricity is mainly by reducing the generation and the accumulation of static electricity.

1. Reducing the Generation of Static Electricity.
   In order to reduce the generation of static electricity, the antistatic materials or materials after antistatic treatment should be used to lay the floor; materials or areas which generate or carry static electricity should be sprayed with efficient antistatic agent; operators' clean room suits should be made of antistatic cloths or cloths after antistatic treatment. These are very effective antistatic measures. After antistatic treatment, the clean room suits can reduce electrostatic potentials by 80% and reduce dust adhesion rates by 90%.
2. Reducing the Accumulation of Static Electricity.
   In order to reduce the accumulation of static electricity and to prevent people from getting electrostatic shock, the leakage resistance on the indoor floor that people may be in contact with at any time should be limited. The smaller the resistance value is, the more easily the static electricity on human body can leak from the ground, and people are less likely to get electric shock. In addition, special attention should be paid to the limits of electrostatic shock under various situations. For example, the electrostatic potential of electrostatic shock to nonconductor is about 10 kv, while the electrostatic potential of electrostatic shock to human body is about 3 kv. Therefore, some measures should be taken to make sure that the potential of charged object is lower than the potential of electrostatic shock.

Cleanliness

In the air of our daily living environment and ordinary workshop environment, there are a lot of dust, particles, and other substances. These dust and particles will not have any adverse effect on ordinary machining methods, but things are quite different for precision machining and ultraprecision machining. The existence of dust and particles often reduces the machining accuracy, because the size of the dust and particles in the air can't be ignored when compared with the requirements of machining accuracy. For example, if the hard dust in the air is mixed in the polishing process of computer hard disk surface, the machined surface will be scratched and fail to record the information correctly. In most serious situations, the disk will be scraped. In the manufacture process of large-scale integrated circuit components, if the silicon wafers are mixed with the dust in the air, it may become an uncontrollable diffusion source in the subsequent process and seriously affect the pass rate of the product (Zhang and Zhang 2004).

As can be seen from Table 4, the air contains a lot of dust and particles with a diameter of 0.5 μm or more, and even in areas where people think it is very clean (e.g., the operating room), there are more than 50,000 particles with a diameter of 0.5 μm or more in every ft^3 of air. Therefore, in order to ensure the quality of precision machining and ultraprecision machining, the air environment must be purified and treated, which means cleanliness control. The so-called cleanliness is the amount of dust in the air. The lower the dust concentration is, the higher the air cleanliness is. China's proposed air cleanliness registration standards are listed in Table 4. Table 5 shows the dust concentration limit of the cleanliness class, which is the average value of indoor air dust concentration.

Table 4 Air dust concentration in daily environment

Place	Number of dust particles(/ft^3)
Factory, station, school	2,000,000
Department store, office, pharmacy	1,000,000
Residence	600,000
Outdoor (residential area)	500,000
Inpatient ward, outpatient department	150,000
Operating room	50,000

Table 5 Air cleanliness class

Class	Number of dust particles ≥0.5 μm diameter per cubic meter	Number of dust particles ≥5 μm diameter per cubic meter
Class 100	≤35*100	0
Class 1000	≤35*1000	≤250
Class 10,000	≤35*10000	≤2500
Class 100,000	≤35*100000	≤25,000

Table 6 The upper limit concentration of various cleanliness classes

	Diameter/μm				
Class	0.1	0.2	0.3	0.5	5
1	35	7.5	3	1	–
10	350	75	30	10	–
100	–	750	300	100	–
1000	–	–	–	1000	7
10,000	–	–	–	10,000	70
100,000	–	–	–	100,000	700

With the rapid development of the semiconductor industry, the requirements for air cleanliness are becoming more demanding. The controlled particle diameter is reduced from 0.5 μm to 0.3 μm and even from 0.1 μm to 0.01 μm. So the Class 1 and Class 10 cleanliness were added into US Federal Standard 209D. Table 6 shows the concentration limit values of different diameter particles of various cleanliness classes stipulated by US Federal Standard 209D. We can know clearly from this table that the number of particles with a diameter $\geq$ 0.5 μm per ft^3 decides the class of cleanliness. For example, cleanliness of Class 100 means the number of particles with a diameter $\geq$ 0.5 μm per ft. 3 is over 100.

In the industrial application, air purification should meet the following requirements.

1. Low Fume Formation Rate.
   Low fume formation rate means that fume in the clean room should be as few as possible and there is no fume in the clean area. The operator should wear dust-free clothing and take an air shower: then they can enter the clean room. The tools and articles they need must be pre-disinfected and delivered to the clean room through the transit box to prevent the unpurified air from entering the clean room. Shorten the operating route of the operator, and avoid unnecessary actions to minimize the dust.
2. Remove the Dust when They Appear.
   Operating in the clean room will produce the dust. Thus, it is important to remove the dust when they appear so that they will not reside and spread. To do this, the materials used during the interior decoration should not hold dust and generate static electricity. Discharging the air near the area where dust particles gather can prevent the dust from spreading and avoid secondary pollution.
3. Supply Clean Air.
   Dust particles are usually 0.5 μm and cannot be removed through the common air-filtering methods. Generally, the filtering system used in the clean room for precision machining and ultraprecision machining is high-efficiency particulate air (HEPA) filter to ensure the supply of the clean air. Although the clean room meets the strict requirements of airtightness, it still unavoidably has some leaks. To ensure that there is pressure difference between the clean room and the dust

can be removed immediately, the most critical measure is to supply clean air continuously and keep the air clean.

The air clean room and air filter are mainly used to improve the cleanliness of the air. The air filter is the key equipment for air purification. The performance of the filter is mainly decided by efficiency, resistance, dust capacity, wind speed, and filtration rate. Filtration efficiency is a more important index, which refers to the amount of dust captured by the filter as the percentage of the dust entering the filter before filtering at rated air volume. Thus the filter efficiency η is obtained:

$$\eta = \frac{Vc_1 - Vc_2}{Vc_1} \times 100\% = \left(1 - \frac{c_2}{c_1}\right) \times 100\% \tag{4}$$

where V means the air volume flowing through the filter.

c_1 means the air dust concentration before the filter.
c_2 means the air dust concentration after the filter.

The resistance of the filter is another important index, which is expressed by pressure drop Δ_{PH}. It varies according to the air volume flowing through the filter, which refers to the rated air volume. Obviously, the resistance will continue to increase due to dust retention with the increasing time of filter use. Usually the resistance of the non-sticky new filter is called the initial resistance, and the resistance of the filter to be replaced is called the final resistance. Generally, the final resistance is stipulated twice as the initial resistance.

Taking a spray purification system as an example, the system is mainly composed of water circulation power system, humidity monitoring system, temperature monitoring system, PM2.5 monitoring system, other auxiliary functions, control system, and so on (Fig. 7).

The design of water circulation power system is to adopt the principle of vacuum pump and water ring pump to absorb the air from the clean room, so that the air is in full contact with the mixed liquid and produces chemical reaction. Finally, the purpose of filtration and purification can be achieved.

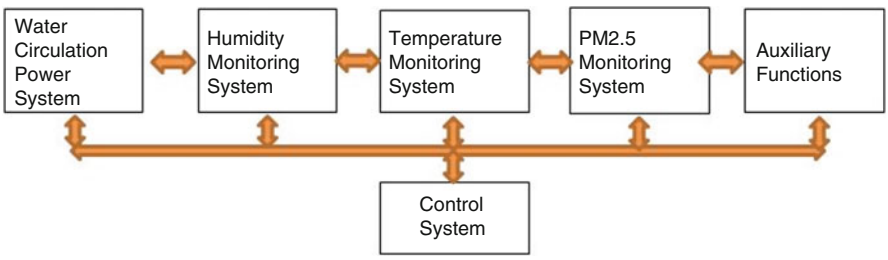

Fig. 7 The principle diagram of constant temperature, constant humidity, and cleaning devices

Humidity monitoring system is used to monitor the humidity of the air in real time.

The temperature monitoring system is used to monitor the temperature of the air in real time. In the meanwhile, customers who do not install the constant temperature device should add a cooling or heating device in this device for auxiliary purpose.

PM2.5 monitoring system is used for real-time monitoring of air PM2.5 content.

Other auxiliary functions are mainly used for the extended purposes, such as oxygen generation system, sterilization, deodorization, degradation of formaldehyde, dust removal, smoke removal, and so on.

The main function of control system is to control the speed of water circulation and to monitor and display parameters including temperature, humidity, PM2.5, and so on; data transmission includes wireless Bluetooth transmission, wireless WIFI data transmission, RS232 wire transmission, or limited transmission of the Internet access.

Figure 8a shows the system prototype, and Fig. 8b shows the relation diagram of purification time and PM2.5 concentration.

It can be clearly seen from Fig. 6 that the PM2.5 concentration descends over the time and fluctuates in the process. The preliminary estimate is that the water level in the tank is too low.

III. The Environment Control Device of Precision Machining.

To satisfy the environmental requirements of precision machining and ultra-precision machining, the corresponding facilities are designed. For air environment, the clean room which can control the cleanliness, wind speed, wind direction, and airflow pressure is designed. For thermal environment, constant temperature room and constant humidity room with functions of controlling temperature and humidity are designed. For vibration environment, vibration-isolating room with functions of vibration prevention, vibration isolation, and vibration attenuation is designed. For noise environment, anechoic room which can insulate, absorb, and eliminate noise is designed. For electrostatic environment and electromagnetic wave environment, antistatic chamber and screened room are designed, respectively. As the requirement for cleanliness is the most basic and general in various operations and methods of precision machining and ultra-precision machining, the cleanliness room is introduced in details in the previous chapter. All the aforementioned facilities specially designed for various environments are to assure and support the normal operations of the precision machining and ultraprecision machining. In order to realize the external supporting environment of precision machining and ultraprecision machining, the following five objectives should be made clear.

1. To realize a high-performance manufacturing environment, which should satisfy every strict requirement of precision machining and ultraprecision machining.
2. To lower the original costs of environmental facilities and the costs of operating and maintaining these facilities and to improve the economic efficiency.
3. To ensure the stability of various performance indexes and the continuous and stable operation of machining.

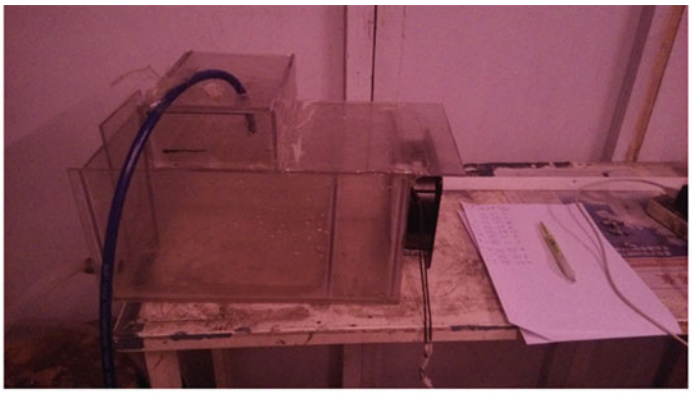

(a) Prototype of spray purification system

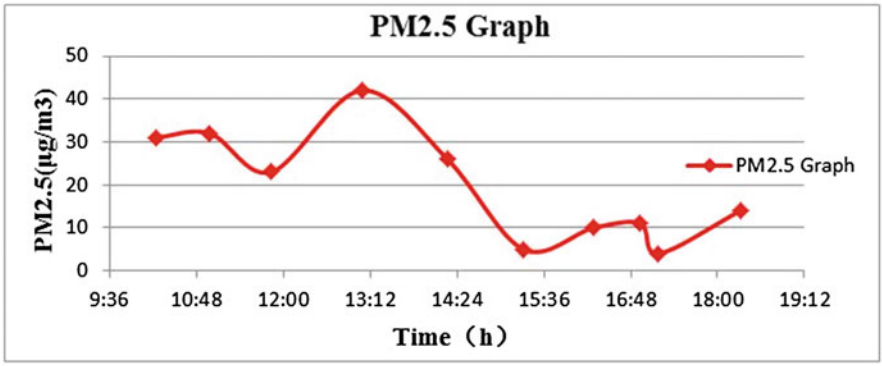

(b) Relation between pm2.5 and time

Fig. 8 Spray purification and humidity system. (**a**) Prototype of spray purification system (**b**) Relation between PM2.5 and time

4. The safety of operators and the environmental contamination should be considered, such as noise, vibration, sewage, exhaust gas, and other environmental pollution.
5. With the fast development of modern technology, the environmental facilities should adapt to the ever-changing requirements of manufacturing process.

As certain operations and methods of precision machining and ultraprecision machining put forward requirements for several external supporting environment, the constant clean room, clean room featuring in constant temperature and vibration isolation, and noiseless clean room featuring in constant temperature and vibration isolation are built to meet these requirements. Below, a university super clean room is taken as an example to illustrate the environmental requirements of precision machining (Fig. 9).

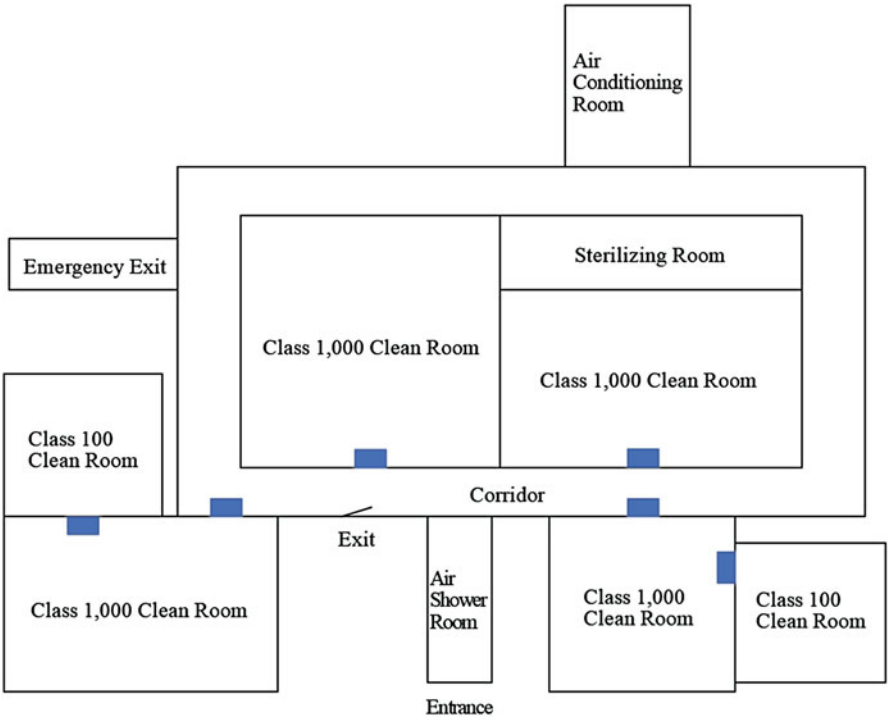

Fig. 9 The diagram of a university super clean room

Before entering into the super clean room, the operator must change into special clean room suits and go through the air shower system to blow off the dust on body surface. The corridor is up to the standard of Class 10,000 cleanliness. When the operator enters into a clean room of higher class from a clean room of lower class, he must go through the air shower system to avoid breaking the cleanliness system of a higher-class super clean room. The air shower is shown as a blue block in the diagram. Besides, the air pressure difference between different clean rooms is 5 Pa.

As shown in the diagram, the external supporting environment for precision machining need is different from the one for ultraprecision machining. Even in the same industry, the environments for different supply and demand conditions are also different. The production of a product usually needs conventional environment, precision environment, and ultraprecision environment. When building these environments, they should be set up by precision level, instead of being set up individually. Thus, when designing of a thermostatic clean room, the outermost layer should be conventional environment, the middle layer should be precision environment (which has higher accuracy of constant temperature and cleanliness level), and the innermost layer should be ultraprecision environment (which has the highest accuracy of constant temperature and cleanliness class). Then, a local environment structure that consists of more than one layer will be built. This design cannot

only create an ultraprecision environment easily and save money but also provide more protection layers to ensure safety and reliability. When planning the production process, please be sure that the materials will be delivered to the conventional environment first and then to the precision environment and the ultra-environment. Please remember that avoiding the wrong flow direction of materials is important for maintaining an ultraprecision environment.

In the precision and ultraprecision machining (e.g., turning the high-precision hemispherical diamond, scraping the high spot on the surface of the hard disk), it is hard to control the temperature, humidity, and cleanness in the cutting area. To solve this problem, keeping the temperature constant in the related area and taking purification measures are recommended.

The high-precision hemispherical diamond lathe installed in the constant temperature clean room is covered by a transparent plastic shell. It has several nozzles and can spray the coolant oil processed at a constant temperature to every area of the lathe to keep the temperature of the processing area at 20 °C (±0.1 °C). Oil returning back to the oil tank will remove not only heat generated in the operating of the lathe and the cutting process but also the debris and dust. This is a typical example of keeping constant temperature in a specific area of a device.

The scraper of high spots on the surface of the computer hard disk coating is installed in a Class 1000 clean room. The gap between the high-speed spinning hard disk and the scraping head made of diamond should be about 0.4 μm. Any spot with the height of 0.4~0.8 μm will be removed by the scraping head and turn into dust. The dust must be removed immediately to prevent the acoustic emission inspection device mounted on the scraping head from giving a false alarm. Thus, a plexiglass cover is added outside of the hard disk and scraping head as a local clean chamber. Supplying clean air to the chamber through a high-efficiency filter can promote the

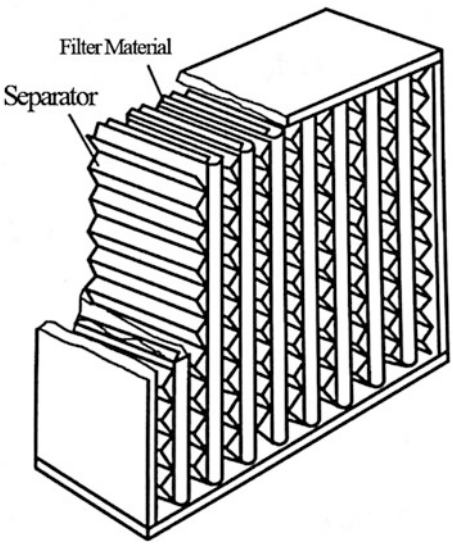

Fig. 10 High-efficiency particulate air (HEPA)filter

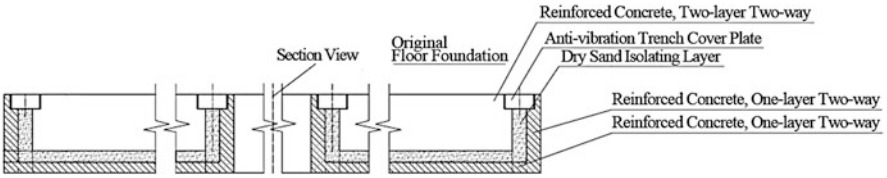

Fig. 11 Diagram of shockproof structure of super clean room

cleanness level to Class 100 in the chamber. This is a typical example of taking purification measures in the processing area.

The entire super clean room is equipped with the air circulation system, where high-efficiency particulate air (HEPA) filter shown in Fig. 10 is installed on the inlet of the air conditioner. The efficiency of the filter with 0.5 μm diameter dust is as high as 99%.

In order to avoid the impact of floor vibration, the super clean room is usually located on the first floor, and the structure of the foundation is shockproof (as shown in Fig. 11), which weakens the vibration and the interaction among various devices in machining.

Above is the introduction of a university clean room. With the fast development of precision machining and ultraprecision machining, the requirements for the performance of a clean room are becoming more and more demanding.

Reference

Choat E.E (1972) Environmental control for precision machining. Oak Ridge Y-12 Plant, Tenn, USA

Debra DB (1992) Vibration Isolation of Precision Machine Tools and Instruments. CIRP Ann Manuf Technol 41(2):711–718

Feng P, Hu GS, Jiang SQ (2008) Compensation and Control of Environmental Magnetic Field. Modern Scientific Instruments

Ghanadan R (2014) Applications of Active Noise and Vibration Control in Precision Machining. Bell Laboratories. Impact And Friction Of Solids, Structures And Intelligent Machines: In: Memoriam of P D Panagiotopoulos (1950–1998), pp 339–339

Jędrzejewski J, Modrzycki W (1997) Intelligent Supervision of Thermal Deformations in High Precision Machine Tools. In: Proceedings of the Thirty-Second International Matador Conference. Macmillan Education UK

Kuznetsov AP (2015) Probability methods of evaluation and control of precision reliability of metal-cutting machine tools under thermal effects. J Mach Manuf Reliab 44(4):363–371

Lee WB, Cheung CF (1999) Materials induced vibration in ultra-precision machining. J Mater Process Technol 89–90(8):318–325

Manning GHE (1976) The taking issue, compensation and environmental issue, compensation and environmental control. Simon Fraser University, Vancouver

Mcclure ER, Thal-Larsen H (1970) Thermal effects in precision machining. ASME, New York

Noh KC, Oh MD, Lee SC (2005) A numerical study on airflow and dynamic cross-contamination in the super cleanroom for photolithography process. Build Environ 40(11):1431–1440

Shinno H, Hashizume H (2002) Machining Environment-Controlled Ultraprecision Machining (Environment Control Technology for Ultraprecision Process and Measurement). J Jpn Soc Precis Eng 68:1171–1174

van den Brink AHTM, Schijndel AWMV (2012) Improved control of the pressure in a cleanroom environment. Build Simul 5(1):61–72

Wernsing H, Gulpak M et al (2014) Enhanced method for the evaluation of the thermal impact of dry machining processes. Prod Eng 8(3):291–300

Zhang TZ, Zhang H (2004) Construction of Superprecision Machining and Measuring Laboratory. Research & Exploration in Laboratory

Zhang C, Zhang JF, Feng PF et al (2013) Research on Modeling and Optimization of a Dual Chamber Air Spring Vibration Isolation System. Adv Mater Res 702:310–317

Thermal Error and Compensation Method for Precision Machines

17

J. P. Xi

Contents

Introduction 460
Effect of Thermal Error for Precision Machines 460
Thermal Error Sources in Machine Tools 461
Influence of Thermal Error 461
Thermal Error Compensation System for Precision Machine Tools 463
Thermal Error Modeling of Machine Tools 465
Thermal Error Detection of Machine Tool 466
Spindle Thermal Error Detection 468
Compensation Method of Thermal Error for Precision Machines 469
Thermal Error Compensation Scheme of the Whole Machine 470
Thermal Error Compensation Scheme of Components 472
Spindle 472
Ball Screw 475
Guide Rail 477
Conclusion 479
References 479

Abstract

As a symbol of national manufacturing and comprehensive national strength, high-grade computer numerical control machine tools have played an increasingly important role in modern industry. Among the various error sources of machine tools, thermal errors account for 40%–70% of the total errors. Therefore, it is important to control and reduce thermal errors for improving the accuracy of precision machine tools. According to studies conducted globally, thermal error compensation technology mainly focuses on three aspects: temperature-sensitive point selection, thermal error modeling, and thermal error compensation. Thus

J. P. Xi (✉)
Zhongyuan University of Technology, Zhengzhou, China
e-mail: xjpyq2010@163.com

Z. Jiang, S. Yang (eds.), *Precision Machines*, Precision Manufacturing,
https://doi.org/10.1007/978-981-13-0381-4_30

far, the theoretical system and compensation implementation technology have been developed and perfected.

Based on the analysis and summary of the research status in thermal error compensation, this chapter discusses the key technologies, including thermal key point optimization and thermal error modeling methods of machine tools.

Keywords

Machine tools · Thermal error · Compensation · Modeling

Introduction

As important equipment in modern industrial production and processing, precision machines have indicated the industrial advancement of a country. The accuracy of precision machine tools is a key factor affecting the development of the manufacturing industry. Therefore, it is important to improve the machining accuracy of precision machine tools.

In recent years, aerospace instruments, optical instruments, automobiles, electronic products, ships, and other high-end technology products have had increasingly higher requirements for the processing of parts, which tend to have high precision, high reliability, and long life. Traditional machine tools can hardly satisfy these requirements. Therefore, it is necessary to develop modern precision and ultra-precision computer numerical control (CNC) machine tools, which are effective processing equipment for such parts (Li Yongxiang 2007).

Thermal errors of machine tools are inevitable during machining. Because of heat transfer between the machine tool and the external environment during operation, both the friction between the parts of the machine tool itself and a part of the energy consumed are converted into heat energy, which are common physical phenomena. Under the action of a heat source, there will be an uneven temperature field. Different parts of the machine tool will produce different degrees of thermal deformation, which will directly affect machining accuracy. Among them, the thermal deformation of the spindle and screw system is significant. If the end of the spindle is connected to a cutting tool, the thermal deformation of the spindle will directly affect the movement path of the tool and reduce machining accuracy. It is of great practical significance to resolve the thermal error problem of machine tools to satisfy the need for high machining accuracy in modern manufacturing industry.

Effect of Thermal Error for Precision Machines

Several factors affect the machining accuracy of machine tools such as the positioning accuracy of machine tool guide rail, error caused by tool wear, geometric error of machine tool parts and installation structure, and error of machining heat deformation. Several studies have demonstrated that thermal error is the largest error source

in CNC machine tools, accounting for approximately 70% of the total errors in machine tools (Li 2007). Consequently, the evaluation of accuracy as well as the machining accuracy of machine tools are seriously affected.

Thermal Error Sources in Machine Tools

Several types of heat sources affect the machining accuracy of machine tools. According to Gakino Yoshiaki, the thermal deformation mechanisms of machine tools can be summarized as follows. During machining, the heat sources that affect the machining accuracy of machine tools can be roughly divided into two categories: internal heat sources and external heat sources (Li 2014). The heat source provided by the external environment is the external heat source, whereas the heat source provided by the internal heating of the machine tool is the internal heat source. Internal and external heat sources can be subdivided according to different conditions.

Internal heat sources are divided into dissipated heat and processing heat. Dissipated heat includes the heat generated by the conversion of the energy consumed by the motor into heat energy, and the heat generated by the friction of the bearings, gears, brakes, guide rail, and other structures, as well as the coolant, lubricating oil, etc. Processing heat includes the heat transferred to the object by the workpiece, tool, cutting fluid, chip, and other process variables. External heat sources can be divided into environment and heat radiation. Variations in external heat sources are caused by environmental factors such as airflow and cold and hot air. Thermal radiation includes lighting equipment, sunlight, and other sources of radiation.

After analyzing the heat sources resulting in thermal error of a machine tool, the installation position of the machine tool should be considered carefully. The machine tool should be installed in a stable environment, away from external heat sources to reduce their unstable influence. Various heat sources have an unstable influence on machine tools, and this influence is complex and controllable. The heat output of heat sources also varies with the environment, processing mode, and processing time. Additionally, machine tools have a certain thermal capacity, and their temperature rise has a time lag phenomenon, such that the thermal deformation of machine tools varies with time (Li 2007).

Influence of Thermal Error

In mechanical processing, the machine tool, fixture, and workpiece together constitute an integral system to realize a certain processing method. The machine tool is a key link of the processing system. During operation, different parts or different positions of the same part have different temperatures under the joint action of internal and external heat sources. Because of the different shapes, structures, materials, and degrees of freedom of different parts of a machine tool, various thermal displacement errors occur during cutting, pulling, pressing, turning,

bending, and other operations, and the errors accumulate. Finally, the parts directly related to the machining accuracy undergo different degrees of displacement deformation. Consequently, the machining process system suffers damage. The position relationship between the cutter and the workpiece, relative motion path, and theoretical deviation leads to a decline in the machining accuracy of the tool.

Blaser et al. (2017) proposed an adaptive learning control method that includes temperature change, load change, boundary condition change, and change in other process variables. It affects the machining accuracy of the machine tool and automatically changes the position of the center point of the tool. There is a chain effect, resulting in the displacement of the tool under the effect of internal and external environments. The objective of the self-adaptive thermal compensation method is to reduce the deviation of the tool center point caused by thermal error and improve the long-term accuracy of the tool with respect to material removal and machine detection. As shown in Fig. 1, several factors of the internal and external environments result in tool center error.

During machining, the interference of internal and external heat sources inevitably causes thermal deformation and decreases the machining accuracy of the tool. The process is shown in Fig. 2. The heat increases the temperature of the parts, causing them to expand and deform, and it is transferred to all parts of the machine tool. However, owing to the different shapes and structures of each part and uneven heating, various thermal displacements such as pulling, pressing, bending, and twisting are generated. These factors affect the condition of the parts, and they

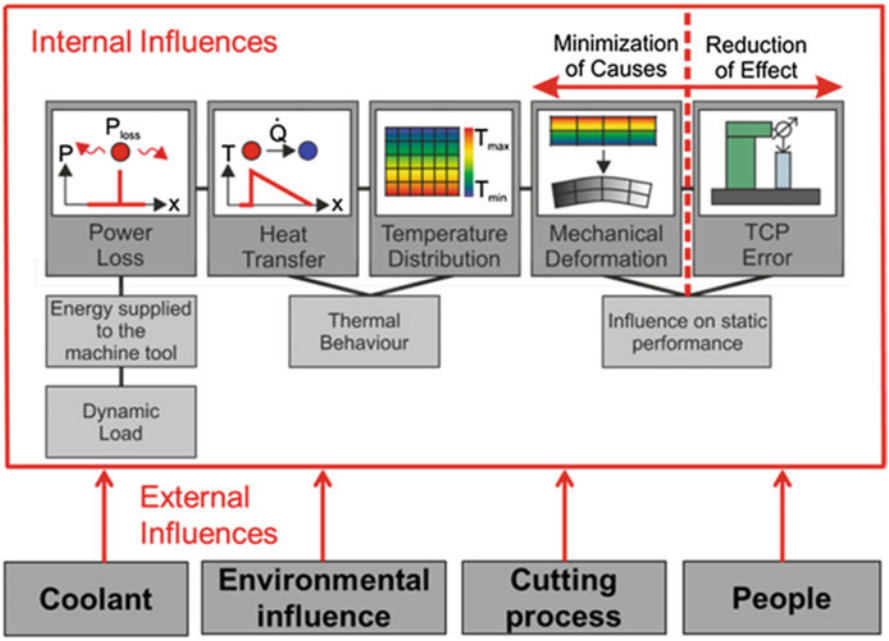

Fig. 1 Thermal chain of causes and tool center point errors

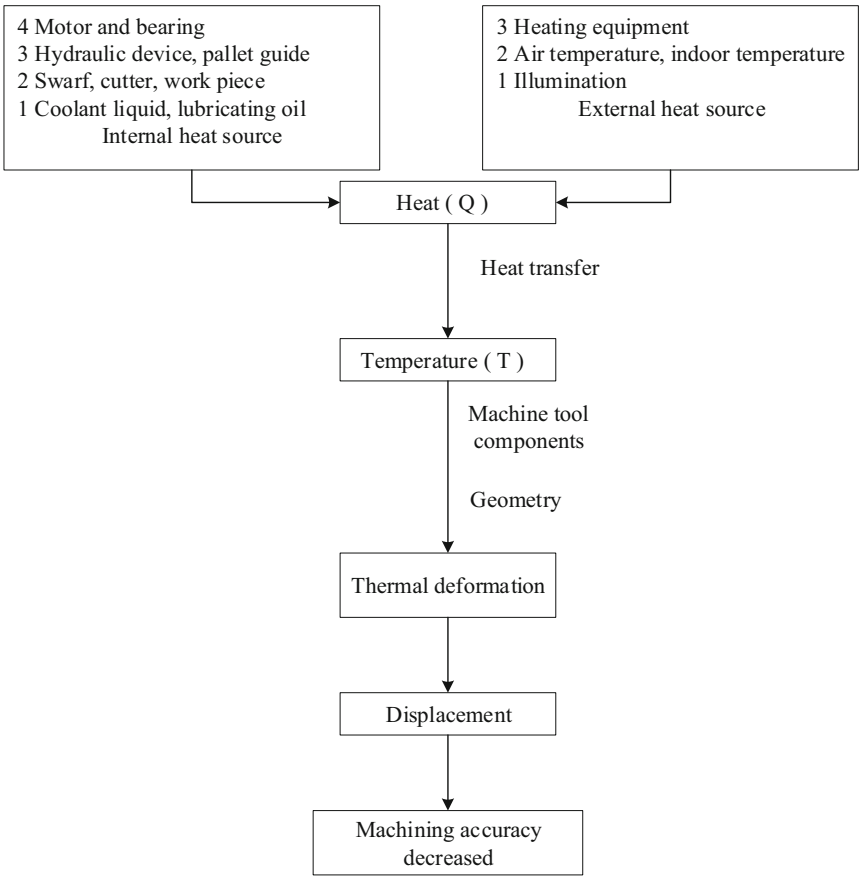

Fig. 2 The influence of heat source on the machine tool

cause a change in the position of the center point of the tool and result in a failure of the tool and the workpiece to move according to the predetermined trajectory.

Thermal Error Compensation System for Precision Machine Tools

Thermal errors of machine tools cannot be avoided in the machining process and are also responsible for a large proportion of the total errors. The two main methods to reduce thermal errors to improve the machining accuracy of tools are the error prevention method and the error compensation method. The error prevention method attempts to eliminate or reduce the number of possible error sources through efficient machine design in terms of variety, performance, and reliability through various design and manufacturing methods (Chen et al. 2015). The error prevention method can be applied by changing the structural layout of the machine tool and considering

ventilation and heat dissipation in the design. However, the error prevention method has significant limitations. The workload related to the redesigning of the machine structural layout is considerable. The design cost increases, and several adverse factors may cause additional problems, such as reducing the processing speed and increasing the vibration. The error compensation method is widely used to reduce thermal errors. This method creates a new error to offset the original error, which may have become a problem. The new error is of approximately the same magnitude as the original error, but with an opposite direction, to reduce the processing error and improve accuracy. The error compensation method cannot change the structural layout of the machine tool itself. It analyses the error source when the machine tool is processed, establishes the mathematical model, calculates the error value, and transmits feedback to the control system to correct the error. Error compensation technology has good adaptability. It can adapt to changes of the error sources. The method can reduce the production and manufacturing costs of machine tools and equipment. With the further development of computer technology, the thermal error compensation method is likely to be widely used.

Thus far, several thermal error compensation routes have been proposed for precision machine tools. The direct compensation method is a simple and effective principle that uses the direct measurement of the displacement of tools and workpieces to make adjustments in real time. However, this method has disadvantages, such as the reduction in the machining efficiency due to frequent measurements, and inability to capture a few thermal changes in time. The indirect compensation method can analyze the problem from two perspectives and implement the compensation scheme. The first perspective is that of principle-based methods such as the finite element (FE) and finite difference methods. However, the establishment of boundary conditions and the accurate acquisition of heat transfer characteristics are difficult, and the formulation of mathematical models is a challenge. The second perspective is based on the relationship between the measured temperature changes and the displacement results of the special position points of the machine tool. The relative position between the tool and workpiece changes, and empirical modeling is performed. The simplest method to associate the measured temperature with the displacement is linear regression. However, the design of linear regression models is time-consuming and laborious.

In recent years, artificial intelligence techniques such as artificial neural network, fuzzy logic, and combinations of various modeling methods have successfully predicted thermal errors. The adaptive neuro-fuzzy inference system (ANFIS) has been proposed (Holkup et al. 2010), and two types of thermal prediction models have been designed. The data space is divided into the ANFIS of rectangular subspace and the ANFIS of the fuzzy c-means clustering method. Based on the grey system theory, the influence grades of all possible temperature sensors on the machine tool structure are obtained. The fuzzy c-means clustering method is used to cluster the influence weights of the thermal sensors, and further correlation analysis is used to reduce the influence weights. ANFIS has been applied in different engineering domains. The basic structure of ANFIS is shown in Fig. 3. This model adopts a five-layer structure,

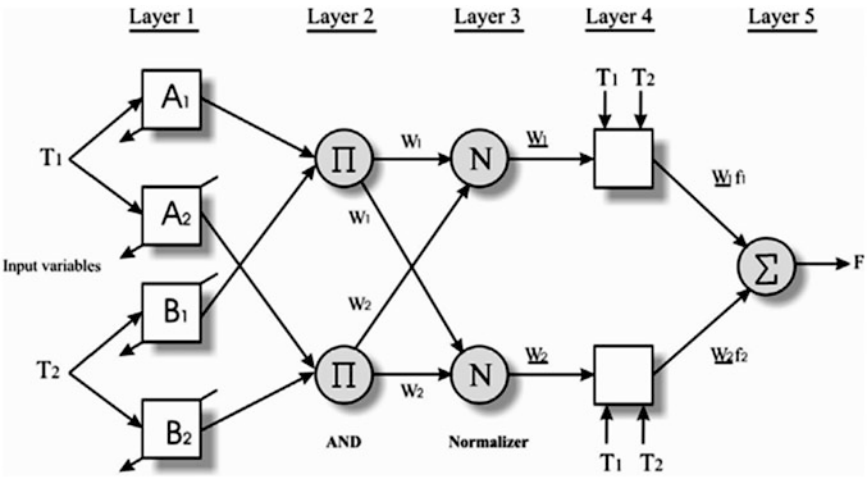

Fig. 3 ANFIS basic structure diagram

and each layer contains several nodes described by a node function. Among these, adaptive nodes are represented by squares, which represent the adjustable parameter sets of these nodes. A fixed parameter set in the model is represented by a circle.

Thermal Error Modeling of Machine Tools

It is important to build a mathematical model that can account for thermal errors in machine tools. The modeling methods of thermal errors are divided into two categories: theoretical and empirical methods. The empirical method is mainly used to compensate the thermal error of machine tools. Based on the identification of the parameters of a statistical model, the thermal error is predicted. The theoretical method is mainly used to prevent thermal errors in machine tools. The equation is established based on the heat transfer relationship and the constraints of force and displacement, and the thermal deformation is obtained using the numerical solution of the differential equation (Wang et al. 2015).

The commonly used modeling methods include artificial neural networks, least square fitting, time series analysis, and grey theory. Artificial neural networks are empirical models. Neural networks and grey theory are two error compensation models that have been widely used in recent years. Although these modeling methods have achieved success in a few applications, it is difficult to establish the mathematical model of thermal error compensation accurately, and the compensation effect is still not ideal (Li 2014).

In addition, aiming to reduce the thermal error of the machine tool feed system, several scholars have studied the thermal error modeling and compensation of machine tools.

A composite prediction method has been proposed to account for the thermal error of the machine feed system (Xin et al. 2019). First, a neural network is used to model the thermal deformation of the screw. Subsequently, the polynomial fitting method is used to determine the relationship between the platform axial thermal error y and the actual thermal deformation x of the lead screw. Accordingly, a platform axial thermal error prediction model called the "two-step method" is established. The two-step method and back propagation neural network method are used for directly predicting the axial thermal error of the platform (direct method) and predicting the experimental value, respectively. The prediction results of the two methods are compared with the measured values of the axial thermal error of the platform.

The generating mechanism of the thermal error in CNC machine tools is complex. Generally, the mathematical modeling of the temperature field monitoring data is used to predict the thermal error. The complexity of processing conditions and environment makes it difficult to evaluate the advantages and disadvantages of the data-driven modeling method. A comprehensive evaluation of the thermal error model of machine tools is required, which can provide information regarding performance metrics such as the robustness, accuracy, effectiveness, stability, and correlation of the thermal error prediction model.

Thermal Error Detection of Machine Tool

The precondition of error compensation is high-precision error detection and identification. Traditional error detection tools include square, dial indicator, level meter, and group gauge block. In recent years, the error detection technology and equipment have included laser interferometer, ball bar instruments, plane grating, R-test (radial test), and machine vision measurement.

The dual-frequency laser interferometer is based on the Doppler effect. The error in a machine tool is calculated by the Doppler frequency shift of transmitted light and reflected light. Different components can be combined with each other to achieve machine tool straightness, perpendicularity, the positioning accuracy of the straight axis and rotation axis, deflection angle, and other error measurements. Common laser interferometry techniques include holography, speckle, and Michelson interferometry. The ball bar instrument is also called a high-precision telescopic linear sensor. Each end has a precision ball. The precision ball is fixed between the precision magnetic bowl seats. A magnetic bowl seat is connected to a machine tool workbench, and the other is connected to the machine tool spindle or spindle box. The distance between the two precision balls changes, and the sensor of the ball instrument can accurately measure this change. When there are errors in the machine tool, the ball bar instruments can measure the actual processing circle track and compare it with the theoretical track, to obtain the overall machine tool accuracy. Plane grating measurement is a noncontact measurement. Plane grating can be used to measure the movement in the two-dimensional space conveniently, and it can measure the movement accuracy when the CNC machine completes the complex trajectory. The R-test device installs a spherical detector on the spindle of the

machine tool, considering the five-axis CNC machine tool as an example. When rotation tool cente point (RTCP) motion is enabled in the five-axis CNC machining center, the three-dimensional error relative to the ideal spatial position is detected by detecting the ball heads of the three contact displacement sensors. The R-test device is more beneficial to reveal the error characteristics of the rotating axis as compared with the ball bar instrument.

Li (2007) developed a real-time detection system to account for the thermal error compensation of CNC machine tools based on the offset of the external coordinate system. This was the first such detection system developed in China. With this detection system, the temperature of machine tools and the thermal error of spindle can be measured automatically, and the thermal error can be compensated in real time by connecting this system to the controller of CNC machine tools.

Narendra et al. (2014) developed a real-time thermal error compensation module and integrated it into an ultra-precision intelligent turning machine. The compensation module designed by the team included a temperature input, a neural network algorithm to compute the deformation error, a real-time calculation using "C" language programming, and open architecture NC controller integration. Three experiments were conducted on intelligent ultra-precision machine tools to draw the thermal error diagram. These experiments were the environmental temperature change error test and the thermal expansion test when the spindle was running and test to measure thermal expansion during axis runs. Figure 4 shows an experiment to measure the thermal expansion when the shaft was running. Through collecting the experimental data, the real-time compensation of the x-axis and z-axis thermal deformation error was realized.

To detect the thermal error in machine tools, Masahiko et al. (2019) proposed a new two-dimensional trajectory measurement method of the thermal deformation of machine tools by using a tracking interferometer. The accuracy of the tool path in the

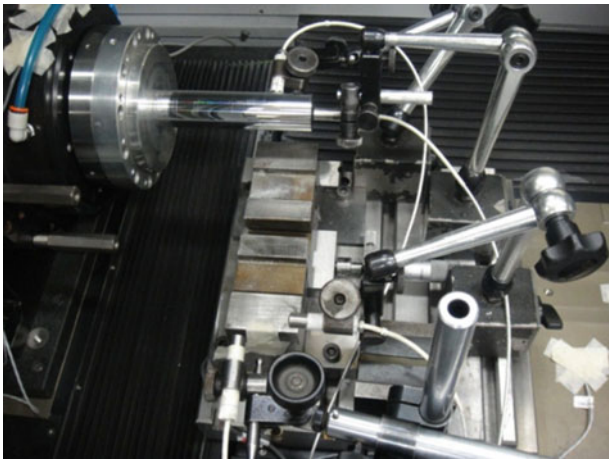

Fig. 4 Thermal error measurement of shaft operation setting

machining space is an important component to evaluate the accuracy of a machine tool. During machining, the measurement and visualization of spatial accuracy change are important to improve the machining accuracy. Masahiko Mori et al. measured the y- and z-plane movement of a vertical machining center and calculated the two-dimensional trajectory using the obtained specific parameters.

Spindle Thermal Error Detection

As mentioned previously, the thermal error has a considerable influence on the spindle and lead screw system of the machine tool. The error caused by the thermal deformation of the spindle accounts for a large proportion of the total thermal errors in a CNC machine tool. Therefore, the measurement and analysis of the thermal error of the spindle system are important to improve the machining accuracy of a machine tool. When there is a difference between the actual condition and the modeling condition, the traditional thermal error models often show poor robustness and prediction accuracy, mainly due to the limitations of modeling data and the dynamics, which are not captured by the model. The heat transfer of a machine tool spindle system is a complex physical phenomenon. There are three basic forms of heat transfer: heat conduction, heat radiation, and heat convection. Heat transfer occurs from the same object or between different objects. Solid heat transfer occurs primarily by conduction, which occurs in two ways when the machine tool rotates. During cutting, the cutting heat is transferred from the cutter head to the cutter body. The heat conduction of a machine tool is in accordance with the Fourier law. Thermal radiation refers to the phenomenon in which an object is at a high temperature, and it radiates electromagnetic waves. In the machining process, thermal radiation refers to the radiation of heat generated by machine tools to the external environment, which conforms to the laws of thermal radiation. Thermal convection refers to the process of the relative displacement and heat transfer of particles in a fluid. For machine tools in operation, there are two main forms of heat convection: heat transfer between the outside air and main axle box and between the lubricating oil and main axle box. Heat convection is generally described by Newton's law of cooling.

Sun et al. (2011) have designed the hardware system of a dynamic thermal error detection instrument for CNC machine tools. It integrates the special fixture, inspection rod, temperature sensor, high-precision capacitive (eddy current) displacement sensor, and programmable control system in the five-point measurement method. It achieves the collection and processing of the multichannel temperature and thermal deformation data of CNC machine tools. The system can satisfy the requirement of high reliability in industrial production. The software system of the dynamic thermal error detection instrument for CNC machine tools has also been developed. The software has five modules: system setup, error measurement, analysis report, error modeling, and help document.

Mayr et al. (2015) studied the thermal error compensation caused by the movement of the rotary unit of the five-axis machine tool and the operation of the spindle.

Three different measuring devices were used to study the thermal error of the rotary axis and the spindle. The main relationship between the thermal positioning error and the input model was determined for the cooling power of the spindle of the machine tool.

Compensation Method of Thermal Error for Precision Machines

Yang et al. (1996) proposed a cerebellar model arithmetic computer (CMAC) neural network for the thermal error modeling of machine tools. CMAC is a systematic learning algorithm that can learn the nonlinear and interactive characteristics between the thermal error and the temperature field. CMAC was studied to account for accuracy prediction, robustness to sensor placement, learning speed, and tolerance to sensor failure. The main axis drift error of horizontal machining centers and NC turning centers was measured and compensated by a capacitance sensor and thermal sensor, respectively.

The temperature field and strain field of the parts of the machine tool and the machine tool itself were calculated using FE analysis. The thermal error of the machine tool was compensated in real time using a microcomputer control system. In addition, the relationship between the thermal load and thermal displacement of the machine tool was studied.

Krulewich (1998) proposed a new method to predict the thermal error of machine tools. The model predicted the positioning error between the tool and the workpiece due to the structural deformation of the machine tool, which was caused by the internal and external heat sources. Figure 5 shows an analysis of the causes of the workpiece error. In this study, the concept of thermal error and temperature integration was used to analyze the temperature field of the machine tools. The number and

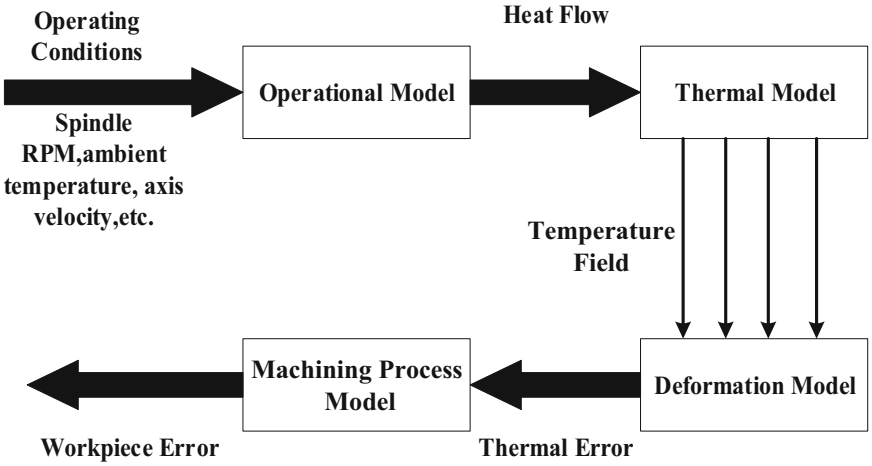

Fig. 5 Cause of workpiece error

position of temperature sensors were regarded as the Gauss integration points, which were distributed in the predicted temperature field. Compared with other methods, the preheating and cooling conditions of this method could be represented as steady-state conditions. In addition, the optimum number and position of temperature sensors were predetermined, which reduced the time required for measuring the temperature of the machine tool.

Thermal Error Compensation Scheme of the Whole Machine

Wang et al. (2007) first used CAD software to perform three-dimensional modeling of the bed of the machine tool to determine the corresponding boundary conditions. Subsequently, ANSYS software was used to perform FE analysis of the thermal characteristics and thermal deformation of the bed of the machine tool. The analysis results adjusted and optimized the parameters of the overall thermal characteristics of the bed of the machine tool.

Liu et al. (2018) proposed the "robust modelling method of the thermal error of unbiased estimation based on grey correlation segmentation." A numerical control machine tool was considered the experimental object, and the machine tool experimental platform is shown in Fig. 6. In the experiment, the degree of thermal deformation in the z-axis was the largest. To simplify the experiment and data processing, only the thermal deformation in the z-axis direction of the machine tool was selected for measurement. Nine batches of experiments were designed. The positions of the temperature and displacement sensors are shown in Fig. 7. The

Fig. 6 Experiment platform

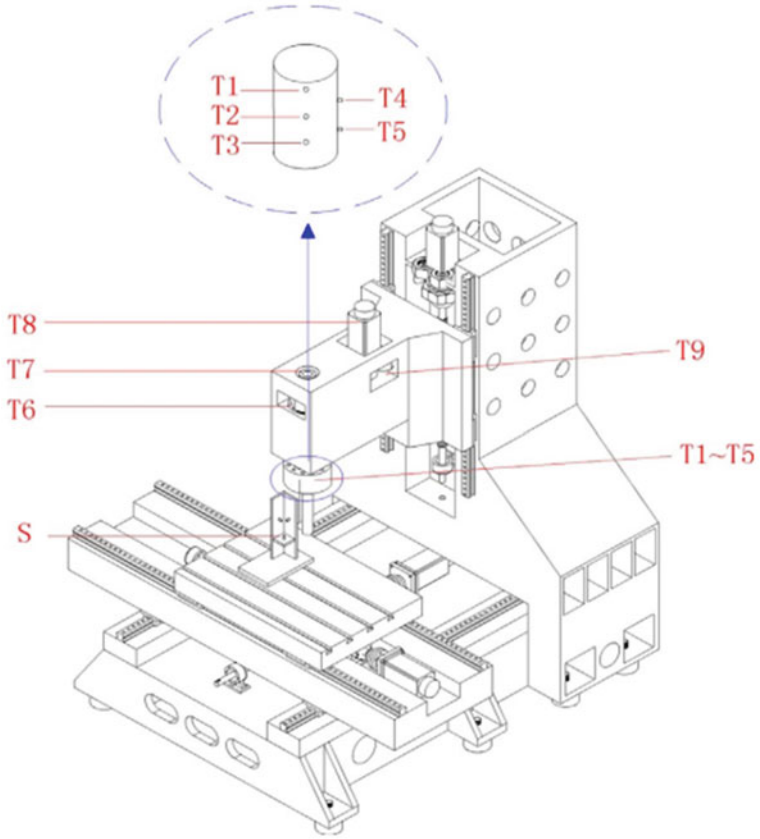

Fig. 7 Schematic of sensor location

experimental results showed that the method could effectively reduce the volatility of the temperature-sensitive points and improve the prediction accuracy and robustness of the model.

Precision machine tools are affected by external heat sources. The types of external heat sources have been analyzed above. For large precision machine tools, the impact of the external environment is evident. It is difficult to place large machine tools in a room temperature environment, and it is difficult to maintain their internal structure at a constant temperature. Tan et al. (2014) proposed a thermal error model for large-scale machine tools considering the effect of environmental thermal lag. Their study described a compensation method using ambient temperature sensors and the information of internal operations. The parameters of time delay components were determined by the calibration program of the system. The time lag between the ambient temperature and the corresponding thermal deformation changed with the change of climate. Figure 8 shows the ambient temperature data measured by a large gantry machine during 20 consecutive days of shutdown.

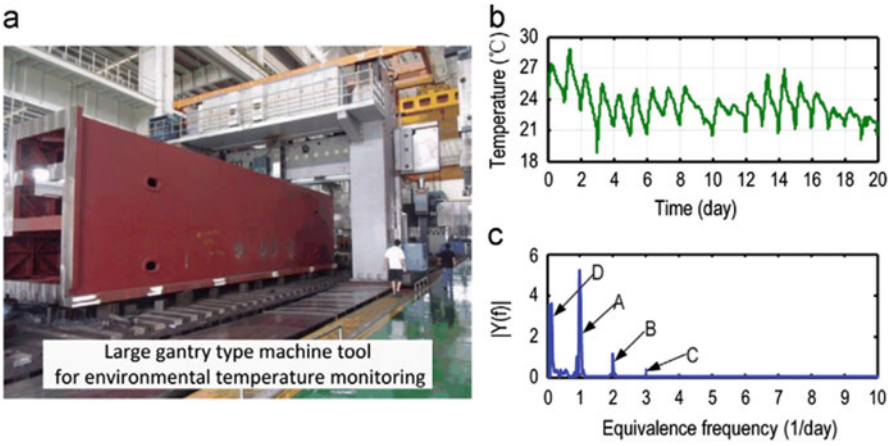

Fig. 8 Periodic characteristics of ambient temperature

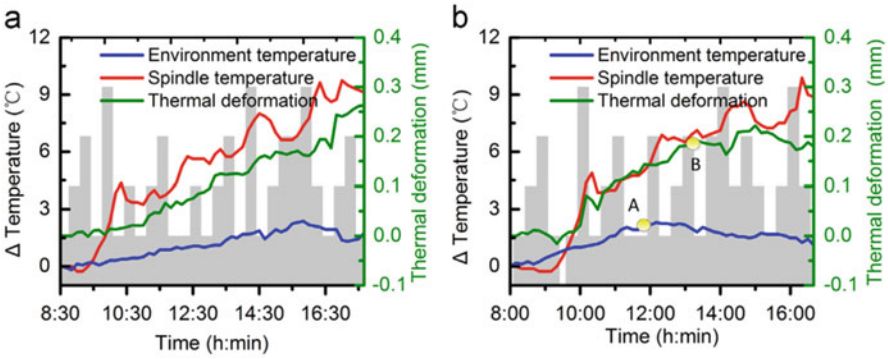

Fig. 9 Hysteresis effect of ambient temperature

Even in different periods of the same day, due to variation in the ambient temperature, small fluctuations lead to the thermal deformation of the structure as shown in Fig. 9.

Thermal Error Compensation Scheme of Components

Spindle

The spindle is one of the key components in machining. Its performance is critical for the cutting speed and machining accuracy of the machine tool. It controls the precision machining of the tool. The spindle of a machine tool produces a significant amount of heat in high-speed operation; hence, it is an important internal heat source. The thermal performance is one of the most important factors affecting the

performance of high-speed machine tools. The thermal characteristics of the spindle determine the cutting speed and machining accuracy of the machine tool. Therefore, it is very important to reduce the influence of thermal error at the design stage of the spindle to improve its thermal characteristics. In the past century, several scholars have explored the thermal design methods of spindles. The thermal design process can be divided into three parts: thermal characteristic analysis, thermal design and optimization method, and thermal characteristic test. Initially, the necessary parameters such as the temperature field distribution, thermal deformation, and thermal balance time are obtained through the modeling and analysis of the thermal characteristics of the main shaft. Subsequently, thermal design measures such as the structural design optimization of the main shaft, material design optimization, and cooling system design are undertaken respectively to obtain the optimum thermal characteristics of the main shaft. Finally, the results of the analysis and design optimization are verified through the process cycles of the thermal characteristic test until satisfactory results are achieved.

Holkup et al. (2010) established a thermal engine spindle model that considered the temperature, deformation, lubricant viscosity coefficient, and the change in bearing stiffness to predict the temperature distribution on the spindle and the change of bearing stiffness and contact load with time. Li et al. (2011) proposed a thermo-mechanical model that could be used to identify the mechanical and thermal properties of the main components of a high-speed spindle, such as bearings, spindle body, spindle boxes, etc. simultaneously. The model could also be used to predict the bearing stiffness, contact load, temperature, and thermal diffusivity of the high-speed spindle. In addition, Professor Jedrzejewski and his team at Wroclaw University of Technology in Poland have conducted extensive research on the thermal analysis of CNC machine tools and used the finite difference and FE methods to establish a hybrid model to analyze the characteristics of the spindle system. A new method was proposed to determine the thermal characteristics of the machine tool based on the power loss of moving system components. When the error source and process parameters, such as spindle speed, ambient temperature, cutting power, and processing time, were determined, the power loss, temperature, thermal deformation, and other results of all the components of the drive system could be calculated automatically.

Creighton et al. (2010) proposed a spindle compensation scheme to reduce the thermal error of the spindle during machining. The FE analysis of a micro milling spindle system was proposed, which related the temperature rise caused by the heating of spindle bearing and motor with the structural deformation. Based on the existing experimental results, the thermal displacement model of the spindle in high-speed micro milling was established, which could effectively predict the displacement of the spindle at different rotational speeds.

For the optimization and compensation of the thermal error of the spindle, Yang et al. (2018) proposed an FE method to establish the thermal structure model of the high-speed spindle system. The experimental design method was used to predict the machining error. Figure 10 shows the model design, and Fig. 11 shows the design of the experimental device.

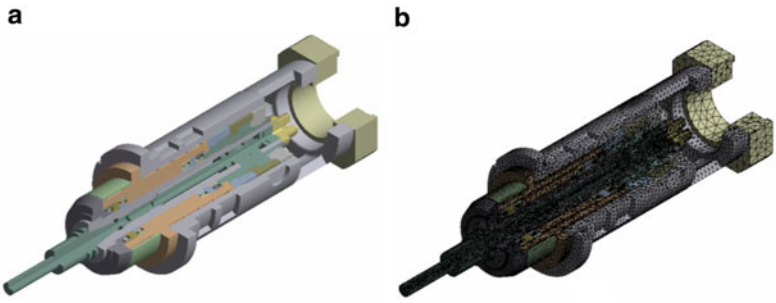

Fig. 10 (a) Model of high-speed spindle (b) FE model of high-speed spindle

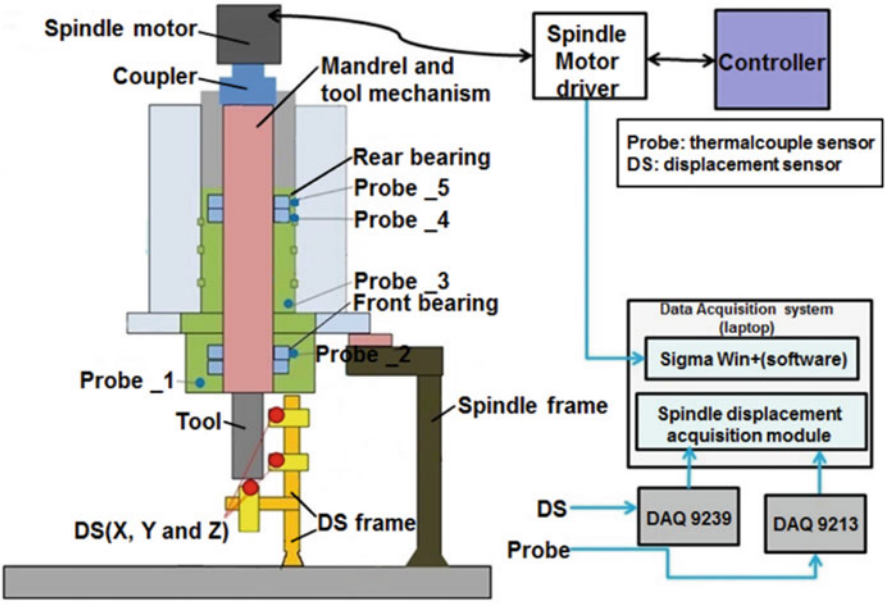

Fig. 11 Experimental device

A better understanding of the thermal error of the spindle is important for designing a thermally optimized spindle. Teng Liu et al. (2017) proposed a mathematical model for analyzing the thermal error of spindle under specific conditions. The conditions were as follows. The linear axial direction of the thermal error of the main shaft was due to the heat transfer from the main shaft of the bearing. The angular thermal error and linear thermal error of the shaft in the radial direction were due to the relative displacement of the thermal change of the bearing. First, the thermal change model of relative displacement of short cylindrical roller bearing and angular contact ball bearing was established. Subsequently, the thermal change model was combined with the finite element simulation of thermal liquid-solid

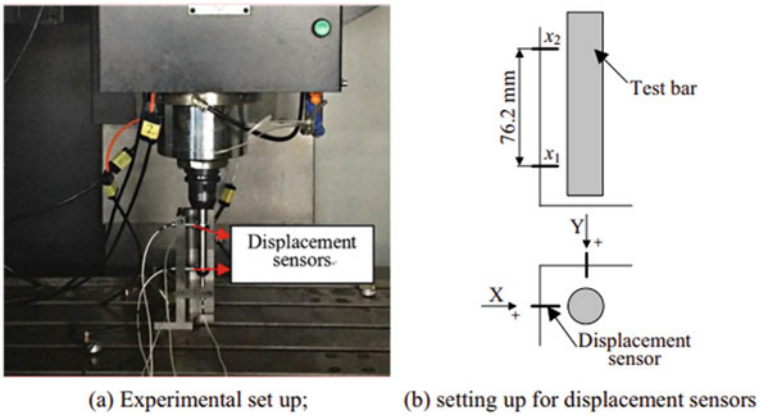

Fig. 12 (a) Experimental setup (b) Displacement sensor setup

coupling. By using the analytical simulation method, the linear thermal error and angular thermal error of the spindle in radial and axial direction were modeled.

The thermal error caused by the spindle includes the thermal growth error in the axial direction and the thermal drift error in the radial direction. In view of the radial thermal drift error, Liu et al. (2016) proposed the modeling and compensation of the radial thermal drift error of the spindle of the vertical machining center. The thermal drift errors in the x-, y-, and z-axes directions of a vertical machining center were measured, and it was determined that the thermal drift error was mainly in the y-axis direction. The thermal drift error in the y-axis direction and the key temperature points of the spindle were measured with different rotating speeds. The thermal drift error model under different attitudes was established, and the compensation scheme was proposed. Figure 12 shows the experimental setup.

Several experts have attempted to reduce the thermal error and improve the thermal accuracy of machine tools through a reasonable structural thermal design based on the thermal characteristics of the machine tool spindle. However, so far, the thermal structure design of a machine tool spindle has not been developed theoretically. With the development of modern manufacturing industry, the demand for high-speed and high-precision machining of machine tools is increasing. Thermal stiffness, static stiffness, and dynamic stiffness have been considered the "three major stiffness values" of a machine tool. The thermal characteristics as well as the static, dynamic, and acoustic characteristics of the machine tool spindle are important characteristics that cannot be ignored.

Ball Screw

In machine tools, the thermal error of a ball screw causes a direct position error. The high-speed ball screw system naturally generates more heat, which leads to greater thermal expansion and has a negative impact on the positioning accuracy. Therefore,

the mathematical modeling of the temperature distribution, thermal deformation laws, and thermal error compensation of the ball screw can enable a better analysis of the influence of thermal error on the machining accuracy of the machine tool.

Otakarhorejs et al. proposed a relationship between the thermal deformation and bearing temperature rise based on the screw preloading effect. Tian et al. (2013) proposed a modeling scheme using the multiple linear regression theory to identify the optimum thermal error detection model of CNC machine tools and achieve high modeling accuracy. Cheng et al. used an Elman neural network for thermal error modeling. The model considered the operation conditions, improved the accuracy, and was robust.

For the ball screw feed system with a closed-loop control, the thermal deformation of the ball screw is offset by the closed-loop control system. Hence, the linear positioning error of the feed system is determined by the deformation of the grating ruler. Kim et al. (2002) studied the mechanism of the influence of the thermal deformation of the grating ruler on the positioning error of the feed shaft of the linear motor and simulated its thermal characteristics and thermal error using the FE method. Xu et al. (2007) combined the FE method with the improved lumped capacitance method.

Hengxi et al. (2006) used the multiple regression method to analyze the thermal deformation of the ball screw of the machine tool. The unrelated temperature variables were considered the key temperature points of the model. An error model that could effectively predict the thermal deformation of the ball screw of the machine tool feed system was established.

Junyong et al. (2008) studied the temperature response and change characteristics of the ball screw by using the heat transfer theory. Finally, the thermal deformation and temperature field of the ball screw were modeled and simulated using FE software under the action of a variable heat source. The thermal dynamic characteristics of the ball screw under the action of a periodic heat source were further obtained.

Zapłata and Pajor (2019) proposed a method of thermal compensation for CNC shafts. The partial differential equation (PDE) of the temperature distribution of the ball screw was solved. The model assumed an unsteady heat source and considered the heat conduction between the screw and the engine body. A temperature sensor was installed inside the screw to record its temperature in real time to verify the correctness of the model. Figure 13 shows the experimental platform. Through experiments, the compensation based on the model using the approximate solution

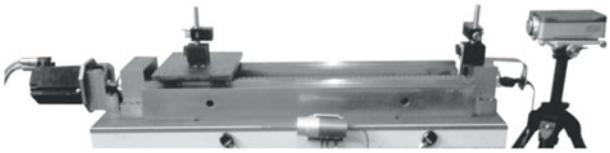

Fig. 13 Experiment platform

of the PDE was determined to be lower than the compensation based on the measured value.

Shi et al. (2015) studied the relationship between the thermal error of the feed transmission system and the axial thermal expansion and temperature of the ball screw. They proposed a thermal error modeling method based on the thermal expansion and the corresponding mathematical expression.

The ball screw is thus a key part of a CNC machine tool feed system, and its thermal deformation affects the positioning error of the machine tool. To improve the accuracy of CNC machine tools, Huijie et al. proposed a thermal error prediction method based on a genetic algorithm-back propagation neural network.

Guide Rail

In the study of tool machining errors, the machine tool guide error cannot be ignored. The machine tool guide is the benchmark of the structural movement of each part of the machine tool, and its accuracy directly affects the machining accuracy of the tool. The tool guide rail mainly includes the following three errors: the straightness error of the guide rail in the horizontal plane, the straightness error of the guide rail in the vertical plane, and the parallelism error of the front and rear guide rails in the same plane. In the machining process, the guide error should be reduced to improve the machining accuracy of the tool.

To study the principle and correlation of Abbe error in the guide rail system, Cha considered a universal three-axis CNC machine tool BV75 as an example, analyzed the Abbe error in each axis, and established a model. The error in the y-axis direction of the guide rail of the stack structure was transmitted to the x-axis direction of the guide rail system to generate an additional Abbe error. The traditional method of analyzing the Abbe error considers the rotation of the worktable to be fixed, and the calculated Abbe arm is inconsistent with the actual size. Therefore, the theory of instantaneous motion of the guide way system was proposed to correct the Abbe arm in all directions accurately. Based on the theory of multi-body system dynamics, a comprehensive error compensation model was established for CNC machine tools in accordance with the actual conditions. The model considered the influence of grating measurement error, the Abbe error of the guide rail system, error correlation, and compensation on the total error of the machine tool.

Compared with the traditional sliding guide, the linear rolling guide has advantages such as fast transmission speed, high positioning accuracy, and superior wear resistance. Therefore, the linear rolling guide is widely used in the positioning system of high-precision CNC machining centers. Gaiyun et al. (2015) studied the influence of the parallelism error of the linear rolling guide on the motion error of the worktable of the machine tool. They also analyzed the relationship between the force on the ball and the contact deformation according to the Hertz contact theory and quantitatively analyzed the motion error of the worktable based on the homogeneous coordinate transformation and the principle of minimum complementary energy.

Finally, through the simulation and comparison of the results, the algorithm was shown to calculate the motion error of the worktable accurately.

Zhili et al. (2011) conducted the FE analysis of a machine tool guide rail and established an FE thermal deformation analysis model for the guide rail. They provided a theoretical basis for analyzing the influence of the thermal deformation of the guide rail on the machining accuracy through analysis and calculation. Haolin et al. (2011) proposed a model calculation method combining an approximate model with numerical simulation for the thermal deformation variable of the machine tool guide rail. The FE objective function of the thermal error of the guide rail was established. Generally, it is difficult to measure the full stroke of the thermal error of the guide rail. This problem was solved using this method to compensate the thermal error of the guide rail. For the thermal error analysis of the guide rail, Yang (2011) proposed a method based on the FE theory, combining the numerical simulation with the actual measurement experiment, which proved the validity and feasibility of the method.

The thermal deformation of the machine tool also affects the movement of the guide rail. Lee et al. (2003) studied the influence of thermal deformation on the contact condition of the guide rail (Sun-Kyu et al. 2003). The typical characteristics of the linear velocity and the variation of friction coefficient with the external load were studied. This led to a study of the thermal effects of sliding motion. The thermal deformation of the sliding table was measured with the time of motion. The linear motion and friction power of the sliding table were monitored, which were directly compared with the thermal deformation. In addition, it was required to predict and compensate the motion error caused by the thermal deformation, properly. Figure 14 shows the experimental setup.

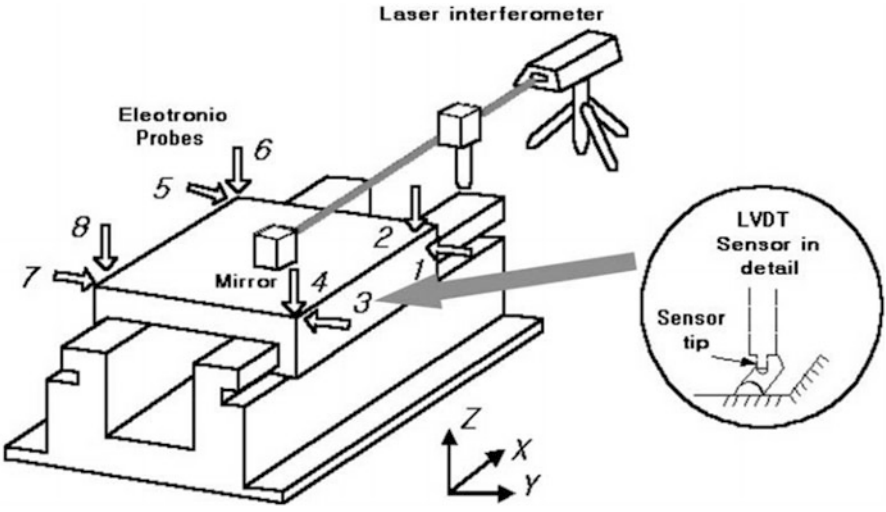

Fig. 14 Thermal effect measurement

Conclusion

In this chapter, the formation mechanism of the thermal error and its influence on machine tools are briefly described. Reducing the effect of the thermal error of machine tools on the improvement of machine tool accuracy is also discussed. Analyzing two measures to reduce the influence of the thermal error, this chapter summarizes and analyzes the main measure, which is the error compensation method, and also summarizes the empirical and theoretical thermal error models. In addition, various compensation schemes are listed for machine tools and various parts. The spindle, guide rail, and ball screw are the main parts of the machine tool, and hence, it is of great significance to study the thermal error.

The thermal error compensation based on thermal error detection is a method with significant economic benefits and can effectively improve the machining accuracy of machine tools. The study of the thermal error compensation technology is the key to improving the machining accuracy of high-precision machine tools, and it is also conducive to improving the machining accuracy of general machine tools.

References

Blaser P, Pavliček F, Mori K, Mayr J, Weikert S, Wegener K (2017) Adaptive learning control for thermal error compensation of 5-axis machine tools. J Manuf Syst 44

Chen L, he Z (2015, Research on error compensation of precision machine tool feed system) Sci Technol Enterp (21):238

Creighton E, Honegger A, Tulsian, Mukhopadhyay D (2010) Analysis of thermal errors in a high-speed micro-milling spindle. Int J Mach Tools Manuf 50(4):386–393

Gaiyun H, Wang K, Guo L, Bohui D (2015) Modeling and analysis of the influence of guideway parallelism error on the motion error of worktable. J Mech Sci Technol 34(11):1705–1709

Gao J, Yueping C, Deng H, zepeng Y, Xin C (2013) Compensation method of in-situ detection error for machining accuracy of complex curved surface parts. J Mech Eng 49(19):133–143

Grama SN, Mathur A, Badhe AN (2018) A model-based cooling strategy for motorized spindle to reduce thermal errors. Int J Mach Tools Manuf 132:3–16

Gurauskis D, Kilikevičius A, Borodinas S, Kasparaitis A (2019) Analysis of geometric and thermal errors of linear encoder for real-time compensation. Sens Actuators A Phys 296

Holkup T, Cao H, Kolar P et al (2010) Thermo-mechanical model of spindles. CIRP Ann Manuf Technol 59(1):365–368

Jianzhong F, Xinhua Y, Yong H, Hongyao S (2010) Development of thermal error compensation technology for CNC machine tools. Aviat Manuf Technol (04):64–66

Li Hengxi, Hu Zhiling (2006) Influence of machine tool guide error on machining quality. Mach Manuf Autom (03):34–35 + 40

Liu Hongwei, Yang Rui, Li Bo, Chen Guohua (2018) Research on measurement and compensation method of machine tool guide rail error. Modul Mach Tool Autom Process Technol (11):110–112

Kim SM, Lee KJ, Lee SK (2002) Effect of bearing support structure on the high-speed spindle bearing compliance. Int J Mach Tools Manuf 42(3):365–373

Krulewich DA (1998) Temperature integration model and measurement point selection for thermally induced machine tool errors. Mechatronics 8(4):395–412

Lee S-K, Yoo J-H, Yang M-S (2003) Effect of thermal deformation on machine tool slide guide motion. Tribol Int 36(1):41–47

Li Y (2007) New method and application of thermal error modeling for CNC machine tools. D. Shanghai Jiao Tong University
Li J (2014) Research on some key technologies of precision CNC lathe D. Northeast University
Li J, Huang M, Zhu W, Dou X, he G, Jianguo Y, Jiangsheng X, Chun L (2001) Temperature and thermal error detection system of CNC machine tools. Jiangsu Mach Manuf Autom (04):82–83. + 85
Li HL, Ying XJ, Chi YL (2011) Approximate model method in thermal error optimization calculation of machine tool guide rail. China Mech Eng 22(04):423–427
Liu K, Sun M, Zhu T, Wu Y, Yu L (2016) Modeling and compensation for spindle's radial thermal drift error on a vertical machining center. Int J Mach Tools Manuf 105:58–67
Liu T, Gao W, Zhang D, Zhang Y, Chang W, Liang C, Tian Y (2017) Analytical modeling for thermal errors of motorized spindle unit. Int J Mach Tools Manuf 112:53–70
Liu H, Miao E, Zhuang X, Wei X (2018) Thermal error robust modeling method for CNC machine tools based on a split unbiased estimation algorithm. Precis Eng:51
Masahiko Mori, Irino N, Shimoike M (2019) A new measurement method for machine tool thermal deformation on a two-dimensional trajectory using a tracking interferometer. CIRP Ann Manuf Technol 68(1)
Mayr J, Egeter M, Weikert S, Wegener K (2015) Thermal error compensation of rotary axes and main spindles using cooling power as input parameter. J Manuf Syst 37
Enming Miao, Yi Liu, Hui Liu, Zenghan Gao, Wei Li (2015) Study on the effects of changes in temperature-sensitive points on thermal error compensation model for CNC machine tool. Int J Mach Tools Manuf 97
Morishima T, van Ostayen R, van Eijk J, Schmidt R-HM (2015) Thermal displacement error compensation in temperature domain. Precis Eng 42
Narendra Reddy T, Shanmugaraj V, Vinod P, Gopi Krishna S, Narendranath S, Shashi Kumar PV (2014) Real-time thermal error compensation module for intelligent ultra precision turning machine (iUPTM). Procedia Mater Sci 6
Pan B (2018) Thermal error analysis and compensation for digital image/volume correlation. Opt Lasers Eng 101
Shi H, Ma C, Yang J, Liang Z, Mei X, Gong G (2015) Investigation into effect of thermal expansion on thermally induced error of ball screw feed drive system of precision machine tools. Int J Mach Tools Manuf 97:60–71
Sun Zhili, Yang Qiang, Gao Pei, Yan Ming (2011) Study on thermal characteristics of machine tool guide rail based on finite element method. J Northeast Univ (NATURAL SCIENCE EDITION), 32 (07): 1000–1003
Sun-Kyu Lee, Jae-Heung Yoo, Moon-Su Yang (2003) Effect of thermal deformation on machine tool slide guide motion[J]. Tribol Int 36(1):41–47
Tan B, Mao X, Liu H et al (2014) A thermal error model for large machine tools that considers environmental thermal hysteresis effects. Int J Mach Tools Manuf 82-83(7):11–20
Tian Guofu, Hu Jun, Guo Yuxue (2013). Application of multiple linear regression theory in thermal error compensation of nc machine tools. Mech Eng Autom (02):128–131
Wang B (2013) Research on error compensation technology and cutting performance of ultra precision machine tools. D. Harbin Univ Technology
Wang Y, Chaoquan T, Qiang L, Songmei Y, Gao J, Jingyi L (2007) Parametric analysis of thermal characteristics of machine tool bed based on finite element method. Mach Tool Hydraul (08): 5–7. + 83
Wang H, Li T, Wang L, Li F (2015) Summary of thermal error modeling of machine tools. J Mech Eng 51(09):119–128
Wang Q, Peng Y, Wiemann A-K, Balzer F, Stein M, Steffens N, Goch G (2019) Improved gear metrology based on the calibration and compensation of rotary table error motions. CIRP Ann Manuf Technol 68(1):511–514
Xia Junyong, Hu Youmin, Wu Bo, Shi Tielin (2008) Thermal dynamic characteristics of ball screw considering thermal elasticity. J Huazhong Univer Sci Technol (NATURAL SCIENCE EDITION) (03):1–4

Xinyuan Wei, Enming Miao, Wei Wang, Hui Liu (2019). Real-time thermal deformation compensation method for active phased array antenna panels Precis Eng, 60

Xicong Z (2018) Sensitivity analysis and in place compensation technology research on geometric error of three-axis ultra precision lathe. D. Harbin University of technology

Xin Zongyi, Feng Xianying, Du Fuxin, Li Hui, Li Peigang (2019) Thermal error modeling and analysis of machine tools based on BP neural network. Modul Mach Tools Autom Process Technol (08):39–43

Xu M, JiAng SHY, Cai Y (2007) An improved thermal model for machine tool bearings. Int J Mach Tools Manuf 41(1):53–62

Yang J (1998) Comprehensive error compensation technology and application of CNC machine tools. Shanghai Jiaotong University, Shanghai

Yang D (2011) Thermal error analysis of machine tool guide rail based on finite element method. Machine 38(08):47–50. + 58

Yang Y (2013) Thermal error mechanism analysis and real-time error compensation of machining center. D. Shanghai Jiaotong University

Yang S, Yuan J, Ni J (1996) The improvement of thermal error modeling and compensation on machine tools by CMAC neural network. Int J Mach Tools Manuf 36(4):527–537

Yang Li, Wanhua Zhao, Shuhuai Lan, Jun Ni, Wenwu Wu, Bingheng Lu (2015) A review on spindle thermal error compensation in machine tools. Int J Mach Tools Manuf 95

Yang A S, Yu X H, Zhuang J R, et al (2018) DOE-FEM based design improvement to minimize thermal errors of a high speed spindle system. Therm Sci Eng Progress

Ye X, Cheng H, Dong Z, Tam H-Y (2015) Error compensation for three-dimensional profile measurement system. Front Optoelectron 8(4)

Zapłata J, Pajor M (2019) Piecewise compensation of thermal errors of a ball screw driven CNC axis. Precis Eng 60

Zhu Jia, Li, Xingfei, Tan, Wenbin, Xiang, Hongbiao, Chen, Cheng (2010). Method of geometric error detection for measuring machine. J Mech Eng, 46(10):25–30

Performance Characterization of Precision Machines

18

Shuming Yang, Guofeng Zhang, and Zhuangde Jiang

Contents

Introduction 484
Geometric Error Analysis and Characterization of Machine Tools 485
Error Parameters Description and Its Modeling 485
Error Characterization of Machine Tool 486
On-Machine Measurement for Process and Product Quality Control 495
Conception of OMM 495
Probing Techniques for Geometric Parameters of Workpieces 497
Measurement Tools for Process Control and Tool Setting 501
Measurement of Distance Between Tool and Workpiece 503
Integration of Online Machining and Process Monitoring 504
Conclusion 506
References 508

Abstract

Geometric error measurements are performed to evaluate a variety of machining factors and conditions as well as the work done on the machine tools. With the increasing complexity of machining processes and ever-growing requirements for accuracy and precision, the demand for advanced methods and instruments for process optimization has also increased. To meet this demand, error measurements and compensations for machine tool components, and on-machine measurement for process, require an expansion of manufacturing metrology to

S. Yang (✉) · Z. Jiang
State Key Laboratory for Manufacturing Systems Engineering, Xi'an Jiaotong University, Xi'an, Shaanxi, China
e-mail: shuming.yang@mail.xjtu.edu.cn

G. Zhang
State Key Laboratory for Manufacturing Systems Engineering, School of Mechanical Engineering, Xi'an Jiaotong University, Xi'an, Shaanxi, China
e-mail: zgf0110@stu.xjtu.edu.cn

Z. Jiang, S. Yang (eds.), *Precision Machines*, Precision Manufacturing,
https://doi.org/10.1007/978-981-13-0381-4_14

include comprehensive closed-loop control of the machining process. In this chapter, we firstly review the measurement methodologies of volumetric error generated in the machine tools from the perspective of measurement instruments and strategies. Then we review technical trends in on-machine measurements for process and product quality control, discussing the probing techniques for geometric parameters of workpieces and measurement tools for tool setting in detail, respectively. To eliminate the effects of disturbances on machining process and adjust the control quantities to optimal values for robustness, integration of online machining and process monitoring is essential. Spreading measurement targets and applications are comprehensively reviewed.

Keywords

Error · Machine tool · Characterization · On-machine measurement · Process monitoring

Introduction

Machine tools and measuring machines have been applied in enormous numbers and various fields of modern production. With the development of hi-tech and new tech, the requirements for machining accuracy have risen from micron to submicron and even nanometer level. The trend toward individualized products and smaller lot sizes with high precision increases the demands of higher machining reliability and flexibility in production. However, many factors still result in deviations compared to the design model, involving kinematics errors, thermal errors, cutting force-induced errors, servo errors, machine structural errors, vibration and tool wear, etc. Among them, the geometric error of machine tool components and structures is one of the uppermost sources of inaccuracy. In the past decades, considerable research has been conducted to compensate these geometric errors which can be preprocessed due to repeatability, aiming to improve the machining accuracy. The compensation techniques (Hsu and Wang 2007) are summarized into three steps: (i) to develop an error model for machine tools; (ii) to measure errors; and (iii) to conduct error compensation using the error model. The preprocess of error compensation is indispensable and a foremost technique to guarantee the machining accuracy.

However, the final machining error is a comprehensive interaction of various error sources including random errors such as vibration, tool wear, and environmental factors. It can be considered that the machining error is indirectly reflected in the relative position between the tool and workpiece. Hence the timely inspection of the workpiece and tool is essential in the process of machining (Roth et al. 2007). During conventional process, workpiece inspection is implemented with stand-alone equipment such as coordinate measuring machine, which is usually located at a separate room apart from the machine tool. This increases the overall machining cost and time to obtain the final products, and the production bottleneck may be caused by the product stagnation due to the time lag between the machining and inspection process in case of the flexible machining system. To increase the availability of

metrology for applications in advanced manufacturing, a shift in the approach of metrology from offline, lab-based solutions toward the use of monitoring probes integrated into manufacturing platforms is urgently needed. On-machine metrology can avoid the errors caused by repositioning workpieces and use the machine axes to extend the measuring range and improve the measuring efficiency. For the critical requirement of machining quality, the errors induced by removal and remounting process would deteriorate the quality if re-machining processes are necessary. Therefore, development of on-machine measurement will enable the reduction of measurement cycle time, in addition to a potential improvement of machining quality.

Geometric Error Analysis and Characterization of Machine Tools

Error Parameters Description and Its Modeling

The main factors affecting the machining accuracy of CNC machine tools are the original errors of machine tools and the errors produced in the machining process. The main errors and their causes are shown in Fig. 1. From the perspective of the different mechanisms of error generation, the error sources can be divided into four categories: geometric and kinematic error, thermal error, servo control error, and cutting force error. Among the various error sources of the machine tool, the thermal error and the geometric error are the main errors, which account for 65% of the total error.

The geometric error of machine tools refers to the difference between the actual position and ideal position of the platform or tool in the process of motion. The term "volumetric error" is firstly introduced to define the ability of a machine tool to produce accurate 3D shapes. To analyze the geometric errors, the International

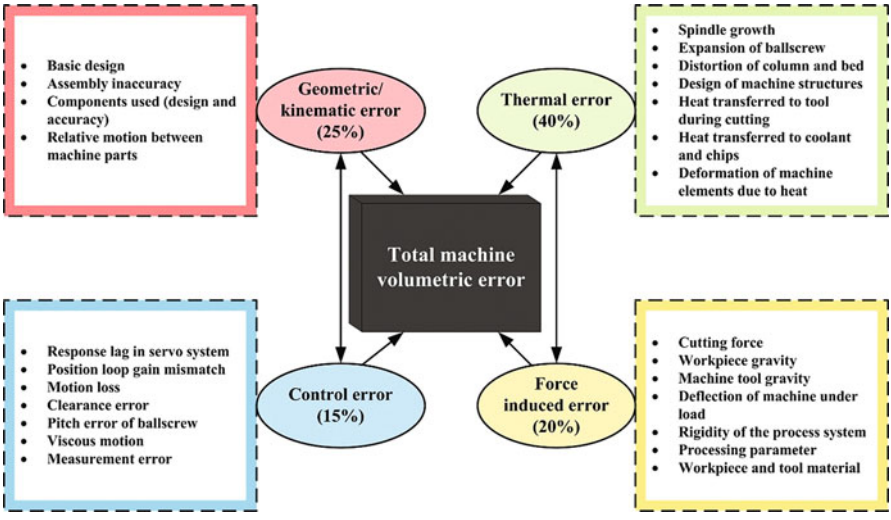

Fig. 1 The main error sources of CNC machine tools

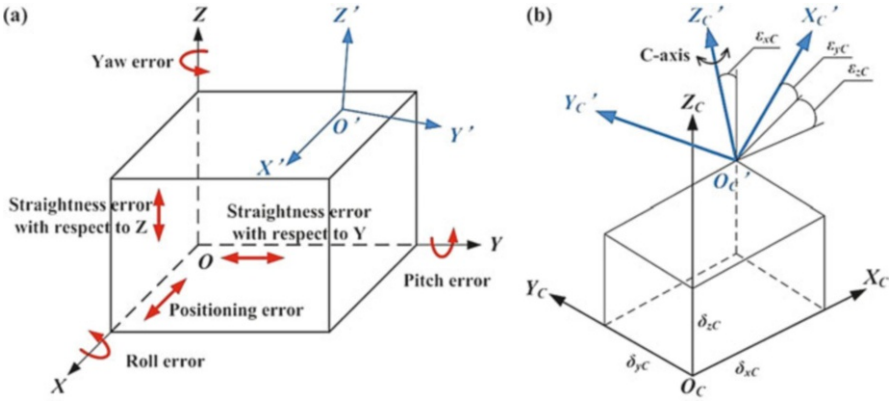

Fig. 2 Geometric errors of (**a**) X-slideway and (**b**) C-rotary table

Table 1 Notations of uniaxial kinematic errors

	Linear errors in respect to			Angular errors in respect to		
Error sources	X	Y	Z	X	Y	Z
X-slideway	δ_{xx}	δ_{yx}	δ_{zx}	ε_{xx}	ε_{yx}	ε_{zx}
C-rotary axis	δ_{xC}	δ_{yC}	δ_{zC}	ε_{xC}	ε_{yC}	ε_{zC}

Standards such as ISO 230 series have been developed to measure three main components of the machine tool, movable guide rails or linear axes, swiveling tables or rotary axes, and spindles, among which the spindles and the rotary axes can be bracketed together. Hence the main measurement objects, including five-axis machine tools, can be simplified as a linear axis and a rotary axis.

It is universally known that when an object moves in the three-dimensional space, it has six degrees of freedom (DOF); therefore, its position description has six errors. In a machine tool, similarly, there are six positional errors when a component moves along an axis. Taking X-slideway as an example, the six geometric error parameters are shown in Fig. 2a. The notation of error parameters is shown in Table 1.

For a 3-axis machine tool, there are 21 geometric error parameters, including positioning error (δ_{xx}), straightness error (δ_{yx}, δ_{zx}), pitch error (ε_{yx}), yaw error (ε_{zx}), roll error (ε_{xx}) of each axis, and squareness errors between every 2 axes. For multi-axis machine tools in precision and ultraprecision manufacturing, each rotation axis brings six geometric errors. Figure 2b shows the six geometric errors (δ_{xC}, δ_{yC}, δ_{zC}, ε_{xC}, ε_{yC}, ε_{zC}) of C-rotary table of a five-axis machine tool with a rotation-tilting table.

Error Characterization of Machine Tool

Measurement methodologies of geometric errors are divided into direct and indirect measurements. Direct measurements are used to measure linear positioning error,

straightness error, angular error, etc. of individual axes, whereas indirect measurements are adopted to analyze volumetric error.

Single Error

Direct measurement methods (Uriarte et al. 2013) allow to measure component of errors separately regardless of the kinematic model of the machine and the motion of the other axes. Single error measurements can be classified in three separate subgroups according to their metrological reference: (i) Gauge-based methods, which are primarily subject to their dimensions and materials, use artifacts such as line scales, straightedges, and step gauges; multidimensional artifacts, such as ball plates, have gained widespread use in recent years, as they helped to overcome the drawback of elementary material standards which typically represent only one special use in terms of dimension or measuring task. (ii) Gravity-based methods, typically use devices such as inclinometers or spirit levels, allow angular error measurement around horizontal axes, while not measurable are angular motions around vertical axes; in inclinometers, a differential capacitive displacement transducer enables detection of even very small deviations. (iii) Laser-based methods use the laser light linear propagation and its wavelength as a reference. Laser interferometry is the most widely applied method for machine tool calibration because of high measurement accuracy.

The first demonstration of using light interference principles as a measurement tool was achieved by Michelson who developed the first interferometer in the 1880s. Laser interferometers have been applied to machine tool calibration tasks as the laser beam is particularly suitable for displacement/length measurement (Wuerz and Quenelle 1983). Due to their long-coherence length, the use of interferometric techniques for high-precision measurements is possible even for long axes. The most accurate and time-saving approach for either short or long machine axis is the use of laser interferometers. However, some error sources should be considered for a correct length measurement: errors in laser wavelength; beam deflection that occurred due to temperature changes and gradients; Abbe errors caused by misalignment between interferometer and axis of motion; and any movement of the equipment during the measurement process. These methods that based on laser interferometer principally measure the individual errors of machines (e.g., positioning, straightness, angular and squareness errors). Some measurement systems that combine multiple sensors are available for the measurement of rotary axes.

Positioning Error

Figure 3a presents the equipment setup to measure the Y-axis positioning errors on a cantilever-type lathe. The linear interferometer is placed on the machine table. The retroreflector is mounted on the end of the spindle. During linear measurement the laser system measures the change in relative distance between a reference and measurement optical path. Either optic can be moving, providing the other optic remains stationary. This setup measures linear displacement accuracy of an axis by comparing the movement displayed on the machine's controller with that measured

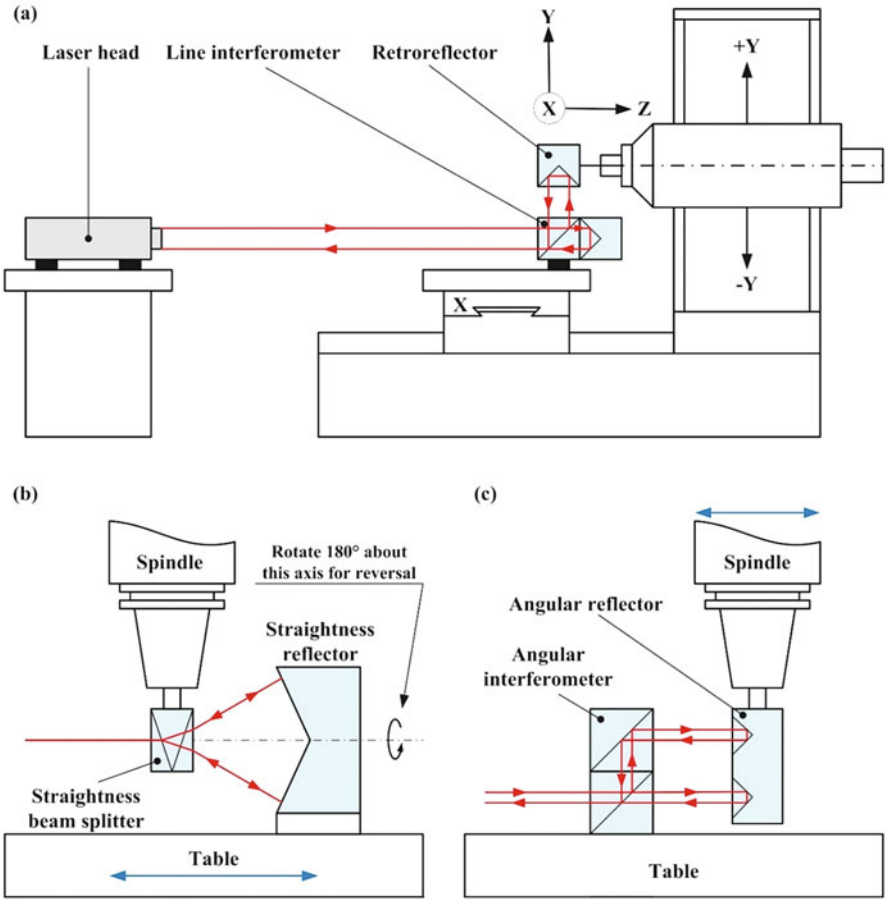

Fig. 3 Laser interferometers for (**a**) positioning error, (**b**) straightness error, and (**c**) angular error measurement

by the laser. Existing commercial laser interferometer can provide an accuracy of ±0.5 ppm with a resolution of 1 nm (Barman and Sen 2010).

Straightness Error

Straightness measurements record errors in the horizontal and vertical planes perpendicular to an axis movement. As is shown in Fig. 3b, a straightness interferometer is used comprising a Wollaston prism and a straightness reflector (Chen et al. 2005). The straightness reflector is mounted to a fixed position on the table even if it moves. The Wollaston prism should then be mounted in the spindle. Straightness measurements are made by monitoring the change in optical path generated by the lateral displacement of the straightness reflector or straightness beam splitter. The Wollaston prism performs as a beam splitter generating two separate beams that exit

the prism at an angle. Both are reflected and recombined to generate an interference signal that allows the lateral displacement of the reflector to be determined. A combination of two straightness measurements makes it possible to assess the parallelism of independent axes.

Angular Error

Pitch and yaw angular errors are among the largest contributors to machine tool positioning errors. Even a small error at the spindle can cause a significant effect at the tool tip. The use of an angular interferometer (Bryan et al. 1994) to measure the angular errors is shown in Fig. 3c. Two parallel beams are generated with a beam splitter mounted in a fixed position on the machine table and are reflected by an angular reflector mounted on the end of the spindle. Angular measurements are made by monitoring the change in optical path generated by the movement of the angular reflector. Current instruments can measure maximum angular deflections of up to $\pm 10^{\circ}$ with a resolution of 0.01 arcseconds. Laser interferometers have been designed to operate with three parallel measurement beams, so the positioning, pitch, and yaw errors can be measured simultaneously.

Rotary Axis Error

Figure 4 illustrates the use of a laser and angular interferometer to measure small angles of rotation of a rotary axis. As the axis rotates, the laser system detects the relative change between the optical path lengths in the two arms of the interferometer. As the axis rotates by angle θ, the laser beam in Arm 1 will get shorter by $S{\cdot}\sin(\theta)$, and the laser beam in Arm 2 will get longer by $S{\cdot}\sin(\theta)$ where S is the separation between the two retroreflectors. The total relative change in the path lengths, between arm 1 and arm 2, is therefore $2S{\cdot}\sin(\theta)$. This change in path

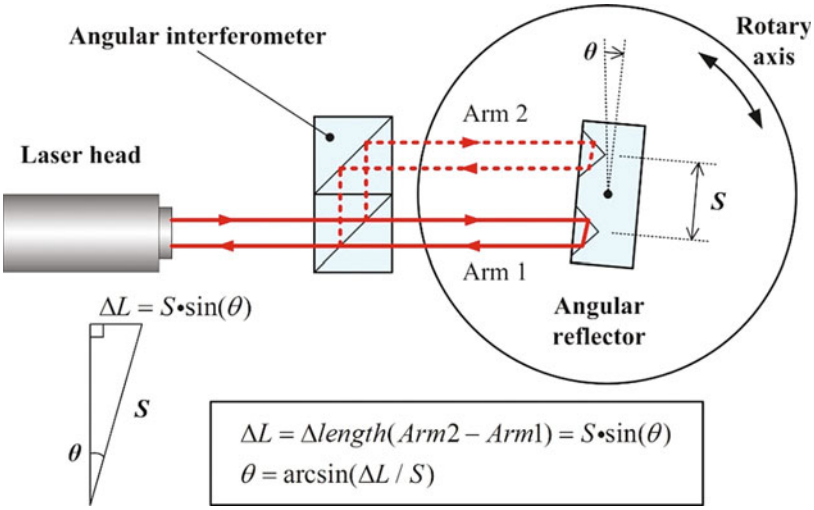

Fig. 4 Angle measurement principle of rotation of a rotary axis

lengths is detected by an interference fringe counter inside the detector unit of laser. The resulting fringe count is converted into a linear distance, ΔL, by multiplying by the $\lambda/2$. In angular mode the laser system software then converts ΔL into an angular measurement by calculating $\arcsin(\Delta L/S)$.

This arrangement is only suitable for checking angular movements over a range of about $\pm 10°$, because, at larger angles, the rotation of the angular reflector will cause misalignment of the returned laser beams and a corresponding loss of signal strength. However, this limitation can be readily overcome by combining measurements from the laser interferometer with those from a high-accuracy rotary axis, such as Renishaw XR20, which allows calibration of the axis over 360°, even over multiple revolutions.

Squareness Error

The squareness measurement is to measure the straightness of two nominal orthogonal axes according the same reference, which is the extension of the straightness measurement in the two-dimensional direction. The squareness of the two axes can be obtained by comparing the straightness. The reference usually refers to the optical alignment axis of the mirror. The mirror is neither moved nor adjusted during measurements to maintain the reference line unchanged. The optical square is used for at least one measurement, allowing the laser beam to be aligned with the former straight line without moving the mirror straightness.

Multi-degrees of Freedom Measurement

Multidimensional laser interferometers have been adopted to measure more than one degree of freedom (DOF) simultaneously, so that several error components of a machine axis are calibrated with a unique measurement system setup through single error measurement methods. These multidimensional measuring solutions provide two main possibilities: (i) measuring time that is greatly reduced because different setups and measuring systems are not needed anymore and (ii) the possibility to be embedded into a machine tool, where the position of tool center point could be detected in real time by monitoring six DOFs of each machine movement at the same time, with multiple measurement systems performing all at once. Two main multidimensional solutions are available based on the straightness measurement principle: One is a multi-interferometer-based method, where the source of the interferometer is divided into three beams to perform a five-DOF measurement; another method uses the laser beam as a straight and a position-sensitive device as a pointing sensor unit to measure straightness error, which is suitable for small- and medium-size machine tools (Schwenke 2012).

Volumetric Error

Comprehensive volumetric error measurement is to separate the error parameters through mathematical identification model and to use the measuring instruments to measure the multiple volumetric errors of machine tools at the same time. Since the 1980s, error measurement mainly focused on the application of new types of

precision measuring instruments of machine tools, such as the test bar and unidimensional probe, the disk gauge and bidimensional probe, double ball bar (DBB), capacitance ball probe (CBP), plane two-link mechanism, plane four-link mechanism, laser ball bar (LBB), etc. With the guidance of research works in the early 1980s (Bryan 1982; Knapp 1982), the tendency to take the abduction method of regular circular motion error measurement as the mainstream is basically formed. The ISO has added the motion test method for circular interpolation of CNC machine tools in the ISO 231. As a typical representative of the circular testing methods, DBB is widely applied and has been developed up to now. The CBP and LBB methods can all be regarded as the modifications of DBB.

Another established volumetric error indirect measurement method is the adoption of calibrated 1D, 2D, and 3D (Bringmann et al. 2005) artifacts. Figure 5 shows the 1D ball artifacts that were used to calculate the errors of the X-axis (Acosta et al. 2018). The artifacts have reference elements that are calibrated in two or three coordinates. By comparing measured coordinates to their calibrated values, error vectors resulting from the superimposed kinematic errors of the machine can be detected. By combining the data from several measurements at different orientations, an analytical or a best fit solution can be derived for the single kinematical errors. In general, this method has a higher requirement for the precision of the standard artifacts and can only measure a limited number of errors, so it is not widely used in practice. Recently, the research works have been focused on the improvement and application of mainstream methods such as laser interferometer and DBB, as well as the development and application of new detection methods and instruments, such as R-test and cross-grid encoder.

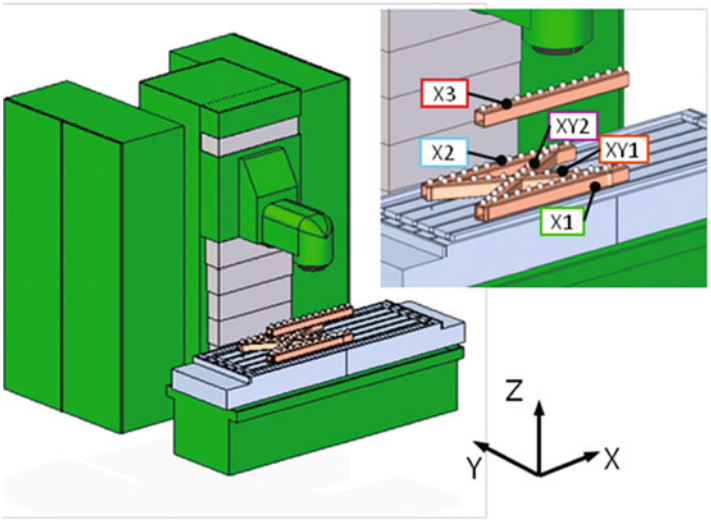

Fig. 5 Positions of the 1D artifact used to calculate the errors of the X-axis. (From Acosta et al. 2018)

Laser Interferometry

With the development of laser interferometry, the traditional interferometer-based single error measurements and comprehensive error measurements such as 12- and 14-line and 15- and 22-line methods have been widely applied in machine tool error measurement and identification. However, in actual measurement, most of these methods are extremely difficult to adjust, time-consuming, and long in measurement cycle, and additional expensive optical components are needed. ISO 230-6 defines the diagonal test method that the machine moves along each body diagonal of the machine's workspace, and the diagonal displacement is measured by using a laser interferometer (Ibaraki and Hata 2010). Diagonal test can calibrate the squareness errors of line axes, while the sensitivity to measurement error or noise is high in case of high aspect ratio of the measured volume. As an extension of diagonal measurement, the step-diagonal measurement has been put forward by Charles Wang (2000). The step-diagonal measurement modifies the diagonal measurement by performing a diagonal as a sequence of single-axis motions.

Conventional laser interferometers have long working range, but the variation of the measurement direction requires manual interaction. DBB can simply generate several measurement directions but is limited in the usable stroke. A combination can be seen in the use of the tracking laser interferometer or laser tracker. It is a laser interferometer with a steering mechanism to change the direction of the laser beam to track a target reflector which is usually mounted on the tool holder of the machine tool. Figure 6 (Gąska et al. 2014) shows a schematic grid of reference points within the distribution of probability and the laser tracker used to determine the distribution of errors, as reproduced by the machine. Since the angular measurement uncertainty of a tracking interferometer directly brings about the measurement uncertainty of the target's position, it is difficult to ensure the measurement uncertainty small enough to calibrate machine tools. Meanwhile, the tracking interferometers based on

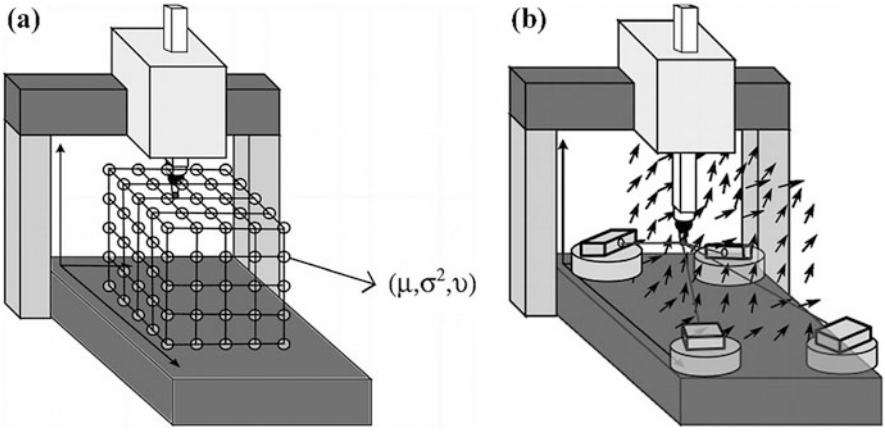

Fig. 6 (**a**) Grid of reference points. (**b**) Residual errors in nodes of reference grid and method of their identification. (From Gąska et al. 2014)

multilateration principle has been developed for machine tool measurement, in which the target of 3D position is calibrated by the distance from four or more tracking interferometers to the target (Ibaraki et al. 2014). Unlike traditional tracking interferometers which calibrate the target position from the distance and the laser beam direction, the multilateration measurement does not use the laser beam direction in its calculation and thus does not need higher angular positioning accuracy to ensure higher measurement accuracy of target position.

DBB

A ball bar usually consists of a kinematic artifact linking two precision balls, where precision linear variable differential transformers (LVDTs) are located between the two balls. A typical setup of a commercially available ball bar, where the measuring ball is fixed on the table of a machine tool and the center ball is attached to the spindle of the machine tool, can measure one-dimensional length variation and is ideal for quick checking of three-axis machine tools by means of the XY, YZ, and XZ planar circular tests (Kwon and Burdekin 1998). Figure 7 illustrates a DBB measurement in the X-Y plane (Lee et al. 2014); the two tested axes are driven simultaneously, causing the measuring ball to move on a circular path relative to the center ball. The change of distance between the two balls results from motion or dynamic errors of the two driven axes and is measured by a displacement sensor in the ball bar. Error origins can be rapidly diagnosed by comparing the resulting error trace with a set of reference trace patterns.

DBB is used extensively to calibrate the geometric and dynamic performance of linear machine tools. The main advantage of the DBB test methods is that it can find a servo mismatch of the simultaneously driven axes, while the laser interferometer and other optical displacement measuring devices only find positioning errors of a single axis. However, researches using DBB methods to test the rotary axes of

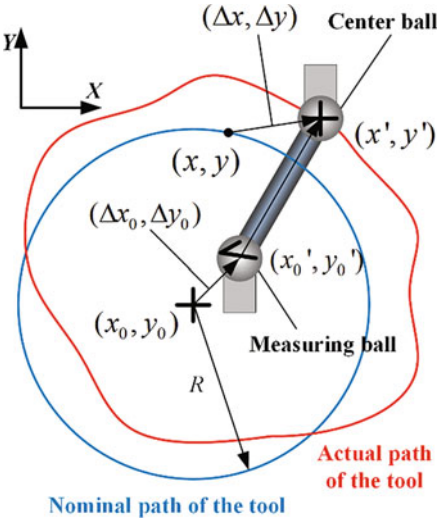

Fig. 7 DBB measurement in the X-Y plane

multi-axis machine tools simply, quickly, and effectively are deficient. Since ball bar measurement is one-dimensional, it often requires at least a couple of different setups to identify all location errors. A method for a tilting rotary-type five-axis machine tool has two steps to identify the imprecision of the rotary axes caused by the position-independent geometric errors (Jiang and Cripps 2017). The first step is designed to evaluate two rotary axes with one setup which performs fast diagnosis efficiency. A further accurate but slower check is carried out in the second step which aims to test the two rotary axes separately, each in two sub-steps. By means of varying the position of the pivot, the A- and C-axes can be tested individually. Both steps are performed with only one axis moving, thus simplifying the error analysis.

R-Test

As is described in ISO/CD 10791-6, many of the DBB tests presented above can be equivalently implemented by using a precision sphere and a linear displacement sensor (Utsumi et al. 2006). The 3D displacement of the sphere can be measured by using a nest of three (or more) linear displacement sensors. The R-test method was proposed based on this supposition (Weikert 2004; Bringmann and Knapp 2006). As depicted in Fig. 8a, the typical R-test device consists of a magnetic socket and three analogous distance sensors being arranged orthogonally to each other in a way that they are uniformly inclined to the horizontal plane. A ceramic sphere is adopted in contact with the three sensors at the same time. Using nominally flat contact geometries between the sensors and the sphere to be touched, the displacement of the center of the sphere is directly transferred by the three sensors (Hong et al. 2012). The three orthogonally aligned distance sensors presented in ISO 230-7 can be seen the same in principle. Furthermore, to identify all the geometric errors of the swiveling head in five-axis machine tools and to simplify the identification process, a new measuring approach (Fig. 8b) by indirectly using the R-test probing system is designed with the assistance of an auxiliary fixture (Li et al. 2017).

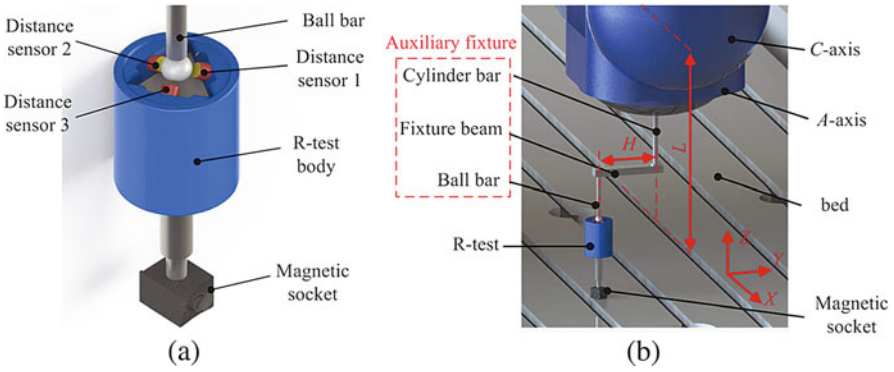

Fig. 8 R-test probing system. (**a**) Structure and (**b**) installation of the auxiliary fixture. (From Li et al. 2017)

Cross-Grid Encoder

The above methods have the problem that the installation, adjustment, and operation are very difficult and time-consuming. Aiming which, a cross-grid encoder (KGM) measurement system was developed by Heidenhain. It is a diffraction grating-type encoder to measure 2D position of an optical head by using a grid plate where grids are aligned orthogonally to each other. The KGM grid encoders consist of a grid plate with a waffle-type graduation, which is embedded in a mounting base, and a scanning head. During measurement, the scanning head moves over the grid plate without making mechanical contact. The KGM encoders capture any motions in a plane and separately transmit the values measured for the two axes. The cross-grid encoder test has many advantages such as high resolution, great agility of contact-free scanning measurement that permits free-form tests over any contours in two axes, and less restriction of relative motion speed. The resolution can reach 5 nm after subdivision, and the actual measurement speed can be up to 15 m/min, which means it is suitable for on-machine measurement (Du et al. 2010). The common KGM is 220 mm in diameter, making it unusable for error detection in the whole volume of a workspace.

On-Machine Measurement for Process and Product Quality Control

Various error measurement and compensation techniques and instruments have been developed and applied to greatly improve the performance of the machine tools. However, due to the mechanical and thermal deformations of the machine structure, motion errors of movable parts, and assembly error accumulated in a machine tool, the final machining accuracy disagrees with the output obtained from the embedded scales. In addition, clamping error of workpiece and tool wear also affect the final product quality. Progress in machine tools and measuring instruments requires the consideration of machine tool elements as well as setting and machining conditions, and it is essential to ensure the machining accuracy by providing the correct relative position between the cutting tool and workpiece. Therefore, on-machine and in-process measurements for the geometric parameters of workpiece and the tool setting are of equal importance.

Conception of OMM

A typical OMM system as illustrated in Fig. 9 is implemented using a workpiece measuring probe, which is usually stored in the tool library like a machining tool, and it is transferred to perform a certain measurement before or after a machining process. Integrating a workpiece measuring probe to the machine tool can deliver significant reductions in production time and cost and can be widely used for process improvement, automating, and speeding part processing, even eliminating part errors of the process. The machine tool should also be equipped with a tool setting probe

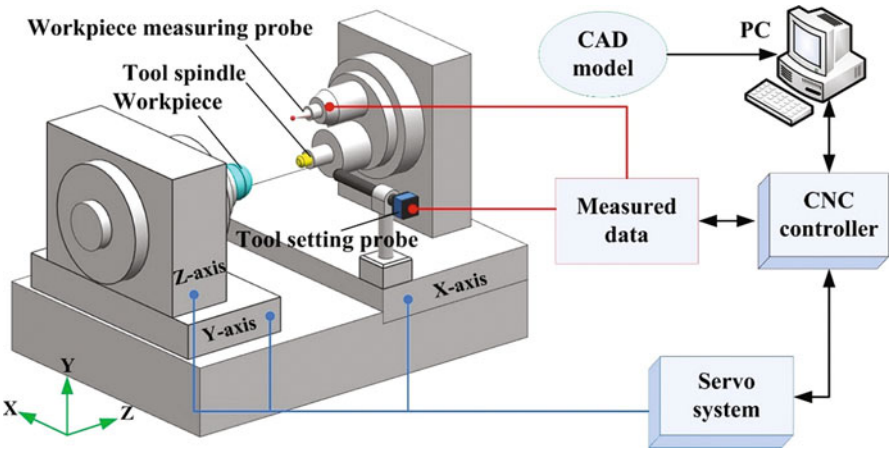

Fig. 9 Schematic diagram of on-machine measurement system structure

which is normally attached to the machine table or frame. Determining geometric information and the current condition of a cutting tool can help to improve the manufacturing process, including checking that the correct tool for the scheduled machining program has been loaded, correcting for tool wear, and automation of tool offset updating.

NC data generated using the part model is fed to the CNC controller for use in the first-step machining. After the machining process is finished, the workpiece measuring probe replaced with a cutting tool starts the measurement in the normal direction to the machined surface. Since a probe measures parts moving along the erroneous machine tool axes, the measured data inevitably include the probing errors originated from the structural characteristics of a touch probe and the positioning errors originated from the inaccurate axis motion of a machine tool. These errors should be eliminated from the measured data to obtain the true machining error. If the true machining error is larger than the given tolerance, the new toolpath is generated using the error compensation algorithm for the next-step machining. Machining and OMM processes are repeated until the required part tolerance is obtained, resulting in the closed-loop machining system.

ISO 230-10 has specified the test procedures for evaluating the measurement performance of contacting probe systems integrated with CNC machine tools. However, ultraprecision manufacturing that requires nanoscale measurement accuracy has accelerated their industrial application. On the other hand, the machine tools have largely spread to simultaneously multi-axis control machining to meet the ever-growing demands for precision parts with complex geometric properties, such as free forms and fine surface figures (Fang et al. 2013). To compensate for time-variable machining errors for the manufacture of complex structures in real time, on-machine measurement techniques with high accuracy are urgently needed.

Probing Techniques for Geometric Parameters of Workpieces

Contact Touch Probes

Contact touch probes can be classified into discrete and scanning groups based on the type of data being acquired, as shown in Fig. 10. Discrete probes, or touch-trigger probes (TTP), have the superiority of being cheaper than other options and are suitable for few data point acquisitions such as the position or size measurement. Scanning probes continuously touch the object as the probe is moved along the expected contour, which perform well in high-speed data acquisition on an object's form characteristics.

Machine-mounted probes are often referred to as TTPs, kinematic resistive probes, and strain gauge probes (Ali 2010), because they use switches that are triggered upon contact between the probe stylus and the workpiece being measured. As for kinematic resistive probes, most TTPs make use of a kinematic seating arrangement for the stylus. Three equally spaced rods rest on six tungsten carbide balls providing six points of contact in a kinematic location. An electrical circuit is formed through these contacts. The mechanism is spring loaded which allows deflection when the probe stylus contacts the part and also allows the probe to reseat in the same position within 1 μm when in free space. Under load of the spring, contact patches are created through which the current can flow. Reactive forces in the probe mechanism cause some contact patches to reduce which increases resistance of those elements. The variable force on the contact patch is measured as a change in electrical resistance. When a defined threshold is reached, a probe output is triggered. However, if the pivot distance varies depending on the direction in which the contact force acts in relation to the probe mechanism, pre-travel variation occurs to affect measurement performance. The use of strain gauge probes has improved the performance limitations mentioned above in kinematic resistive probes, because modern compact electronics and solid-state sensors have been embedded. The strain gauges are arranged to sense all stylus forces, which are summed together to acquire the measuring point. As a result, a lower trigger force is needed, and uniform pre-travel variation is achieved in all directions.

Analog scanning probe ensures a permanent and continuous contact between the probe and the component under measurement, so it is particularly suitable for

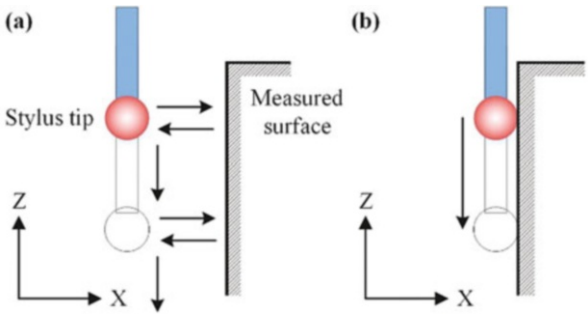

Fig. 10 Types of probes. (**a**) Touch-trigger probe, (**b**) scanning probe

free-form and contoured shaped components as well as for the measurement of large sheet metal assemblies, such as automobile components. Continuous analog scanning is a relatively new technology. Its main advantage is the high acquisition speed, which reduces dramatically the measuring time while offering a high density of data acquisition for a full definition of the size, position, and shape, enabling completely new opportunities for on-machine metrology (Weckenmann et al. 2004). To enable touch probing system to measure the shapes of both the workpiece and the tool during an electrical discharge machining process, a multiple-degrees-of-freedom arm for holding the probe with passive joints was reported (Furutani et al. 1999), which has the potential to be applied to OMM of a machined workpiece with a complex shape using multi-axis machine tools.

Optical Probes

Optical probes such as triangulation, interferometry, and confocal sensors have the advantages that they are non-contacting and nondestructive and, by using visual sensors, they also have a higher speed than contact methods, which can be used for rapid sampling. Interferometric probes among these methods have been widely applied because of high sensitivity and nano-level vertical resolution. In addition, the confocal laser probes can produce a very small spot with a resolution of up to 10 nm, which are suitable for the measurement of microstructure parts.

Optical Triangulation

Laser triangulation probes are increasingly considered as a viable alternative to touch probes for rapid dimensional measurements in a variety of applications. The main components of a triangulation probe are a collimated light source (generally a laser diode) and a detector unit consisting of an imaging lens and a detector (CCD line or position-sensitive diode). The optical axes of the light source and the imaging lens form a fixed angle, the so-called triangulation angle. The object surface is brought close to the point in which both axes intersect and the diffuse reflection of the light spot on the workpiece surface is imaged onto the detector. The position of the image on the detector is a function of the distance between sensor and specimen, as shown in Fig. 11a (Muralikrishnan et al. 2012). If a structured pattern generator is used to generate a laser line onto the target workpieces, the reflected laser line that follows the profile of the object is imaged back on the image sensor (Huang and Kovacevic 2011). The height of each point on the surface of the target stripe can be precisely determined based on the mathematical relationship derived from geometrical optics as illustrated in Fig. 11b. Another improvement is the realization of 3D scanning by adopting a galvanometer in a laser triangulation measurement system (Yang et al. 2018).

Interferometry

OMMs are very important for ultraprecision machining because it requires tolerance on the order of several tens of nanometers. The practical purpose is to make the repeated correction processes efficient and enable compensation for accidental and systematic machining errors by direct process control. To meet these demands,

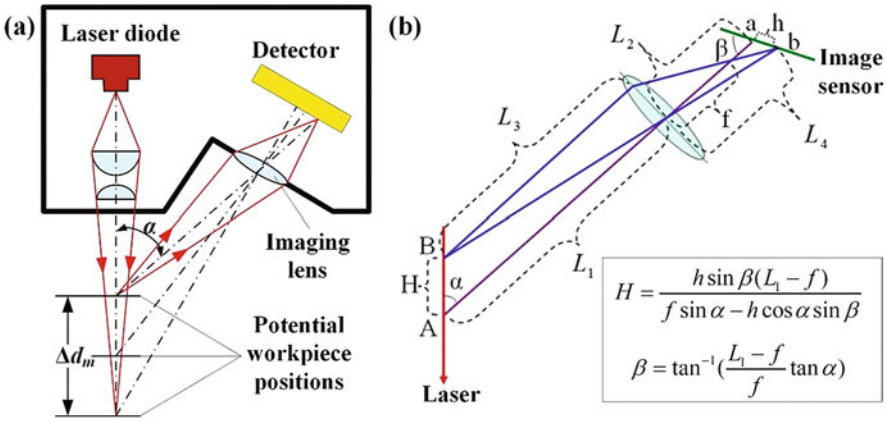

Fig. 11 Laser triangulation probe. (**a**) Structure, (**b**) measurement principle

high-precision optical interference measurement methods were initially developed. Many commercial compact laser interferometers (Muralikrishnan et al. 2016) are stable and reliable enough for dimensional measurement such as position, size, and profile scanning, while the shape and surface measurements using wavefront interferometry seem to be easily affected by disturbances such as vibration and air turbulence in the optical paths. Improved measuring instruments such as Fizeau interferometer, zone-plate interferometer, and lateral-shearing interferometer were mounted on a modified lathe to examine the measurement performance while the machine was running. Nomura (Nomura et al. 1998) invented a common-path lateral-shearing interferometer for machine running combined with fringe-scanning method, which was little affected by mechanical vibrations and air turbulence.

Phase-shifting laser interferometer (Tian and Liu 2016) is a common full-field shape measurement equipment for spherical or aspherical optical mirrors that are machined by ultraprecision diamond turning. When it comes to in-process or on-machine measurements, however, multiple frames of data are required over many milliseconds, which means vibration and turbulence have enough time to degrade the measurement results. A better approach for reducing these effects is to capture all the phase-shifting frames fall on a single CCD camera at once (Millerd et al. 2017). As shown in Fig. 12, a holographic optical element (HOE) is used to split interferograms into four separate beams. The four beams pass through a phase-shifting mask and a polarizer with its transmission axis at $\pi/4$ to the direction of the polarization of the test and reference beams placed in front of the CCD array. In this way a single detector array captures all four phase-shifted interferograms in a single shot.

To achieve trans-scale and close-to-machine measurement with low uncertainty, a complementary integrated system that combines the large-aperture DHI and the sub-aperture stitching WLI was proposed (Yang and Zhang 2018). As shown in Fig. 13, the DHI subsystem is used to complete a rough measurement of the overall profile of the object, and thus establish a reasonable way of path planning, and then guide the WLI probe to measure the local detail features with nanometer accuracy.

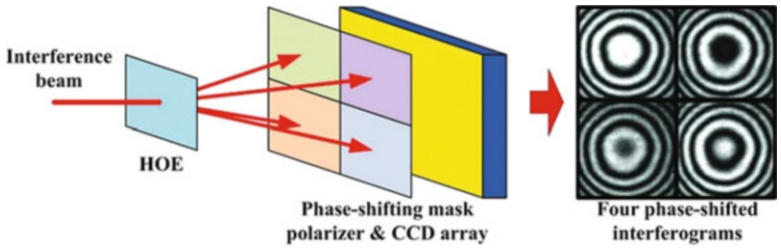

Fig. 12 A single-shot detector to capture four separate, phase-shifted interferograms

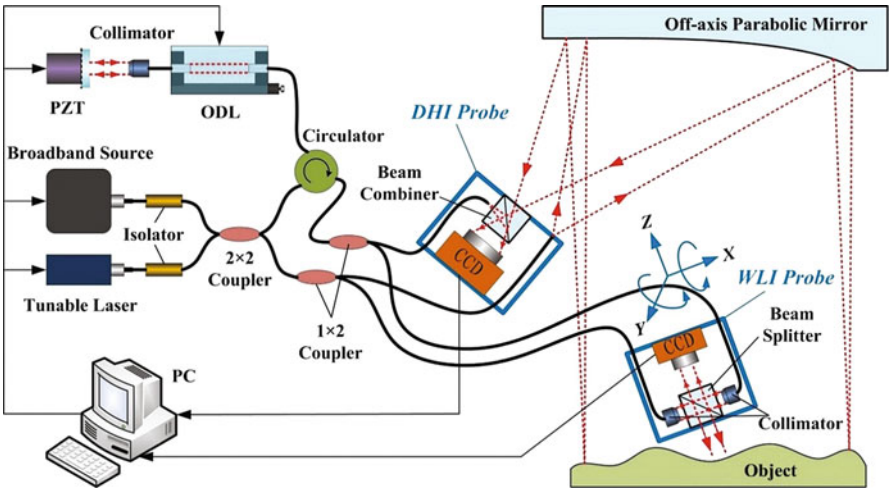

Fig. 13 A complementary integration of the large-aperture DHI and the sub-aperture stitching WLI. *ODL* optical delay line

Confocal Probing

Chromatic confocal sensing is a well-known measurement technique that is able to evaluate the position of a point on an object surface along the optical axis of the system with high accuracy. The optical principles of an improved chromatic confocal probe are illustrated in Fig. 14a (Zou et al. 2017). The white light point source passes through an objective lens, which diffracts the emerging light according to its wavelength. Only light of a wavelength λ_M is focused at a point M on the surface being measured. The backscattered light passes back through the objective lens and is then directed toward the detector by a beam splitter. The pinhole located at the image of *M* plays an essential role in this system because it filters out all wavelengths except λ_M that derive from points located on the optical axis above or below *M*. A confocal probe-based OMM system is shown in Fig. 14b. The system is composed of an aerostatic spindle and vacuum chuck, two horizontal hydrostatic slideways (x- and z-axes), an orthogonal y-axis precision stage, a chromatic confocal probe mounted on the y-axis translation stage, a standard radius sphere affixed in the vacuum chuck (the master sphere), and a second standard radius sphere

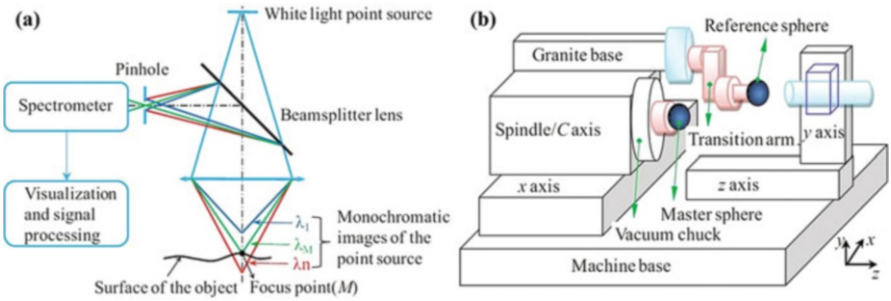

Fig. 14 A chromatic confocal probe. (**a**) The optical principle, (**b**) schematic diagram of the OMM system. (From Zou et al. 2017)

(the reference sphere) mounted to a granite base located on top of the spindle via a dedicated transition arm attached to a standard System 3R holder.

The chromatic confocal probe and y-axis translation stage form an integrated component of the OMM system, and the reference sphere and transition arm form another integrated component. The y-axis precision stage is bolted onto the z-directional slideway. The optical axis of the measurement probe is adjusted to be collinear to z-direction. The spindle and vacuum chuck are positioned on the x-directional slideway. The standard spheres must be of sufficiently high geometric accuracy and are employed to calibrate the relative distance between the rotary axis of the spindle and the center of the reference sphere.

Shack-Hartmann Wavefront Sensing

Shack-Hartmann wavefront sensing (Platt and Shack 2001) is one of the well-known optical measuring methods for lens aberration or concave mirror surface figure. The basic structure of the Shack-Hartmann wavefront sensor is composed of a microlens array and a CCD camera. Each lens takes a small part of the aperture (sub-aperture) and forms an image of the light source. According to the relationship of simple geometrical optics, the average slope of the wavefront can be calculated by measuring the difference between the centroid coordinate position of the actual imaging spot and the centroid coordinate position of the actual imaging spot and the centroid coordinate position of the reference imaging spot. The actual wavefront can be reconstructed between the slope data and the Zernike coefficients. The Shack-Hartmann wavefront sensor has a large dynamic range and high measurement accuracy, low environmental requirements, short detection time, and easy operation which is used for the on-machine measurement of the position and displacement and aspheric and free-form surfaces.

Measurement Tools for Process Control and Tool Setting

Machining accuracy is largely affected by tool conditions including the geometric features of the tool, tool setting, and tool behavior during machine running. Generally, systematic machining error is caused by the geometric features of a

tool and the tool setting, while accidental machining error is introduced due to the tool behavior during machine running. The specific geometrical tool conditions related to systematic machining error are the tool length, tool diameter, cutting-edge sharpness, and tool setting with respect to the position of the tool tip and the dynamic balance. However, unexpected behavior and fluctuation of the tool such as deflection and dynamic and thermal conditions and tool wear during machining make the machining conditions unstable. With the help of OMMs, an essential control of machining process capability can be achieved by improving the machining repeatability.

Touch-trigger probe or laser-based technologies are usually applied for tool setting. The touch-trigger tool setter uses the same kinematic technology as workpiece inspection probe which has been introduced in section "Contact Touch Probes." Noncontact laser tool setting system uses a beam of laser light, passing between a transmitter and a receiver, positioned within the machine tool so the cutting tools can be passed through the beam. The passage of a tool into the beam causes a reduction in laser light seen at the receiver, from which a trigger signal is generated. This latches the machine position at that instant, providing the information to determine a tool's dimension. With approaches from several directions, tool geometry can also be accurately determined. These systems can also be used to detect broken tools, by rapidly moving the tool into a position where it should intersect the laser beam; if light reaches the receiver, the tool tip must be missing.

Tool cutting-edge profile is an essential factor that significantly affects the machining process capability index, and it is expected to remain changed during machining, ideally for stable and high machining accuracy. During ultraprecision cutting, the depth must be controlled within nanometers. Therefore, it is important for assurance of the machined surface quality to make periodic checks on the tool cutting edge without moving the tool from the machine. A measuring instrument consisting of an atomic force microscope (AFM) and an optical alignment probe was developed for fast measurement of 3D cutting-edge profiles of single-point diamond cutting tool (Gao et al. 2009).

The reduction of accidental machining error by monitoring the dynamic conditions of the tool, such as the tool wear which is the result of a combination of load factors (mechanical, thermal, and chemical) affecting the cutting edge of the tool, is an important technical issue. Various sensors have been developed while the machine vision sensors performed online monitoring with high-speed (real time) and noncontact capability. In addition, as machine vision and artificial intelligence are natural partners, integration of the two technologies is to provide a better understanding of the tool wear problem (Malekian et al. 2009). The edge radius of the tool is used for the monitoring of the tool conditions, and it could be measured by counting pixels from the vision system and comparing the number with the scale on the reticle. On the other hand, cutting forces (static and dynamic), AE, and vibration (acceleration) are considered the most widely applicable parameters. Advances and increased sophistication in instrumentation technology employed for measuring these parameters make them viable,

practical, cost-effective, robust, and easy to mount and have the quick response needed to indicate changes for online monitoring of machining process (Teti et al. 2010).

Measurement of Distance Between Tool and Workpiece

Control of the relative distance between a tool and a workpiece is quite important in ultraprecision machining because the relative distance determines their interaction and the quality of a machining result. In general, the position of a tool or a workpiece is controlled with embedded scales of positioning systems. However, due to the mechanical and thermal deformations of the machine structure, motion errors of movable parts, and assembly error accumulated in a machine tool, the final relative distance between a tool edge and a workpiece surface disagrees with the output obtained from the embedded scales. In addition, clamping error of workpiece and tool wear are also added to the relative distance. Thus, a direct measurement of the distance between the tool edge and the workpiece surface is especially required.

Figure 15 shows a measurement model of laser diffraction for tool setting clearance between the tool tip and workpiece surface (Shi et al. 2015). The clearance between the tool and the workpiece is set for x, the wavelength of the laser beam is set for λ, and the diffraction light angle is set for θ. When the laser passes through the tool workpiece clearance, diffraction fringes will be generated. Then the diffraction fringes go through the Fourier lens with the focal length f and finally irradiate on the CCD screen. The computer will process intensity information of the diffraction fringes obtained from the CCD camera. According to the integral formula of Fraunhofer diffraction, the distance between the tool tip and the workpiece surface can be calculated.

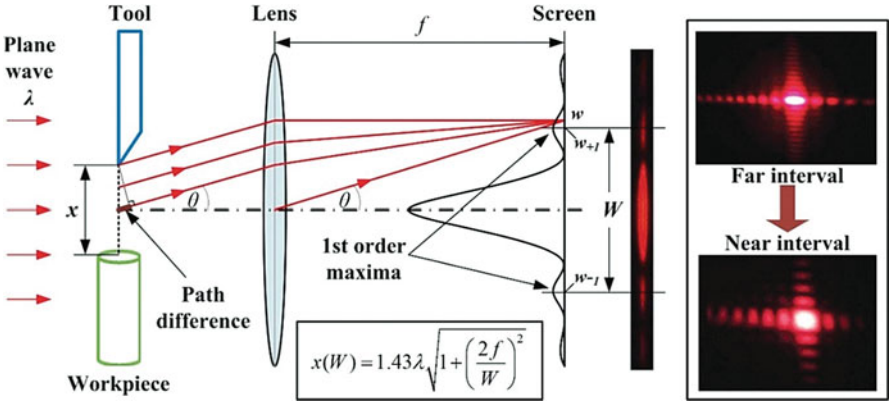

Fig. 15 Laser diffraction application on distance measurement

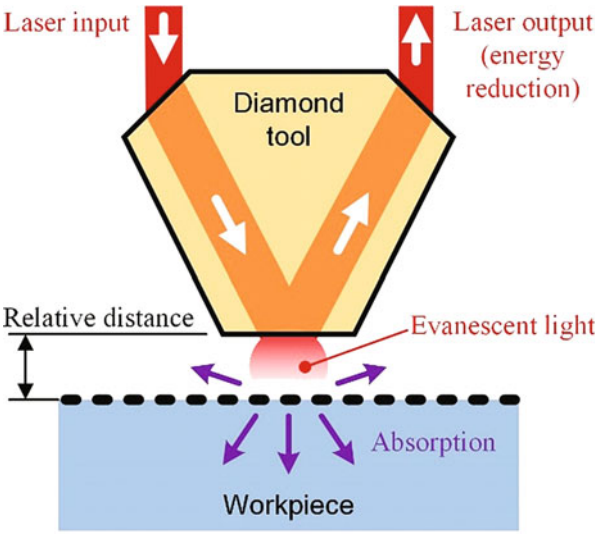

Fig. 16 Evanescent light application on distance measurement

Single crystal diamond tools are widely used as a tool in ultraprecision cutting, and the diamond crystal has a large index of refraction. As shown in Fig. 16, when a laser beam is irradiated to the tool edge over the critical angle, the total reflection of laser beam generates evanescent light in the sub-micrometer area from the tool edge. Evanescent light has the intensity distribution depending on a distance from the tool edge (Yoshioka et al. 2014). Approach of the tool to a workpiece results in absorption and dispersion of evanescent light, and it decreases the intensity of reflected light. Thus, the distance can be estimated by monitoring of the intensity of reflected light.

Integration of Online Machining and Process Monitoring

Various developments in machine tool metrology and OMM technology lead to increasing the automation, flexibility, and productivity of machine tools. The process capability is evaluated as being worse than the actual capability because of the measurement uncertainty (Mutilba et al. 2017). Therefore, when the improvement of process capability is attempted, the measurement uncertainty should be suppressed to determine the control target based on process capability indices estimated as accurately as possible. Meanwhile, it is important to enable further fine-tuning of the control qualities during the machining process for high repeatability and robustness. To achieve this progress in machine tools, a fusion of machining and measurement technologies is required to optimize the assessment and control of the machining process during machining.

In most developments of OMM, the measuring instruments were implemented or mounted externally to the machine tools. However, to develop more advanced methods for direct control of the machining process, machine tools with internal sensors were required. The sensing techniques for monitoring and controlling the machine force can be considered as in-process measurements that are independent of external and internal factors. And much research effort has gone into the autonomous determination of machining parameters for conducting feedback control while minimizing human intervention. This was developed to enable even a non-expert machine operator to perform highly productive and accurate machining processes. This is because in conventional NC machining, the process control of an expert machine operator can be provided as feedback control that includes the decisions of the human operator. Furthermore, it is suggested that the application of process monitoring and control to specific machining problems has practical values, which include micromachining and machining of new and difficult-to-cut material areas in which even expert human operators find effective process planning difficult. This productive insight was supported by the development of an adaptive spindle with three built-in force sensors, which enables active compensation of static and dynamic tool deflections and stabilization of milling processes (Möhring et al. 2010). For the simultaneous measurement of the grinding force and workpiece form error during cylindrical-plunge grinding, capacitive probes are embedded in the work spindle to produce normal and tangential grinding forces, and an additional capacitive probe is applied to measure the size of the workpiece.

Integration of online machining and inspection is an effective way for machining process control to improve machining quality. The conventional approach for the integration of the machining and inspection operations is that, first, inspect the workpiece after certain machining processes or just the final state of the machined workpiece using a CMM or using online inspection devices on machine tools and then compensate or adjust the tool path according to the inspection results. Construction of uniform information model and definition of standardized interfaces are the primary methods for the integration of machining and inspection. It is also important and beneficial to alert an abnormal state of a machining process and address the issue in a timely manner through the integration of machining and monitoring functions. Monitoring signal data analysis is the approach for machining condition recognition based on the sensor signals. Typical signal data analyzing methods include artificial intelligence algorithms, multi-signal fusion methods, and wavelet analysis methods. The ultimate goal of monitoring is used for adjusting the machining strategy timely to improve the machining stability and machining quality, i.e., modifying tool path and changing machining parameters and operation sequence and conditions. The current research efforts mainly include cutting parameter adjustment to stabilize the cutting force, decrease vibration, suppress machining chatter, and avoid surface defect of workpiece. Figure 17 describes an integrated manufacturing process planning and online control based on intelligent software agents and multidimensional manufacturing features (Liu et al. 2014).

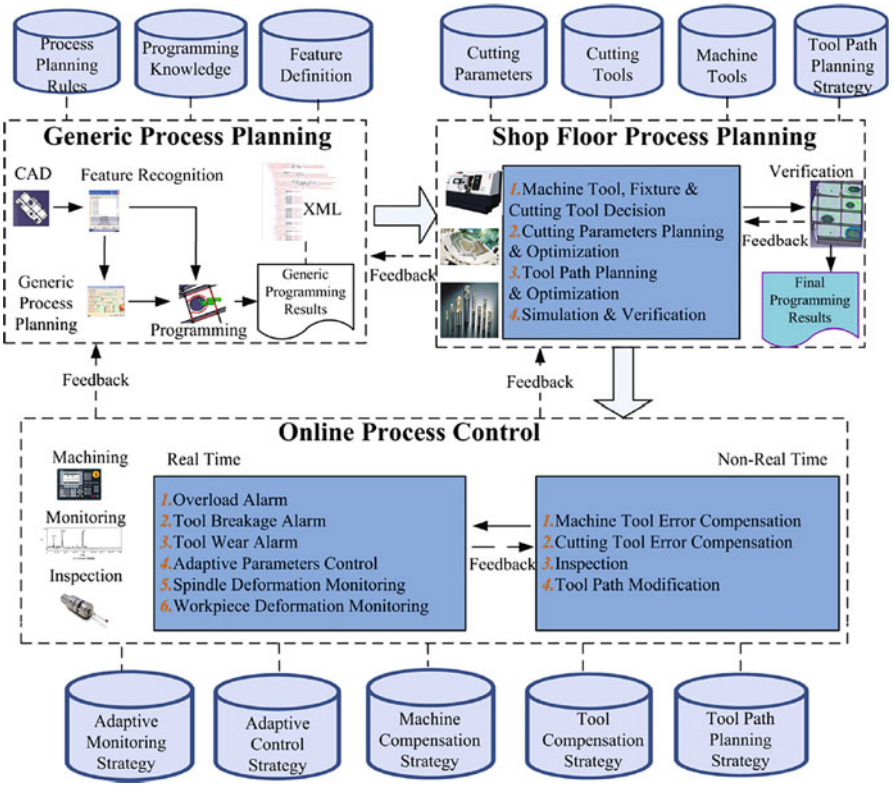

Fig. 17 Architecture of process planning and control system. (From Liu et al. 2014)

Conclusion

With the rapid development of hi-tech and new tech, the requirements for machining accuracy of parts have risen from micron- to submicron and even nanometer level. The trend toward individualized products and smaller lot sizes with high precision increases the demands of higher machining reliability and flexibility in production. However, many factors still result in machining errors which can be considered as the original errors of machine tools and the errors produced in the machining process, involving kinematics errors, thermal errors, cutting force-induced errors, servo errors, machine structural errors, vibration and tool wear, etc.

For the original errors of machine tools, various error measurement and compensation techniques and instruments have been developed and applied to greatly improve the performance of the machine tools. Measurement methodologies are divided into direct measurements and indirect measurements. Direct measurements are used to measure single errors such as the linear positioning error, straightness error, and angular error of individual axes, whereas indirect measurements are

adopted to analyze volumetric error. Laser interferometers are undoubtedly the best choice for single error calibration because of its high measurement accuracy and long working range, and a series of mature commercial instruments have been launched to such applications. Some systems combine multiple interferometers for simultaneous measurement of positioning, straightness, and angular errors. However, the environmental factors have a non-negligible impact on the laser wavelength and optical path difference, which are directly transferred into errors in the measurement results. Comprehensive volumetric error measurement is to separate the error parameters through mathematical identification model and to use the measuring instruments to measure the multiple volumetric errors of machine tools at the same time. Recent research works focus on the improvement and application of mainstream methods such as the tracking laser interferometer and DBB, as well as the development and application of new detection methods and instruments, such as R-test and cross-grid encoder. These methods still have many limitations as follows:

1. Measurable dimension: DBB tests measure only one-dimensional displacement of the tool center position. Interferometer-based diagonal and step-diagonal tests also perform one-dimensional measurements.
2. Measurable positions: Artifact-based measurement can measure only at pre-calibrated positions. Motion trajectories for DBB tests are limited by the position of the fixed ball. Tracking laser interferometers can measure arbitrary positions in large workspace, although their measurement uncertainty may change considerably according to the target position.
3. Axis separation: DBB tests for rotary axes and R-tests are typically performed with two or three linear axes driven synchronously with a rotary axis of interest. The measurement result will be influenced by all axes involved. Most volumetric error measurement methods have the problem about the separation of error motions of linear axes and rotary axes in kinematic model construction.
4. Angular errors: Quasi-static measurement of artifact can evaluate angular errors directly. DBB tests and R-tests only measure the position of the reference sphere center, because the sphere does not define any direction. Angular errors can be assessed only when the kinematic model is best fitted by measuring data at multiple points.

The final machining errors are generated due to the interaction of geometric errors, thermal errors, force errors, and servo errors of machine tools. The mechanism of these error interactions is not clear, which brings difficulties to error measurement and modeling. A great variety of instruments recommended by the ISO 230 series generally have shortcomings such as long measuring period and low measuring efficiency, which make the overall measurement and compensation of machine tools error can't really be implemented and become a technical bottleneck that restricts the improvement of measurement accuracy and manufacturing level. Therefore, how to achieve the high accuracy and fast measurement of multi-error parameters has become one of the key problems that need to be solved urgently for the error compensation of machine tools.

Due to the mechanical and thermal deformations of the machine structure, motion errors of movable parts during machine running, and assembly error accumulated in a machine tool, the final machining accuracy disagrees with the output obtained from the embedded scales. In addition, the final machining error is a comprehensive interaction of various error sources including random errors such as vibration, tool wear, and environmental factors. It can be considered that the machining error is finally reflected directly in the machining quality of the products and indirectly in the relative position between the tool and workpiece. Progress in machine tools and measuring instruments requires the consideration of machine tool elements as well as setting and machining conditions, and it is essential to ensure the machining accuracy by providing the correct relative position between the cutting tool and workpiece. In-process and on-machine measurements constitute the simplest method for achieving high accuracy and small uncertainty values, as well as reducing the measurement procedures. Nevertheless, the system requires optimal trade-off between machining time and measurement performance. The conventional approaches focus on achieving good measurement performance without a clear trade-off and on the practical benefit of introducing in-process and on-machine measurements.

"Industry 4.0" represents an initiative for the future development of machine tools. The conception aims to combine the manufacturing industry and measurement technology to make production more flexible, where the flexibility offers the possibility to manufacture customized products through efficient manufacturing processes. As demand fluctuates and batch sizes fall, efficiency in process adjustment and production control operations become crucial. During production, machine tool performance, cutting tool conditions, cutting parameters, and workpiece geometry and properties change all the time. The integration of online machining, inspection, and monitoring is a final solution to addressing the problems mentioned above. Efforts have been made in online adjustment of cutting parameters and emergency actions and online tool path compensation. Advanced sensors and sensor systems such as dynamometers, accelerometers, AE sensors, and current and power sensors have been adopted for intelligent monitoring of machining process. However, more work should be devoted to online process control, information fusion, and optimization for dynamic and complex machining conditions.

References

Acosta D, Albajez JA, Yague-Fabra JA (2018) Verification of machine tools using multilateration and a geometrical approach. Nanomanuf Metrol 1(1):39–44

Ali S (2010) Probing system characteristics in coordinate metrology. Meas Sci Rev 10:120–129

Barman S, Sen R (2010) Enhancement of accuracy of multi-axis machine tools through error measurement and compensation of errors using laser interferometry technique. Mapan 25:79–87

Bringmann B, Knapp W (2006) Model-based 'chase-the-ball' calibration of a 5-axes machining center. CIRP Ann Manuf Technol 55:531–534

Bringmann B, Kung A, Knapp W (2005) A measuring artifact for true 3D machine testing and calibration. CIRP Ann 54:471–474
Bryan JB (1982) A simple method for testing measuring machines and machine tools, part 1and 2. Precis Eng 4(2, 3):61–69. 125–138
Bryan JB, Carter DL, Thompson SL (1994) Angle interferometer cross axis errors. CIRP Ann Manuf Technol 43:453–456
Chen Q, Lin D, Wu J et al (2005) Straightness/coaxiality measurement system with transverse zeeman dual-frequency laser. Meas Sci Technol 16:2030
Du Z, Zhang S, Hong M (2010) Development of a multi-step measuring method for motion accuracy of NC machine tools based on cross grid encoder. Int J Mach Tools Manuf 50:270–280
Fang FZ, Zhang XD, Weckenmann A et al (2013) Manufacturing and measurement of freeform optics. CIRP Ann Manuf Technol 62:823–846
Furutani K, Iwamoto K, Takezawa H et al (1999) Multiple degrees-of-freedom arm with passive joints for on-the-machine measurement system by calibrating with geometric solids. Precis Eng 23:113–125
Gao W, Asai T, Arai Y (2009) Precision and fast measurement of 3D cutting edge profiles of single point diamond micro-tools. CIRP Ann Manuf Technol 58:451–454
Gąska A, Krawczyk M, Kupiec R et al (2014) Modeling of the residual kinematic errors of coordinate measuring machines using LaserTracer system. Int J Adv Manuf Technol 73(1–4):497–507
Hong C, Ibaraki S, Oyama C (2012) Graphical presentation of error motions of rotary axes on a five-axis machine tool by static R-test with separating the influence of squareness errors of linear axes. Int J Mach Tools Manuf 59:24–33
Hsu YY, Wang SS (2007) A new compensation method for geometry errors of five-axis machine tools. Int J Mach Tools Manuf 47(2):352–360
Huang W, Kovacevic R (2011) A laser-based vision system for weld quality inspection. Sensors 11:06–21
Ibaraki S, Hata T (2010) A new formulation of laser step diagonal measurement – three-dimensional case. Precis Eng 34:516–525
Ibaraki S, Nagae K, Sato G (2014) Proposal of "open-loop" tracking interferometer for machine tool volumetric error measurement. CIRP Ann Manuf Technol 63:501–504
Jiang X, Cripps RJ (2017) Accuracy evaluation of rotary axes of five-axis machine tools with a single setup of a double ball bar. Proc Inst Mech Eng B J Eng Manuf 231:427–436
Knapp W (1982) Test of the three-dimension uncertainty of machine tools, part 1 and 2. Precis Eng 4:459–464
Kwon HD, Burdekin M (1998) Measurement and diagnostics of machine tool errors during circular contouring motions. Proc Inst Mech Eng B J Eng Manuf 212:343–356
Lee HH, Lee DM, Yang SH (2014) A technique for accuracy improvement of squareness estimation using a double ball-bar. Meas Sci Technol 25:094009
Li J, Xie F, Liu X et al (2017) A geometric error identification method for the swiveling axes of five-axis machine tools by static R-test. Int J Adv Manuf Technol 89:3393–3405
Liu C, Li Y, Shen W (2014) Integrated manufacturing process planning and control based on intelligent agents and multi-dimension features. Int J Adv Manuf Technol 75:1457–1471
Malekian M, Park SS, Jun MB (2009) Tool wear monitoring of micro-milling operations. J Mater Process Technol 209:4903–4914
Millerd J, Brock N, Haye J et al (2017) Vibration insensitive interferometry. In: International conference on space optics – ICSO 2006, 10567:105671P
Möhring HC, Litwinski KM, Gümmer O (2010) Process monitoring with sensory machine tool components. CIRP Ann Manuf Technol 59:383–386
Muralikrishnan B, Ren W, Everett D et al (2012) Performance evaluation experiments on a laser spot triangulation probe. Measurement 45:333–343
Muralikrishnan B, Phillips S, Sawyer D (2016) Laser trackers for large-scale dimensional metrology: a review. Precis Eng 44:13–28

Mutilba U, Gomez-Acedo E, Kortaberria G et al (2017) Traceability of on-machine tool measurement: a review. Sensors 17:1605

Nomura T, Kamiya K, Miyashiro H et al (1998) Shape measurements of mirror surfaces with a lateral-shearing interferometer during machine running. Precis Eng 22:185–189

Platt BC, Shack R (2001) History and principles of Shack-Hartmann wavefront sensing. J Refract Surg 17:S573–S577

Roth JT, Mears L, Djurdjanovic D et al (2007) Quality and inspection of machining operations: review of condition monitoring and CMM inspection techniques – 2000 to present. In: ASME 2007 international manufacturing science and engineering conference, pp 861–872

Schwenke H (2012) The latest trends and future possibilities of volumetric error compensation for machine tools. In: Proceedings of the 15th international machine tool engineers' conference, IMEC, Tokyo, Japan 2–3, pp 57–71

Shi G, Liu J, Yu Z, Shi G (2015) Laser diffraction application on detection technology of online tool setting. In: International conference on optoelectronics and microelectronics (ICOM), pp 62–64

Teti R, Jemielniak K, O'Donnell G et al (2010) Advanced monitoring of machining operations. CIRP Ann Manuf Technol 59:717–739

Tian C, Liu S (2016) Two-frame phase-shifting interferometry for testing optical surfaces. Opt Express 24:18695–18708

Uriarte L, Zatarain M, Axinte D et al (2013) Machine tools for large parts. CIRP Ann Manuf Technol 62:731–750

Utsumi K, Kosugi T, Saito A et al (2006) Measurement method of geometric accuracy of five-axis controlled machining centres (measurement by a master ball and a displacement sensor): measurement by a master ball and a displacement sensor. Trans Jpn Soc Mech Eng C 72:2293–2298

Wang C (2000) Laser vector measurement technique for the determination and compensation of volumetric positioning errors. Part I: basic theory. Rev Sci Instrum 71:3933–3937

Weckenmann A, Estler T, Peggs G et al (2004) Probing systems in dimensional metrology. CIRP Ann Manuf Technol 53:657–684

Weikert S (2004) R-test, a new device for accuracy measurements on five axis machine tools. CIRP Ann Manuf Technol 53:429–432

Wuerz LJ, Quenelle RC (1983) Laser interferometer system for metrology and machine tool applications. Precis Eng 5:111–114

Yang S, Zhang G (2018) A review of interferometry for geometric measurement. Meas Sci Technol 29(10):102001

Yang S, Yang L, Zhang G et al (2018) Modeling and calibration of the galvanometric laser scanning three-dimensional measurement system. Nanomanuf Metrol 1:180–192

Yoshioka H, Shinno H, Sawano H et al (2014) Monitoring of distance between diamond tool edge and workpiece surface in ultraprecision cutting using evanescent light. CIRP Ann Manuf Technol 63:341–344

Zou X, Zhao X, Li G et al (2017) Non-contact on-machine measurement using a chromatic confocal probe for an ultra-precision turning machine. Int J Adv Manuf Technol 90:2163–2172

Measurement Technology for Precision Machines

19

Shuming Yang, Changsheng Li, and Guofeng Zhang

Contents

Introduction 513
Principles of Measurement for Machine Tool Metrology 513
Measurement of Dimension 514
  Gauge Block 515
  Length Bars 515
  Dial Gauges, Dial Test Indicators, and Inductive Gauges 516
Measurement of Angle 520
  Sine Bar 521
  Angle Gauges 522
  Precision Polygons 523
Autocollimator 524
  Straightness, Squareness, and Parallelism Calibration 525
  Flatness Calibration 526
  Angular Calibration of a Precision Polygon 528
  Calibration of a Rotary Table 529
Micro-alignment Telescope 530
  Principle 530
  Applications 531

S. Yang (✉) · C. Li
State Key Laboratory for Manufacturing Systems Engineering, Xi'an Jiaotong University, Xi'an, Shaanxi, China
e-mail: shuming.yang@xjtu.edu.cn; li.changsheng@stu.xjtu.edu.cn

G. Zhang
State Key Laboratory for Manufacturing Systems Engineering, School of Mechanical Engineering, Xi'an Jiaotong University, Xi'an, Shaanxi, China
e-mail: zgf0110@stu.xjtu.edu.cn

Z. Jiang, S. Yang (eds.), *Precision Machines*, Precision Manufacturing,
https://doi.org/10.1007/978-981-13-0381-4_15

Clinometers 533
Principle 533
Straightness and Parallelism Calibration 534
Flatness Measurement 536
Interferometry 537
Linear Measurement 538
Angular Measurement 538
Straightness Measurement 539
Rotary Axis Measurement 540
Flatness Measurement 542
Squareness Measurement 542
3D/6D Laser Interferometer 544
Tracking Laser 546
Principle 546
Applications 547
Variations 549
Telescoping Ballbars 549
Principle 550
A Closer Examination of Machine Tool Inaccuracies 551
Variations of Ballbar 553
Measurement of Spindle Error 556
Principle and Instrument 556
Error Separation 558
References 560

Abstract

wThe precision of machine tools is the foundation of machining to achieve high precision. Therefore, an investigation on the measurement technology for precision machines is extremely important for precision/ultraprecision machining. This chapter provides an overall introduction to the measurement of precision machines, including the precision along linear axes and rotary axes, e.g., the precision of length, precision of angle, straightness, squareness, parallelism, flatness, and runout. The basic principles, achievable accuracy, application, and characteristics of a wide variety of measurement methods and instruments with precision in the nanoscale or below are discussed. It is found that digitization, automation, and flexibility are the development trends of modern instruments used for the measurement of precision machine tools. Though a number of measurement methods have been developed during these years, the existed methods face challenges to comprehensively characterize the performance of machine tools, especially for ultraprecision machine tools with a precision better than 100 nm. In addition, online measurement still remains to be investigated to improve the performance of precision machining.

Keywords

Measurement · Metrology · Online measurement · Machine tool · Precision machining

Introduction

There is standard nomenclature for defining the possible errors in a mechanical system. A rigid body has 6 degrees of freedom, i.e., three in translation, *x*, *y*, and *z* (including linear position, horizontal straightness and vertical straightness), and three in angular motion or "tilt" commonly referred to as "roll," "pitch," and "yaw," as shown in Fig. 1a. In addition, each axis must be perpendicular to one another (i.e., totaling three squareness relationships). Therefore, an arrangement of three-axis orthogonal machine tool produces potential uncertainties in motion of 21 degrees of freedom. For a nominal rotational movement, the six component errors are two radial error motions, one axial error motion, the angular position error, and two tilt error motions. Figure 1b shows these component errors for a C movement.

Principles of Measurement for Machine Tool Metrology

Nakazawa (1994) gives four principles of measurement that point out some of the basis of good measurement or metrology. They are summarized here:

1. When measuring the dimensions of an object, one must know its temperature. The temperature differences in the structure will introduce errors due to linear expansion of machine elements, and the magnitude depends on the temperature difference, dimension, and coefficients of expansion.

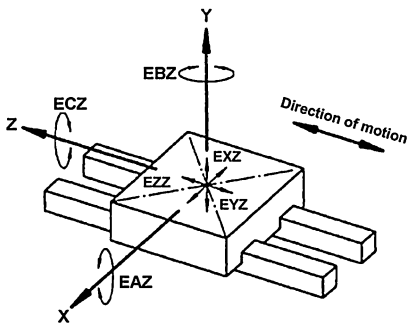

EXZ: horizontal straightness error motion of Z (straightness error motion of Z in X direction)
EYZ: vertical straightness error motion of Z (straightness error motion of Z in Y direction)
EZZ: positioning error
EAZ: pitch error motion of Z (tilt error motion around X)
EBZ: yaw error motion of Z (tilt error motion around Y)
ECZ: roll error motion

(a)

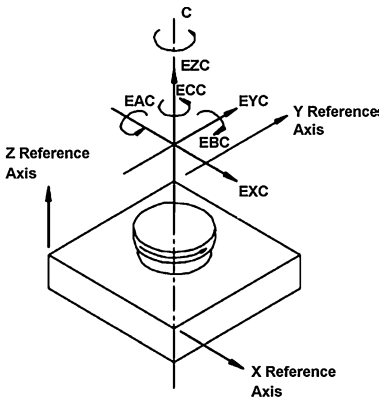

EXC: radial error motion of C in X direction
EYC: radial error motion of C in Y direction
EZC: axial error motion of C
EAC: tilt error motion around X of C
EBC: tilt error motion around Y of C
ECC: angular positioning error

(b)

Fig. 1 (**a**) Component errors of horizontal Z-axis according to ISO 230-1 (ISO 230-1). (**b**) Component errors of C-axis according to ISO 230-7 (ISO 230-7)

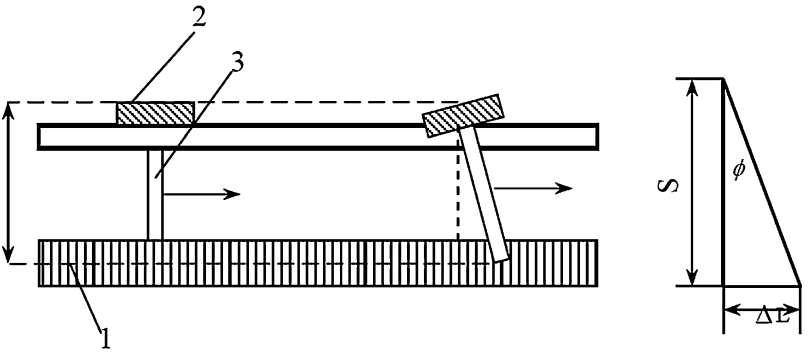

Fig. 2 A one-dimensional measurement system which violates the Abbé's principle (Yetai et al. 2010)

2. Avoid the application of force. Noncontact methods of measurement are preferable to contact methods. Contact stresses generated by the contact of two bodies under load will generate deformation due to the elasticity of the bodies, and the magnitude depends on the contact force, the equivalent modulus of elasticity of the two bodies, and the equivalent radius of contact, as revealed by Hertz.
3. The precision of the measuring instrument must be five or ten times higher than the expected precision of the measured object. This is because the precision of the measuring instrument is one key component of the measurement uncertainty.
4. Be aware of the behavior of the instrument. It is important for machinist or metrologists to understand the factors that influence the performance of the instrument to use it properly.

Abbé's principle is one of the basic rules for the metrology of machine tools. Abbé observed that "If errors in parallax are to be avoided, the measuring system must be placed co-axially with the axis along which displacement is to be measured on the workpiece" (Bryan 1979). Figure 2 shows a one-dimensional measurement system, which violates the Abbé's principle. Abbé arm S exists between the standard scale 1 and measured line 2. If the measuring frame 3 generates an inclination angle ϕ for the straightness deviation of the lead rail movement, it will produce a measurement error of

$$\Delta L = S \tan \phi = S\phi$$

Measurement of Dimension

In practical metrological measurements for the inspection and calibration work undertaken on machine tools, the use of equipment such as gauge blocks, length bars, angle gauges, straightedges, and dial gauges together with dial test indicators forms the foundation for machine verification.

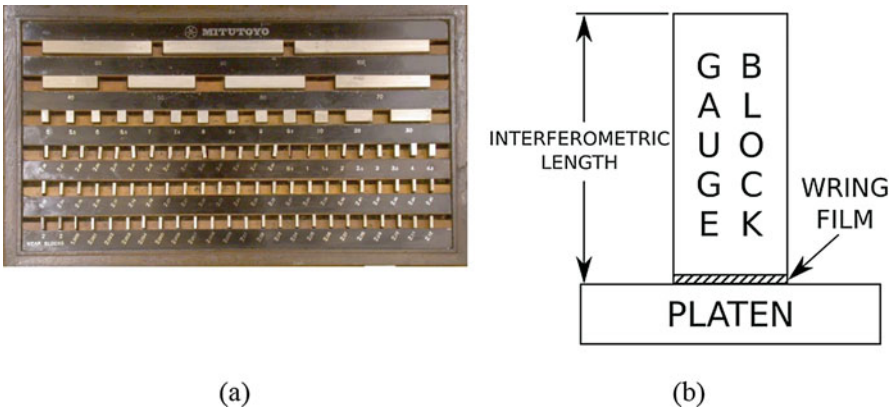

Fig. 3 (**a**) Metric gauge block set (courtesy of Mitutoyo Corporation); (**b**) How gauge blocks are calibrated

Gauge Block

The individual gauge block is a metal or ceramic block that has been ground and lapped to a specific thickness. Gauge blocks come in sets of blocks with a range of standard lengths, as shown in Fig. 3a. The blocks are joined by the combined action of sliding and a pressure process called wringing, which causes their ultraflat surfaces to adhere together. By utilizing blocks from, say, a large set of 105 blocks, one may create any of the required lengths up to its dimensional additive capacity – in 0.001 mm incremental steps.

Length Bars

When it becomes impractical to utilize gauge blocks for longer length measurements, it is the normal practice to use length bars instead. These length bars are normally produced from high-carbon high-chromium steel with a round section of Φ30 mm for greater stability and ease of handling, as shown in Fig. 4. Both of their ends are threaded and recessed and precision lapped to meet with the stipulated standards requirements of finish, flatness, parallelism, and gauge length. They have a threaded hole in the center which allows the bars to be safely and accurately joined together in various combinations. Airy points (Airy 1846) are utilized for accurate and precision metrology. The length standard is supported in such a way as to lessen its anticipated bending, or droop, while allowing the ends of the length bar to become parallel or square (Fig. 5a). These Airy points are symmetrically arranged around the center of the length bar and are separated by a distance.

The Bessel support points (i.e., after Friedrich William Bessel) are the support positions for an evenly loaded bar, where the droop for both the middle and ends of the bar are at a minimum (i.e., termed its neutral axis). These supporting points

Fig. 4 Boxed set of highly accurate and precise length bars. (Courtesy of Thomas Salvesen Enterprises Ltd)

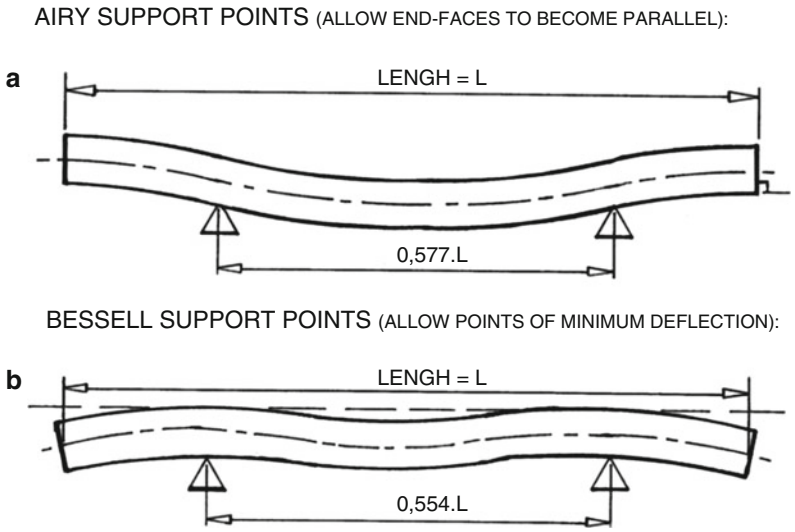

Fig. 5 Support points of length bars

(Fig. 5b, bottom), often known as the points of minimum deflection, are not valid for end standards such as length bars but can be utilized more effectively for the support points for flat metrology tables or similar level items.

Dial Gauges, Dial Test Indicators, and Inductive Gauges

Dial gauges are probably the most universal metrology instruments utilized in basic inspection/verification/calibration activities. The ubiquitous dial gauge is usually available in two distinct types: (i) plunger-type (Fig. 6a) with the digital variety shown in Fig. 6b and (ii) lever-type (Fig. 6c) often referred to as a dial test indictor. Dial indicators typically measure ranges from 0.25 to 300 mm (0.015–12.0 in), with graduations of

Fig. 6 (**a**) Mahr mechanical dial indicator with 1 mm measuring span and 0.001 mm graduation value; (**b**) Mahr digital indicator with 12.5 mm measuring span and 0.001 mm graduation value; (**c**) Mahr test indicator with ±0.07 mm measuring span and 0.001 mm graduation value; **(d)** TESA GT21 inductive gauge. (Courtesy of Mahr Group and TESA Technology)

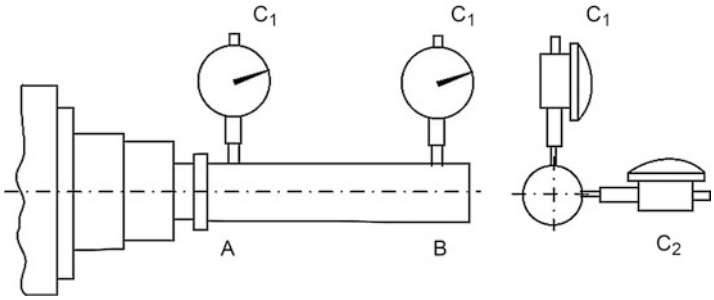

Fig. 7 Dial gauges are employed for machine tool' headstock calibration

0.001–0.01 mm. The smallest graduation of dial gauges is normally 1 μm. It can be replaced by the inductive gauge if high precision is required. For example, the precision of TESA GT21 inductive gauge (Fig. 6d) can be lower than 0.1 μm.

When mounting the dial gauge and then inspecting with a test mandrel in, say, a turning center's headstock as shown in Fig. 7, the dial gauge/test mandrel alignment procedure should be carefully performed so that the dial gauge's sensor axis is both perpendicular and aligned to the axis to be inspected, thus ensuring that both sine and cosine errors are effectively minimized. The actual difference in shaft center lines will be half the total indicator runout (TIR).

Straightness Calibration with Straightedges

Straightness measurement systems consist of a straightness reference and a displacement indicator. In order to measure the straightness errors with a material reference, the straightedge reference is placed in direction of the machine axis. As a straightness reference, a calibrated ruler or a stretched wire (for long axes) can be used. The axis is then moved, while a distance sensor (capacitance gauges, electronic gauges, or dial gauges) measures the lateral displacement.

One of the most common straightness measurement systems is the combination of a straightedge and a dial gauge. Straightedges can be produced from a variety of materials

which include steel, cast iron, granite, Zerodur™, etc. They are usually provided with feet-invariably set at the Bessel points for minimum deflection. A Zerodur™ straightedge shown in Fig. 8 is an axis-calibrating nanocenter lathe. This type of straightedge material is produced in Germany by Schott AG. It is made from lithium aluminosilicate glass ceramic. Its low coefficient of thermal expansion, high 3D homogeneity, and good chemical stability make it a very good solution for high-precision metrology.

The accuracy and precision of straightness of the working faces for straightedges are tested by direct comparison with say, a master surface table, as shown in Fig. 9. Two calibration-grade and equal-sized gauge blocks are situated on the surface table just below the Bessel support points, with the straightedge on its working face being situated over these paired gauge blocks. And the gap (i.e., vertical distance) between the lower working face of the straightedge and the datumed surface table is measured at various

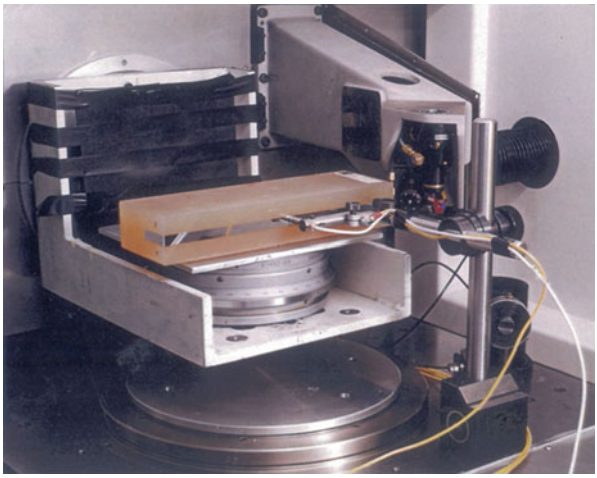

Fig. 8 "Zerodur™" straightedge and proximity sensor can be utilized to calibrate a nanocenter's X-axis to a very high level of accuracy/precision, in a temperature-controlled machining environment. (Courtesy of Cranfield Precision/Atomic Weapons Establishment, Aldermaston)

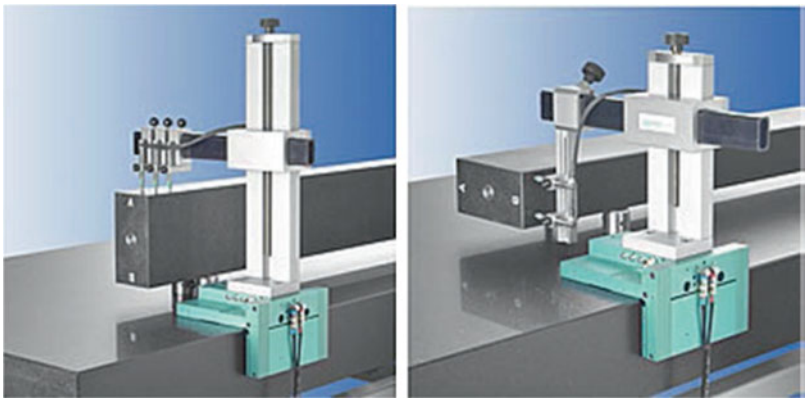

Fig. 9 Exacting-calibration procedure for the overall inspection of a large granite straightedge, for its length and breadth dimensions and its geometric characteristics (Smith 2016)

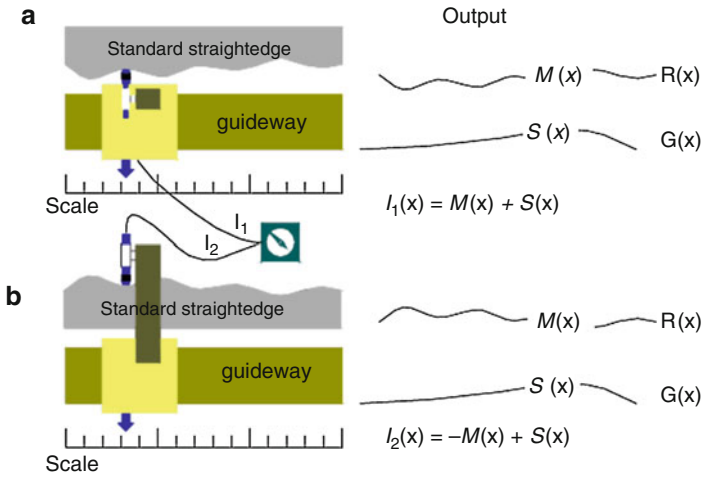

Fig. 10 Schematic of the reversal technique for the straightness errors measurement (Di Giacomo et al. 2004)

points along its length by lightly and gently sliding in gauge blocks of appropriate size, which gives an indication of the parallelism degree along the length of straightedge.

By employing reversal methods (rotating the standard), the calibration errors and the reference errors can be separated. However, gravitational deformation will always point in the same direction. For the reversal method, the separation of reference errors is customarily achieved by reversing the position of a reference object along with the sensitive direction of the instrument and then simply repeating a sequence of measurements as a function of linear position or angle. In the first orientation, the machine error will be added to the result, while in the second orientation, the machine error will be subtracted from the result. For example, in an experimental setup shown in Fig. 10, an indicator is mounted on the travelling carriage in such a way that it is aligned in the direction of interest (i.e., usually orthogonal to the axis), touching a straightedge mounted in the desired vicinity. Assuming that the machine slide straightness is given by a function "$M(x)$" and the departure of the straightedge is given by a function "$S(x)$," it is then possible to calculate the indicator output for this position by adding these two functions of '$M(x)$' and '$S(x)$' together and then calling it "$I_1(x)$."

Once satisfactorily completed, it simply reverses the straightedge by rotating along with its long axis and remounting the indicator so that it is touching the straightedge, but it now has had its direction or sign reversed. This action is important to note, because now when one calculates the indicator output "$I_2(x)$," it is possible to see an apparent reversal of the machine axis; the ostensible lack of change in the straightedge output being despite the fact that this straightedge has been reversed.

Spindle calibration with Cylindrical Precision Mandrels

Cylindrical precision mandrels often have a self-holding taper and are also known as inspection mandrels, which are utilized for calibrating both the alignment of machine tool's spindle axis and its runout. Typically, cylindrical taper mandrels (shown

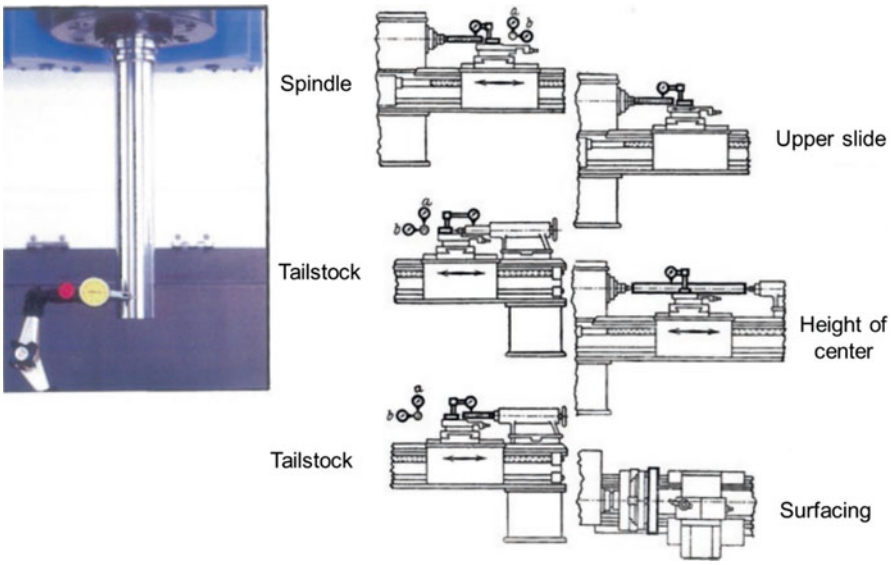

Fig. 11 Calibrate a spindle with dial gauges and mandrels (Smith 2016)

Fig. 11, left) are usually made of hardened and stabilized alloy steel. Standard sizes and accuracy of these straight and taper mandrels are typically manufactured to ISO 2063:1962.

Squareness Calibration with Precision Squares

Precision squares are commonly made from cast iron or granite (Fig. 12), which can be used for the calibration of the squareness of machine tool axes with the aid of dial gauges. The reversal method can be also used for the squareness calibration. The disadvantages are that the requirement for testing environment is relatively high and the measuring range is limited, generally no more than 1 m. An appropriate indicator is used on the slideway(s) of the machine to derive angular information (I_n), as shown in Fig. 13 (Evans et al. 1996). α is the out of squareness of the machine axes and β the test square:

$$\alpha = \frac{l_1 + l_2}{2} \tag{1}$$

$$\beta = \frac{l_2 - l_1}{2} \tag{2}$$

Measurement of Angle

Sine bar, angle gauges, polygonal mirrors, serrated tooth circle dividers, and rotary encoders are used for establishing motion through an angle or measuring angles.

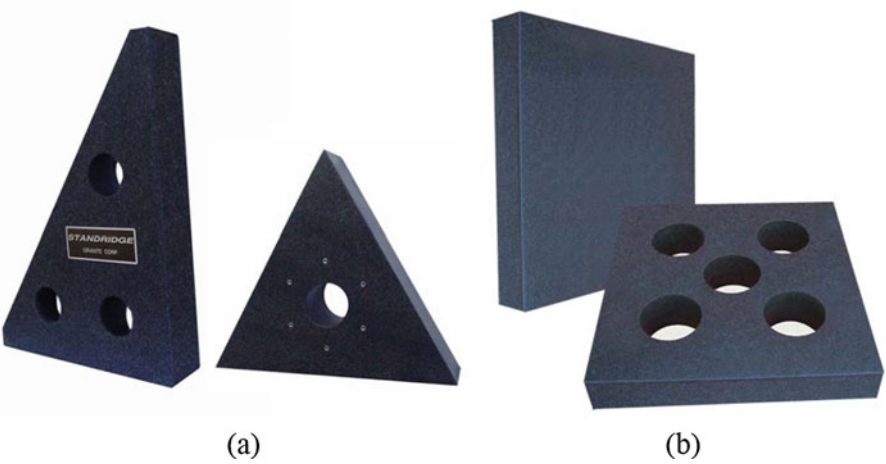

Fig. 12 (**a**) Granite triangular squares: one large face and two edges are finished flat and square to each other with lightening holes; (**b**) granite master squares: finished on five faces. One large face and four edges are finished flat, square, and parallel with lightening holes. (Courtesy of Standridge Granite Inc.)

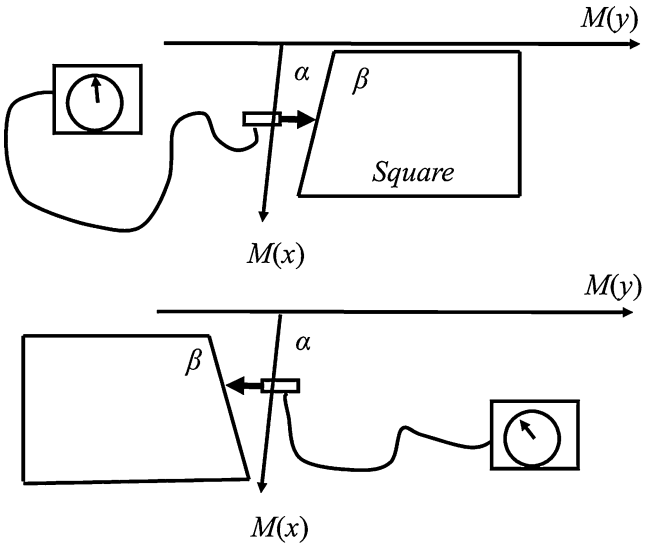

Fig. 13 Square reversal (Evans et al. 1996)

Sine Bar

Firstly, we will mention here the traditional method of using a sine bar to establish an angle. This method is comprised of a sine bar, a block (like a gauge block – with a precise length), and an auxiliary flat surface (Fig. 14) from Nakazawa (1994). The

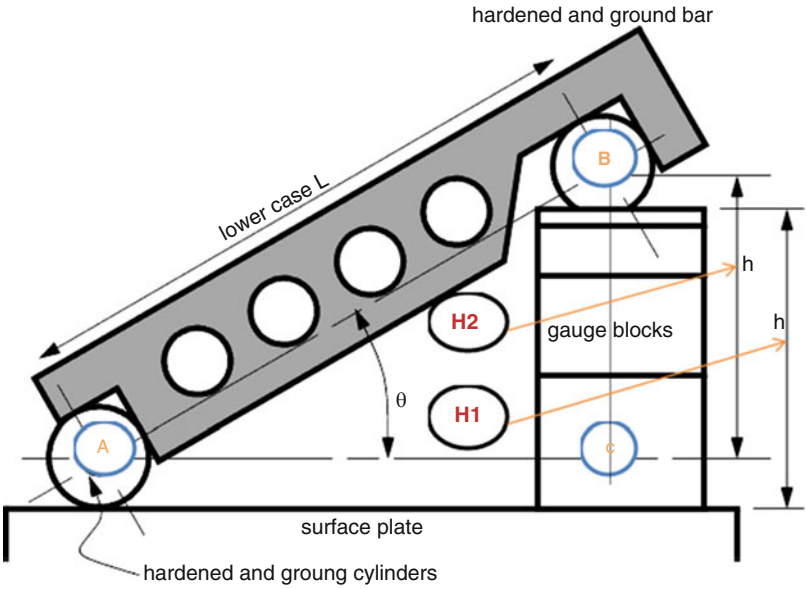

l = distance between centres of ground cylinders (typically 5" or 10")
h = height of the gauge blocks
θ = the angle of the plate

$$\theta = \text{asin}\left(\frac{h}{l}\right)$$

Fig. 14 Angle measurement using a sine bar

sine bar is designed to act as a gage or angle reference or to make angular measurements of mechanical parts mounted on it. Usually, a stack of gauge blocks is set in the correct combination to form length *h*. The corners of the right triangle, A and B, are hardened gage pins. The inclined surface is hardened, ground, and lapped to a high degree of flatness. The device is fairly reliable at low angles, less than 15°, but becomes increasingly inaccurate as the angle increases.

Angle Gauges

A combination set of angle gauges normally consists of a specific range of separate gauges as shown in Fig. 15, which may be utilized in conjunction with one square block and one parallel straightedge. Like linear gauge blocks, angle gauge blocks can also be wrung together to build up a desired angle. In addition, they can also be subtracted to form a smaller angle as a difference of two larger angles. These angle gauges are normally made of hardened alloy steel, and the actual measuring faces are previously lapped and polished to a high degree of accuracy and flatness, similarly to that of gauge

Fig. 15 A typical 27-piece combination angle gauge set. (Courtesy of Thomas Salvesen Enterprises Ltd)

blocks. Flatness of each lapped face is 0.2 μm or less, and the faces are square to the ground sides within 2 μm. The contents of 27-piece, 16-piece, and 15-piece sets have been calculated so that it is possible to wring together gauges to form 32,400 different angles from 0° 0′ 0″ to 90° 0′ 0″ in 10-second increments. Additionally, the 27-piece set is also able to produce obtuse angles. The deviation from the marked angle for the laboratory master grade angle gauges is smaller than ±0.25 sec.

Precision Polygons

Optical polygons (Fig. 16a) are designed for use with autocollimators (Fig. 17) in the precise measurement of angle spacing and calibration of the circular-divided scales (with circles for optical-dividing equipment, such as rotary tables). Many of the precision polygons of today are produced from fused silica, with a special aluminum protective coating. The largest metallic precision polygon usually has 72 faces at an included angular interval of 5°. However, a typical precision polygon might have 12 sides at an interval of 30°, which is suitable for most types of inspection/verification/calibration work. These polygons commonly have equiangular faces, but for certain special purposes, unequal angles can also be provided by the optical manufacturers. In practical use, the polygon might be mounted on the indexing plate to be verified/calibrated, or a circular scale to be divided, as shown in Fig. 16b. The autocollimator is set to receive a reflection from any one of the faces of the polygon, and the reading is noted down accordingly. Then the polygon is rotated until the same reading is observed by the autocollimator, and thus obviously, the angle of the rotation will be equal to the angle between the polygon faces. It is possible to divide the circle as well as undertake any required recalibration.

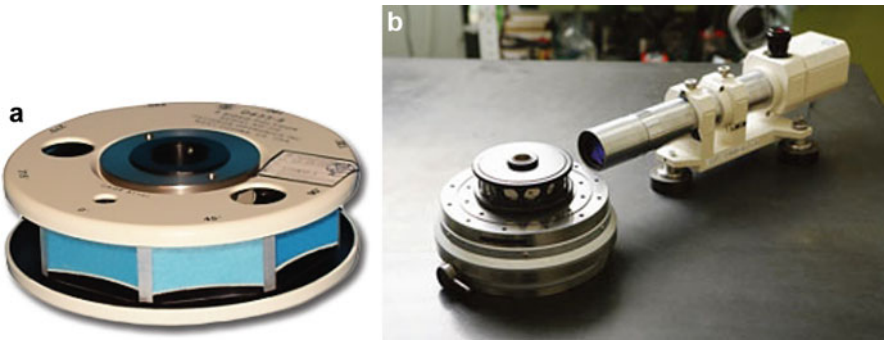

Fig. 16 (**a**) Optical polygons. (Courtesy of Davidson Optronics, Inc.). (**b**) An example of angle indexing for a polygon mirror. The device equipped with a tube is an autocollimator

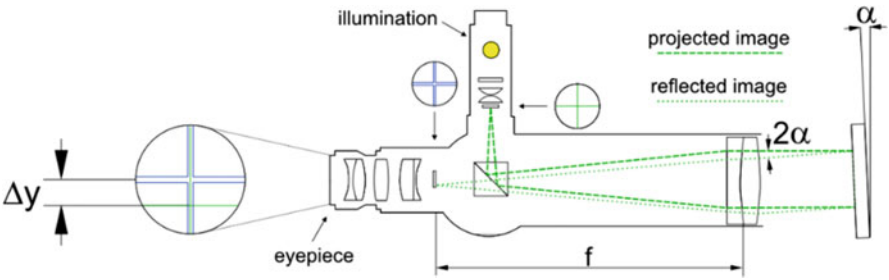

Fig. 17 In this diagram of an autocollimator, the angle of the *y*-axis mirror displacement (α) is calculated using the formula $\alpha = \Delta y/2f$ where f is the focal length of the autocollimator

Davidson Optical Polygons are available in standard configurations of 8, 9, 12, 18, 24, and 36 facets and may be ordered with any number of facets, up to 72. The flatness of facets is $\lambda/10$ and accuracy of polygons is ± 5 arc seconds. As a result, its calibration of 1/10 arc second can be achieved.

Autocollimator

Although interferometry was applied to the establishment of standards of measure and eventually replaced the autocollimator as the preferred means for measurement of angular errors of form in mechanisms and workpieces, the autocollimator is still in use and serves as a practical instrument or a component of many measurements. If the autocollimator is used in conjunction with a reflecting mirror, it can accurately measure very small deviations from a datum angle. A visual autocollimator operates by projecting an image onto a target mirror/reflector as shown in Fig. 19, which is then used to measure the deflection of the returned image against a graduated scale, either visually (Fig. 18(a) or by means of an electronic detector – such as in the digital autocollimator/digital autocollimator (Fig. 18(b)). With the optical

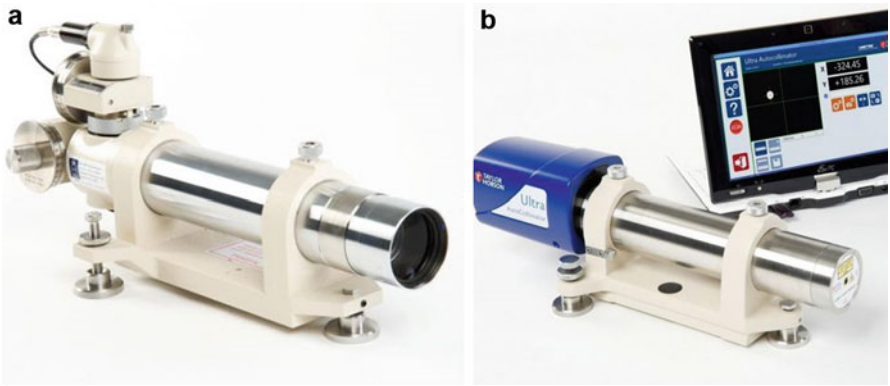

Fig. 18 (**a**) A dual axis visual autocollimator (TA51) and (**b**) a dual axis digital autocollimators with touchscreen software. (Courtesy of Taylor Hobson)

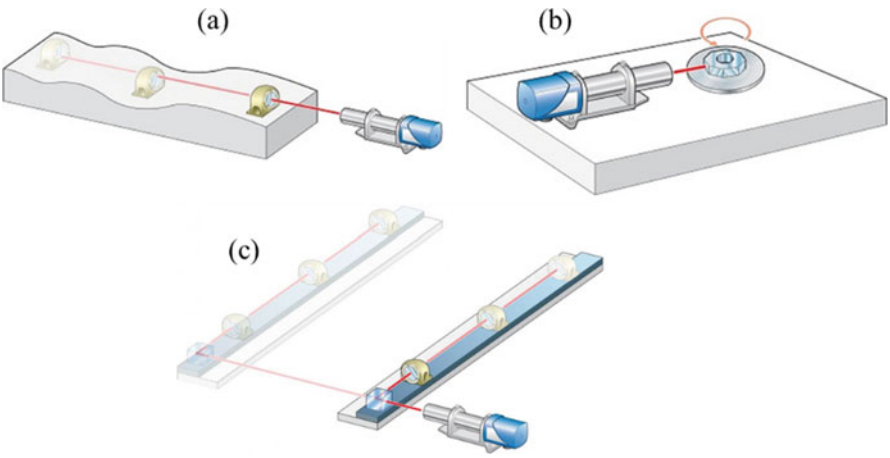

Fig. 19 (**a**) Straightness measurement, (**b**) checking indexing heads and polygons, and (**c**) checking parallelism/squareness of rails using the autocollimator. (Courtesy of Taylor Hobson)

autocollimator, it can quantify angles as small as 0.5 arc seconds or even be $\geq$100 times more accurate for electronic/digital autocollimator.

Autocollimators can be used to measure angle (indexing head accuracy), straightness (machine tool slides in two axes), squareness (column to slideways), parallelism (slideways), etc.

Straightness, Squareness, and Parallelism Calibration

Figure 19a shows the schematic of measuring straightness with an autocollimator. Using a reflector (on a carriage) and a dual axis autocollimator, up

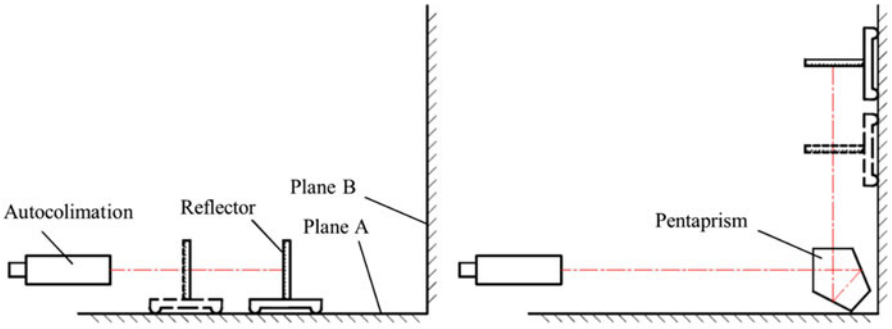

Fig. 20 The schematic diagram of autocollimation method for squareness measurement (Jia et al. 2015)

to 200 measuring steps can be taken for straightness checking by moving the reflector carriage along the slideway in equidistant steps. Any out-of-straightness in either of the two slideway surfaces *X* and *Y* (side and top of the slide) will cause the reflector carriage to change angle with respect to the autocollimator, and it is these changes which are measured and computed to determine the errors in straightness. Measurement of parallelism of two machine tool rails can be achieved using an autocollimator with an optical square and mirror, as shown in Fig. 19c.

Autocollimation can also measure the squareness using a pentaprism that can deflect the light path with 90° (Jia et al. 2015). As shown in Fig. 20, straightness of plane *A* was firstly measured by the autocollimation and reflector, and then straightness measurement of plane *B* was carried out by the pentaprism. This method is particularly suitable for large objects, such as machine tool guide, large workpiece, and so on.

Flatness Calibration

The autocollimator can also be used for the calibration of flatness of a granite or cast iron table, as shown in Fig. 21a. The table should be labeled according to the Moody method or grid method. The Moody method (Espinosa et al. 2008; Meijer and Heuvelman 1990) was founded by JC Moody in 1955 and has been widely accepted to provide a quick calibration method for round, rectangular, and square surface tables. It is also referred to as the "Union Jack" method. It provides a map where all measurements must be conducted to grade the surface table. It is consisting of eight measuring lines in which each line can be divided into a multiple of measuring stations. For a rectangular plate, the Moody map is consist of three long lines, three short lines, and two diagonal lines as shown in Fig. 21a. For a square surface plate, we will have six equal lines and two diagonal lines. The same can also be assumed for a round surface table as it was seen in Fig. 21a.

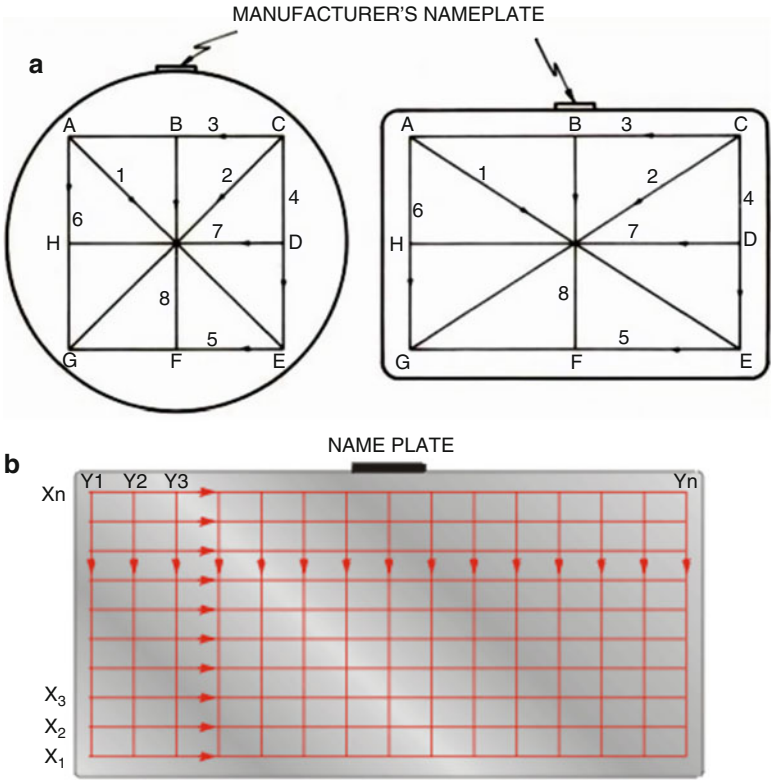

Fig. 21 (**a**) Measuring lines on a surface table by Moody method; (**b**) grid map of surface plate

The number of measuring stations is determined by the length of the line and the agreed increment on measurement which is called the foot spacing. Figure 22 shows the procedures to measure the flatness of a granite table using the Moody method. This method does have one disadvantage – all of the points on all of the eight lines must be measured and plotted. This can cause problems in defining a foot spacing which will meet this requirement, particularly on slotted tables/surfaces where the position of one or more slots may coincide with the required position of one of the feet of the flatness base. With the grid method (Kim and Raman 2000), any number of lines may be taken in two orthogonal directions across the surface as shown in Fig. 21b. While the incremental nature of the measurement technique requires that all points on a given line are measured, it is not necessary to take measurements on all lines. This allows the measurement lines to be configured to avoid "obstructions" or to provide details in a given area. A disadvantage of both grid methods is that they require a reference plane. An alternative technique such as the Moody method is needed to define the reference plane.

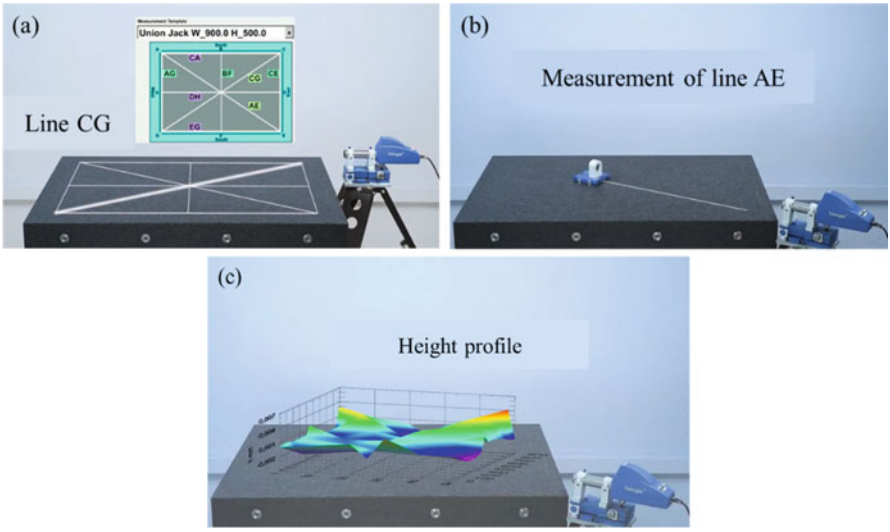

Fig. 22 The procedures to measure the flatness of a granite table using the Moody method. (**a**) Label the table with measuring lines; (**b**) measure all the eight measuring lines; (**c**) calculate the height of measuring points and draw the height profile. (Courtesy of Trioptics. Inc.)

Angular Calibration of a Precision Polygon

The autocollimator with the multiangular prism angle measurement principle has long been considered as the most precise means of angular positional determination. This technique of angle determination remains the national angle reference in many countries. Consequently, the calibration of such features of the angular measurement, namely, by the multiangular prism/polygon, can be considered as extremely important. A precision polygon can be calibrated by utilizing two autocollimators based upon the known fact that a circle is a continuous function, namely, whatever the values of the individual polygon's angles, they exactly total to 360°; the setup which is typically configured is depicted in Fig. 23. For example, if an eight-sided polygon requires calibration prior to use, then the two autocollimators are positioned at an included angle of 45° with respect to each other. So, if "R_1" and "R_2" are the readings taken on the autocollimators and identified as "1" and "2," respectively, with "S" being the angle between the normals of faces "A" and "B" and, "T" being the angle between these autocollimators, then by simple geometry we get

$$S + R_1 = T + R_2 \tag{3}$$

In order to complete the polygon's geometrical faces for all values of "S," "T," and ("$R_2 - R_1$")

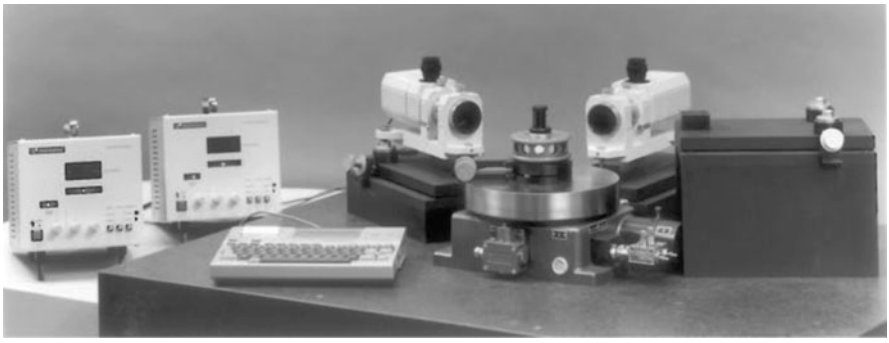

Fig. 23 Calibration of a precision polygon utilizing two photoelectronic autocollimators angularly displaced at the included angle of each polygon face

$$\sum S = \sum T + \sum (R_2 - R_1) \tag{4}$$

"$\Sigma S = 360°$," so

$$360 = \sum T + \sum (R_2 - R_1) \tag{5}$$

By dividing through by the number of sides of the polygon, n, i.e.,

$$360/n = \sum T/n + \sum (R_2 - R_1)/n \tag{6}$$

A complete set of readings "$\Sigma(R_2 - R_1)$" can be established, enabling the value of "T" to be determined. "T" can be substituted back into equation, for each face, enabling the angle for each of these faces to be simply determined.

Calibration of a Rotary Table

Figure 24 shows the setup to calibrate the rotary table (Smith 2016). To ensure proper alignment, the polygon is mounted on the rotary table using an inside diameter as a reference. The inside diameter center line is parallel to the faces and square to the base. After alignment, one of the mirror faces on the polygon is rotated toward the autocollimator and zeroed; then the rotary table readout is zeroed. During inspection the table is rotated until its readout is the nominal angle of the polygon (45° increments for an eight-sided polygon). The next face should be aligned to the autocollimator. If not, the error can be read on the autocollimator. An alternative to the polygon is the ultraprecision index table. The typical angular accuracy of an index table is 0.25 arc second. A 360-position index table yields 1° resolution. To use an index table, a plane mirror is placed on the center of rotation and parallel to the axis of rotation. The index table is aligned in the same manner as a polygon.

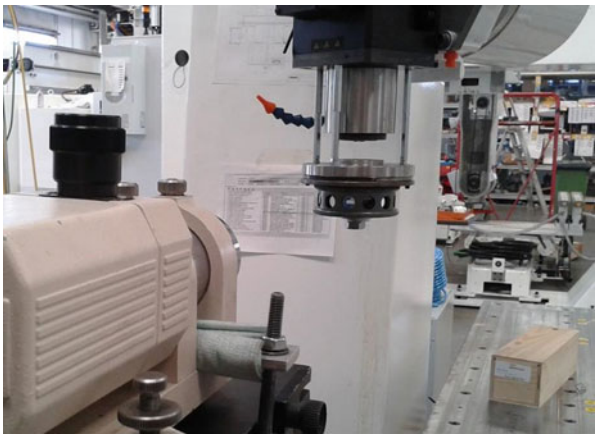

Fig. 24 Use an autocollimator to check indexing on vertical spindles (Smith 2016)

During inspection, the rotary table is rotated to 23°, for example, and the index table is counter-rotated 23°. If not again, the error can be read on the autocollimator.

Micro-alignment Telescope

The alignment telescope decomposes the autocollimator into two optical tools, the collimator and the telescope. Similar to the autocollimator, micro-alignment telescope is used for checking and setting, for example, alignment (series of bores or bearings); squareness (column to a base); parallelism (series of rollers); level/flatness (machine bed foundation); and straightness (rails or guideways).

Principle

The alignment telescope consists of two separate elements, a collimating unit and a focusing telescope, as shown in Fig. 25; the body of each of which is cylindrically ground to a truly accurate and precise known outside diameter. The collimator is an optical instrument consisting of a well-corrected objective lens with an illuminated reticle at its focal plane. The emerging beam is parallel (collimated beam), so that the image of the reticle is projected at infinity. It is customary for the collimating unit to contain the light source and condensers, in front of which is positioned a reticle in the focal plane of the collimating lens.

The telescope (Fig. 26) is an optical tool that images an object at a far distance (usually preset to infinity) into the image plane of the objective lens. The image is then magnified and visually inspected by an eyepiece. For measurement purposes usually a graduated reticle is located in the image plane. The magnification of the telescope is given by the ratio of the objective focal length and the eyepiece focal length. Two micrometer drums are situated within the telescope unit with the thimble being graduated with intervals of 0.02 mm, situated either side of the zero position

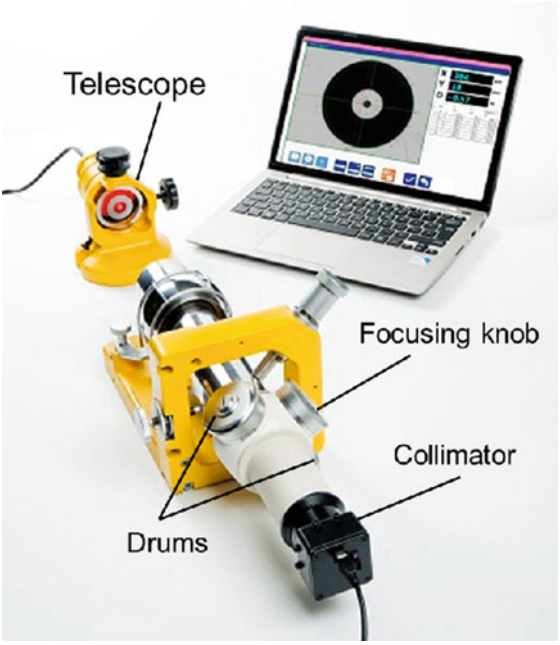

Fig. 25 Digital micro-alignment telescope. (Courtesy of Taylor Hobson)

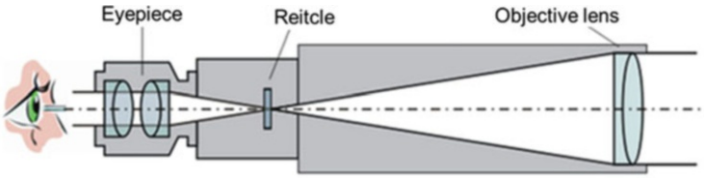

Fig. 26 Principle of a telescope

and being click stop adjustable. These two micrometre drums are set at 180° apart and when the alignment telescope is mounted. The focusing knob is normally positioned at 45° to the vertical, as shown in Fig. 25. In this telescope orientation, the left-hand drum controls the movement of the line-of-sight in a horizontal plane, while the right-hand drum controls the movement in the vertical plane.

Applications

With its optical and mechanical axes aligned to within 3 arc seconds, a typical accuracy of 50–70 μm at 30 m is achievable with the micro-alignment telescope. Closer distances produce better results with a best accuracy of around 5–10 μm. The micro-alignment telescope generates a straight line-of-sight (LOS) from zero to infinity, as shown in Fig. 27. This forms the basic reference from which all

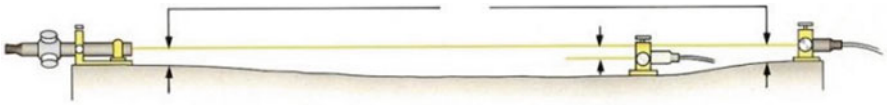

Fig. 27 Micro-alignment telescope creates a straight line-of-sight from zero to infinity. (Courtesy of Spectrum Metrology)

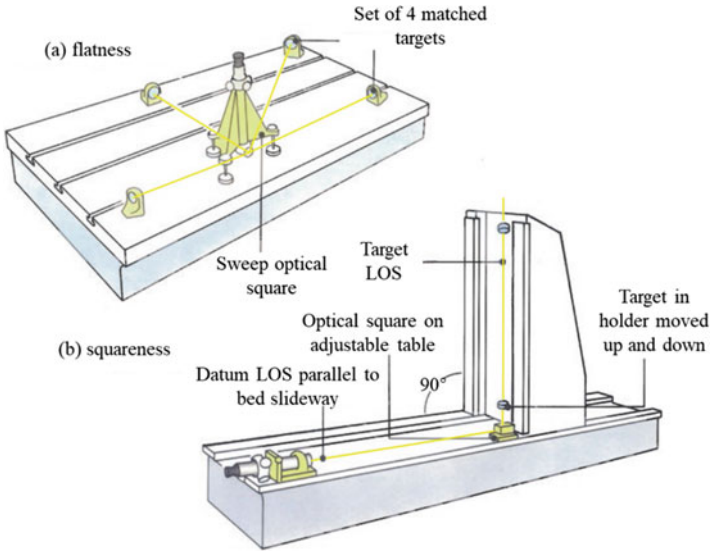

Fig. 28 Micro-alignment telescope showing two of its principle features, for (**a**) flatness and (**b**) squareness. (Courtesy of Spectrum Metrology)

measurements are taken. To measure squareness or parallelism, a pentaprism is used to deviate the straight line through exactly 90°. A similar rotating pentaprism (sweep optical square) is used to generate a plane for flatness measurement, as shown in Fig. 28(a).

The setting or checking of squareness (shown in Fig. 28b) utilizes a lamphouse to illuminate the crosslines, with the telescope being focused to infinity. Accordingly, from this telescope the rays of light are collimated and are successively reflected back along their own path from a mirror set square to this line-of-sight, forming a reverse image of the crosslines, on the actual original crosslines. A specific feature of the crossline patterns is two pairs of short heavy lines which produce a bold reverse image for precise setting. In consequence, if the mirror is slightly tilted, this crossline image will be displaced. It is worth to emphasize the point that when the telescope is focused at infinity, the micrometers are then ineffective; they cannot be employed in measurement process; no graticule or target other than the crosslines are utilized for autocollimation. A representative micro-alignment telescope system offers the following advantages when either inspecting or calibrating machines: optical and

mechanical axes alignment to $\leq$3 arc seconds and concentric within 6 μm, an achievable accuracy and precision to $\leq$0.05 mm at 30 m, and an extensive field of view of which ranges from 50 mm at 2 m to 600 mm at 30 m. In addition to the performance of the autocollimators and alignment telescope themselves, the earth curvature and atmospheric refraction will also influence their calibration precision. The effective radius of the earth curvature becomes more noticeable over much longer linear distances, especially when a line-of-sight configuration with the telescope is compared with a level surface setup by a gravity-controlled instrument. The line-of-sight deviates from a straight line owing to refraction within the same atmosphere due to the density gradient in the atmosphere resulting from differential heating/cooling of the layers of air at varying heights above the earth surface.

Clinometers

The Taylor Hobson Talyvel electronic levels and a range of precision clinometers are used for level and flatness measurement (surface plates and granite tables), straightness and twist (roll) measurement (machine slides), squareness measurement (of machine columns), angle measurement (remote monitoring of movement of structures), parallelism measurement, etc.

Principle

The traditional type of clinometer utilizes the spirit-level principle (Fig. 29). In this metrological application, the clinometer incorporates a spirit level mounted onto a rotary assembly member, which is then carried within an instrument's housing. One face of the housing forms the base of the instrument. Situated within this housing is a

Fig. 29 TESA spirit inclinometer with micrometer element scale division of and error limit of 1 and 1.5 arcmin, respectively. (Courtesy of courtesy of Tesa/Hexagon Metrology)

Fig. 30 The Taylor Hobson Talyvel 6 precision digital clinometer offers a larger measuring range (+/−45°), accuracy of within 2 min of arc, and a resolution of 0.01° (in certain display settings 4 s of arc or 0.02 mm/m). (Courtesy of Taylor-Hobson plc)

circular scale that is incorporated with the angle of inclination of its rotary member carrying the level being relative to the datum base. The angle inspected can then be established by the in situ circular scale.

Recently the compact digital inclinometers without a bubble level are widely used, as shown in Fig. 30. Incorporating a highly stable pendulum transducer in the level unit and a rechargeable battery, the Talyvel 6 is simple to calibrate and operate, with a fast measurement response time and exceptional stability. Talyvel 6 provides rapid and simple reading of angle of tilt and measurement relative to gravity; it can also function as a comparator to detect departures from a preset attitude, which may not necessarily be level. As shown in Fig. 31, a pendulum is suspended from a low stiffness torsion spring. Pendulum rotation can be induced by a linear acceleration along its sensitive axis (acceleration mode) or by a component of the gravity force along that axis caused by tilt (tilt mode). The pendulum displacement is sensed by a photoelectric position sensor, the output of which is amplified and fed to the coil of an electromagnetic torque attached to the pendulum. The polarity of the connection is chosen to produce a reaction torque which tends to return the pendulum to its zero position (negative feedback). Since the input and reaction torque's exactly balance each other, the current producing the reaction torque is a very accurate and linear function of the acceleration and is used as output. In the tilt measuring mode, the output is proportional to the sine of the angle of tilt. This fact limits the effectivity of the sensor for tilt angles approaching $\pm 90°$.

Straightness and Parallelism Calibration

A clinometer can be used to measure the straightness of a slideway by moving the clinometer with a constant interval. For some metrological inspection applications, e.g., parallelism, two of these level units may be required – denoted here as "*A*" and "*B*" (see Fig. 32) which can then be controlled from the single display unit.

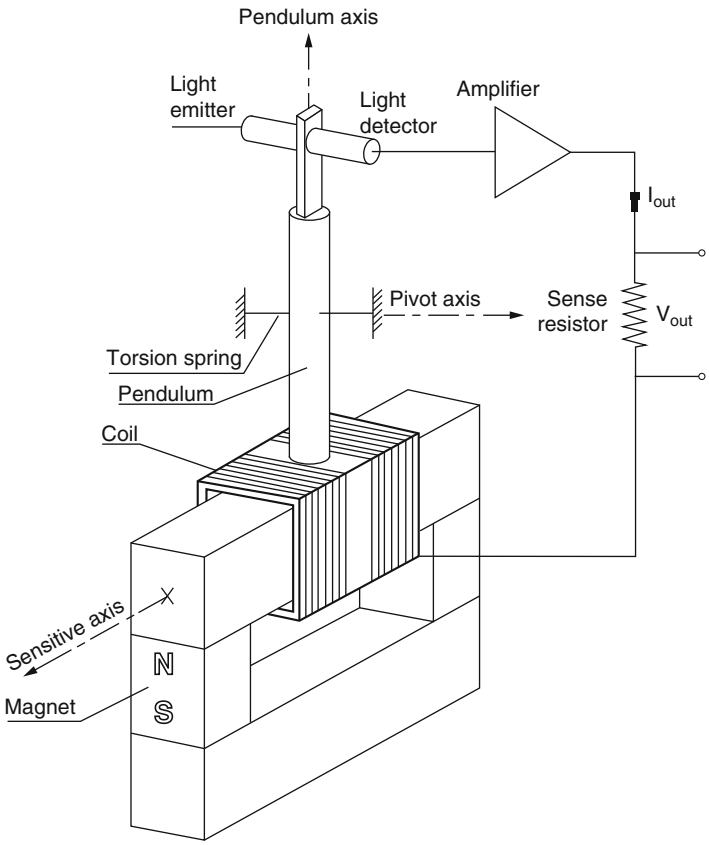

Fig. 31 Principle of dual axis inclinometer

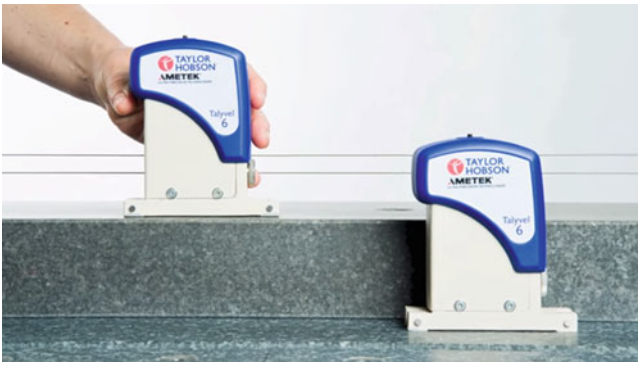

Fig. 32 Two Talyvel Clinometers measure the actual difference in the inclination of two surfaces. (Courtesy of Taylor-Hobson plc)

A clinometer provides a differential system for measuring the actual difference in the inclination of two surfaces, as well as their departure from absolute level. This metrological application of differential levelling is of particular value in specific applications such as measuring the relative deflections, while machines are in actual production and in the accurate assembly of precision machinery, furthermore for the monitoring twist, or deflection on exceptionally slowly tilting surfaces.

Flatness Measurement

One of its most common uses of Talyvel electronic level is checking the flatness of granite and cast iron tables. Flatness can be measured and displayed by employing either the union jack (i.e., Moody) method or by the grid method. Figure 33 shows the Talyvel electronic level that was used to conduct the flatness measurement by participant *A* to grade the UUT (unit under test). The electronic level was firstly validated with the aid of three gauge blocks. It was then zeroed on the first measuring station. Then it moved to the next measuring station and noted down the angle reading on the dial. This was repeated for all measuring lines to capture the data on all measuring stations. The data was then fed to a Taylor and Hobson flatness program to compute the results. The uncertainly budget was also calculated by taking all the contributors into consideration.

To operate the electronic level, the level is first adjusted, so the meter reads zero at the starting position (at the beginning of each line for evaluation). The electronic level is then translated along a straightedge, which acts as guide, as shown in Fig. 33. Measurements are taken at evenly spaced distances along the line to be evaluated. The actual flatness of the measurement line will be the algebraic sum of the readings, as shown in Fig. 34. Finally, the flatness map can be drawn according to the error of all the measuring points, as shown in Fig. 35. Two electronic levels can be used to eliminate the influence of level weight. The first level remains stationary and the second is translated along the straightedge. The difference between the two

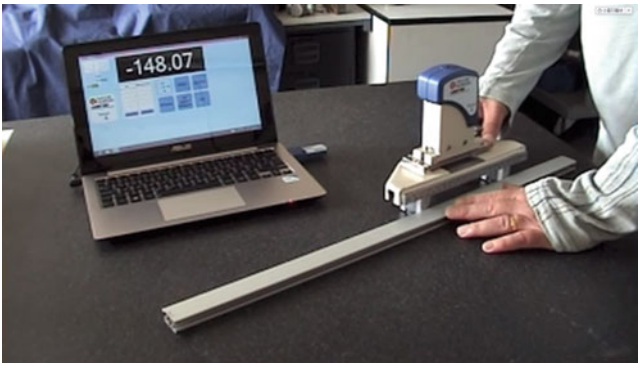

Fig. 33 Talyvel 6 precision electronic level. (Courtesy of Taylor-Hobson plc)

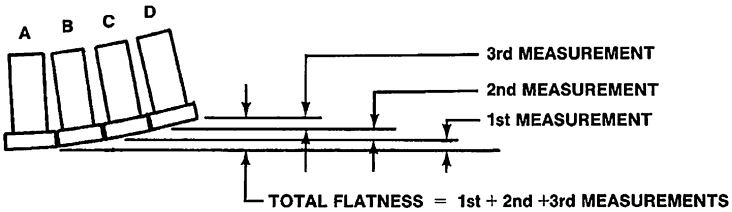

Fig. 34 Increments equal to 1 ft-spacing during flatness measurements (Espinosa et al. 2008)

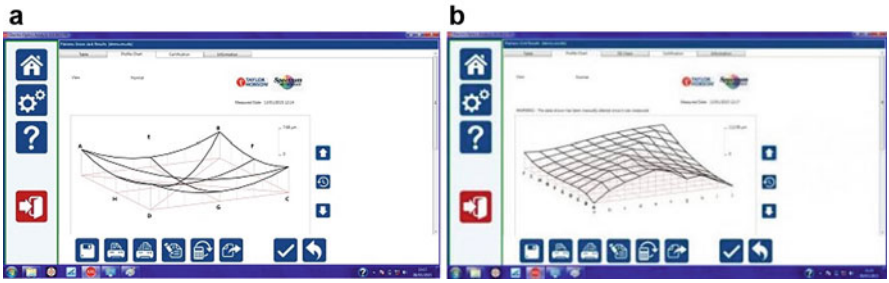

Fig. 35 (**a**) Error maps of flatness measurement by the Union Jack method and (**b**) grid method. (Courtesy of Taylor-Hobson plc)

measurements is recorded. If the surface plate tilts due to the weight of the translating level, the differential measurement will not be effected, while an absolute measurement made with a single level would be effected.

Interferometry

Interferometry is most widely used for displacement/length measurement today as well as some form measurement. It can also be used for measurement of positioning accuracy and straightness of the moving axis, positional accuracy of a rotary axis, surface form of a surface plate, perpendicularity of two nominally orthogonal axes, etc. It is a measure of relative movement (measurement from an initial position) rather than an absolute measurement (measurement of a specific position). Different selections of optics pass the laser beam through different paths, allowing a variety of measurement modes (e.g., linear, angular, straightness) to be taken from a single laser unit. Without reliable and accurate wavelength compensation, linear measurement errors of 20 ppm (parts per million) would be common in typical conditions. These errors can be reduced to ± 0.5 ppm by applying precise environmental compensation, which is better than many other methods including tracker laser system or ballbar testing.

Renishaw XL-80 laser interferometer (Beno et al. 2013; Józwik and Czwarnowski 2015; Parkinson et al. 2012) is one of the most widely used

Table 1 Achievable specifications of XL-80 laser measurement system. (Courtesy of Renishaw plc)

Measurement	Range	Resolution	Accuracy
Linear	0–80 m	0.001 μm	±0.5 ppm
Angular	±10°	0.01 arc sec	±0.0002A ±0.1 ±0.007F arc sec
Straightness	0.1–4.0 m (short range)	0.01 μm (short range)	±0.005A ±0.5 ±0.15 M^2 μm (short range)
	1–30 m (long range)	0.1 μm (long range)	±0.025A ±5 ± 0.015 M^2 μm (long range)
Rotary	Up to 25 revolutions	0.01 μm	±5 μm/m
Flatness	±1.5 mm	0.01 μm	±0.002A ±0.02 M^2 μm
Squareness	±3/M mm/m	0.01 μm	±0.005A ±2.5 ±0.8 M μrad (short range)
			±0.025A ±2.5 ±0.08 M μrad (long range)

A = displayed squareness reading
M = measurement distance in meters of the longest axis

high-precision interferometers for machine tool calibration. Key XL system components are a compact laser head (XL-80), an independent environmental compensator system (XC-80), and a comprehensive and powerful software suite. Together with the measurement optics, they form a highly accurate measurement and analysis system. The achievable specifications of XL-80 are shown in Table 1.

Linear Measurement

The setup measures linear positioning accuracy of an axis (Fig. 36) by comparing the movement displayed on the machine's controller with that measured by the laser. The setup provides an accuracy of ±0.5 ppm (parts per million) with a resolution of 1 nm. During linear measurement the laser system measures the change in relative distance between a reference and measurement optical path. Either optic of the linear beam-splitter and the retro-reflector can be moving, providing the other optic remains stationary.

Angular Measurement

Pitch and yaw angular errors are among the largest contributors to machine tool and CMM positioning errors. Even a small error at the spindle can cause a significant effect at the tool tip. The setup shown in Fig. 37 can measure maximum angular deflections of up to ±10° with a resolution of 0.01 arc secs. Angular measurements are made by monitoring the change in optical path generated by the movement of the

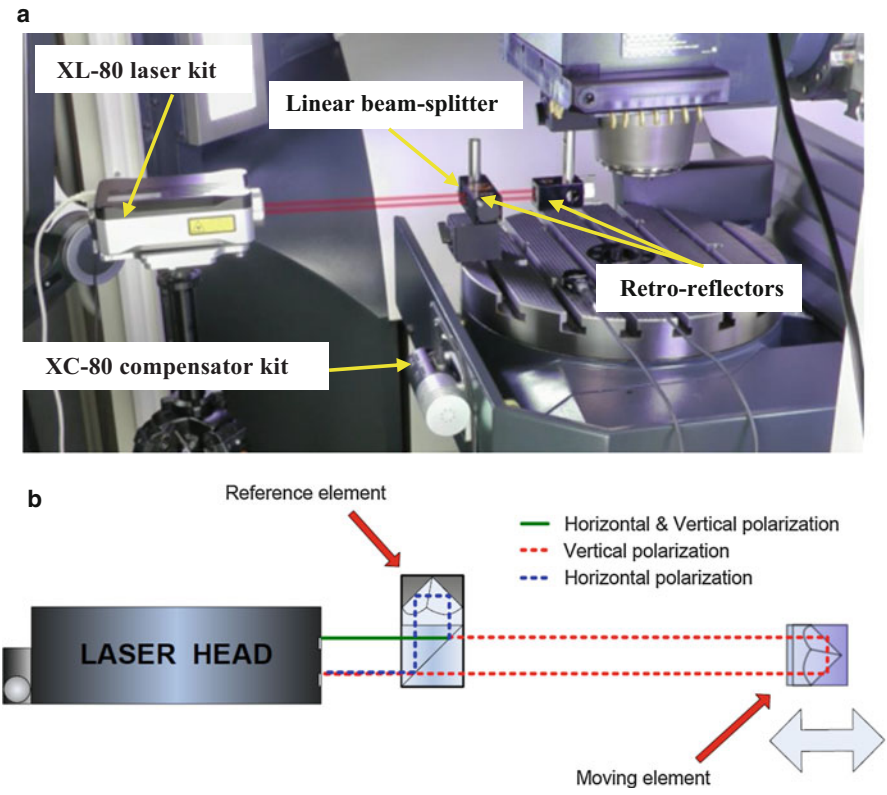

Fig. 36 Renishaw XL-80 laser interferometer for linear measurement. (Courtesy of Renishaw plc). (**a**) Setup; (**b**) illustration of the principle

angular reflector. The angular interferometer is best mounted in a fixed position on a machine. The angular reflector is then mounted to the moving part of the machine.

Straightness Measurement

Straightness measurements (Fig. 38) record errors in the horizontal and vertical planes perpendicular to an axis movement. Straightness errors will have a direct effect on the positioning and contouring accuracy of a machine. The components used in this measurement comprise a straightness beam splitter (Wollaston prism) and a straightness reflector. The straightness reflector is mounted to a fixed position on the table even if it moves. The straightness beam splitter should then be mounted in the spindle. Straightness measurements are made by monitoring the change in optical path generated by the lateral displacement of the straightness reflector or straightness beam splitter. A combination of two straightness measurements makes it possible to assess the parallelism of independent axes.

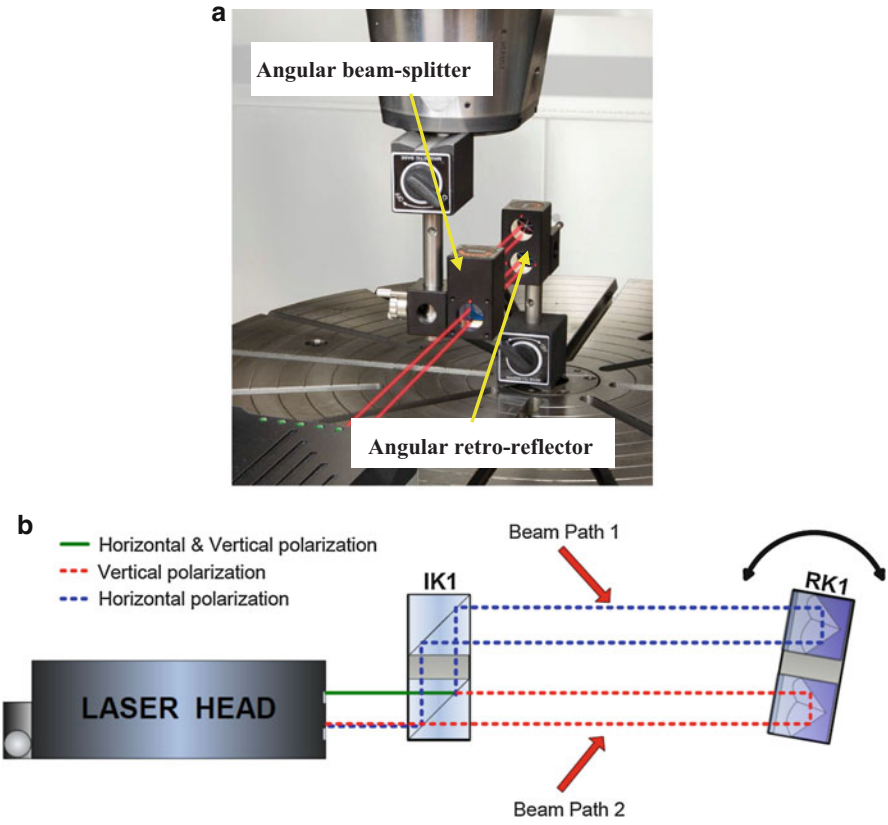

Fig. 37 Renishaw XL-80 laser interferometer for angular measurement. (Courtesy of Renishaw plc). (**a**) Setup; (**b**) illustration of the principle

Rotary Axis Measurement

Recent international standards state a rotary axis should be calibrated in a number of ways, which include 0.1° increments through 5°; 3° intervals through 360°; and 0°, 90°, 180°, and 270° positions and nine further random angular positions through 360°. It is extremely difficult to complete these measurements using autocollimators and optical polygons. Automated testing with rotary axis calibrator enables rotary axes to be checked at any angular position and far more quickly than with any other methods with precision down to 1 arcsec. The rotary setup uses an XL-80 laser, an XR20-W rotary axis calibrator, and an angular interferometer (Józwik and Czwarnowski 2015). A typical rotary axis calibrator setup is shown in the machining center configuration in Fig. 39a. An angular reflector is mounted on top of the rotary axis calibrator, which in turn is also mounted on top of the machine tool's rotary table axis. In this case, it is an integral rotary table which is presently being calibrated. As the machining center's axis under test is rotated

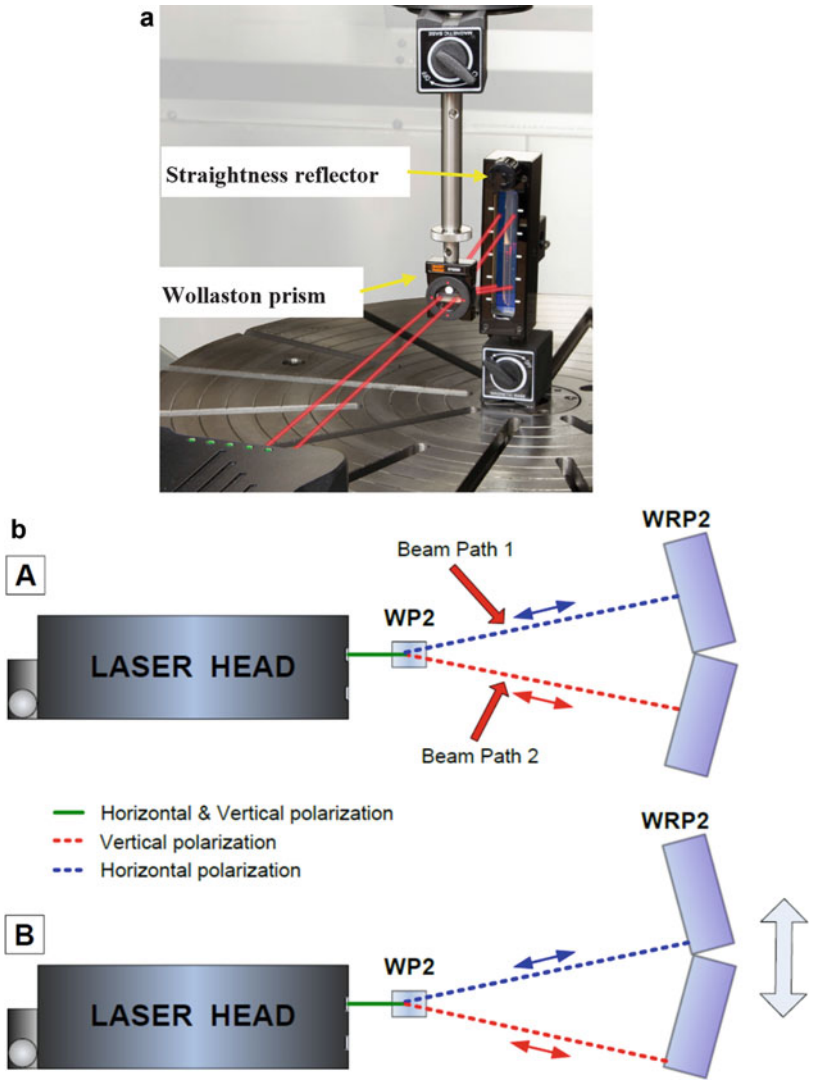

Fig. 38 Renishaw XL-80 laser interferometer for straightness measurement. (Courtesy of Renishaw plc). (**a**) Setup; (**b**) illustration of the principle

from one target position to the next, the rotary axis calibrator is driven in the opposite direction in order to maintain alignment with that of the angular interferometer. When the axis under test stops at each target position, the positioning error is calculated by comparing this target position, with the arithmetic sum of the angular readings from the laser interferometer and from that of the rotary axis calibrator. This specific rotary action allows the calibration of the axis over a full 360° or even over multiple revolutions.

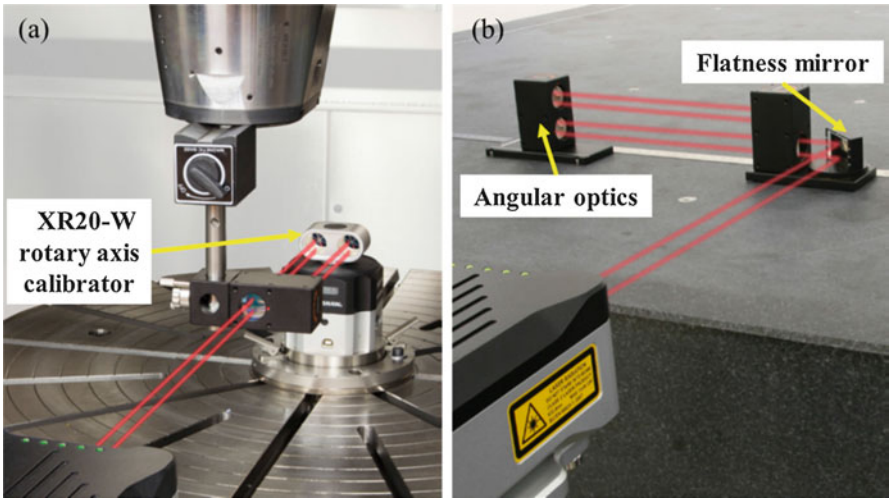

Fig. 39 (**a**) The Renishaw XL-80 laser interferometer optic for rotary axis measurement; (**b**) optics for flatness measurement. (Courtesy of Renishaw plc)

Flatness Measurement

Flatness measurement analyzes the form of a surface. This enables a 3D picture to be built up and documents the deviations from a perfectly flat surface. The flatness kit contains two flatness mirrors and three flatness bases to suit the size of the surface (Fig. 39b). The flatness mirrors not only rotate horizontally but also tilt vertically. This allows horizontal and vertical adjustment of the laser beam. In addition, angular measurement optics are required for flatness measurements. Two standard methods of conducting flatness measurements are supported by the laser software, i.e., the Moody method in which measurement is restricted to eight predefined lines and the grid method in which any number of lines may be taken in two orthogonal directions across the surface.

Squareness Measurement

The measurement of the squareness (Józwik and Czwarnowski 2015) is the extension of the straightness measurement in the two-dimensional direction. The setup and principle of squareness are shown in Figs. 40 and 41. The squareness measurement is to measure the straightness of two nominal orthogonal axes according the same reference. Then compare the straightness of the two axes to get the squareness of the two axes. The reference usually refers to the optical alignment axis of the mirror during two measurements. The mirror is neither moved nor adjusted during two measurements to maintain the reference line

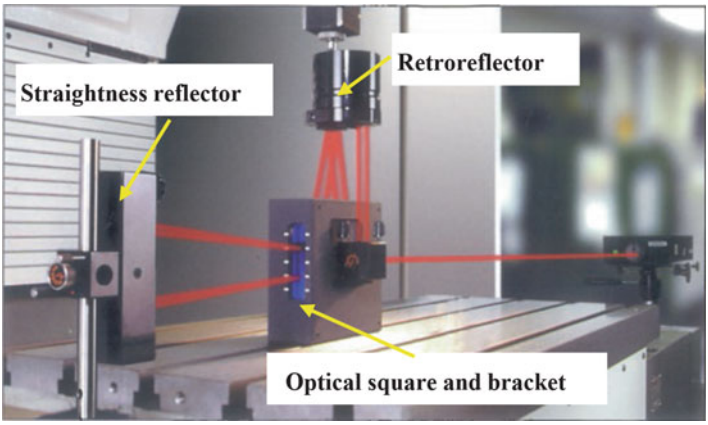

Fig. 40 X-Z axis squareness measurement. (Courtesy of Renishaw plc)

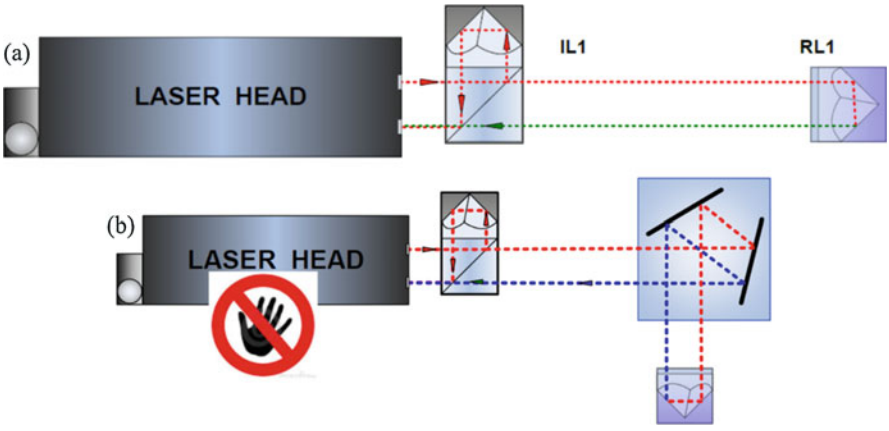

Fig. 41 Optical path setup for 3D squareness measurement in (**a**) the first axis and (**b**) the second axis

unchanged. The optical square is used for at least one measurement, allowing the laser beam to be aligned with the former straight line without moving the straightness of the mirror. Laser interferometer measurement is one of the most reliable ways to measure squareness. However, the Abbe's offset combined with angular errors during the motion of an axis causes Abbe's error. In addition, difficulty in the optical square setup causes restrictions on other optics and limitations of the measurable range. Recently, Lee et al. present mathematical approaches that can be used to eliminate Abbe's error and to estimate squareness over the full range by using the best fit of straightness data without an optical square (Józwik and Czwarnowski 2015).

3D/6D Laser Interferometer

A 3D interferometer design is usually based on that of the 1D interferometer with added optoelectronic circuits (e.g., CCD cameras, PSDs, four-field detectors) to enable the simultaneous measurement of the lateral motions of the reflector. The accuracy of measurement along the given axis is equal to that of the interferometer, while in the other two axes, it is usually lower. An example of such a design is the laser interferometer with a four-field detector, shown in Fig. 42 (Kwaśny et al. 2011). It is a bifrequency interferometer exploiting the heterodyne method. In the case of bifrequency lasers, laser beam stabilization is of major importance, which consists in measuring the frequency resulting from the Doppler effect. A major drawback of this solution is the limitation of the measuring arm travel speed in one direction to about 0.3 m/s. If a proper splitter is used, it is possible to measure the other axis, but then the laser beam power drops by 50%. This may make it difficult or impossible to perform measurements on larger machine tools.

By adding more optoelectronic circuits, 6D lasers were built. By using the latter, the measuring time can be reduced up to 80%. Besides measuring the positioning error, horizontal and vertical straightness, and angular errors (pitch and yaw), a 6D laser system can be used to measure the roll error. This means that the components of a 6D laser measuring system need to be set and calibrated only once for each of the measured machine tool axes. The 6D XD™ Laser from Automated Precision Inc. (API) is a multidimensional laser measurement system that simultaneously measures

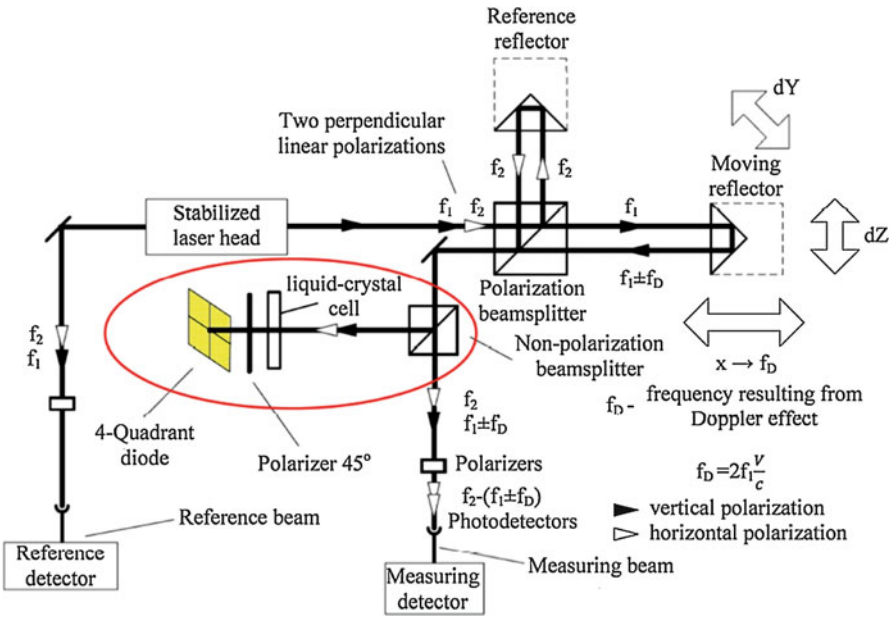

Fig. 42 Modification of 1D laser to 3D laser (Kwaśny et al. 2011)

Table 2 Measuring accuracy of API XD laser systems compared to 1D interferometer and 3D interferometer (Kwaśny et al. 2011)

Laser configuration			Error	Accuracy	
				Regular	High precision
6D	3D	1D	Linear positioning (μm/m)	0,5	0,2
			Vertical and horizontal straightness (μm)	± (1,0+0,2/m)	± (0,2+0,05/m)
		3D	Pitch & yaw (arc-sec)	± (1,0+0,1/m)	± (0,2+0,02/m)
	6D		Roll/squareness (arc-sec)	±1,0	±0,5

linear, angular, straightness, and roll errors for rapid machine tool error assessment. Table 2 shows the measurement accuracies of the API XD laser system compared to 1D interferometer and 3D interferometer.

The main sources of error/uncertainty arising from the use of laser calibration systems are well known and documented and must be minimized if valid readings are to be obtained from the machine or equipment under test. The so-called weather station automatically compensates for the linear displacement readings from the laser on behalf of any variations in both the air refractive index and material temperature. So just some significant values of uncertainty are incurred when setting up and utilizing laser systems on machines, including:

- Cosine error. This will be present when the machine tool's travel is not identical to that of the interferometer's beam.
- Abbé offset error. This is when the position of the laser measurement is shifted away (i.e., offset) from the position of the actual axis cutter travel.
- Dead path errors. These are influenced by ambient conditions in the same manner as the displacement part of the beam. So, the interferometer reasons that the path length is the distance moved by the mirror, but in actuality this path length is affected by ambient conditions, the distance from the interferometer block to the matched mirror.

The system does not perceive that there is additional air in the measurement arm and as a result will not compensate for changes in the wavelength of the laser in that portion of the beam. As a consequence, the general equation for the air dead path error (E_{ADP}) is provided as follows:

$$E_{\mathrm{ADP}} = D(\lambda_{\mathrm{air}} - \lambda_0)/\lambda_0 \tag{7}$$

where "E_{ADP}" is the air dead path error, "D" is the separation between the optics at datum (i.e., the dead path), "λ_{air}" is the current laser wavelength, and "λ_0" was the laser wavelength – when the system was datumed. The general equation for material dead path error (E_{MDP}) is

$$E_{\mathrm{MDP}} = D\alpha T \tag{8}$$

where E_{MDP} is the material dead path error, 'α' is the linear coefficient of expansion of the material in the dead path, and "T" is the change in temperature of the material since the system was first datumed.

Normally, material dead path errors are potentially much more significant than its associated air dead path errors. The optimum methodology to lessen these undesirable conditions is to apply good metrology practices.

The material dead path – this should be made by situating the setup of the laser as closely and directly as possible to the point of metrological interest.

Any changes in material temperature during measurement – this should be made by initially stabilizing the temperature and/or promptly completing the measurements.

The optics separation (when the system is datumed) – this should be made either by utilizing a preset reading or by employing a beam splitter as the moving optic.

Tracking Laser

The original laser tracker was patented in the USA in 1987. These now very popular trackers can be considered as polar coordinate measuring systems, being capable of high-accuracy measurements over quite long linear distances. For example, in one of the systems now being utilized by NPL, it can measure at distances of up to 40 m to within discrete accuracies of measurement of ± 60 μm. The current laser trackers can make measurements to ~10 μm accuracy without any special geometry or data processing. By choosing advantageous geometry, by calibrating repeating errors, and by averaging random errors, the instrument's tracking allows it to measure to even tighter levels of <1 μm.

Principle

Laser trackers take measurements using a spherical coordinate system as shown in Fig. 43a, which means that any given point is specified by three numbers: (a) the radial distance of the point from the tracker; (b) the polar or zenith angle, which measures elevation; (c) the azimuth angle, measured on a reference plane that passes through the tracker and is orthogonal to the zenith. The numbers for the zenith and azimuth angles are determined by means of two angular encoders which measure the orientation in the tracker's gimbal along its mechanical axes. The radial distance of the point from the tracker is determined using an interferometer (IFM), an absolute distance meter (ADM) or a combination of the two.

Laser trackers equipped with IFMs split their lasers in two: one beam travels directly to the interferometer, while the other travels to a target device in contact with the component being measured. The two lasers interfere with one another inside the interferometer (hence the name), resulting in a cyclic change equal to one quarter of

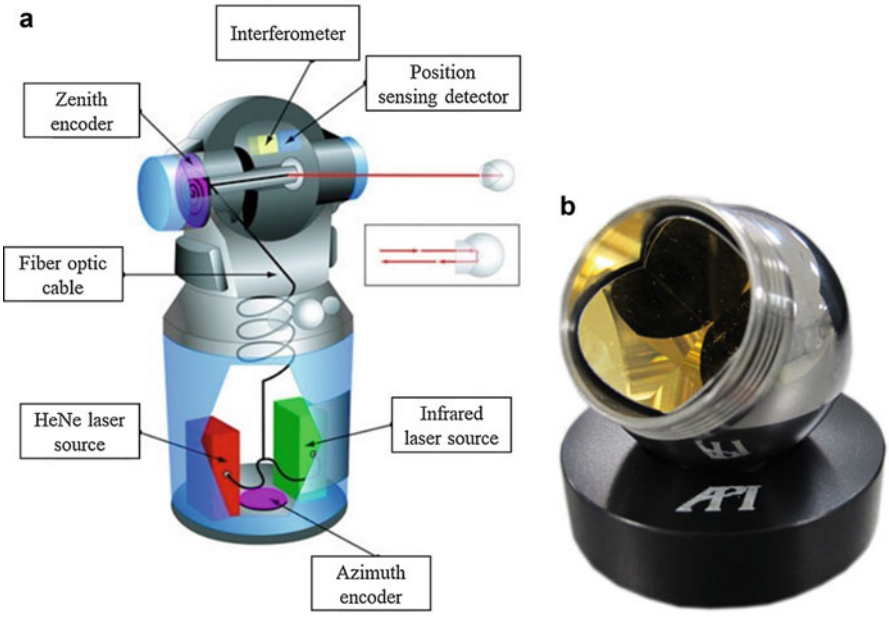

Fig. 43 (**a**) Schematic of a tracker; (**b**) a SMR target

the laser's wavelength – approximately 0.0158 μm. Each time the target device changes its distance from the tracker. By counting these cyclic changes, what's known as fringe counting, the laser tracker can determine the distance the laser has travelled. ADMs use infrared light from a semiconductor laser which bounces off the target device and reenters the tracker. The infrared light is then converted into an electrical signal for time-of-flight analysis.

Applications

The basic laser tracker setup consists of the tracker itself (Fig. 43a), a target device (Fig. 43b), and a computer running the tracker's application software. The most common target device is a retroreflector, which reflects the laser beam back in the direction from which it came. The most common retroreflector design is the spherically mounted retroreflector (SMR) as shown in Fig. 43b, which has the advantage of keeping the center of the retroreflector at a constant distance from the surface being measured. To take measurements with the tracker, the inspector firstly sets up a laser tracker on a tripod, with an unobstructed view of the object to be measured (see Fig. 44). Then the inspector removes a target from the base of the tracker and carries it to the object, for certain regions of its features to be measured, moving smoothly to allow the laser tracker to follow these movements of the target. During this procedure, the inspector individually places this target against the object, triggering measurements to be taken at preselected points.

Fig. 44 Calibrate a machine tool with an eTALON LaserTRACER-NG. Measuring uncertainty for spatial displacement (95%) is 0.2 μm + 0.3 μm/m, and resolution reaches 0.001 μm. (Courtesy of Etalon AG)

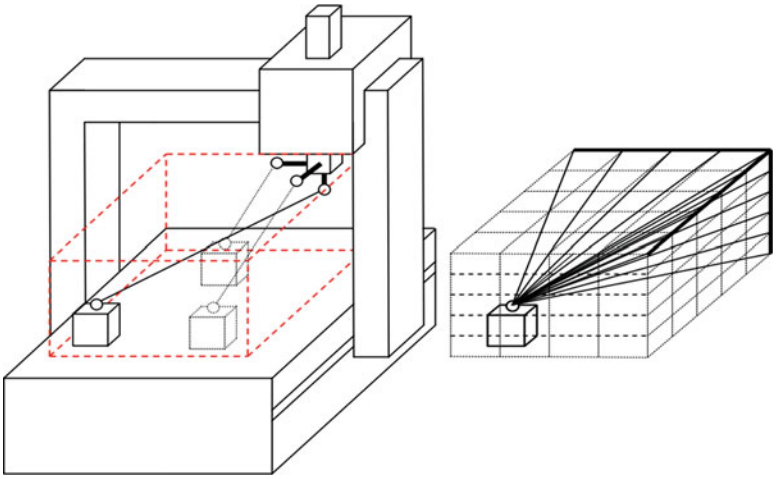

Fig. 45 A laser tracker in at least three positions on the workpiece table: (**a**) tracker positions, (**b**) spatial grid. (Schwenke et al. 2005)

PTB and NPL have jointly developed a method for error mapping of machine tools (Schwenke et al. 2005). The concept is based on displacement measurements between reference points that are fixed to the base and offset points fixed to the machine head. These measurements are realized by a tracking interferometer that is mounted on the workpiece table and a retroreflector that is attached to the machine head. Figure 45 shows a setup in principle. For each of the three laser positions, the machine tool performs spindle motions maximally filling its workspace. In each point of the space grid, the axis motions are stopped, and the displacement of the

reflector relative to the stationary reference ball is recorded. Machine tool errors are defined as the differences between the programmed displacements and the measured ones.

Variations

Having in mind higher precision in determining the position of a point in space, research on the realization of the multilateration procedure in accordance with the GPS (global positioning system) principle, i.e., through the use of not one but several electronically interconnected transmitters, is underway (Schwenke et al. 2005; Wang et al. 2011). The MultiTrace system made by Etalon (Fig. 46) has been designed for this purpose. Such a solution may substantially reduce test time.

As part of the project entitled "Volumetric Accuracy for Large Machine Tool," carried out jointly by Boeing, Siemens, Mag Cincinnati, and Automated Precision Inc. (API), methodology enabling the precise calibration of large multiaxis machine tools in a very short time (in a matter of hours) has been developed (Kwaśny et al. 2011). A special tracking laser, called API T3, using the company's volumetric error compensation (VEC) technology (Bangert 2009), working in tandem with the patented active target (Fig. 47) is used. Active target devices are new-generation retroreflectors equipped with two drives; hereby they can automatically position and track the laser beam, preventing it from being interrupted. The angle of laser beam incidence on the retroreflector can change to a rate of 50°/s. Since the retroreflector can rotate by a large angle, only one tracking laser position is required for measuring volumetric error.

Telescoping Ballbars

Component dimensional and finish defects may result from bad tooling, worn spindles, or workpiece clamping, but the major causes of defects can usually be attributed to positioning errors in the machine tool itself. In the past the workpiece accuracy may have been achieved by machining test or "master" parts and then

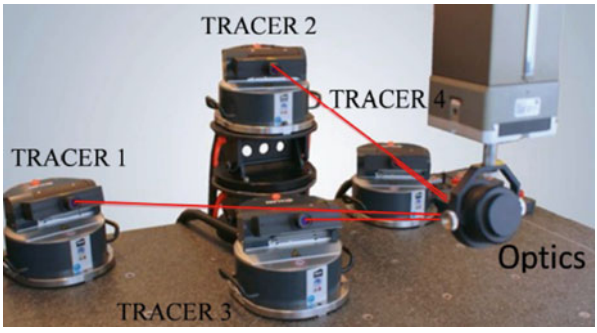

Fig. 46 Multilateration system MultiTrace by Etalon. (Courtesy of Etalon AG)

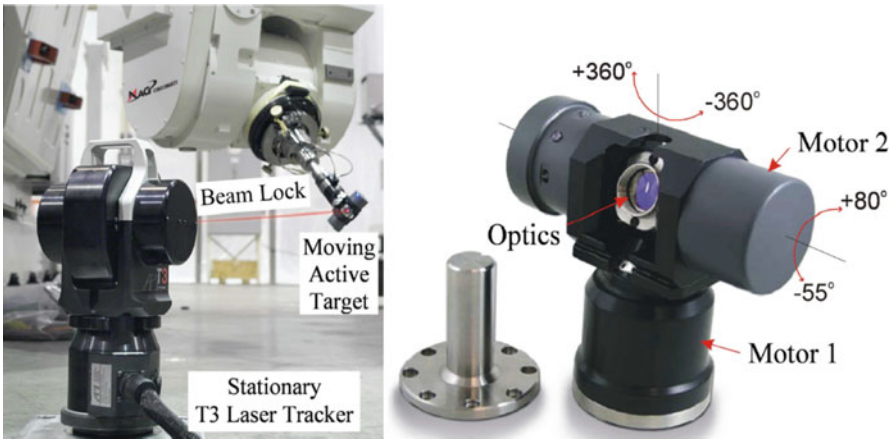

Fig. 47 Active target API T3 laser tracker. (Courtesy of Automated Precision Inc.)

inspecting them. However, this was time-consuming and gave limited confidence when machining parts with geometries different to the master part. Ballbar testing first developed by Bryan provides the quickest (typically 10 min), easiest, and most effective way to monitor machine tool condition and quickly diagnose problems that may require maintenance and the error sources that produce them.

Principle

The basis of the Renishaw QC20-W ballbar is shown in Fig. 48a. Any of the errors of a machine tool will cause the radius of the circle to deviate from the programmed circle. If you could accurately measure the actual circular path and compare it with the programmed path, you would have a measure of the machine's performance. The heart of the system is the ballbar itself, a very high accuracy, telescoping linear sensor with precision balls at each end. In use the balls are kinematically located between precision magnetic cups, one attached to the machine table and the other to the machine spindle or spindle housing. This arrangement enables the ballbar to measure minute variations in radius as the machine follows a programmed circular path. The resolution and accuracy of the QC20-W ballbar system are 0.1 μm and $\pm$ (0.7 + 0.3% L) μm. The error of the distance transducer alone does not exceed $\pm$0.5 mm. The Bluetooth device enables data transmission for a distance of up to 10 m. Figure 48b shows the schematic diagram of ballbar testing.

In an archetypal ballbar test, the ballbar might be assembled to sweep, say, a 150 mm radius, but for other tests the ballbar's radii can be changed, ranging from 50 mm to that a larger radius of >1000 mm becomes possible. A longer radial ballbar length could be employed to increase sensitivity to geometry errors such as squareness; conversely a very small ballbar radius might be utilized to highlight any dynamic errors such as servo mismatch.

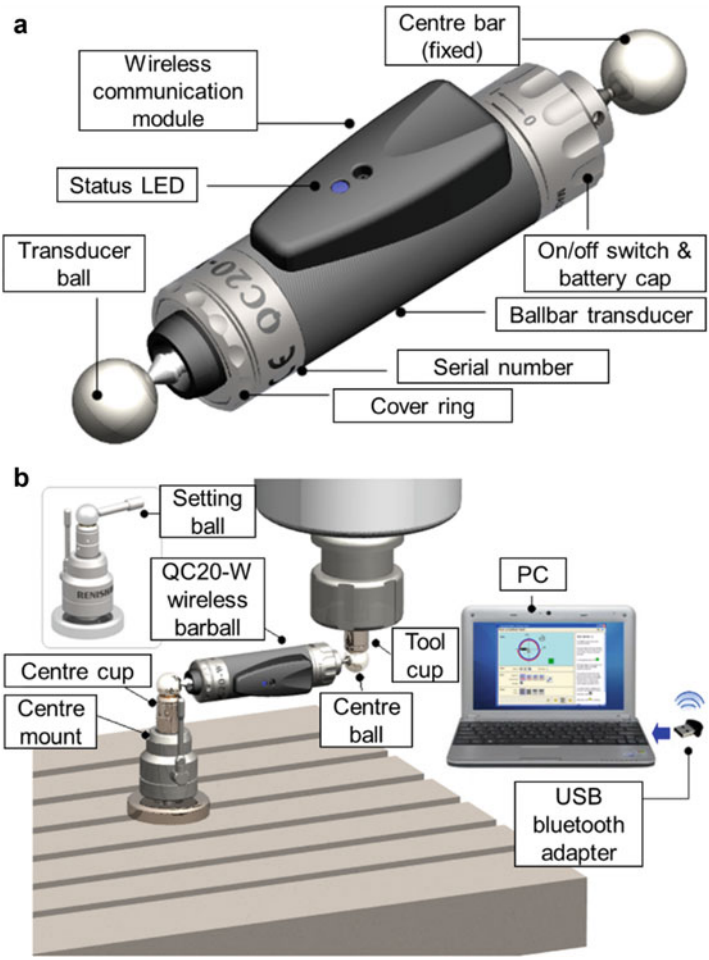

Fig. 48 (**a**) The structure of the ballbar; (**b**) the schematic diagram of ballbar testing. (Courtesy of Renishaw plc)

A Closer Examination of Machine Tool Inaccuracies

Diagnostic testing with a telescoping ballbar for machine tool verification can reveal a number of machine-related problems. According to the ballbar troubleshooting guide, the problems of the machine tools can be identified, and corresponding measures can be taken. Take the squareness, for example. This error geometry is shown as an oval ballbar plot (Smith 2016) (Fig. 49), usually occurring when orthogonal axes are no longer moving at 90°, relative to one another. This type of error may possibly be due to a bent axis or some other form of axis misalignment. This squareness error ovality on the plot will tilt it at 45° with respect to the two axes, remaining in the same position regardless of the direction of travel of the ballbar.

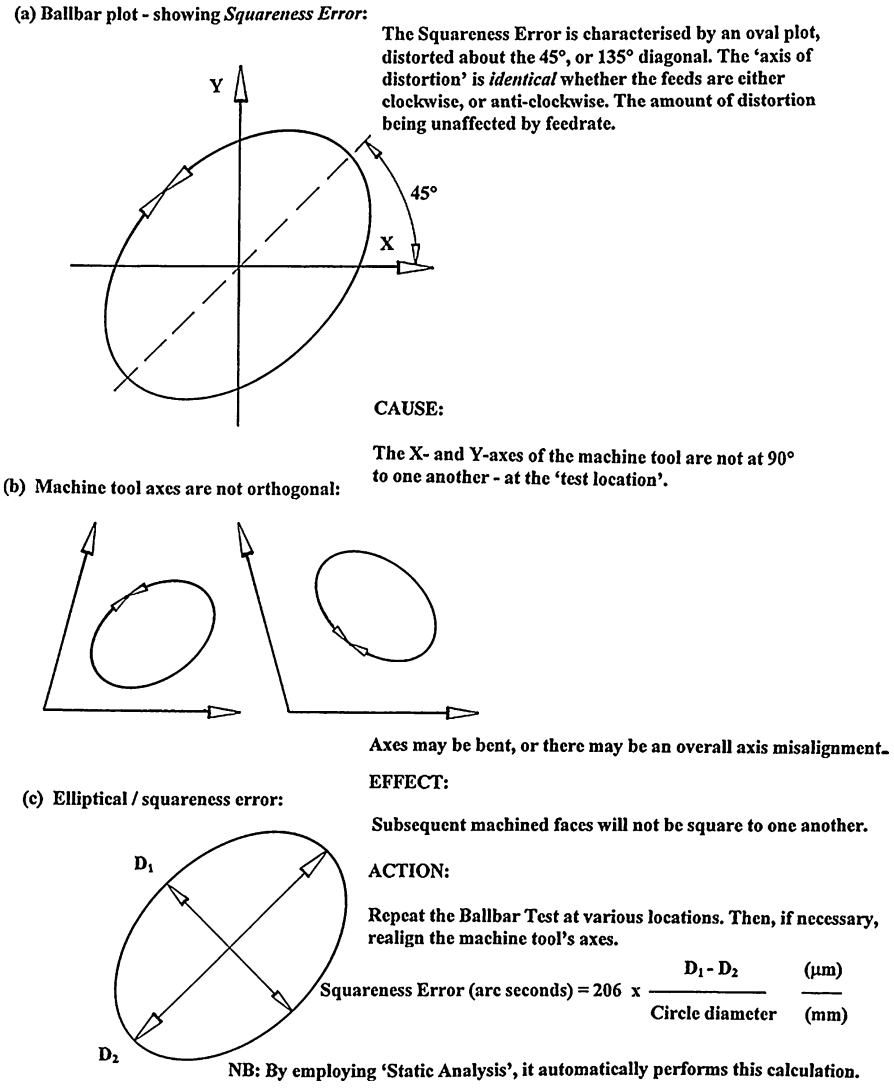

Fig. 49 Squareness on ballbar plot, with its likely cause, effect, and action (Smith 2016)

Since it was designed for only simple three-axis milling centers and three-axis lathe centers with ball screws and feed drives, the expert system aiding inference about the causes of errors is a series limitation of the above method. Consequently, only simple circular interpolation tests can be carried out for other machines, both conventional ones and with parallel kinematics. Another drawback of the ballbar device is that measurements are taken only in a selected part of the machine tool workspace. Despite the above drawbacks, the ballbar enables machine tool diagnostics and does not necessitate long

breaks in the manufacturing process, mainly owing to measurement simplicity and speed.

Variations of Ballbar

Similar to the magnetic ballbar, the laser ballbar (LBB) (Schmitz et al. 2001; Ziegert and Mize 1994) uses the telescoping assembly to maintain beam alignment with the moving retroreflector and features a much longer range of motion than does Bryan's with relative displacements measured via laser interferometry. It consists of a two-stage telescoping tube with a precision sphere mounted at each end. A heterodyne displacement measuring interferometer is aligned inside the tube and measures the relative displacement between the two sphere centers.

Once initialized, the LBB uses trilateration to measure the spatial coordinates of points along a CNC part path (Schmitz and Ziegert 2000). The six edges of a tetrahedron formed by three base sockets (rigidly attached to the machine table) and a tool socket (mounted in the spindle) are measured, and, by geometry, the spatial coordinates of the tool position in the LBB coordinate system are calculated. The three lengths between the three base sockets (denoted L_{B1}, L_{B2}, L_{B3}) shown in Fig. 50 are measured once and are assumed to remain fixed during the motion of the tool socket. The three base-to-tool socket lengths (denoted L_1, L_2, L_3 in Fig. 50) are measured simultaneously during a single execution of the applicable CNC part program. Then the coordinates of the tool point are calculated from the ballbar readings to define the contouring accuracy.

Another kind of laser ballbar is laser vector measurement technique (Janeczko et al. 2000; Wang and Liotto 2002) for the determination and compensation of

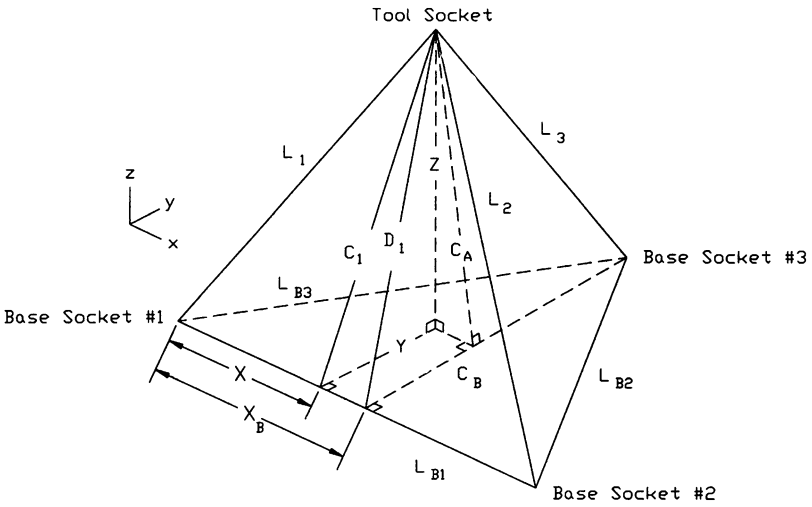

Fig. 50 Simultaneous trilateration (Schmitz and Ziegert 2000)

volumetric position errors. A laser noncontact measurement of static positioning and dynamic contouring accuracy of a CNC machine tool (Figs. 51 and 52) is a relatively recent machine tool calibration technique, its operation being based upon a single-aperture Laser Doppler Displacement Meter (LDDM) using the laser vector method. Briefly, when a laser beam is reflected from a target, the Doppler frequency shift is proportional to the velocity. Since the frequency shift is the change of the phase and the velocity is the change of the position, after the integration with respect to time, the Doppler phase shift is proportional to the position. Once the phase is measured, the position can be determined. The foremost features are that the measurement is noncontact where the circular path radii can be varied continuously, ranging from 1 to 150 mm; the laser/ballbar uses a laser displacement meter for the measurement, and the accuracy is typically 1 ppm and traceable to NIST. However, two sets of measurements with two setups are needed for the laser/ballbar to generate the circular path compare to telescoping ballbar, only one setup and one set of measurement.

Although ballbar and the latest laser ballbar (LBB) are capable of two-axis error measurements, they are still sensitive to one dimension only. A novel design that integrates the merits of a LBB and laser tracking systems (LTSs) has been proposed for the three-dimensional measurement of moving objects in real time. The system, called the 3D Laser Ballbar (3D LBB) (Fan et al. 2004), is based on the spherical coordinate principle containing only one precision laser linear measurement device

Fig. 51 A typical laser ballbar setup

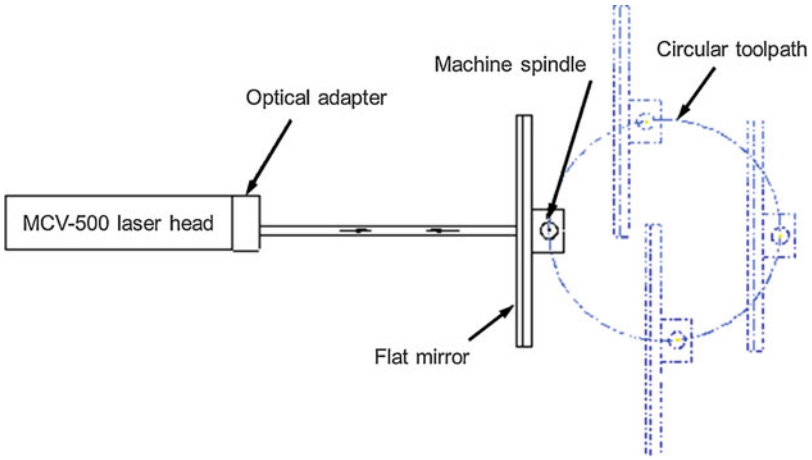

Fig. 52 Schematic of laser circular test

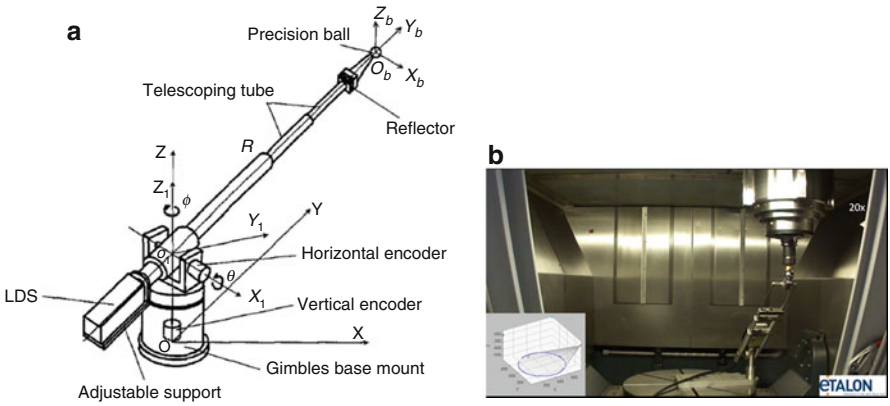

Fig. 53 (**a**) Structure of the 3D Laser Ballbar (Fan et al. 2004); (**b**) measuring the C-axis (by rotating the rotary table) and linear axis (by moving the linear axis) by means of Etalon LaserTRACER-MT system. (Courtesy of Etalon AG)

and two precision laser rotary encoders in the gimbal base with an extendable ballbar (Fig. 53a). Three sensors simultaneously record the ball positions and transform into the Cartesian coordinate in real time. The LaserTRACER-MT (MT, mechanical tracking) system made by ETALON (Fig. 53b) is an exemplary commercial implementation of the above idea. The system can be used to calibrate small- and medium-sized machine tools with their assemblies shifted by up to 1.5 m.

The main limitation of the LBB and 3D LBB devices is the minimum length of the telescoping tube, which determines the dead part of the workspace and the maximum size of the workspace in which measurements can be made. The state-of-the-art tracking laser systems have no such limitations.

Measurement of Spindle Error

The performance of precision spindles is a significant contributor to the overall accuracy of a precision machine or instrument. For years, the error motion of the highest precision spindles was essentially too small to reliably quantify because the measurement uncertainty exceeded the measurand (a few nanometers for the best spindles). However, improvements in sensors, instrumentation, data acquisition, signal processing, and structural design are closing this gap and enabling low uncertainty spindle metrology.

Principle and Instrument

A conventional method for the calibration of rotary axis is described in ISO 230-1 (ISO 230-1 1996) which proposes the use of a dial gauge to measure the radial and axial runout deviation at the center hole of the rotary axis. If the gauge cannot be applied at the center hole, it can be used in combination with precise manufactured check gauges which are mounted on the rotary axis. Another possibility is the use of capacitive (Chapman 1985; Marsh et al. 2006) or inductive (Frennberg and Sacconi 1996) sensors, which measure contactless and can be used at much higher rotational speed. Capacitance gauging has several advantages over the alternative Eddy current gauging or inductive sensing, which most notably is that capacitance: insensitive to metal alloy variations, not affected by variations in the surface, allows measuring equipment to be readily calibrated in an approved calibration laboratory, and can be traceable to an international standard.

The spindle error motions (dynamic and thermal) is commonly measured and analyzed by the Spindle Error Analyzer (SEA) system (Grejda et al. 2005; Marsh et al. 2006) as shown in Fig. 54. Master target with a maximum roundness error of 50 nm and its fixture are mounted on the machine tool spindle and will provide the reference surface for measurements taken by this SEA system. A standard setup consists of three sensors mounted in X-, Y-, and Z-direction, respectively. The sensors measure simultaneously the master ball allowing a real-time dynamic radial and axial measurement. With five sensors the tilt of the spindle can also be determined in X- and Y-direction. For five axes of measurement as shown in Figure, a probe is mounted from the bottom to measure movement in the Z-axis. A pair of probes is mounted at right angles (top view) to measure movement in the X and Y axes. A second pair of X and Y probes are mounted to measure a second master ball. The combination of these probe pairs generates tilt measurements. The last degree of freedom is the error of the rotation angle itself, which can be measured with a laser interferometer in combination with a self-centering device and the optical components for an angular measurement.

The most widely used method to present error motion of an axis of rotation is to plot error motion versus the angle of rotation of the spindle in a polar chart (PC) as is shown in Fig. 55 (Shu et al. 2017). The most widely recognized evaluation method is

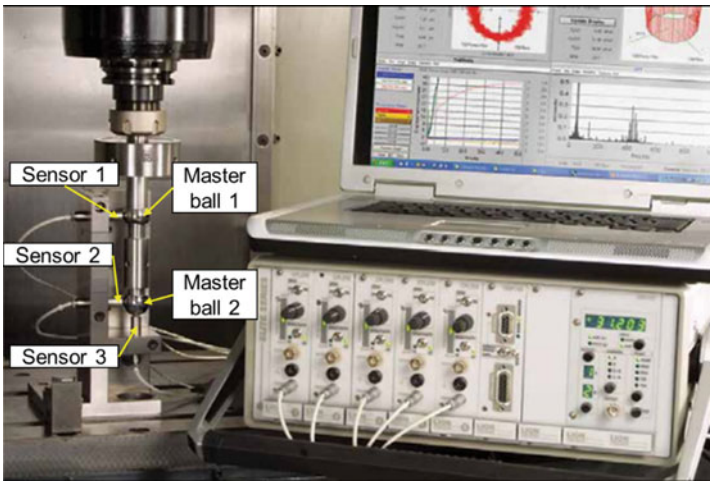

Fig. 54 Spindle Error Analyzer (SEA) system can measure real-time dynamic radial and axial movement and tilt along X- and Y-axis. (Courtesy of Lion Precision)

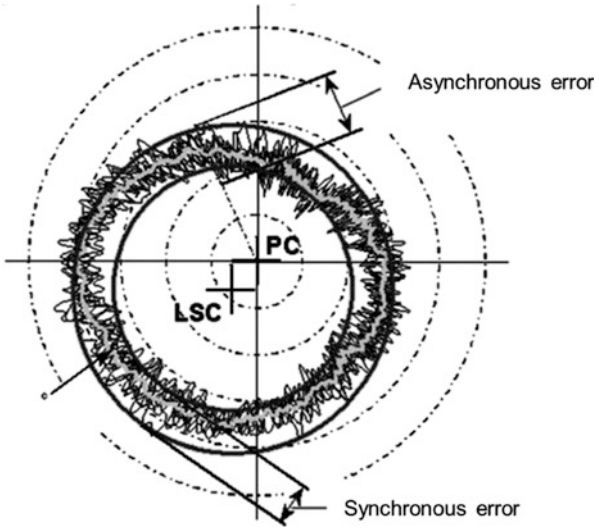

Fig. 55 Illustration of synchronous and asynchronous motion in a polar chart (Shu et al. 2017)

based on least-squares center (LSC) of the polar chart. The LSC is the center of a circle that minimizes the sum of the squares of radial deviations measured from it to the error motion polar plot. The synchronous error motion value is the scaled difference in radius of two concentric circles from LSC just sufficient to contain the synchronous error motion polar plot, while asynchronous error motion value is the maximum scaled width of the asynchronous error motion polar plot, measured along a radial line through the polar chart (PC) center.

Error Separation

Generally, error motion of a spindle is directly measured with a capacitive probe targeting a spherical or cylindrical artifact mounted on the top of the spindle. However, this traditional method no longer applies to error motion measurement for an ultraprecision axis of rotation because of form error of the artifact. As a result, several error separating methods have been developed. The most well-known methods such as Donaldson reversal, multistep, and multiprobe have been demonstrated to have uncertainty of the order of 6–20 nm. The basic concept of Donaldson reversal is the reversed characteristic of artifact form error based on that complete error separation is achieved (Donaldson 1972). As shown in Fig. 56, spindle radial motion is given by $R(\theta)$, and the ball roundness is given by $B(\theta)$. Assuming that angular information is derived from the spindle position, the indicator outputs, $I(\theta)$, for the two positions are

$$I_1(\theta) = R(\theta) + B(\theta) \tag{9a}$$

$$I_2(\theta) = -R(\theta) + B(\theta) \tag{9b}$$

$$R(\theta) = \frac{I_1(\theta) - I_2(\theta)}{2} \tag{9c}$$

$$B(\theta) = \frac{I_1(\theta) + I_2(\theta)}{2} \tag{9d}$$

Multistep is another well-known error separation method. With sufficient measurement steps and elaborately designed multistep method (Anandan and Ozdoganlar 2016), it is possible to achieve measurement accuracy of nanometer level, although harmonic suppression exists. Figure 57 shows the procedure for multistep method. Record probe readings around several cycles before rotating the

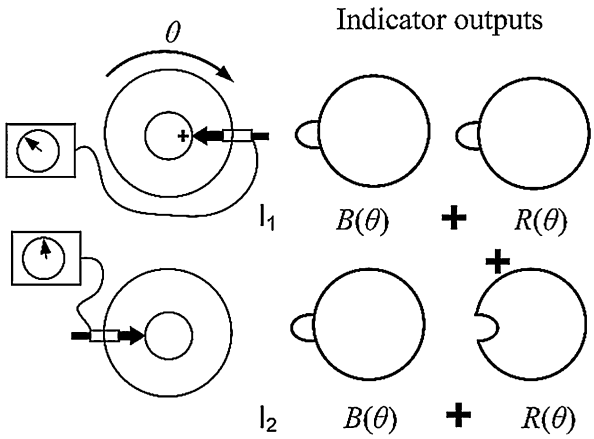

Fig. 56 Donaldson reversal error separating method (Evans et al. 1996)

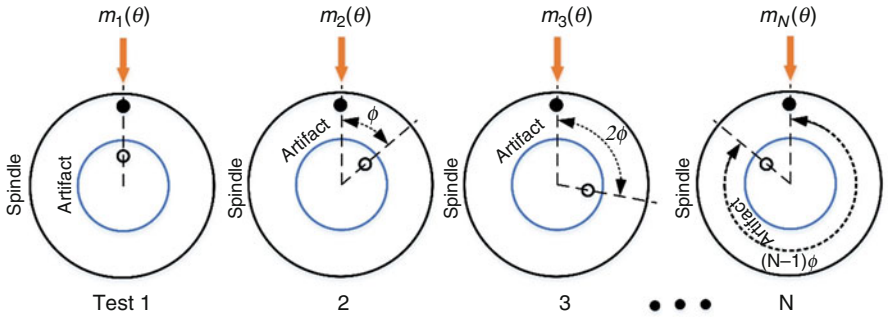

Fig. 57 Schematic of the multistep error separation method after B89.3.4M (Marsh et al. 2006)

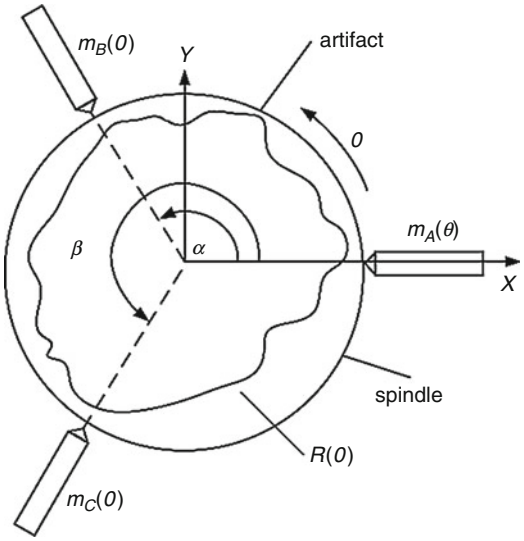

Fig. 58 Three-probe method for separating form error of an artifact (Shu et al. 2017)

artifact by an angle ϕ until N measurements are completed, such that $N\phi = 360^{\circ}$. Each measurement should be made at the same starting point, and all the data should be sampled at evenly spaced positions around one cycle of the rotator. Let $m_i(\theta)$ be the ith measurement, and the radial error motion of spindle axis $S(\theta)$ is given by

$$S(\theta) \approx \frac{1}{N}\sum_{i=1}^{N} m_i(\theta) \tag{10}$$

Averaging the multistep measurements separates the error motion of the spindle from the artifact form, except at frequencies that are at integer harmonics of the number of steps. Therefore, caution should be used when interpreting the results. However, when a sufficient number of steps (e.g., 20) are used, the first distorted

harmonic occurs at a relatively high frequency. For high quality lapped artifacts, the amplitude of artifact error occurring at these higher harmonics is relatively small (normally a few nanometers) (Marsh et al. 2006).

The multiprobe method, as illustrated in Fig. 58, involves more than two probes spaced at given angles with each other. Compared with multistep methods, multiprobe methods are more suitable for on-machine measurements, because the repeat measurement of the spindle error is not necessary.

References

Airy GB (1846) On the flexure of a uniform bar supported by a number of equal pressures applied at equidistant points, and on the positions proper for the applications of these pressures in order to prevent any sensible alteration of the length of the bar by small flexure. Mem R Astron Soc 15:157

Anandan KP, Ozdoganlar OB (2016) A multi-orientation error separation technique for spindle metrology of miniature ultra-high-speed spindles. Precis Eng 43:119–131

Bangert M (2009) Easier error compensation: volumetric error compensation technology shortens and simplifies the calibration process. Quality 48(2):30–32

Beno M, Zvoncan M, Kovac M, Peterka J (2013) Circular interpolation and positioning accuracy deviation measurement on five axis machine tools with different structures/Mjerenje devijacija tocnosti kruzne interpolacije i pozicioniranja na petoosnim alatnim strojevima razlicitih konstrukcija. Tehnicki Vjesn-Tech Gaz 20(3):479–485

Bryan JB (1979) The Abbe principle revisited: an updated interpretation. Precis Eng 1(3):129–132

Chapman P (1985) A capacitance based ultra-precision spindle error analyser. Precis Eng 7(3):129–137

Di Giacomo B, de Magalhães RDCA, Paziani FT (2004) Reversal technique applied to the measurement of straightness errors

Donaldson RR (1972) Simple method for separating spindle error from test ball roundness error. California Univ., Lawrence Livermore Lab, Livermore

Espinosa OC, Diaz P, Baca MC, Allison BN, Shilling KM (2008) Comparison of calibration methods for a surface plate. Sandia National Laboratories (SNL-NM), Albuquerque

Evans CJ, Hocken RJ, Estler WT (1996) Self-calibration: reversal, redundancy, error separation, and 'absolute testing'. CIRP Ann-Manuf Technol 45(2):617–634

Fan K-C, Wang H, Shiou F-J, Ke C-W (2004) Design analysis and applications of a 3D laser ball bar for accuracy calibration of multiaxis machines. J Manuf Syst 23(3):194–203

Frennberg M, Sacconi A (1996) International comparison of high-accuracy roundness measurements. Metrologia 33(6):539

Grejda R, Marsh E, Vallance R (2005) Techniques for calibrating spindles with nanometer error motion. Precis Eng 29(1):113–123

ISO. 230-1:1996, Test code for machine tools. Part 1. Geometric accuracy of machines operating under no-load or finishing conditions. Geneva

ISO. 230-7:2006(E), Test code for machine tools. Part 7. Geometric accuracy of axes of rotation. Geneva

Janeczko J, Griffin B, Wang C (2000) Laser vector measurement technique for the determination and compensation of volumetric position errors. Part II: experimental verification. Rev Sci Instrum 71(10):3938–3941

Jia MQ, Zhang J, Gao R, Zhao D-S, Peng T-T (2015) Precision measurement of squareness of large rectangular square. In: Paper presented at the ninth international symposium on precision engineering measurement and instrumentation

Józwik J, Czwarnowski M (2015) Angular positioning accuracy of rotary table and repeatability of five-axis machining centre DMU 65 MonoBLOCK. Adv Sci Technol Res J 9(28):89–95
Kim W-S, Raman S (2000) On the selection of flatness measurement points in coordinate measuring machine inspection. Int J Mach Tools Manuf 40(3):427–443
Kwaśny W, Turek P, Jędrzejewski J (2011) Survey of machine tool error measuring methods. J Mach Eng 11
Marsh E, Couey J, Vallance R (2006) Nanometer-level comparison of three spindle error motion separation techniques. J Manuf Sci Eng 128(1):180–187
Meijer J, Heuvelman C (1990) Accuracy of surface plate measurements – general purpose software for flatness measurement. CIRP Ann-Manuf Technol 39(1):545–548
Nakazawa H (1994) Principles of precision engineering. Oxford University Press, Oxford
Parkinson S, Longstaff A, Crampton A, Gregory P (2012) The application of automated planning to machine tool calibration. In: Paper presented at the ICAPS
Schmitz T, Ziegert J (2000) Dynamic evaluation of spatial CNC contouring accuracy. Precis Eng 24(2):99–118
Schmitz T, Davies M, Dutterer B, Ziegert J (2001) The application of high-speed CNC machining to prototype production. Int J Mach Tools Manuf 41(8):1209–1228
Schwenke H, Franke M, Hannaford J, Kunzmann H (2005) Error mapping of CMMs and machine tools by a single tracking interferometer. CIRP Ann-Manuf Technol 54(1):475–478
Shu Q, Zhu M, Liu X, Cheng H (2017) Radial error motion measurement of ultraprecision axes of rotation with nanometer level precision. J Manuf Sci Eng 139(7):071017
Smith GT (2016) Machine tool metrology: an industrial handbook. Springer
Wang C, Liotto G (2002) A laser non-contact measurement of static positioning and dynamic contouring accuracy of a CNC machine tool. In: Paper presented at the proceedings of the measurement science conference
Wang Z, Mastrogiacomo L, Franceschini F, Maropoulos P (2011) Experimental comparison of dynamic tracking performance of iGPS and laser tracker. Int J Adv Manuf Technol 56(1):205–213
Yetai F, Ping S, Xiaohuai C, Qiangxian H, Liandong Y (2010) The analysis and complementarity of Abbe principle application limited in coordinate measurement. In: Paper presented at the proceedings of the world congress on engineering
Ziegert JC, Mize CD (1994) The laser ball bar: a new instrument for machine tool metrology. Precis Eng 16(4):259–267

On-Machine Measurement System and Its Application in Ultra-Precision Manufacturing

20

Xiangqian Jiang, Zhen Tong, and Duo Li

Contents

Introduction 564
Surface Metrology 565
Definition of Surface Metrology 565
Surface Features and Characterization 566
Procedures of Surface Measurement 566
Measurement Systems Used in Manufacturing Process 568
Classification of Optical Measurement Systems 568
Advantages of Embedded On-Machine Surface Metrology 569
Requirements for Embedded Metrology System 570
Typical Embedded Measurement Systems 570
Contact Profilometer 570
Machine Version 572
Confocal Chromatic Microscopy 572
Optical Interferometry 574
Phase-Measuring Deflectometry 579
Focus Variation 581
Embedded Metrology in Ultra-Precision Manufacturing 583
Contact Profilometer Based On-Machine Measurement System 583
Non-contact Optical On-Machine Measurement System 588
Conclusion 596
References 597

X. Jiang (✉) · Z. Tong (✉) · D. Li
EPSRC Future Metrology Hub, Centre for Precision Technologies, University of Huddersfield, Huddersfield, UK
e-mail: x.jiang@hud.ac.uk; z.tong@hud.ac.uk

Z. Jiang, S. Yang (eds.), *Precision Machines*, Precision Manufacturing,
https://doi.org/10.1007/978-981-13-0381-4_16

Abstract

The increasing complexity of functional surface structures in terms of structure size and area shape and scale brings considerable challenges on the existing ultra-precision manufacturing and surface measurement technologies. The discrete nature of manufacturing cycle in industry where the measurement instrument used for quality assessment is normally in an offline manner significantly limits productivity and flexibility.

This chapter gives a brief coverage to the historical development of surface metrology and measurement systems embedded within the manufacturing process. The current typical metrological techniques and instrumentation for carrying out embedded surface metrology are presented from the aspects of working principle, advantages, applications, and limitations. The specific emphasis has been put on the applications of embedded measurement system in ultra-precision manufacturing environment. It is found that with embedded metrology, it is possible to further improve the processing efficiency and reliability of high-precision manufacturing. The merits and limitations of embedded measurement systems used in ultra-precision manufacturing are compared and discussed.

Keywords

On-machine measurement · Surface functionality · Ultra-precision manufacturing · Surface measurment · Embedded metrology

Introduction

Freeform and micro-/nanostructured functional surfaces have been widely used in astronomy, aerospace, automotive, semiconductors, telecommunicating, IT facilities, and medical and foods safety, changing our lives in terms of increased living standards. To ensure the designed functionality, it normally requires surfaces to have sub-micrometer form of accuracy and nanometer surface topography (Jiang and Whitehouse 2012). Diamond machining including diamond turning, high-speed micro milling, fast tool servo, slow tool servo, and fly cutting plays a key role in the fabrication of functional structured surfaces with mirror finishes. However, the increasing complexity of surface structures in terms of scale (both the structure size and the area of structured surface) and shape of the products (e.g., sphere, aspheric, freeform) impose considerable challenges on the existing ultra-precision fabrication and surface measurement technologies. The measurement systems used for product quality assessment in industry are usually in an offline manner where the samples are measured within the field of view of the instrument. The discrete nature of production cycle limits the further development of productivity while allowing high reliability and flexibility.

Indeed, in many high-precision applications, the removal and remounting of workpieces in post-process metrology would cause unavoidable alignment error if re-machining processes need to be carried out. For example, the polishing of large telescope optics (Walker et al. 2006) and the mounting of the sample on a fixed measurement platform are very challenging and even impossible when the sample dimensional size exceeds the measurement scale of current measurement equipment having nanometer form resolution. The movement of components from manufacturing environment to measurement instruments also increases production cycle times and component cost. The integration of metrology into manufacturing environment will preserve the consistency between the machining and measurement coordinates and thus allows further improvement of machining accuracy and efficiency by eliminating repositioning operations.

Additionally, for some demanding advanced production line such as the manufacture of flexible photovoltaics (PV), printable electronics, structured films, and other roll-to-roll (R2R) manufacturing processes (Elrawemi et al. 2015), offline or post-process measurement is not applicable anymore. The high throughput of the manufacturing processes means that detection of defects post-manufacture would result in the wastage of a large quantity of products. Although the existing machine-vision inspection solutions can help detect surface defects, it is incapable to provide height information for the characterization of all defects. Thus, it is imperative to shift the approach of metrology from offline lab-based solutions to embedded measurement in manufacturing platforms (Jiang and Whitehouse 2012). With embedded metrology it is possible to enhance the material processing and reliability of high added-value critical components, ultimately leading to cost-effectively eco-manufacturing.

This chapter will briefly introduce the historical development of surface metrology and measurement systems and highlight the requirements for embedded measurement used in manufacturing process. Typical metrological techniques and instrumentation for embedded surface metrology are introduced from the aspects of working principles, advantages, and typical applications in ultra-precision manufacturing as well as their limitations.

Surface Metrology

Definition of Surface Metrology

Surface metrology refers to the measurement that describes the surface deviation between a structured surface and its ideal shape (Whitehouse 2004). Surface metrology is used in engineering to understand the creation and behavior of surface topographies. It specifically covers measurements such as surface texture, surface roughness, surface shape, surface finish, form, etc.

The surfaces are generally manufactured to provide specially designed functional properties. These surfaces are produced by variety of processes such as diamond turning, milling, grinding, polishing, molding, etc. High-precision

engineered surfaces of desired functionality are usually manufactured by manipulating geometrical features on surfaces. Functional properties directly relate to the geometrical features, and hence measurements of such features are extremely important. The measurement results also give valuable feedback to manufacturing units for controlled manufacturing.

Surface Features and Characterization

Surface features are generally characterized along the vertical direction by height parameters and along the horizontal direction by spatial (wavelength) parameters. The structures on the surfaces are basically various components of frequency related to the manufacturing process or the production technique used. According to the spatial frequency, a surface profile can be generally divided into three types of surface features, namely, roughness, waviness, and form.

Roughness refers to the highest-frequency components present on a surface of interest. Roughness depends on the type of manufacturing method employed rather than the machine type.

Waviness results due machine deflections and vibration and is defined as repeating irregularities with spacing greater than roughness. In terms of frequency, the next lower order frequency components on the surface represents waviness.

Form error is the overall parameter describing the maximum of the local deviations of the real form of a line or surface from the nominal – geometrically ideal feature. Form error is generated due to lack of rigidity of the workpiece during the machining process allowing it to flex or bend. This contains lowest frequency components on a surface. Several factors such as material strain, temperature changes during machining, and excessive surface residual stress can cause form error.

With the development of novel and robust mathematical tools, the characterization interest has shifted from profile to areal, from stochastic to tessellated, and from simple geometries to complex freeform surfaces. For areal surface characterization, the concept of scale-limited surface has been developed. The scale-limited surface contains S-F surface and S-L surface, which are created by a combination of S-filter, L-filter, and F-operator as shown in Fig. 1 (ISO Standard 25178-2 2012).

Procedures of Surface Measurement

Surface measurement involves three basic steps: acquisition of data by an instrument, filtration, and analysis by parameterization (Fig. 2). Sometimes fitting of the acquired data is required to remove any underlying shape due to the tilt of sample relative to the measuring instrument. Filtering is used either to remove the undesired aspects of surface topography or to select the elements which are needed for analysis or evaluation. So, filtering wherever employed must be carried out with utmost care so that the desired information always remains. After filtering the

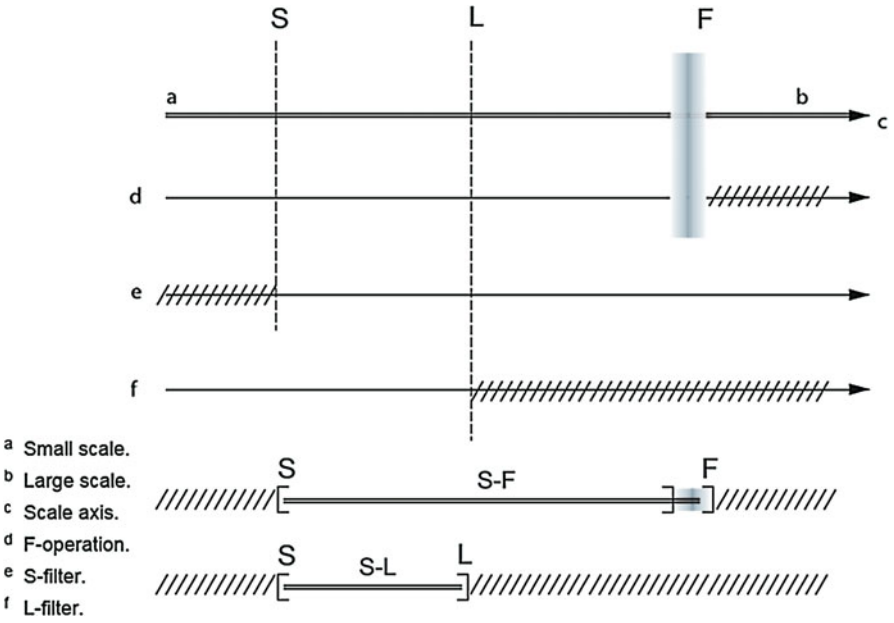

Fig. 1 Relationships between the S-filter, L-filter, F-operation, and S-F and S-L surfaces (ISO Standard 25178-2 2012). **S-filter**, which defined as a filter that removes small-scale lateral components from the surface resulting in the primary surface. **L-filter**, which is used to remove large-scale lateral components from the primary surface or S-F surface. **F-operator**, which removes the form from the primary surface. An S-F surface results from the use of an S-filter and an F-operator in combination on a surface and an S-L surface by the use of an L-filter on an S-F surface

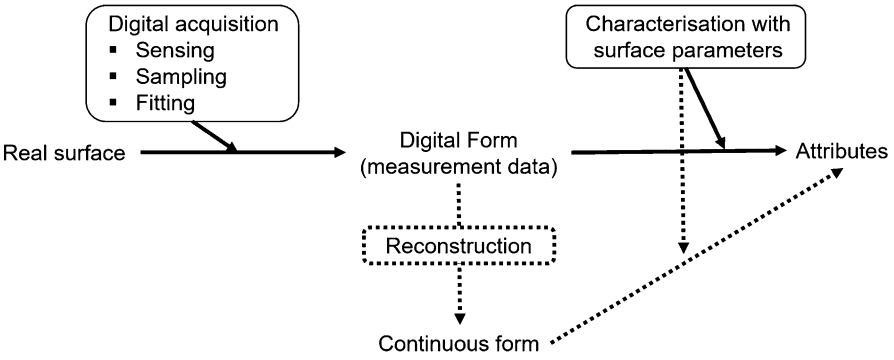

Fig. 2 General procedures for the measurement of a patch of surface topography

data is analyzed to describe the surface features in some numbers called parameterization.

Large numbers of surface parameters are developed to characterize the surface topography. These surface parameters have been categorized into mainly four

groups: height parameter, shape parameter, wavelength parameter, and combination of these known as hybrid parameter. Similarly, statistical function gives detailed statistical description of surface properties. Examples of statistical functions are the power spectral density function, the autocorrelation function, the amplitude density function, and the bearing area curve.

Measurement Systems Used in Manufacturing Process

Structured surfaces have enabled functional advancements such as lubrication, adhesion, wear diagnostics, friction, and so on. As the dimensions of products are getting smaller, the surface features and its properties become a dominant factor affecting the functionality of products. With advanced surface metrology techniques, there is high possibility of improving material processing processes, making manufacturing more efficient, reliable, economic, and less environmentally sensitive.

Classification of Optical Measurement Systems

Many reviews have been written regarding various optical methods, offering a detailed list of categories such as polarization interferometry, speckle interferometry, heterodyne interferometry, white-light interferometry, moiré and structured light methods, holographic methods, confocal microscopy, optical scattering, focus variation, etc. All these categories can be divided into two types, namely, non-interferometric and interferometric techniques. The surface characterization can be performed at different conditions according to requirements of applications. Vacharanukul and Mekid provided a classification for the act of measurement during the manufacturing process in three groups, namely, in- process, in situ, and post-process (Vacharanukul and Mekid 2005).

In-process or in-line metrology can be defined as any measurement method which occurs while the manufacturing process continues. This may include use of the metrology as part of a control system to provide real-time feedback information for compensation of manufacturing errors or later in the manufacturing chain for continuous processes. The harsh factory environment brings big challenges for in-process measurement. The in-process metrology system should be robust enough to allow the motion of the measurand, vibration, and heat generation. The system should also be protected from manufacturing contaminants such as swarf, dust, and cooling fluids. Examples of in-process metrology include the measurement of moving webs in a roll-to-roll manufacturing line as well as the measurement of conveyed products.

On-machine, in situ, online, or embedded metrology is the process of measuring surfaces without removal of the workpiece from the manufacturing platform. The manufacturing is actually halted during the measurement process. Typical examples of on-machine metrology like grinding tool wear measurement, characterization of tip geometry of milling cutters, measurement of both the molds,

components in precision injection molding, measurement of surface roughness, form deviation of freeform surfaces produced by diamond machining, etc. Compared to in-process measurement, it not only significantly relaxes the challenges for implementation due to a mild assessment surroundings but also takes the advantages of not having to remove/refit workpiece in terms of further surface modification. Challenges faced are those such as machining platform motion errors, environmental disturbances, and process contaminants.

Post-process or offline metrology describes the measurement through instruments located remotely from the manufacturing process. The maturity of measurement technologies and the ability to perform measurement at a specific temperature, humidity, pressure, as well as anti-vibration environment are advantages of office metrology. However, the discrete nature between production and measurement, the cost of upkeep of a separate facility, as well as the operator costs of nonautomated metrology are significant drawbacks of using offline metrology. It is also time consuming to fix and realign the workpiece on a machine tool for further surface modification.

Advantages of Embedded On-Machine Surface Metrology

Compared with offline surface measurement, the following benefits of on-machine measurement are offered:

(A) Increased inspection efficiency

From the production perspective, the integration of measurement system in manufacturing environment increases the inspection efficiency and production throughput and reduces the cost associated with transportation labor and tools, staff training, and maintenance of offline measurement equipment.

(B) Improvement of machining accuracy

The coordinate system between machining and measurement process is consistent through the whole manufacturing process when machining with assist of on-machine measurement system. This is particularly important when machining ultra-precision surfaces requiring sub-micrometer and even nanometer level form tolerance.

(C) Improvement of automation level

The automated nature of on-machine metrology makes it indispensable for autonomous and intelligent manufacturing. The machined surface can be inspected in situ, and the extracted information can be promptly fed back to machine control system for product quality control. The intimate knowledge of measurement strategy and other operation experiences can be integrated into CNC machine control system, which means that operator experience is less necessary in the product manufacturing.

Requirements for Embedded Metrology System

In general, the embedded system used in manufacturing platform need to be compact and flexible enough to allow for an easy installation. Furthermore, they must be capable of reaching the same performance as their commercial standalone equivalents (Jiang and Whitehouse 2012). In order to match and exceed the performance of offline metrology tools, the selected embedded measurement instrument must meet as many of the following requirements as achievable:

- **Robust to environment**. The effects of temperature, humidity, vibration, and atmospheric pressure and the presence of lubricants/contaminants must not adversely affect the quality of measurement.
- **Compact design**. The instrument is supposed to be compact enough to be integrated into a machine.
- **Measurement rate**. The measurement rate/speed of the instrument should match the production line requirement. High measurement rate will help reduce the effects of environmental noise on measurement results and save the time for a complete measurement.
- **Measurement range**. The measurement range of the instrument should be large enough to cover all the features of interest.
- **Dynamic range**. The ratio of axial range to resolution is important to (a) increase the instrument versatility in measurement and (b) reduce the cost associated with the requirement for many probes/objectives to cover a range of measurement regimes.
- **Measurement precision**. The measurement precision of embedded metrology system must equal or exceed existing offline methods due to the ever-decreasing feature sizes of engineered surfaces.

Typical Embedded Measurement Systems

In general, an appropriate measurement technique used for a surface metrology should be determined according to the function of the surface and its applications. In this section, typical embedded measurement systems are selected and briefly introduced from the aspects of working principle, typical applications, advantages, and limitations.

Contact Profilometer

Stylus profilometry (Fig. 3) and scanning probe microscopes (SPMs, Fig. 4) are two typical contact profilometers. A tactile probe is used in contact profilometer to collect the surface topography information. The stylus-based profilometer traces a contacting stylus through a transducer (acting as a gauge) and measures the vertical variation of the stylus

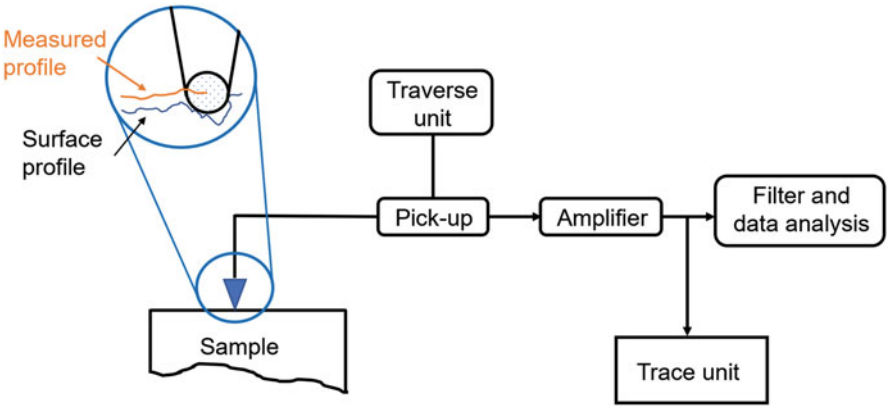

Fig. 3 Schematic representation of stylus profilometer

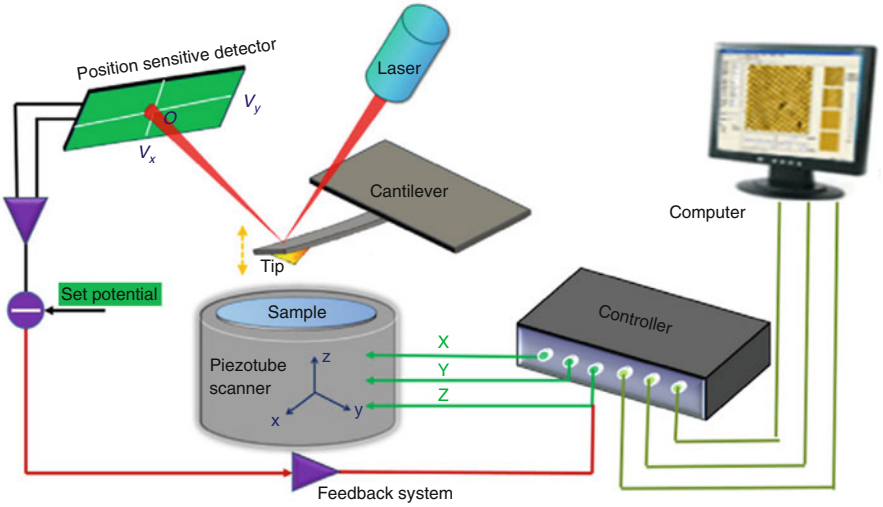

Fig. 4 Schematic diagram of the basic working principle of AFM (Guo et al. 2013)

as it traverses across the surface of interest. The lateral resolution is determined by the radius of curvature of stylus tip and the slopes of the surface irregularities. Currently the measurement range can achieve up to several millimeters in height with a vertical resolution in nanoscale. Equipped with an extra translational stage, a stylus profilometer is able to measure areal surfaces in a raster scanning mode. Many commercial products have been developed by the Taylor Hobson Limited, typically Talysurf PGI (surface form measurement) and Talyrond series (roundness measurement).

SPMs are developed based on the scanning tunneling microscope (STM) and the atomic force microscope (AFM). It has much common with the stylus-based

instrument but uses STM/AFM fine level tips to scan surfaces. The surface information collected by STM/AFM is the charge density or atomic forces, not the height data.

The contact profilometer is preferred for measurement of large deviation freeform surfaces due to its high lateral/vertical resolution and large measurable range. However, the contact stylus tips have high risk to be damaged in harsh measurement environment. It is also not suitable to measure soft and dedicate surfaces as the surface would get scratched or even functionally damaged when the stylus tip scanning the surface. The finite size of stylus tip also makes it impossible to penetrate into all valleys of the true surface and thus introduces a nonlinear distortion to the measured envelope. The image resolution is highly dependent on the tip geometry, and the point-by-point scanning of contact profile meter also makes the measurement of surface topography time-consuming. From these point of views, contact profilometers are usually considered not applicable to the metrology in manufacturing environment. However, several attempts have been conducted recently to use scanning probe microscopes (SPMs) with finer tips to realize the on-machine measurement of ultra-precision machined microstructures. More details are introduced in the following section.

Machine Version

Machine vision is imaging-based optical metrological system which is commonly used for surface inspection in industry such as die attach bond inspection, ball grid array inspection, solar and PV device inspection, metal surface inspection, print inspection, etc. As shown in Fig. 5, it consists of four main parts, namely, illumination system, imaging optical system, detector, and computer system. The tested surface is illuminated by a light source, and then the features within the field of view (FOV) are imaged by a high-speed camera. The recorded grayscale images are analyzed by data processes algorithms such as averaging and filtering to characterize the surface features of interest. The selection of illumination source depends on the applications. Bright field transmission illumination is normally used for transparent or nearly transparent material, while dark field illumination system is preferred for glossy surfaces. For low-contrast surface, a diffuse illumination is recommended, and directional lighting source is usually applied for structured surface (Harding 2013). The selection of high-speed camera is normally depended on the requirement of web speed and the minimum feature size on the tested surface. The commercial CMOS cameras usually can offer line rates up to 140 KHz with 4 K pixels and 10 μm pixel size. However, the technique can only provide 2D surface information, and it remains very difficult to obtain the depth information of the tested surface.

Confocal Chromatic Microscopy

Confocal chromatic microscopy (CCM), also known as confocal chromatic sensing (CCS) and confocal chromatic spectrometry (CCS), takes advantage of using two

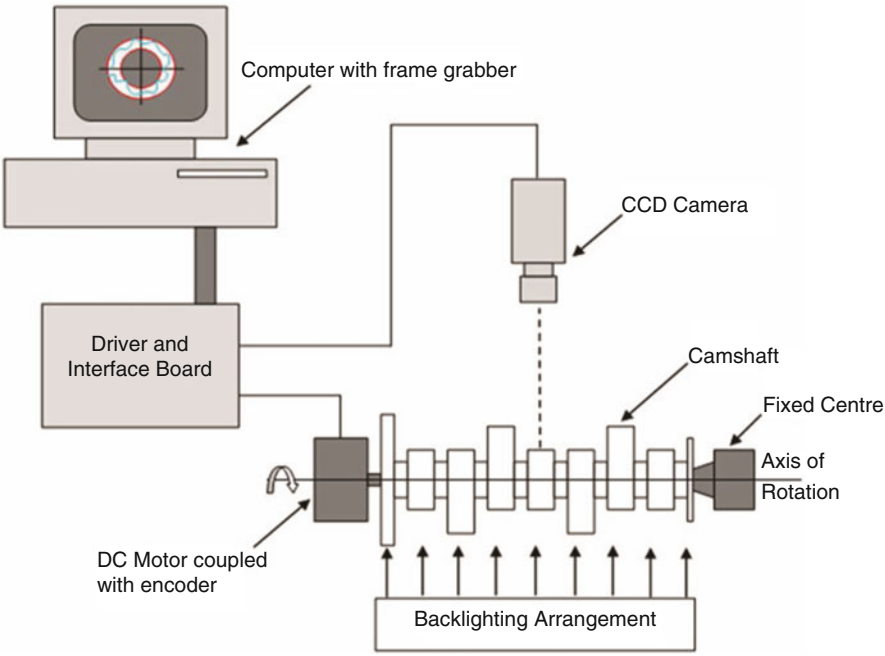

Fig. 5 Configurations for in-line inspection calibration and in situ roundness measurement (Ayub et al. 2014)

pinhole apertures as spatial filters for focused rays (as schematically shown in Fig. 6). Monochromatic or white-light source travels through one pinhole and converges on the sample surface. The other pinhole works as a filter in front of the detector which only allows the reflected focused rays to transmit through it and reached the detector or a spectrometer. Mechanical vertical scanning is required for monochromatic confocal microscopy to get the height information of a point. CCM of white-light source takes advantage of the chromatic aberration introduced by a lens and the range of focal lengths of a broadband light source. Each wavelength of the illumination corresponds to a focal plane along the optical axis. After calibration of the instrument, a range of focal lengths can be used to achieve parallelization scanning in depth direction (Ruprecht et al. 2004). In order to reconstruct surface topography, scanning the surface in XY plane is required.

The confocal microscopy can be potentially applied in in-process metrology due to its compact system design, high measurement rate, and data processing speed. Most recently, company such as Precitec, Nanofocus, and Micro-Epsilon can supply CCM instrument with different performance. However, the confocal microscopy still suffers from the same problems as other microscopy instruments – physical limitation of objective. The vertical measurement range and lateral resolution are largely restricted by the working distance and diffraction limit of objective used if not camera limited (Leach and Sherlock 2013). Another problem

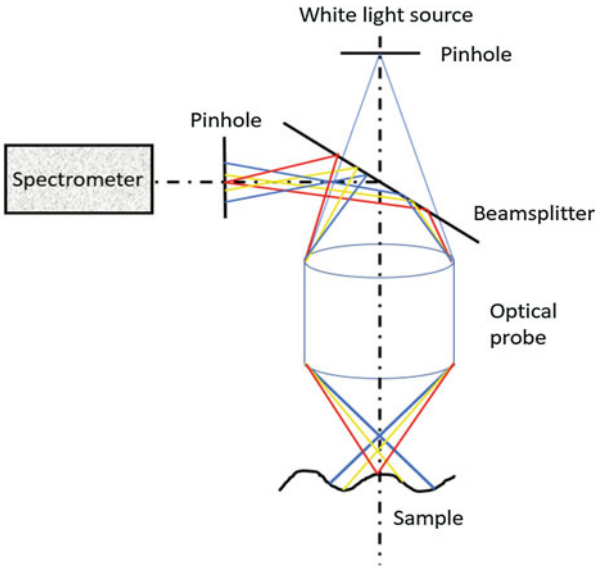

Fig. 6 Schemas of confocal microscopy

with CCM is the occurrence of self-imaging when measuring surfaces with curved profiles such as lens arrays, curved trenches, and grooves with radii (Lyda et al. 2012). The local radius of the surface refocuses wavelengths of the source light that should be out of focus at the measured surface. These refocused lights will travel back into the measurement apparatus and result in a false reading of the surface height.

Optical Interferometry

In the past decades, many interferometry-based metrology instruments have been developed to achieve high measurement accuracy. Optical interferometry is based on the analysis of the fringes generated by two light beams with the same frequency. The beams originate from the same source but traveling along different paths. An optical objective is required to bring two or more beams to interfere. According to the way to split the beam into reference and measurement beams, the interferometric objective can be broadly classified into four types, namely, Linnik, Michelson, Mirau, and Fizeau. The most popular interferometers are phase-shifting interferometry (PSI), white-light interferometry (WLI), and wavelength scanning interferometry (WSI). Interference signal is obtained by varying the path length between the test object and the reference beams. The path length variation is generally induced by either vertical scanning or phase-shifting techniques which involve mechanical scanning. It can also be induced by nonmechanical means such as wavelength scanning and dispersive methods. Vertical resolution of nanoscale level can be achieved by the interference signal, while the lateral resolution is limited by the objectives used.

Phase-Shifting Interferometry

Phase-shifting interferometry (PSI), also known as temporal phase measurement, makes the use of phase changes occurring in an interferogram during a controlled phase shift. These phase change can be induced by rotating polarizers, moving diffraction gratings, translation of mirrors, or tilt of glass slides. The 3-point, 4-point, and 5-point algorithms are commonly used to calculate the interferogram phase. Higher frame number algorithms usually have higher resistance to errors at the expense of measurement rate. Other algorithms such as the Carré algorithm allow calculation of interferogram phase without application of a known phase shift, assuming that the applied phase shifts are equal each time.

The PSI with a single-wavelength light source with long coherence length offers outstanding axial resolution. It is renowned as having sub-nanometer resolution with an achievable repeatability of less than 1 nm independent of field size (Leach 2011). However, the high axial resolution of temporal PSI is offset by its measurement rate. The measurement rate is reduced proportional to the number of camera-captured frames required by the chosen PSI algorithm. This limitation makes PSI particularly susceptible to environmental influence, for example, the vibration, where changes in surface position between frames result in measurement errors.

Another limitation of temporal PSI is the fatigue and failure associated with the translation and mechanical settling of heavy optics thousands of times throughout the life cycle time of the instrument. The relative nature of PSI also results in the phenomenon that the measured surface height wraps around every time the surface height deviates by half the illuminating wavelength or more. The PSI is thus recommended to measure smooth surfaces or step heights less than a quarter of a wavelength.

In contrast to the temporal PSI, the spatial phase-shifting interferometry also known as instantaneous interferometry is an optical measurement method where the required phase shifts occur instantaneously in time. The phase shift of spatial PSI can be induced by polarization of measurement and reference beams and use of multiple detectors. As compared to temporal PSI, the instantaneous nature of spatial PSI can inherently increase the measurement rate by elimination of the requirement for multiple camera frames per measurement. It also avoids the difficulties associated with temporal PSI such as vibration and sample movement. However, the difficulties in calibrating multiple image sensors and the measurement errors introduced by the non-common path nature of spatial PSI are the inherent limitations of the spatial PSI.

A variation of spatial PSI, namely, a single-shot phase-shifting interferometer, has been developed to circumvent the problems suffered by previous traditional PSI. It produces four phases shifted interferograms through use of a quarter wave plate and a pixelated birefringent mask in front of a single detector (Millerd et al. 2006) (Fig. 7). The single-shot nature and much improved measurement rate allow areal measurement of surfaces without sensitivity to vibration or air flow through interferometer paths, making this method potentially advantageous for on-machine measurement of moving films, webs, and other continuous production processes. Zeeko has used this kind of metrology instruments (commercialized by 4D Technology) as part of their on-machine stitching interferometer (OMSI) module for

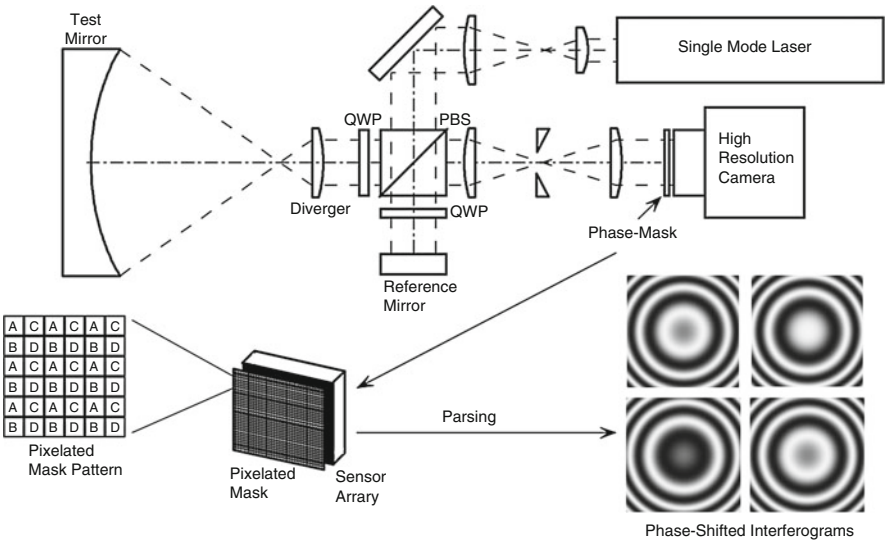

Fig. 7 Twyman-Green configuration for pixelated interferometer (Millerd et al. 2006). It produces four phases shifted interferograms through use of a quarter wave plate and a pixelated birefringent mask in front of a single detector (Millerd et al. 2006) (Fig. 7).

seven axis precision polishing and grinding machines. Nevertheless, dynamic interferometry is limited to near-perpendicular measurement of surfaces and still suffers from the phase ambiguity problem which is common to all phase-shifting techniques (Williamson 2016) (Fig. 7).

Vertical Scanning Interferometry

Vertical scanning interferometry (VSI), also known as white-light interferometry (WLI) or coherence correlation interferometry (CCI), uses the short-coherence length of a wide bandwidth source (typically several hundred nanometers bandwidth) along with the fact that the interference fringes have highest contrast when the path lengths of the interferometer arms are matched. By mechanically varying the length of one arm of the interferometer, the intensity of the interferogram at each pixel is modulated, and a pixel-wise intensity pattern of the surface is generated. The absolute distance of tested surface with respect to reference plane is determined by retrieving the locations of coherence peaks from the captured interferograms. Surface topography is acquired after tracking all coherence peaks within the field of view of the interferometric objective (as shown in Fig. 8).

The absolute (as opposed to relative) nature of coherence scanning methods allows the metrological application to rough surfaces and structured surfaces with large discontinuities. Its vertical measurable range is dependent on the working distance of the objective and the scanning range of the translation system, usually a few micrometers to a few centimeters. Many commercial products using VSI technique have been developed, such as Talysurf CCI 6000 from the Taylor Hobson

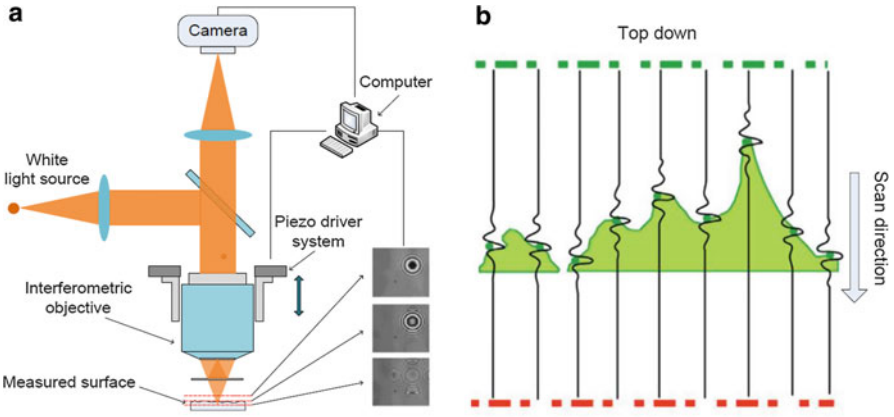

Fig. 8 (**a**) Schematic of vertical scanning interferometry; (**b**) localization of coherence peak using VSI technique (Tang 2016)

Ltd. (vertical resolution of 0.1 Å), NewView 7300 (vertical resolution smaller than 0.1 nm), and APM650 (areal measurement of high aspect ratio features) from the ZYGO Corporation. However, a large amount of interferograms are required to calculate the coherence profile, which significantly limits the measurement rate of VSI. The vertical mechanical scanning also requires extra calibration and compensation process before the in situ/offline measurement.

Wavelength Scanning Interferometry

Wavelength scanning interferometry (WSI) is proposed for the first time by Takeda and Yamamoto (1994). It takes advantage of shifting the phase by tuning wavelengths of broadband light source without any mechanical scanning. As the wavelength varies, the phase difference between the measurement arm and reference arm changes, resulting in sinusoidal intensity variations of individual pixels. Absolute surface position of each point can then be determined through frequency analysis of the intensity variations. To analyze the fringes and retrieve the phase information, various algorithms have been developed based on the zero-crossing technique, fast Fourier transform (FFT), and convolution and Carré algorithm. WSI can characterize both the rough and smooth surfaces without 2π phase ambiguity. It can also be extended to measure film thickness measurement through separation of interference signals from the top and the bottom of film surface in frequency domain (Gao et al. 2012; Ghim and Kim 2009).

Compared with CCI/VSI, the wavelength change rate is over mechanical scan rate. The camera exposure time and the computing time for data processing are factors limiting measurement rate of WSI. It is highly computationally intensive for areal measurement as a large number of frames need to be captured and analyzed for each areal measurement. The wavelength change is also very sensitive to the environmental noises such as mechanical vibration and air turbulence. To minimize the environmental effects and achieve the high measurement accuracy, Jiang et al.

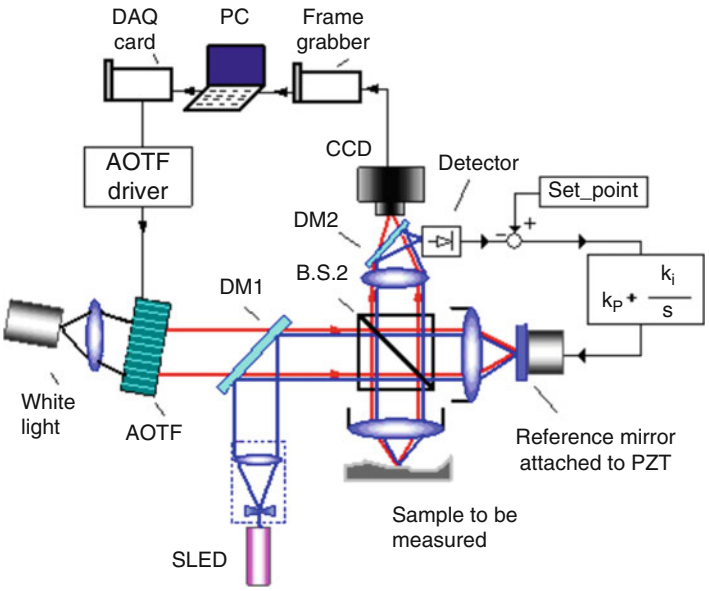

Fig. 9 An enhanced WSI with an active servo system to eliminate the environmental noise (Muhamedsalih et al. 2013)

proposed an enhanced WSI which introduced an active servo control system (reference interferometer) to monitor environment noise and compensate the environment-induced measurement error, as shown in Fig. 9. This reference interferometer is utilized as a feedback source for a close loop control system to stabilize the entire interferometry (Muhamedsalih et al. 2013). Most recently, this improved WSI has been successfully used in R2R process for surface defect inspection (Muhamedsalih et al. 2015).

Dispersive Interferometry

Dispersive interferometry, normally named spectrally resolved white-light interferometry (SRWLI) or white-light channeled spectrum interferometry (WLCSI), achieves phase shifting through wavelength variations without mechanical scanning. The interference beam is spatially dispersed by a diffraction grating or prism before being focused onto the camera, through which a channeled spectrum is obtained, and the phase information is encoded as a function of wavenumber along the chromaticity axis of the camera. Therefore, the surface profile can be obtained in a single shot, which largely improves the measurement rate of the interferometry with respect to the VSI and the WSI. Scanning the surface in XY plane is usually required for a dispersive interferometer to reconstruct surface topography.

In order to integrate the dispersed interferometry into production line, several variations of dispersive interferometry have been proposed recently, such as the spatially dispersed short-coherence interferometry (SDSCI), the line-scan dispersive

interferometry (LSDI), and the dispersed reference interferometry (DRI). In particular, the DRI adds a dispersive element in the reference arm of the interferometer to separate the source light angularly by the wavelength. Because of the short-coherence nature of the light source used in DRI, the length of the measurement arm is determined by the most strongly interfering wavelength of light. Surface topography measurements are based on phase shifts due to wavelength variations, avoiding the problems caused by optical path difference scanning and phase-shift calibration (Fig. 10). The DRI has high axial resolution (nanometer level) and robustness to discontinuous and structured surfaces. In order to enable DRI the ability to perform on-machine surface topography measurement, a small, light, and compact fiber-linked probe was applied to separate the bulky and comparatively fragile interrogation optics from the measurement probe. High-resolution position data (2 nm resolution in axial direction) has been achieved by applying a template matching technique (Williamson et al. 2016).

Phase-Measuring Deflectometry

Phase-measuring deflectometry (PMD), also known as structured light and fringe projection, detects the distortions of a sinusoidal fringe projection upon a surface to determine the surface topography. The working principle of PMD is illustrated in Fig. 11. A digital laser projector (DLP) generates sinusoidal fringes on a rear projection screen (normally use computer software), and the fringes are projected onto the surface under test. From different viewpoints, the reflected fringe patterns from the specular surfaces appear deformed with regard to the slope variation of the measured surfaces. The distortions of fringes are then observed by one or more areal detectors, for example, a charged couple device (CCD) camera. After the proper calibration, the surface height information can be reconstructed through numerical integration of gradient data derived from the deformed fringes. Because two orthogonal local slopes data are needed to be integrated to reconstruct a 3D surface tomography, vertical and horizontal fringe patterns are usually needed to be displayed sequentially on an LCD screen. To further improve the measurement speed, cross-fringe pattern and color-fringe pattern (Fig. 12) were proposed to code multiple fringe patterns in one image (Zhang et al. 2017).

A significant strength of deflectometry is the adaptability to measure both specular and diffuse surfaces. Owning to its advantages of large dynamic range, non-contact operation, and high measurement rate, the PMD technique has been applied in several areas such as the measurement of freeform car body sheets (Sárosi et al. 2010), large aspherical and/or spherical mirrors (Su et al. 2012), and flaw detection of specular or semi-specular reflective surfaces (Chan 2008). Though robust to movements and environmental effects, the vertical resolution of current PMD system is still limited to microscale, and thus it is unsuitable for surface topography measurement. The measurement error resulted from the parasitic reflections from the rear surface of transparent screen optics should be

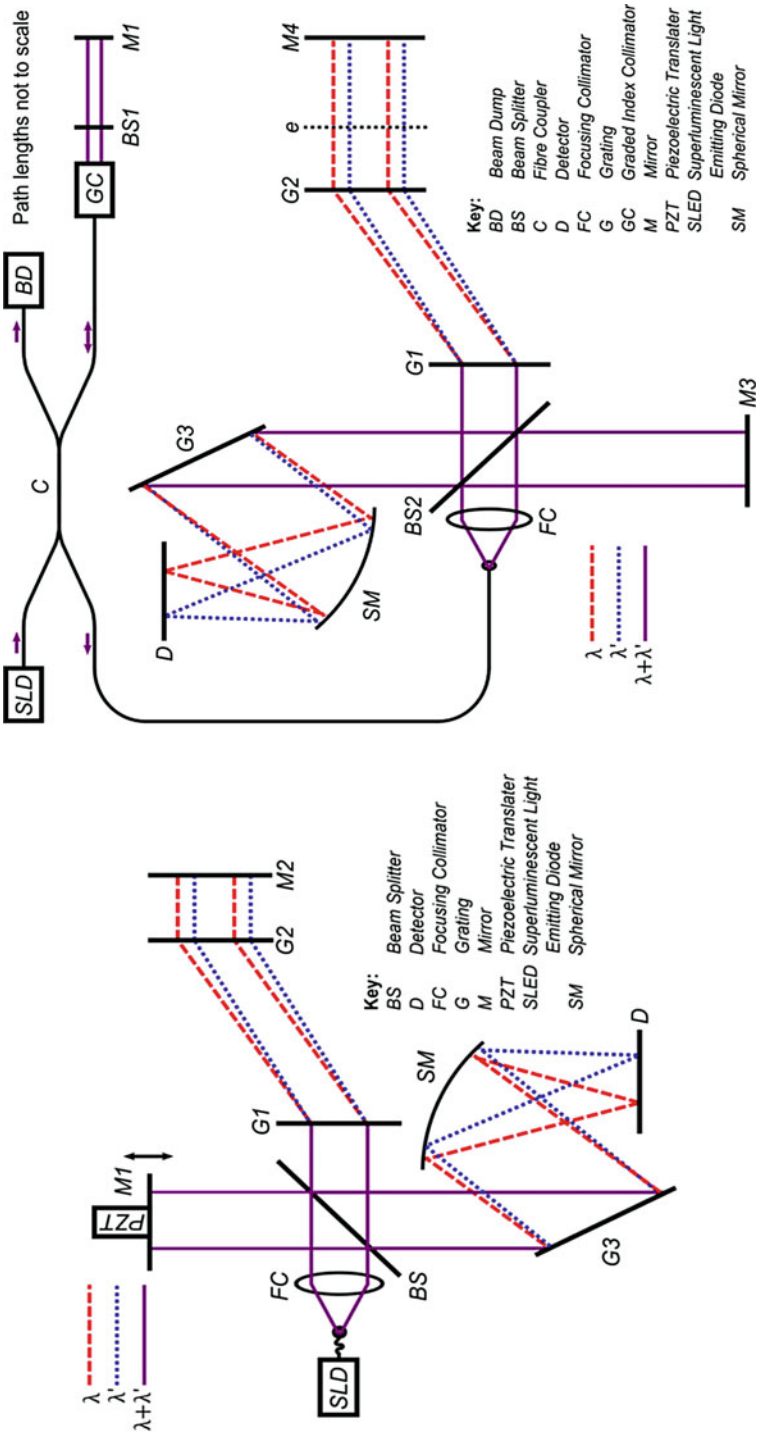

Fig. 10 Schematic of the experimental bulk optics dispersed reference interferometer (left) and DRI interrogation interferometer with a fiber-linked probe (right) (Williamson 2016)

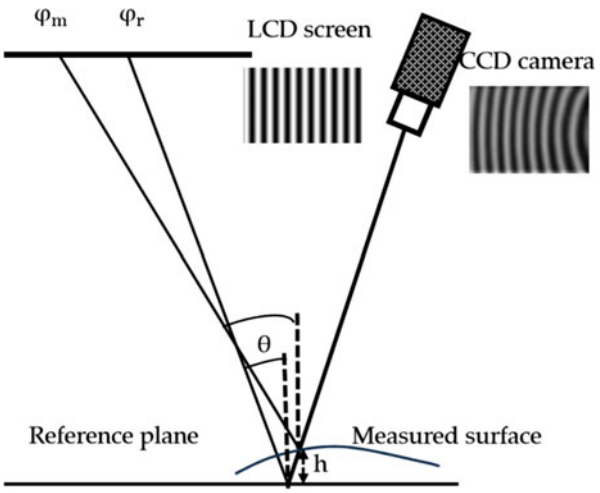

Fig. 11 Working principle of classical PMD to measure specular objects (Zhang et al. 2017)

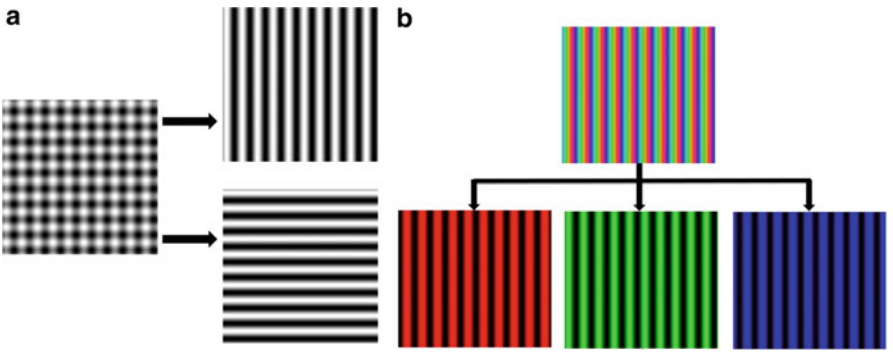

Fig. 12 (**a**) One crossed fringe pattern containing two orthogonal fringe patterns and (**b**) color composite fringe pattern containing three fringe patterns (Zhang et al. 2017)

carefully considered in order to further improve PMD measurement accuracy (Faber et al. 2012).

Focus Variation

Focus variation tracks the changing of image sharpness across the depth of field when mechanically moving an objective lens or the measured sample. The 3D topographical surface data is obtained through pixel-by-pixel calculation of image focus. As schematically shown in Fig. 13, the collimated beam is first brought to an objective and is focused onto the sample surface. All reflected rays then go back to the objective and are gathered by a camera through an imaging lens. Unlike other optical techniques where coaxial illumination usually is the only choice, various

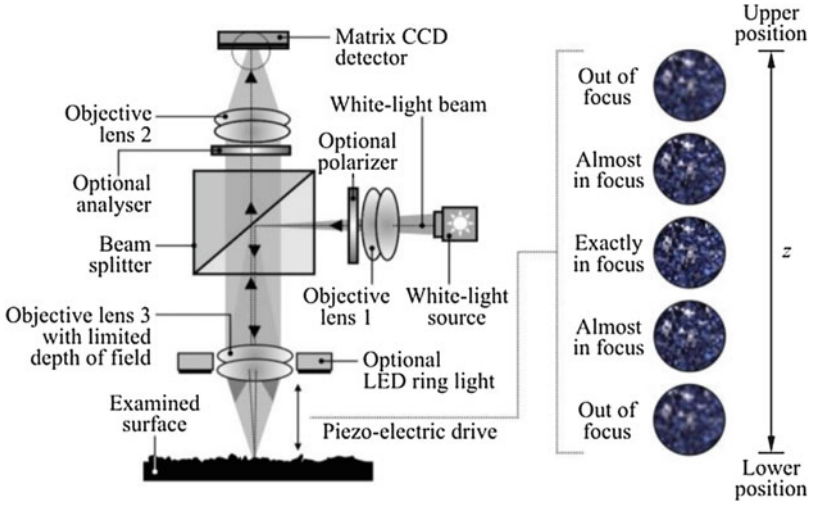

Fig. 13 Schematic diagram of measurement device based on focus variation (Wojciech Kapłonek et al. 2016)

illumination schemes can be used in focus variation instrument, for example, a ring light illumination can greatly enhance the measurable slopes of the system up to 80° (Danzl et al. 2011). The axial measurable range is dependent on the scanning range and the working distance of the objective. Additionally, the polarizer and analyzer showed in Fig. 13 can be used as filters to polarize the light when measuring metallic surfaces with steep and flat surface elements. Commercially this has resulted in the infinite focus range of offline measurement instruments by Alicona Imaging GmbH (Fig. 13).

The absolute nature of the focus variation method allows measurement of discontinuous surfaces containing steep, broken or rough regions, and the spatially separated regions. This method has excellent measurement range (up to 25 mm) with 10 nm achievable axial resolution, making it applicable to surfaces with complex structures and large discontinuities. Compared with interferometric-based methods, it is less susceptible to short-term variations in ambient light, temperature, humidity, and pressure.

However, the requirement for mechanical scanning in height direction makes the focus variation somehow a slow method. The measurement rate is less than 1 Hz, making it sensitive to vibration and inappropriate for in-line/on-machine measurement. Another negative aspect is the necessity for nanoscale surface roughness to back scatter sufficient light for sharpness detection.

Despite these limitations Alicona offer the IF-SensorR25, IF-Portable, and IF-Robot for metrology in production environments. IF-SensorR25, a miniaturized version (126 × 153 × 202 mm) for integration with machine tools, has been reported as beneficial for measurement in electro-discharge machining (EDM) centers, allowing a fourfold increase in machining accuracy (Williamson 2016).

IF-Portable and IF-Robot are offered as roughness, waviness, and form measurement tools for use in production environments with a focus on the ability to measure on and around traditionally difficult to measure larger components and assemblies. Focus variation instrument from Alicona was also applied as one of the characterization methods to investigate the additive manufacturing process such as selective laser melting and electron beam melting (Triantaphyllou et al. 2015).

Embedded Metrology in Ultra-Precision Manufacturing

Contact Profilometer Based On-Machine Measurement System

Several contact profilometers have been employed for embedded on-machine surface measurement (OMSM) because of its technological maturity and the ease of integration. To ensure the similar or higher performance of measurement system used in OMSM, several modifications and specific setups are usually required. In this section, the applications of embedded on-machine measuring system (OMMS) in ultra-precision manufacturing based on contact profilometer are introduced with emphasis on the principle and accuracy achieved.

Suzuki et al. (Suzuki et al. 2008) applied a new contact type of on-machine measuring system to measure aspherical optical parts with a steep surface angle. In this measuring system, a ceramic air slider was adopted for the measurement probe, and a high-accuracy glass scale was employed to reduce the thermal drift of the displacement gauge. To reduce the change in the probe friction force, the air slider or the measuring probe was tilted to 45° against the aspherical workpiece axis. This configuration will keep the contact angle between the probe axis and the contact surface constant (Fig. 14b) when the probe was scanned over the workpiece surface.

Chen et al. employed a compensation approach to grind the tungsten carbide aspheric molds. In this approach, a contact probe based on-machine measurement was employed to eliminate the profile error (Fig. 15). A sapphire microprobe of 0.5 mm in radius was used to measure the ground profile on-machine. A new method was proposed to reconstruct the actual ground profile based on the measured profile data. The overall profile error after grinding was obtained by subtracting the target profile from the actual ground profile along normal direction and was then used to generate a new tool path for compensation grinding. The experimental results showed that after three compensation grinding cycles, the aspheric surface had a profile accuracy of 177 nm (in PV) with a roughness of 1.7 nm (in Ra) (Chen et al. 2010).

Contact probing systems are nowadays provided as accessories in some commercial ultra-precision machining tools. For example, Moore Nanotech provides an on-machine measuring probing system, which is composed of a linear variable differential transformer (LVDT) sensor and air bearings. It has been reported that this on-machine measurement function can improve the diamond machining accuracy for freeform optical surfaces. The on-machine contact measurement was utilized to align the remounting workpiece into the modified machining coordinate, while surface

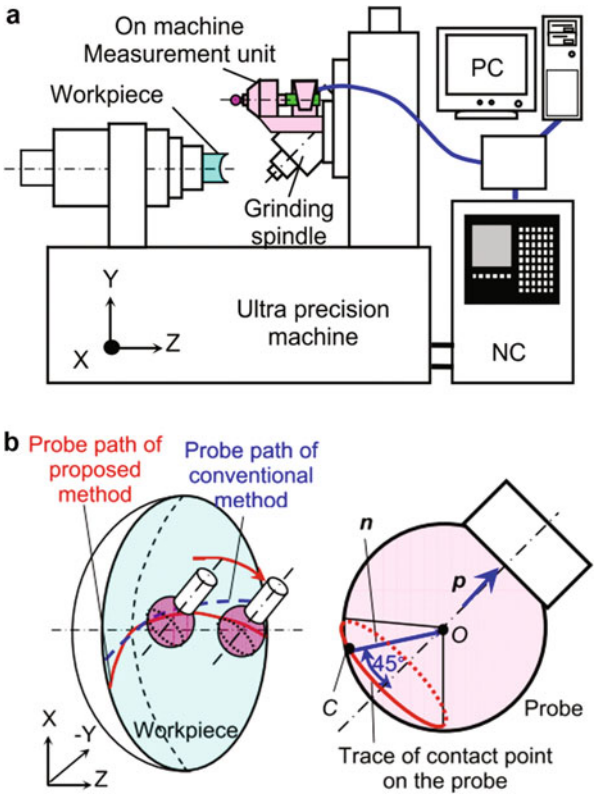

Fig. 14 (**a**) Schematic of on-machine contact probing for optics grinding process; (**b**) tilted angle probe configuration (Suzuki et al. 2008)

error derived from offline measurement was used for compensation machining (Zhang et al. 2015).

Nevertheless, the ruby ball used in the conventional contact probing system often has probe radius of several millimeters, which inherently limits lateral resolution of the measurement. Several attempts have been conducted to use scanning probe microscopes (SPMs) with tiny tips to realize on-machine measurement of ultra-precision machined micro-/nanostructured surface. As shown in Fig. 16, Gao et al. have designed an AFM head to measure diamond turned sinusoidal microstructures. A robust linear encoder was adopted in the AFM head for the measurement of profile height in the presence of electromagnetic noise. The OMMS was able to measure microstructured surfaces with 0.5 nm resolution in a spiral path (Gao et al. 2007).

Zhu et al. developed a scanning tunneling microscope (STM) probing system and applied the system in the ultra-precision fly-cutting process (Fig. 17) (Zhu et al. 2016). The probe tip follows the surface variations of the machined microstructure at a constant distance through the control of the difference between detected tunneling current and the default value. A piezoelectric translator (PZT) was used to drive the probe during the measuring process. A capacitance sensor was used to record the displacement of the driven piezoelectric translator (PZT) which reflects the profile

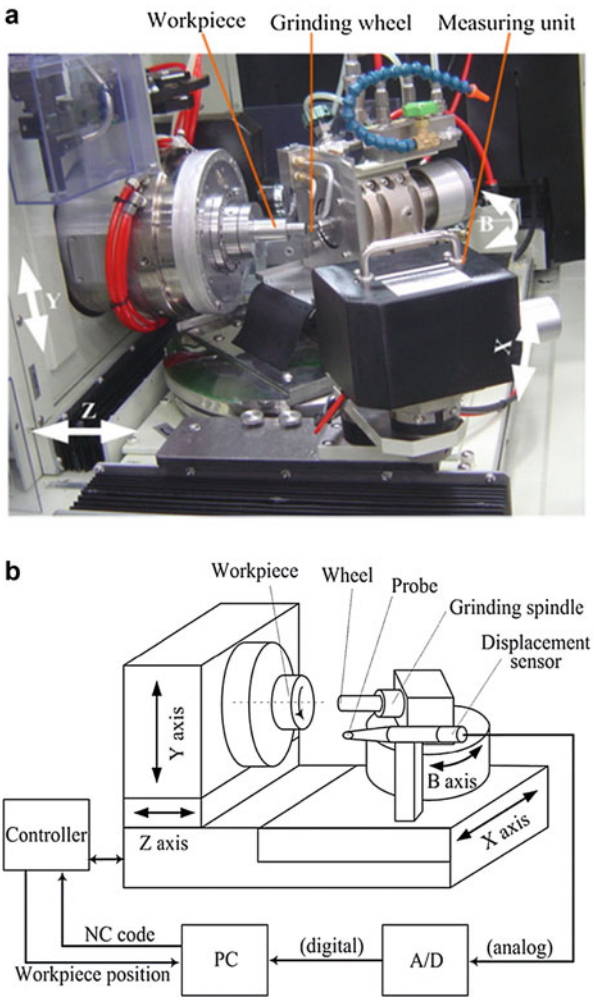

Fig. 15 (**a**) Mold grinding machine with integrated probing unit; (**b**) schematic of compensation grinding strategy (Chen et al. 2010)

measured surface. The geometrical size of the probe plays a key role on the measurement accuracy. Chemical etching process is well suited for the fabrication of tungsten probe with a stabilized stylus contour and ultra-sharp apex radius in high production reproducibility. Currently, tungsten probes with a controllable aspect ratio from 20:1 to 450:1, apex radius less than 20 nm and cone angle smaller than 3° can be achieved by the etching process (Ju et al. 2011).

Zhu et al. has employed this STM-based probing system to assist the precision fabrication of rectangular pyramid arrays. The STM-based probing system was mounted on the main spindle of an ultra-precision turning machine. The form accuracy of high-slope microstructures was significantly improved by cutting depth compensation of fly cutting in 120° direction through feedback of on-machine measured results (Zhu et al. 2016). The same probing system was also employed to

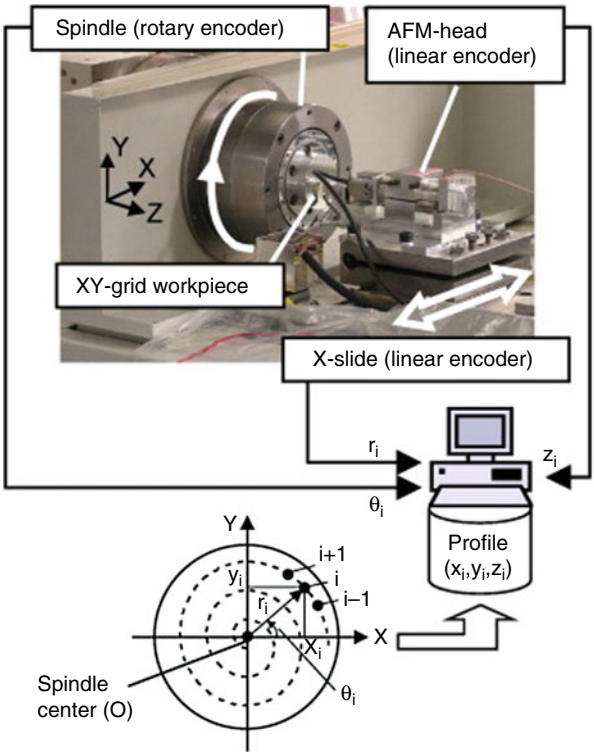

Fig. 16 Robust AFM based on-machine measuring system (Gao et al. 2007)

measure 3D curved compound eye surfaces machined by STS technique (Zhu et al. 2015). A tip-tracking strategy was proposed to extend the measuring ranges with more flexibility. Distortion caused by central alignment errors was analyzed based on the characteristic points.

Moreover, a piezoelectric force sensor was innovatively integrated into a FTS device to constitute a force-displacement servo unit termed as FS-FTS (Chen et al. 2015). The FS-FTS acted as a cutting tool with force sensor during the machining, and it was employed as a contact probe after the machining. The characteristic enabled the unit to perform structured surface machining, profile measurement, defect identification, and cutting tool reposition. With the assistance of FS-FTS, Chen et al. proposed an in-process identification and repairment of diamond turned micro-lens arrays on a roll mold (Figs. 18 and 19). The thrust force was monitored during the machining process as an indicator to reflect cutting status and singular forces map with respect to the cutting tool position. After the defects were identified by FS-FTS scanning, the repair process was subsequently carried out (Fig. 19).

Additionally, a concept of relay fabrication was proposed based on the capability of FS-FTS on repositioning a new tool to the former cutting spot after the replacement of the worn tool (Chen et al. 2014). A bidirectional scanning strategy was

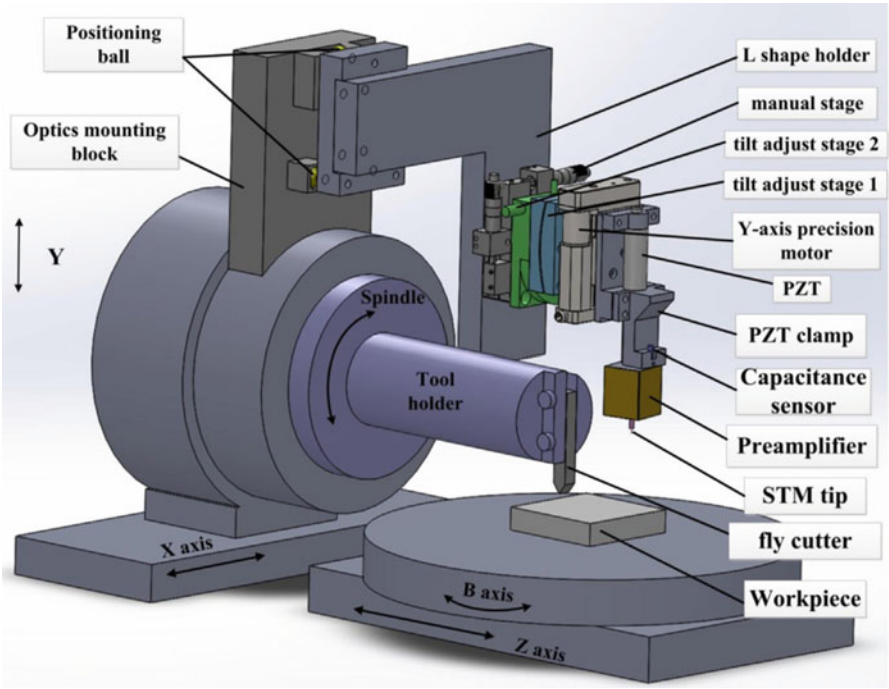

Fig. 17 STM-based on-machine measuring system with ultra-sharp tips (Zhu et al. 2016)

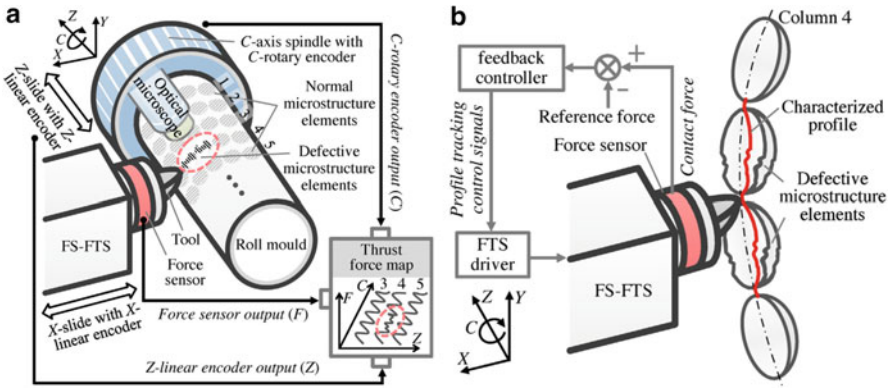

Fig. 18 Steps of the in-process measurement method for repair of destructive microstructures on a roll mold. (**a**) Step 1 for real-time detection of the micro-defect positions. (**b**) Step 2 for characterization of the micro-defect surface profiles (Chen et al. 2015)

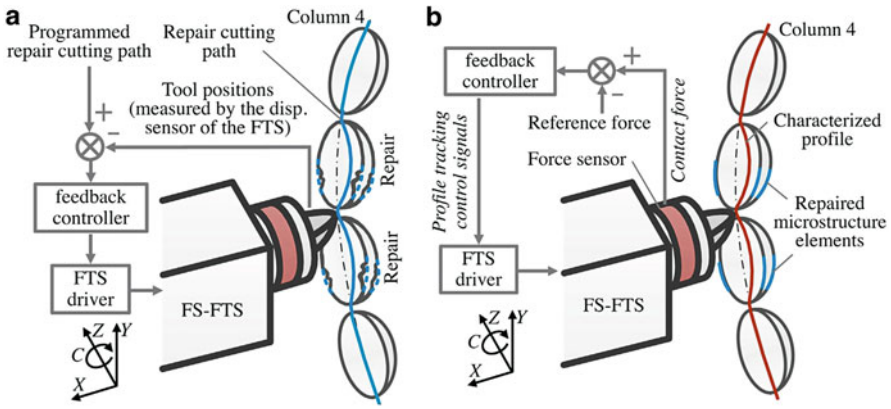

Fig. 19 The repair and evaluation steps. (**a**) Step 3 for repairing the defective microstructure elements. (**b**) Step 4 for evaluating the repair results (Chen et al. 2015)

employed to increase the positioning accuracy due to the delay of the feedback control loop. Stitching fabrication of a microgroove line array and filling fabrication of a micro-lens lattice pattern demonstrated the feasibility of the tool position measurement method.

Table 1 summarizes state-of-the-art researches on the contact profilometer-based OMMS and corresponding applications in ultra-precision machining processes.

Non-contact Optical On-Machine Measurement System

Non-contact optical measurement techniques are nondestructive and usually have high measurement rate, which makes them suitable for on-machine and in-process applications. Particularly for ultra-precision machining processes, on-machine interferometry has received a lot of attention from researchers for its nanometric precision and high-speed acquisition.

Shore et al. employed a Twyman-Green phase-shifting interferometer to conduct on-machine measurement of form accuracy of machined individual multi-mirror arrays used in the James Webb Space Telescope. The interferometer is mounted on a 3-axis machine with submicron positioning ability as shown in Fig. 20a. The measurement of form and radius was carried out using the cat's eye position (Fig. 20b), where the interferometer was focused on the surface and gave a quick measurement of mirror radius by measuring the displacement required to move from cat's eye to confocal positions. Achievable form accuracy of the individual mirror is reported below 20 nm RMS (Shore et al. 2006).

King et al. proposed an integrated solution for polishing and on-machine measurement of large-scale optics up to 1 m in diameter (King 2010). As shown in Fig. 21, it consisted of a Zeeko IRP 1000 polishing machine and a 5-axis motorized stage housing 4D dynamic interferometer. The dynamic interferometry

Table 1 Contact profilometer-based OMMS and applications

No	Author	Principle	Instrument	Performance	Applications	Remarks
1	Suzuki et al. (2008)	Contact ball	A high-accuracy glass scale with a ceramic air slider	Contact force <0.3 mN; 0.14 nm scale resolution	Steep optical mold grinding	The tilted angle configuration reduced the variation in the probe friction force
2	Chen et al. (2010)	Contact ball	N.A.	Similar to offline profilometer in terms of form deviation	Aspheric mold grinding	Normal-compensation tool path was generated according to the reconstructed profile from OMSM
3	Zhang et al. (2015)	Contact ball	A LVDT sensor with an air bearing slide	20 nm resolution; measurement standard deviation 10 nm	Freeform diamond turning	A novel compensation method is proposed using a combination of on-machine and off-machine measurement
4	Gao et al. (2007)	SPM	AFM head with a robust linear encoder	0.5 nm resolution	Microstructured surface FTS machining	The use of linear encoder increases the robustness of AFM head, and alignment issue was investigated for accurate measurement
5	Zhu et al. (2015)	SPM	Position-servo STM with ultra-sharp stylus	5 nm vertical resolution	Fly-cutting and STS machining	A tip-tracking strategy was proposed to extend the measuring ranges. It is capable of scanning steep microstructured surfaces (V-grooves and compound eyes)
6	Chen et al. (2015)	Piezo-force sensing	FS-FTS	Sub-mN contact force; 30 nm resolution	Microstructured surface machining	Defect repair and relay fabrication of micro-lens arrays were achieved with FS-FTS

is a variation of traditional PSI. Four phase-shifted interferograms are simultaneously generated through the use of a quarter wave plate and a pixelated birefringent mask in front of a single detector. The single-shot nature of the dynamic interferometry allows fast surface measurement without sensitivity to vibration or airflow through interferometer paths. The large optics were measured in situ without the need of risky transportation to offline metrology platforms, and corrective

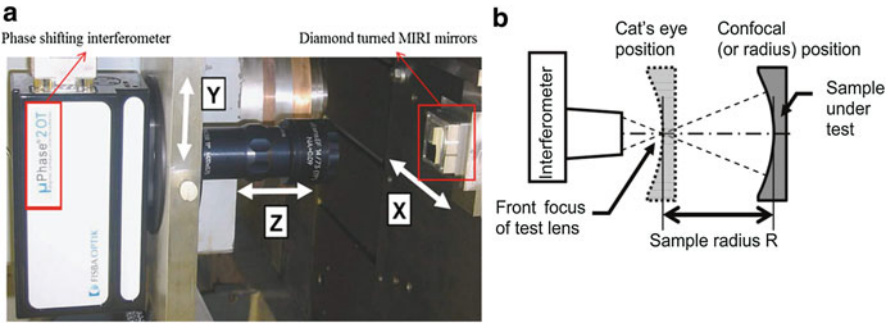

Fig. 20 PSI on-machine measurement of diamond turned mirror arrays (**a**) measurement system configuration; (**b**) measurement of form and radius (Shore et al. 2006)

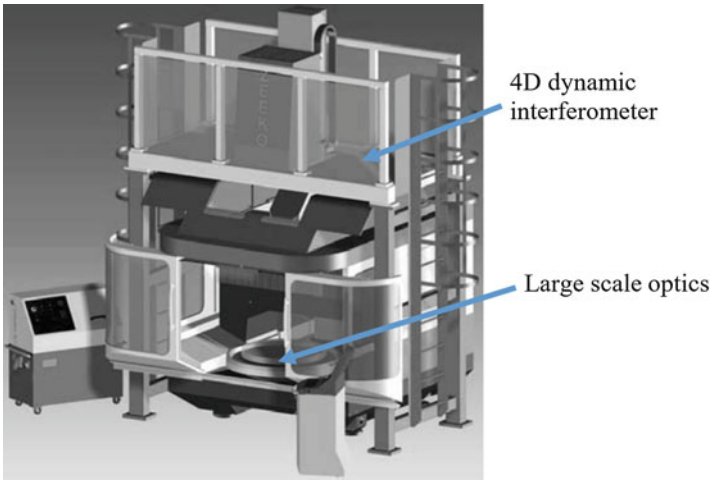

Fig. 21 Zeeko IRP 1000 machine, 5-axis motorized stage, and 6″ Fizeau interferometer (King 2010)

polishing was subsequently carried out. The measurement system was also equipped with different CGH elements to measure aspheric and freeform optics. Besides, a white-light interferometer for texture measurement and a laser tracker for radius measurement were integrated as optional accessories of the polishing machine.

In terms of microscale topography measurement, a wavelength scanning interferometer (WSI) based on wavelength division multiplexing was developed recently for the measurement of diamond machined-structured surfaces on a large drum turning machine. Jiang et al. created a new kind of full-field measurement to replace electromechanical scanning with white-light interferometry and to form a compact system that is fast, robust, and suitable for in situ surface measurement (Fig. 22) (Jiang 2011). An experimental system was developed for the manufacture of

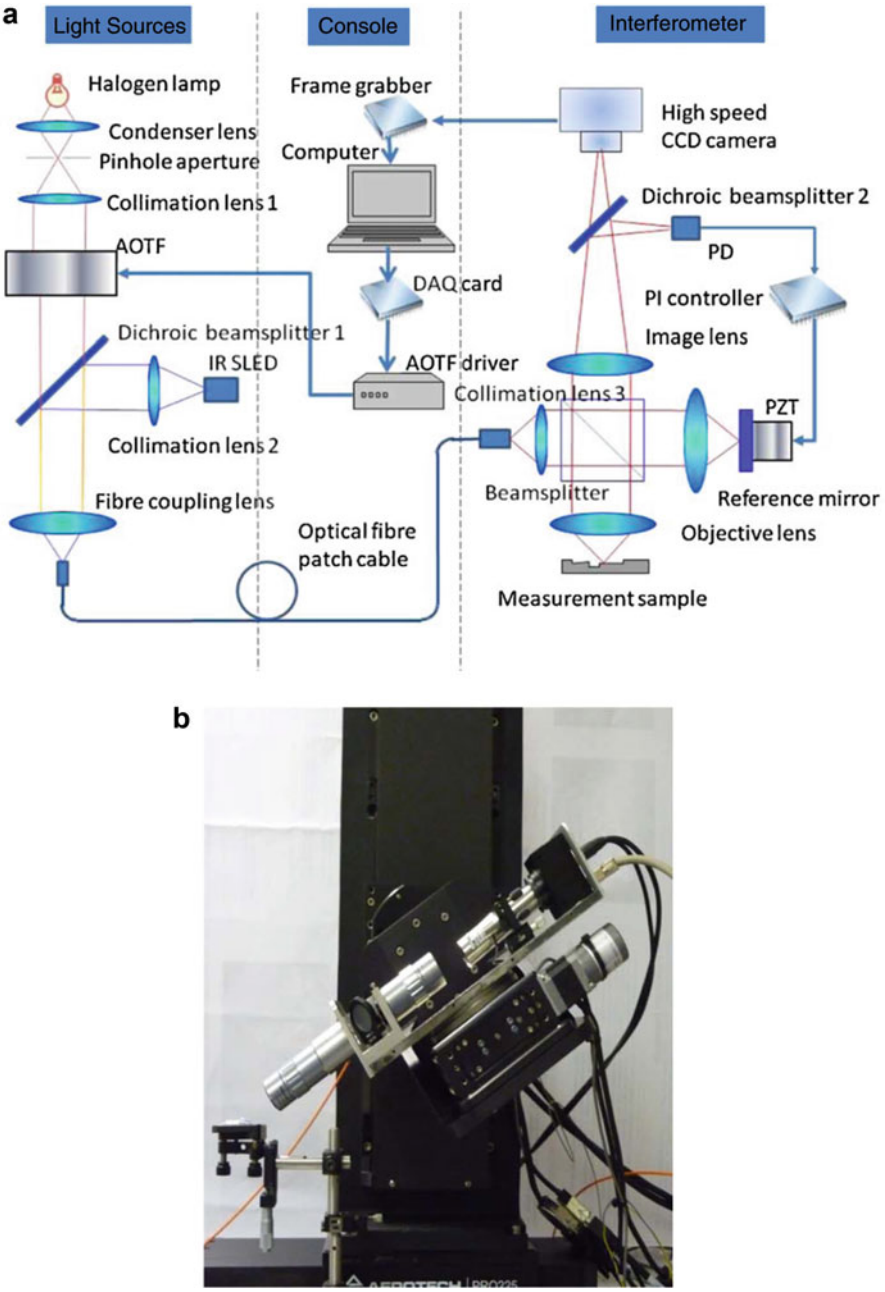

Fig. 22 The wavelength scanning interferometry system. (**a**) A schematic diagram; (**b**) a prototype system (Jiang 2011)

diamond turned/fly cut microstructured surfaces on a large drum diamond-turning machine. Nanometer precision surface measurement results were achieved for microscale structured samples. The instrumentation will have numerous further applications in precision machining, micro-machining, and the general manufacture of surface reliant products such as embossed steel sheet (Fig. 23) (Jiang 2011).

Due to the sensitivity to environmental disturbances and complex system configuration of interferometric instruments, non-interferometric OMMS have also been investigated in recent years. Röttinger et al. presented a setup of miniaturized deflectometry on a diamond-turning machine and measured high-precision specular surfaces without re-chucking operations (shown in Fig. 24). The development of global calibration and parasitic reflections reduction will boost the usage of deflectometry. The advantages of on-machine deflectometry include the

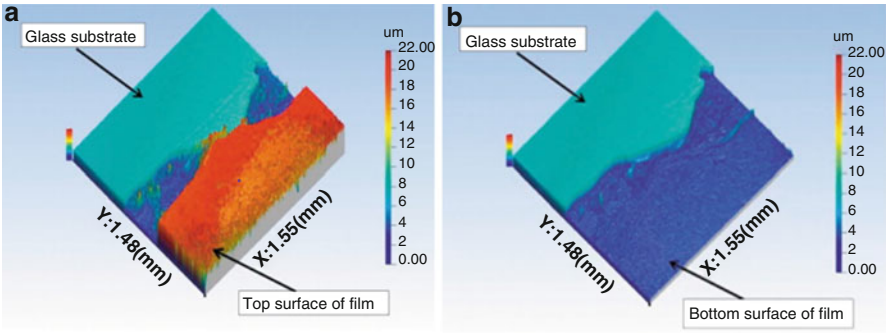

Fig. 23 Thin film measurement. (**a**) The top surface of the film forms a step upward on the glass substrate. (**b**) The bottom of the film surface forms a step downward on the glass substrate (Jiang 2011)

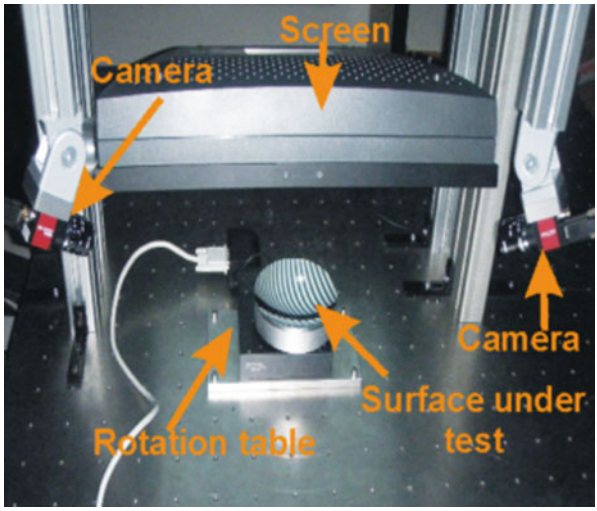

Fig. 24 Setup of PMD on a multi-axis ultra-precision machine tool (Röttinger et al. 2011)

environmental robustness and the capability of measuring arbitrary freeform surfaces within micron accuracy without additional null testing. By rotating the object with the machine's rotational axis, the field of measurement was easily increased to cover the large aperture and steep mirrors (Röttinger et al. 2011).

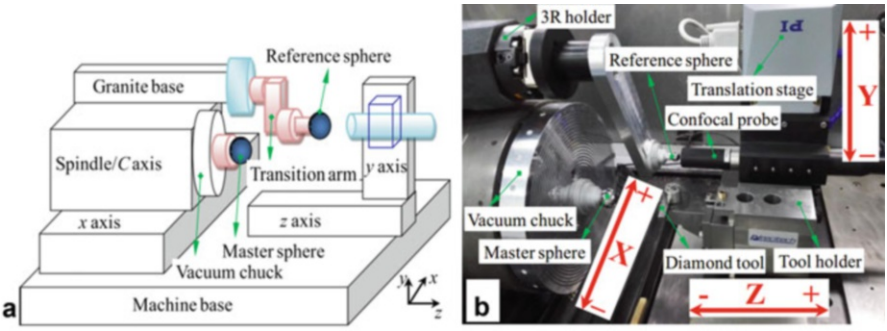

Fig. 25 Chromatic confocal based on-machine measurement for ultra-precision turning processes (**a**) schematic diagram of the OMM system; (**b**) image of the OMM system (Zou et al. 2017)

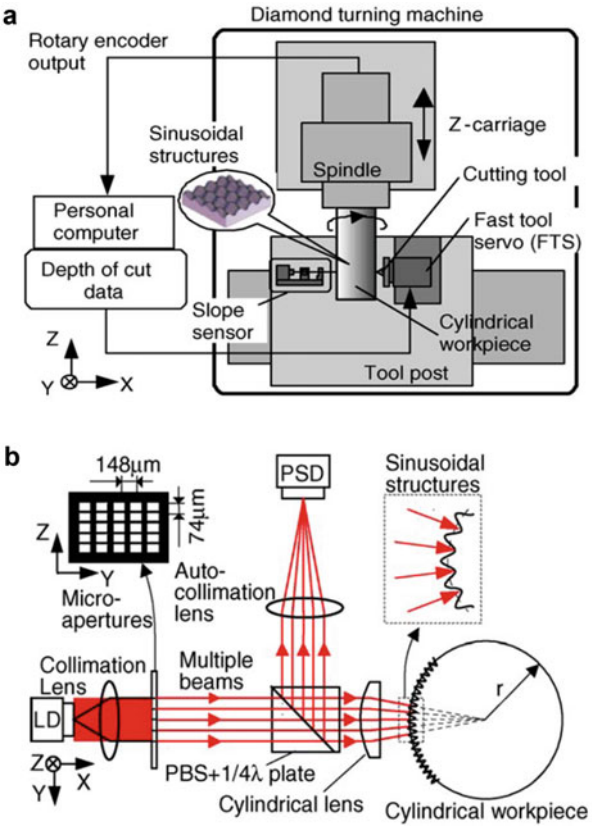

Fig. 26 Optical slope sensor for on-machine measurement of FTS machined sinusoidal structures. (**a**) Schematic of the fabrication and measurement system for the cylindrical master grid; (**b**) schematic of the slope sensor (Gao et al. 2006)

Confocal microscopy is an effective tool for surface measurement in the micro-scale. Compared with other optical methods, the maximum detectable slope can be as large as 75 degree with enough scattered light enhanced by software and hardware. All these characteristics make it applicable to measure complex and high-slope structured surfaces in the manufacturing environment. Zou et al. integrated a chromatic confocal sensor on a self-developed ultra-precision turning lathe for 3D measurement of diamond turned aspheric surfaces. As shown in Fig. 25, the sensor was mounted perpendicular to the vacuum chuck plane and aligned with a reference sphere. The combined standard uncertainty of the measurement system was estimated to be 83.3 nm, which mainly resulted from the flatness uncertainty of the scanning hydrostatic slide (Zou et al. 2017).

Moreover, in order to characterize the functional-related geometric properties, several special OMMSs have been developed for corresponding applications. For instance, Gao et al. developed a two-dimensional optical slope sensor with a multi-spot light beam for on-machine measurement of local slopes of the FTS turned sinusoidal surface (Gao et al. 2006). As illustrated in Fig. 26, the sensor unit was mounted opposite to the cutting tool on the feeding slide. A cylindrical lens was integrated in the sensor so that slopes of the sinusoidal structures could be detected without the influence of curvature of the cylindrical workpiece. After machining, the surface was measured on the machine without removing the workpiece from the

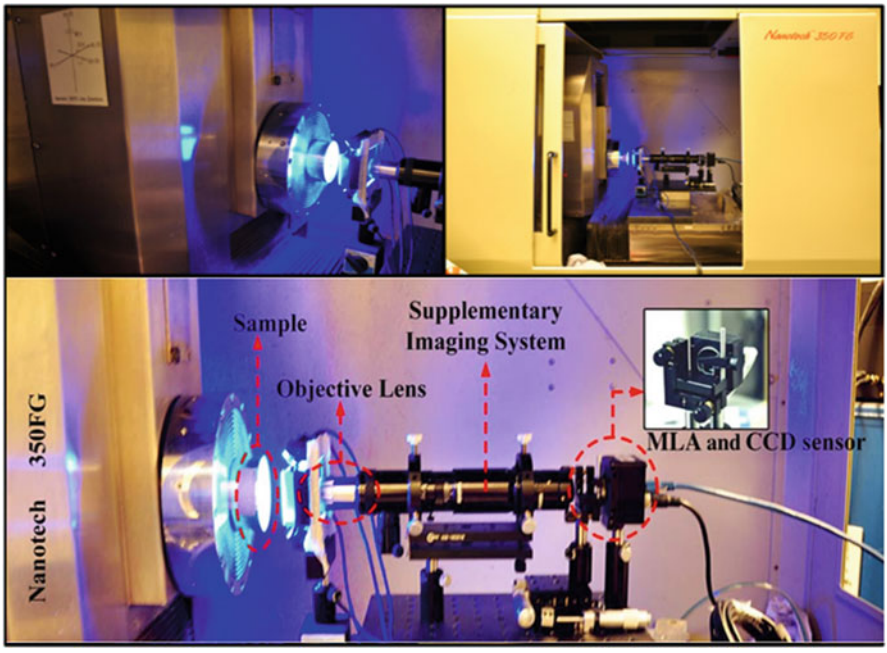

Fig. 27 Disparity pattern-based autostereoscopic system for in situ inspection of diamond turned microstructures (Li et al. 2015)

Table 2 Non-contact optical type of OMSM and applications

No	Author/ year	Principle	Instrument	Performance	Applications	Remarks
1	Shore et al. (2006)	Interferometry	Trioptics μphase PSI	1.9 nm repeatability	MIRI mirror diamond turning	Relative locations of confocal positions are evaluated with the aid of OMSM
2	King 2010	Interferometry	4D dynamics interferometry	30 μs acquisition time; 0.002λ wavelength precision	Large-scale optics polishing	Single shot and vibration insensitive measurement
3	Jiang (2011)	Interferometry	Wavelength scanning interferometer	15 nm vertical resolution; anti-vibration <300 Hz	Microstructures diamond turning on drum rolls	Real-time vibration compensation with a monitoring interferometer
4	Röttinger et al. (2011)	Deflectometry	Mini-PMD	Sub-micron accuracy	Freeform ultra-precision machining	Environmentally insensitive and able to measure arbitrary freeform without null testing
5	Zou et al. (2017)	Chromatic confocal	STIL confocal point sensor	Relative measurement error 0.022%; combined standard uncertainty 83.3 nm	Diamond turning	Measurement uncertainty mainly resulted from the flatness of the scanning slide
6	Gao et al. (2006)	Autocollimation	Optical slope sensor with a cylinder lens	N.A.	FTS machining of cylindrical sinusoidal structures	The surface slope errors caused by the tool nose geometry were corrected with the integrated slope sensor
7	Li et al. (2015)	Auto-stereoscopy	Disparity pattern-based autostereoscopic 3D system	Sub-micrometer measuring repeatability	Pyramid structured surfaces machining	Compact, fast capturing, and environmental robust

spindle. Post-process compensation was carried out to further improve the machined surface quality. The results indicated that the error component caused by the round nose geometry of the tool was reduced from 0.632 mrad (10.1 nm in height amplitude) to 0.112 mrad (1.8 nm in height amplitude) through the post-process compensation, indicating the effectiveness of the proposed on-machine measurement system.

To overcome the rigorous environmental requirements for on-machine optical measurement system, Li et al. proposed a pattern-based autostereoscopic (DPA) 3D metrology system to capture raw 3D information of the measured surface in a single snapshot by a CCD camera (as shown in Fig. 27). A micro-lens array was used to capture raw 3D information, and the 3D digital model of the target surface was used to directly extract disparity information (Li et al. 2015). The direct extraction of disparity information (DEDI) method is highly efficient when performing the direct 3D mapping of the target surface because the tomography-like operation excluded the defocused information of every depth plane. Precise measurement results have shown that the proposed DPA 3D metrology system is capable of measuring 3D microstructured surfaces with sub-micrometer measuring repeatability for high precision and in situ measurement of microstructured surfaces.

The state-of-the-art research work on the non-contact optical OMMS and corresponding applications in ultra-precision machining processes are summarized in Table 2 with highlights on the performance and application remarks.

Conclusion

The ability to effectively monitor the machining process and measure products rapidly in manufacturing environment has become a fundamental limiting factor in the deterministic manufacturing of micro-/nanostructured surfaces with specific functions. Most of the measuring (dimensional and surface topography) systems used in micro-/nanoscale manufacturing is relatively slow, expensive, and in an offline manner.

This chapter has briefly introduced the typical embedded measurement systems used in manufacturing process. They have different performances with respect to range, resolution, measurement rate, and ability to measure discontinuous surfaces.

Contact methods have been commonly used for on-machine metrology for its technological maturity. Compared with optical methods, contact methods are applicable to measure high-slope surface geometries. However, the contact methods normally operate at a low-scanning speed, and the contact nature makes them unsuitable to measure the soft and delicate surfaces. Some SPMs are developed for some ultra-precision machining applications. However, the tip wear issue is still a big challenge for large area and long-time measurement. Non-contact methods which have fast measurement rate, high data density, and in nature preventing damage to delicate measurands or to the measurement instrument itself have been widely explored in this case such as machine vision, phase-shifting interferometry (PSI), white-light interferometry (WLI), wavelength scanning interferometry (WSI), dispersive interferometry, etc. With the development of calibration and processing

algorithms, non-interferometric methods such as deflectometry and confocal chromatic microscopy (CCM) are receiving more attention in specific measurement conditions. However, for ultra-precision machining applications, robust interferometry is still the best choice because of its high measurement resolution (nanometer and even sub-nanometer).

Acknowledgment The authors would like to acknowledge the supports from the UK's Engineering and Physical Sciences Research Council (EPSRC) under Grant No. EP/P006930/1 and the European Union's Horizon 2020 research and innovation program under grant agreement No. 767589.

References

Ayub MA, Mohamed AB, Esa AH (2014) In-line inspection of roundness using machine vision. Procedia Technol 15:807–816

Chan FW (2008) Reflective fringe pattern technique for subsurface crack detection. NDT E Int 41 (8):602–610

Chen F, Yin S, Huang H, Ohmori H, Wang Y, Fan Y, Zhu Y (2010) Profile error compensation in ultra-precision grinding of aspheric surfaces with on-machine measurement. Int J Mach Tools Manuf 50(5):480–486

Chen Y-L, Gao W, Ju B-F, Shimizu Y, Ito S (2014) A measurement method of cutting tool position for relay fabrication of microstructured surface. Meas Sci Technol 25(6):064018

Chen Y-L, Wang S, Shimizu Y, Ito S, Gao W, Ju B-F (2015) An in-process measurement method for repair of defective microstructures by using a fast tool servo with a force sensor. Precis Eng 39:134–142

Danzl R, Helmli F, Scherer S (2011) Focus variation–a robust technology for high resolution optical 3D surface metrology. Strojniški Vestn-J Mech Eng 57(3):245–256

Elrawemi M, Blunt L, Muhamedsalih H, Gao F, Fleming L (2015) Implementation of in process surface metrology for R2R flexible PV barrier films. Int J Autom Technol 9(3):312–321

Faber C, Olesch E, Krobot R, Häusler G (2012) Deflectometry challenges interferometry: the competition gets tougher! In: Interferometry XVI: techniques and analysis. International Society for Optics and Photonics, p 84930R

Gao W, Tano M, Sato S, Kiyono S (2006) On-machine measurement of a cylindrical surface with sinusoidal micro-structures by an optical slope sensor. Precis Eng 30(3):274–279

Gao W, Aoki J, Ju B-F, Kiyono S (2007) Surface profile measurement of a sinusoidal grid using an atomic force microscope on a diamond turning machine. Precis Eng 31(3):304–309

Gao F, Muhamedsalih H, Jiang X (2012) Surface and thickness measurement of a transparent film using wavelength scanning interferometry. Opt Express 20(19):21450–21456

Ghim Y-S, Kim S-W (2009) Spectrally resolved white-light interferometry for 3D inspection of a thin-film layer structure. Appl Opt 48(4):799–803

Guo D, Xie G, Luo J (2013) Mechanical properties of nanoparticles: basics and applications. J Phys D Appl Phys 47(1):013001

Harding K (2013) Handbook of optical dimensional metrology. CRC Press, Boca Raton

ISO standard 25178-2 (2012) Geometrical product specifications (GPS) surface texture: areal part 2

Jiang X (2011) In situ real-time measurement for micro-structured surfaces. CIRP Ann-Manuf Technol 60(1):563–566

Jiang XJ, Whitehouse DJ (2012) Technological shifts in surface metrology. CIRP Ann-Manuf Technol 61(2):815–836

Ju B-F, Chen Y-L, Ge Y (2011) The art of electrochemical etching for preparing tungsten probes with controllable tip profile and characteristic parameters. Rev Sci Instrum 82(1):013707

Kapłonek W, Nadolny K, Królczyk GM (2016) The use of focus-variation microscopy for the assessment of active surfaces of a new generation of coated abrasive tools. Meas Sci Rev 16(2):42–53

King CW (2010) Integrated on-machine metrology systems. In: International symposium on ultraprecision engineering and nanotechnology (ISUPEN), Japan Society for precision engineering semestrial meeting 2010 JSPE autumn conference

Leach R (2011) Optical measurement of surface topography, vol 14. Springer, Berlin

Leach R, Sherlock B (2013) Applications of super-resolution imaging in the field of surface topography measurement. Surf Topogr: Metrol Prop 2(2):023001

Li D, Cheung CF, Ren M, Whitehouse D, Zhao X (2015) Disparity pattern-based autostereoscopic 3D metrology system for in situ measurement of microstructured surfaces. Opt Lett 40(22):5271–5274

Lyda W, Gronle M, Fleischle D, Mauch F, Osten W (2012) Advantages of chromatic-confocal spectral interferometry in comparison to chromatic confocal microscopy. Meas Sci Technol 23(5):054009

Millerd J, Brock N, Hayes J, North-Morris M, Kimbrough B, Wyant J (2006) Pixelated phase-mask dynamic interferometers. In: Osten W. (eds) Fringe 2005. Springer, Berlin, Heidelberg

Muhamedsalih H, Jiang X, Gao F (2013) Accelerated surface measurement using wavelength scanning interferometer with compensation of environmental noise. Procedia CIRP 10:70–76

Muhamedsalih H, Blunt L, Martin H, Hamersma I, Elrawemi M, Feng G (2015) An integrated optomechanical measurement system for in-process defect measurement on a roll-to-roll process. In: Laser Metrology and Machine Performance XI, LAMDAMAP 2015. EUSPEN, Huddersfield, UK, pp. 99–107. ISBN 978-0-9566790-5-5

Röttinger C, Faber C, Olesch E, Häusler G, Kurz M Uhlmann E (2011) Deflectometry for ultraprecision machining–measuring without rechucking. In: Proceedings of DGaO, p 28

Ruprecht AK, Koerner K, Wiesendanger TF, Tiziani HJ, Osten W (2004) Chromatic confocal detection for high-speed microtopography measurements. Proc. SPIE 5302, Three-dimensional image capture and applications VI. San Jose, California, United States

Sárosi Z, Knapp W, Kunz A, Wegener K (2010) Detection of surface defects on sheet metal parts by using one-shot deflectometry in the infrared range. In: Infrared camera applications conference 2010. ETH Zurich, IWF, pp 243–254

Shore P, Morantz P, Lee D, McKeown P (2006) Manufacturing and measurement of the MIRI spectrometer optics for the James Webb space telescope. CIRP Ann-Manuf Technol 55(1):543–546

Su P, Wang Y, Burge JH, Kaznatcheev K, Idir M (2012) Non-null full field X-ray mirror metrology using SCOTS: a reflection deflectometry approach. Opt Express 20(11):12393–12406

Suzuki H, Onishi T, Moriwaki T, Fukuta M, Sugawara J (2008) Development of a 45 tilted on-machine measuring system for small optical parts. CIRP Ann-Manuf Technol 57(1):411–414

Takeda M, Yamamoto H (1994) "Fourier-transform speckle profilometry: three-dimensional shape measurements of diffuse objects with large height steps and/or spatially isolated surfaces," Appl. Opt. 33, 7829–7837.

Tang D (2016) Investigation of line-scan dispersive interferometry for in-line surface metrology. Doctoral thesis, University of Huddersfield, UK

Triantaphyllou A, Giusca CL, Macaulay GD, Roerig F, Hoebel M, Leach RK, Tomita B, Milne KA (2015) Surface texture measurement for additive manufacturing. Surf Topogr: Metrol Prop 3(2):024002

Vacharanukul K, Mekid S (2005) In-process dimensional inspection sensors. Measurement 38(3):204–218

Walker DD, Beaucamp ATH, Doubrovski V, Dunn C, Evans R, Freeman R, Kelchner J, McCavana G, Morton R, Riley D, Simms J, Yu G, Wei X (2006) Automated optical fabrication: first results from the new precessions 1.2 m CNC polishing machine. Proc. SPIE 6273, Optomechanical Technologies for Astronomy, 627309. Orlando, Florida, United States

Whitehouse DJ (2004) Surfaces and their measurement. Elsevier, Oxford

Williamson J (2016) Dispersed reference interferometry for on-machine metrology. Doctoral thesis, University of Huddersfield, UK.

Williamson J, Martin H, Jiang X (2016) High resolution position measurement from dispersed reference interferometry using template matching. Opt Express 24(9):10103–10114

Zhang X, Zeng Z, Liu X, Fang F (2015) Compensation strategy for machining optical freeform surfaces by the combined on-and off-machine measurement. Opt Express 23(19):24800–24810

Zhang Z, Wang Y, Huang S, Liu Y, Chang C, Gao F, Jiang X (2017) Three-dimensional shape measurements of specular objects using phase-measuring deflectometry. Sensors 17(12):2835

Zhu W-L, Yang S, Ju B-F, Jiang J, Sun A (2015) On-machine measurement of a slow slide servo diamond-machined 3D microstructure with a curved substrate. Meas Sci Technol 26(7):075003

Zhu W-L, Yang S, Ju B-F, Jiang J, Sun A (2016) Scanning tunneling microscopy-based on-machine measurement for diamond fly cutting of micro-structured surfaces. Precis Eng 43:308–314

Zou X, Zhao X, Li G, Li Z, Sun T (2017) Non-contact on-machine measurement using a chromatic confocal probe for an ultra-precision turning machine. Int J Adv Manuf Technol 90(5–8):2163–2172